Reconstructing the History of the Antarctic Ice Sheet Using Internal Reflecting Horizons from Radio-Echo Sounding

Julien Bodart



Thesis submitted for the degree of Doctor of Philosophy

The University of Edinburgh

2023

Declaration

I declare that this thesis has been composed solely by myself and that it has not been submitted, in whole or in part, in any previous application for a degree. Except where stated otherwise by reference or acknowledgment, the work presented is entirely my own.

Julien Bodart
May 2023

"Man is the most insane species. He worships an invisible God and destroys a visible Nature. Unaware that this Nature he's destroying is this God he's worshiping"

Hubert Reeves (1932 -)
Canadian astrophysicist

Abstract

Understanding the contribution of the Antarctic Ice Sheet (AIS) to past and future sea-level rise has emerged as a scientific priority over the last four decades. Whilst our knowledge of ice-dynamical changes occurring as a result of current anthropogenic forcing has improved considerably since the start of the satellite era, significantly less is known about the evolution of the AIS during the pre-industrial Holocene (the last ∼11.7 thousand years; ka). Quantifying these changes is crucial, however, as this time period corresponds to a time when the ice sheet was retreating from its maximal extent at the Last Glacial Maximum (LGM; ∼20 ka) and environmental conditions were similar to today. Therefore, improving our understanding of this period may provide a long-term context to the decadal changes observed in recent times and how these may evolve in the future. Whilst point-based geochronological measurements of ice and sediment cores, or surface exposure dating, can be used to assess past ice-sheet changes over the AIS, it remains unclear how representative they are of a wider region. A complementary and spatially extensive resource across the ice sheet are Internal Reflecting Horizons (IRHs) as imaged by Radio-Echo Sounding (RES) techniques, which provide a cumulative record of accumulation, basal melt and ice dynamics that, if dated precisely at ice cores, can be used to inform numerical ice-sheet models projecting past and future changes on large spatial scales. The aim of this thesis is therefore to develop and extend age-depth models from IRHs across the AIS to assess the past stability of the ice sheet.

In this thesis, an age-depth model of Pine Island Glacier spanning the LGM and Holocene periods is derived from spatially extensive IRHs. The connection between RES profiles and the WAIS Divide ice core enables the direct dating of the IRHs, and reveals that they match large peaks in sulphate concentrations which are unparalleled in the 68,000 year-old record, thus suggesting that the cause of these IRHs is from past explosive volcanic eruptions. By connecting this IRH stratigraphy with a previously developed age-depth model across the Institute and Möller Ice Streams (IMIS), I show that a precisely dated age-depth model now exists over 20% of the West Antarctic Ice Sheet (WAIS). One of these IRHs, precisely

dated at ∼4.7 ka, is then used as input into a one-dimensional ice-flow model to estimate past accumulation rates during the mid-Holocene over the catchments encompassing Pine Island Glacier, Thwaites Glacier, and IMIS, together representing 30% of the WAIS. The inferred mid-Holocene accumulation estimates are then compared with modern rates derived from climate models and observational measurements to show that accumulation rates were 18% greater during the last five millennia compared to the present over the Amundsen-Weddell-Ross Divide. These results match previous findings from isolated ice-core measurements and spatially targeted studies over the divide, and correspond to periods of grounding-line retreat and readvance during the Holocene over the WAIS. Together, these show the potential for extracting further IRH information from other sectors of the AIS in order to build an age-depth model of the ice sheet. However, the underlying RES data necessary for this work were, until recently, relatively inaccessible to the wider scientific community, thus restricting the extraction and interpretation of age-depth models across the AIS. This motivated the release of ∼300,000 line-km of RES profiles acquired by the British Antarctic Survey between 2004 and 2020. In addition to standardising and releasing these data, this thesis shows that large sections of continuous englacial layering exist widely across both East and West Antarctica, suggesting that, together with previously developed age-depth models of both regions and nearby ice-core stratigraphies, these newly released RES datasets will be critical in our aim to build an ice-sheet wide age-depth model of Antarctica, as motivated by the AntArchitecture Initiative.

Together, the findings from this thesis reveal the spatially extensive nature of IRHs across West and East Antarctica and demonstrate how these can be used to infer past ice-sheet changes. This thesis also highlights the need to extract further age-depth models, particularly across East Antarctica, in order to provide important boundary conditions such as past accumulation rates and ice-elevation change which can be used by numerical ice-sheet models to help improve predictions of past and future ice-sheet change and ensuing sea-level rise contributions.

Résumé

L'une des priorité scientifique majeure des dernières décennies est d'estimer la contribution passée, présente, et future de la calotte de l'Antarctique sur l'évolution du niveau global de la mer. L'étude de ces changements dynamiques, durant les quatre dernières décennies, s'est améliorée considérablement grâce, en partie, à l'utilisation grandissante des satellites. Cependant, notre connaissance de l'évolution passée de l'Antarctique, particulierement durant la période pré-industrielle de l'Holocène (les dernières ∼11 700 années), reste limitée.

Des études déjà publiées sur l'évolution de l'Antarctique durant cette période se sont concentrées principalement sur l'utilisation de données statiques; comme les carottes de glace ou de sédiments, qui malheureusement, nous donnent souvent une compréhension restreinte et parfois non-représentative de l'environnement à l'échelle régionale. Les réflexions internes visibles sur les données radars (aussi connues sous le nom de Internal Reflecting Horizons, ou IRHs) sont une alternative à plus grande échelle spatiale.

Ces réflexions proviennent principalement de changements d'acidité de la neige et reflètent un effet cumulatif des changements de taux d'accumulation de neige, fonte de la glace, ou bien d'autres procédés internes, qui, si ils sont datés à l'aide de la stratigraphie d'une carotte de glace, peuvent être employés dans des modèles mathématiques de l'écoulement de la glace qui ont pour but de projeter temporellement et spatialement les changements de masse de la calotte glaciaire dans le passé et le future.

À cet effet, le but de cette thèse est d'étendre notre connaisance de ces réflexions à travers l'Antarctique pour pouvoir améliorer notre compréhension des processus qui contrôlent la stabilité du continent.

Cette thèse rapporte la découverte de quatre réflexions continues sur des données radars à travers le glacier de Pine Island. Elles ont été datées vers la fin de la période quaternaire grâce à l'analyse d'une carotte glaciaire profonde. Les

résultats montrent qu'il y a une correspondance claire entre ces réflexions et d'autres réflexions tracées par plusieurs études précédentes sur les glaciers de Institute et Möller; ce qui suggère qu'il existe un assortiment unique de réflexions glaciaires qui s'étendent sur au moins 20% de la surface de l'Antarctique de l'Ouest durant l'Holocène. Ces réflexions correspondent à des pics de concentration de sulfate sans précédent dans l'historique des 68 000 dernières années de la carotte glaciaire profonde de *WAIS Divide*; ce qui suggère que les causes de ces réflexions proviennent d'éruptions explosives volcaniques massives.

L'étude de l'une de ces réflexions quasi-omniprésente à travers l'Antarctique de l'Ouest, par l'utilisation d'un modèle mathématique d'approximation de couche locale, permet à cette thèse de montrer que le taux d'accumulation de neige était 18% plus élevé durant les ∼5 000 dernières années que les taux observés aujourd'hui à travers la ligne de partage des secteurs de Amundsen, Weddell et Ross. Ce résultat concorde avec les conclusions précédentes d'études plus restreintes, qui, elles, ont utilisé des carottes glaciaires et d'autres techniques géophysiques; et renforce l'explication de l'évolution des changements dynamiques glaciaires sur la zone de transition entre la glace terrestre et marine de l'Antarctique de l'Ouest durant l'Holocène. Ensemble, ces résultats démontrent le potentiel des IRHs pour mieux comprendre les procédés passés à travers l'Antarctique.

Malheureusement, l'accès aux données radars nécessaires pour extraire les IRHs était jusqu'à présent restreint, ce qui limitait la capacité de la communauté scientifique à extraire plus d'information sur le passé de l'Antarctique. Ceci a motivé cette thèse à publier plus de 300 000 kms de nouvelles données radars sur le continent acquis par la British Antarctic Survey depuis 2004. De larges sections de réflexions continues à travers l'Antarctique ont pu être détectées, via l'utilisation d'un algorithme automatique d'extraction de réflexions continues, sur ces nouvelles données radars. Cela révèle enfin d'importantes zones à prioriser afin de pouvoir extraire plus d'informations sur les processus dynamiques passés de l'Antarctique.

Plain Language Summary

Given that the Antarctic Ice Sheet has the potential to raise sea level by 58 metres if completely melted, it is crucial that we fully understand the factors controlling its stability. Even though satellites have revolutionised our understanding of how the ice sheet has responded to a changing climate over the last four decades, the long-term (centennial to millennial) context within which these changes fall is much less understood, impacting in turn our wider understanding of ice-sheet processes which may affect the future stability of the ice sheet and its contribution to sea-level rise.

Traditionally, millennial-scale information of Antarctic ice-sheet change has come from ice and sediment cores; however, it remains unclear how representative these records are of a wider region and thus whether they can be used to compare Antarctic-wide predictions from numerical ice-sheet models. A complementary resource to these point-based measurements are Internal Reflecting Horizons (IRHs), otherwise known as palaeosurfaces, which appear as bright reflections on ice-penetrating radar data. These reflections are commonly the result of acidic impurities from past volcanic activity which have been retained from when they fell onto the ice surface during snowfall events, and subsequently buried under additional snowfall, thus forming a vertical stratigraphic profile through the ice column. Crucially, the nature of these IRHs in the ice column reflects the cumulative history of past ice-sheet conditions, such as snow accumulation rates, melting in the ice column, or changes in ice-flow conditions. This stratigraphy can therefore be used to reconstruct past climate and ice-sheet processes, which can then be compared with current satellite observations or future ice-sheet model predictions to provide a long-term record of ice-sheet conditions. Therefore, the aim of this thesis is to develop and extend such IRH stratigraphies across Antarctica to assess the past stability of the ice sheet.

In this thesis, an IRH stratigraphy spanning the last ∼16,500 years is extracted from the Pine Island Glacier in West Antarctica and compared with other IRH stratigraphies and ice-core records in the region. The connection with a deep ice-

core stratigraphy reveals that these IRHs match large concentrations of volcanic deposit that are unparalleled in the 68,000 year-old ice-core record, thus suggesting that the origin of this particular IRH stratigraphy is from past explosive volcanic eruptions. Using one of these IRHs dated at ∼4,700 years before the present and a one-dimensional ice-flow model reveals that rates of snow accumulation were 18% higher in the last five millennia compared with current rates over the slow-flowing parts of West Antarctica. These results also match recent evidence of spatial and temporal changes over West Antarctica's ice-sheet margins during the pre-industrial Holocene period (the last ∼11,700 years), thus suggesting that the higher rates of snow accumulation observed here may have contributed to such changes. Together, these results motivate the future recovery and linking of IRH stratigraphies across Antarctica in order to build a continuous and wide-ranging stratigraphy spanning the entire ice sheet. However, whilst technically feasible, the ice-penetrating radar data that are necessary for this work were, until recently, relatively inaccessible to the wider scientific community. This motivated the standardisation and publication of ∼300,000 km of radar data acquired by the British Antarctic Survey between 2004 and 2020 in this thesis. Analyses of the presence and continuity of IRHs in these radar data show that large sections of well-preserved IRH stratigraphies exist over key sectors of East Antarctica. This suggests that, alongside existing IRH stratigraphies over the region, these newly published datasets could be critical in our aim to create a continuous and wide-ranging stratigraphy from IRHs across the ice sheet, as motivated by the international AntArchitecture initiative.

Acknowledgments

I am firstly grateful to the NERC E^3 Doctoral Training Partnership based at the School of GeoSciences for funding my PhD and providing me with the opportunity to study at The University of Edinburgh. Thanks in particular to Stephanie Robin, Sophie Ramette, and Richard Essery for overseeing the programme so well, and for being so flexible and understanding with regards to PhD extensions during COVID times. I am also grateful for the financial support I received from SAGES for my six-week research visit to UTIG, which formed the basis of my second results chapter.

I also want to thank my supervisor, Rob Bingham, for his encouragements and help during my PhD. You offered me the opportunity to create a good network of collaborators and be included in exiting science collaborations, which is not always guaranteed for early-career researchers. Thank you also for involving me in the ITGC GHOST field season and for letting me be actively engaged with AntArchitecture.

My thanks also go to my *not-so-official* supervisor, Dave Ashmore, who was one of the first people I met when I started my PhD, and who introduced me to the very basics of radar and helped me get through the technical details of data processing early on. Thank you for your patience and for always explaining concepts in a simple way without making me feel like a complete idiot! I always appreciated that.

I have also had the pleasure to work and interact with many other colleagues throughout the last four years. Duncan Young, Don Blankenship, Erica Quartini and Jamin Greebaum at UTIG who welcomed me and even gave me an office with a window (however short that lasted...), and for taking me out for pizza and burgers regularly during my six-week stay. Thanks to Joe MacGregor for being a great teacher and patient mentor during the last year of my PhD, and for always having a word of encouragement regardless of the results. Thanks also to the whole AntArchitecture community for the great interactions over the years, par-

ticularly Neil Ross, Olaf Eisen, Nanna Karlsson, Johannes Sutter, and Gwendolyn Leysinger Vieli. Thank you to Peter Fretwell and Hamish Pritchard for involving me in the Bedmap project and inviting me to steering group meetings where I learned a lot, and Kenny Matsuoka for getting me involved in data analysis for the RINGS project in the last year of my PhD. I am also grateful to the Coastal Hydrology Research Lab at Vancouver Island University for offering me a desk in the last year of my PhD. I am also particularly thankful to T.J. Fudge for a great review of our PIG paper and for unselfishly helping us to connect our results with the sulphate record from the WAIS Divide ice core, which turned out to be one of the highlights of the paper (at least for me!). My thanks also go to the late David Vaughan for his involvement in my PhD and for always providing wise advice when discussing my next steps. Lastly, thank you to the many great non-Edinburgh ECRs I met during the last four years, especially James Kirkham, Rebecca Schlegel, Marie Cavitte, Rebecca Sanderson, and T.J. Young.

One of the most memorable part of my PhD was undoubtedly the three months I spent in Antarctica as part of the ITGC GHOST project. There are many people to thank for this, particularly Andy Smith for 'pencilling' me back in 2018 to go South and for subsequently employing me as a field assistant for four months with BAS; Ed King for training us on the DELORES radar system and for his invaluable advice and knowledge; the 2022-2023 GHOST team, particularly Elizabeth Case, Louise Borthwick, Rebecca Pearce, Ole Zeising, Florian Koch, Coen Hofstede, Luke Glazzard, Knut Christianson, Andrew Hoffman, Nate Stevens, and Amanda Willet, as well as the whole ITGC programme for the many interesting science interactions over the last four years.

The ten months I spent at the British Antarctic Survey will probably remain one of the most interesting and productive times I've had during my PhD. I want to particularly thank Alice Frémand for encouraging me throughout my post and including me in what turned out to be really exciting science projects which have helped me grow both professionally and personally. My thanks also go to the Polar Data Centre team, particularly Helen Peak and Beatrix Schlarb-Ridley for welcoming me so well during my stay, as well as the aerogeophysics teams of Tom Jordan, Carl Robinson, Hugh Corr, Fausto Ferraccioli, and Àlvaro Arenas Pingarròn for being so actively engaged with our work. Lastly, I am also grateful to Jo Johnson and Rob Larter for involving me in discussions on the ITGC review paper and engaging so nicely with my research.

I want to also thank the staff and students at The University of Edinburgh's School of GeoSciences for fun exchanges at the cafeteria and in the offices/class

rooms. Particularly, I want to thank my adviser Mikael Attal for being so approachable, and other friends and colleagues, including Amit Acharya, Carry Arnold, Ashley Buchan, Richard Delf, Dan Goldberg, Noel Gourmelen, Andy Hein, Nick Homer, Anthony Newton, Helen Ockenden, Jess Rickenback, Donny Wahyudi, and Aythya Young. Lastly, I also want to particularly thank Pete Nienow and David Rippin for a great viva examination and providing wise advice for the future.

This thesis would not have been possible without the excellent formatting years I have received from the School of Interdisciplinary Studies at the University of Glasgow (Dumfries Campus) during my undergraduate. Particularly, I would like to thank Matt Davies for being an inspirational mentor and getting me interested in research early on in my first year (sorry I dropped out of Ecology..). Thanks also to Steven Gillespie, Bethan Davies, and David Clark for continuously encouraging me and pushing me to do my best, both academically and personally. I wouldn't have done this without your help all these years ago.

More personally, I want to thank my family and friends for all their support, laughter, and love. Maman et Del sans qui cette thèse n'aurait jamais été possible sans votre accompagnement depuis toujours malgré les difficultés, Granny et Pepée pour nous avoir tellement aidé durant toutes ces années, et Marraine pour m'avoir toujours écouté et encouragé à continuer mes études en Sciences comme tu l'as fait, toi, il y a tant d'années. J'espère vous avoir rendu fièrs. Rosie for being the best thing that happened to me in the last four years (after getting a PhD obviously...). You've been my source of laughter and fun, but also my rock over the years, even despite being asked about 2,000 times "can you please help me with this equation?". Here's to many years of fun and happiness together. Thank you also to my closest friends and family who've always been here and without which life would definitely be less fun: Davi & Joanna, John, Laurence & Saori, Youri, Max & Juliette, Katymum, Philippe, Adrien, petite Agathe - merci d'être encore là depuis si longtemps malgré la distance.

Table Of Contents

Declaration iii

Abstract v

Résumé vii

Plain Language Summary ix

Acknowledgments xi

List of Figures xviii

List of Tables xxi

List of Abbreviations xxiii

List of Variables xxvi

Chapter 1: Introduction 1
- 1.1 Thesis motivations . . . 1
  - 1.1.1 Internal Reflecting Horizons: An alternative proxy for reconstructing past ice-sheet changes . . . 3
  - 1.1.2 AntArchitecture: Towards the development of a continent-wide age-depth model of Antarctica . . . 5
- 1.2 Thesis aims and overview . . . 5

Chapter 2: Background 7
- 2.1 Past, present and future evolution of the Antarctic Ice Sheet . . . 7
  - 2.1.1 Past AIS changes . . . 7
  - 2.1.2 Present AIS changes . . . 9
  - 2.1.3 Future AIS changes . . . 13
- 2.2 Traditional methods for inferring past changes over Antarctica . . . 14

2.3 RES as a means to infer current and past ice-sheet processes 16
2.3.1 Internal Reflecting Horizons in RES data 20
2.3.1.1 IRHs to constrain past accumulation rates 23
2.3.1.2 IRHs to constrain past ice-dynamical processes . . 27
2.3.2 Data requirements for the development of an ice-sheet wide age-depth model 31
2.4 Summary of key points and gaps in knowledge 33
2.5 Thesis objectives 34

Chapter 3: Age-Depth Stratigraphy of Pine Island Glacier 35
3.1 Abstract 35
3.2 Introduction 36
3.3 Datasets and methods 38
3.3.1 Data 38
3.3.2 IRH-tracing workflow 40
3.3.3 Catchment-wide depth uncertainties 46
3.3.3.1 Electromagnetic wave in ice 46
3.3.3.2 Firn-density correction 46
3.3.3.3 Radar range precision 47
3.3.3.4 Combining uncertainties 48
3.3.4 Age-depth attribution 48
3.3.4.1 Connection to the WAIS Divide ice-core chronology 48
3.3.4.2 Age-depth modelling 49
3.3.4.2.1 Past accumulation rates 52
3.3.4.2.2 Basal shear layer thickness 53
3.4 Results 55
3.4.1 Englacial stratigraphy 55
3.4.2 Age-depth estimates 57
3.5 Discussion 58
3.5.1 IRH comparison across the WAIS 58
3.5.2 Linkage with the WAIS Divide ice-core record 62
3.5.3 Accumulation rate and IRH-age comparison 64
3.5.4 Characteristics of englacial stratigraphy 65
3.6 Conclusions 67
3.7 Data availability 68

Chapter 4: Holocene Accumulation over West Antarctica 69
4.1 Abstract 69
4.2 Introduction 70
4.3 Data and methods 73
4.3.1 Along-track IRH data 73

4.3.2 Inferring accumulation rates . . . 75
4.3.2.1 Assessing the suitability of the 1-D model . . . 76
4.3.2.2 Model limitations and uncertainty . . . 79
4.3.3 Gridding and filtering . . . 84
4.3.4 Comparison with modern observations . . . 85
4.4 Results . . . 86
4.4.1 Catchment-scale accumulation estimates . . . 87
4.4.2 Elevation-dependent accumulation estimates . . . 91
4.5 Discussion . . . 92
4.5.1 Comparison with other Holocene accumulation estimates . . . 92
4.5.2 Impact for ice-sheet elevation change during the Holocene . . . 94
4.5.3 Impact for grounding-line evolution during the Holocene over the WAIS . . . 95
4.6 Conclusions . . . 96
4.7 Data availability . . . 97

Chapter 5: A Community Resource of Aerogeophysical Data Across Antarctica: Application to the study of IRHs across the AIS 98
5.1 Abstract . . . 99
5.2 Introduction . . . 99
5.3 Background . . . 102
5.3.1 Aerogeophysical surveys for the period 1994-2004 . . . 103
5.3.2 Aerogeophysical surveys for the period 2004-2020 . . . 104
5.3.2.1 2004-2015 . . . 104
5.3.2.2 2015-2020 . . . 110
5.4 Data acquisition and processing . . . 111
5.4.1 Data acquisition and instrumentation . . . 113
5.4.1.1 Gravity . . . 113
5.4.1.2 Magnetics . . . 115
5.4.1.3 Radar . . . 115
5.4.1.4 GPS and lidar . . . 119
5.4.2 Data processing . . . 120
5.4.2.1 Gravity . . . 120
5.4.2.2 Magnetics . . . 121
5.4.2.3 Radar . . . 122
5.5 FAIR data publishing . . . 127
5.5.1 Interoperability: data formats and attributes . . . 127
5.5.2 Findability: metadata and digital object identifiers . . . 131
5.5.3 Accessibility: Polar Airborne Geophysics Data Portal . . . 133

5.5.4 Re-Usability: user guide and tutorials . . . 134
5.6 Discussion . . . 134
5.6.1 Internal Layering Continuity Index . . . 134
5.6.2 Polar Airborne Geophysics Data Portal . . . 141
5.6.3 Future work . . . 141
5.7 Conclusion . . . 143
5.8 Data availability . . . 144

Chapter 6: Discussion **146**
6.1 Thesis overview . . . 146
6.2 Thesis outcome . . . 147
6.3 Thesis limitations and future developments . . . 148
6.3.1 Chapter 3 . . . 148
6.3.2 Chapter 4 . . . 154
6.3.3 Chapter 5 . . . 158

Chapter 7: Conclusion **162**

References **165**

Appendix **214**
Appendix A: *Journal of Geophysical Research: Earth Surface* paper . . . 215
Appendix B: *The Cryosphere* paper . . . 240
Appendix C: *Earth System Science Data* paper . . . 258

List of Figures

1.1 Map of Antarctica with notable landmarks 2
1.2 Radargram from the British Antarctic Survey Polarimetric Airborne Survey INstrument (PASIN) system over the Wilkes Subglacial Basin (East Antarctica) showing clear IRHs and bed topography on the shallow- and deep-sounding RES modes 4

2.1 Reconstructions of the AIS for four time periods between 20-5 ka BP 8
2.2 Mass change and sea-level contribution of the four main Antarctic regions between 1992 and 2017 10
2.3 Recent Antarctic mass change between 2003 and 2019 from satellite altimetry 11
2.4 Schematic of Marine Ice-Sheet Instability (MISI) for a glacier with a retrograde slope 12
2.5 Future ice-sheet simulations from 2015 to 2300 over the Amundsen Sea sector following the more fossil-fuel intensive scenario (RCP 8.5; DeConto and Pollard, 2016; their Figure 4) 13
2.6 Future AIS contribution to GMSL by 2300 under different RCP scenarios (DeConto et al., 2021; their Figure 1) 15
2.7 Photographs showing the evolution of airborne RES data acquisition over Antarctica 18
2.8 Diagram demonstrating the use of ground-based and airborne RES systems to obtain information on IRHs and bed characteristics . . . 21
2.9 Radargram from a 200-km segment of the Institute-Möller Antarctic Funding Initiative (IMAFI) survey by BAS using (a) the PASIN shallow-sounding pulse and (b) the PASIN deep-sounding chirp . . 22
2.10 Reconstruction of accumulation and temperature rates from the WAIS Divide ice core between 31 ka and the present 26
2.11 Classification of the continuity of englacial layering across Pine Island Glacier 30
2.12 Map showing the availability of RES data from Bedmap 1-3 32

3.1 Map of study area with the datasets and key locations mentioned in this chapter 40
3.2 Subset of the control line with the unmodulated pulse (a) and chirp (b) modes from the PIG-PASIN survey along transect AA–AB . . . 41
3.3 Radargram and radar trace profile showing IRH characteristics and return power on the PIG-PASIN data 43
3.4 Map showing the spatial extent of IRHs R1-4 across our study area (grey lines) and selected crossover points for IRHs traced on PIG-PASIN and OIB-MCoRDS2 45
3.5 3-D radar profile connecting the Pine Island Glacier with the WAIS Divide ice core 50
3.6 Normalised (a-d) and fractional (e-h) depth for the four IRHs traced over the PIG-PASIN and OIB-MCoRDS2 data from shallowest to deepest 56
3.7 Comparison between our IRHs and Karlsson et al. (2014) and Ashmore et al.'s (2020a) IRHs 61
3.8 Sulphate concentration (μg kg^{-1}) as a function of depth (m) at the WAIS Divide ice-core site for: (a) the brittle section of the WDC06A ice core (577-1,300 m) from Cole-Dai (2014); and (b) for depths of 1,300-3,404 m at WD2014 Ice Core from McConnell (2017) 63
3.9 Ice thickness (m) below R3 (a) and R4 (b) traced over the PIG-PASIN and OIB-MCoRDS2 data 66

4.1 Map of the datasets and key locations in this study. 74
4.2 Suitability of the LLA over the PIG, THW, and IMIS catchments for the 4.72 ka IRH 78
4.3 Strain rate patterns across the survey area 81
4.4 Histograms of inferred accumulation rates from both the Nye and shallow-strain rate models 82
4.5 Uncertainties in inferred accumulation rates based on the radar and ice-core age uncertainties and from the accumulation rates returned from the shallow-strain rate model 83
4.6 Maximum distance to the nearest 500-m along-track point used for the interpolation of the 4.72 ka IRH depth and accumulation grids . 85
4.7 Gridded depths for the 4.72 ka IRH across the model domain 87
4.8 Gridded estimates of ice-equivalent accumulation rates for the last 4.72 ka and modern times across the model domain 88
4.9 Scatter plot showing the difference in accumulation rates between the modern (cores and RACMO2) and the Holocene (4.72 ka) . . . 89
4.10 Relative change in accumulation rates between the 4.72 ka-to-present estimates and modern rates 90

4.11 Comparison of ice-equivalent accumulation rates between the 4.72 ka-to-present estimates and modern rates (RACMO2) binned by 50-m elevation bands across the three main catchments considered here (Amundsen, Weddell, and Ross) 91

5.1 Map showing all the published datasets included in this data release 101
5.2 Maps of gravity, magnetic, and radar (bed elevation and ice thickness) point measurements for all surveys published as part of this data release 108
5.3 Sample radargrams from the ten 2-D radar datasets released with this paper 109
5.4 Workflow describing the data acquisition, processing, and publishing for the BAS aerogeophysical data included in this data release . 112
5.5 Photographs of the aerogeophysical set-up on the BAS Twin Otter aircraft "VP-FBL" for PASIN-2 114
5.6 Digitised version of the diagram describing the set-up for the "BAS-built" radar system (Corr and Popple, 1994) 118
5.7 Diagram describing the set-up for the PASIN-1 radar system 118
5.8 Diagram describing the set-up for the PASIN-2 radar system 119
5.9 A 25 km segment of flight line 15d of the 2010–2011 IMAFI survey, showing the three radar products and processing attributes 126
5.10 Example of a segmented quick-look image from the 2005–2006 WISE-ISODYN survey 130
5.11 The ILCI for the ten PASIN datasets for which the fully processed 2-D radar data were released as part of this chapter 137
5.12 Zoomed-in sections of the ILCI 139
5.13 Segment A-A' from the AGAP survey (flightline: A10B) showing continuous layering at depth and high ILCI values 140
5.14 Screenshots of the Polar Airborne Geophysics Data Portal showing the three aerogeophysical products for the 2012–2013 ICEGRAV survey with different basemaps 142

6.1 Sulphate concentrations (μg kg^{-1}) as a function of depth (m) at the South Pole ice core 151
6.2 Comparison of age-depth relationships between two 1-D ice-flow models and the WAIS Divide ice core profile 156
6.3 Coverage of dated IRH stratigraphies across Antarctica against existing RES data from Bedmap2-3 and the newly released data from Chapter 5 159

List of Tables

3.1 Characteristics and resolution of the two airborne RES systems used in this study . . . 39
3.2 Crossover depth analysis for ten locations (I1-10, Fig 3.4) where R1-4 intersect each other at flight path crossovers on the PIG-PASIN data . . . 44
3.3 Crossover depth analysis for five locations (K1-5) where R4 traced on the OIB-MCoRDS2 data (this study) intersects the 17.5 ± 0.5 ka layer (Jacobel and Welch, 2005) . . . 45
3.4 IRH depths (m) at three locations where the SPRI/NSF/TUD survey intersects the PIG-PASIN survey . . . 52
3.5 Accumulation rates (m a^{-1}) for each IRH at Site A and B, as calculated using the four accumulation datasets . . . 54
3.6 Summary statistics for each IRH traced throughout the PIG-PASIN and OIB-MCoRDS2 surveys . . . 55
3.7 IRH mean depths (m), ages (ka; in years before 2020 AD), and uncertainties (Δ) at the WD2014 site for R2-4 . . . 57
3.8 Modelled IRH age-range estimates (ka) returned from the 1-D steady-state model for varying accumulation datasets and basal shear layer thickness (h, in metres) scenarios at Site A and B for IRHs R1-4 . 58

4.1 Characteristics of each IRH dataset used in this study that contain the 4.72 ka IRH . . . 75
4.2 Summary statistics for the modern (modelled and observational) and 4.72 ka-to-present ice-equivalent accumulation rates at the catchment-scale and over the Amundsen-Weddell-Ross Divide . . . 89

5.1 Information on the period, region, sub-region, type of data acquired, total line coverage (km), total coverage area (km^2), and key reference for each survey included in this data release . . . 106
5.2 Radar parameters for the three radar systems deployed by BAS between 1994 and the present day . . . 117

5.3 PASIN-2 Radar Transmit (Tx) and Receive (Rx) Description 119
5.4 Short digital object identifiers (DOIs) for the gravity, magnetic, bed-pick, and 2-D radar datasets of each survey flown by BAS and included in this data release 128
5.5 Attributes for each variable stored in the NetCDF files 132

6.1 Largest volcanic events in the WAIS Divide ice core during the Holocene 150

List of Abbreviations

ADC	Analogue-to-Digital Converter
AGAP	Antarctica's Gamburtsev Province Project
AFI	Antarctic Funding Initiative
AGASEA	Airborne Geophysical Survey of the Amundsen Embayment
AIS	Antarctic Ice Sheet
APIS	Antarctic Peninsula Ice Sheet
ASE	Amundsen Sea Embayment
BAS	British Antarctic Survey
BP	Before the Present
CD	Central Amundsen-Weddell-Ross Divide
CE	Common Era
CF	Climate Forecast
CReSIS	Center for Remote Sensing of Ice Sheets
DELORES	DEep LOok Radio Echo Sounder
DEM	Digital Elevation Model
DJ	Dansgaard-Johnsen model
DMS	Discovery Metadata System
DML	Dronning Maud Land
DOI	Digital Object Identifier
DTP	Doctoral Training Partnership
EAIS	East Antarctic Ice Sheet
ECMWF	European Centre for Medium-Range Weather Forecasts
EM	Electromagnetic wave
ESA	European Space Agency
FAIR	Findable, Accessible, Interoperable, Reusable
FISS	Filchner Ice-shelf System
FPGA	Field-Programmable Gate Array
GCMD	Global Change Master Directory
GHOST	Geophysical Habitat of Subglacial Thwaites
GMSL	Global Mean Sea Level
GNSS	Global Navigation Satellite System

GOCE	Gravity Field and Steady-State Ocean Circulation Explorer
GPR	Ground Penetrating Radar
GPS	Global Positioning Systems
GRADES	Glacial Retreat in Antarctica and Deglaciation of the Earth System
HM	Hudson Mountain Range
HiCARS	High Capacity Airborne Radar Sounder
ICECAP	International Collaborative Exploration of the Cryosphere through Airborne Profiling
IGRF	International Geomagnetic Reference Field
IIS	Institute Ice Stream
ILCI	Internal Layer Continuity Index
IMAFI	Institute and Möller Antarctic Funding Initiative
IMAGE	Inverse Modelling of Antarctica and Global Eustasy
IMBIE	Ice Sheet Mass Balance Inter-comparison Exercise
IMIS	Institute and Möller Ice Streams
IPCC	Intergovernmental Panel on Climate Change
IPY	International Polar Year
IQR	Interquartile Range
IMU	Inertial Measurement Unit
IRH	Internal Reflecting Horizon
ITASE	International Trans-Antarctic Scientific Expedition
ITGC	International Thwaites Glacier Collaboration
LGM	Last Glacial Maximum
LIDAR	Light Detection and Ranging
LIMA	Landsat Image Mosaic of Antarctica
LLA	Local-Layer Approximation
MAMOG	Magmatism as a Monitor of Gondwana breakup
MAR	Modèle Atmosphérique Régional
mCDW	modified Circumpolar Deep Water
MISI	Marine Ice Sheet Instability
MCoRDS	Multichannel Coherent Radar Depth Sounder
MODIS	Moderate Resolution Imaging Spectroradiometer
NASA	National Aeronautics and Space Administration
NCAR	National Committee for Antarctic Research
NERC	National Environmental Research Council
NSF	National Science Foundation
OIB	Operation IceBridge
PASIN	Polarimetric Airborne Survey INstrument
PDC	Polar Data Centre
PIG	Pine Island Glacier

PPP	Precise Point Positioning
PRI	Pulse Repetition Interval
PRF	Pulse Repetition Frequency
RAISED	Reconstruction of Antarctic Ice Sheet Deglaciation
RACMO	Regional Atmospheric Climate Model
RAMADA	Repository for Archiving and MAnaging Diverse DAta
RCP	Representative Concentration Pathway
RES	Radio-Echo Sounding
RMSE	Root Mean Square Error
RF	Radio Frequency
SAGES	Scottish Alliance for Geoscience, Environment and Society
SAR	Synthetic Aperture Radar
SCAR	Scientific Committee on Antarctic Research
SF	Sampling Frequency
SI	Sampling Interval
SMB	Surface Mass Balance
SNR	Signal-to-Noise Ratio
SPARC	Superterranes in the Pacific Margin Arc
SPRI	Scott Polar Research Institute
TORUS	Targeting ice-stream Onset Regions and Under-ice Systems
TU	Technical University
TUD	Technical University of Denmark
THW	Thwaites Glacier
UTIG	University of Texas Institute for Geophysics
VEI	Volcanic Explosivity Index
VL	Very Large
WAIS	West Antarctic Ice Sheet
WD2014	WAIS Divide Ice Core
ZLS	Zero-Length Spring

List of Variables

Chapter 3

a	accumulation rate	m a^{-1}
$\Delta a_{\Delta depth}$	IRH age uncertainty from radar	ka
Δa_{core}	IRH age uncertainty from ice core	ka
B	radar bandwidth	MHz
c_0	speed of light in a vacuum	km s^{-1}
ϵ'	dielectric constant of ice	-
H	ice thickness	m
h	basal shear layer thickness	m
k	window widening factor	-
Δr	radar vertical range resolution	m
t	IRH age	ka
t_{IRH}	IRH two-way travel time	μs
v_{ice}	speed of electromagnetic waves through ice	m μ^{-1}
Z_f	firn correction	m
z	IRH depth	m
Δa_{comb}	combined age uncertainty	ka
Δa_{total}	total age uncertainty	ka
$\sigma(r^*)$	radar range precision	m

Chapter 4

a	IRH age	ka
$\dot{b}$	accumulation rate	m a^{-1}
$\dot{b}_a$	accumulation rate for age a	m a^{-1}
$\dot{b}_{modern}$	accumulation rate for the present	m a^{-1}
$\Delta\dot{b}$	accumulation rate difference	m a^{-1}

$d\dot{b}$	accumulation rate gradient	m a^{-1}
D	D parameter	-
$\dot{\epsilon}_{xx}$	vertical strain rate	a^{-1}
$\Sigma_{total}\ \dot{b}$	total accumulation rate	Gt a^{-1}
H	ice thickness	m
$L_{\dot{b}}$	accumulation rate characteristic length	km
L_H	ice-thickness characteristic length	km
L_{path}	path length of particle of ice	km
$\overline{u}$	modern ice-flow velocities	m a^{-1}
Z_a	IRH depth	m
$\tilde{\mu}$	median	-
$\dot{\epsilon}^a_{zz}$	longitudinal strain rates	a^{-1}
$\hat{u}_{\parallel}$	modern surface velocity unit vector	a^{-1}

Chapter 5

ψ	Internal Layer Continuity Index	-
Δr	depth	m
P_i	reflected relative power	dB
N	selected section length	-
n	sample number of reflected relative power values	-

1 Introduction

1.1 Thesis motivations

The Antarctic Ice Sheet (AIS) is one of the key contributors of global mean sea level rise, with a contribution of 2.1 ± 0.19 cm over the last three decades and a three-fold increase in mass loss observed between the periods 1992-1996 (105 Gt yr^{-1}) and 2016-2020 (372 Gt yr^{-1}) (Otosaka et al., 2023). However, this mass loss and associated sea-level rise are not evenly distributed across the three main regions of the AIS (namely the Antarctic Peninsula, West Antarctica, and East Antarctica) (Fig. 1.1), whereby the East Antarctic Ice Sheet (EAIS) is thought to be in a state of balance in contrast to the West Antarctic Ice Sheet (WAIS) which currently experiences high rates of mass loss approximating 82 ± 9 Gt yr^{-1} between 1992 and 2020 (Otosaka et al., 2023).

However, placing the recent downward trend in overall mass loss within the context of long-term changes in ice-sheet dynamics and sea-level rise is challenging due to the short observation record, which in turn impacts our understanding of how the AIS may react to further changes in atmospheric and oceanic forcings. Whilst progress has been made in recent years to model past and future changes and compare them to the current observational record (e.g. DeConto and Pollard, 2016; Sutter et al., 2016; Golledge et al., 2021), physics-based models are only as good as the data used to constrain them. It is therefore increasingly important to obtain past records of long-term ice-sheet change to better understand the centennial to millennial response of the ice sheet to future anthropogenic forcing.

Physical records of past changes used in ice-sheet models have traditionally come from ice and sediment cores (WAIS Divide Project Members, 2013; Arnd et al., 2017; Kingslake et al., 2018; Venturelli et al., 2020; Buizert et al., 2021; Neuhaus et al., 2021; Sproson et al., 2022), or from surface exposure dating (Johnson et al., 2014; Hein et al., 2016a; 2016b; Nichols et al., 2019; Braddock et al., 2022). Whilst ice cores are particularly useful for recovering changes at high



Figure 1.1: Map of Antarctica with notable landmarks. Figure is from the Landsat Image Mosaic of Antarctica (LIMA) dataset (Bindschadler et al., 2008).

temporal scales, it is challenging to put the results from these point-based measurements into a regional or continental-scale setting. For example, Antarctic ice-sheet models rely primarily on past records of temperature and snow accumulation at the Last Glacial Maximum (LGM) from two ice cores situated in East Antarctica (i.e. Vostok and Dome C) as forcing parameters to model ice-sheet change and sea-level rise (Chavaillaz et al., 2013; DeConto and Pollard, 2016; Bracegirdle et al., 2019). However, evidence has shown that ice cores may not be representative of a wider regional area (Koutnik et al., 2016; Cavitte et al., 2022), thus intro-

ducing a bias in the models over different regions of Antarctica. Additionally, recent evidence from the WAIS Divide ice core (Fudge et al., 2016) has shown that there is considerable variability in accumulation rates between the LGM and the present, which other ice cores over the EAIS do not show (Koutnik et al., 2016). Whilst this is likely specific to the WAIS, it is important to understand the spatial extent of this variability at a catchment scale if we are to better model past and future changes in the sea-level rise contribution of the AIS. In addition to issues of spatial representativeness from ice cores, sediment cores or surface exposure dating acquired over previously glaciated areas of the ice sheet only provide information on past boundary conditions of a retreated ice sheet, as opposed to the terrestrial history of the current ice sheet. Therefore, an alternative that can provide both high temporal and spatial records of past ice-sheet change is required.

1.1.1 Internal Reflecting Horizons: An alternative proxy for reconstructing past ice-sheet changes

Internal Reflecting Horizons (IRHs), as imaged by Radio-Echo Sounding (RES) techniques, are a useful alternative to point-based geochronological measurements for inferring past changes over the ice sheet (Siegert, 1999; Bingham and Siegert, 2007) (Fig. 1.2). When isochronous and continuous in the horizontal direction, IRHs can be traced across large swaths of RES profiles spanning hundreds of kilometres, and connected to ice-core stratigraphies to create an age-depth profile of the ice sheet, as previously conducted across Greenland (Fahnestock et al., 2001a-b; MacGregor et al., 2015) and selected parts of Antarctica (Siegert et al., 1998; Siegert and Payne, 2004; Jacobel and Welch, 2005; Siegert et al., 2005; Leysinger-Vieli et al., 2011; Steinhage et al., 2013; Cavitte et al., 2016; Holschuh et al., 2018; Koutnik et al., 2016; Muldoon et al., 2018; Winter et al., 2019; Beem et al., 2021).

Crucially, the information that these IRHs provide can be used to infer past ice-sheet changes, such as estimating past accumulation rates or basal melting rates (Siegert, 2003; Waddington et al., 2007; Neumann et al., 2008; Carter et al., 2009; Leysinger-Vieli et al., 2011; Karlsson et al., 2014; Koutnik et al., 2016; Parrenin et al., 2017; Cavitte et al., 2018), assessing changes in the position and stability of ice divides (Jacobel et al., 2000; Carter et al., 2009; Conway and Rasmussen, 2009), assessing changes in past ice-sheet configurations (Siegert et al., 2004a; Kingslake et al., 2018; Ashmore et al., 2020a), or identifying suitable sites for drilling deep ice cores (Parrenin et al., 2017; Karlsson et al., 2018; Beem et al., 2021; Fudge et al., 2022), amongst others.

Despite their significant potential for inferring past changes over large spatial

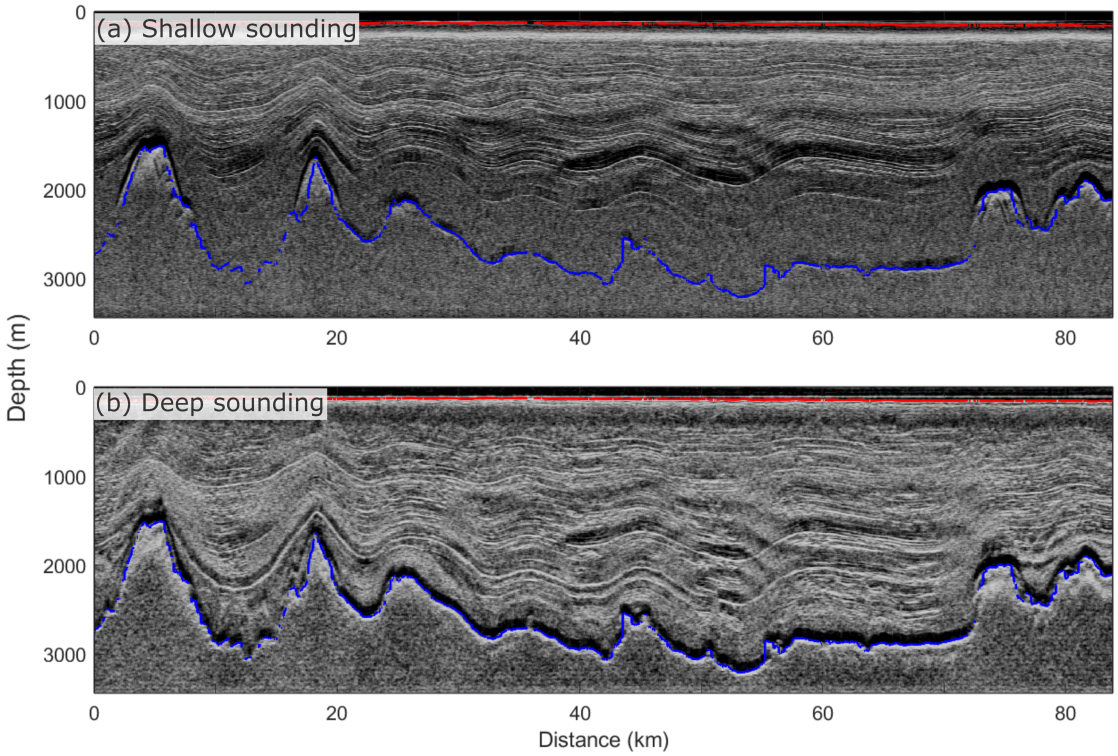

Figure 1.2: Radargram from the British Antarctic Survey Polarimetric Airborne Survey INstrument (PASIN) system over the Wilkes Subglacial Basin (East Antarctica), showing clear IRHs and bed topography on the shallow- and deep-sounding RES modes. The shallow RES mode in (a) shows better resolved layer stratigraphy in the upper part of the ice thickness, but fails to identify any englacial layering below 2 km depth. The deep-sounding RES mode in (b) shows thicker englacial layers than in (a) due to system resolution but is able to sound clear englacial layering down to the bed. The surface and bed picks are shown in red and blue respectively.

scales, most studies focusing on the extraction of IRH stratigraphies over Antarctica have done so along spatially focused areas (Neumann et al., 2008; Koutnik et al., 2016; Holschuh et al., 2018; Beem et al., 2021) or along individual RES profiles (Siegert et al., 1998; Siegert and Payne, 2004; Jacobel and Welch, 2005), and fewer have been able to extract an age-depth model from larger glacier catchments (Medley et al., 2013; Muldoon et al., 2018; Ashmore et al., 2020a; Cavitte et al., 2020). Further work is therefore required to extend IRH stratigraphies at a regional and continental scale in order to extract further past information which can be used to better constrain present and future ice-sheet changes.

1.1.2 AntArchitecture: Towards the development of a continent-wide age-depth model of Antarctica

Within this context, the Antarctic scientific community, under the auspices of the Scientific Committee for Antarctic Research (SCAR), set up the AntArchitecture Action Group with the aim to develop the first continent-wide age-depth model of Antarctica using dated IRHs. This resource has the potential to provide significant boundary conditions that will help determine the stability of the AIS over past glacial cycles, as recently demonstrated by Sutter et al. (2021). Previous attempts at developing an ice-sheet wide age-depth model over Greenland have been highly successful (MacGregor et al., 2015); however, significant challenges have so far prevented a similar product over Antarctica. This is primarily due to the variety of institutions and countries acquiring data over the continent which, as opposed to Greenland where this is largely limited to a single data provider, has led to differences in the quality and availability of RES data. Additional challenges include the relatively low amount of deep ice-core stratigraphies with respect to the size of Antarctica and the lack of RES profiles connecting these ice cores together across the continent.

By being firmly embedded within the AntArchitecture initiative, this thesis contributes to building and connecting regional-scale age-depth models across West Antarctica to extract past ice-sheet information, and provides a new community resource that will enable the development of other regional age-depth models across the AIS, as motivated by AntArchitecture.

1.2 Thesis aims and overview

The previous section highlighted the need to build a continent-wide age-depth model of the AIS from IRHs to inform ice-sheet models aiming to model past and future ice-sheet conditions. Therefore, the overall aim of this thesis is to develop and extend age-depth models from IRHs across Antarctica to assess the past stability of the AIS. To answer this overall aim, this thesis is divided into individual chapters, summarised as follows:

Chapter 2 provides the necessary background for this thesis by reviewing the literature relating to (a) the evolution of the AIS in the past, present and future; (b) the history of RES data acquisition in Antarctica; (c) the use of IRHs to estimate past accumulation rates and assess past ice-sheet dynamics; and (d) the requirements necessary for the development of an ice-sheet wide age-depth model. This chapter ends with a review of the key research gaps and how this thesis will

aim to address some of them.

Chapters 3, 4, and 5 describe the research that has been conducted as part of this PhD to address each of the objectives listed in Chapter 2. These three results chapters have been written in formats suitable for publication in peer-review journals. Chapter 3 was published in *Journal of Geophysical Research: Earth Surface*, Chapter 4 was published in *The Cryosphere*, and Chapter 5 was published in *Earth System Science Data*.

Chapter 6 synthesises the results from this thesis, with a particular focus on some of the key knowledge gaps that have been filled as a result of the work presented here, as well as the progress made since the publication of Chapters 3, 4, and 5. Lastly, this chapter discusses the limitations associated with the three results chapters and provides suggestions for future studies.

Chapter 7 summarises the main findings from this thesis and provides an outlook for future studies. Finally, the scientific contributions from this thesis are also presented in their published form in the Appendix section.

2 Background

2.1 Past, present and future evolution of the Antarctic Ice Sheet

The Antarctic Ice Sheet (AIS) has the potential to raise sea levels by 58 m if completely melted (Alley et al., 2005; IPCC AR6, 2022), therefore understanding how the ice sheet is responding to current anthropogenic changes and how the magnitude and extent of these changes compare with the evolution of the ice sheet during past glacial cycles is of high societal importance. In turn, improving our understanding of past and current changes will provide better forecasting of the likely future evolution of the ice sheet and reduce the uncertainties associated with those predictions (Jones et al., 2022). The following sections provide a background of our knowledge of past, present and likely future changes over the AIS.

2.1.1 Past AIS changes

Evidence from geochronological proxy records and numerical ice-sheet models have shown that the AIS has evolved considerably over past glacial cycles (Jones et al., 2022; Siegert et al., 2022; Stokes et al., 2022). Previous studies focused on reproducing the evolution of the AIS during the last interglacial period (130-115 ka Before the Present; BP) using ice-sheet models indicate that the AIS contributed between 2.5 and 7.5 m of Global Mean Sea Level (GMSL) rise (DeConto and Pollard, 2016; Sutter et al., 2016; 2019), a significant shift from its previous maximal extent reached towards the end of the mid-Pleistocene climate transition (1.2-0.9 Myr ago), which coincided with a significant buildup of ice over the West Antarctic Ice Sheet (WAIS; Elderfield et al., 2012; Sutter et al., 2019).

During its most recent maximal extent, referred to as the Last Glacial Maximum (LGM; ∼20 ka BP), the AIS was significantly thicker than today and its grounding line reached the continental-shelf edge, with an estimated GMSL-rise potential that was ∼6 to 19 metres greater than the ice sheet's current GMSL-rise

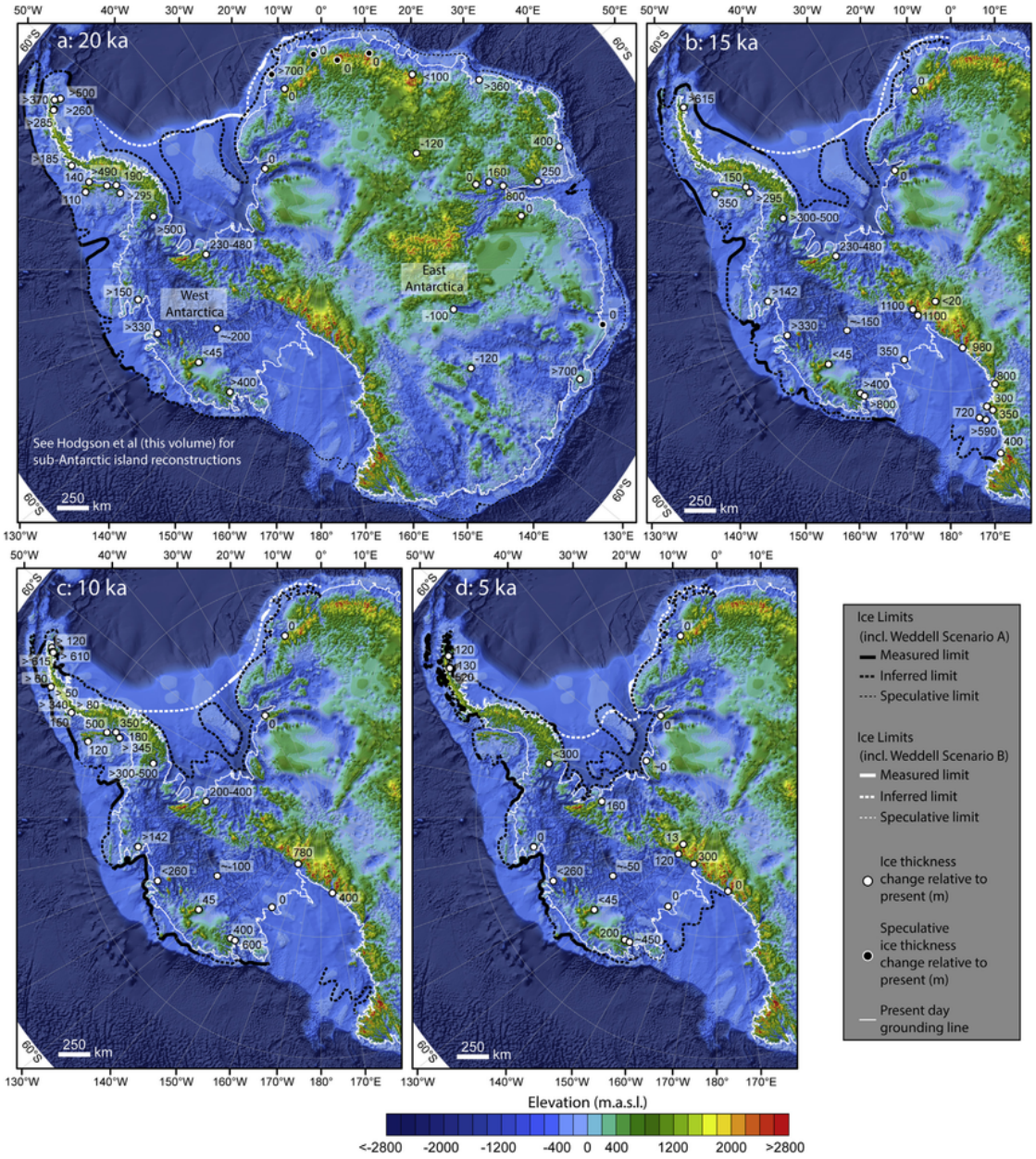

Figure 2.1: Reconstructions of the AIS for four time periods between 20-5 ka BP. The background is bed topography from Bedmap2 (Fretwell et al., 2013). Each inset represents the reconstruction of ice-sheet extents at (a) 20 ka, (b) 15 ka, (c) 10 ka, and (d) 5 ka. The different line styles represent uncertainty in grounding-line positions (low uncertainty: thick line; high uncertainty: dashed line). The two different and currently debated scenarios for grounding-line evolution over the Weddell Sea sector at the start of the Holocene are also shown, with Scenario A (black line) representing the grounding-line position close to present in the Southeastern Weddell Sea, and Scenario B (white line) representing the grounding-line position at the northern tip of Berkner Island at 10 ka. Figure from RAISED (Reconstruction of Antarctic Ice Sheet Deglaciation) Consortium (2014; their Figure 2).

potential (Denton and Hughes, 2002; Siegert et al., 2022). The AIS then subsequently retreated to its modern extent by ∼3 ka BP, although evidence has shown that this retreat was not homogeneous across all sectors of the AIS (Anderson et al., 2002; Pollard and DeConto, 2009; Hein et al., 2016b; Kingslake et al., 2018). In East Antarctica, the ice sheet may have started retreating from the continental-shelf edge around 18-14 ka BP in response to an abrupt rise in sea levels associated with Meltwater Pulse 1a (14.7-13.5 ka BP), followed by full deglaciation of the region between 12 and 6 ka BP from enhanced ocean warming (Mackintosh et al., 2014).

Whilst most studies of past ice-sheet evolution have focused on changes occurring prior to, or at the LGM, less is known of the evolution of the AIS during the pre-industrial Holocene (the last ∼11 ka; Siegert et al., 2013; RAISED consortium, 2014), a period that resembles current climatic conditions and ice-sheet extent. In West Antarctica, evidence had, until recently, suggested that the grounding line retreated gradually from the LGM to reach its current position in the late Holocene (Conway et al., 1999; Anderson et al., 2002; RAISED consortium, 2014; Fig. 2.1), with added uncertainty about the extent of the grounding line in the Weddell Sea sector (Scenarios A and B; Fig. 2.1). However, recent evidence has shown that the WAIS likely experienced retreat of its grounding line beyond its modern position up to ∼10 ka BP, followed by a readvance during the late Holocene, particularly over the Weddell and Ross Sea sectors due to glacial isostatic rebound and a likely change in climatic conditions (Siegert et al., 2013; Bradley et al., 2015; Kingslake et al., 2018; Siegert et al., 2019; Wearing and Kingslake, 2019; Venturelli et al., 2020; Neuhaus et al., 2021; Johnson et al., 2022). A similar pattern has also recently been identified over Totten and Denman Glaciers in the East Antarctic Ice Sheet (EAIS; King et al., 2022), although our understanding of the extent of this pattern remains constrained to these two glaciers.

Filling the knowledge gap around past ice-sheet configurations on large spatial scales, particularly with regards to the position of the grounding line during the Holocene, is important, as it would allow us to put current ice-sheet changes occurring on decadal timescale into the perspective of millennial-scale changes, and thus better predict the impacts of anthropogenic emissions on the short and long-term future evolution of the AIS (RAISED consortium, 2014; Siegert et al., 2013).

2.1.2 Present AIS changes

Mass loss from glaciers and ice sheets has been one of the dominant drivers of GMSL rise during the 20th Century, contributing 41% of the total 20 ± 5 cm

of GMSL for the period 1901-2018 (IPCC AR6, 2021). Estimates of Antarctica's ice-mass discharge into the oceans show a continent-wide mass loss of 92 ± 18 Gt yr^{-1} between 1992 and 2020, the equivalent of approximately 2.1 ± 0.19 cm of GMSL rise for that time period (Otosaka et al., 2023; Fig. 2.2).

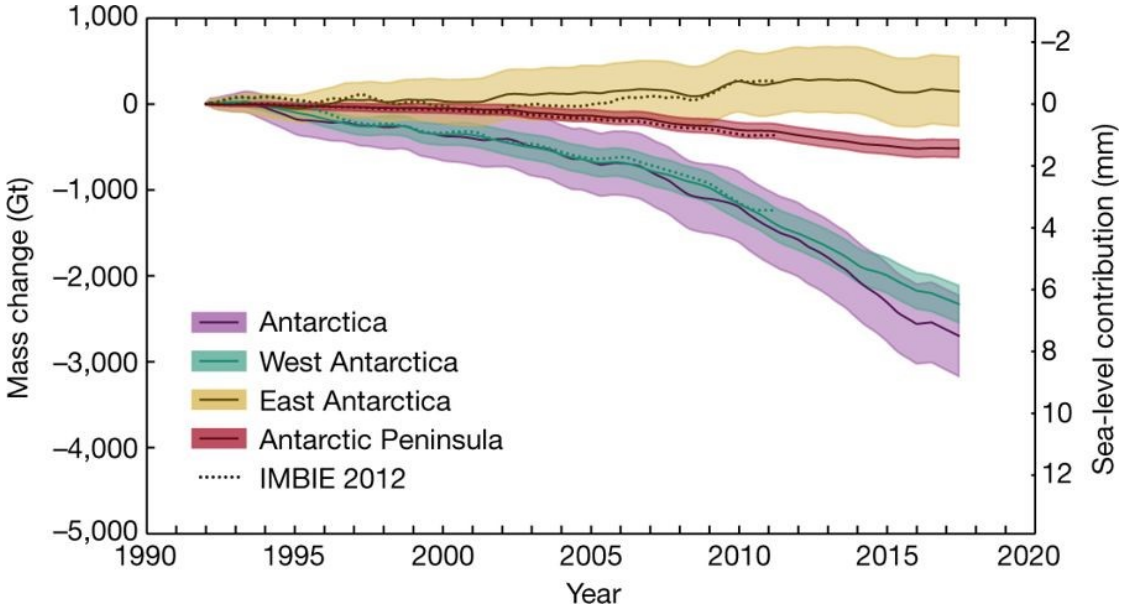

Figure 2.2: Mass change and sea-level contribution of the four main Antarctic regions between 1992 and 2017. Figure from Shepherd et al. (2018; their Figure 2)

Current net mass loss from the AIS is not uniform and exhibits strong regional variations, with a much larger mass loss of 82 ± 9 Gt yr^{-1} and 13 ± 5 Gt yr^{-1} for West Antarctica and the Antarctic Peninsula respectively, compared with a small mass gain of 3 ± 15 Gt yr^{-1} for the EAIS for the period 1992-2020 (Otosaka et al., 2023; Fig. 2.2 and 2.3). The mass loss on West Antarctica and the Antarctic Peninsula is dominated by glacial discharge from melting and calving events along their fast-flowing ice streams (Holland et al., 2010; Rignot et al., 2013; Gardner et al., 2018) (Fig. 2.3), whereas East Antarctica has primarily experienced mass gains due, in part, to an increase in precipitation rates over the East Antarcic plateau (Fig. 2.3; Shepherd et al., 2012; Medley et al., 2018; Otosaka et al., 2023). However, it is worth highlighting that the small mass gain in East Antarctica is concealing rising mass loss from marine basins in the region, including the Totten and Denman Glaciers where increased mass loss has been observed in recent years (Li et al., 2015; Rignot et al., 2019; Miles et al., 2021; Fig. 2.3). Overall, basal melting is responsible for 70% of mass loss over West Antarctica's Amundsen-Bellingshausen Sea ice shelves, whilst it only account for 40% of the average melt

ratio over the rest of the continent (Depoorter et al., 2013).

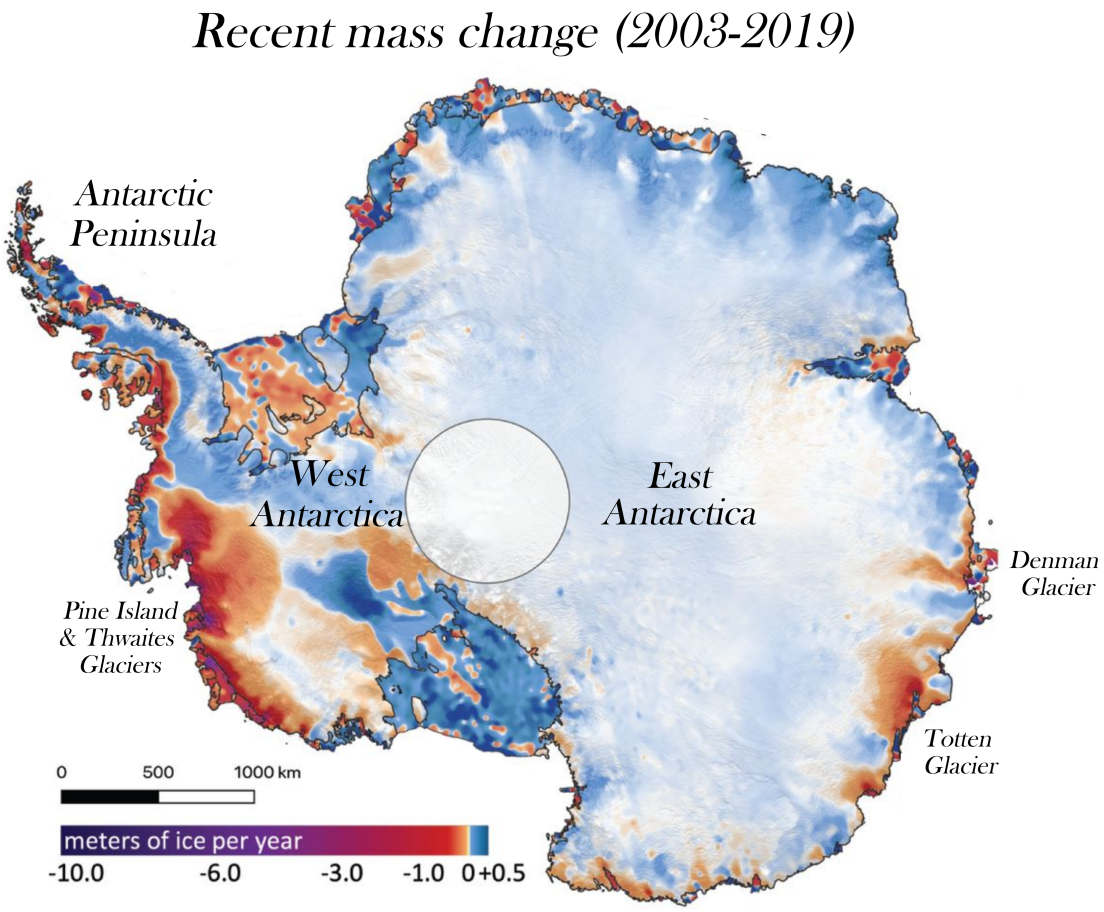

Figure 2.3: Recent Antarctic mass change between 2003 and 2019 from satellite altimetry. The annotations on the map refer to locations mentioned in this chapter. Figure adapted from Smith et al. (2020; their Figure 3).

There is now widespread concerns that parts of the WAIS and EAIS may collapse under a process called the Marine Ice-Sheet Instability (MISI), akin to glaciers where subglacial bedrock slopes inland (also known as retrograde slope) (Fig. 2.4; Weertman et al., 1974; Schoof, 2007; Pollard et al., 2015). Particularly vulnerable sectors of the WAIS and EAIS include Pine Island, Thwaites, and Totten Glaciers, where rapid disintegration of their ice shelves in response to warmer atmospheric temperatures (Joughin et al., 2014; Scambos et al., 2017; Edwards et al., 2019; Pelle et al., 2020) and the incursion of modified Circumpolar Deep Water (mCDW) beneath their ice shelves (Favier et al., 2014; Mouginot et al., 2014; Rignot et al., 2014; Smith et al., 2020) may lead the grounding line to retreat inland

where thicker ice is present, thus creating a positive feedback that may destabilise the entire ice sheet (Fig. 2.4). So far, West Antarctica's Pine Island Glacier has contributed approximately half (∼3.0 mm) of the total sea-level-rise contribution of the WAIS between 1979-2017 (Rignot et al., 2019), whereas Thwaites Glacier has contributed 1.8 mm of sea-level rise over the same period (Rignot et al., 2019). When taking into account their sea-level-rise potential however, both Pine Island and Thwaites Glaciers could contribute 51 and 65 cm of GMSL rise respectively, if completely melted, draining in turn the rest of the WAIS and contributing up to five metres of GMSL rise (Rignot et al., 2019). Over the EAIS, recent evidence has shown that large cavities underneath Totten Glacier could allow intrusion of mCDW to melt the ice shelf from beneath and thus lead to the potential destabilisation of this glacier, which could contribute 3.5 m of GMSL rise from East Antarctica (Greenbaum et al., 2015; Nitsche et al., 2017; Rignot et al., 2019).

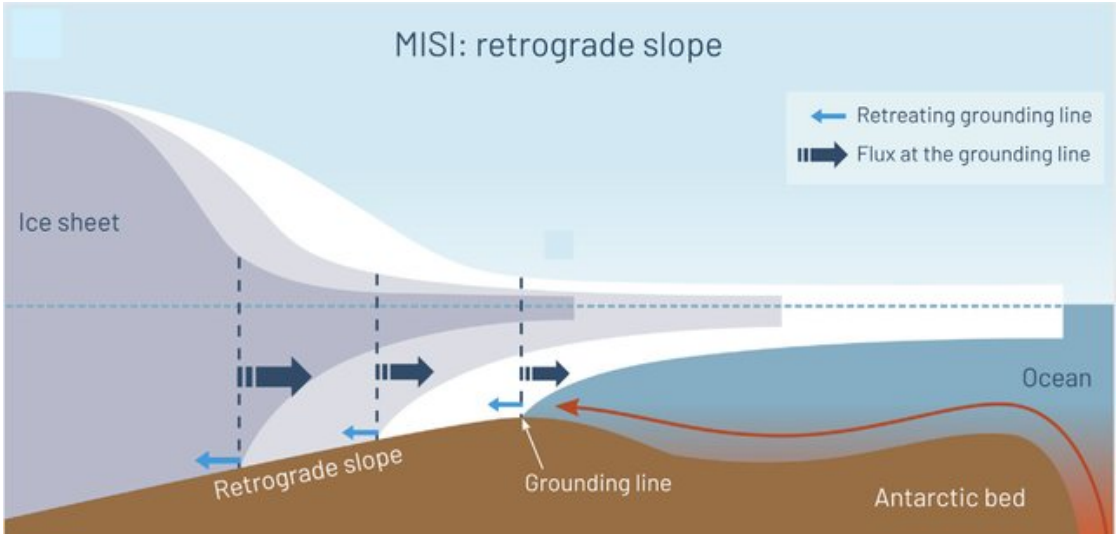

Figure 2.4: Schematic of Marine Ice-Sheet Instability (MISI) for a glacier with a retrograde slope. Figure adapted from Siegert et al. (2020; their Figure 2).

Unfortunately, significant uncertainties still remain with regards to modelling MISI and its associated effects on the ice sheet, in parts due to the spatial resolution required to model grounding-line processes and the tight interactions between bedrock characteristics and ice flow which will likely dictate whether the ice sheet can stabilise itself in the future (e.g. around pinning points) (Ritz et al., 2015; Robel et al., 2019; DeConto and Pollard, 2022). One alternative to reducing these uncertainties, and improving our understanding of whether large ice streams over the WAIS and EAIS have been affected by MISI in the past, is to use geochronological proxy records. These may provide the required context to understand and

forecast how the current changes we are observing today may affect future ice-sheet evolution (Edwards et al., 2019). I come back to these in more detail in Sections 2.2 and 2.3.1.

2.1.3 Future AIS changes

Future predictions of the evolution of the AIS under increasing anthropogenic emissions differ widely amongst emission scenarios and temperature targets, ranging from total collapse of the WAIS and a sea-level rise contribution approximating ten metres by 2300 under the most fossil-fuel intensive scenarios (Representative Concentration Pathway (RCP) 8.5; Fig. 2.5), to less than one metre of GMSL-rise contribution from the AIS by 2300 under conditions where global temperature rise is limited to 1.5°C (Fig. 2.6).

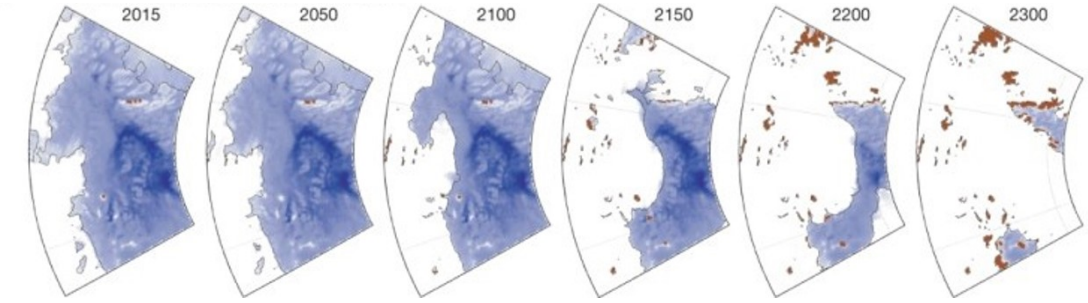

Figure 2.5: Future ice-sheet simulations from 2015 to 2300 over the Amundsen Sea sector following the more fossil-fuel intensive scenario (RCP 8.5; DeConto and Pollard, 2016; their Figure 4).

Recent modelling efforts aimed at assessing the evolution of the AIS with respect to the Paris Agreement target of limiting global temperature rise to 2°C or less, has shown that AIS mass loss is likely to continue at the same pace as current rates throughout the 21st Century, which would represent up to 9 cm of GMSL rise in 2100 (DeConto et al., 2021; Fig. 2.6). Scenarios consistent with current policies, which would likely lead to a global rise in temperatures of 3°C, would result in a rapid increase in ice-mass loss beyond 2060 equivalent to 0.5 cm of GMSL rise per year to 2100, which represents an order of magnitude greater than current rates (DeConto et al., 2021; Fig. 2.6). This rapid mass loss is partly dominated by the collapse of Thwaites Glacier in most ice-sheet models, which is likely to lead to the destabilisation of the WAIS in the later part of the 21st Century (DeConto and Pollard, 2016; Seroussi et al., 2020; DeConto et al., 2021; IPCC AR6, 2021; Fig. 2.5). Failure to meet the Paris Agreement temperature and emission targets would lead to increased thinning across the AIS from the lack of buttressing due to

ice-shelves disintegration, and result quickly in rapid collapse of the ice sheet and unstoppable GMSL rise equivalent to 34 cm by 2100 and 9.6 m by 2300 (DeConto et al., 2021; Figs. 2.5-2.6).

It is worth noting that numerical model predictions of the evolution of the AIS over the next few centuries do not all agree with each other in terms of the magnitude of change (IPCC AR6, 2021). This is partly due to uncertainties in model parameters used to represent the physical system (e.g. bedrock topography or geothermal heat flux), model resolutions which are too coarse to reproduce small-scale processes at the grounding line, uncertainties in future CO_2 emissions, and uncertainties in modern and geochronological measurements used to constrain the models, amongst others (Bracegirdle et al., 2019; Pattyn and Morlighem; 2020, Seroussi et al., 2020; DeConto et al., 2021; Sutter et al., 2021). In particular, the climate forcings used in ice-sheet models lead to large uncertainties in the response of the AIS to future climate change (Robel et al., 2019; Seroussi et al., 2020). However, despite varying degrees of uncertainty in future model projections, most model predictions indicate that under all emission scenarios, the AIS will lose mass and contribute significantly to sea-level rise in the future, with most thinning concentrated over West Antarctica's Amundsen Sea Sector and East Antarctica's Totten Glacier (IPCC AR6, 2021).

2.2 Traditional methods for inferring past changes over Antarctica

The downward trend in the current mass balance of ice sheets have precipitated the development of complex ice-sheet models that rely on in situ data to calibrate model predictions (Bracegirdle et al., 2019). Such data may come from past estimates of accumulation and temperature rates, ice thickness, or ice-sheet extent.

Previous assessments of past ice-sheet conditions have primarily come from surface exposure dating of bedrock and glacially transported debris on nunataks and mountain ranges, or from sediment cores collected either offshore of the current margins of the AIS or by drilling below the current ice sheet (Jones et al., 2022; Siegert et al., 2022). The results from these geochronological records have provided more insights into how the ice sheet evolved over past glacial cycles, including changes in grounding-line position during the Holocene and beyond (Bentley et al., 2010; Hillenbrand et al., 2013; 2017; Kingslake et al., 2018; Venturelli et al., 2020; Neuhaus et al., 2021; Sproson et al., 2022), as well as changes in past

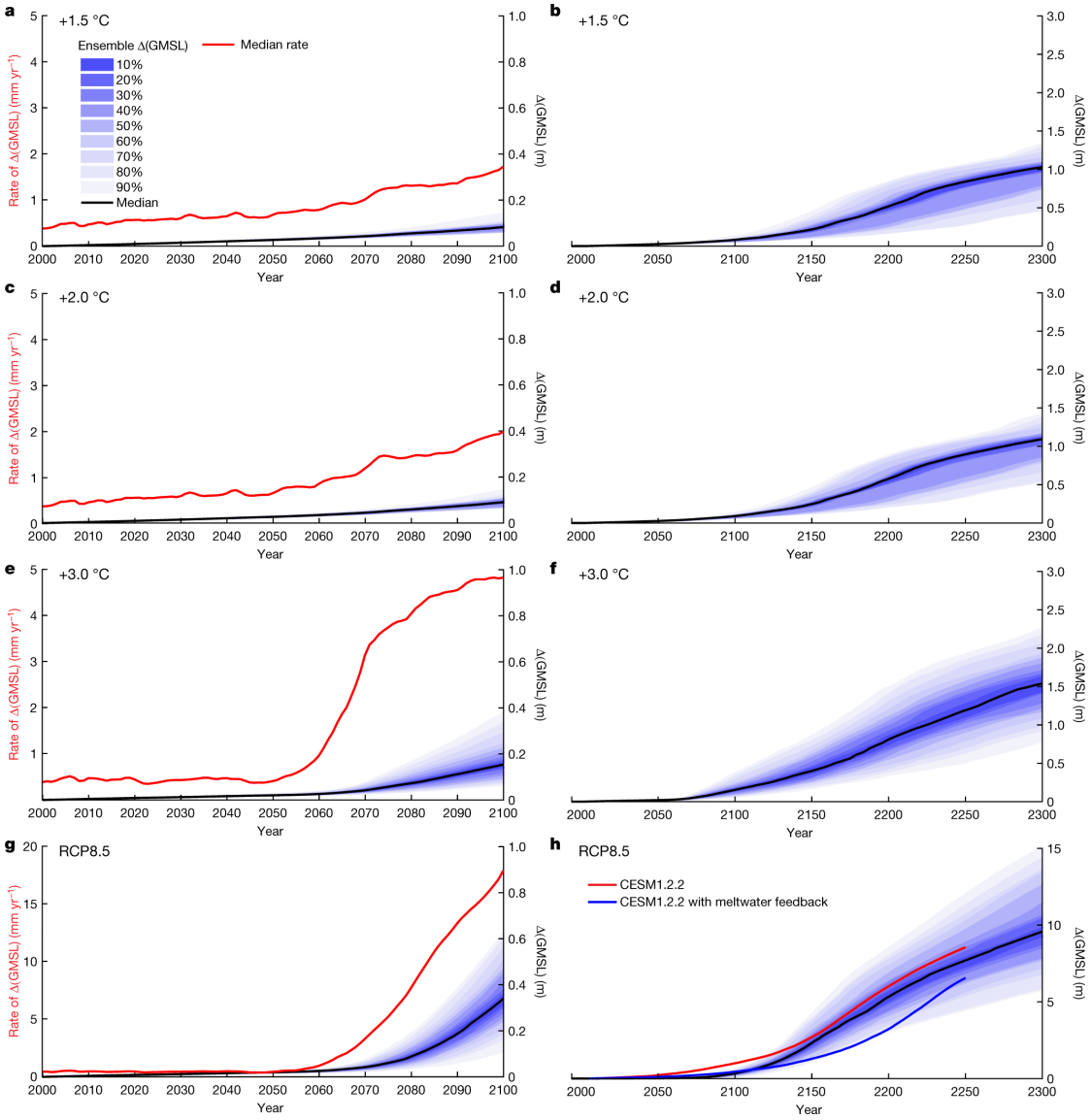

Figure 2.6: Future AIS contribution to GMSL by 2300 under different RCP scenarios (DeConto et al., 2021; their Figure 1). (a, c, e and g) and (b, e, f and h) show AIS contribution to GMSL by 2100 and 2300 respectively. The red line in (a, c, e and g) shows median rates of GMSL rise. (a-b), (c-d), (e-f), and (g-h) represent the future AIS contribution to GMSL based on emissions consistent with a rise in global temperatures of 1.5°C (a-b), 2°C (c-d), 3°C (e-f), and RCP 8.5 emission scenario (g-h), respectively. The blue and red lines in (h) represent the additional RCP 8.5 simulations with and without Antarctic meltwater feedback (see DeConto et al. (2021) for more details).

ice-sheet elevations and ensuing sea-level rise contributions (Johnson et al., 2008; 2014; Hein et al., 2016a; 2016b; Nicholls et al., 2019; Spector et al., 2019; Johnson

et al., 2020; Balco et al., 2023).

The extraction of deep ice cores from Antarctica have provided long-term records of temperature and CO_2 concentrations, which have broadened our understanding of past global climate and atmospheric compositions (Petit et al., 1999; EPICA Community Members, 2004; WAIS Divide Project Members, 2013), and provided more insights into Antarctic-wide changes of past temperature and accumulation rates, which have been used in ice-sheet models to estimate past ice-sheet configurations (Ritz et al., 2001; Fudge et al., 2016; Holloway et al., 2016; Koutnik et al., 2016; Werner et al., 2018).

However, whilst these geochronological measurements provide information at relatively high-temporal resolutions, their spatial representativeness is often limited since they are taken at one location, thus making their results challenging to extrapolate across a wider catchment or region, and potentially introducing a bias when using them as a boundary conditions in numerical ice-sheet models to recreate past ice-sheet wide changes (Koutnik et al., 2016; Cavitte et al., 2022). Additionally, data from surface exposure dating and sediment cores acquired over previously glaciated areas only provide information on past boundary conditions of the retreated ice sheet, as opposed to a terrestrial record of the current ice sheet.

One alternative technique for extracting past records of ice-sheet change on large-spatial scales come from ice-penetrating radars mounted on airborne platforms, hereafter referred to as Radio-Echo Sounding (RES).

2.3 RES as a means to infer current and past ice-sheet processes

RES was first used as a means of locating and mapping the ice-bed interface beneath ice sheets, with the aim of constraining ice volume and bedrock morphology (Robin et al., 1970; Evans et al., 1972; Robin et al., 1977; Drewry et al., 1982; Bingham and Siegert, 2007). However, it was quickly discovered that RES data also contained significant englacial layering that result primarily from acidity contrasts caused by past volcanic activities, which RES systems are sensitive to due to changes in the conductivity of the ice (Harrison, 1973; Hammer, 1977; 1980; Millar, 1981; 1982). This made RES an essential tool for quantifying current ice-sheet volume and flow, as well as for constraining past ice-sheet conditions via the interrogation of englacial layering (Siegert, 1999; Plewes and Hubbard, 2001; Bingham and Siegert, 2007).

The first large-scale RES surveys of Antarctica were conducted between 1967 and 1979 by a consortium from the Scott Polar Research Institute (SPRI), the United States National Science Foundation and the Technical University of Denmark (Fig. 2.7), resulting in the acquisition of 400,000 line-km of RES data at multiple frequencies optimised to observe bedrock topography (60 MHz frequency) and near-surface englacial layering (300 MHz frequency) (Drewry et al., 1982; Siegert, 1999; Schroeder et al., 2019). These surveys were so successful that by the early 1980s, it is estimated that approximately 50% of the ice sheet had at least some RES measurement within 50 to 100 km (Drewry et al., 1982; Siegert, 1999). Whilst significant in terms of data coverage, the data from these surveys were primarily acquired on optical films and video tapes using analogue radar systems and lacked precise navigational techniques; with initial navigation based on basic imagery and dead reckoning prior to the 1970s but transitioning quickly to the use of inertial navigation systems with a reported accuracy of 5 km (Drewry et al., 1982; Schroeder et al., 2019; 2020).

The end of the 20th Century marked a significant shift in RES data acquisition over Antarctica, primarily through the improvement of surveying equipment, which included the use of modern digital RES equipment and Global Positioning Systems (GPS) for navigational purposes (Schroeder et al., 2020). This led to a significant increase in the acquisition of RES data over Antarctica, with the primary aim to characterise bed properties below key glacier catchments, such as over Pine Island Glacier (Vaughan et al., 2006; Bingham et al., 2017; Davies et al., 2018), Thwaites and Smith Glaciers (Holt et al., 2006), the Bailey-Slessor sector (Rippin et al., 2004; Bamber et al., 2006), the Weddell Sea sector (Ross et al., 2012; Jordan et al., 2013; Rippin et al., 2014; Siegert et al., 2016), the Ellsworth Subglacial Highlands (Ross et al., 2014), the Ross Sea and Marie Byrd Land sectors (Gades et al., 2000; Blankenship et al., 2001; Luyendyk et al., 2003; Studinger et al., 2004), and Dronning Maud Land (Nixdorf et al., 1999), amongst others. Following the long-term funding of ice-sheet-wide RES surveying in the mid-2000s, large-scale missions such as NASA Operation IceBridge (OIB) and the International Collaborative Exploration of the Cryosphere through Airborne Profiling (ICECAP) surveys began acquiring widespread RES data over large sectors of West and East Antarctica, as well as over the grounding line of the Antarctic Peninsula (Young et al., 2011; MacGregor et al., 2021). Together, the extensive RES coverage acquired over the last five decades made RES second to satellite data in providing spatially extensive observations of the ice sheet.

Whilst the initial focus of most of these campaigns was to constrain bedrock



Figure 2.7: Photographs showing the evolution of airborne RES data acquisition over Antarctica. (a) LC-130 aircraft used during the 1970s RES surveys of Antarctica with the SPRI radar antennas mounted on the wings (credit: Charles Swithinbank; shared by Martin Siegert); (b) Twin-otter aircraft equipped with the University of Texas Institute for Geophysics (UTIG)'s High Capability Airborne Radar Sounder (HiCARS) system during the 2004-2005 Airborne Geophysical Survey of the Amundsen Embayment (AGASEA) survey of Thwaites Glacier (credit: Matt Fields-Johnson; shared by Duncan Young); (c) Basler aircraft during the 2008-2009 ICECAP survey using UTIG's HiCARS RES system (credit: Andrew Wright; shared by Martin Siegert); (d) Twin-otter aircraft equipped with the British Antarctic Survey (BAS)'s Polarimetric Airborne Survey INstrument (PASIN) system flying over the Antarctic Peninsula (credit: Carl Robinson).

topography and ice-sheet volume, the use of RES data quickly evolved to other scientific applications, including constraining the roughness of the basal interface and its relation to ice flow under large Antarctic ice streams (Siegert et al., 2004b, Taylor et al., 2004; Rippin et al., 2006a; Bingham et al., 2007; Bingham and Siegert, 2009; Rippin et al., 2011; 2014; Bingham et al., 2015; Eisen et al., 2020), constraining ice-crystal fabric orientation to assess ice deformation from polarimetric RES techniques (Matsuoka et al., 2012; Das et al., 2020; Young et al., 2021), determining the wetness and material property of the basal interface via the assessment of bed reflectivities (Gades et al., 2000; Catania et al., 2003; Ashmore et al., 2014; Chu et al., 2020), characterising the subglacial hydrological system of ice shelves and ice streams (Jordan et al., 2010; Wright et al., 2012; Le Brocq et al., 2013; Schroeder et al., 2013; Rose et al., 2014; Drews et al., 2017; Dow et al., 2022), and identifying the presence of subglacial water bodies (Siegert et al., 2000; Carter et al., 2007; Wright et al., 2014; Young et al., 2016; Diez et al., 2019; Napoleoni et al., 2020). More recently, Schroeder et al. (2019) showed that analogue RES data acquired in the 1970s can be used to provide a multidecadal-scale record of ice-sheet change from RES data alone, with a particular focus on reconstructing the history of basal channels and ice-shelf stability between older and more recent RES profiles. Importantly for this thesis, RES data have also been used extensively to study englacial structures with the aim to better understand past ice-flow processes and climatic conditions (Harisson, 1973; Clough et al., 1977; Siegert, 1999). I come back to these in more detail in Section 2.3.1.

The large amount of data originating from these surveys led to the development of gridded maps of bed elevation and ice thickness, starting with the SPRI Glaciology and Geophysical Folio series (Drewry, 1983). This eventually led to the Bedmap1 data product (Lythe et al., 2001), which provided, for the first time, digital gridded datasets of bed elevations and ice thickness acquired from RES and seismic data over Antarctica. The increase in new RES surveys over the AIS led to subsequent iterations of this dataset, namely Bedmap2 (Fretwell et al., 2013) and BedMachine (Morlighem et al., 2017). Each iteration of these gridded products quickly became cornerstone datasets for glaciological and geophysical studies of the AIS, especially ice-sheet models that use the interpolated bedrock topography and ice thickness data as boundary conditions in their models (e.g. Pollard and DeConto, 2009; Pattyn, 2010; Seroussi et al., 2019; DeConto et al., 2021; Sutter et al., 2021). These products also motivated the acquisition of new RES surveys aimed at filling large gaps in RES data coverage over the AIS, including over Recovery Glacier (Diez et al., 2018) and Princess Elizabeth Land (Cui et al., 2020), which are now both included in the updated iteration of the Bedmap product (namely Bedmap3; Frémand et al., 2023).

Whilst these surveys have improved considerably our understanding of bed properties and ice-dynamical processes over Antarctica, a relatively under-utilised resource originating from RES data are Internal Reflecting Horizons (IRHs). Crucially, and in a similar method to the interpolation of bed elevations and ice thickness data in Bedmap and BedMachine, IRHs extracted from RES data can be gridded to provide spatially extensive boundary conditions for ice-sheet models (e.g. Sutter et al., 2021). However, until now, the tracing and interpretation of IRHs over the AIS has so far been restricted to individual glacier catchments and RES surveys (e.g. Leysinger-Vieli et al., 2004; Cavitte et al., 2016; Muldoon et al., 2018; Winter et al., 2019; Ashmore et al., 2020a; Beem et al., 2021). The following sections provide a summary of their applications to date, and review the necessary requirements for making these an essential dataset for future glaciological applications, namely with regards to the development of an ice-sheet wide age-depth model, as motivated by the AntArchitecture initiative (Sect. 1.1.2).

2.3.1 Internal Reflecting Horizons in RES data

A powerful complementary resource to geochronological measurements such as sediment and ice cores, or surface exposure dating, are IRHs as imaged by RES techniques (Fig. 2.8 - 2.9; Siegert, 1999; Bingham and Siegert, 2007). The evidence for englacial reflections within the ice, as represented by echoes from the incoming radar pulse, can be interpreted as changes in the dielectric properties of ice with depth, which are influenced by contrasts in ice density, electrical conductivity, or ice-crystal fabric (Harrison, 1973; Millar, 1981; Siegert, 1999; Bingham and Siegert, 2007).

In the shallower part of the ice column, most englacial reflections are associated with variations in ice density, represented by contrasts between the snow and firn, and occasional ice lenses (Moore, 1988). In a thick ice sheet ($>$ 3.5 km), englacial reflections found between $\sim$1 km and 3 km under the surface mainly originate from variations in the conductivity of the ice, resulting from fluctuations in acidity mainly associated with volcanic ash deposited on the surface of the ice sheet during snowfall events (Millar, 1981). In very deep ice ($>$3 km), large englacial stresses can affect the orientation of crystal fabric (i.e. anisotropy) which lead to changes in the permittivity of the ice, which RES systems are sensitive to (Harrison, 1973). Crucially, whilst reflections found in the shallow firn and the middle part of the ice thickness can be considered isochronous (i.e. palaeosurfaces of the same age in the horizontal direction; Siegert, 1999), most reflections found in the deeper part of the ice column are not (King, 2009; Ross et al., 2020; Das et al., 2020; Young et al., 2021). In this thesis, I use the terms deeper IRHs to refer to

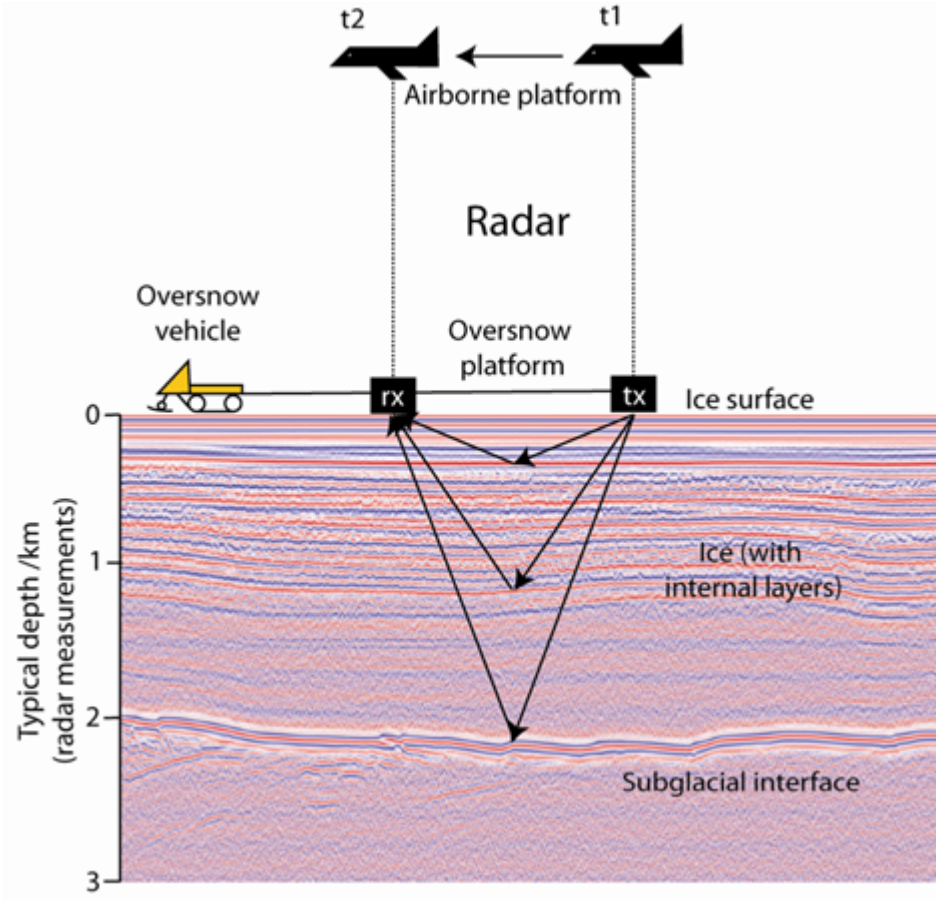

Figure 2.8: Diagram demonstrating the use of ground-based and airborne RES systems to obtain information on IRHs and bed characteristics. Rx and Tx refer to the receiving and transmitting antennas respectively. Figure adapted from Bingham et al. (2010; their Figure 3).

isochronous englacial reflections found in the middle part of the ice column, and ignore englacial reflections caused by variations in density in the first few hundred metres of the ice column, or variations in ice permittivity in the bottom part of the ice column.

When dated precisely at ice cores, IRHs can provide a high temporal and spatial record of accumulation rates, basal melting, and ice flow (Siegert, 2003; Carter et al., 2009; Leysinger-Vieli et al., 2011; Cavitte et al., 2018), thus making them important palaeo proxies for assessing past ice-sheet changes. For example, changes in past ice flow or basal melting can leave englacial imprints on IRH shape, which are often characterised by a divergence between IRH geometries and that of the surface topography above or bed topography below, or in extreme cases in

a complete erasure of their signature in the ice (Jacobel et al., 2000; Fahnsetock et al., 2001a; Siegert et al., 2003; Rippin et al., 2006b; Catania et al., 2010). In particular, the ability to trace dated IRHs across hundreds of kilometres makes them a very powerful tool for extracting spatially extensive records of past ice-sheet configurations (Siegert, 1999), which in turn makes them a suitable guide to compare boundary forcings in numerical ice-sheet models (Sutter et al., 2021). However, despite their potential, well-dated IRHs remain poorly constrained over Antarctica, mainly due to the labour-intensive aspect of digitising individual IRHs across large sections of RES profiles, the relatively low number of deep ice cores across the continent, and the large amount of data providers which complicates the access to RES data optimised for the tracing of IRHs.

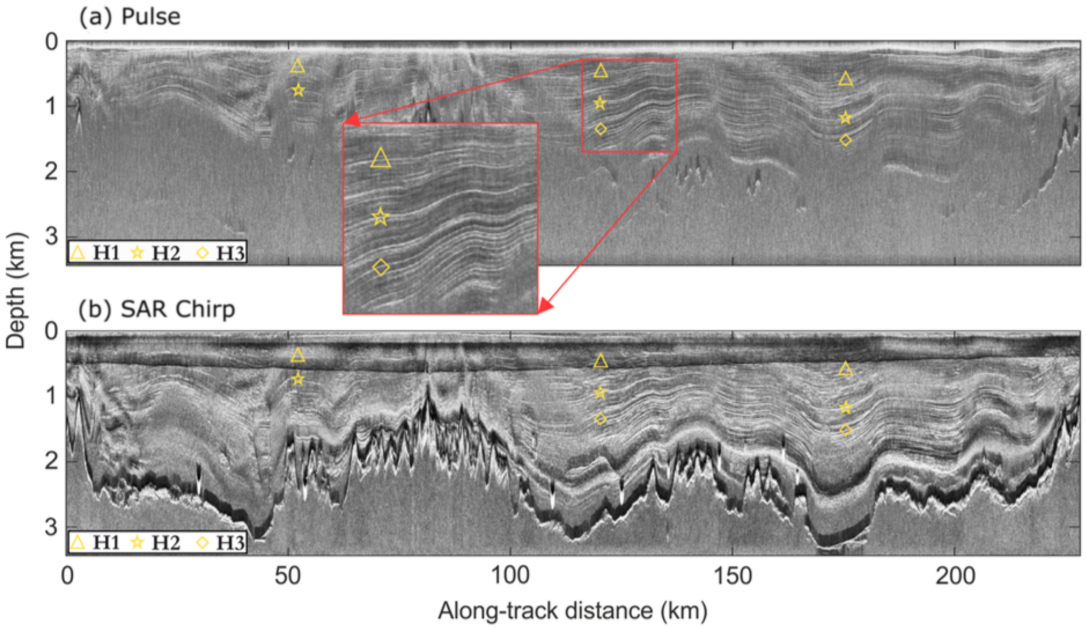

Figure 2.9: Radargram from a 200-km segment of the Institute-Möller Antarctic Funding Initiative (IMAFI) survey by BAS using (a) the PASIN shallow-sounding pulse and (b) the PASIN deep-sounding chirp. The red rectangle shows a zoomed inset of the IRH stratigraphy on the pulse radargram, and the yellow symbols represent three prominent IRHs traced over the IMIS catchment by Ashmore et al. (2020a). Figure adapted from Ashmore et al. (2020a; their Figure 1)

Previous mapping and dating of IRHs has primarily focused on the slow-flowing parts of the East Antarctic plateau, where several deep ice-core stratigraphies exist (Siegert et al., 1998; Siegert, 2003; MacGregor et al., 2009; Leysinger-Vieli et al., 2011; Cavitte et al., 2016; Parrenin et al., 2017; Winter et al., 2019; Beem et al., 2021). Over the WAIS, IRH tracing has primarily been restricted to ground-based

RES data (Jacobel et al., 2005; Neumann et al., 2008; Woodward and King, 2009; Koutnik et al., 2016; Holschuh et al., 2018), due to the sparse coverage of deep ice cores and the faster flowing conditions of ice streams draining the WAIS, which can affect the horizontal continuity of IRHs. More recently, and using extensive airborne RES data, Karlsson et al. (2014) and Ashmore et al. (2020a) identified three IRHs over the slow-flowing parts of Pine Island Glacier and IMIS (Fig. 2.9), however the lack of suitable RES profiles connecting these two catchments to deep ice-core stratigraphies precluded them from precisely dating the IRHs. Until now, the only spatially extensive and precisely dated IRH stratigraphy over the WAIS is of Thwaites Glacier, where Muldoon et al. (2018) were able to identify four IRHs spanning the Holocene and late Pleistocene (4.7-24.9 ka) periods and which they dated precisely using the Byrd and WAIS Divide ice cores.

Motivated by the AntArchitecture initiative, increasing attention is now being placed on extracting further IRH stratigraphies over Antarctica to improve our understanding of past ice-sheet changes, particularly over sensitive sectors of the WAIS and EAIS. The following two sub-sections explore the findings from previous IRH studies; focusing firstly on the use of IRHs to constrain past accumulation rates (Sect. 2.3.1.1), and secondly on the use of IRHs to constrain past ice-dynamical processes (Sect. 2.3.1.2).

2.3.1.1 IRHs to constrain past accumulation rates

Records of past accumulation rates typically come from reconstructions of water-stable isotope records or from annual layer counting in ice cores (Fudge et al., 2016). Whilst these are useful in providing a highly accurate temporal record of accumulation rates, it remains unclear how representative past accumulation rates reconstructed at ice-core sites are of a wider region (Fudge et al., 2016; Koutnik et al., 2016; Dattler et al., 2019; Cavitte et al., 2022).

Promisingly, and when employed with ice-core stratigraphies, spatially extensive IRHs can be used to extend age-depth relationships away from ice cores and thus reconstruct past accumulation rates over large spatial scales (Whillans, 1976; Nereson et al., 2000; Spikes et al., 2004; Siegert, 2003; Rotschky et al., 2004; Eisen et al., 2008; Verfaillie et al., 2012). Using shallow firn cores and spatially extensive IRHs in the upper 100 metres of the ice thickness, Medley et al., (2013; 2014) showed that gridded reanalysis and modelled Surface Mass Balance (SMB) products over Pine Island and Thwaites Glaciers agreed well with reconstructed accumulation estimates derived from IRHs at regional scales. Follow-up studies employing similar methods, but this time using ground-based RES systems on ice rises in East Antarctica, showed that SMB rates derived at ice cores are only

representative of a small surface area (∼250-500 m radius) (Cavitte et al., 2022). Together, these studies show that IRHs can be used as a benchmark to constrain SMB estimates derived from climate models and ice-core records.

Whilst shallow IRHs can be used to constrain decadal to centennial accumulation rates with relatively little complexity (Eisen et al., 2008; Verfaillie et al., 2012; Medley et al., 2013; 2014; Cavitte et al., 2022), extracting millennial accumulation rates from deeper IRHs requires the use of complex ice-flow models that account for the effects of vertical and horizontal strain rates, or basal melting, on the position of IRHs in the ice thickness (Waddington et al., 2007). A particular challenge associated with this approach is that it is an ill-posed inverse problem, as both changes in ice flow and accumulation-rate variations can affect IRH geometries (Waddington et al., 2007). Indeed, in an inverse problem, the existing data result from known processes (e.g. surface speeds, ice thickness, layer-depth geometries) which depend on an unknown process or parameter value (e.g. accumulation-rate history) that we wish to calculate (Waddington et al., 2007). In order to solve this inverse problem, we need both a forward algorithm (e.g. an ice-flow model) and an inverse algorithm. The forward algorithm can be provided with initial guesses on the unknown boundary conditions to generate an estimate of the corresponding values (Waddington et al., 2007). The inverse algorithm then evaluates the misfit between the modelled observables and the existing data in order to estimate the best set of unknown parameter values (Waddington et al., 2007). Ice-flow models of different complexities have been developed to account for these challenges, including relatively simple one-dimensional (1-D) ice-flow models that account for vertical strain rates and basal melting (Nye, 1957; Dansgaard and Johnsen, 1969; Fahnestock et al., 2001b; Parrenin et al., 2007; MacGregor et al., 2016), to more physically complete multi-dimensional models that can account for vertical and horizontal advection of IRHs as a result of convergent or divergent flow patterns (Leysinger-Vieli et al., 2007; Waddington et al., 2007; Hindmarsh et al., 2009; Karlsson et al., 2014; Koutnik et al., 2016). Over Antarctica, 1-D models have been used primarily in relatively slow-flowing areas of the ice sheet where such disturbances are limited (Siegert, 2003; Leysinger-Vieli et al., 2004; Siegert and Payne, 2004; Waddington et al., 2007), whereas more complex 2-D and 3-D models have been used to model accumulation rates from deeper IRHs, as well as in faster-flow areas or where basal melting is particularly high (Neumann et al., 2008; MacGregor et al., 2009; Leysinger-Vieli et al., 2011; Koutnik et al., 2016).

Whilst choosing an appropriate ice-flow model is essential in order to recover realistic accumulation rates, another factor that can affect the accuracy of those estimates is how precisely an IRH has been dated. Generally, this can be done us-

ing two approaches; either using the accurate age-depth relationship derived from layer counting at an ice core (e.g. Sigl et al., 2016), or by using simple 1-D ice-flow models to provide an approximate age-range (e.g. Dansgaard and Johnsen, 1969). Dating IRHs at ice cores is the most accurate alternative, as it reduces age uncertainties to less than a few decades for shallower IRHs and up to a few centuries for deeper IRHs (1% and 3% for ages ranging between 0–15 ka and 15–31 ka, respectively; Sigl et al., 2016), whereas ice-flow models can only provide an approximate age envelope which can be as much as an order of magnitude more than for ice-core dated IRHs (e.g. Karlson et al., 2014; Ashmore et al., 2020a).

Past reconstructions of accumulation rates over the EAIS have previously been calculated from deeper IRHs extracted from large RES surveys situated in the vicinity of deep ice cores, namely Vostok and EPICA Dome C. Using IRHs traced on SPRI-acquired data from the 1970s and a 1-D ice-flow model, Siegert (2003) and Leysinger-Vieli et al. (2004) showed that accumulation rates were substantially greater during the Holocene than during full glacial conditions over this sector of East Antarctica, with rates of 3.0-5.5 cm a^{-1} during the last 10 ka compared with 1.4-1.8 cm a^{-1} for the period 125-15 ka BP (Siegert, 2003). Crucially, they also showed that no spatial changes in accumulation patterns occurred over this sector across glacial-interglacial cycles (Siegert, 2003; Leysinger-Vieli et al., 2004). Using the same RES data, but also employing a 3-D numerical ice-flow model, Leysinger-Vieli et al. (2011) showed that spatial accumulation patterns were similar to the present at 17.5 ka but differed for deeper IRHs from beyond the current interglacial period. More recently, Cavitte et al. (2018) used a series of well-dated IRHs (ranging from 10.0 to 73.4 ka), and a 1-D ice-flow model that incorporates a basal melting parameter, to estimate past accumulation rates and patterns over EPICA Dome C Ice Core. They showed that accumulation-rate patterns over the EAIS plateau have been spatially stable over the last 73 ka, reflecting current modelled and observed precipitation estimates.

In contrast to the EAIS, reconstructions of accumulation rates from IRHs over the WAIS have primarily come from spatially targeted RES surveys (Siegert and Payne, 2004; Neumann et al., 2008; Koutnik et al., 2016). Using a 1-D model and a single RES profile connecting the coastal area of the Amundsen Sea sector and the Amundsen-Weddell Divide, Siegert and Payne (2004) showed that accumulation rates over the WAIS have not changed significantly over the last 3.1 ka compared to today, but that accumulation rates between 16-6.4 ka were around half that of the present. Using more complex 2-D models, Neumann et al. (2008), and later Koutnik et al. (2016) using the new WAIS Divide ice-core record, showed that accumulation rates over the Amundsen-Weddell Divide were 40% higher than

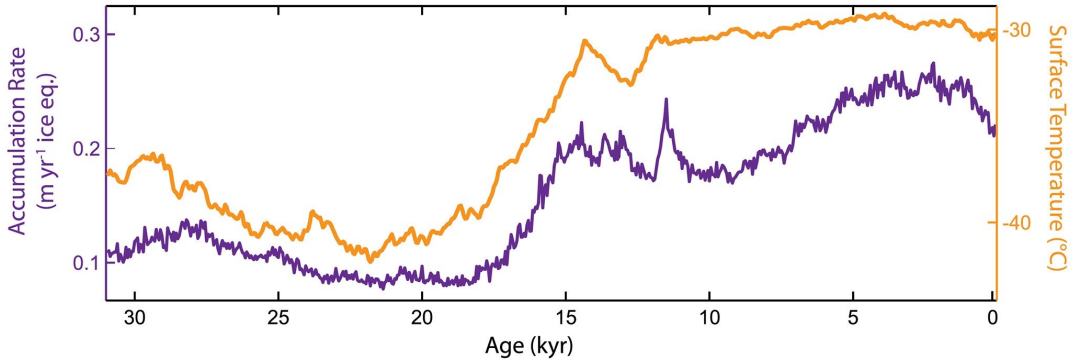

Figure 2.10: Reconstruction of accumulation and temperature rates from the WAIS Divide ice core between 31 ka and the present. Figure adapted from Fudge et al. (2016; their Figure 2).

present rates between 9-2 ka BP, and similar to today in the last 2 ka. In particular, Koutnik et al. (2016) showed that these higher Holocene accumulation rates compared to the present would likely lead to an increase in ice thickness of tens of metres at the divide. Providing that dynamic losses further downstream (i.e. from melting and/or calving) did not counteract this thickening at the divide, this study points to the potential for the ice sheet interior to have thickened over a relatively short period of time from accumulation rate alone, with possible wider implications for changes in ice-sheet configuration during the Holocene (Koutnik et al., 2016). Over Pine Island Glacier, and this time using a 3-D ice-flow model, Karlsson et al. (2014) reported that at least two changes in accumulation patterns occurred during the LGM-Holocene transition, at a time when the WAIS was retreating from its maximal ice-sheet extent. Together, these studies point to the possibility for significant variability in accumulation rates since the LGM in certain parts of the WAIS. However, so far, these findings have lacked a wider regional setting, which has restricted our understanding of past changes in spatial accumulation patterns and rates across the wider WAIS. Evidence from the WAIS Divide ice core shows that accumulation rates varied considerably during the Holocene, with up to 40% more accumulation between the early and late Holocene (Fudge et al., 2016; Koutnik et al., 2016; Fig. 2.10) compared with present rates. It is therefore critical to assess whether this variability is observed across wider swaths of the WAIS, or whether it reflects local conditions in the vicinity of the ice core. This is important, because higher accumulation rates in the past compared to the present over large spatial scales may delay, or even reverse, the retreat of the WAIS after the LGM (Koutnik et al., 2016; Kingslake et al., 2018), which may have wider implications for the contribution of the WAIS to past sea-level rise (Neuhaus et al., 2021).

2.3.1.2 IRHs to constrain past ice-dynamical processes

Aside from serving as a useful proxy for estimating past accumulation rates, IRHs also hold crucial information on past ice flow and ice-sheet dynamics. For example, using IRHs over the Greenland Ice Sheet and a 1-D ice-flow model, MacGregor et al. (2016) showed that the ice-sheet interior is slower now than it was during the Holocene, partly as a result of higher Holocene accumulation rates and the presence of a layer of softer ice from the last glacial period buried under stiffer Holocene ice, thus resulting in current ice-sheet thickening in the interior. This study demonstrates that a discrepancy between IRH-derived balance velocities for the past 9 ka and the current ice-sheet configuration is able to explain the current dominant pattern of ice-sheet thickening and ice-flow deceleration in the interior, which is large enough to affect Greenland-wide interpretations of ongoing mass loss observed by altimetry studies (MacGregor et al., 2016). In comparison to Antarctica, however, IRH stratigraphies over Greenland are now well constrained, partly due to there being only one data provider which facilitates access to consistent data onto which IRHs can be traced, and as a result of the large amount of deep ice cores over Greenland which facilitate the precise dating of IRHs (MacGregor et al., 2015). By comprehensively incorporating IRHs into ice-flow models to assess ice-dynamical changes over Greenland, this study provides a motivation for further work to extract an age-depth model of the AIS so that it can be used as a proxy for assessing past ice-dynamical changes over large spatial scales.

Previous studies employing IRHs over the AIS have shown that IRHs can be used as a reliable indicator of current or past changes in ice-sheet dynamic, albeit on much smaller spatial scales (Jacobel et al., 1993; Bell et al., 1998; Siegert et al., 2004a). Indeed, whereas past accumulation rates leave little imprint on IRH geometries aside from potential changes in layer thickness, changes in past ice flow and basal melting can significantly alter IRH geometries. Assessing their influence is primarily done by evaluating the continuity, disturbance, or absence of englacial layering in the ice column, which can be caused by fast or slow flowing ice or alternatively by the complete erasure of their signature in the ice as a result of basal melting (Fahnsetock et al., 2001a; Siegert et al., 2003; Rippin et al., 2006b; Catania et al., 2010). For example, the interpretation of buried crevasses, relict shear margins and highly disturbed IRHs underlying continuous layering over Kamb Ice Stream were interpreted as evidence for the shutdown of the ice stream ∼150 years ago (Retzlaff and Bentley, 1993; Conway et al., 2002; Catania et al., 2006).

Other studies have also linked the continuity of IRHs with current or past ice-flow conditions over key glacier catchments, whereby continuous bed-parallel IRHs typically correspond to areas where ice-flow speeds are relatively slow, whereas

buckled or distorted IRHs typically correspond to areas experiencing faster flow conditions such as the main trunk and tributaries of marine-terminating ice streams (Rippin et al., 2006b; Bingham et al., 2007; Karlsson et al., 2009; Woodward and King, 2009; Bingham et al., 2015; Holschuh et al., 2018). The continuity of englacial layering was initially assessed using manual classification methods (Siegert et al., 2003; Rippin et al., 2003b; Bingham et al., 2007; Karlsson et al., 2009; 2012; Fig. 2.11a-c), which assigned IRHs into three categories: (1) continuous, (2) discontinuous, or (3) absent, as per Siegert et al. (2003):

1. **Continuous:** well-preserved and continuous layering which can be traced for large distances without significant gaps in the horizontal direction. These layers are typically flat or follow the underlying bed topography. The amplitudes of all undulations (or wavelengths) are less than those of the bed.

2. **Discontinuous:** disrupted layering that do not follow the underlying bed topography and contain significant gaps which prevent them from being traced for long distances. At times, these can be overlain by continuous englacial layering in the shallow part of the ice column. Critically, the amplitudes of the short wavelengths are higher than those of the bed.

3. **Absent:** complete lack of englacial layering at all depths. This may be the result of a loss in radio-wave power caused by a sudden change in aircraft altitude, or alternatively due to the dynamical effects of fast flow or basal melting.

Using these criteria, Siegert et al. (2003) showed that discontinuous and continuous englacial layering occurs respectively inside and outside of all of the tributaries of Bindschadler Ice Stream (West Antarctica), thus suggesting that the recent ice-flow reconfiguration of the neighbouring Kamb Ice Stream did not affect the configuration of Bindschadler Ice Stream. Using the same analogue RES data over ice streams draining the Wilkes Subglacial Basin (East Antarctica) and calculations of balance velocities, Rippin et al. (2003b) showed that disrupted layering is not only found in areas of fast flow (i.e. in the downstream end of fast-flowing ice streams), but also in areas of enhanced flow (i.e. several hundred kilometres upstream of the grounding line). Additionally, they showed that mean balance velocities in areas where englacial layering is disrupted are nearly three times higher than for areas with continuous englacial layering (Rippin et al., 2003b). A similar analysis over South Pole showed that satellite-derived ice-surface speeds correspond to RES profiles characterised by smooth bed topography but disrupted layering (Bingham et al., 2007), thus demonstrating that englacial layering can be used as a proxy for estimating past or present enhanced ice flow in areas where satellite or ground-based surface speed measurements are not available. Further

work assessing the continuity of englacial layers over tributaries of Slessor Glacier (East Antarctica), provided the first evidence of ice-stream reconfiguration in East Antarctica (Rippin et al., 2006b). This study showed that although surface speeds are currently low, the bed topography is smooth and englacial layering is heavily disrupted, which contrasts with evidence at the time that suggested that high basal motions corresponded with areas of smooth bed topography (through subglacial erosion; Rippin et al., 2004), and by extent disrupted englacial layering; whereas low basal motions typically corresponded to rough bed topography, and by extent, continuous layering (Siegert et al., 2003; Bingham et al., 2007). Whilst previous observations of such change had been made at the time for West Antarctica (e.g. Jacobel et al., 2000; Siegert et al., 2003; Ng and Conway, 2004), the ice-flow reconfiguration over this sector is unique in that this tributary is topographically controlled by deep subglacial troughs which would typically prevent lateral migration (Rippin et al., 2006b). By dating a series of IRHs over this sector, they suggested that the switch from fast to slow flow must have occurred after the LGM, likely as a result of ice-sheet thinning and basal freeze-on associated with a warmer EAIS during the Holocene (Rippin et al., 2006b).

While manually classifying IRH continuity is useful for determining spatial patterns in englacial layering and its association with surface speeds, this process is time-consuming and often subjective, as it does not enable the quantitative assessment of, for example, how buckled a layer must be in order to be characterised as continuous or discontinuous (Siegert et al., 2003). To address this challenge, Karlsson et al. (2012) developed a quantitative alternative to assessing the continuity of englacial layering, named the Internal Layer Continuity Index (ILCI; Fig. 2.11). This method classifies the continuity of englacial layers by considering the gradient in the amplitude of A-scope RES profiles (Fig. 2.11d-f). In other words, A-scope profiles from regions of ice dominated by continuous layering will exhibit high-amplitude fluctuations as the radio-wave passes through different boundaries of high dielectric contrast bounded by values of lower reflected relative power, leading to higher ILCI values (Fig. 2.11; Karlsson et al., 2012). In contrast, in A-scope records with low englacial layering, the radio-wave will penetrate through less dielectric boundaries and thus result in lower amplitudes, leading in turn to low ILCI values (Fig. 2.11; Karlsson et al., 2012). After having been tested successfully over a subset of RES data from Pine Island Glacier (Karlsson et al., 2012), the ILCI was subsequently employed over other sectors of East Antarctica (Karlsson et al., 2018; Luo et al., 2020) and West Antarctica (Bingham et al., 2015; Winter et al., 2015). Analysis over the IMIS sector in particular, showed that most of this sector has retained its current configuration at least throughout the Holocene, apart from one area in the upstream section of IMIS where the continuity of englacial layer-

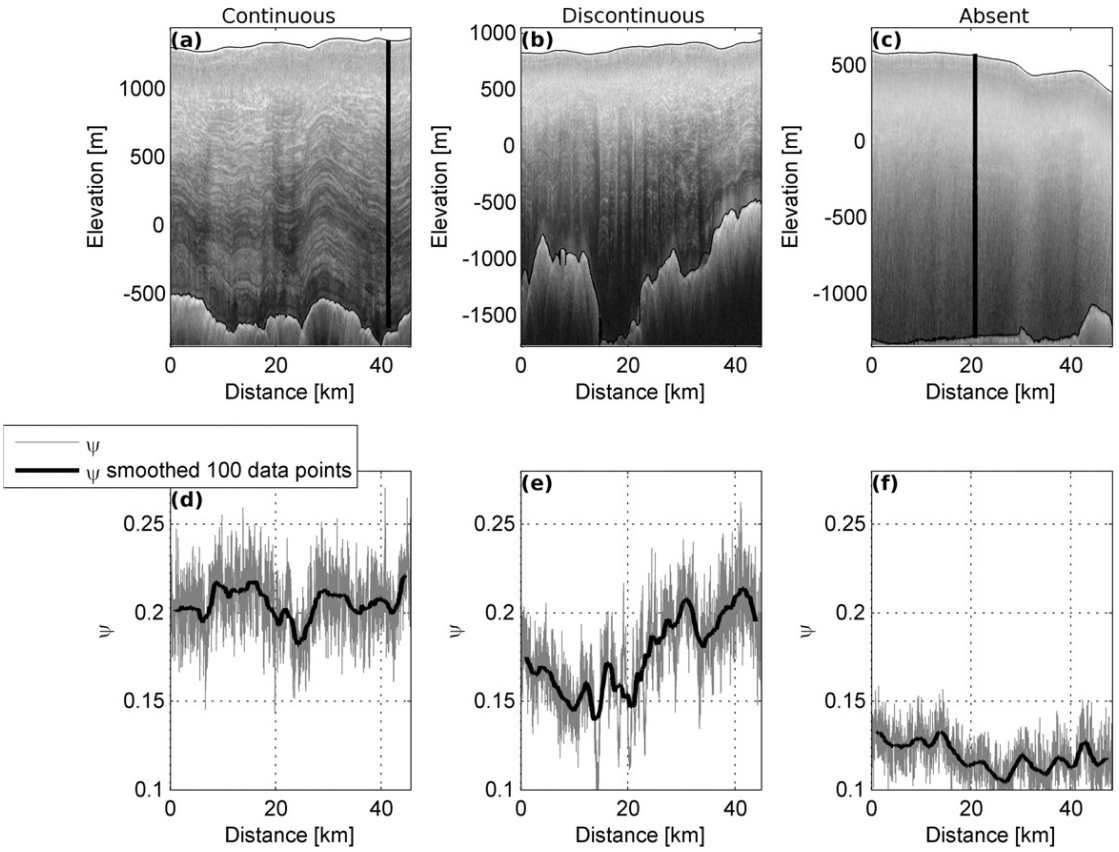

Figure 2.11: Classification of the continuity of englacial layering across Pine Island Glacier. Manual classification for (a) continuous, (b) discontinuous, (c) absent layering in Z-scope profiles. (d-f) Automatic classification of englacial layering using the ILCI, ψ, for each A-scope trace shown in a-c. The grey and black lines in d-f show the non-smoothed and smoothed (running mean of 100 samples) versions. Figure from Karlsson et al. (2012; their Figure 2).

ing is not consistent with depth and does not match current surface flow speeds (Bingham et al., 2015; Winter et al., 2015). Using the same ILCI results, Ashmore et al. (2020a) further demonstrated that the ILCI was statistically higher where manually picked IRHs could be traced over IMIS, thus demonstrating that this method can be reliably used to identify areas where IRH tracing is particularly suitable. This is important, as it enables the rapid identification of RES profiles that guarantee the recovery of an extensive IRH stratigraphy.

Aside from assessing the continuity of englacial layering to infer changes in past ice-flow conditions, the geometry of IRHs has also been used to assess the stability of ice divides across West Antarctica. For example, by comparing GPS measurements of current ice-flow speeds with the shape of IRHs, Ross et al. (2011)

showed that the Amundsen-Weddell Divide has maintained a stable ice-flow regime and ice-divide position throughout the Holocene. Additionally, the stability of ice rises, and by extent, ice divides, has also been assessed using the geometry of IRHs, and in particular whether they exhibit a clear convex-like "Raymond Arch" pattern which is typically found over stable divides (Conway, 1999; Martín et al., 2006; Drews et al., 2015). In contrast, a tilt in the arch's axial plane, or the total absence of an arch on RES data, can be indicative of past divide migration, wider ice-flow reorganisation from nearby ice streams, or alternatively basal sliding from high rates of geothermal heat flux (Nereson et al., 1998; Neumann et al., 2008; Hindmarsh et al., 2011).

Other applications of IRHs to infer past ice-dynamical processes include the assessment of IRH drawdown in the ice column, which have been associated with basal melting caused by high geothermal heat flux beneath Antarctica (Carter et al., 2009; Beem et al., 2018; Jordan et al., 2018; Ross and Siegert, 2020). Lastly, the geometries of IRHs in the East Antarctic plateau have also been interpreted as buried eolian unconformities created by wind scouring at the surface and subsequently buried by snow, which, if dated, could be used as a record of vertical strain rates (Cavitte et al., 2016; Luo et al., 2022).

2.3.2 Data requirements for the development of an ice-sheet wide age-depth model

Whilst the bed elevation and ice thickness data which were incorporated into each iteration of the Bedmap and BedMachine products are now fully accessible to the wider scientific community (Frémand et al., 2023), the underlying RES data which were used to obtain these datasets remain relatively inaccessible (Fig. 2.12). However, these RES data are crucial for extracting an age-depth model of Antarctica, as IRH tracing requires the fully processed Z-scope RES profiles (Fig. 2.11a-c). Efforts have been made in recent years to make these data more accessible. In particular, most of the open-access RES data currently available come from NASA OIB which has made its fully processed RES data freely available on open-access servers (CReSIS, 2018) (Fig. 2.12), which is equivalent to ∼150,000 line-km of data acquired between 2009-2020 (MacGregor et al., 2015). This data release has been highly successful, evidenced by the amount of studies that have used these data for wide-ranging applications, such as investigating ice-sheet stratigraphy, ice-sheet hydrology, as well as ice-dynamical and snow-accumulation processes (MacGregor et al., 2021). Other institutes have also made similar data releases, including UTIG who released large swaths of RES data acquired between 2009 and 2016 over Wilkes Land, Dronning Maud Land and South Pole (Blankenship

et al., 2017; Young et al., 2021); and BAS, who released the RES data associated with the IMAFI survey over the Weddell Sea sector of the WAIS (Siegert et al., 2017) (Fig. 2.12).

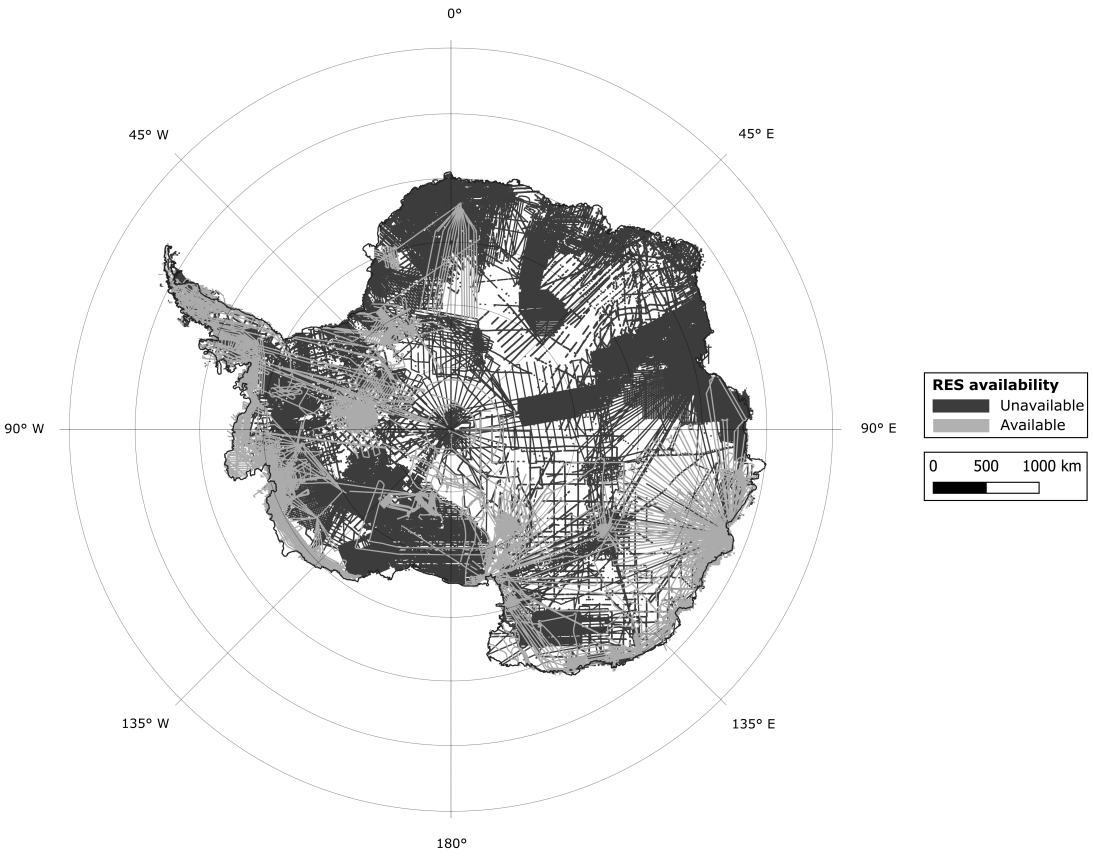

Figure 2.12: Map showing the availability of RES data from Bedmap 1-3. RES Availability is defined as whether the fully processed RES profiles are publically available according to the FAIR data principles on open-access repositories, as of 2021.

However, many RES datasets that cover large parts of East and West Antarctica remain unavailable in open-access formats, which restricts their wider use, particularly for tracing or otherwise characterising the ice-sheet stratigraphy, as envisaged by the AntArchitecture initiative. Of particular relevance to AntArchitecture is whether these RES data contain continuous englacial layering which can be used to leverage information on past ice-sheet extent. Whilst the underlying RES data that was acquired with analogue RES systems is likely to be of lesser immediate priority due to the lack of precise navigational information at time of acquisition, RES data collected since the early 2000s with digital RES systems

and modern GPS equipment likely contain large sections of continuous englacial layering which may be used to develop an age-depth model of the AIS. However, relatively little is known on the quality of englacial reflections in these data and whether additional processing or data acquisition is required. Therefore, and as motivated by AntArchitecture, opportunities now exist for such work to take place in order to gain more information on the availability and quality of existing RES data and how these can be used further to build an ice-sheet-wide age-depth model.

2.4 Summary of key points and gaps in knowledge

Section 2.1 summarised the evidence that important changes have occurred over the AIS in recent decades, but that significant uncertainties still exist with regards to how the ice sheet evolved during past climatic transitions, and how it will evolve in the future as a result of enhanced anthropogenic forcings. Section 2.2 discussed the traditional geochronological point-based measurements used across the AIS to constrain numerical ice-sheet models, and highlighted their limitation in terms of spatial representativeness. Section 2.3 provided an overview of the application of RES techniques to study ice-sheet conditions over Antarctica, and how RES data can be used to infer current and past ice-sheet processes. Section 2.3.1 discussed the use of IRHs, as imaged by RES techniques, to infer past ice-sheet changes, with a particular focus on the reconstruction of past accumulation rates (Sect. 2.3.1.1) and ice-dynamical processes (Sect. 2.3.1.2). Lastly, Section 2.3.2 discussed the requirements necessary for the development of an ice-sheet wide age-depth model and highlighted potential barriers to achieving this goal with current RES data.

Despite significant advances in our understanding of how IRHs can be used to infer past ice-sheet changes, particularly over the EAIS, I showed that there is still a gap in our understanding of these changes over the WAIS, primarily due to the lack of suitable RES and IRH datasets over this region of Antarctica. Additionally, whilst age-depth models have been developed in recent years, their use to infer past ice-sheet changes such as accumulation rates, has so far been limited to spatially targeted areas of the ice sheet. This, in turn, affects our ability to put current changes occurring over the AIS in the context of the longer term evolution of the ice sheet, particularly during the Holocene, a period often regarded as resembling much of today's climate and ice-sheet conditions. Lastly, I showed that the RES data required to build the first age-depth model of the ice sheet remains largely inaccessible to the wider scientific community, which limits

our ability to characterise IRH stratigraphies across large sectors of the AIS and connect existing age-depth models, as motivated by the AntArchitecture Initiative.

2.5 Thesis objectives

Based on the overview provided in this chapter, it can be seen that a more detailed assessment of IRHs across Antarctica is required to provide a spatially extensive record of past ice-sheet processes that can be compared to predictions of the future evolution of the AIS from numerical ice-sheet models. To achieve this will require: (a) the development of regional IRH datasets over key missing sectors of Antarctica; (b) the interpretation of these IRHs at a regional scale by, for example, reconstructing accumulation rates over past glacial-interglacial periods; and (c) the development of an ice-sheet wide dataset of RES data that can be used to extend existing age-depth models to other sectors of the AIS, as motivated by the AntArchitecture Initiative.

Following on from the main aim of this thesis (see Chapter 1) and the key research gaps highlighted in this chapter, three research objectives are identified, each of which underpin the results presented in Chapters 3, 4, and 5, as follows:

Thesis Objective 1: To obtain a spatially extensive age-depth model of the Pine Island and upper Thwaites Glacier catchments from airborne RES data and high-resolution ice-core stratigraphy.

Thesis Objective 2: To estimate mid-Holocene accumulation rates over the WAIS from a pervasive IRH and the use of a 1-D ice-flow model.

Thesis Objective 3: To provide a community resource of standardised aerogeophysical data and identify areas of continuous IRH profiles that will facilitate the development of an age-depth model of the AIS.

3 Age-Depth Stratigraphy of Pine Island Glacier

A version of this chapter has been published in *Journal of Geophysical Research: Earth Surface* as:

Paper details: Bodart, J.A., Bingham, R.G., Ashmore, D.W., Karlsson, N.B., Hein, A.S., Vaughan, D.G., 2020. Age-Depth Stratigraphy of Pine Island Glacier Inferred from Airborne Radar and Ice-Core Chronology. *Journal of Geophysical Research: Earth Surface*, 126(4), e2020JF005927. DOI: 10.1029/2020JF005927 (see Appendix A for a copy of the published paper)

Author contributions: I conceived the study with R.G. Bingham. I developed the methods, performed all of the primary data analysis and interpretation, and wrote the paper. D.W. Ashmore conducted the post-processing of the radar data. D.G. Vaughan led the airborne data acquisition from Pine Island Glacier in 2004-2005. All co-authors provided inputs to the final manuscript.

3.1 Abstract

Understanding the contribution of the West Antarctic Ice Sheet (WAIS) to past and future sea level has been a major scientific priority over the last three decades. In recent years, observed thinning and ice-flow acceleration of the marine-based Pine Island Glacier has highlighted that understanding dynamic changes is critical to predicting the long-term stability of the WAIS. However, relatively little is known about the evolution of the catchment during the Holocene. Internal Reflecting Horizons (IRHs) provide a cumulative record of accumulation, basal melt and ice dynamics that, if dated, can be used to constrain ice-flow models. Here, we use airborne Radio-Echo Sounding (RES) data to trace four spatially extensive IRHs deposited in the late Quaternary across the Pine Island Glacier catchment. We use the WAIS Divide ice-core chronology to assign ages to three IRHs: 4.72 ± 0.28,

6.94 ± 0.31, and 16.50 ± 0.79 ka. We use a 1-D model, constrained by observational and modelled accumulation rates, to produce an independent validation of our ice-core-derived ages and provide an age estimate for our shallowest IRH (2.31-2.92 ka). We find that our upper three IRHs correspond to three large peaks in sulphate concentrations in the WAIS Divide ice-core record and hypothesise that the origin of these spatially extensive IRHs is from past volcanic activity. The clear correspondence between our IRHs and the ones previously identified over the Weddell Sea Sector, altogether representing ∼20% of the WAIS, indicates that a unique set of stratigraphic markers spanning the Holocene exists over a large part of West Antarctica.

3.2 Introduction

The West Antarctic Ice Sheet (WAIS) has been losing mass at an accelerating rate since satellite records began, averaging 94 ± 27 Gt yr^{-1} of mass loss since 1992 (Shepherd et al., 2018). Approximately 40% of this loss was through Pine Island Glacier (PIG), which alone has contributed ∼3 mm of the total ∼7 mm sea-level-rise contribution of the WAIS between 1979 and 2017 (Rignot et al., 2019). The increasing mass-loss trend of PIG has been primarily driven by interannual and decadal-scale atmospheric and oceanic forcing, triggering grounding-line retreat and consequent inland dynamical adjustments (Dutrieux et al., 2014; Favier et al., 2014; Christianson et al., 2016; Konrad et al., 2017; Smith et al., 2017; Bodart and Bingham, 2019; Holland et al., 2019; Rignot et al., 2019). However, placing the observed changes over the last four decades within the context of longer-term dynamic changes and sea-level-rise contribution is challenging (Palerme et al., 2017; Medley et al., 2018), as the short observational satellite record captures only slight perturbations in the forcing and response which are not sufficient to predict a future in which changes are likely to be rapid and large. This lack of long-term observations currently limits our understanding of the likely future evolution of this sensitive sector of the WAIS. Reaching further back into the past will help us capture a wider set of ice-sheet configurations, and so create a more robust basis for future predictions of the Antarctic Ice Sheet evolution (Ritz et al., 2001; DeConto and Pollard, 2016; Bracegirdle et al., 2019).

Past research has focused primarily on using in situ observations and ice-sheet models to reconstruct the evolution of the WAIS since the Last Glacial Maximum (LGM, ∼20 ka BP), indicating that the WAIS contained significantly more ice than at present, with the potential to have raised sea level by more than 9 m at the LGM (Denton and Hughes, 2002). Several studies have reported evidence of short-lived episodes of rapid grounding-line retreat in the Amundsen Sea Embayment (ASE)

between the LGM and the start of the Holocene (∼11.5 ka BP) (Jakobsson et al., 2011; Lowe and Anderson, 2002; Hillenbrand et al., 2013). However, much less is known about the interior ice-sheet history of this region during the Holocene. Cosmogenic nuclide studies on isolated nunataks across the ASE suggest significant ice thinning occurred during the early- to mid-Holocene in the central ASE (Lindow et al., 2014; Johnson et al., 2017; 2020), with thinning complete by the mid-Holocene in the eastern ASE near PIG (Johnson et al., 2008; 2014). More recent evidence, based on sediment cores, Radio-Echo Sounding (RES), and ice-sheet modelling, showed possible retreat and readvance of the WAIS grounding line over millennial timescales during the Holocene (Kingslake et al., 2018), although evidence of such behaviour is not available in the ASE region.

Internal Reflecting Horizons (IRHs), as observed by RES systems, provide a powerful and complementary resource to point-based geochronological measurements. Excluding basal ice and erosional surfaces, the majority of specular, continuous IRHs are isochronous (Whillans, 1976); many can be traced for several hundreds of kilometres and provide a record of accumulation rates and patterns, convolved with key information on past ice-dynamical processes (Siegert et al., 1998; Eisen et al., 2005; Bingham and Siegert, 2007; Eisen et al., 2008). IRHs can thus serve as a valuable resource for constraining past changes in surface mass balance and ice-flow velocities (e.g. Rotschky et al., 2004), and, where they can be dated, can be incorporated into ice-flow models, as previously shown for Greenland (Fahnestock et al., 2001a; MacGregor et al., 2016) and Antarctica (Waddington et al., 2007; Leysinger Vieli et al., 2011; Koutnik et al., 2016; Cavitte et al., 2018).

Despite the large spatial coverage of Radio-Echo Sounding (RES) data across Antarctica, information on dated IRHs is limited over much of the WAIS. This is partly due to the restricted availability of deep ice cores, the multitude of RES-system families operating at varying frequencies and using different post-processing methods to generate the RES data, and the challenge in tracing deep continuous IRHs, particularly through areas of high strain rate (i.e. at the onset of fast-flowing tributaries). Nonetheless, previous studies over the WAIS have used IRHs for the direct purpose of linking major deep ice cores together (Neumann et al., 2008; Koutnik et al., 2016), while others have used a wider, catchment-scale approach to constrain information on past accumulation rates and ice-flow reconfiguration. Such studies have ranged across the central WAIS (Siegert and Payne, 2004; Jacobel and Welch, 2005; Muldoon et al., 2018), or focused on specific sub-regions, e.g., Siple Dome (Jacobel et al., 1996), Kamb Ice Stream (Catania et al., 2006; Holschuh et al., 2018) and Thwaites Glacier (THW; Muldoon et al., 2018).

Over PIG, Karlsson et al. (2014) identified two IRHs spanning much of the slow-flowing parts of the catchment, which they roughly dated to 5.3-6.2 and 8.6-13.4 ka. More recently, Ashmore et al. (2020a) recovered three IRHs ranging across Institute and Möller Ice Streams (IMIS) and crossing the Institute/PIG divide which they broadly dated at 1.9-3.2, 3.5-6.0, and 4.6-8.1 ka. They demonstrated a correspondence between their IRH package and the IRHs previously identified by Karlsson et al. (2014) and Siegert et al. (2005), suggesting that a spatially extensive network of IRHs may span much of the WAIS.

Here, we build on previous studies to present a spatially extensive, dated-radiostratigraphy of PIG. We use RES data collected from two airborne platforms to trace four IRHs throughout PIG. We use a published ice-core chronology as well as a steady-state vertical-strain model to date these IRHs, and show that they span much of the late Pleistocene and Holocene. We first discuss the specifications of the RES systems and their respective uncertainties, and then describe the methods used to assign ages to each of our four IRHs. We present the dated age-depth stratigraphy of the catchment and make inferences for the rest of WAIS by comparing our recent findings to other age-depth studies. Finally, we investigate the link between sulphate activity in the WAIS Divide ice-core record and the depth of our upper three IRHs, and discuss the potential to recover records of older (i.e. pre-LGM) ice in the region using currently available RES datasets.

3.3 Datasets and methods

3.3.1 Data

The principal data used in this study were acquired during two large-scale airborne RES surveys of West Antarctica.

The first of these was acquired over the 2004-2005 austral season, when PIG's 175,000 km^2 catchment was surveyed extensively using the British Antarctic Survey's Polarimetric Airborne Survey INstrument (PASIN) system (Vaughan et al., 2006). This survey, hereafter termed "PIG-PASIN", acquired ∼35,000 line-km of airborne RES data across the region (Fig. 3.1). Data were collected with two interleaved radar modes. The first was a deep-sounding, 150 MHz centre-frequency, 4-μs, 10 MHz chirp mode, which has been used previously to identify and trace the bed (Vaughan et al., 2006) and some IRHs (Karlsson et al., 2009; 2014). The second was a 150 MHz, 0.1-μs pulse mode designed to image shallow IRHs but from which we are also able to recover IRHs deeper (∼2 km, see Fig. 3.2a) in the ice column. Over much of the surveyed region flight lines form 30 km spaced

grids that contain multiple crossovers, ensuring consistency when tracing IRHs across neighbouring lines (Fig. 3.1). Following techniques outlined in Ashmore et al. (2020a), here we used both modes of PASIN interchangeably during our IRH-tracing procedures (see Section 3.3.2). For the purposes of linking our stratigraphy further across the WAIS, we also refer to further PASIN-acquired data from a survey of IMIS undertaken in 2010-2011 (hereafter "IMAFI-PASIN"), which provided tie-lines connecting PIG with its neighbouring basins (Fig. 3.1; see Ashmore et al., 2020a, and references therein, for further details).

The second survey was conducted in 2016 and 2018 by NASA's Operation IceBridge (OIB) mission, and yielded ∼3,000 line-km of airborne RES data over PIG, IMIS and THW (Fig. 3.1). The system deployed by the Center for Remote Sensing of Ice Sheets (CReSIS) was the Multichannel Coherent Radar Depth Sounder 2 (MCoRDS2) with a 190 MHz centre frequency and 50 MHz bandwidth. We used the CReSIS L1B standard products, produced with pulse compression, focused-SAR processing and along-track motion compensation. More information on the RES system and processing is given by CReSIS (2018). Critically for this study, one of the OIB flight tracks over PIG also flew over the WAIS Divide ice core (79.48°S, 112.11°W; hereafter referred to as WD2014) (Fig. 3.1), making it possible to assign relatively unambiguous dates to the traced IRHs.

TABLE 3.1: Characteristics and resolution of the two airborne RES systems used in this study. Note: For the PASIN system, we provide values for both the chirp- and pulse-acquisition mode in the bandwidth/pulse width column, as well as in the vertical resolution column. The vertical resolution of the chirped systems was calculated as per CReSIS (2018) using a scaling factor k which accounts for resolution degradation due to receiver characteristics and processing (see Eq. (3.2)).

System	Platform	Centre Frequency	Bandwidth / Pulse Width	Vertical Sampling Frequency	Vertical Resolution	Horizontal Sampling Distance
PASIN	Twin Otter	150 MHz	10 MHz / 100 ns	22 MHz	12.89 / 8.42 m	45 m
MCoRDS2	DC8	190 MHz	50 MHz	150 MHz	2.58 m	14 m

More details on each of the RES systems are provided in Table 3.1. For the purposes of increasing IRH traceability on the PIG-PASIN data, we quadratically detrended each radar trace, normalised each pixel in a moving vertical window, and then applied a 10-trace horizontal average to reduce incoherent noise (after Ashmore et al., 2020a). For both the PIG-PASIN and the OIB-MCoRDS2 data, we removed the air-to-ice two-way travel time and shifted the surface elevation to time zero, prior to exporting the data to standard 2-D SEG-Y format for data interpretation.

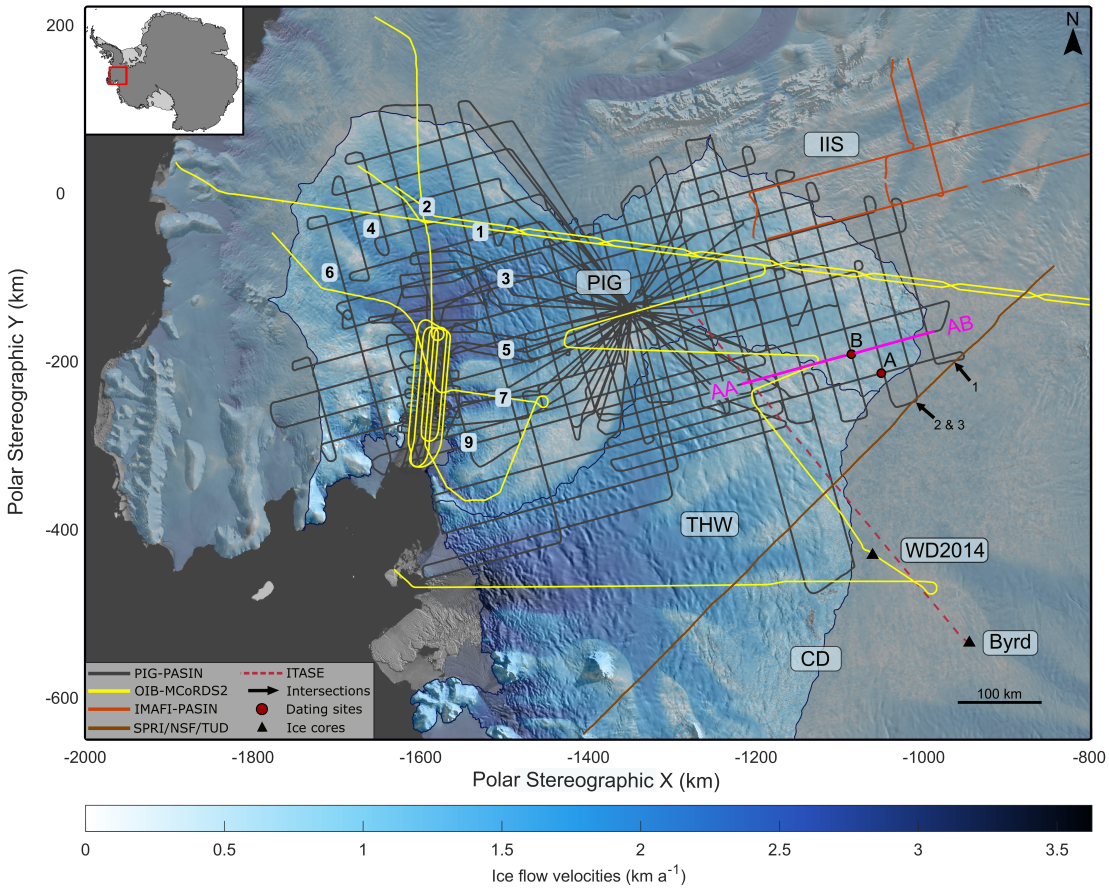

Figure 3.1: Map of study area with the datasets and key locations mentioned in this chapter. The inset in top left corner shows the region of interest (red box). Airborne survey lines included in this study: PIG-PASIN (grey), OIB-MCoRDS2 (yellow), IMAFI-PASIN transects flown over Institute Ice Stream (IIS) and intersecting the PIG catchment (orange), SPRI/NSF/TUD line (brown), overlaid on top of ice flow velocities from Rignot et al. (2017) and Moderate Resolution Imaging Spectroradiometer (MODIS) Mosaic of Antarctica (Scambos et al., 2007). Also included is the long, ITASE GPR-transect (dashed red) through which the 17.5 ± 0.5 ka layer from Jacobel and Welch (2005) was traced. The numbers shown over PIG's trunk represent the eight fast-flowing tributaries (1-7, 9) mentioned in this chapter. The WAIS Divide (WD2014) and Byrd ice cores are represented by the two black triangles, and the black arrows represent the three intersections between the SPRI/NSF/TUD-traced IRHs and this study. The two red circles show the two sites (Site A and B) where the 1-D age-depth model was used. The AA-AB segment (magenta) shows a subset of the control line where IRHs were first identified over PIG-PASIN (see Figure 3.2). The position of the Central Amundsen-Weddell-Ross Divide (CD) is also shown. The ICESat IMBIE basins of PIG and THW (Zwally et al., 2012) are annotated on the map and delimited by the blue outline lines.

3.3.2 IRH-tracing workflow

We conducted all IRH-tracing in the Schlumberger Petrel 3-D seismic software using a semi-automated tracing algorithm that uses an adjustable window to track

the local maxima of received reflected power between traces.

We initiated our workflow on the PIG-PASIN dataset as it is the most spatially extensive survey of the PIG catchment. From a "control line" crossing the ice divides between PIG, THW and IIS (Fig. 3.1), in which clearly-visible englacial stratigraphy is ubiquitous in both chirp- and pulse-mode data, we identified four prominent IRHs that we term R1-4 (Fig. 3.2). The upper three IRHs (R1-3) were chosen on the basis of high spatial continuity, high signal-to-noise ratio (SNR), and as being analogous to "IRH packages" traced over part of PIG by Karlsson et al. (2014) and through IMAFI-PASIN RES profiles by Ashmore et al. (2020a). All four IRHs occur in the middle part of the ice column where IRHs likely result from contrasts in acidity from past volcanic eruptions (Gow and Williamson, 1971; Millar, 1981; 1982), rather than the result of density variations occurring primarily at the near-surface (Gow, 1970; Clough, 1977; Moore, 1988) or orientation of anisotropic material due to ice foliation in the basal zone (Harrison, 1973; Fujita et al., 1999); and thus can be assumed to be isochronous (Whillans, 1976; Siegert et al., 1998).

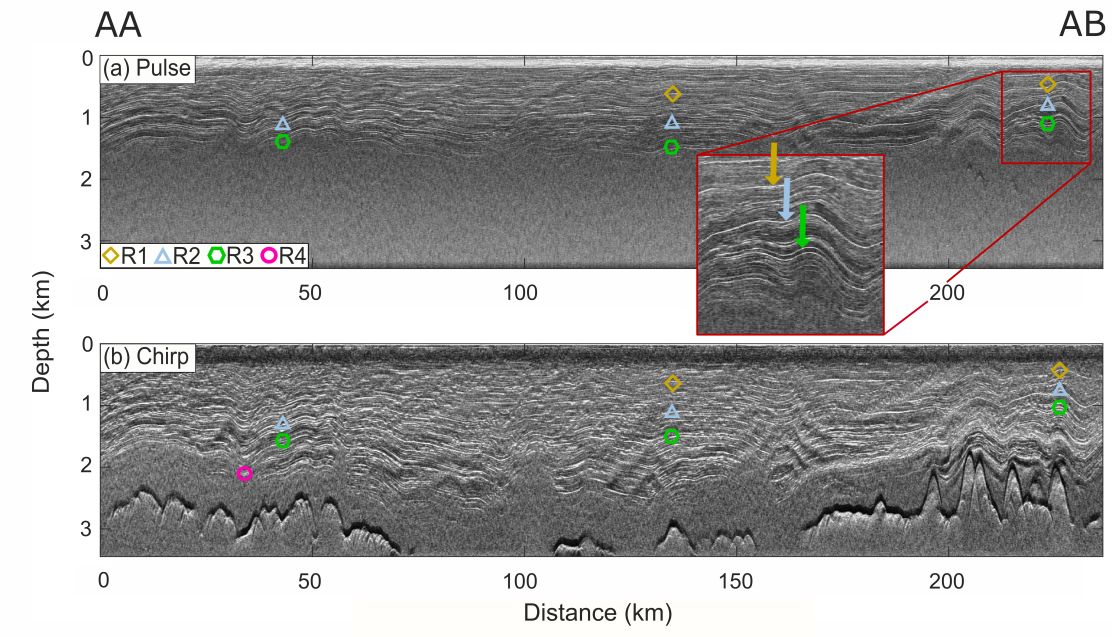

Figure 3.2: Subset of the control line with the unmodulated pulse (a) and chirp (b) modes from the PIG-PASIN survey along transect AA–AB (see Figure 3.1). Traced IRHs are marked as per the legend on panel (a). The zoomed inset on the pulse radargram shows the characteristics of R1-3 in more detail, with the colour of the arrows corresponding to the legend in (a).

Expanding out from the control line, we progressively traced and mapped IRHs across the catchment using IRH intersections at each crossover as calibration points. This ensured reliability in our reflection tracing as the software is capable of detecting intersecting IRHs at the crossover with orthogonal RES lines. Since our tracing strategy was based on reflector echo strength and continuity, the reflection tracing was terminated when it was no longer possible to distinguish visually between adjacent reflections, either as a result of similar brightness levels or a loss in continuity. This was particularly common in areas of steep bed topography causing IRHs to dip significantly, or where enhanced ice-flow speeds disrupted IRH continuity, notably into the main flow features of PIG's northern catchment. In some places, IRHs faded without such clear topography/flow-induced reasons, likely due to the attenuation of the radar signal with depth or the type of processing used (Holschuh et al., 2014). In some locations more distant from the upper PIG catchment (i.e. westward of tributary 6; Fig. 3.1), extensive englacial layering was visible in RES profiles but, due to a dearth of connecting lines and crossovers, we could not, with confidence, identify R1-4.

When tracing between crossovers, we relied upon the distinctiveness of our IRHs. At the vertical resolution of PASIN, R1 and R2 manifest as single-amplitude peaks, with R2 representing a particularly bright reflector widely visible across our RES data (Figs. 3.2 - 3.3). R3 consists of the shallowest of a series of closely-spaced bright horizons, often manifested as a couplet (zoomed inset in Figure 3.2 and Figure 3.3), and previously identified by Karlsson et al. (2014; their "Layer 2") and Ashmore et al. (2020a; their "H3"). The lowermost IRH, R4, forms the upper part of a band of bright reflectors visible at the intersection with the 17.5 ± 0.5 ka layer widely imaged on RES data from the International Trans-Antarctic Scientific Expedition (ITASE) connecting the PIG catchment with the Byrd Ice Core chronology (Hammer et al., 1997; Jacobel and Welch, 2005) (Figs. 3.1 - 3.3).

Once R1-4 were traced through the PIG-PASIN survey, we looked for the same IRHs on the OIB-MCoRDS2 data using available crossovers between each survey (Figs. 3.1 and 3.4). We found R2-3 to be equally distinguishable in OIB-MCoRDS2 profiles, with R2 representing a particularly bright reflector similar to that on PIG-PASIN, whilst R3 also formed the shallower part of an easily distinguishable couplet. We did not recover R1 independently on the OIB-MCoRDS2 profile crossing the WAIS Divide ice core and used intersections with PIG-PASIN to trace it across to IIS catchment. Similarly, we used several intersections with the 17.5 ± 0.5 ka layer from Jacobel and Welch (2005) in and around the WD2014 site to recover R4 in the OIB-MCoRDS2 data (Figs. 3.1 and 3.5).

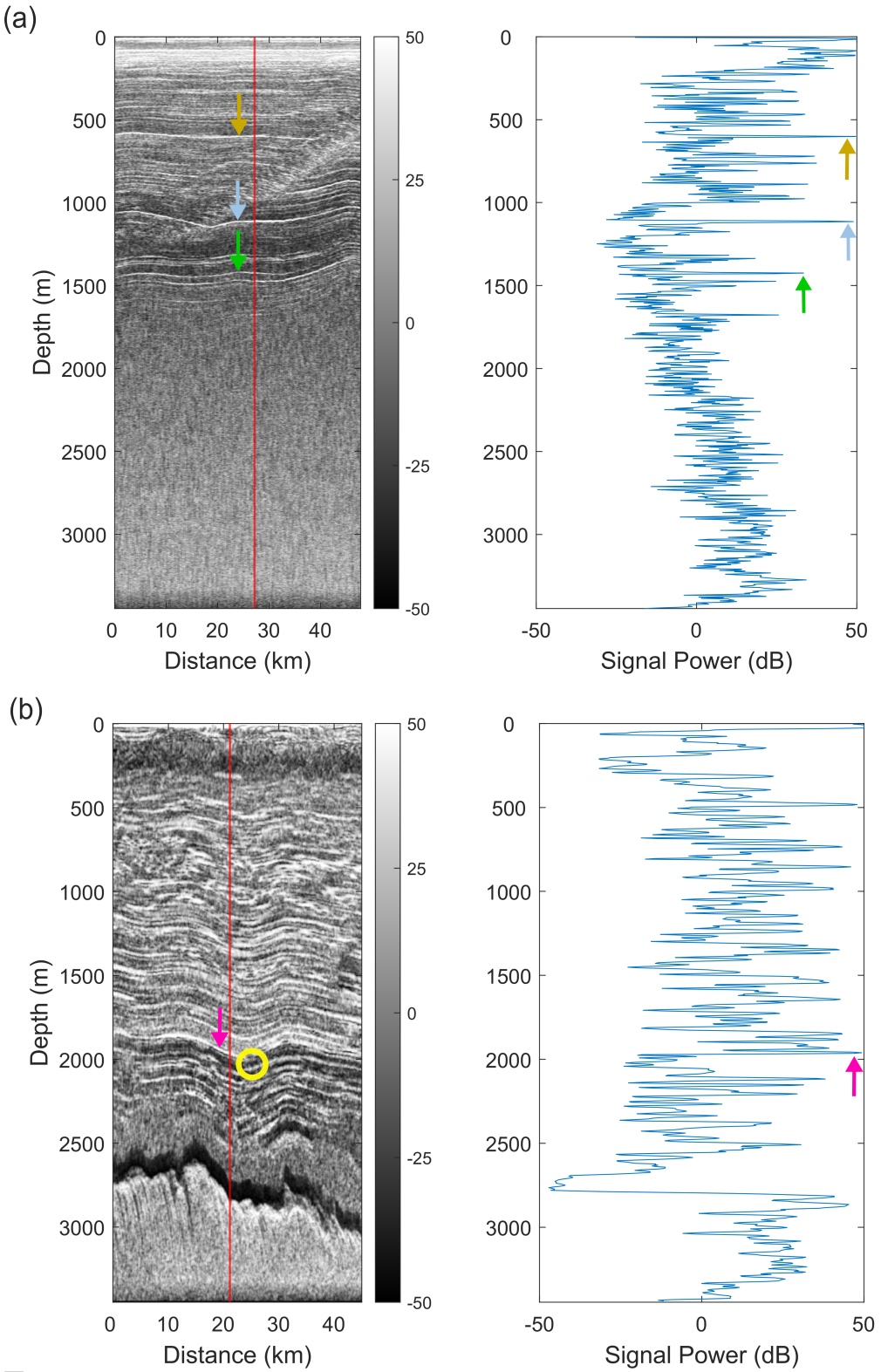

Figure 3.3: Radargram and radar trace profile showing IRH characteristics and return power on the PIG-PASIN data. Colours of arrows are per legend in Figure 3.2. (a) Pulse radargram along the control line (segment AA-AB, Figures 3.1 and 3.2) showing IRHs R1-3 and their peak power, with R1 (yellow), R2 (blue), R3 (green). The red line on the radargram shows the location of the radar trace. (b) Same as for (a) but on PIG-PASIN flight line 1 (chirp mode) with R4 (pink) shown as well as the depth and location of where Jacobel and Welch's (2005) 17.5 ± 0.5 ka layer (yellow circle) intersects our data.

TABLE 3.2: Crossover depth analysis for ten locations (I1-10, Fig 3.4) where R1-4 intersect each other at flight path crossovers on the PIG-PASIN data. Depth uncertainty for PIG-PASIN is ±17 m.

	IRH	*Depths at intersection (m)*			*IRH*	*Depths at intersection (m)*	
I1	R1	467	470	**I6**	R1	816	814
	R2	890	896		R2	1,488	1,503
	R3	1,193	1,197		R3	1,592	1,596
	R4	-	-		R4	-	-
I2	R1	525	503	**I7**	R1	723	728
	R2	947	942		R2	1,099	1,100
	R3	1,286	1,284		R3	1,410	1,412
	R4	2,086	2,085		R4	-	-
I3	R1	532	537	**I8**	R1	559	558
	R2	1,181	1,176		R2	802	806
	R3	1,483	1,479		R3	989	1,004
	R4	2,021	2,016		R4	-	-
I4	R1	796	797	**I9**	R1	599	598
	R2	1,223	1,224		R2	958	954
	R3	1,499	1,502		R3	1,161	1,160
	R4	2,072	2,058		R4	-	-
I5	R1	-	-	**I10**	R1	956	946
	R2	1,488	1,503		R2	1,577	1,576
	R3	1,796	1,797		R3	2,010	1,993
	R4	2,197	2,192		R4	-	-

It is worth noting that the OIB-MCoRDS2 data were acquired 12-14 years later than the PIG-PASIN survey, and so the same IRHs will, in principle, lie slightly lower in the ice column. However, considering a present-day mean accumulation rate of ∼0.30-0.35 m a^{-1} (metres of ice equivalent per year) at the intersection between the two surveys, the maximum change in IRH depth is <5 m. This is well within the bounds of the total depth uncertainty calculated for each RES system (see Section 3.3.3) and does not affect the pattern of englacial layering or the identification of our IRHs across the different surveys. Crossover analysis at key intersections on the airborne RES data showed that the mean depth difference for R1-4 fall within the uncertainty range of all surveys (Fig. 3.4, Tables 3.2-3.3) (see Section 3.3.3). At 10 intersections on PIG-PASIN, the mean depth difference for R1-4 is <6 m. Similarly, mean depth difference for R2-3 at 11 intersections between PIG-PASIN and OIB-MCoRDS2 is 14 m and 29 m respectively, and <18 m at five intersections between R4 on OIB-MCoRDS2 and the 17.5 ± 0.5 ka from

Jacobel and Welch (2005) (Fig. 3.4, Tables 3.2-3.3).

TABLE 3.3: Crossover depth analysis for five locations (K1-5, Fig 3.4) where R4 traced on the OIB-MCoRDS2 data (this study) intersects the 17.5 ± 0.5 ka layer (Jacobel and Welch, 2005). Depth uncertainty for the OIB-MCoRDS2 IRH is ±14 m. Estimated uncertainty for the 17.5 ± 0.5 ka layer from Jacobel and Welch (2005) is ±10 m.

	Depths at intersection (m)	
	Jacobel and Welch (2005)	This Study
K1	1,439	1,424
K2	1,848	1,824
K3	1,784	1,764
K4	1,725	1,743
K5	1,917	1,905

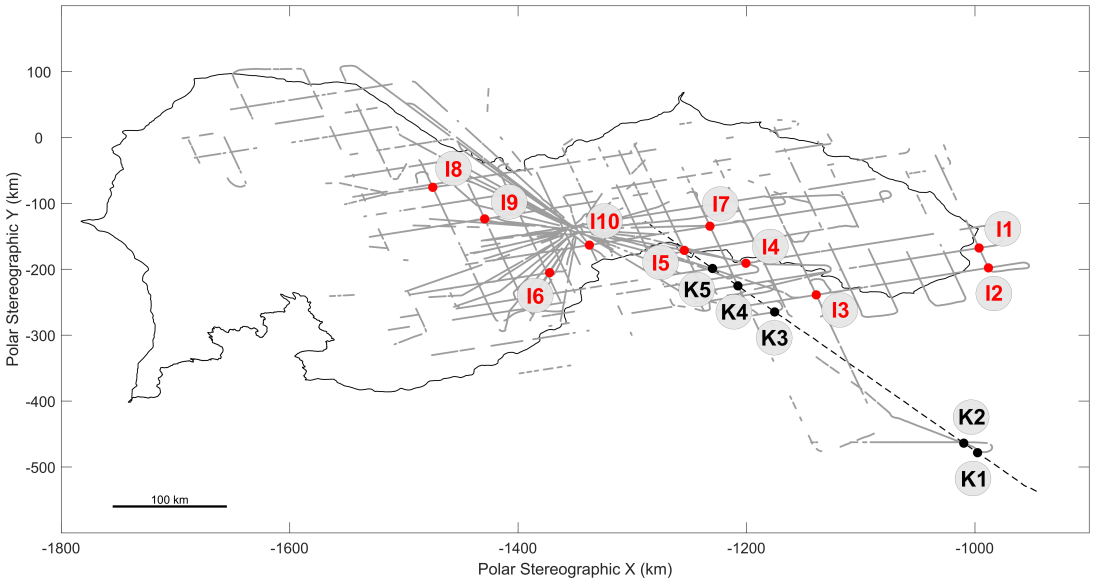

Figure 3.4: Map showing the spatial extent of IRHs R1-4 across our study area (grey lines) and selected crossover points for IRHs traced on PIG-PASIN and OIB-MCoRDS2. The red dots I1-10 show the ten intersections where we directly compared the depth of IRHs R1-4 traced on the PIG-PASIN data. The black dots K1-5 are where we directly compared the depths of R4 (this study) with the depth of the 17.5 ± 0.5 ka layer (Jacobel and Welch, 2005). The black dotted line is where Jacobel and Welch's (2005) profile intersects our dataset. The black outline in the background is the ICESat IMBIE basin containing the Pine Island Glacier (Zwally et al., 2012).

With our objective being to produce an age-depth radiostratigraphy across

PIG, we converted all IRHs traced above in the time domain (t_{IRH}) to depth (d_{IRH}) using

$$d_{IRH} = \frac{v_{ice} t_{IRH}}{2} + Z_f, \tag{3.1}$$

where v_{ice}=168.5 m μ^{-1} is the speed of electromagnetic (EM) waves through ice (c.f. Fujita et al., 2000) and Z_f=10 m is a spatially invariant firn correction, appropriate for West Antarctica (Ashmore et al., 2020a). All our depth measurements are given in metres below the surface. We then calculated IRH depth as a function of ice thickness using the ice-thickness measurement from each respective RES mission, and complemented these with ice-thickness measurements from BedMachine (Morlighem et al., 2020) in places where the radar did not sound the bed.

3.3.3 Catchment-wide depth uncertainties

To assess the accuracy of our IRH depths at the catchment scale, we considered the uncertainties associated with the imaging of IRHs with RES systems. These uncertainties primarily depend on three factors: variations in the speed of EM waves through the ice, the firn-density correction, and the RES system's range precision (Cavitte et al., 2016). These are described in more details in the following three sub-sections (Sect. 3.3.3.1 - 3.3.3.3).

3.3.3.1 Electromagnetic wave in ice

The greatest source of uncertainty when calculating the depth of an IRH is the true speed of EM wave in the ice, which varies based on impurity concentrations, anisotropy and temperature, and ranges from p= v_{ice} [∼U 168.0, 169.5] m μ^{-1} (Fujita et al., 2000). Because this error increases with depth, the maximum uncertainty can be found on the deepest IRH. The maximum uncertainty arising from selecting an EM value ranging between 168 and 169.5 m μ^{-1} is 16 m on the maximum depth of the deepest reflection on PIG-PASIN and 14 m on OIB-MCoRDS2.

3.3.3.2 Firn-density correction

The radar signal travels at a faster rate in the lower-density firn (∼350-900 kg m^{-3}) than in the higher-density solid ice (∼917 kg m^{-3}). To correct for this, RES studies typically calculate a spatially invariant firn correction Z_f and add this value in the vertical direction (see Eq. (3.1)) (Dowdeswell and Evans, 2004). Previous studies over West Antarctica (i.e. Ross et al., 2012; Siegert et al., 2013)

used a value of Z_f=10 m, based on the high-resolution density profiles at WAIS Divide (see Ashmore et al., 2020a). Since our IRHs are in close proximity to the WD2014 site, we also used this nominal value of 10 m and applied it to all our IRHs. We estimate the uncertainty associated with the firn correction to be ±3 m, owing to minor variations in firn densification across the catchment (see Ashmore et al., 2020a for details).

3.3.3.3 Radar range precision

The precision of IRH depth estimates also depends on the range precision of the RES system (also known as the range accuracy), $\sigma(r^*)$, which refers to how accurately changes can be located in 3-D space (Cavitte et al., 2015; King, 2020).

In order to determine the range precision of the RES system, the vertical range resolution, which is mainly a function of sampling frequency, bandwidth, source wavelets, and the type of post-processing applied, must first be calculated. The range resolution represents the ability of a RES system to detect between two closely-spaced targets with similar reflection strengths. Denoted Δr, it is given by the bandwidth of a chirped RES system, B, the dielectric constant of ice, ϵ'= 3.17, the speed of light in a vacuum, c_0, and a window widening factor, k, of 1.53 for a 20% Tukey time-domain, as per CReSIS (2018). This results in the following equation:

$$\Delta r = \frac{k c_0}{2B\sqrt{\epsilon'}}. \tag{3.2}$$

Following Eq. (3.2), the range resolution for each system from coarser to finer is: PASIN chirp (12.89 m), PASIN pulse (8.42 m), and MCoRDS2 (2.58 m) (Table 3.1). The SNR for each reflector for a point target is a function of the reflector signal power and noise power, as per Cavitte et al. (2016). It is used alongside the range resolution to calculate the range precision, which is the standard deviation of the range estimate for each reflector at the 68% confidence level, as per the following equation:

$$\sigma(r^*) = \frac{\Delta r}{\sqrt{SNR}}. \tag{3.3}$$

This provides us with an estimate of the distance between the platform and a single reflecting target. SNR calculated for each IRH traced on the OIB-MCoRDS2 system at WD2014 varied between 6.54 and 7.68 dB. Using Eq. (3.3), this resulted in a maximum range precision $\sigma(r^*)$ = 1.01 m. As per Ashmore et al. (2020a), we did not estimate SNR directly for PASIN and instead used a realistic range accuracy of ±4 m to calculate our RES depth uncertainties. This is estimated by

comparing the range resolution of the University of Texas's HiCARS system, which has a slightly higher range resolution (8.6 m) compared with PASIN (12.9 m; see Table 3.1) and for which RES range accuracy varies between 0.9 and 3.9 m over East Antarctica (Cavitte et al., 2016) (see Ashmore et al., 2020a for more details). Considering the chirped version of the RES system flown over IMIS has the same centre frequency and a similar bandwidth to the Pine Island Glacier survey (2010 IMAFI-PASIN: 12 MHz, 2004 PIG-PASIN: 10 MHz), we estimate that using the same conservative value of ±4 m for the range precision is appropriate here.

3.3.3.4 Combining uncertainties

We undertook an empirical error analysis to calculate the maximum uncertainty associated with the deepest IRH by calculating the root-mean-square error of the depth uncertainties from EM wave through the ice, the firn correction, and the RES range precision. We obtained a combined maximum uncertainty of ±17 m and attached this uncertainty to all IRHs traced on the PIG-PASIN data (see Section 3.8.1). Similarly, we estimated a combined maximum uncertainty of ±14 m on the OIB-MCoRDS2 data (see Section 3.8.1). Given that this uncertainty represents the maximum uncertainty on the deepest IRH over our entire dataset, we also calculated IRH-specific uncertainties at the ice-core site (see Section 3.3.4.1).

3.3.4 Age-depth attribution

To estimate the absolute age of our IRHs, we employed two primary dating methods. We used (a) the WAIS Divide ice-core chronology to provide a direct age to our three deepest IRHs, namely R2-4; and (b) the Dansgaard-Johnsen 1-D model to independently compare the ages calculated at the ice core and to provide an approximate age range to our shallowest IRH, R1. Once dated, we also compared the ages and depths of R1-3 with dated IRHs traced across PIG (Siegert and Payne, 2004; Karlsson et al., 2014) and IMIS (Ashmore et al., 2020a); as well as the age and depth of R4 with the 17.5 ± 0.5 ka layer dated using the Byrd ice-core chronology (Hammer et al., 1997) and traced across the WAIS (Jacobel and Welch, 2005). Finally, we also compared the depth and age of our upper three IRHs with sulphate concentrations from the WD2014 ice-core record (Cole-Dai, 2014; McConnell et al., 2017).

3.3.4.1 Connection to the WAIS Divide ice-core chronology

We used the 2016 OIB-MCoRDS2 data linking central PIG to the WD2014 site to date IRHs across PIG relative to the ice-core chronology, where annual-layer counting goes back to the last ∼31 ka BP (Buizert et al., 2015; Sigl et al.,

2016). We used the recorded depth at the ice core which most-closely matches our IRH depth at WD2014 to calculate the upper and lower age bounds using the RES depth and ice-core uncertainties. Following MacGregor et al. (2015), the age uncertainty (Δa_{comb}) associated with each IRH is the root-mean-square combination of the age uncertainty associated with the unweighted mean IRH depth at the ice core ($\Delta a_{\Delta depth}$) and the age uncertainty associated with the ice core at the IRH depth (Δa_{core}), following

$$\Delta a_{comb} = \sqrt{\Delta a_{\Delta depth}{}^2 + \Delta a_{core}{}^2}, \tag{3.4}$$

where (Δa_{core}) is a function of the age of the individual IRH at the ice core site (Sigl et al., 2016) and the published uncertainty associated with the ice core age (1% and 3% for ages ranging between 0-15 ka and 15-31 ka BP respectively; Sigl et al., 2016), while ($\Delta a_{\Delta depth}$) is a function of the depth uncertainty of each IRH at the ice-core site. Since the uncertainty in the EM wave through the ice increases with depth, using the maximum uncertainty calculated on the deepest IRH to calculate $\Delta depth$ at a catchment scale (see Section 3.3.3) would result in less accurate age uncertainties at the ice core. We have therefore calculated a depth uncertainty for each individual IRH at the ice core, and undertook the same empirical error analysis to calculate $\Delta depth$ at WD2014. This resulted in IRH-specific RES depth uncertainties which we used to calculate the age uncertainty for each IRH at WD2014, as per Eq. (3.4).

Whilst Δa_{comb} represents the combined maximum uncertainty from the RES system and the ice-core chronology, we found that our IRHs are systematically lower in the ice column compared with strong peaks in acidity concentrations at WD2014 matching closely the age and depth of our IRHs and which we can assume to be the likely cause of our IRHs (see Section 3.5.2). To account for this offset in ages between the IRHs and the strong sulphate peaks observed at WD2014, we calculated a total age uncertainty (Δa_{total}), which represents the maximum age difference between our IRHs and the sulphate peaks at the ice core. This was obtained by adding a systematic factor of 0.22 ka to Δa_{comb}, which represents the total age difference between the maximum IRH age calculated using Δa_{comb} and the age of the strong sulphate peaks (see Section 3.5.2). We provide the total uncertainty values in Section 3.4.2.

3.3.4.2 Age-depth modelling

To provide an independent validation of our ice-core derived IRH ages, we also applied the Dansgaard and Johnsen (1969) 1-D vertical ice-strain rate model to

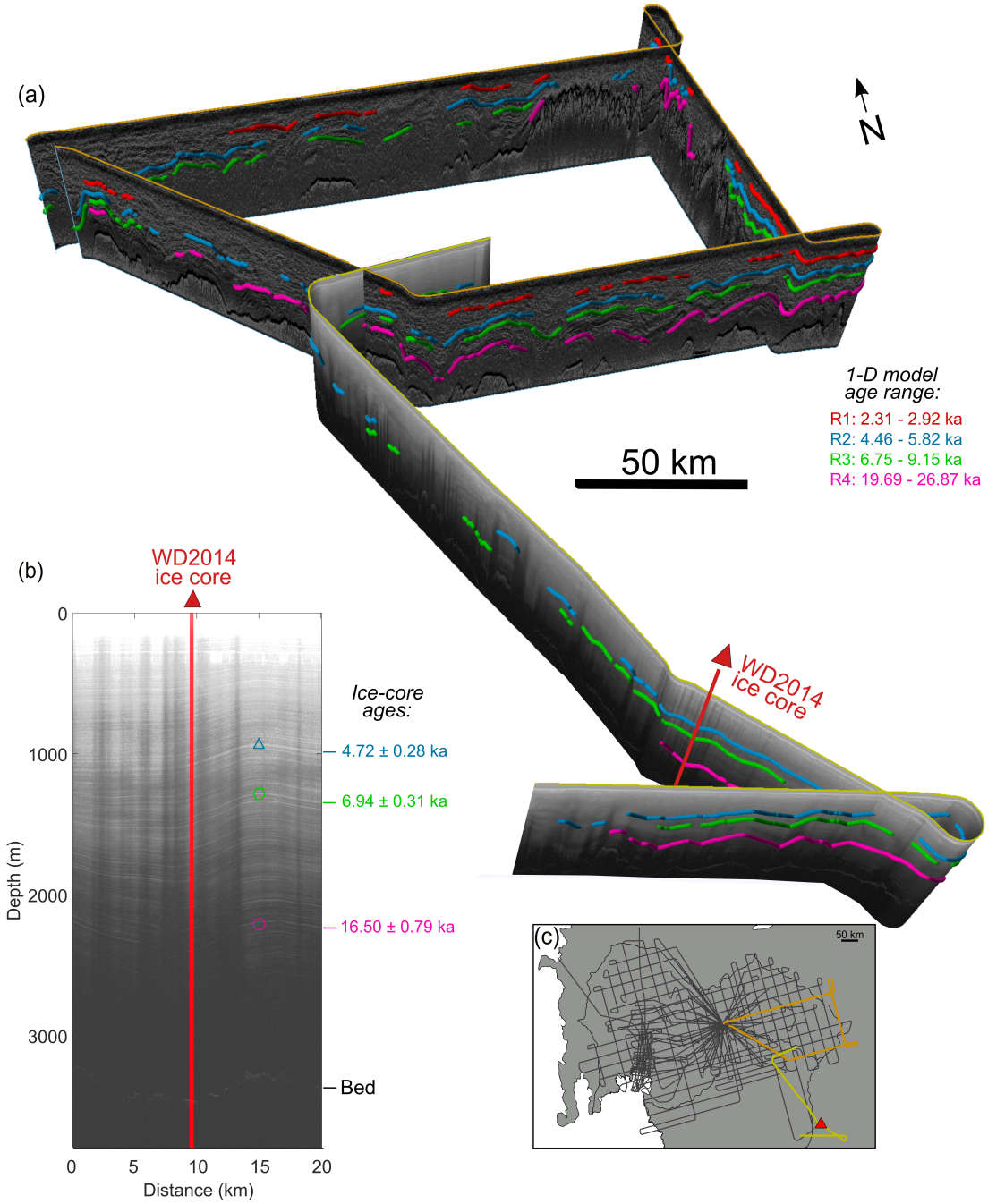

Figure 3.5: 3-D radar profile connecting the Pine Island Glacier with the WAIS Divide ice core. (a) Intersecting RES profiles from PIG-PASIN and OIB-MCoRDS2 with IRHs R1 (red), R2 (blue), R3 (green) and R4 (pink) traced along radargrams. The age range shown on the PIG-PASIN profile in the top right corner are from the 1-D model for R1-4 (see Section 3.4.2). (b) Englacial layering on the OIB-MCoRDS2 RES profile where it intersects the WD2014 ice core (red line), with ages and total age uncertainties for R2-4 inferred from the ice-core chronology (see Section 3.4.2) shown on the right-hand side. (c) Inset showing the PIG-PASIN (orange line) and OIB-MCoRDS2 (yellow line) profiles in (a) and the full PIG-PASIN RES flight lines shown in grey in the background, as well as the position of the WD2014 ice core (red triangle).

derive approximate dating of the IRHs traced over the central PIG catchment. This model has been used previously to date IRHs across West Antarctica (Corr and Vaughan, 2008; Karlsson et al., 2012; 2014; Ashmore et al., 2020a), assess divide migration (Waddington et al., 2005), and calculate past accumulation rates at or near ice divides (Siegert and Payne, 2004; Jacobel and Welch, 2005). We chose the Dansgaard–Johnsen model here for its simplicity and as it allows us to test the effect of ice deformation on the ages of our IRHs. However, we note that other alternatives exist such as the Nye (Nye, 1957) and Lliboutry (Lliboutry, 1979) models, or the more developed quasi-Nye model (MacGregor et al., 2015).

Under the assumption that the ice sheet is, and has been, in steady state, close to an ice divide, the Dansgaard-Johnsen model gives

$$t = \frac{2H - h}{2a} \ln \left(\frac{2H - h}{2z - h} \right), h \leq z \leq H, \tag{3.5}$$

where t (ka; thousand years) is the age of an IRH, H (m) is the ice thickness (assumed constant in time), h (m) is the thickness of the basal shear layer, a (in m a^{-1} ice-equivalent) is the average accumulation rate since deposition of the IRH, and z (m) is the elevation of the IRH above the bed (Dansgaard and Johnsen, 1969).

For this model, several assumptions are made: (a) negligible horizontal velocity component; (b) time-averaged accumulation rates and no temporal change in accumulation patterns; and (c) constant ice deformation from the surface to some depth, h, below which vertical strain rate is assumed to decrease linearly towards the bed. Considering the above, we initiated the model on the PIG-PASIN data at two sites (A and B in Figure 3.1) located ∼50km from the ice divide where horizontal ice flow is minimal (<3 m a^{-1}), the ice is thick (>3 km) and the bed relatively flat. Site A (80.15°S, 101.56°W) was selected due to its relative proximity within PIG to WD2014 (∼215 km). At this site, R1-3 were traced, as well as R4. This provided us with initial constraints for age-depth estimates for the upper IRHs (namely R1-3), and allowed us to evaluate the model results based on the approximate known age of R4. To ensure representativeness, however, we also selected a second site, Site B (79.87°S, 100.03°W), where R1-3 were traced but not R4.

In order to obtain direct ages for our IRHs using Eq. (3.5), the model also requires a good approximation of past accumulation rates, a, and basal shear layer thickness, h, which are both unknown over our grid. The following two sections provide more details on how these were calculated.

3.3.4.2.1 Past accumulation rates

We based our estimates for a in Eq. (3.5) on advection-corrected accumulation rates from the WD2014 ice core (Fudge et al., 2016) for each IRH R1-4, and with current accumulation estimates to correct for any elevation-dependent change in accumulation between the WD2014 site and our PIG Sites A and B.

To obtain estimates of accumulation rates for R1-3 at the Ice Core, we first needed to assign broad ages to our IRHs which were independent from those calculated at the Ice Core. For this, we used a profile from the 1974-75 Scott Polar Research Institute/National Science Foundation/Technical University of Denmark (SPRI/NSF/TUD) survey containing IRHs that were traced and dated at their intersection with the Byrd Ice Core chronology (Hammer et al., 1997; Siegert and Payne, 2004) and that cross R1-3 traced on PIG-PASIN. At three crossovers (marked on Figure 3.1), we used the age-depth profile of Siegert and Payne (2004) to assign broad ages to our upper three IRHs. Table 3.4 shows the close correspondence between our traced IRHs and those from Siegert and Payne (2004) at Intersections 1-3. Acknowledging the spatial uncertainties associated with pre-GPS navigation in the SPRI/NSF/TUD records (Schroeder et al., 2019), we treated these as initial constraints to refine the input parameters of the age-depth modelling we describe in this section.

TABLE 3.4: IRH depths (m) at three locations where the SPRI/NSF/TUD survey intersects the PIG-PASIN survey. The intersections mentioned here are shown as black arrows in Figure 3.1. Age and uncertainty for each of Siegert and Payne's (2004) IRHs is also shown here. The maximum depth uncertainty associated with our IRHs at a catchment-scale is ±17 m on PIG-PASIN (see Section 3.3.3). The uncertainty associated with Siegert and Payne's (2004) IRHs is ±40 m.

IRH depths at Intersections 1-3						
	This study			*Siegert and Payne (2004)*		
	R1	R2	R3	L07 (3.10 ± 0.16 ka)	L10 (5.60 ± 0.18 ka)	L11 (6.40 ± 0.18 ka)
I1	520.8	882.3	1,146.0	500.8	896.7	1,056.8
I2	508.4	975.0	1,478.8	531.3	1,034.4	1,222.9
I3	569.6	999.6	1,475.3	557.0	1,055.5	1,193.4

Tentatively treating our R1-3 as broadly equivalent to three of Siegert and Payne's (2004) dated IRHs, we derived mean advection-corrected accumulation rates at WD2014 for each reference age: 0.247 ± 0.062 m a^{-1} (3 ka BP, with BP defined as years before 1950 CE), 0.248 ± 0.062 m a^{-1} (5 ka BP), and 0.243 ± 0.061 m a^{-1} (7 ka BP), as well as a rate of 0.226 ± 0.051 m a^{-1} (17.5 ka BP)

based on the intersection with Jacobel and Welch (2005). The errors correspond to uncertainties in the firn-densification model used by Fudge et al. (2016). These provided us with estimates of what would be required to reproduce each layer if accumulation had remained constant between the time of the deposition of the layer and the present at WD2014.

Under the assumption that spatial accumulation patterns have not changed during the Holocene over the WAIS (Siegert and Payne, 2004; Neumann et al., 2008; Koutnik et al., 2016), and considering that accumulation rates at the Ice Core are generally smaller than at Site A and B (Table 3.5), we used modern accumulation rates from modelled and observational data to calculate the regional difference between accumulation at WD2014 and our Sites A and B. The four sources of modern accumulation data used here are: (a) surface mass balance (SMB) estimates for the period 1979-2015 using the Modèle Atmosphérique Régional (MAR, Version 3.6.4; Agosta et al., 2019); (b) SMB estimates for the period 1979- 2018 from the Regional Atmospheric Climate Model 2 (RACMO2; van Wessem et al., 2018); (c) accumulation rates interpolated from ground measurements and AMSR-E polarisation (Arthern et al., 2006; hereafter referred to as ART06); and (d) a combination of catchment-wide, snow and accumulation RES measurements obtained in 2009-11 from ultra-wideband airborne platforms and intersecting a series of shallow ice cores (Medley et al., 2014), combined with a set of GPR tracks acquired in 2002-04 over the Central Amundsen-Weddell Divide (Neumann et al., 2008) (hereafter referred to as MED14). To ensure consistency across all observational and modelled products, and capture intra-cell variability in accumulation rates, we bilinearly interpolated the resolution of the MAR (35 x 35 km), RACMO2 (27 x 27 km), and ART06 (100 x 100 km) products to match the 3-km resolution of MED14. We then obtained the closest grid value that corresponded to WD2014 and each of Site A and B, and converted the accumulation value from kg m^{-2} a^{-1} to m a^{-1} of ice-equivalent using a density value of 917 kg m^{-3}.

From these datasets, we then calculated a percentage of change between WD2014 and Site A-B and applied this to the mean advection-corrected rates calculated at WAIS Divide for R1-4 (Table 3.5). Together, these provided us with a range of realistic values of a for each IRH at Site A-B to use as input into the 1-D model.

3.3.4.2.2 Basal shear layer thickness

The thickness of the basal shear layer, h, is largely unknown as it is dependent on accurate knowledge of the bed topography, ice thickness, and temperature of

TABLE 3.5: Accumulation rates (m a^{-1}) for each IRH at Site A and B, as calculated using the four accumulation datasets. Note that at Site B, R4 was not retrieved. The accumulation rate is given in m a^{-1} (metres of ice equivalent per year) using an ice density value of 917 kg m^{-3}. Δ% refers to the percentage change in accumulation rates between the WD2014 site and Site A and B respectively.

	Site A					*Site B*			
	R1	R2	R3	R4	Δ %	R1	R2	R3	Δ %
MAR	0.253	0.255	0.249	0.210	2.659	0.266	0.268	0.261	7.742
ART06	0.268	0.270	0.264	0.223	8.817	0.276	0.278	0.271	11.831
RACMO2	0.305	0.307	0.300	0.253	23.560	0.331	0.333	0.326	34.200
MED14	0.311	0.314	0.307	0.259	26.308	0.325	0.325	0.318	30.888

the ice (Neumann et al., 2008). Previous studies have used a value of h=400 m for Greenland and West Antarctica (Fahnestock et al., 2001b; Siegert and Payne, 2004; Jacobel and Welch, 2005; Karlsson et al., 2012), whilst Karlsson et al. (2014) and Ashmore et al. (2020a) explored the effects of fuller ranges of $100 \leq h \geq 1200$ m. Considering that the vertical velocity profile under present-day conditions is dependent on a good approximation of the flow and bed conditions at the divide, Neumann et al. (2008) tested two scenarios to estimate the basal shear layer thickness over the Central Amundsen-Weddell Divide. The parameterisation of their model used both h=0.2H (corresponding to a divide where basal sliding or divide migration is occurring) and h=0.7H (representing a stable divide with frozen bed). They showed that values where h>0.2H required increasingly more accumulation at the divide to match the age of the RES-detected IRHs dated at Byrd ice core. Schwander et al. (2001) used h=0.373H at Dome Concordia (East Antarctica), but accumulation is lower there than at the Divide and ice flow has likely changed little since the last interglacial. Owing to the above, and considering that ice thickness at Site A is H=3,605 m and at Site B is H=3,430 m (±23 m; Vaughan et al., 2006), using a range of values for h of 100–1,200 m as per Ashmore et al. (2020a) and Karlsson et al. (2014) is not appropriate.

We therefore refined this range to between $0.2 \leq h \geq 0.3H$, rounding to the nearest 100, hence investigating the effect of h ranging from 700 to 1,100 m at both sites. We note, however, that large uncertainties in basal deformation at WD2014 (Cuffey et al., 2016; Fudge et al., 2019) could result in h values being smaller than 20% of the ice thickness and thus lead to an overestimation of our ages.

3.4 Results

3.4.1 Englacial stratigraphy

We successfully traced four IRHs R1-4 across a large proportion of the PIG catchment, including in areas where annual velocities reach up to ∼350 m a^{-1} (Fig. 3.6). The most extensive IRH traced in our study is R2, closely followed by R3 (Fig. 3.6), with mean depths across the catchment of 1,175 and 1,463 m respectively (Table 3.6). The shallowest IRH, R1, was located on average at ∼30% of the ice depth, whilst the deepest, R4, was on average found at ∼68% depth (Table 3.6).

TABLE 3.6: Summary statistics for each IRH traced throughout the PIG-PASIN and OIB-MCoRDS2 surveys. We provide these for both depth below the surface and depth as a fraction of ice thickness. "1σ" refers to one standard deviation, "Range" refers to the minimum and maximum values, and "IQ Range" refers to the interquartile range (25th and 75th percentile). A maximum uncertainty of ±17 m is assumed here.

IRH depth statistics								
	Depth below the surface (m)				*Depth as fraction of ice thickness*			
	Mean	1σ	Range	IQ Range	Mean	1σ	Range	IQ Range
R1	722	191	204 - 1,302	623 - 873	0.30	0.10	0.12 – 0.63	0.22 – 0.36
R2	1,175	240	304 - 2,014	1,069 - 1,347	0.46	0.09	0.21 – 0.82	0.40 – 0.52
R3	1,463	298	650 - 2,486	1,324 - 1,650	0.54	0.08	0.29 – 0.82	0.48 – 0.60
R4	1,929	257	697 - 2,640	1,799 - 2,080	0.68	0.05	0.42 – 0.92	0.66 – 0.71

The traceability of R1-3 does not vary greatly and is primarily constrained by topography (Fig. 3.6a-c). By contrast, R4 was only detected across the upper THW/PIG catchments (Fig. 3.6d), even though it has previously been detected much further north into the PIG basin in the ITASE survey (Jacobel and Welch, 2005), likely due to the different frequency range used by the two RES systems. We come back to this point in Section 3.5.1. We were also able to trace R1-3 in the upper parts of the IMIS catchment, and R2-4 in the upper parts of the THW catchment toward the WD2014 site (Fig. 3.6). The traced IRHs are generally deeper southward of the onset of PIG tributaries 7 and 9 and at the centre of the PIG catchment, and relatively shallow at its southern margin and at the divides with THW and IIS (Fig. 3.6e-h). We were unable to identify the IRHs in several locations, mainly north of the main trunk of PIG near the Hudson Mountains range and west of tributary 6 (Fig. 3.6a). We were also unable to detect continuous IRHs in any PIG-PASIN profiles traversing the main trunk and tributaries of THW, nor those that cover the main trunk and fast-flowing tributaries of PIG (Fig. 3.6).

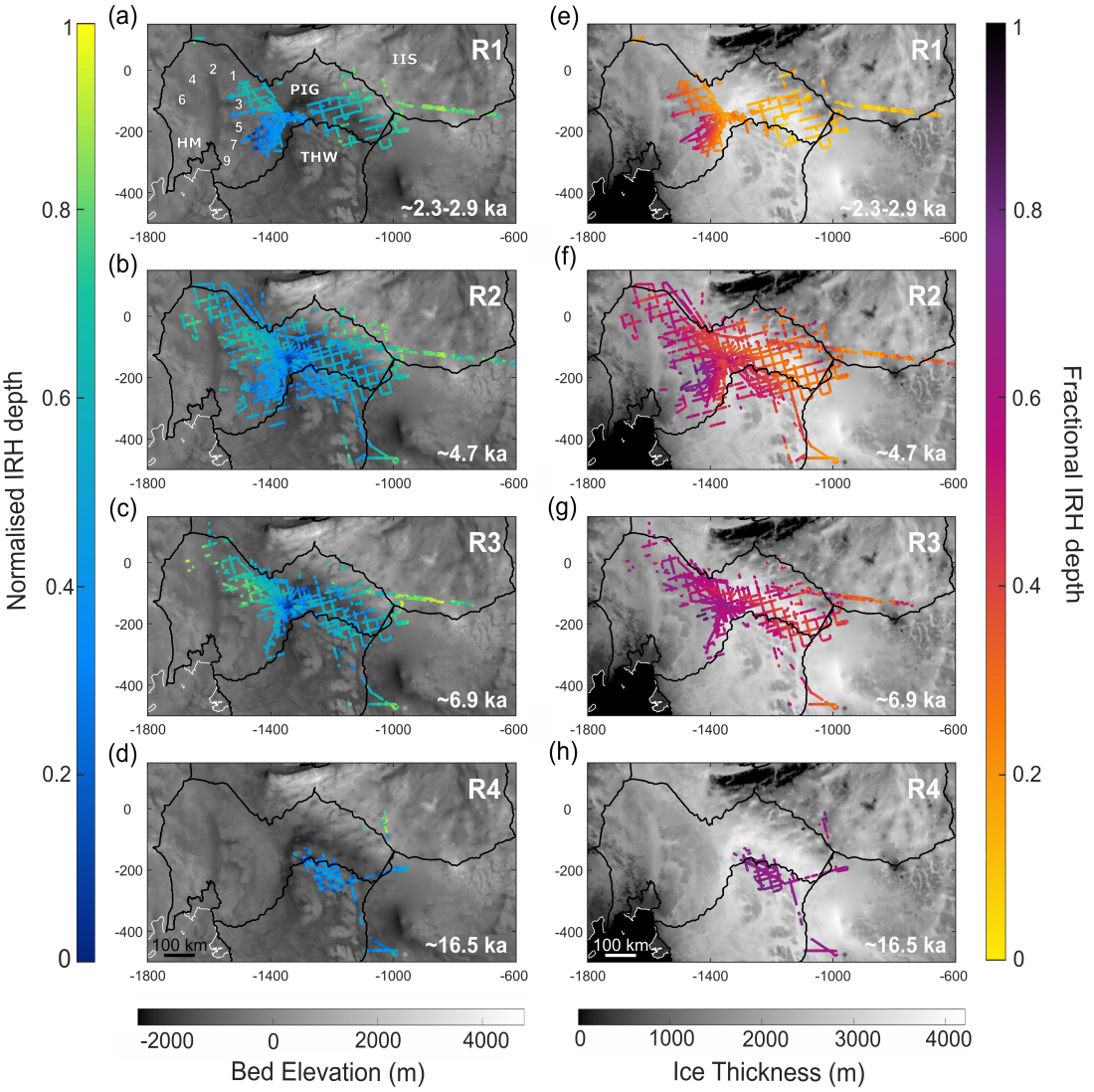

Figure 3.6: Normalised (a-d) and fractional (e-h) depth for the four IRHs traced over the PIG-PASIN and OIB-MCoRDS2 data from shallowest to deepest. Also shown are the IRH ages (ka) (see Section 3.4.2) for R1 (age-range estimate from 1-D model) and R2-4 (ages from WD2014 ice-core intersection). For (a-d), lower (blue) values correspond to relatively deep IRH depths, higher (yellow) values correspond to shallow IRH depths. Background is bed elevation in metres (referenced to the WGS84 ellipsoid) from BedMachine (Morlighem et al., 2020). For (e-h), lower (yellow) values correspond to the shallowest IRHs, higher (purple) values correspond to the deepest IRHs. Background is ice thickness in metres from BedMachine (Morlighem et al., 2020). The white line is the Antarctic coast line. The numbers and annotations in (a) are the eight fast-flowing tributaries (1-7, 9) of Pine Island Glacier, the location of the Hudson Mountain Range (HM), and the ICESat IMBIE basins containing PIG, THW and IIS (Zwally et al., 2012).

3.4.2 Age-depth estimates

Having clearly identified R2-4 near the WD2014 site, we attempt to date these using the WD2014 chronology. The OIB-MCoRDS2 RES profile passes within ∼1.2 km of the ice-core site, and the stable ice conditions in the area means that flow-induced disturbance on layer geometry is relatively limited (Laird et al., 2010). Following MacGregor et al. (2015), we calculate the unweighted mean reflection depth within a distance of ±250 m along transect from the trace that is closest to the ice-core site to obtain $\Delta a_{\Delta depth}$, resulting in mean depths at the ice core of 1,060 ± 7 (R2), 1,430 ± 9 (R3), and 2,371 ± 14 m (R4) (Table 3.7). Considering the RES-depth and ice-core uncertainties (Eq. (3.4)), and to account for the age offset between our IRHs and the strong sulphate peaks at the ice core (see Sections 3.3.4.1 and 3.5.2), we determined the age and associated age uncertainty for each IRH at WD2014 as: 4.72 ± 0.28 (R2), 6.94 ± 0.31 (R3), and 16.50 ± 0.79 ka (R4) (Table 3.7).

TABLE 3.7: IRH mean depths (m), ages (ka; in years before 2020 AD), and uncertainties (Δ) at the WD2014 site for R2-4. Column *"a (ka)"* refers to the IRH age obtained from the RES-depth and the depth at the WD2014 ice core. Column "Δa_{comb}" refers to the combined age uncertainty from the RES and the ice-core chronology, whilst "Δa_{total}" refers to the maximum age uncertainty of our IRHs calculated from the age difference between our IRHs and the strong sulphate peaks at WD2014 (see Section 3.3.4.1 and 3.5.2).

	depth (m)	$\Delta depth$ (± m)	*a* (ka)	$\Delta a_{\Delta depth}$ (± ka)	Δa_{core} (± ka)	Δa_{comb} (± ka)	Δa_{total} (± ka)
R2	1,060	7	4.72	0.04	0.05	0.06	0.28
R3	1,430	9	6.94	0.06	0.07	0.09	0.31
R4	2,371	14	16.50	0.28	0.50	0.57	0.79

To compare the ages independently from the WD2014 chronology and provide an approximate age-range estimate for our shallowest isochrone R1, we use the 1-D model at Site A and B. The age estimates returned from the 1-D model at both sites are as follows: R1 (2.31-2.92), R2 (4.46-5.82), R3 (6.75-9.15), and R4 (19.69-26.87 ka) (Table 3.8).

TABLE 3.8: Modelled IRH age-range estimates (ka) returned from the 1-D steady-state model for varying accumulation datasets (see Section 3.3.4.2) and basal shear layer thickness (*h*, in metres) scenarios at Site A and B for IRHs R1-4 (see Section 3.3.4.2). Note: At Site B, R4 was not retrieved. The accumulation rates (m a^{-1}) used to obtain each IRH age estimate can be found in Table 3.5. We calculate an empirical error estimate of between ±2 and 4% for each modelled age estimate based on the uncertainties in RES-derived depth (±17 m) and ice thickness (±23 m, Vaughan et al., 2006).

		Site A			Site B		
		h = 700	*h = 900*	*h = 1,100*	*h = 700*	*h = 900*	*h = 1,100*
R1	MAR	2.84	2.85	2.86	2.89	2.90	2.92
	ART06	2.68	2.69	2.70	2.78	2.80	2.81
	RACMO2	2.36	2.37	2.38	2.32	2.33	2.34
	MED14	2.31	2.32	2.33	2.36	2.37	2.38
R2	MAR	5.72	5.77	5.82	5.55	5.61	5.67
	ART06	5.40	5.44	5.49	5.35	5.40	5.46
	RACMO2	4.75	4.79	4.84	4.46	4.50	4.55
	MED14	4.65	4.69	4.73	4.57	4.62	4.67
R3	MAR	8.88	9.01	9.15	8.41	8.54	8.69
	ART06	8.38	8.50	8.63	8.10	8.23	8.37
	RACMO2	7.38	7.48	7.60	6.75	6.86	6.98
	MED14	7.22	7.32	7.43	6.92	7.03	7.15
R4	MAR	24.22	25.40	26.87	-	-	-
	ART06	22.85	24.00	25.40	-	-	-
	RACMO2	20.13	21.10	22.32	-	-	-
	MED14	19.69	20.64	21.84	-	-	-

The ages calculated for R2-3 at WD2014 (Table 3.7) are within the upper and lower bounds of the modelled age-range estimates from the 1-D model (Table 3.8), with the MED14 and RACMO2 accumulation products best able to reproduce the ages at WD2014 to within <10%. However, the returned age estimate for R4 at Site A, 19.69-26.87 ka, is 20 to 60% greater than the age of R4 at WD2014 (16.50 ± 0.79 ka) and that of Jacobel and Welch (2005) (17.5 ± 0.5 ka). We come back to these points in Sections 3.5.1 and 3.5.3.

3.5 Discussion

3.5.1 IRH comparison across the WAIS

Karlsson et al. (2014) traced two distinctive IRHs through the middle ice depths across parts of the central PIG catchment using the same PIG-PASIN dataset as that used here, but only focusing on flight lines flown at constant elevation and only exploiting the data in its chirp mode. This earlier study highlighted

the existence of a distinctive IRH package between an upper bound, "Layer 1", approximately dated to 5.3-6.2 ka, and a lower bound "Layer 2", approximately dated to 8.6-13.4 ka. Here, by additionally exploiting the full spatial extent of the PIG-PASIN dataset, the simultaneously-acquired pulse-mode PASIN data, and complementing these with recent OIB-MCoRDS2 data, we have expanded the reach of that earlier radiostratigraphy across the fuller PIG catchment, and across the ice divides into neighbouring regions, notably THW and IIS. Direct comparison between both sets of results suggests that Karlsson et al.'s (2014) Layer 1 and 2 are equivalent to the IRHs traced in this study as R2 and R3, with a median difference ranging between 6 and 12 m, which is within the depth uncertainty of the IRHs (Fig. 3.7).

Throughout the neighbouring IMIS catchments, Ashmore et al. (2020a) also recently traced three prominent IRHs (H1-3), broadly dated at 1.9–3.2 (H1), 3.5–6.0 (H2), and 4.6–8.1 ka (H3), using the same 1-D model described here. They posited that their deeper two IRHs (namely H2-3) were also similar to Karlsson et al.'s (2014) Layers 1 and 2 (and hence are likely equivalent to our R2 and R3), but the association was untested with any direct crossovers. Here, we were able to trace our upper three IRHs R1-3 along an OIB-MCoRDS2 profile extending across the upper IIS catchment (Fig. 3.6a-c), intersecting eight IMAFI-PASIN profiles in which H1-3 were traced. Across these intersections, the mean difference between OIB-MCoRDS2 R1-3 and IMAFI-PASIN H1-3 is 15 m, which is within the uncertainty bounds of the respective RES systems (±14 m for OIB-MCoRDS2; ±15 m for IMAFI-PASIN, Ashmore et al. (2020a)), and hence provides additional evidence that we observe the same IRHs across both catchments. Two sets of parallel profiles, laterally offset by ∼1.5 km, and acquired across the PIG/IIS divide in the PIG-PASIN and IMAFI-PASIN datasets (Fig. 3.1), provide a further opportunity to confirm these equivalences with data from the same RES system. Only in three short sections of these transects could we compare our IRHs with those from the IMAFI-PASIN study (inset in Figure 3.7a); in these locations, we could not identify R1 and R3. Nevertheless, at two intersections (black arrows in inset on Figure 3.7a), the respective depths for PIG-PASIN R2 and IMAFI-PASIN H2 were 794 and 797 m at Intersection 1 and 776 and 778 m at Intersection 2 respectively, which is remarkably close considering ice thickness in this area exceeds 2 km. This, alongside the crossovers on the OIB-MCoRDS2 data, gives us high confidence that our R2, Ashmore et al.'s (2020a) H2, and therefore Karlsson et al.'s (2014) Layer 1, all represent the same internal marker in the ice. This study, by using additional data that allowed direct dating at the WD2014 site, is therefore able to ascribe more accurate and precise ages to the IRH package ranging across PIG and IMIS of 4.72 ± 0.28 ka (Layer 1/H2/R2) and 6.94 ± 0.31 ka (Layer

2/H3/R3) respectively based on the WD2014 ice-core chronology.

We also note that all three studies identify R2 as their most spatially extensive IRH, indicating the presence of a particularly ubiquitous isochrone, similar in age to a 4.72 ± 0.24 ka isochrone detected and also extensively mapped elsewhere across central West Antarctica (Muldoon et al., 2018). Whilst we were not able to provide a more refined age to our shallowest IRH, R1, from direct intersection with the WD2014 Ice Core, the 1-D model returned an age-range estimate (2.31-2.92 ka) that is in broad agreement with that of Ashmore et al. (2020a) (1.9–3.2 ka; their H1) and Siegert and Payne (2004) (3.10 ± 0.16 ka; their L07). Together, these studies demonstrate considerable promise for unifying an age-depth stratigraphy across the WAIS back to at least ∼7 ka, while tying our IRHs to the WD2014 Ice Core has yielded more accurate, and younger, ages, for the isochrones detected across PIG and, by extension, IMIS.

The age assigned to R4 at WD2014 (16.50 ± 0.79 ka) is slightly younger than the 17.5 ± 0.5 ka layer tied by Jacobel and Welch (2005) to the Byrd Ice Core (Hammer et al., 1997), although there is an overlap of 0.29 ka when fully accounting for the age uncertainties. We offer two potential explanations for this disparity. Firstly, the low-frequency ground-based RES system used as part of the ITASE survey has a much longer wavelength than the high-frequency airborne systems used here, meaning that the 17.5 ± 0.5 ka layer appears as a single-amplitude peak measuring tens of metres in thickness (c.f. Jacobel and Welch, 2005), whereas the shorter-wavelength on the airborne RES systems allows for the delineation of individual peaks, thus resolving the strong singular reflector from Jacobel and Welch (2005) as a series of closely spaced reflectors. As a result, when attempting to connect the ITASE profile with the airborne RES data, it is likely that the closest bright reflector identified on the airborne RES data forms the upper part of the wider reflector imaged by Jacobel and Welch (2005), thus leading to younger ages at the intersection with the WD2014 Ice Core. Secondly, the uncertainties in the RES data at the intersection between OIB-MCoRDS2 (± 14 m) and Jacobel and Welch's (2005) profile (± 10 m) increase the chance to misinterpret the correct position of the 17.5 ka layer over the airborne data, although we show in Table 3.3 that the mean depth difference between R4 and Jacobel and Welch's (2005) layer is <18 m, which is within the uncertainty range of both studies. Whilst these points are relevant when comparing the ages of R4 at WD2014 with the age of Jacobel and Welch's (2005) layer, it is worth mentioning that the exact age and depth of the strong reflector at WD2014 are known from electrical conductivity and chemistry measurements. At the ice core, this layer is characterised by nine distinctive peaks ranging in depths between 2,420 m and 2,427 m and dated at

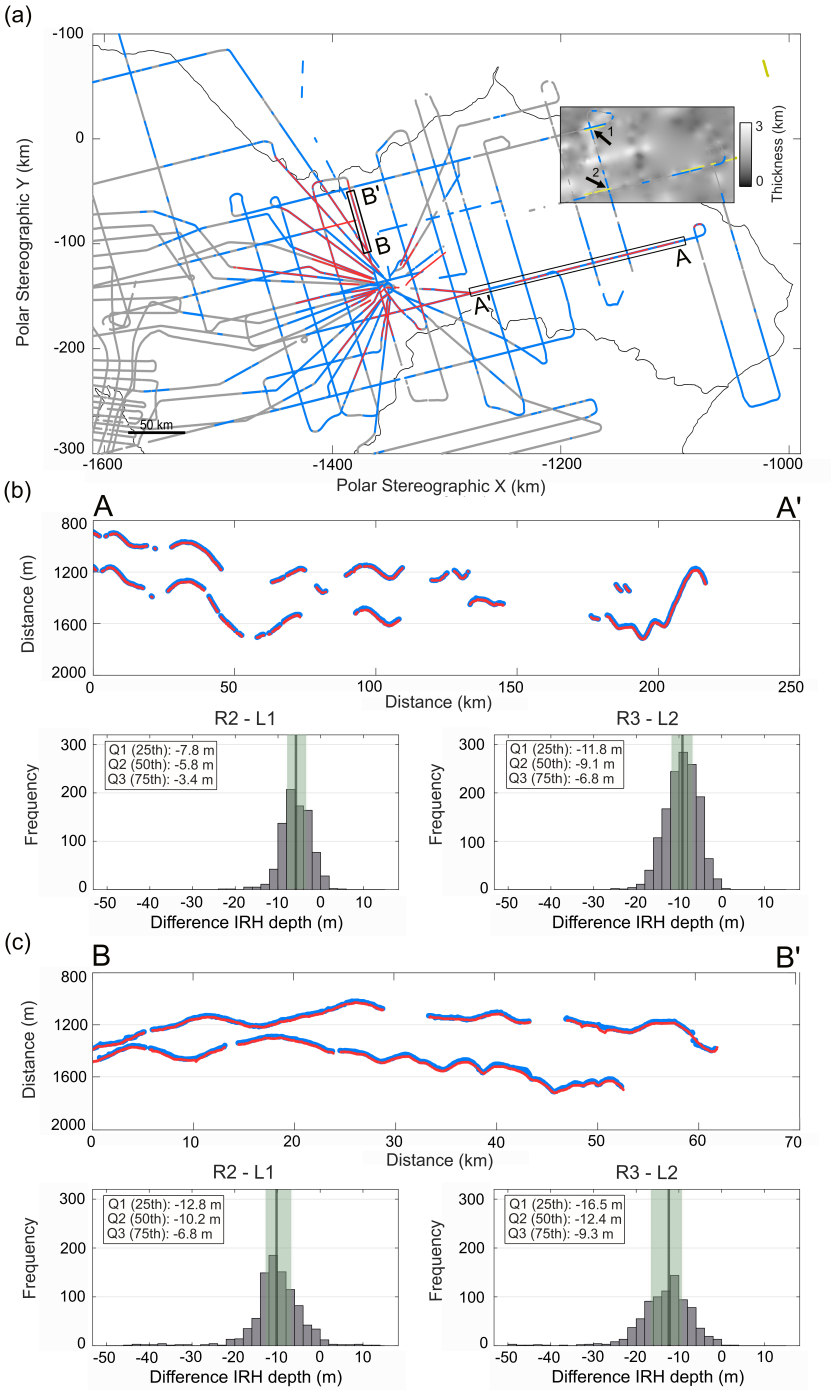

Figure 3.7: Comparison between our IRHs and Karlsson et al. (2014) and Ashmore et al.'s (2020a) IRHs. (a) Spatial extent of traced IRHs over Pine Island Glacier using the PIG-PASIN dataset: subset of R2-3 package from this study (blue), Karlsson et al.'s (2014) Layer 1-2 (abbreviated in the figure as L1-2) (red). The grey lines in the background show a subset of the PIG-PASIN flight lines onto which Karlsson et al.'s (2014) Layer 1-2 were traced. The black outline lines are the ICESat IMBIE basins containing PIG and THW (Zwally et al., 2012). Inset in top right shows the location where Ashmore et al.'s (2020a) H2-3 (yellow) from the PIG-PASIN survey (see Figure 3.1) intersect our IRHs over PIG, with ice thickness (m) from BedMachine (Morlighem et al., 2020) in the background. The black arrows are where we directly compare Ashmore et al.'s (2020a) H2 and our R2. (b) Comparison between R2-3 (blue) and Karlsson et al.'s (2014) L1-2 (red) (top) and histograms showing the key statistics of the difference between R2/L1 and R3/L2 (bottom) for segment A-A' (see (a)). The median is represented by the thick green line and the 25th and 75th interquartile range is shown in shaded green. (c) As (b) but for segment B-B'. Note that the segments A-A' and B-B' shown here are distinct from the AA-AB segment shown in Figure 3.1.

17.75 ± 0.19 ka (Sigl et al., 2016; McConnell et al., 2017), a full 35 m below the depth of R4 at WD2014. Even taking into account the maximum depth of our IRH along the ±250 m transect (2,378 ± 14 m; see Table 3.7), R4 is still found 28 m above the depth of the 17.75 ± 0.19 ka at WD2014. Considering all the above, it is likely that R4 is not the same layer as the strong volcanic layer dated at 17.75 ± 0.19 ka at WD2014 (McConnel et al., 2017), but rather forms the upper part of the wide reflector imaged by Jacobel and Welch (2005) in the ground-based RES data.

3.5.2 Linkage with the WAIS Divide ice-core record

Whilst determining the cause of R4 remains ambiguous due to the limitations mentioned above, the existence of R2 and R3 offer an opportunity to link them directly to the ice-core sulphate record at WD2014. High sulphate content from volcanic sulphuric acid is known to correspond to high acidity levels in englacial layers in ice cores (Gow and Williamson, 1971; Hammer et al., 1997; Millar, 1982; Castellano et al., 2005) and, because the radar is sensitive to acidity contrasts (Millar, 1981; Fujita et al., 1999), we can attempt to link the sulphate record at the ice core with our IRH stratigraphy. Figure 3.8 shows the presence of three large peaks in sulphate concentration at the WD2014 ice core which are particularly close in age and depth to IRHs R2-3 traced on the OIB-MCoRDS2 profile near WD2014. In particular, a layer dated at 4.94 ka (depth: 1,099 m) contains sulphate concentrations that are unmatched (405 μg kg^{-1}) for much of the core up until a depth of ∼2,400 m (equal to the last ∼18,000 years BP) (Fig. 3.8). Even taking into account the entire profile, this layer contains the fourth largest amount of sulphate concentrations in the last ∼68,000 years BP. We also notice the presence of two closely-spaced peaks in the sulphate record which are dated at 7.25 ka (depth: 1,475 m; sulphate concentration: 306 μg kg^{-1}) and 7.64 ka (depth: 1,526 m; sulphate concentration: 271 μg kg^{-1}), corresponding to the 9th and 10th highest sulphate concentrations on record (Fig. 3.8b). Not only do these ages match closely the age of R3 at the ice core, they also match the characteristics of R3, which is often found as a couplet across most of PIG, upper THW, and IMIS catchments on the airborne RES data (Figs. 3.2 and 3.3). Additionally, the second largest peak on record before ∼18,000 years BP is found at a depth of 584 m and dated at 2.45 ka (sulphate concentration: 309 μg kg^{-1}), which falls within the modelled age-range estimate for R1 (2.31-2.92 ka) at Site A and B (Table 3.8, Fig. 3.8a).

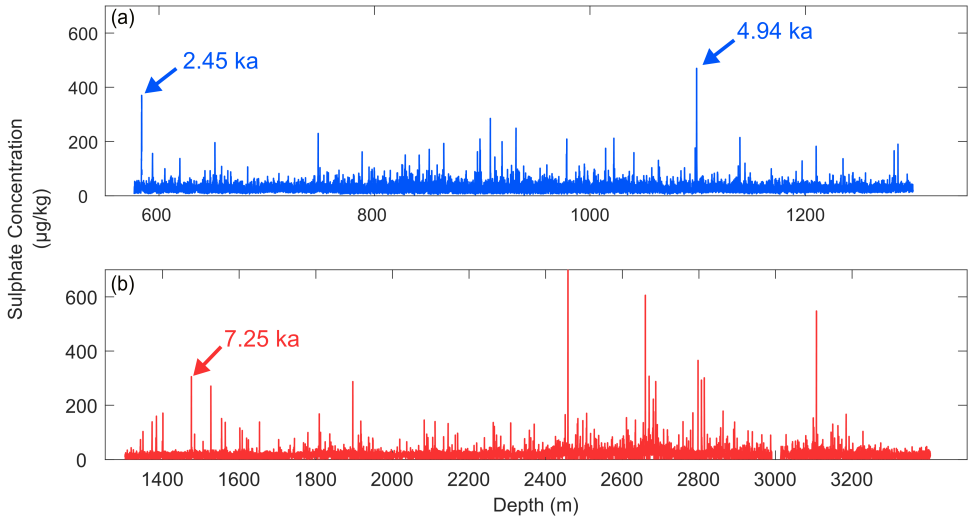

Figure 3.8: Sulphate concentration (μg kg^{-1}) as a function of depth (m) at the WAIS Divide ice-core site for: (a) the brittle section of the WDC06A ice core (577-1,300 m) from Cole-Dai (2014); and (b) for depths of 1,300-3,404 m at WD2014 Ice Core from McConnell (2017). Peaks of sulphate concentration matching the age-depths of R1-3 and dated at 2.45 ka, 4.94 ka, and 7.25 ka are also shown. The ages shown are from the WD2014 chronology and are in years before 2020 AD.

Whilst this offers us the opportunity to directly link our IRHs to the WAIS Divide record, we note that the depths of R2-3 at WD2014 are slightly shallower (R2: 1,060 ± 7 m; R3: 1,430 ± 9 m) than the sulphate peaks in Figure 3.8, resulting in slightly younger ages at the ice core. We cannot exclude the possibility that we traced a layer that is slightly above R2 and R3 at the ice-core site, although this is unlikely as we base our tracing on depth intersections (Fig. 3.4) and IRH characteristics (Figs. 3.2 and 3.3). Even taking into account the maximum depth of R2-3 along our ±250 m transect to account for the fact the OIB-MCoRDS2 line did not fly directly over the WD2014 site but instead ∼1.2 km away (Sect. 3.3.4.1), R2 (1,069 ± 7 m) and R3 (1,438 ± 9 m) would still be found 23 m and 28 m higher than the sulphate peaks at the ice core respectively. Whilst this is a relatively small disparity considering ice thickness in the area exceeds ∼3.5 km and that we are effectively comparing airborne-RES data (metre-scale accuracy) with ice-core data (mm-scale accuracy), the reason for our IRHs not aligning more closely with the sulphate peaks remains unclear. One potential explanation could relate to the distance between our transect and the location of the WD2014 ice-core site. Although Laird et al. (2010) suggested that flow-induced disturbance on layer geometry is limited in the area around the WD2014 site, changes in bed roughness were found to affect englacial stratigraphy near WD2014. This could lead to small undulation in IRH elevations between our transect and WD2014

and thus likely result in several metres of discrepancy. To acknowledge this, and considering that the sulphate peaks are most likely the cause of our IRHs as we show above, we have increased the age uncertainty of our IRHs to account for the offset between our IRH ages and the age of the sulphate peaks (Sect. 3.3.4.1, Table 3.7). This results in more conservative uncertainties for our deeper three IRHs dated at the ice core: 4.72 ± 0.28 (R2), 6.94 ± 0.31 (R3), and 16.50 ± 0.79 ka (R4).

By linking three of our four IRHs to the sulphate record at WAIS Divide, we can hypothesise that the origin of our spatially extensive IRHs is from past explosive volcanic activity during the Holocene. Previous studies in Antarctica have demonstrated the correspondence between bright reflectors in the RES data and past volcanic activity (e.g. Jacobel and Welch, 2005; Corr and Vaughan, 2008). Karlsson et al. (2014) previously attempted to link their deeper layer (Layer 2/R3) to acidity peaks at Byrd Ice Core, however the absence of a direct link between the PIG catchment and a complete ice-core chronology was lacking at the time. The evidence presented here suggests that our IRHs may also originate from past explosive volcanism; though the precise source of these eruptions, whether regional or global, remains unknown.

3.5.3 Accumulation rate and IRH-age comparison

The correspondence in isochrone-age estimates for IRHs R2-3 derived from intersecting the WD2014 site (Table 3.7) and using the 1-D model (Table 3.8) at the PIG/THW divide (∼250 km away) (our Sites A and B; Fig. 3.1) suggests that accumulation patterns have remained broadly similar across the Amundsen-Ross divide for at least the last ∼7 ka. Whilst this is based on a relatively limited amount of data points, it complements previous studies (Neumann et al., 2008; Fudge et al., 2016; Koutnik et al., 2016), including Siegert and Payne (2004) who, using the same SPRI/NSF/TUD RES transect as that in Figure 3.1, concluded that accumulation patterns have remained stable over the last 6.4 ka. We suggest future research make use of the accurately dated IRHs provided here to model Holocene accumulation rates and patterns, as well as regional ice-sheet balance velocities, as previously conducted over Greenland (e.g. MacGregor et al., 2016) and on individual sections of the WAIS (Koutnik et al., 2016; Neuman et al., 2008). This will provide additional information on the terrestrial ice-sheet history of the Amundsen Sea Embayment during the Holocene, and in turn help us to constrain better the future of the WAIS.

Previous studies have successfully combined ice-core records with modelled modern-day accumulation rates to reconstruct Holocene accumulation (Fudge et al., 2016; Cavitte et al., 2018; Nielsen et al., 2018), although non-climatic noise in

the observations and model biases have resulted in small discrepancies between ice-core and model reconstructions (Cavitte et al., 2020; Dalaiden et al., 2020). When assessing the ability of the 1-D model to reproduce the ages for R2-3 derived at the WD2014 Ice Core, we find that the best match (to within <10%) is achieved using the modern accumulation rates provided by the MED14 and RACMO2 products. This is not surprising as both have higher spatial resolution than MAR and ART06, but it also likely reflects the fact that MED14 is an observational product and that RACMO2 has been shown to agree well with geophysical estimates of accumulation rates (Lenaerts et al., 2012; Medley et al., 2014; Wang et al., 2016; van Wessem et al., 2018). In contrast, when using present-day accumulation estimates from ART06 and MAR to calculate past accumulation rates, model-derived ages are up to 1.1 ka (∼23%) greater for R2 and 2.2 ka (∼32%) greater for R3 compared with ice-core derived ages (Tables 3.7-3.8). This discrepancy is primarily dominated by different modern accumulation gradients estimated between WD2014 and the PIG/THW divide (i.e. Site A and B), with the MED14 and RACMO2 products suggesting a slightly more homogenous gradient than ART06 and MAR (Table 3.5). Lower in the ice, the poor correspondence between the age of R4 derived by links to the WD2014 (16.50 ± 0.79 ka) relative to the age returned by the 1-D model (19.69-26.87 ka) is worthy of investigation. Even taking into account the maximum age uncertainty at the ice core, the minimum and maximum age returned by the 1-D model is 2.6 (15%) and 9.8 ka (57%) greater than at the ice core (Tables 3.7-3.8), a difference that cannot solely be attributed to the different modern-day accumulation gradients mentioned above. The most likely explanation is that the assumptions required for the 1-D model (see Section 3.3.4.2) break down for older IRHs, where local accumulation rate is no longer a primary factor in determining the depth of an IRH. This could be due to complex flow dynamics such as longitudinal strain or lateral shearing at the boundary between slow and fast-flowing ice, resulting in high internal stress impacting IRH stratigraphy in the deeper part of the ice column (Waddington et al., 2007). Moreover, R4 (16.50 ± 0.79 ka) was deposited pre-Holocene as the WAIS was transitioning from a glacial to an interglacial period during which ice thickness has likely not remained constant (Golledge et al., 2014; Johnson et al., 2017), implying possible changes in ice-flow configurations for which the steady-state model is not able to account.

3.5.4 Characteristics of englacial stratigraphy

Previous research over East Antarctica has shown that common bright reflectors can be interchangeably traced over long distances using RES systems operating at different centre frequencies (Cavitte et al., 2016; Winter et al., 2017). Our findings provide further evidence of this over West Antarctica, having successfully identified common IRHs across different airborne RES systems. However,

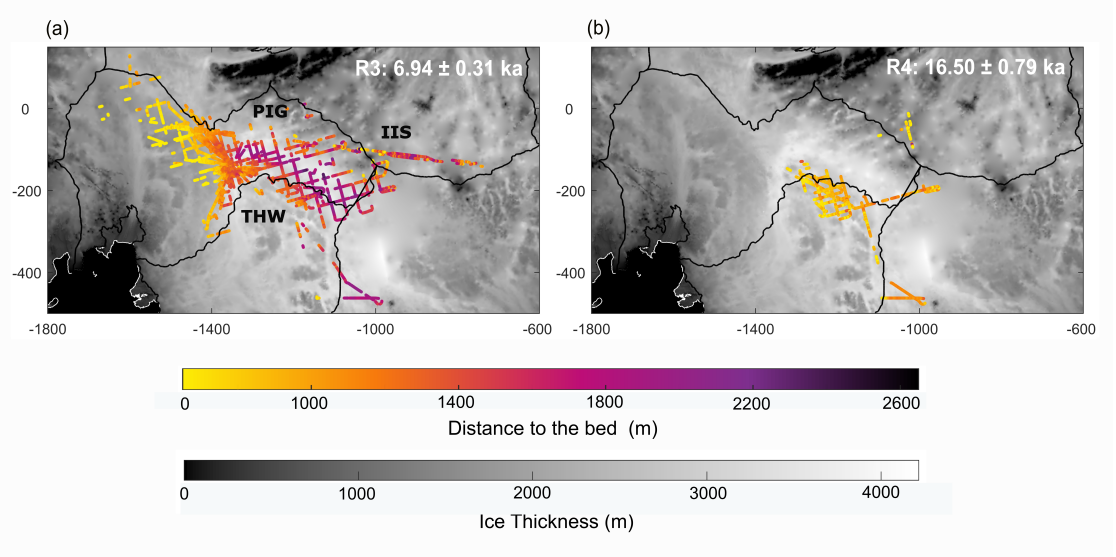

Figure 3.9: Ice thickness (m) below R3 (a) and R4 (b) traced over the PIG-PASIN and OIB-MCoRDS2 data. The ages are from the intersection with the WD2014 ice-core site (see Table 3.7). Background is ice thickness in metres from BedMachine (Morlighem et al., 2020). The white line is the Antarctic coast line and the black outlines are the ICESat IMBIE basins containing the PIG, THW, and IIS (Zwally et al., 2012).

although IRHs younger than 7 ka can be traced widely across the WAIS using existing datasets, tracing deeper, pre-Holocene IRHs has not been widely possible across PIG (this study) nor the Weddell Sea Sector (Ashmore et al., 2020a). Relative to the interior of East Antarctica, where much lower snow accumulation and ice-flow velocities have facilitated the tracing of isochrones pre-dating the Last Glacial Maximum (∼20 ka BP) and even the past glacial-interglacial periods (up to ∼366 ka BP) (Steinhage et al., 2013; Cavitte et al., 2016; Parrenin et al., 2017; Winter et al., 2019), the extremely variable deep-ice conditions in the WAIS will challenge the recovery of pre-Holocene radiostratigraphy. Compounding the challenge, Ross et al. (2020) have demonstrated that large packages of ice older than ∼16 ka in the Weddell Sea sector of the WAIS are rheologically different to the ice above, containing large proportions of deformed and folded ice. These packages typically show poor continuity of englacial stratigraphy across IMIS (Bingham et al., 2015) and, indeed, where we could see IRHs deeper than R4 in PASIN and MCoRDS2 for this study, very few were continuous for long distances. Over other parts of the WAIS, an IRH dating back to 24.9 ± 0.3 ka has been traced in limited RES profiles connecting the Byrd and WAIS divide ice cores, where it was found at 68% and 80% of ice depth at Byrd and WD2014 respectively (Muldoon et al., 2018); however they were also unable to recover deeper continuous IRHs more widely.

Overall, with the existing datasets available across the WAIS, the prospects for tracing and dating Holocene radiostratigraphy widely across the ice sheet with existing data are excellent, but diminish rapidly for older ice, going back to the LGM and beyond. Yet, much deeper, and thus older IRHs, are visible throughout the ice column with ground-based RES systems (e.g. Laird et al., 2010; King, 2011; Bingham et al., 2017) and hence the interrogation of older ice in the WAIS may be best suited to strategic ground campaigns that can be linked into the airborne-derived radiostratigraphy. In the PIG catchment, older ice is suggested by our results to lie below the PIG/THW divide, where on average ∼900 m of ice (30% of the mean ice thickness) underlies R4 (17 ka) (Fig. 3.9).

3.6 Conclusions

We have identified four spatially extensive Internal Reflecting Horizons (IRH) in airborne RES surveys that are present across much of the Pine Island Glacier (PIG) catchment in West Antarctica. Extending into neighbouring Thwaites Glacier (THW) and Institute Ice Stream, these IRHs can be considered isochrones that span the late Pleistocene and Holocene, with ages of 2.31-2.92, 4.72 ± 0.28, 6.94 ± 0.31, and 16.50 ± 0.79 ka derived from intersecting the WAIS Divide ice core and the use of a 1-D ice-flow model. Our most spatially extensive IRH, R2, is remarkably similar in age and depth to another extensive IRH previously identified by other studies over Pine Island Glacier, Institute and Möller Ice Streams, and the Marie Byrd Land region. More broadly, we have also shown that our IRH package is similar to previously-traced IRHs over the Weddell Sea sector of the WAIS, which, together with the Pine Island Glacier catchment represents ∼20% of West Antarctica. Lastly, we have shown that our upper three IRHs correspond to large peaks in sulphate concentrations at the WAIS Divide ice core, suggesting that our IRHs are of volcanic origin.

When assessing the presence of older ice across the catchment, we observe that the relative proportion of ice older than R4 in the ice column is limited and does not contain many continuous reflections. Indeed, we find that the deepest (and thus oldest) continuous IRH identified in this study, R4, is found at an average depth of 68% in the ice column despite its age (∼17 ka) only representing 25% of the estimated age of the oldest ice recovered at the WAIS Divide ice core (∼68 ka). This indicates that the majority of ice older than the LGM is found within the bottom ∼30% of the ice thickness across PIG/upper THW. Whilst this is to be expected as the age-depth profile of an ice sheet does not increase linearly, the absence of continuous reflections dating back to the Last Glacial Maximum and

older currently limits our ability to reconstruct longer-term changes using existing airborne datasets.

As isochronous features, the dated IRHs generated here offer a new set of large-scale boundary conditions that could be a valuable resource, if incorporated into ice-flow models seeking to improve our understanding of past ice-sheet evolution. We anticipate that these well-dated IRHs will provide constraints for models simulating past accumulation rates and patterns, which in turn will shed more light onto the terrestrial ice sheet history of this very sensitive catchment of the WAIS.

3.7 Data availability

The RACMO2 and MAR SMB outputs were downloaded from https://www.projects.science.uu.nl/iceclimate/publications/data/2018 and https://zenodo.org/record/2547638 respectively. The IRH from Ashmore et al. (2020a) can be found at: https://doi.org/10.5281/zenodo.4945301 (Ashmore et al., 2020b). The BAS airborne RES data which were used to extract the IRHs used in this chapter are fully available at the UK Polar Data Centre via the Polar Airborne Geophysics Data Portal (see Frémand, Bodart et al., 2022). Parts of the figures included in this study were produced with outputs from the Antarctic Mapping Toolbox in MATLAB (Greene et al., 2017). The full picking information for each IRH can be downloaded from the UK Polar Data Centre (https://doi.org/10.5285/f2de31af-9f83-44f8-9584-f0190a2cc3eb; Bodart et al., 2021b).

4 Holocene Accumulation over West Antarctica

A version of this chapter has been published in *The Cryosphere*, as:

Paper details: Bodart, J.A., Bingham, R.G., Young, D.A., MacGregor, J.A., Ashmore, D.W., Quartini, E., Hein, A.S., Vaughan, D.G., and Blankenship, D.D. 2023. High mid-Holocene accumulation rates over West Antarctica inferred from a pervasive ice-penetrating radar reflector. *The Cryosphere*, 17(4), 1497-1512. DOI: 10.5194/tc-17-1497-2023 (see Appendix B for a copy of the paper).

Author contributions: I conceived the study with input from R.G. Bingham, D.A. Young and D.D. Blankenship. I developed the methods, performed the primary data analysis and interpretation, and wrote the paper. J.A. MacGregor provided guidance for the 1-D models and the calculation of the model's structural uncertainty. All co-authors provided inputs to the final manuscript.

4.1 Abstract

Understanding the past and future evolution of the Antarctic Ice Sheet is challenged by the availability and quality of observed palaeo-boundary conditions. Numerical ice-sheet models often rely on these palaeo-boundary conditions to guide and evaluate their models' predictions of sea-level rise, with varying levels of confidence due to the sparsity of existing data across the ice sheet. A key data source for large-scale reconstruction of past ice-sheet processes are Internal Reflecting Horizons (IRHs) detected by Radio-Echo Sounding (RES). When IRHs are isochronal and dated at ice cores, they can be used to determine palaeo-accumulation rates and patterns on large spatial scales. Using a spatially extensive IRH over the Pine Island Glacier (PIG), Thwaites Glacier (THW), and the Institute and Möller Ice Streams (IMIS, covering a total of 610 000 km2 or 30% of the West Antarctic Ice Sheet (WAIS)), and a local layer approximation model, we infer mid-Holocene

accumulation rates over the slow-flowing parts of these catchments for the past ∼4,700 years. By comparing our results with modern climate reanalysis models (1979 – 2019) and observational syntheses (1651 – 2010), we estimate that accumulation rates over the Amundsen-Weddell-Ross Divide were on average 18% higher during the mid-Holocene than modern rates. However, no significant spatial changes in the accumulation pattern were observed. The higher mid-Holocene accumulation-rate estimates match previous palaeo-accumulation estimates from ice-core records and targeted RES surveys over the ice divide, and they also coincide with periods of grounding-line readvance during the Holocene over the Weddell and Ross sea sectors. We find that our spatially extensive, mid-Holocene-to-present accumulation estimates are consistent with a sustained late-Holocene period of higher accumulation rates occurring over millennia reconstructed from the WAIS Divide Ice Core (WD2014), thus indicating that this ice core is spatially representative of the wider West Antarctic region. We conclude that future regional and continental ice-sheet modelling studies should base their climatic forcings on time-varying accumulation rates from the WAIS Divide ice core through the Holocene to generate more realistic predictions of the West Antarctic Ice Sheet's past contribution to sea-level rise.

4.2 Introduction

Improving our knowledge of past climatic changes over the Antarctic Ice Sheet is required if we are to understand its present evolution and model its future under increasingly rapid climatic changes (IPCC, 2021). Most studies of past ice-sheet behaviour over Antarctica have focused on modelling changes in ice volume and grounding-line retreat following the Last Glacial Maximum (LGM, ∼20 ka BP; Before the Present) (Denton and Hughes, 2002; Golledge et al., 2012; 2013; Hillenbrand et al., 2013; 2014; Le Brocq et al., 2011; Kingslake et al., 2018); however, less attention has been paid to ice-sheet evolution during the Holocene (∼11.7 ka BP). Recent evidence suggests that parts of the grounding line of West Antarctica may have retreated several hundred kilometres inland from its current position at ∼10 ka and subsequently readvanced to reach its modern position sometime during the Holocene, due to isostatic rebound and climate-induced changes, particularly over the Weddell Sea and western Ross Sea sectors (Siegert et al., 2013; Bradley et al., 2015; Kingslake et al., 2018; Wearing and Kingslake, 2019; Venturelli et al., 2020; Neuhaus et al., 2021; Johnson et al., 2022). However, the atmospheric and ice-dynamical conditions farther inland, which could also have induced grounding-line migration, remain poorly constrained. An early investigation by Whillans (1976) using radar data near the Byrd ice core indicated stability during the Late Pleistocene and Holocene epochs. Records of temperature and

precipitation from the WAIS Divide ice core (hereafter abbreviated as WD2014; Fig. 4.1) in the central West Antarctic Ice Sheet (WAIS) suggest higher accumulation rates during the Holocene than at present (Fudge et al., 2016), a trend that is also observed across small parts of the Amundsen-Weddell-Ross Divide (Fig. 4.1) where isolated Radio-Echo Sounding (RES) surveys have shown 15-30% higher accumulation rates during the mid-Holocene compared to modern values (Siegert and Payne, 2004; Neumann et al., 2008; Koutnik et al., 2016).

Many numerical ice-sheet models that aim to predict Antarctica's long-term (past and future) contribution to sea-level rise use past ice-sheet reconstructions from after the LGM to guide and evaluate their models (Chavaillaz et al., 2013; DeConto and Pollard, 2016; Bracegirdle et al., 2019). However, even well-used ice-sheet reconstructions assume that the ice sheet retreated continuously throughout the Holocene (e.g. RAISED Consortium, 2014), a finding that has been challenged recently for the WAIS (e.g. Kingslake et al., 2018). Further, significant discrepancies between model simulations and the palaeo-proxy record currently impede our ability to confidently predict how the ice sheet will respond to future changes in the climate (e.g. Johnson et al., 2021). While improvements in model parameterisations are needed to close this gap (Bracegirdle et al., 2019; Sutter et al., 2021), considerable improvement in the availability and quality of palaeo-proxy records, particularly during the Holocene, is also needed to provide better constraints for ice-sheet models and ultimately better resolve past ice-sheet changes (Kingslake et al., 2018; Jones et al., 2022). Palaeo-proxy data have traditionally come from point-based measurements, such as ice cores (e.g. Petit et al., 1999; Parrenin et al., 2007; WAIS Divide Project Members, 2013; Buizert et al., 2021), sediment cores (e.g. Hillenbrand et al., 2013; Arnd et al., 2017; Hillenbrand et al., 2017; Kingslake et al., 2018; Venturelli et al., 2020; Neuhaus et al., 2021; Sproson et al., 2022), or surface-exposure dating (e.g. Stone et al., 2003; Suganuma et al., 2014; Johnson et al., 2014; Hein et al., 2016b; Nichols et al., 2019; Johnson et al., 2020; Braddock et al., 2022). A complementary and spatially extensive alternative data source for inferring past climate across an ice sheet is provided by Internal Reflecting Horizons (IRHs) detected by RES. They primarily result from englacial acidity contrasts and are often detected for hundreds of kilometres on RES data (Harrison, 1973; Bingham and Siegert, 2007). When employed in combination with ice-core stratigraphies, IRHs can be used to extend age-depth relationships away from an ice core by following peaks in electromagnetic return power in the radar data (e.g. Beem et al., 2021; Bodart et al., 2021a; Cavitte et al., 2016; Jacobel and Welch, 2005; MacGregor et al., 2015; Whillans, 1976; Winter et al., 2019).

In contrast to East Antarctica and Greenland, the IRH extension of WAIS ice cores has been challenging so far due to fewer deep ice cores there and, until recently, the lack of well-dated IRH datasets. However, efforts have intensified in recent years to improve our understanding of ice stratigraphy over this sector. In particular, four recent studies using airborne RES data (Karlsson et al., 2014; Muldoon et al., 2018; Ashmore et al., 2020a; Bodart et al., 2021a) all identified a distinct and bright IRH dated using the Byrd and WD2014 ice-core chronologies to 4.72 ± 0.28 ka BP (Muldoon et al., 2018; Bodart et al., 2021a). A comparison of volcanic sulphate deposition within the WD2014 and Siple Dome ice cores revealed a large peak in sulphate concentration that matches the age and depth of this ubiquitous IRH (Kurbatov et al., 2006; Bodart et al., 2021a; Cole-Dai et al., 2021; Sigl et al., 2022), which we hereafter term the "4.72 ka IRH". This IRH has now been observed by multiple RES systems and extends throughout much of the slower-flowing ice of the Amundsen and Weddell sea embayments (<400 m a^{-1}), including across the divides demarcating regions draining into the Amundsen, Weddell, and Ross seas.

Despite their potential wide-ranging applications, the incorporation of IRHs into ice-sheet models has been limited so far compared to other types of palaeo-proxy data, primarily because the inference of accumulation-rate or ice-flow history from IRHs is an ill-posed inverse problem (Waddington et al., 2007). Previous applications using IRHs to inform regional and continental models include the following: (a) constraining decadal-scale Surface Mass Balance (SMB) estimates from atmospheric models using annually resolved IRHs found in the shallow firn (Medley et al., 2013; 2014; Van Wessem et al. 2018; Dattler et al., 2019; Kaush et al., 2020; Cavitte et al., 2022); (b) inferring past accumulation rates going back further in time (i.e. hundreds to thousands of years) with the aim of comparing past accumulation estimates with modern times (e.g. Leysinger Vieli et al., 2004; Siegert and Payne, 2004; Neumann et al., 2008; MacGregor et al., 2009; 2016; Leysinger Vieli et al., 2011; Cavitte et al., 2017); or (c) integrating both their characteristics (e.g. elevation in the ice) and the information inferred from them (e.g. accumulation or basal-melt rates) to evaluate the output from regional and continental ice-sheet models (Leysinger Vieli et al., 2011; 2018; Holschuh et al., 2017; Sutter et al., 2021). Promisingly, Sutter et al. (2021) recently showed that spatially extensive Antarctic IRHs can provide unique benchmarks for constraining ice-sheet model parameterisations (i.e. climate forcing and simulated ice flow), which are then used to simulate palaeo ice-sheet evolution. Together, these studies indicate multiple avenues for ice-sheet models to assimilate IRHs to further improve estimates of past, current, and future ice-sheet changes.

Here, we estimate mid-Holocene accumulation rates across the WAIS from first-order calculations using a one-dimensional (1-D) model, constrained by the spatially extensive 4.72 ka IRH. We first describe the data, the model used and their limitations and uncertainties (Sect. 4.3). We then present our accumulation-rate estimates and compare them to observed and modelled modern accumulation rates to reveal a longer-term perspective on changes between the mid-Holocene and the present (Sect. 4.4). Finally, we place our results in the context of previous studies that consider WAIS evolution during the Holocene (Sect. 4.5).

4.3 Data and methods

4.3.1 Along-track IRH data

We used data from extensive (∼91,000 km) RES surveys acquired across West Antarctica between 2004 and 2018. The main contributing surveys are the University of Texas Institute for Geophysics (UTIG) 2004-2005 AGASEA (Airborne Geophysical Survey of the Amundsen Embayment) survey, flown over the Thwaites Glacier (THW) and Marie Byrd Land which deployed the 60-MHz High Capability Airborne Radar Sounder (HiCARS) radar system (Holt et al., 2006; Peters et al., 2007); the British Antarctic Survey (BAS) 2004-05 BBAS survey over Pine Island Glacier (PIG); and the 2010-2011 Institute-Möller Antarctic Funding Initiative (IMAFI) survey over the Institute and Möller Ice Streams (IMIS) which deployed the 150-MHz Polarimetric Airborne Survey INstrument (PASIN) radar system (Vaughan et al., 2006; Corr et al., 2007; Ross et al., 2012; Frémand, Bodart et al., 2022) (Fig. 4.1; Table 4.1). Additional profiles from NASA's Operation Ice Bridge (OIB; MacGregor et al., 2021) 2016 and 2018 surveys, flown with the 195-MHz Multichannel Coherent Radar Depth Sounder 2 (MCoRDS-2) radar system (CReSIS, 2018), were also used to extract IRH information near the WD2014 and upper IMIS catchments (Bodart et al., 2021a; Fig. 4.1; Table 4.1). We refer the reader to the above references for comprehensive details on each system's capabilities.

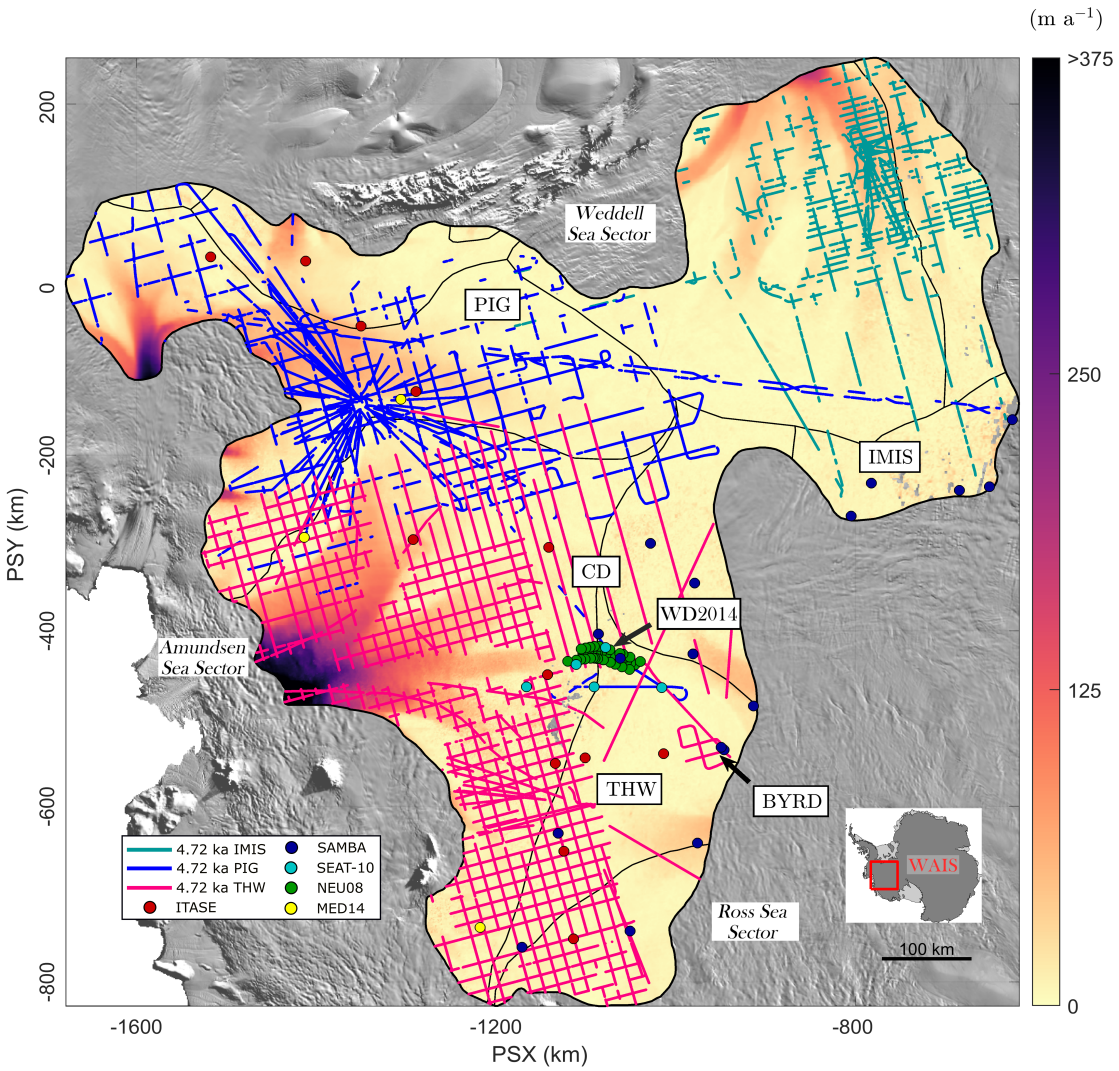

Figure 4.1: Map of the datasets and key locations in this study. The three datasets that contain the 4.72 ka IRH are colour-coded as IMIS (green), PIG (blue), and THW (pink). IRH data points found in areas where we estimate the Local-Layer Approximation (LLA) to be likely unsuitable (i.e. $D > 1$; see Section 4.3.2.1 and Figure 4.2) are excluded. Points represent the snow, firn, and ice cores used in this study to compare modern accumulation rates with those inferred from the 4.72 ka IRH (Sect. 4.3.4). The background colour map shows modern surface speeds from Rignot et al. (2017). Locations mentioned in this paper are abbreviated on the map as follows: BYRD (Byrd Ice Core), IMIS (Institute and Möller Ice Streams), PIG (Pine Island Glacier), THW (Thwaites Glacier), WAIS (West Antarctic Ice Sheet), CD (Central Amundsen-Weddell-Ross Divide), WD2014 (WAIS Divide ice core). Major ice divides are from Mouginot et al. (2017). The background image is the 2014 Moderate Resolution Imaging Spectroradiometer (MODIS) mosaic of Antarctica (Haran et al., 2018). For all analyses and figures in this study, the Scientific Committee on Antarctic Research (SCAR) Antarctic Polar Stereographic projection is used (PSX/PSY; EPSG: 3031).

These RES surveys were used to track and date six IRHs spanning the Late Pleistocene and Holocene (25.7 – 2.3 ka BP) that collectively cover much of the WAIS, including IMIS (Ashmore et al., 2020a), PIG (Karlsson et al., 2014; Bodart et al., 2021a), and THW (Muldoon et al., 2018). Here we only consider the 4.72 ka IRH mapped in all four studies and shown in Figure 4.1, as it is by far both the most spatially extensive and the only commonly traced IRH across all studies. We first merged all data points from the 4.72 ka IRH across the three catchments, resulting in a cumulative distance of ∼40,000 line-km of IRH profiles (44% of the RES surveys' total coverage; Table 4.1). Although the along-track RES data were acquired with a trace spacing of between 10 and 35 m, depending on the dataset used, we resampled these points to 500 m in the along-track direction. We then added a spatially invariant firn correction of 10 m onto the Muldoon et al. (2018) dataset to match the same firn correction applied by the other studies to correct the IRH depth. Finally, we calculated the median value of all ice thicknesses and IRH depths falling within each 500 m interval.

TABLE 4.1: Characteristics of each IRH dataset used in this study that contain the 4.72 ka IRH. 'Reflector 1' in Muldoon et al. (2018) is abbreviated here as 'R1'.

Survey name	***Survey provider***	***RES system***	***Dataset reference***	***Cumulative IRH distance (10^3 km)***
IMAFI	BAS	PASIN 150-MHz	H2 in Ashmore et al. (2020a)	6
BBAS /OIB	BAS/NASA	PASIN 150-MHz / MCoRDS-2 195-MHz	R2 in Bodart et al. (2021a)	15
AGASEA	UTIG	HiCARS 60-MHz	R1 in Muldoon et al. (2018)	19

4.3.2 Inferring accumulation rates

To infer accumulation rates from the 4.72 ka IRH, we used the Nye model, a 1-D ice-flow model widely used for estimating accumulation rates and age-depth relationships over relatively slow-flowing parts of an ice sheet (Nye, 1957; Fahnestock et al., 2001a). This model invokes the local-layer approximation (LLA; Figs. 4.2-4.6), i.e. it assumes that the time-averaged accumulation rate that the IRH has experienced since its upstream inception at the surface can be adequately represented by its depth where it is observed presently. Other 1-D models exist, including the Dansgaard-Johnsen (Dansgaard and Johnsen, 1969) and the shallow-strain rate model (MacGregor et al., 2016), but were less suitable for estimating accumulation rates here due to uncertainty in the basal shear layer thickness across

our survey area and because we are limited to only one IRH to constrain the ice-flow model, respectively. The Nye model assumes that ice thickness is constant and therefore that the ice sheet has been in a steady state since the deposition of the IRH, an acceptable assumption for the period under investigation here, as we show in the following sections (see Figures 4.2-4.5). The Nye model states:

$$\dot{b}_a = \ln(\frac{z_a}{H}\frac{H}{a}), \tag{4.1}$$

where $\dot{b}_a$ is the mean accumulation rate during the Holocene epoch between an IRH of age a and the present, z_a represents the depth of the IRH dated at the ice core, and H is the ice thickness. The model assumes that the vertical strain rate, $\dot{\epsilon}^a_{zz}$, is also constant and vertically uniform, so that it exactly balances the overburden of local ice accumulation:

$$\dot{\epsilon}^a_{zz} = \frac{\dot{b}_a}{H}. \tag{4.2}$$

We iterated Eq. 4.1 over the resampled 500-m spaced dataset using the depth of the 4.72 ka IRH for z_a and used the median radar-derived ice-thickness measurement resampled over the 500-m grid to obtain H, when this information was available. In areas where the radar did not sound the bed, we used the BedMachine Antarctica v2 gridded product to obtain a value for H (Morlighem, 2020; Morlighem et al., 2020). Note that accumulation-rate values presented in this study are all reported in metres per annum (m a^{-1}) of ice equivalent using an ice density value of 917 m^{-3}.

4.3.2.1 Assessing the suitability of the 1-D model

To quantify the suitability of the LLA, which is used here to estimate accumulation rates, we calculated the effects of horizontal gradients in modern ice thickness and accumulation rates along particle paths in their ability to affect IRH depths across our grid, as per Waddington et al. (2007). Where these gradients are large, estimates of accumulation rates from IRHs likely require a more complete treatment of ice flow and its effect upon IRH depths, which multi-dimensional models and more physically complete models can better resolve (e.g. Waddington et al., 2007; Leysinger Vieli et al., 2011; Karlsson et al., 2014; Nielsen et al., 2015; Koutnik et al., 2016;). However, such models are significantly more computationally expensive over such a larger area and depend on well-constrained boundary conditions from along-flow radar profiles which are not often available at an ice-sheet

level (MacGregor et al., 2009).

We quantified the effect of horizontal gradients on an IRH of age a by first estimating the total horizontal particle path length L_{path} that each "particle" of the 4.72 ka IRH has travelled since a, and then the characteristic lengths of variability in ice thickness (L_H) and apparent accumulation rate ($L_{\dot{b}}$). The input datasets used for this calculation were modern ice thickness from BedMachine v2 (Morlighem, 2020), modern SMB (1979 – 2019) from the Regional Atmospheric Climate Model 2.3p2 (hereafter RACMO2; Van Wessem et al., 2018), and modern surface velocities (1996 – 2016) from the InSAR MEaSUREs v2 dataset (Rignot et al., 2017). These were all regridded to a single 1-km grid using bilinear interpolation and smoothed using an exponentially decaying filter equivalent to ten ice thicknesses in length, before subsampling the data to a common 5-km grid for data analysis. Following MacGregor et al. (2016), we re-calculated surface speed directions for slower ice-flow regions (<100 m a^{-1}) in the interior of the ice sheet using surface-elevation gradients from the BedMachine product. To calculate L_{path} (Fig. 4.2a), we then produced a reverse flowline for each grid cell based on modern ice-surface velocity, $\overline{u}$, and calculated where, along the reverse flowline, we obtained age, a:

$$L_{path} = \overline{u}a. \tag{4.3}$$

We then interpolated the ice-thickness and accumulation-rate grids onto each flowline and conducted a first-order polynomial fit to obtain the ice-thickness and accumulation-rate gradients along the flowline. The ensuing gradients were then combined with the mean values along the flowline ($\overline{H}$ and $\overline{\dot{b}}$ to calculate the characteristic lengths L_H and $L_{\dot{b}}$ (Fig. 4.2b-c), as follows:

$$\frac{1}{L_H} = \mid \frac{1}{\overline{H}} \frac{dH}{dx} \mid, \tag{4.4}$$

$$\frac{1}{L_{\dot{b}}} = \mid \frac{1}{\overline{\dot{b}}} \frac{d\dot{b}}{dx} \mid . \tag{4.5}$$

Taken together, the ice-thickness and accumulation-rate gradients are combined to obtain a characteristic length scale, which was used to compare with L_{path} to generate the non-dimensional parameter D (Fig. 4.2d):

$$D = L_{path}(\frac{1}{L_H} + \frac{1}{L_{\dot{b}}}). \tag{4.6}$$

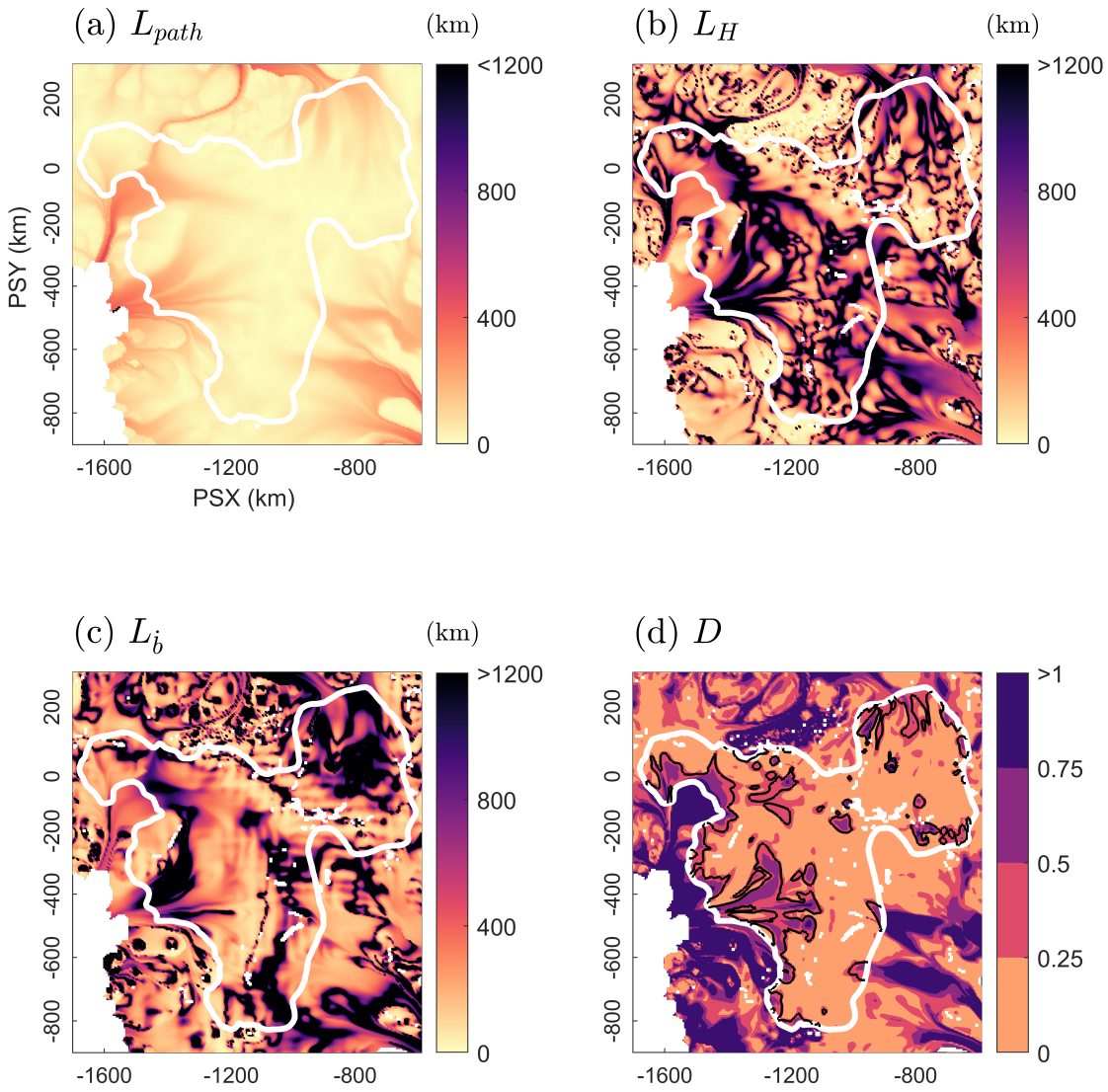

Figure 4.2: Suitability of the LLA over the PIG, THW, and IMIS catchments for the 4.72 ka IRH. (a) Horizontal path length, L_{path}, of a 4.72 ka particle of ice to reach its present location, calculated using modern surface velocities (Rignot et al., 2017). (b) Characteristic length of ice-thickness variability, L_H, along the 4.72 ka particle path, estimated using modern ice thickness measurements from BedMachine v2 (Morlighem, 2020). (c) Characteristic length of accumulation variability, $L_{\dot{b}}$, along the 4.72 ka particle path, estimated using modern modelled SMB data from RACMO2 (Van Wessem et al., 2018). (d) The D parameter for the 4.72 ka IRH used to quantify the suitability of the LLA for the survey area (black contours represent the upper limit of the interquartile range for the D parameter ($D \leq 0.34$), whereby all values situated inside of this boundary may satisfy the $D \ll 1$ criteria and those outside may require re-evaluating with the use of multi-dimensional models). The white outline represents the model domain boundary used to model Holocene accumulation rates where $D \leq 1$, whereas the black outline represents the upper limit of the interquartile range for the D parameter (i.e. $D \leq 0.34$) which we use to assess the level of confidence in the inferred Holocene accumulation rates.

We used the D parameter as a confidence metric for our inferred accumulation rates. Both Waddington et al. (2007) and MacGregor et al. (2009) suggested a value of $D \ll 1$ over Antarctica, whereas MacGregor et al. (2016) used a maximum value of $D = 1$ to estimate where the LLA is acceptable over Greenland. Since D cannot be translated simply into an uncertainty in an LLA-inferred accumulation rate, it is not yet clear what exact value is appropriate. Smaller values of D indicate that local horizontal gradients in ice thickness and accumulation rates have a smaller effect on IRH depth of age a, and thus that the LLA may be valid (Waddington et al., 2007; MacGregor et al., 2009; 2016). Where $D \geq 1$, the depth of an IRH is less likely to be the result of accumulation rates at the surface or vertical strain rates further down, and thus a more sophisticated model is likely required (Sect. 4.3.2.2) (Waddington et al., 2007). However, MacGregor et al. (2009) found that even along a flow band across Lake Vostok where the mean value of D is 0.50 for a 41-ka IRH, the difference in accumulation rate inferred from the LLA and from a more sophisticated flow-band model could be relatively small (4-16%). This similarly suggests that accumulation rate can be inferred acceptably using the LLA where D is higher.

For our study area, D values are mostly well below unity (median: 0.19; 25th quartile: 0.09; 75th quartile: 0.34), which suggests relatively little effect from ice-dynamical processes upon IRH depths across most of our grid. We used the upper quartile of the D distribution across our model domain (i.e $D \leq 0.34$) to show areas where we can have confidence that accumulation rate remains the dominant factor influencing the vertical position of our IRHs in the ice column (i.e. where the $D \ll 1$ criterion is likely met; Fig. 4.2d). While accumulation rates inferred from IRHs situated in the upper quartile (Fig. 4.2d) may still be valid, we suggest additional caution in interpreting our results there due to the potential impact of larger flow gradients on IRH depths.

4.3.2.2 Model limitations and uncertainty

One of the main limitations of the Nye model is that it assumes that gradients in sliding velocity are mostly concentrated in a thin layer at the ice-bed interface and that the ice column deforms by pure shear only (Nye, 1957; Fahnestock et al., 2001a). For this reason, the Nye model is generally only appropriate for IRHs found in the upper part of the ice column, as is the case here. Additionally, the use of the model is restricted to areas where ice flow is relatively slow and horizontal strain rates are also relatively low.

Here, we focus on a shallower IRH situated in the upper part of the ice column (median: 40%; 25th quartile: 30%; 75th quartile: 50%; Fig. 4.7b-c), for which we

can reasonably assume that the ice sheet has remained close to steady state and where IRHs are likely shallow enough not to have experienced appreciable flow disturbances that would affect the Nye model assumptions. Additionally, due to the inherent nature of tracking IRHs through RES data, our coverage is limited to areas where ice-flow speeds are relatively low and IRHs are undisturbed. In some portions of our study area, the IRH is found deeper in the ice column or in faster-flowing sections of the ice sheet (e.g. in the downstream sectors of our grid, Figs. 4.1 and 4.7b-c), both of which challenge the assumptions that the 1-D model is based upon and thus where uncertainties in accumulation estimates are likely to be higher.

Estimating uncertainty in accumulation rates from the Nye model is non-trivial. Because the Nye model does not directly take into account the effect of strain rates on IRH depth and position within the ice column, it is not possible to assess its impact on the inferred accumulation rates, particularly in areas where strain rates are higher and the IRHs are deeper in the ice. In turn, this limits our ability to quantify the model's structural uncertainty. Because the model's structural uncertainty is likely larger than that related to the IRH age, it is important to quantify it to assess the significance of accumulation-rate change from modern values that we detect. Previous studies have used the misfit between the accumulation rate calculated using multiple proximal IRHs in the ice column (e.g. Fahnestock et al., 2001a; 2001b; Leysinger Vieli et al., 2004; MacGregor et al., 2016). Unfortunately, this method is not suitable here due to the dearth of spatially extensive IRHs younger than 4.72 ka over our model domain.

To overcome this issue, we used the shallow-strain rate model developed by MacGregor et al. (2016) which directly includes a strain-rate parameter that is independent from ice thickness, rather than one that is tied to ice thickness, as in the Nye model (Eq. 4.7). The accumulation rates produced by this model are then used here to estimate lower and upper bounds in the accumulation rates that partly consider the effect of non-Nye vertical strain on the ice column and thus on the accumulation rate needed to reproduce the depth of the 4.72 ka IRH in the Nye model. The shallow-strain rate model for age, a, is:

$$a(z) = \frac{1}{\dot{\epsilon}^a_{zz}} \ln\left(\frac{\dot{b}_a + \dot{\epsilon}^a_{zz} z_a}{\dot{b}_a}\right). \tag{4.7}$$

The strain-rate parameter in Eq. 4.7 would typically be $\dot{\epsilon}^a_{zz}$ from Figure 4.3a, but because this is calculated based on the results from Eq. 4.1 it is not independent from the inferred accumulation rates presented here and is thus not a suitable input for evaluating accumulation-rate uncertainty inferred from the Nye model.

In the absence of well-constrained vertical strain rates across our grid, by continuity, we tested whether longitudinal strain rates ($\dot{\epsilon}_{xx}$; Fig. 4.3b) could be used as an alternative to $\dot{\epsilon}^a_{zz}$ in the shallow-strain rate model (ignoring lateral strain).

These were calculated from gradients in the x and y-direction for modern surface speeds ($\overline{u}$) projected onto the appropriate surface velocity unit vectors ($\hat{u}_{\parallel}$) (MacGregor et al., 2013):

$$\dot{\epsilon}_{xx} = \frac{\partial u}{\partial x} = \overline{\nabla}|\overline{u}| \cdot \hat{u}_{\parallel}. \tag{4.8}$$

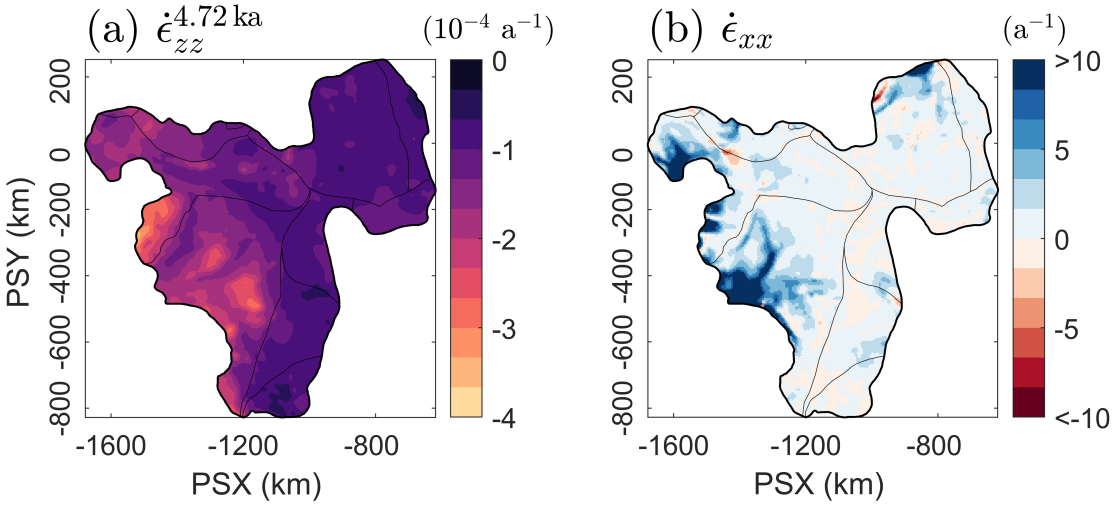

Figure 4.3: Strain rate patterns across the survey area. (a) Mean Nye-inferred vertical strain rates, $\dot{\epsilon}^a_{zz}$, for the 0-4.72 ka portion of the ice column calculated from Eq. 4.2. (b) Longitudinal strain rates, $\dot{\epsilon}_{xx}$, obtained from Eq. 4.8.

To assess whether $\dot{\epsilon}_{xx}$ can be used as a proxy for $\dot{\epsilon}^a_{zz}$, we solved Eq. 4.7 for $\dot{b}_a$, replaced $\dot{\epsilon}^a_{zz}$ for $\dot{\epsilon}_{xx}$, and then compared the accumulation-rate results inferred from the shallow-strain model to the Nye-inferred accumulation rates over our grid from Figure 4.8a. Note that $\dot{\epsilon}_{xx}$ can only be used as a proxy for $\dot{\epsilon}^a_{zz}$ where $\dot{\epsilon}_{xx} > 0$, as positive $\dot{\epsilon}^a_{zz}$ values are typically only found in areas where the ice column is expanding, such as the ablation zone, and are thus non-physical for our model domain. As a result, all negative $\dot{\epsilon}_{xx}$ values were replaced by extremely low, but positive strain-rate values (10^{-7} a^{-1}). The results shown in Figure 4.4 demonstrate that both the Nye and shallow-strain models produce similar results, but with decreasing similarity where $D > 0.34$, which is likely related to ice-dynamical processes affecting the assumptions of the Nye model further downstream (Fig. 4.5).

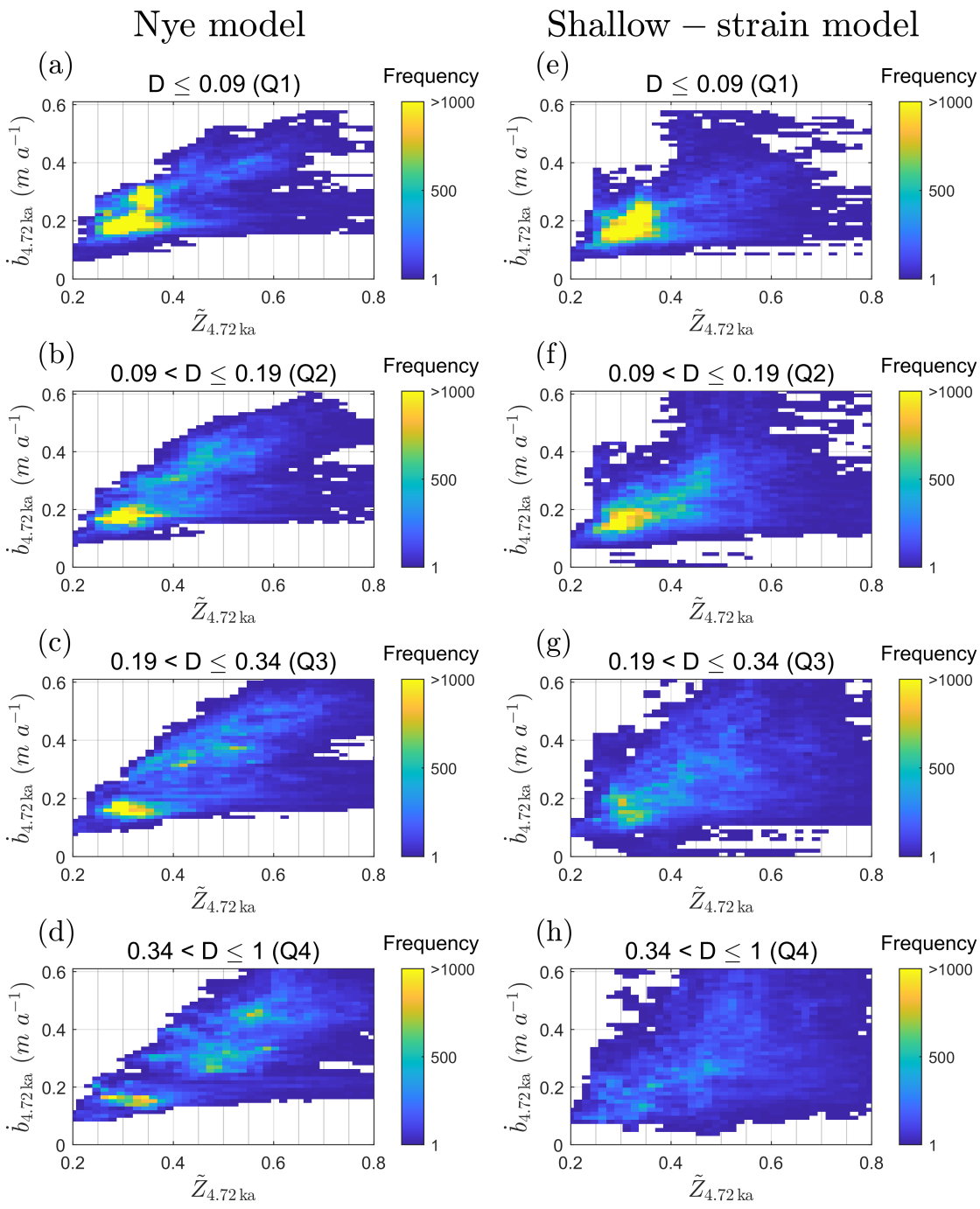

Figure 4.4: Histograms of inferred accumulation rates from both the Nye and shallow-strain rate models. (a-d) Inferred accumulation rates using the Nye model plotted against normalised IRH depths and binned into the four D quartiles (e.g. panel a is for all grid cells that fall within the lower quartile (Q1), b is for all those that fall within the second quartile (Q2), etc. (e-h) same as (a-d) but for the shallow-strain rate model.

This analysis increases confidence that $\dot{\epsilon}_{xx}$ can be used in the shallow-strain rate model from MacGregor et al. (2016) as a proxy for the vertical strain parameter, $\dot{\epsilon}^a_{zz}$, to infer accumulation rates over the time period and location considered here, and thus ultimately has value for constraining uncertainty in the Nye-inferred accumulation rates (Fig. 4.8a). While this method likely produces more conservative uncertainty estimates than with the more challenging use of inverse flow-band models that solves for the effect of changing flow, temperature and strain conditions along targeted flow bands, it enables a straightforward uncertainty quantification across a large area.

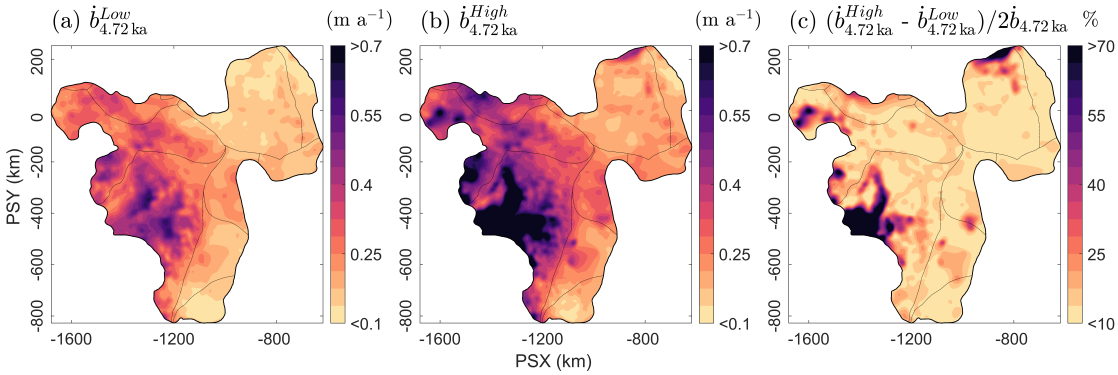

Figure 4.5: Uncertainties in inferred accumulation rates based on the radar and ice-core age uncertainties and from the accumulation rates returned from the shallow-strain rate model. (a) Lower bound accumulation estimates, which are the product combination of the combined uncertainty from the radar and ice-core uncertainties in the age of the 4.72 ± 0.28 ka IRH (Muldoon et al., 2018; Bodart et al., 2021) and the accumulation rate returned from the shallow-strain rate model. (b) same as (a) but for the upper bounds in accumulation rates. (c) Relative uncertainty in Nye-inferred accumulation rates for the 4.72 ka IRH (Fig. 4.8a) based on the lower and upper bound estimates from (a-b).

Following on from these steps, we then produced two sets of upper and lower accumulation-rate uncertainties ($\dot{b}^{Low}_{4.72\,\mathrm{ka}}$ and $\dot{b}^{High}_{4.72\,\mathrm{ka}}$) for each of the following products over our grid: (1) using the Nye model from Eq. 4.1 with the age uncertainty (± 0.28 ka) of the 4.72 ka IRH; and (2) same as (1) but using the shallow strain-rate model from Eq. 4.7 using $\dot{\epsilon}_{xx}$ as a proxy for $\dot{\epsilon}^a_{zz}$. We then calculated the maximum $\dot{b}^{Low}_{4.72\,\mathrm{ka}}$ and $\dot{b}^{High}_{4.72\,\mathrm{ka}}$ values for each grid cell (Fig. 4.5a-b) and averaged these to generate a relative uncertainty to the Nye-inferred accumulation rates (Fig. 4.5c). From this assessment, we estimate a median relative uncertainty in the Nye-inferred accumulation rates for the 4.72 ka IRH of 14% across our grid. The largest relative uncertainties to the Nye-inferred accumulation rates (>70%) are found primarily across the downstream end of THW, and to a smaller extent over the edges of the grid of PIG and IMIS where longitudinal strain rates are

higher due to faster flowing ice. Relatively low uncertainties are found across the Amundsen-Weddell-Ross Divide and most of the region where $D \leq 0.34$, reflecting the small effect of spatially variable strain rates on the inferred accumulation rates. When combined with the assessment of the suitability of the LLA and exclusion of IRHs where the $D > 1$, we conclude that it supports our application of a 1-D modelling approach here.

4.3.3 Gridding and filtering

Once IRH depths and accumulation rates for the 4.72 ka IRH were obtained at regular 500-m points along RES flight paths, we filtered the results using a moving-average Gaussian filter of length 30 samples (equivalent to ∼15 km) to reduce along-track noise in the IRH depth. We then gridded the filtered result using a Delaunay-triangulation-based natural neighbour interpolation method onto a 1-km polar stereographic grid. We further smoothed the gridded data using an 18-km square cell mean filter to limit the localised interpolation artefacts in areas of poor survey coverage. Figure 4.6 shows the maximum distance away from the nearest 500-m along-track point used to produce Figures 4.7-4.8, and thus where errors in the interpolated grids are expected to be larger. The median value of this maximum distance is 5 km and its maximum value is 75 km, which is comparable to previous studies that infer SMB from IRHs in the shallow firn (e.g. Medley et al., 2014). We evaluated other possible interpolation methods (e.g. kriging and using different semi-variogram models), but they resulted in similar or poorer quality and were thus discounted.

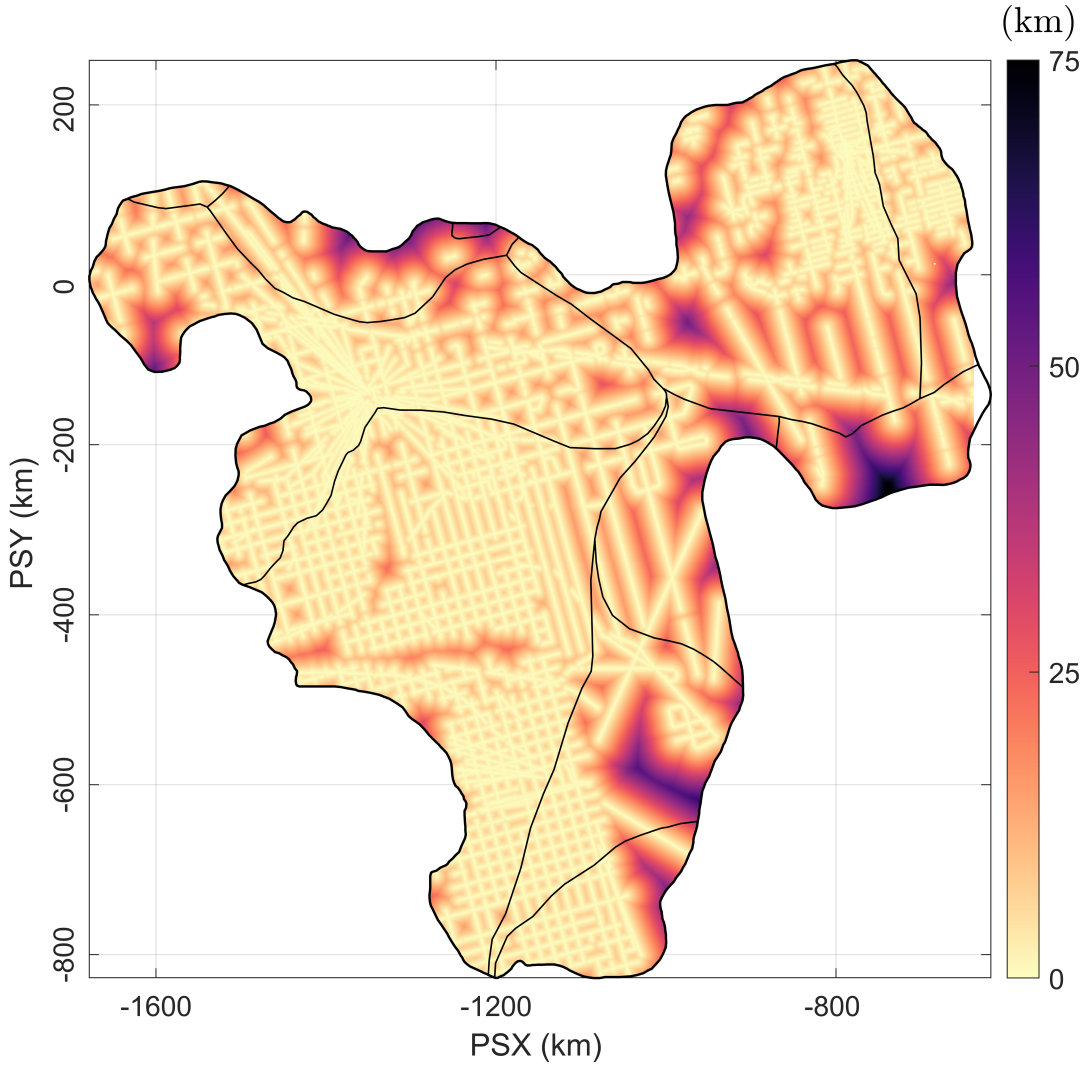

Figure 4.6: Maximum distance to the nearest 500-m along-track point used for the interpolation of the 4.72 ka IRH depth and accumulation grids.

4.3.4 Comparison with modern observations

To compare our inferred accumulation estimates for the past 4.72 ka with modern values (defined here as 1651-2019), we derived information on modern accumulation rates from two sources, one modelled (gridded) and one from a series of observational (point-based) datasets.

We used modelled gridded accumulation rates from the RACMO2 SMB product forced at its margin with the ERA-Interim product (native resolution: 27 km)

as an estimate for modern accumulation rates (Van Wessem et al., 2018). Although SMB is not technically equivalent to the accumulation rate, runoff and sublimation are negligible in our survey area (Medley et al., 2013), so we assume that SMB is equal to accumulation rate in this region. We converted modelled values from kilogrammes per square metre per year (kg m^{-2} a^{-1}) to metres per annum (m a^{-1}) of ice equivalent using an ice density value of 917 m^{-3}, calculated the 40-year mean, and then bi-linearly interpolated the gridded RACMO2 product to the same 1-km grid resolution as our 4.72 ka-to-present accumulation grid (Sect. 4.3.3) to ensure consistency when comparing both datasets.

Observational point-based measurements were obtained from a series of snow, firn and ice cores from the ITASE (Mayewski and Dixon, 2013), MED14 (Medley et al., 2014), SAMBA (Favier et al., 2013), and SEAT-10 (Burgener et al., 2013) datasets, as well as from a network of centennially averaged modern accumulation rates derived from shallow IRHs traced on ground-based RES data over the Central Amundsen-Weddell-Ross Divide and dated using a shallow ITASE Ice Core (Neumann et al., 2008) (Fig. 4.1). This resulted in 79 point-based accumulation measurements from cores covering the period 1651-2010 CE (Common Era) and spread across our model domain (see Figure 4.1). Further detail on these datasets can be found in the above references.

To compare the Holocene gridded product with the point-based measurements, we first calculated the average value of the accumulation rate at the point measurement for the entire period. We converted these values to ice-equivalent accumulation rates and then extracted two paired values, i.e. the value for the point measurement for modern accumulation rates and the value for the nearest grid cell in the gridded 4.72 ka-to-present accumulation estimates to this measurement.

4.4 Results

The final grids for depth and accumulation rates for the 4.72 ka IRH are shown in Figures 4.7-4.8. In total, these grids are made of ∼89,000, 500-m spaced points, which cover an area of ∼610,000 km^2, or 30% of the total surface area of the WAIS. The grids span most of the PIG and THW catchments, as well as the Ronne (upper Rutford, Institute, and Möller) and upper western Ross (Bindschadler, Kamb, MacAyeal, and Whillans) catchments (IPY Antarctic boundaries G-H, J-Jpp, and Ep-F; Mouginot et al. (2017); Figs. 4.7-4.8). Overall, the 4.72 ka IRH is shallower within the IMIS and upper PIG and THW catchments, as well as on the Ross side of the central divide where ice thickness is particularly deep (Fig.

4.7b). Conversely, the 4.72 ka IRH is deeper in the ice near a 400-m high bedrock plateau that separates the northern and southern basins of PIG (Vaughan et al., 2006) and at two locations in the upstream parts of the main trunk of THW where ice flows over highs in subglacial topography (Fig. 4.7b).

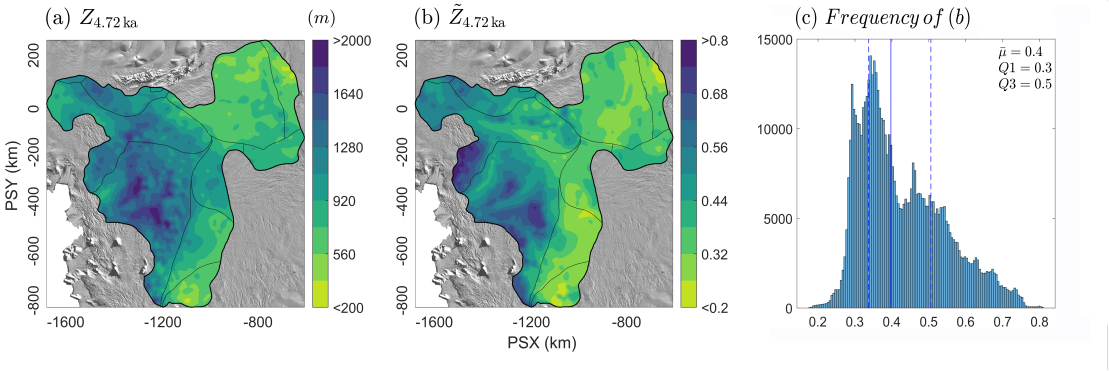

Figure 4.7: Gridded depths for the 4.72 ka IRH across the model domain. (a) Gridded depth of the 4.72 ka IRH. (b) Normalised depth of the 4.72 ka IRH relative to ice thickness. (c) Histogram showing the distribution of values in (b) with the median ($\tilde{\mu}$) and interquartile range (i.e. 25th (Q1) and 75th (Q3) quartiles) shown as solid and dashed blue lines respectively. The background image is the 2014 MODIS mosaic of Antarctica (Haran et al., 2018).

4.4.1 Catchment-scale accumulation estimates

Figure 4.8 shows a comparison of the ice-equivalent accumulation rates we inferred for the 4.72 ka IRH (Fig. 4.8a) and modern SMB estimates from RACMO2 (Fig. 4.8b). We observe that the IRH accumulation rate pattern for the last 4.72 ka is similar to the modern pattern of accumulation rates for the Amundsen Sea sector of the WAIS, which is dominated by higher coastal accumulation rates that progressively decrease inland to reach their lowest rates over the Ross side of the divide (Fig. 4.8a-b). Differences in accumulation rates between the 4.72 ka-to-present estimates and modern values are mainly observed directly upstream of the main trunks of PIG and THW, where modern rates are much higher (up to 0.2 m a^{-1} ice equivalent) than for the 4.72 ka-to-present estimates (Fig. 4.8c). In comparison, higher accumulation rates for the last 4.72 ka relative to modern rates are observed for the entire stretch of the Amundsen-Weddell-Ross Divide (Fig. 4.8c; Table 4.2). Over the IMIS catchment, little change is observed between the two periods. Over the entire model domain, we observe a median percentage change value of 6% higher accumulation since 4.72 ka compared with modern rates (Figs. 4.9 and 4.10); however, when considering only the values that fall within 100 km of either side of the Amundsen-Weddell-Ross Divide (i.e. in the accumulation zone of the Amundsen, Weddell, and Ross sea sectors and where mean surface speeds

average 7 m a^{-1}), we obtain a median percentage change value of 18% higher accumulation compared with modern accumulation rates (Figs. 4.9 and 4.10).

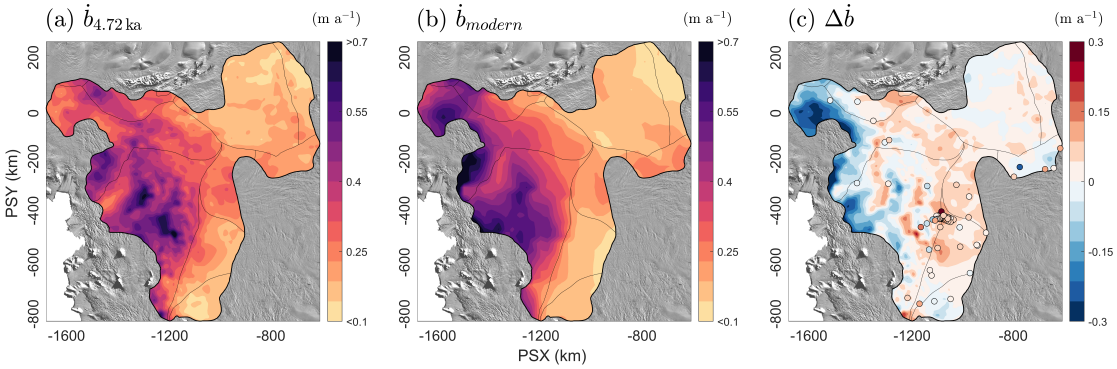

Figure 4.8: Gridded estimates of ice-equivalent accumulation rates for the last 4.72 ka and modern times. (a) Gridded accumulation rates inferred from the 4.72 ka IRH. (b) Modern (1979 – 2019) modelled SMB rates from RACMO2. (c) Difference between 4.72 ka-to-present and modern accumulation rates (red = 4.72 ka-to-present accumulation higher than modern times, blue = 4.72 ka-to-present accumulation lower than modern times). The dots represent the difference between the value for the nearest grid cell in (a) and time-averaged accumulation rates at each of the 79 core locations (see Section 4.3.4; Fig. S6). The background image is the 2014 MODIS mosaic of Antarctica (Haran et al., 2018).

Comparison between our 4.72 ka-to-present accumulation-rate estimates and 79 core-derived point-based accumulation measurements for modern times (1651-2010 CE) are shown in Figures 4.8-4.10. This evaluation shows that the 4.72 ka-to-present accumulation-rate estimates for the nearest grid cell to each point measurement are, on average, 22% higher for cores situated across the entire grid ($p < .0015$, n=79) and 23% higher for cores found within 100 km of the divide compared with modern accumulation rates ($p < .0001$, n=59; Figs. 4.9 and 4.10). In comparison, a similar analysis between grid cells from the 4.72 ka-to-present accumulation-rate estimates and RACMO2 at these 79 core locations shows mid-Holocene accumulation rate estimates are, on average, 32% ($p < .00002$, n=79) higher for cores situated across the entire grid and 36% higher for cores found within 100 km of the divide ($p < .00001$, n=59; Fig. 4.9). This result confirms that the relative change for gridded accumulation rates between the 4.72 ka-to-present and modern modelled accumulation rates is consistent with modern rates from point-based measurements.

TABLE 4.2: Summary statistics for the modern (modelled and observational) and 4.72 ka-to-present ice-equivalent accumulation rates at the catchment-scale and over the Amundsen-Weddell-Ross Divide (abbreviated CD for Central Divide here). Values for the Amundsen-Weddell-Ross Divide are for all points that fall within 100 km of either side of the divide (see dashed line in Figure 4.10). $\tilde{\mu}$ refers to the median and IQR represents the interquartile range calculated by computing the difference between the 75th and 25th percentiles. Note that the values provided in the text represent the median relative change from the cell-by-cell change between each grid (Fig. 4.10), rather than the relative change of the median values provided here.

	Catchment-wide		***CD only***	
Accumulation rate (m a^{-1})	$\tilde{\mu}$	***IQR***	$\tilde{\mu}$	***IQR***
Modern (model)	0.23	0.23	0.22	0.10
Modern (cores)	0.24	0.12	0.24	0.09
4.72 ka-to-present	0.27	0.18	0.27	0.11

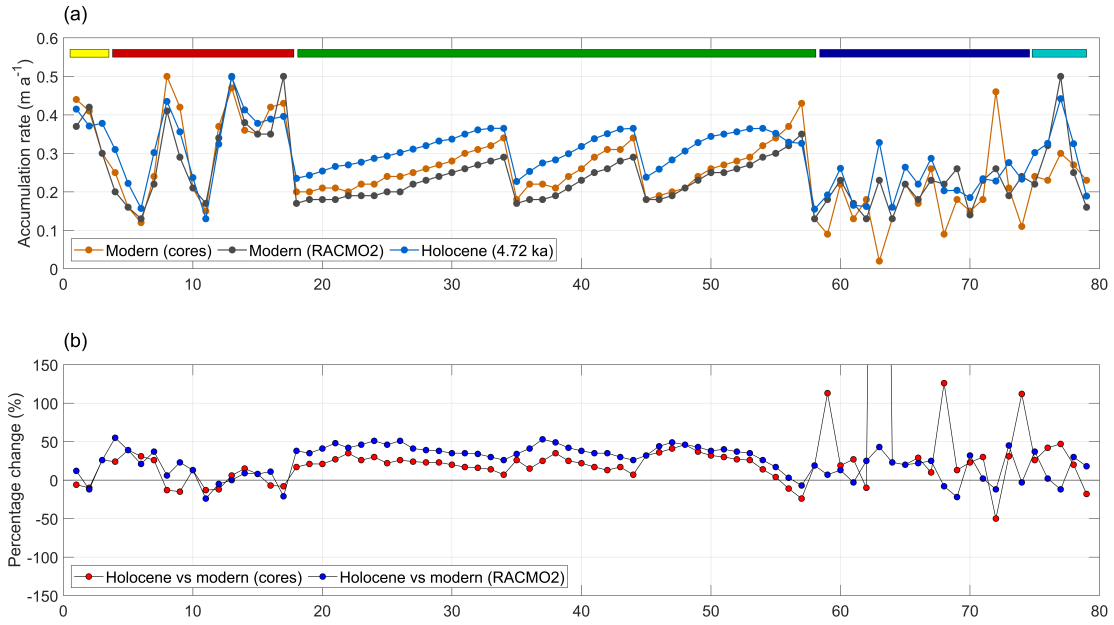

Figure 4.9: Scatter plot showing the difference in accumulation rates between the modern (cores and RACMO2) and the Holocene (4.72 ka) based on data showed in Figures 4.8c and 4.10. (a) Accumulation rates for each of Modern (cores), Modern (RACMO2), and Holocene (4.72 ka) at each of the 79 core locations shown in Figure 4.1. The five colour boxes at the top of (a) indicate the datasets to which each point belongs and are colour-coded as per the legend in Figure 4.1 (from left to right: MED14, ITASE, NEU08, SAMBA, SEAT-10). (b) Percentage change between Holocene and modern (cores; red) and Holocene and modern (RACMO2; blue) at the 79 core locations shown in Figure 4.1.

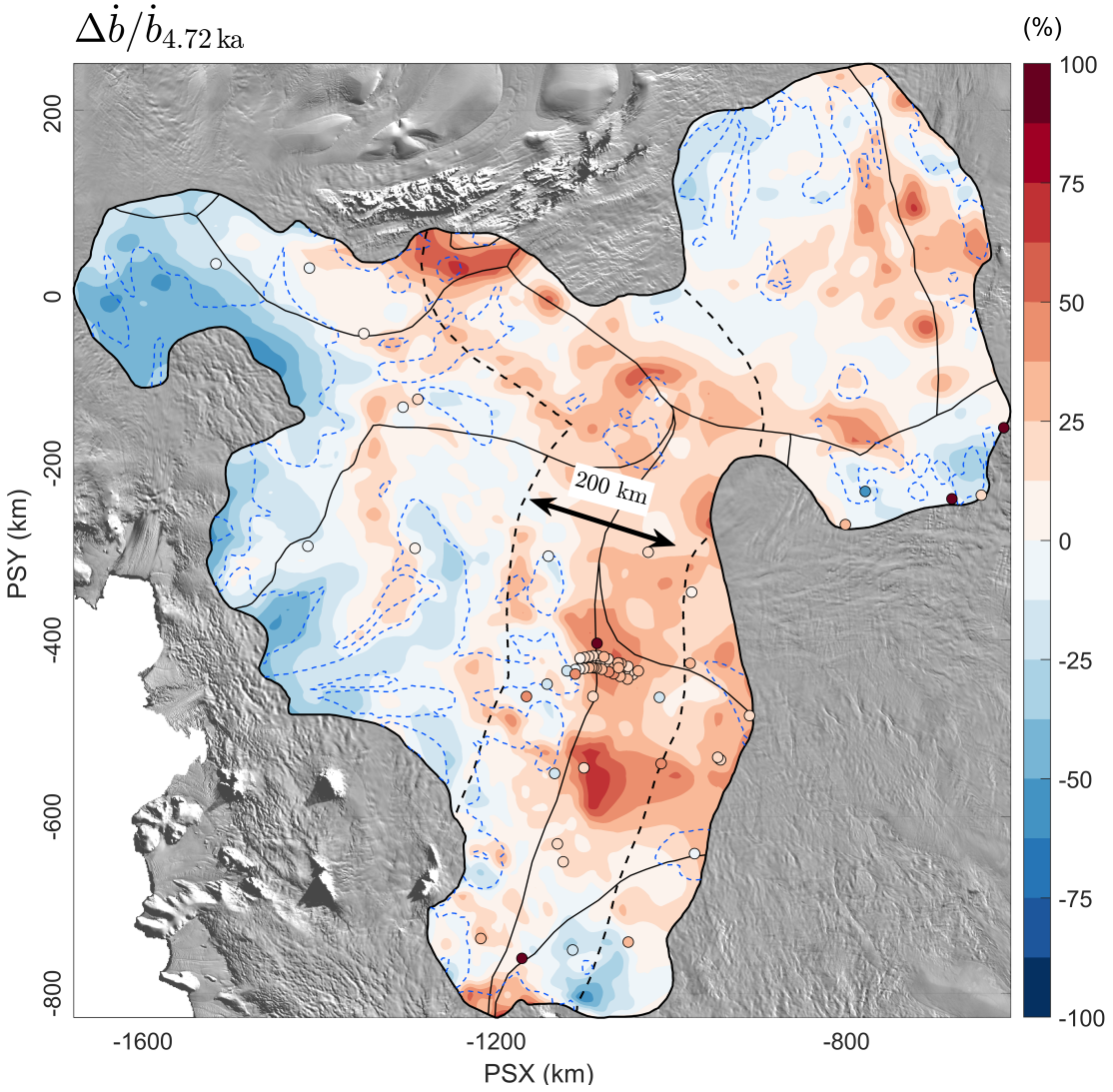

Figure 4.10: Relative change in accumulation rates between the 4.72 ka-to-present estimates and modern rates. The points on the map represent the relative change in ice-equivalent accumulation rate between the nearest grid cell in the 4.72 ka-to-present grid and the 79 modern observations from cores (Figs. 4.1 and 4.9; Sect. 4.3.4). The dashed black outline line represents the 100-km boundary on either side of the Amundsen-Weddell-Ross Divide used to provide the summary statistics in Section 4.4.1 and Table 4.2. The dashed blue line shows the contours of the upper limit of the interquartile range for the D parameter ($D \leq 0.34$), whereby all values situated inside of this boundary may satisfy the D 1 criteria and those outside may require re-evaluating with the use of multi-dimensional models (Sect. 4.3.2.1). The background image is the 2014 MODIS mosaic of Antarctica (Haran et al., 2018).

4.4.2 Elevation-dependent accumulation estimates

While Figures 4.8-4.10 help to assess potential differences in patterns and rates across spatial scales, considering accumulation-rate differences in terms of elevation can inform how topography influences accumulation and whether this has changed over time. We binned the ice-equivalent accumulation values by 50-m elevation bands across the three main catchments covering our grid (Amundsen, Weddell and Ross) for both the 4.72 ka-to-present estimates and modern model rates and calculated the mean accumulation rate and the total accumulation rate for each bin over the entire elevation gradient (Fig. 4.11).

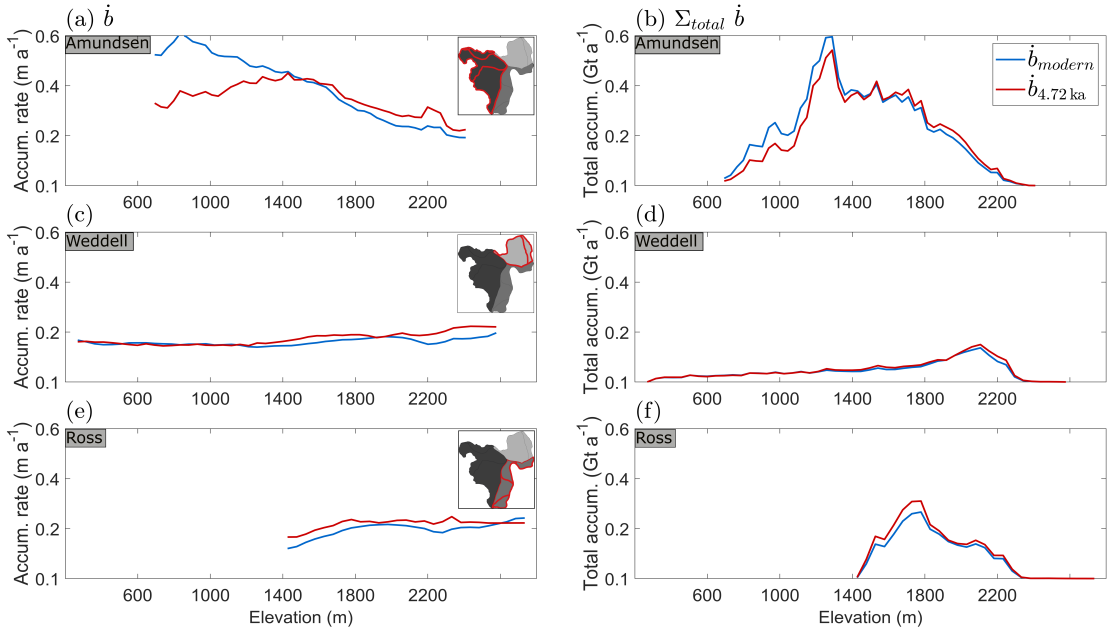

Figure 4.11: Comparison of ice-equivalent accumulation rates between the 4.72 ka-to-present estimates and modern rates (RACMO2) binned by 50-m elevation bands across the three main catchments considered here (Amundsen, Weddell, and Ross). (a, c, e) Mean accumulation rate averaged per 50-m elevation band across the specific catchment area in metres per annum (m a^{-1}). (b, d, f) Total accumulation rate per 50-m elevation band across the specific catchment area in gigatonnes per annum (Gt a^{-1}). The inset in plot a, c and e shows the geographic location that each graph belongs to, with the main drainage basin boundaries shown in red.

We again find that the accumulation-rate estimates for the period since 4.72 ka are lower at low elevations (∼700 – 1,400 m) over the Amundsen sector compared with RACMO2, but they begin to exceed RACMO2 near the 1,400-m elevation band where the 4.72 ka-to-present accumulation rate is higher than modern times across the divide (Fig. 4.11a-b). We also note that whilst an elevation-dependent

gradient in accumulation rates, dominated by high accumulation at the coast and decreasing inland, exists over this sector for the mid-Holocene, it is much less marked than for present rates. This is not surprising, as this sector is where we observe the largest relative uncertainties in inferred accumulation rates across our grid (Fig. 4.5c), indicating that the 1-D model is less able to produce realistic accumulation rates in the downstream end of our grid where ice flow is faster and strain rates are likely higher. In comparison to the Amundsen sector, accumulation rates since 4.72 ka are generally higher at all elevations for the Weddell and Ross sectors compared with the present, although this difference is less than over the Amundsen sector (Fig. 4.11c-f).

4.5 Discussion

4.5.1 Comparison with other Holocene accumulation estimates

Previous studies of past accumulation rates over the WAIS have shown that accumulation varied temporally during the Holocene. Using a single airborne RES profile over the Amundsen Sea sector, Siegert and Payne (2004) showed that accumulation rates were approximately the same at 3.1 ka compared with modern rates, but ∼0.3 m a^{-1} greater (∼15 %) than current rates between 3.1-6.4 ka, before which accumulation was ∼50% of modern rates between 6.4 and 16.0 ka. Similarly, Neumann et al. (2008) found that accumulation rates at the Amundsen-Weddell-Ross Divide were ∼30% higher between 3-5 ka than modern values based on a dense network of IRHs traced on ground-based RES data, while Karlsson et al. (2014) found that accumulation patterns had likely changed twice during the early to mid-Holocene over PIG from the lack of a model fit between the depths and ages of two prominent IRHs. Using the updated WD2014 record, Fudge et al. (2016) showed that accumulation rates were higher there in the mid to late-Holocene (19% between 4.72 ka BP and the present), a trend that was also observed by Koutnik et al. (2016), who found a 20% increase in accumulation rates between 2-4 ka compared with modern rates from a ground-based RES profile across the ice divide.

These studies together point to a period of increasing accumulation observed at the WD2014 from ∼7 ka onwards (Fudge et al., 2016; their Figure 2), with its peak matching the age of the 4.72 ka IRH used here. Thus, our accumulation-rate estimates likely form part of a wider pattern of a sustained increase in accumulation across the Amundsen-Weddell-Ross Divide over several millennia. In showing that mean accumulation rates since 4.72 ka were 18% greater than modern rates

modelled from RACMO2 across the Amundsen-Weddell-Ross Divide, our results provide much wider regional support for the hypothesis that accumulation rates during the mid-Holocene exceeded modern rates across central West Antarctica. A possible explanation for the higher accumulation rates during the mid-Holocene compared with modern values is that they represent a continued climatic transition from the LGM (Steig et al., 2001). Alternatively, it has been suggested that seasonal or interannual variability, such as a weaker circumpolar vortex (van Den Broeke and van Lipzig, 2004; Neumann et al., 2008), or teleconnections to tropical Pacific Ocean warming (Sproson et al., 2022), may also lead to such difference. We did not find evidence for significant changes in accumulation patterns between the mid-Holocene and modern times, suggesting that the current spatial pattern of high accumulation on the Amundsen side of the divide transitioning to low accumulation on the Ross side of the divide was stable throughout the mid-Holocene, as previously suggested by others (Siegert and Payne, 2004; Neumann et al., 2008; Koutnik et al., 2016).

We also find that accumulation estimates for the 4.72 ka-to-present are smaller than modern rates in the lowest elevation bands (<1,400 m), particularly over the Amundsen Sector (Fig. 4.11a-d). This pattern was also found by Medley et al. (2014), who compared modern observational and modelled data over this sector and hypothesised that this discrepancy at low elevations resulted primarily from a lack of sufficient accumulation measurements in the lower sections of their survey area. In our case, these low-elevation values are close to the boundary where we consider the LLA acceptable for the 4.72 ka IRH, albeit where D values are higher than for the rest of the catchment (Figure 4.2d), so it is more likely that accumulation rates calculated there are affected by ice-flow gradients and their influence upon IRH depths leading to lower accumulation rates there. Despite this caveat, Figures 4.11b and 4.11d show that values at low elevations contribute relatively little to the total accumulation (by mass) over our survey area.

We suggest that future ice-sheet modelling studies investigate the difference in accumulation rates inferred from our 1-D model using multi-dimensional flow-band models to assess effects of divergent and convergent flow on IRH depth and ultimately accumulation rates, as previously considered elsewhere in Antarctica (MacGregor et al., 2009). This could be conducted along a flowline transitioning from the slow-flowing regions directly downstream of the Amundsen-Weddell-Ross Divide to the coastal margins of our grid, particularly over THW where we observe the largest uncertainties in accumulation rates. In addition, we suggest that future modelling studies use the accumulation-rate variability from the WD2014 as a climate forcing in their ice-sheet models. Koutnik et al. (2016) previously

showed that the WD2014 record is unique in that it provides a reliable record of accumulation-rate variability during the Holocene, which other East Antarctic ice-core records, often used to reconstruct the evolution of the WAIS, do not possess. We found that these higher accumulation rates are spatially extensive across nearly one third of the WAIS, further suggesting that the WD2014 is indeed representative of the wider WAIS and can be used in regional or continental ice-sheet models as a reliable climate forcing for the region. Future regional and continental ice-sheet models should make use of this record to adjust their climatic boundary conditions to provide improved estimates of ice-elevation change and grounding-line evolution over Antarctica.

4.5.2 Impact for ice-sheet elevation change during the Holocene

Model results from Steig et al. (2001) suggest that the maximum elevation of the WAIS was most likely reached during the early to mid-Holocene (around ∼7 ka) following higher accumulation rates at the late glacial–interglacial transition, after which the WAIS slowly declined to present conditions as the sea-level-rise-induced kinematic wave reached the ice-sheet interior and outpaced the increase in accumulation rates. However, higher accumulation rates in the mid-Holocene relative to the present, which our results suggest occurred spatially across the WAIS, would likely delay the timing of this thinning by several thousand years (Steig et al., 2001).

Using a flow-band model, Koutnik et al. (2016) suggested that an increase of up to 40% in accumulation rates for the period 9 – 2 ka would likely have led to an increase in ice thickness of tens of metres during the mid-Holocene. Although this finding was warranted by physical assumptions around the response time of the ice-sheet interior to adjust to an increase in accumulation in the model, it points to the potential for the divide to have thickened by several metres over a relatively short period of time from increased accumulation rates alone. Because the WAIS is also sensitive to ice-dynamical changes at the ice-sheet margins (e.g. grounding-line retreat or calving), an increase in accumulation rates in the upper part of the ice sheet may not necessarily result in enough thickening to counteract potential dynamical losses farther downstream (Jones et al., 2022). Conway and Rasmussen (2009) reported that the Amundsen-Ross Divide is currently thinning and migrating towards the Ross Sea at a speed of 10 m a^{-1}, but they were unable to determine whether this was in response to long-term (last two millennia) accumulation-rate changes there or short-term (last few centuries) ice-dynamical forcing from the coastal margins of the Amundsen and Ross sectors. More recently, Balco et al.

(2023) showed that THW and Pope Glaciers experienced 35 m of thickening in the mid-to-late Holocene, when accumulation rates were higher than present. While this thickening relative to present was attributed to glacio-isostatic rebound, it is also possible that higher accumulation rates in the upstream sections of the WAIS contributed to this thickening, if sustained over millennia.

The lack of an ice-dynamical component in the model used here precludes us from evaluating any ice-surface-elevation change associated with changing accumulation rates. However, 18% higher accumulation rates during the mid-Holocene relative to the present across 30% of the WAIS could be consistent with an elevation increase of several tens of metres in ice thickness, according to Koutnik et al. (2016). Even if tens of metres of ice-surface-elevation change occurred, it is still unlikely to significantly affect the steady-state assumption of the 1-D model used here (constant ice thickness over time), because such changes are small (a few percent of the ice thickness) and that ice thickness exceeds 3,500 m in places over our survey area.

4.5.3 Impact for grounding-line evolution during the Holocene over the WAIS

Finally, we consider the possibility for Holocene ice thickening at the divide from increased accumulation rates to affect downstream grounding-line evolution. Recent evidence from ice-sheet modelling and field measurements suggest that grounding-line retreat during the Holocene was not monotonic, particularly at the Ross and Weddell sea sides of the WAIS (Bradley et al., 2015; Kingslake et al., 2018; Neuhaus et al., 2021). Rather, Kingslake et al. (2018) showed that the grounding-line position in the Ross and Weddell sea sectors initially retreated from the LGM inland until ∼10.2 – 9.7 ka, and then readvanced to its modern position sometime during the Holocene. Although they attributed this change in grounding-line position to the solid Earth viscoelastic response due to ice-sheet mass change and the subsequent re-grounding around pinning points, it has also been suggested that an increase in accumulation rates upstream of the grounding line could lead to a readvance via ice thickening there and a subsequent increase in ice flow (Steig et al., 2001; Koutnik et al., 2016; Jones et al., 2022). Across parts of the Weddell Sea Embayment, several studies have produced evidence for stability of the LGM ice thickness there until the early to mid-Holocene (Ross et al., 2011; Hein et al., 2016b; Ashmore et al., 2020a), contrary to most of the WAIS, after which abrupt thinning of ∼400 m contributed ∼1.4 – 2 m of sea-level rise (Hein et al., 2016b). A possible explanation for this delayed thinning in the Weddell Sea Embayment is that increased snowfall in the upper WAIS might have

counteracted ice-dynamical processes at the coast until the mid-to-late Holocene (Hein et al., 2016b; Spector et al., 2019). Similarly, over part of the Ross Sea sector, Neuhaus et al. (2021) showed that the grounding line over the Whillans, Kamb, and Bindschadler ice streams retreated to its minimum Holocene position in the mid to late-Holocene, and then readvanced between 2 – 1 ka, coinciding with periods of warmer and colder climates, respectively. They concluded that the reported grounding-line migration was likely dominated by modest climate-induced changes upstream rather than ice dynamics further downstream, as suggested for the Weddell Sea sector (Hein et al., 2016b).

Our results, which provide strong and widespread evidence for higher accumulation along the Amundsen-Weddell-Ross Divide during the mid-Holocene compared with the present, support these hypotheses further, as higher accumulation rates at the divide would likely result in upstream thickening (Sect. 4.5.2). In the absence of ice-dynamical processes counter-balancing this increase in accumulation rates, the grounding-line should advance in these regions. However, we note that the pattern of grounding-line retreat and readvance has not been observed over the Amundsen Sea sector (Kingslake et al., 2018; Johnson et al., 2020; 2021; Braddock et al., 2022) despite the accumulation-rate increase we also observed along the Amundsen-Weddell-Ross Divide and the recent results from Balco et al. (2023). This complication may indicate that the Amundsen sector is more strongly influenced by coastal changes in ice dynamics, for which even moderate changes in accumulation rate cannot compensate.

4.6 Conclusions

Using a ubiquitous internal reflecting horizon found across most of the Pine Island, Thwaites, and Institute and Möller ice-stream catchments, we have estimated mid-Holocene accumulation rates in the relatively slow-flowing parts of West Antarctica, representing 30% of total surface area of the WAIS.

By comparing our Holocene accumulation-rate estimates with a modern climate reanalysis model and observational syntheses, we estimated that accumulation rates across the Amundsen-Weddell-Ross Sea Divide since 4.72 ka were, on average, 18% higher than modern values. Our results suggest that spatial patterns of accumulation across the WAIS have remained stable during this period, i.e. higher accumulation rates on the Amundsen side of the divide transitioning to lower accumulation rates on the Ross side of the divide. The higher accumulation rates reported here for the mid-Holocene compared to the present agree well

with earlier, spatially focused studies of accumulation rates, all of which indicate higher accumulation rates (+15 - 30%) over the past ∼5 ka. This change in magnitude occurred at a time of asynchronous grounding-line migration over the WAIS, including readvances of the grounding line in the Weddell and Ross sectors and evidence for delayed deglaciation in the Weddell Sea side of the WAIS.

The higher mid-Holocene accumulation estimates inferred here over large sectors of the WAIS occurred at a time of sustained, millennial-scale increase in accumulation rates found at the WAIS Divide ice core. This pattern indicates that the ice core is suitably representative of the climatic conditions of the wider region over time. We suggest that future regional or continental ice-sheet modelling studies base their palaeoclimate forcing on modern spatial SMB products that are modulated over time using the WAIS Divide ice-core record. This will enable those models to obtain a more realistic climatic forcing representative of the past conditions of the wider WAIS, and ultimately, constrain ice-sheet volume change and grounding-line evolution during the Holocene.

4.7 Data availability

The IRH information for each of the three surveys used in this paper are archived in open-access repositories (Ashmore et al., 2020b; Bodart et al., 2021b; Muldoon et al., 2023) with references and links provided in the reference list. The BAS airborne radar data which were used to extract the IRHs used in this paper are fully available at the UK Polar Data Centre via the Polar Airborne Geophysics Data Portal (see Frémand, Bodart et al., 2022). The RACMO2 product is available on request from j.m.vanwessem@uu.nl or m.r.vandenbroeke@uu.nl. Links to access the observational point-based datasets used here are available from the respective references mentioned in the text (Sect. 4.3.4). The gridded depth and accumulation output, as well as all the codes associated with this study, are archived in an open-access repository (Bodart et al., 2023a).

5 A Community Resource of Aerogeophysical Data Across Antarctica: Application to the study of IRHs across the AIS

A version of this chapter has been published in *Earth System Science Data* as:

Paper details: Frémand, A.C.*, **Bodart, J.A.***, Jordan, T.A., Ferraccioli, F., Robinson, C., Corr, H.F.J., Peat, H.J., Bingham, R.G., Vaughan, D.G., 2022. British Antarctic Survey's Aerogeophysical Data: Releasing 25 Years of Airborne Gravity, Magnetic, and Radar Datasets over Antarctica, *Earth System Science Data*, 14, 3379–3410. DOI: 10.5194/essd-14-3379-2022 (see Appendix C for a copy of the published paper).

*indicates that these authors contributed equally to the paper.

This chapter contains an extended version of the published paper's Section 5.6.1 on applying the Internal-Layering Continuity Index to the newly released airborne Radio-Echo Sounding data presented in the paper, thereby addressing this thesis' aims and objectives stated respectively in Chapters 1 and 2.

Author contributions: I co-led the data release alongside A.C. Frémand. I created the data portal, with input from A.C. Frémand, T.A. Jordan, and F. Ferraccioli. I led the reprocessing, quality-checking and publication of the radar datasets and accompanying files, with input from A.C. Frémand, T.A. Jordan, and C. Robinson. A.C. Frémand led the standardisation and release of the gravity and magnetic data, with contributions from myself, T.A. Jordan and F. Ferraccioli. I wrote the code and analysed the results from the Internal Layer Continuity Index presented in the paper. I wrote the manuscript and created the figures, with input from A.C. Frémand and all co-authors.

5.1 Abstract

Over the past 50 years, the British Antarctic Survey (BAS) has been one of the major acquirers of aerogeophysical data over Antarctica, providing scientists with gravity, magnetic, and radar datasets that have been central to many studies of the past, present, and future evolution of the Antarctic Ice Sheet. Until recently, many of these datasets were not openly available, restricting further usage of the data for different glaciological and geophysical applications. Starting in 2020, scientists and data managers at BAS have worked on standardising and releasing large swaths of aerogeophysical data acquired during the period 1994–2020, including a total of 64 datasets from 24 different surveys, amounting to ∼450,000 line-km (or 5.3 million km^2) of data across West Antarctica, East Antarctica, and the Antarctic Peninsula. Amongst these are the extensive surveys over the fast-changing Pine Island (BBAS 2004–2005) and Thwaites (ITGC 2018–2019 2019–2020) glacier catchments, and the first ever surveys of the Wilkes Subglacial Basin (WISE-ISODYN 2005–2006) and Gamburtsev Subglacial Mountains (AGAP 2007–2009). Considerable effort has been made to standardise these datasets to comply with the FAIR (Findable, Accessible, Interoperable and Re-usable) data principles, as well as to create the Polar Airborne Geophysics Data Portal (https://www.bas.ac.uk/project/nagdp/, last access: 05 April 2023), which serves as a user-friendly interface to interact with and download the newly published data. This paper reviews how these datasets were acquired and processed, presents the methods used to standardise them, and introduces the new data portal and interactive tutorials that were created to improve the accessibility of the data. Lastly, we exemplify future potential uses of the aerogeophysical datasets by extracting information on the continuity of englacial layering from the fully published airborne radar data. We believe these newly released data will be a valuable asset to future glaciological and geophysical studies over Antarctica and will significantly extend the life cycle of the data. All datasets included in this data release are now fully accessible at https://data.bas.ac.uk (British Antarctic Survey, 2022).

5.2 Introduction

As one of the fastest changing environments on Earth, Antarctica has been at the epicentre of scientific research since the early 1960s. Understanding the past, present, and future of the Antarctic Ice Sheet is of special interest, particularly in the context of rapid climatic changes already affecting large parts of the Antarctic Peninsula and threatening the stability of the West Antarctic Ice Sheet (WAIS; IPCC AR6, 2021). One way to quantify how the ice sheet will respond to these changes is to conduct studies of englacial and basal properties of the ice using geo-

physical techniques such as gravity, magnetic, and radar. By studying the bedrock topography beneath an ice sheet, we can better estimate where a retreating ice stream is more likely to stabilise or destabilise further (Holt et al., 2006; Vaughan et al., 2006; Tinto and Bell, 2011; Ross et al., 2012; Morlighem et al., 2020) and how landforms or subglacial water-routing systems can affect the flow regime of ice streams (Bell et al., 2011; Wright et al., 2012; Schroeder et al., 2013; Ashmore and Bingham, 2014; Siegert et al., 2014; Young et al., 2016; Napoleoni et al., 2020). By studying the subglacial geology, we can better understand magmatic, tectonic, and sedimentary influences on ice flow over timescales of hundreds, thousands or even millions of years (Bell et al., 1998; Blankenship et al., 2001; Studinger et al., 2001; Bamber et al., 2006; Bell et al., 2006; Jordan et al., 2010b; Bingham et al., 2012), and quantify the influence of geothermal heat flux on ice dynamics (Schroeder et al., 2014; Jordan et al., 2018). Finally, the use of gravity techniques enables us to better understand the bathymetry beneath fast-changing ice shelves and ice-stream fronts and quantify areas of high sensitivity (Greenbaum et al., 2015; Millan et al., 2017; Tinto et al., 2019; Jordan et al., 2020).

Since the mid-1960s, the British Antarctic Survey (BAS) has been involved in acquiring aerogeophysical data with a particular focus on radar-data acquisition using a 35 and 60 MHz radio-echo sounder developed at the Scott Polar Research Institute (Robin et al., 1970), and, in collaboration with the Technical University of Denmark, using slightly improved versions of the same analogue radar system until the early 1990s (Robin et al., 1977). The subsequent development of an in-house digital radar system at BAS in 1993–1994 (Corr and Popple, 1994), and accompanying gravity and magnetic instruments, allowed for the first surveys over West Antarctica's Evans Ice Stream to be conducted in 1994–1995, marking the start of modern digital aerogeophysical surveying of the Antarctic by BAS. Further improvements in survey techniques and instruments have allowed BAS to develop its aerogeophysical capabilities further and become one of the leaders in aerogeophysics over the Antarctic.

Since the mid-1990s, aerogeophysical datasets acquired by BAS have played a vital role in understanding past and current ice-dynamical and lithospheric processes over the Antarctic Ice Sheet. In total, BAS flew 24 survey campaigns between 1994 and 2020, representing a total of ∼450,000 line-km of aerogeophysical data over the Antarctic Peninsula as well as over the WAIS and the East Antarctic Ice Sheet (EAIS) (Fig. 5.1, Table 5.1). The total cumulative survey coverage since 1994 is 5.3 million km^2, equivalent to >30% of the total area of the Antarctic Ice Sheet (14.2 million km^2). Many of these surveys were acquired as part of large international collaborative projects such as the International Polar Year

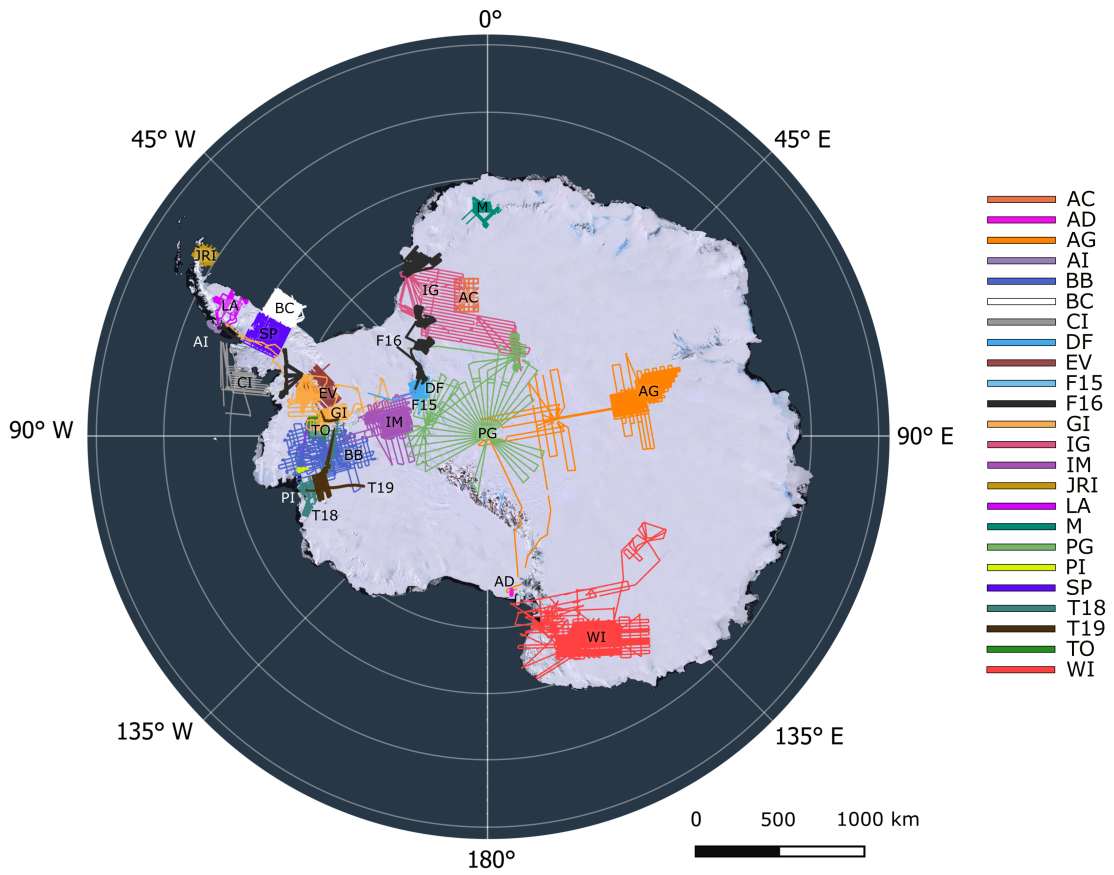

Figure 5.1: Map showing all the published datasets included in this data release. The colours are the same as those used on the data portal interface. Abbreviations are as follows: AC: AFI Coats Land (2001–2002); AD: Andrill HRAM (2008–2009); AG: AGAP (2007–2009); AI: Adelaide Island (2010–2011); BB: BBAS (2004–2005); BC: Black Coast (1996–1997); CI: Charcot Island (1996–1997); DF: DUFEK (1998–1999); EV: EVANS (1994–1995); F15: FISS 2015 (2015–2016); F16: FISS–EC–Halley 2016 (2015–2016); GI: GRADES-IMAGE (2006–2007); IG: ICEGRAV (2012–2013); IM: IMAFI (2010–2011); JRI: James Ross Island (1997–1998); LA: Larsen Ice Shelf (1997–1998); M: MAMOG (2001–2002); PG: PolarGAP (2015–2016); PI: Pine Island Glacier Ice Shelf (2010–2011); SP: SPARC (2002–2003); T18: ITGC (2018–2019); T19: ITGC (2019–2020); TO: TORUS (2001–2002); WI: WISE-ISODYN (2005–2006). The legend on the right-hand side of the figure shows the colour corresponding to each survey. The background image is from the Landsat Image Mosaic of Antarctica (LIMA; Bindschadler et al., 2008).

Antarctica's Gamburtsev Province Project (AGAP), the European Space Agency (ESA) PolarGAP project, and the US–UK International Thwaites Glacier Collaboration (ITGC), amongst others. Importantly, much of the data acquired since then have been central to the output of large international science groups, such as the Scientific Committee on Antarctic Research (SCAR) Bedmap (I/II/III),

ADMAP (I/II), AntArchitecture, and IBCSO projects (Lythe et al., 2001; Arndt et al., 2013; Fretwell et al., 2013; Golynsky et al., 2018).

Despite the importance of these surveys for understanding the Antarctic cryosphere and tectonics, until now the underlying data have been relatively inaccessible to wider scientific communities due to the scale of the data-management task required. This lack of accessibility has hampered the ability of the wider research community to extract further valuable information from these datasets. In 2020, a collaborative project between the UK Polar Data Centre (PDC, https://www.bas.ac.uk/data/uk-pdc/, last access: 05 April 2023) and the BAS Airborne Geophysics science team was set up to improve the FAIR-ness (Wilkinson et al., 2016) of these data. The main objectives of this collaboration were to comply with national and international policies on data sharing and accessibility, foster new collaborations, and allow the further re-use of these data beyond the lifespan of the science projects.

This chapter presents the result of this successful collaboration between data managers and scientists to standardise and release most of BAS' aerogeophysical data acquired to date using modern instruments from 1994 onwards. Data acquired prior to this, while particularly useful to long-term monitoring of ice sheet conditions, are much more challenging and time-consuming to update to modern standards (see Schroeder et al., 2019; Sect. 5.6.3), and are thus not included in the data release discussed here. Section 5.3 of this chapter reviews the main scientific findings from each survey flown between 1994 and 2020. Section 5.4 describes the various instruments and techniques used to acquire and process the data. Section 5.5 outlines the format and data publishing strategy for our datasets following the FAIR data principles, as well as the creation of a new data portal and interactive, open-access tutorials. Finally, Section 5.6 provides a case study for the re-usability of the newly released aerogeophysical data, as well as suggestions on future uses of the data portal and aspirations for future data releases.

5.3 Background

The following section reviews the main scientific findings related to the acquisition of aerogeophysical data from BAS for the period 1994–2020 and is divided into two sub-sections: (i) findings from surveys conducted pre-2004 using older aerogeophysical instruments and for which the fully processed 2-D radar data are not published as part of this data release (see Table 5.1, Sect. 5.6.3), and (ii) surveys conducted post-2004 using the Polarimetric Airborne System INstrument

1 (PASIN-1) (2004–2015) and PASIN-2 (2015–2020) radar systems and more modern data-acquisition methods. Figures 5.2-5.3 present the wide-ranging datasets of gravity and magnetic anomalies, bed elevation and ice thickness, and 2-D radar profiles ensuing from the surveys discussed in Sections 5.3.1 and 5.3.2.

5.3.1 Aerogeophysical surveys for the period 1994-2004

The first surveys conducted by BAS since the mid-1990s involved extensive gravity and magnetic surveying of the western and eastern Antarctic Peninsula and Weddell Sea Embayment. Surveys over Evans Ice Stream (1994–1995), Black Coast (1996–1997), Charcot Island (1996–1997), and James Ross Island (1997–1998) (Fig. 5.1, Table 5.1) provided new insights into the history of crustal boundaries between the eastern Antarctic Peninsula and the Filchner Block (Ferris et al., 2002), evidence of crustal thinning below Evans Ice Stream (Jones et al., 2002), and new understanding of the magmatic and tectonic processes around the Mount Haddington stratovolcano on James Ross Island (Jordan et al., 2009). A further study covering the Larsen Ice Shelf (Antarctic Peninsula) was conducted conjointly by BAS and the Instituto Antártico Argentino in 1997–1998. The radar data acquired during this survey were used in ocean (Holland et al., 2009) and firn-density (Holland et al., 2011) models to improve our understanding of ice–ocean interactions and ice-surface elevation changes on the ice shelf. In 1998–1999, extensive aeromagnetic surveying of the Dufek Massif (West Antarctica/East Antarctica) revealed the presence of a Jurassic dike swarm that likely acted as a magma transport and feeder system to the Ferrar Large Igneous Province (Ferris et al., 2003). In 2001–2002, an additional survey was flown as part of the initiative, Targeting ice-stream Onset Regions and Under-ice Systems (TORUS), to assess the factors controlling the dynamics of the Rutford Ice Stream using gravity, magnetic, and radar instruments over a high-resolution grid spacing of ∼10 km (Vaughan et al., 2008). Lastly, for the WAIS, the 2002–2003 Superterranes in the Pacific Margin Arc (SPARC) campaign over northern Palmer Land (Antarctic Peninsula) used gravity and magnetic instruments to reveal subglacial imprints of crustal growth linked with the Gondwana margin (Ferraccioli et al., 2006).

Over East Antarctica, two surveys conducted in 2001–2002 acquired detailed gravity, magnetic, and radar measurements over Slessor Glacier (as part of the Antarctic Funding Initiative (AFI) Coats Land survey) and Jutulstraumen Ice Stream (as part of the Magmatism as a Monitor of Gondwana breakup survey; MAMOG). The AFI Coats Land survey, a UK initiative between BAS and the University of Bristol, provided the first accurate measurements of ice thickness and bed elevation in the area (Rippin et al., 2003a) (Fig. 5.2), and led to the discovery of a ∼3 km thick sedimentary basin associated with a weak till layer at

the bed which enhances basal motion and affects the flow regime of this part of the EAIS (Rippin et al., 2003a; Bamber et al., 2006; Shepherd et al., 2006). The MAMOG survey revealed the presence of a subglacial Jurassic continental rift in the area of western Dronning Maud Land, providing early evidence for the initial Gondwana breakup (Ferraccioli et al., 2005a, b).

5.3.2 Aerogeophysical surveys for the period 2004-2020

Building on the surveys prior to 2004, which were relatively small in areal extent, BAS began surveying larger areas from the mid-2000s onwards (Table 5.1), primarily due to enhanced international collaborations and improvements in data acquisition and instruments, which led to data being acquired both at higher resolution and over larger spatial scales. The acquisition strategy was to collect data from multiple geophysical sensors mounted on BAS' Twin Otter aircraft across every survey, giving a holistic view of vast and previously unsurveyed regions (Figs. 5.2-5.3). The core sensor suite included gravity and magnetic instruments used to understand the geological nature of the subglacial basins and mountains along with their tectonic structure, together with the radar system used to map ice thickness and bed elevation. The development of a new radar system, the PASIN system (PASIN-1, 2004–2015) (see Section 5.4.1.3), and an improved version of the same system (PASIN-2, 2015–2016 onwards), allowed for the efficient collection of high-quality digital radar data for BAS-led campaigns in the Antarctic.

We divide the findings from these surveys into two sub-sections (Section 5.3.2.1 for surveys between 2004 and 2015 and Section 5.3.2.2 for surveys between 2015 and 2020) to reflect the acquisition of data prior to and following the upgrade of the PASIN system (see Section 5.4.1.3).

5.3.2.1 2004-2015

The first mission to utilise the PASIN-1 radar system was the 2004–2005 BBAS survey of Pine Island Glacier, which aimed to characterise the subglacial conditions of this sensitive glacier of West Antarctica (Vaughan et al., 2006). This survey provided two key findings: (a) the discovery of a narrow subglacial trough that is 500 m deep and 250 km long, through which Pine Island Glacier flows; and (b) the existence of well-constrained valley walls, which would likely provide a buffer against a potential catastrophic collapse of the WAIS via Pine Island Glacier (Vaughan et al., 2006). Further studies utilising this dataset focused primarily on bed characteristics and the subglacial hydrology of the catchment (Rippin et al., 2011; Napoleoni et al., 2020; Chu et al., 2021), as well as tracking englacial layers

and quantifying past accumulation rates (Corr and Vaughan, 2008; Karlsson et al., 2009, 2014; Bodart et al., 2021a). The survey was also conducted simultaneously with another covering the Thwaites Glacier catchment led by the University of Texas Institute for Geophysics and the National Science Foundation of the United States (Holt et al., 2006), enabling a comparison of the surveying capabilities where the surveys overlapped (e.g. Chu et al., 2021).

Following on from the BBAS data, the suite of geophysical instruments on board the BAS Twin Otter aircraft were used to survey the Wilkes Subglacial Basin, Dome C, and the Transantarctic Mountains as part of the 2005–2006 WISE-ISODYN survey between BAS and the Italian Programma Nazionale di Ricerche in Antartide (Bozzo and Ferraccioli, 2007; Corr et al., 2007; Ferraccioli et al., 2007; Jordan et al., 2007). This project revealed, for the first time, the crustal architecture of the Wilkes Subglacial Basin (Ferraccioli et al., 2009; Jordan et al., 2013) and the distribution of a well-preserved subglacial sedimentary basin underlying the Wilkes catchment (Frederick et al., 2016). The following year, the 2006–2007 survey, Glacial Retreat in Antarctica and Deglaciation of the Earth System – Inverse Modelling of Antarctica and Global Eustasy (GRADES-IMAGE), comprising surveys over the transitional area between the Antarctic Peninsula and the WAIS, provided detailed information on subglacial properties of Evans Ice Stream (Ashmore et al., 2014). Ice-thickness measurements along the grounding line were also used as key calibration for the Landsat-derived "ASAID" grounding-line product (Bindschadler et al., 2011), and englacial layers through Bungenstock Ice Rise were used to assess ice-divide stability and the wider ice-flow history and stability of the WAIS's Weddell Sea sector during the Holocene (Siegert et al., 2013).

Over two austral field seasons from 2007 to 2009, AGAP, coordinated as part of the fourth International Polar Year between the UK, USA, Germany, Japan, Australia and China, comprised a comprehensive survey of the interior of the EAIS, yielding important aerogeophysical data used to interrogate the origin and geophysical characteristics of the Gamburtsev Subglacial Mountains. Significant scientific discoveries generated by the AGAP survey included observations of widespread freeze-on at the bottom of the ice which leads to thickening of the EAIS from the base (Bell et al., 2011), a thick crustal root formed during the Proterozoic aeon (1 Gyr ago) surrounded by a more recent ∼2,500-km-long rift system (Ferraccioli et al., 2011), and the existence of ancient pre-glacial fluvial networks at the present ice bed which confirmed the presence of the Gamburtsev Subglacial Mountains prior to the start of glaciation at the Eocene–Oligocene climate boundary (ca. 34 Ma) (Rose et al., 2013; Creyts et al., 2014).

TABLE 5.1: Information on the period, region, sub-region, type of data acquired, total line coverage (km), total coverage area (km^2), and key reference for each survey included in this data release. For "Data", the abbreviations are as follows: gravity (G), magnetic (M), radar (R). For "Regions", abbreviations are as follows: APIS (Antarctic Peninsula Ice Sheet), EAIS (East Antarctic Ice Sheet), WAIS (West Antarctic Ice Sheet). "DML" stands for Dronning Maud Land and "PIG" for Pine Island Glacier. *For AGAP, the data release only consists of the BAS-acquired data, which represents approximately half of the total (∼120,000 km) survey coverage from the whole AGAP expedition (see Section 5.3.2.1).

Survey	Year	Region	Sub-Region	Data	Total line coverage (km)	Total coverage area (km^2)	Reference
EVANS	1994-95	WAIS/APIS	Evans Ice Stream	G, M, R	11,500	1.06 x10^5	Jones et al. (2002)
Black Coast	1996-97	APIS	Black Coast / Weddell Sea	M	10,000	8.96 x10^4	Ferris et al. (2002)
CHARCOT	1996-97	APIS	Charcot Island	M	7,500	1.67 x10^5	Johnson et al. (1999)
James Ross Island	1997-98	APIS	James Ross Island	G, M, R	10,000	3.32 x10^4	Jordan et al. (2009)
LARSEN	1997-98	APIS	Larsen Ice Shelf	M, R	5,800	5.96 x10^4	Holland et al. (2009)
DUFEK	1998-99	WAIS/EAIS	Dufek Massif	G, M, R	8,300	4.66 x10^4	Ferris et al. (2003)
AFI Coats Land	2001-02	EAIS	Slessor Glacier	G, M, R	5,000	6.53 x10^4	Rippin et al. (2003a)
MAMOG	2001-02	EAIS	Jutulstraumen Ice Stream / DML	G, M, R	15,500	5.79 x10^4	Ferraccioli et al. (2005a)
TORUS	2001-02	WAIS	Rutford Ice Stream	G, M, R	8,600	1.12 x10^5	Vaughan et al. (2008)
SPARC	2002-03	APIS	Northern Palmer Land	G, M	20,000	1.07 x10^5	Ferraccioli et al. (2006)
BBAS	2004-05	WAIS	Pine Island Glacier	G, M, R	35,000	4.09 x10^5	Vaughan et al. (2006)
WISE-ISODYN	2005-06	EAIS	Wilkes Land	G, M, R	61,000	7.91 x10^5	Jordan et al. (2013)
GRADES-IMAGE	2006-07	WAIS/APIS	Evans & Rutford Ice Streams	M, R	27,500	3.06 x10^5	Ashmore et al. (2014)
AGAP	2007-09	EAIS	Gamburtsev / Dome A	G, M, R	73,000*	6.22 x10^5	Ferraccioli et al. (2011)
ANDRILL HRAM	2008-09	WAIS	Ross Ice Shelf & Coulman High	M, R	1,200	1.48 x10^3	-
Adelaide Island	2010-11	APIS	Adelaide Island	M, R	5,500	3.76 x10^3	Jordan et al. (2014)
IMAFI	2010-11	WAIS	Institute & Möller Ice Streams	G, M, R	25,000	1.96 x10^5	Ross et al. (2012)
PIG Ice Shelf	2010-11	WAIS	Pine Island Shelf	M, R	1,500	1.80 x10^3	Vaughan et al. (2012)
ICEGRAV	2012-13	EAIS	Recovery & Slessor glaciers, Bailey Ice Stream	G, M, R	29,000	4.75 x10^5	Diez et al. (2018)
FISS 2015	2015-16	WAIS	Foundation Ice Stream / Bungenstock Ice Rise	M, R	7,000	1.43 x10^4	-
PolarGAP	2015-16	EAIS	South Pole	G, M, R	38,000	8.71 x10^5	Jordan et al. (2018)
FISS 2016	2016-17	WAIS	Filchner Ice Shelf /English Coast / Recovery & Support Force glaciers	G, M, R	26,000	5.99 x10^5	Hofstede et al. (2021)
ITGC 2018	2018-20	WAIS	Thwaites Glacier	G, M, R	9,872	6.43 x10^4	Jordan et al. (2020)
ITGC 2019	2019-20	WAIS	Thwaites Glacier / Rutford Ice Stream	G, M, R	4,432	4.85 x10^4	-

Between 2008 and 2011, three surveys utilised the magnetic and radar instruments on board the BAS Twin Otter to conduct high-spatial-resolution surveying of Coulman High on Ross Ice Shelf as part of the Antarctic Drilling – High Resolution Aeromagnetic (ANDRILL HRAM) project, Adelaide Island (Antarctic Peninsula), and Pine Island Glacier Ice Shelf (West Antarctica). The 2010–2011 Adelaide Island survey provided high-resolution aeromagnetic data to underpin a better understanding of the complex magmatic structure of the Antarctic Peninsula Cenozoic arc/forearc boundary (Jordan et al., 2014). The Pine Island Glacier Ice Shelf survey of the same year revealed a network of sinuous subglacial channels, 500 to 3,000 m wide and up to 200 m high, in the ice-shelf base, which, combined with surface and basal crevasses formed as a result of the basal melting, could lead to structural weakening of the shelf in the future (Vaughan et al., 2012).

The early 2010s saw the deployment of the PASIN system used as part of two large collaborative projects, namely the 2010–2011 Institute–Möller Antarctic Funding Initiative (IMAFI) survey over the Institute and Möller Ice Streams of West Antarctica, and the 2012–2013 ICEGRAV survey over the Recovery and Slessor region of East Antarctica.

The 2010–2011 IMAFI project was a UK initiative between BAS and the universities of Edinburgh, York, Aberdeen and Exeter. The key aims were to investigate the potential stability of this sector of West Antarctica and test the ability of the subglacial sedimentary structure to control the flow of two large ice streams draining the WAIS into the Weddell Sea Embayment (Ross et al., 2012). Radar data revealed the presence of a reverse-bed slope with a 400 m decline over a 40 km distance away from the grounding line and that this region was relatively close to flotation, indicating the potential instability of this sector in light of future grounding-line migration upstream of its current position (Ross et al., 2012). Additional analysis using gravity and magnetic data revealed the extent of the Weddell Sea Rift System, adding further evidence for the early stages of the Gondwana breakup and Jurassic extension in the region (Jordan et al., 2013). Further analysis of the radar data acquired during the IMAFI survey led to a new digital elevation model of the subglacial topography around the ice streams of the Weddell Sea Embayment at 1 km resolution, revealing deep subglacial troughs between the ice-sheet interior and the grounding line, and well-preserved landforms associated with alpine glaciation (Ross et al., 2014; Jeofry et al., 2018), as well as evidence for a temperate former WAIS via the discovery of extensive subglacial meltwater channels (Rose et al., 2014). The data have also been used to assess the roughness of the subglacial bed (Rippin et al., 2014), investigate englacial properties across the catchment as an indicator of past ice-flow dynamics (Bingham et

al., 2015; Winter et al., 2015; Ashmore et al., 2020a; Ross et al., 2020), and show the presence of sub-ice shelf channels generated by water flowing from beneath the present ice sheet (Le Brocq et al., 2013).

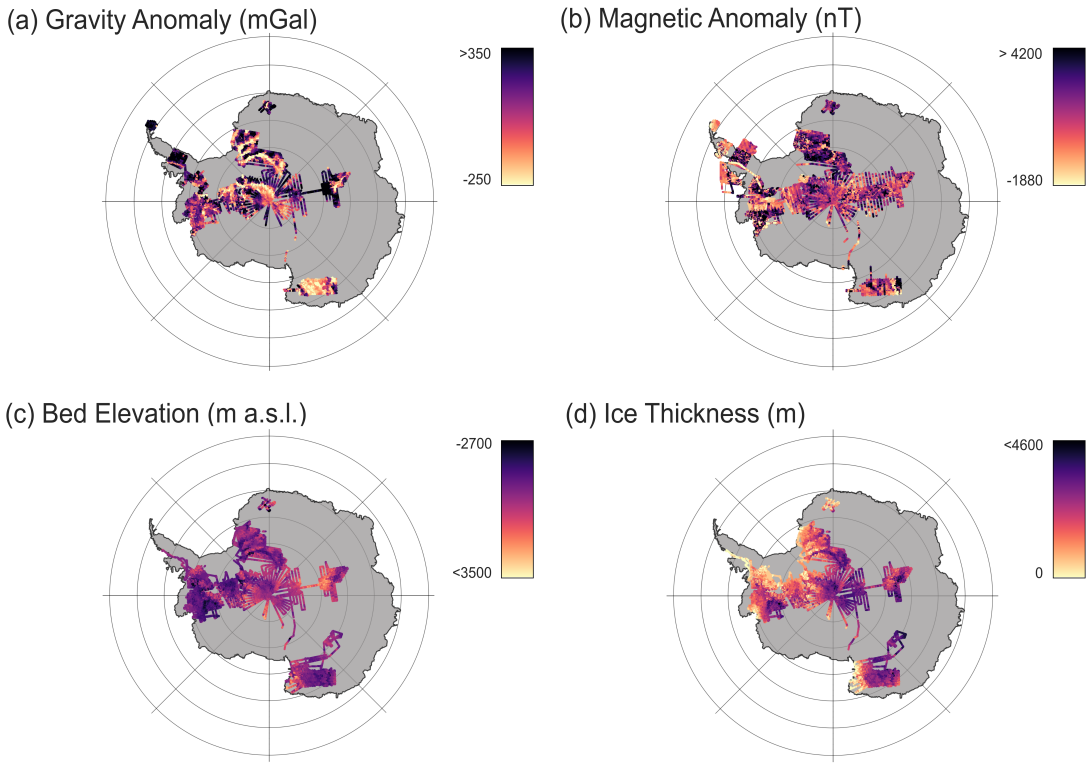

Figure 5.2: Maps of gravity, magnetic, and radar (bed elevation and ice thickness) point measurements for all surveys published as part of this data release. (a) Gravity anomaly points (in milligal, or mGal), (b) magnetic anomaly points (in nanotesla, or nT), (c) bed-elevation points from radar data (in metres above sea level, or m a.s.l.), (d) ice-thickness points from radar data (metres). In total, this data release consists of 3.62 million gravity, 7.41 million magnetics, and 14.5 million ice-thickness and bed-elevation data points. Note that no correction such as downward continuation has been applied to compile the gravity data shown in (a).

The 2012–2013 ICEGRAV survey, an international collaboration between BAS and the Technical University of Denmark, National Science Foundation, Norwegian Polar Institute, and the Instituto Antártico Argentino, carried out aerogeophysical surveys over the poorly explored Recovery Glacier catchment and Recovery subglacial lakes (Forsberg et al., 2018), revealing a deep 800 km trough underlying Recovery Glacier, with evidence for subglacial water controlling the fast flow in the upstream portion of the ice stream (Diez et al., 2018).

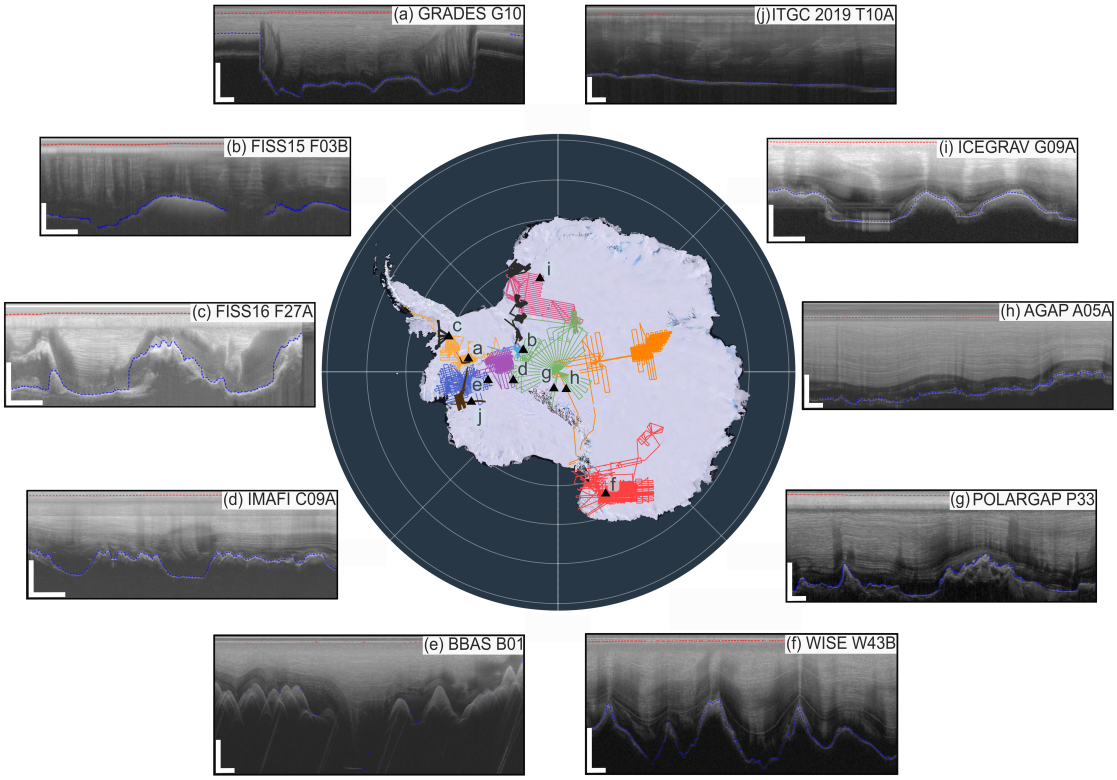

Figure 5.3: Sample radargrams from the ten 2-D radar datasets released with this paper. The colours for each survey on the map are the same as in Figure 5.1 and the data portal. The location of each radargram (a–j) is marked on the map by black triangles. The dashed red and blue lines on the radargrams are the surface and bed picks, respectively. A description of each radargram is provided as follows: (a) flight line G10 (GRADES-IMAGE) showing well-defined subglacial valleys through which Evans Ice Stream flows (ice flow is approximately out of page), with stable layering present before and in the middle of the topographic low; (b) flight line F03B (FISS 2015) showing undulating bed topography and disrupted layering at the onset of Foundation Ice Stream; (c) flight line F27A (FISS 2016) showing variations in subglacial topography at the divide between the Antarctic Peninsula and West Antarctica, with potential evidence of basal freeze-on at the start of the segment; (d) flight line C09A (IMAFI) showing evidence of preserved layering despite changes in local topography at the bottleneck between East and West Antarctica; (e) flight line B01 (BBAS) over Ellsworth Subglacial Mountains showing a ∼1.5 km trough in the ice-sheet bed and one of the deepest points in the PIG basin with ∼3 km of ice underlying the surface; (f) flight line W43B (WISE-ISODYN) showing internal layers draping over the highs and lows in the local Wilkes Subglacial Basin topography, with two particularly bright reflections in the middle and bottom of the ice column; (g) flight line P33 (PolarGAP) showing clear and stable englacial layering throughout the ice column at the onset of the topographic highs of the Transantarctic Mountain Range; (h) flight line A05A (AGAP) showing stable internal layering characteristic of the interior of the EAIS; (i) flight line G09A (ICEGRAV) showing evidence of a bright reflection likely associated with a previously unidentified subglacial lake in the region; and (j) flight line T10A (ITGC 2019) showing a section of inland-sloping bed from a profile in the main trunk of Thwaites Glacier, >200 km from the current grounding line position (ice flow is right to left). The horizontal and vertical white bars at the bottom of each radargram represent ∼3 km in the horizontal direction (i.e. distance) and ∼1 km in the vertical direction (i.e. depth), respectively.

5.3.2.2 2015-2020

The 2015–2016 PolarGAP survey was a major international collaboration, funded by ESA and led by BAS, the Technical University of Denmark, the Norwegian Polar Institute, and the National Science Foundation, to fill a gap in global gravity surveying that the ESA's Gravity field and steady-state Ocean Circulation Explorer (GOCE) satellite network was unable to cover. Alongside the large swath of gravity surveying, opportunistic magnetic and radar data were also acquired over the South Pole and parts of Support Force, Foundation, and Recovery ice streams using a further upgraded radar system, PASIN-2 (see Section 5.4.1.3). Additional funding from the Norwegian Polar Institute also allowed for a number of dedicated flights over the Recovery subglacial lakes. The acquired data have led to major scientific findings, including (a) the presence of anomalously high geothermal heat flux near the South Pole (Jordan et al., 2018), (b) the delineation of two subglacial lakes (Recovery Lakes A and B) totalling ∼4,320 km^2 in size and composed of saturated till, with evidence of bed lubrication and enhanced flow downstream of their location as a result of water drainage (Diez et al., 2019), and (c) the evidence of a large (500–700 km-wide) marginal embayment formed during late Neoproterozoic rifting along the craton margin and which cuts into the East Antarctic basement around the South Pole region (Jordan et al., 2022). Additional evidence showed that the Pensacola-Pole Basin is characterised by a topographic depression of ∼0.5 km below sea level and contains a thick sedimentary layer of 2–3 km in the southern part of the catchment (Paxman et al., 2019). The radar data from the PolarGAP survey have also revealed large troughs at the bottleneck between East and West Antarctica, suggesting that the drawdown of the EAIS via the WAIS is unlikely (Winter et al., 2018).

In the austral summers of 2015–2016 and 2016–2017, two surveys were flown as part of the Filchner Ice Shelf system (FISS) project led by BAS with support from the Alfred Wegener Institute in Germany and several other UK institutions (UK National Oceanography Centre, Met Office Hadley Centre, universities of Exeter, Oxford, and University College London), with the aim to investigate the potential contribution of the Filchner Ice Shelf and feeding ice streams to sea-level rise. The 2015–2016 survey acquired ∼7,000 line-km of aerogeophysical data, primarily over Foundation Ice Stream and to a smaller extent over Bungenstock Ice Rise. In 2016–2017, ∼26,000 line-km of aerogeophysical data were acquired over Academy, Recovery, Slessor, and Support Force glaciers, and parts of the Filchner and Brunt ice shelves. Data were also collected over outlet glaciers of the English Coast (western Palmer Land, Antarctic Peninsula). Early findings from the 2016–2017 aerogeophysical survey revealed subglacial drainage channels beneath Support Force Glacier (Hofstede et al., 2021), provided evidence for a large ∼80 x

30 x 6 km mafic intrusion, likely resulting from mantle melting during the Gondwana breakup (Jordan and Becker, 2018), and helped to delineate the subglacial bathymetry beneath Brunt Ice Shelf (Hodgson et al., 2019).

During the 2018–2019 and 2019–2020 seasons, BAS was involved in aerogeophysical surveying of Thwaites Glacier as part of the UK–US ITGC initiative. The 2018–2019 survey acquired ∼9,900 km of aerogeophysical data over the lower Thwaites Glacier and Thwaites Glacier Ice Shelf. The 2019–2020 survey acquired ∼4,500 line-km over the lower Thwaites Glacier, the WAIS Divide ice-core site, and Rutford Ice Stream. These surveys contributed to a new bathymetric map of Thwaites, Crosson, and Dotson ice shelves from gravity measurements, revealing a deep (>800 m) marine channel extending beneath the ice shelf adjacent to the front of Thwaites Glacier (Jordan et al., 2020). These datasets have also contributed to a new bathymetry model of George VI Sound (Constantino et al., 2020) and were integrated with swath bathymetric data outboard from Thwaites Glacier (Hogan et al., 2020).

5.4 Data acquisition and processing

The typical acquisition and processing workflow for the aerogeophysical data is shown in Figure 5.4. Usually, the aircraft is set up systematically to acquire gravity, magnetic, and radar data together, except in situations where surveying objectives are not compatible with the acquisition of all three datasets at once (i.e. flying at constant terrain clearance for the radar data affects the quality of the gravity data which is better flown at constant altitude, and vice versa); although novel gravity-acquisition methods are increasingly making this issue redundant (see Section 5.4.1.1). As shown in Table 5.1, the conventional gravity–magnetic–radar set-up was used in 15 out of 24 surveys, with the remaining 7 surveys using either a magnetic–radar- or gravity–magnetic-only set-up, and only 2 using a magnetic-only set-up. The data acquisition steps for each type of data are described in Section 5.4.1, and the processing of the data is described in Section 5.4.2.

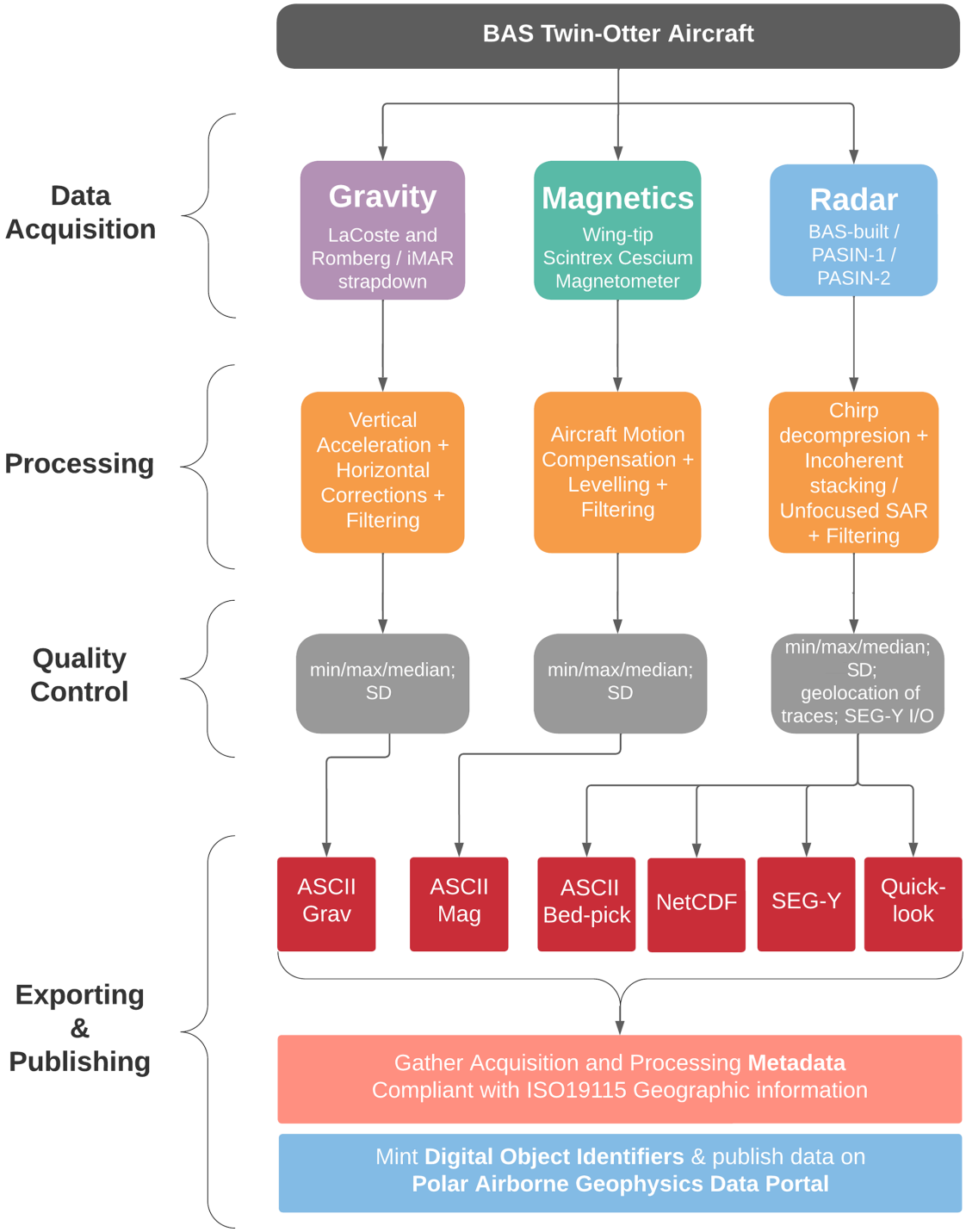

Figure 5.4: Workflow describing the data acquisition, processing, and publishing for the BAS aerogeophysical data included in this data release. Standard deviation is abbreviated as "SD", whilst "I/O" refers to the import of the SEG-Y files into seismic-interpretation software for quality check and the output of the files.

5.4.1 Data acquisition and instrumentation

All BAS aerogeophysical data acquisition is conducted using Twin Otter aircraft due to their remote capabilities, long fuel range (up to 1,000 km), and operability. The aircraft's twin turbo-prop engines enable it to conduct rapid take-off and landing as well as operate in small and remote airfields commonly covered in snow and icy terrains using mounted skis. All data acquisition since the early 1990s has been conducted using the BAS DeHavilland Twin Otter aircraft "VP-FBL" (Fig. 5.5). The aircraft typically flies at a nominal speed of ∼60 m s^{-1}, which results in an along-track distance between each stacked radar trace of 0.2 m (prior to processing). The following sections describe the acquisition of the data for the gravity (Sect. 5.4.1.1), magnetic (Sect. 5.4.1.2), radar (Sect. 5.4.1.3), and GPS and lidar (Sect. 5.4.1.4) instruments on board the aircraft.

5.4.1.1 Gravity

Until 2012, BAS aerogravity measurements were acquired with a LaCoste and Romberg air–sea gravimeter modified by Zero-Length Spring (ZLS) Corporation. The gravimeter was mounted in a gyro-stabilised, shock-mounted platform at the centre of the aircraft to minimise the effect of vibrations and rotational motions.

Starting with the 2015–2016 PolarGAP survey, aerogravity data were acquired using a novel strap-down method which, unlike traditional surveys using a stabilised gravity platform, allowed for the collection of gravity data during draped or turbulent flights (Jordan and Becker, 2018). For this survey, both the LaCoste and Romberg and strap-down systems were operated, together with results from the two systems merged, to provide an optimum data product with the long-term low and predictable drift of the LaCoste and Romberg system and the dynamic stability of the strap-down system. Subsequent surveys used a strap-down sensor alone, removing the need to prioritise the quality of the gravity data over the radar data and allowing for flights at a constant terrain clearance for optimal radar-data collection. The optimum resolution of the system is approximately 100 s along-track (Jordan and Becker, 2018).

The first strap-down sensor deployed by BAS was the iMAR RQH-1003 system provided by the Technical University (TU) of Darmstadt, and consisting of three Honeywell QA2000 accelerometers (mounted in mutually perpendicular directions) and three Honeywell GG1230 ring laser gyroscopes. The subsequent 2018–2019 and 2019–3020 ITGC surveys over Thwaites Glacier used the iMAR iCORUS strap-down airborne gravimeter systems from Lamont-Doherty Earth Observatory and BAS respectively, which have approximately equivalent internal components to the

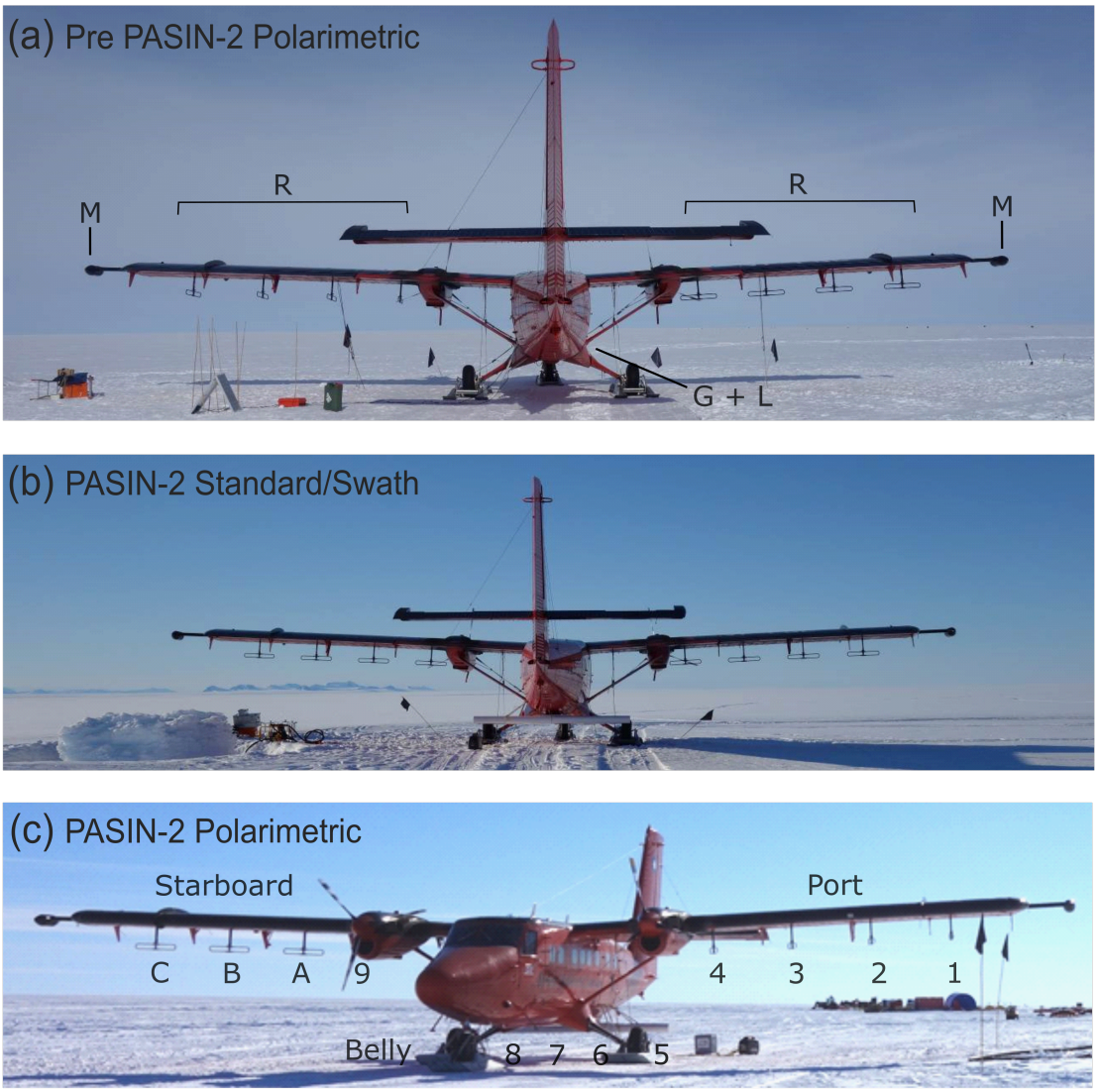

Figure 5.5: Photographs of the aerogeophysical set-up on the BAS Twin Otter aircraft "VP-FBL" for PASIN-2. (a) The pre-PASIN-2 (used in 2015–2016 PolarGAP only) configured to mimic the set-up of PASIN-1 data collection in polarimetric mode. The eight folded dipole transmitting and receiving antennas are fixed under the wings (two transmitting and two receiving antennas on each wing) with the port configured as vertical (V) and starboard as horizontal (H). The annotations show the location of the radar (R), magnetic (M), and gravity and lidar (G + L) instruments on board the aircraft. (b) The PASIN-2 set-up in standard/swath mode. The eight folded dipole transmitting and receiving antennas are fixed under the wings and inside the aircraft and are operated using a radio frequency (RF) switch, and an additional four receiving antennas are situated in the belly enclosure. When in standard swath mode, all antennas are configured in H orientation with the starboard and belly antennas also in H orientation. The PASIN-1 set-up in standard mode (not shown here) had a similar configuration as shown in (b) bar the belly antenna (i.e. only four transmitting on port and four receiving on starboard in H orientation). (c) The PASIN-2 set-up in polarimetric mode. The eight folded dipole transmitting and receiving antennas are fixed under the wings and inside the aircraft and are operated using an RF switch, and an additional four receiving antennas are situated in the belly enclosure. When in polarimetric mode, the port antennas are configured in V orientation and the starboard and belly antennas in H orientation. The PASIN-1 set-up in polarimetric mode (not shown here as rarely flown) had the two pairs of outboard antennas rotated to V configuration and the inboard to H configuration. Photo credit: Carl Robinson.

TU Darmstadt system.

5.4.1.2 Magnetics

The Twin Otter is configured for fixed wing magnetometer operation. The aircraft modifications include inboard-positioned wingtip fuel pumps, pod-boom hard points and a demagnetised airframe to maximise magnetic-data collection. Scintrex CS3 Cesium sensors are used due to their high sensitivity, high cycling rates, excellent gradient tolerance, fast response, and low susceptibility to the electromagnetic interference. The resolution of the magnetometers has greatly increased over time, with the current systems having a measurement accuracy of 0.2 pT compared to the older systems used between 1973 and 1990 (500 pT; Geometrics G-803 Potassium) and between 1991 and 2003 (10 picotesla; Sintrex H8 Cesium).

5.4.1.3 Radar

Prior to 2004, BAS deployed a custom-built, 8-array element radar system, referred to here as "BAS-built" (Corr and Popple, 1994). This was a coherent radar system operating at a centre frequency of 150 MHz and using a transmit power of 1,200 W (Rippin et al., 2003a). The radar system was equipped with eight folded dipole transmitting and receiving antennas fixed under the wings (four transmitting on the port wing, four receiving on the starboard wing). Similar to the current systems, the "BAS-built" system transmitted both a conventional narrow-sounding pulse mode of 0.25 μs and a deep-sounding 4 μs, 10 MHz chirp (Table 5.2). As developments in digital acquisition became commercially available, several technical upgrades were applied to the radar system. These ranged from using a LeCroy scope to acquire logarithmic detected waveforms to accommodate complex coherent acquisition, as well as the replacement of the LeCroy oscilloscope by a low sample-frequency 12-bit dual ADC (analogue-to-digital converted) card in the later years of operation (see Figs. 5.6-5.8). During this time, the dynamic range of the system was extended by the interleaved transmission of different waveforms, which were conventional short wave-train pulses at the centre frequency.

After operating for 10 successive field seasons, the "BAS-built" radar system was retired and replaced by a more modern radar system, PASIN (Corr et al., 2007). In contrast to the "BAS-built" system, PASIN was designed to sound ice much deeper (up to 5 km compared to 3.3 km for the earlier system) thanks to improved digital electronics and added power in the transmitting antennas (see Table 5.2). Additionally, modern methods of digitisation, enabled by the use of ADC cards rather than a digitising scope, allowed phase and not just power to be

recorded in greater resolution on PASIN, which eventually allowed for the use of more advanced processing techniques such as Synthetic Aperture Radar (SAR) to be applied to the data (see Section 5.4.2.3).

The older PASIN-1 (2004–2015) and the newer PASIN-2 (2015–present) systems are bistatic radars operating at a 150 MHz centre frequency and configured as follows: (a) PASIN-1: 10 MHz bandwidth system with eight folded dipole transmitting and receiving antennas fixed under the wings (four transmitting on port wing, four receiving on starboard wing) operating in horizontal (H) orientation when in standard mode, and more rarely with the port (transmit) and starboard (receive) antennas positioned in both H and vertical (V) orientation when in polarimetric mode (see similar set-up of PASIN-2 in Figure 5.5a) (Corr et al., 2007); and (b) PASIN-2: 13 MHz bandwidth system with eight folded dipole transmitting and receiving antennas fixed under the wings and inside the aircraft with radio frequency (RF) switches and an additional four receiving antennas in the belly enclosure (see see Figure 5.5b-c; Table 5.2). The main difference between the PASIN-1 and PASIN-2 systems is the ability for across-track swath processing to be applied to the PASIN-2 data by allowing both transmitting and receiving on the folded dipole antennas via the use of RF switches.

In further contrast with PASIN-1, the PASIN-2 radar has a very flexible configuration, with the standard configuration being as 12-channel swath radar (with 8 transmitting and 12 receiving). However, other configurations are also possible, including a polarimetric mode to give H and V data where the port antennas are rotated 180 (see Table 5.3). A final configuration is a mixed antenna gain path for areas where ice is heavily disrupted and where the starboard signal can be attenuated by several decibels. Since 2016, the PASIN-2 system has undergone minor modifications to reduce noise and improve system operations, including (a) low-pass filters in the RF switches, (b) the use of a 10 GHz waveform generator, and (c) new 1 kW solid-state power amplifiers which have lowered transmitter system noise and increased transmitter and receiver isolation.

Data for both versions of the PASIN system are received using sub-Nyquist digitisation and stacking and stored on removable solid-state disks or tapes, and then copied to duplicate spinning disks for data archiving. On average, a 4.5 h flight will generate ∼150–200 GB of data for PASIN-1 and up to 3 TB of data for PASIN-2. The systems systematically acquire a shallow-sounding 0.1 μs pulse (PASIN-1)/1 μs short-attenuated chirp (PASIN-2), and a deep-sounding 4 μs, 10 MHz (PASIN-1)/13 MHz (PASIN-2) linear chirp (Table 5.2). The shallow-sounding pulse/short-attenuated chirp product is best used to assess internal lay-

TABLE 5.2: Radar parameters for the three radar systems deployed by BAS between 1994 and the present day. Note that PASIN-1/2 have a number of programmable settings for flight-specific objectives (e.g. one to eight waveforms programmable for PASIN-2), and the numbers provided here are for the most commonly used settings. For PASIN-2, a standard set-up consists of five waveforms as follows: 4 μs H (0°S), 4 μs V (0°S), 4 μs H (90°S), 4 μs V (90°S) ,1 μs H (Table 5.3). Abbreviations in the table are as follows. ADC: analogue-to-digital converter; FPGA: field-programmable gate array; SF: sample frequency; SI: sample interval; PRF: pulse-repetition frequency; PRI: pulse-repetition interval. [b]BAS-built and PASIN-1 systems used RF combiners on the receiver to produce a single RF input-to-sample, with PASIN-1 splitting these into a high- and low-gain channel for standard mode (two ADC channels) and combining these for pairs of H and V in polarimetric mode (four ADC channels). [b]Radar Range Resolution is calculated using a radio-wave velocity in ice of 168 m μs^{-1} and does not include the effect of the processing on the vertical resolution of the system, which is expected to be ∼50% greater than the values provided in the table, thus these numbers should be interpreted as the theoretical system performance. Diagrams showing the configurations of the three radar systems are provided in Figs. 5.6-5.8.

Radar parameters	**BAS-built (1994-2004)**	**PASIN-1 (2004-15)**	**PASIN-2 (2015-present)**
Antennas configuration	8x folded dipole (4 Tx / 4 Rx)[a]	8x folded dipole (4 Tx / 4 Rx)[a]	8x folded dipole + 4x belly (8 Tx/Rx / 4 Rx only)
Centre frequency	150 MHz	150 MHz	150 MHz
Transmitted pulse width	0.25 μs (pulse) 4 μs linear (chirp)	0.1 μs (pulse) 4 μs linear (chirp)	1 μs (Tukey envelope chirp) 4 μs linear (Tukey envelope chirp)
Chirp bandwidth	4 MHz (pulse) 10 MHz (chirp)	10 MHz	13 MHz
Antenna gain	11 dBi	11 dBi	11 dBi
PRF/PRI	20,000 Hz (PRI: 50 μs)	15,635 Hz (PRI: 64 μs)	15,635 Hz (PRI: 64 μs)
Peak transmit power	300 W / antennas (1.2 kW total)	1 kW / antennas (4 kW total)	1 kW / antennas (8 kW total)
Receiver SF	25 MHz (scope max single shot)	88 MHz	120 MHz
Receiver FPGA decimation	-	4	-
Receiver effective SF	25 MHz (SI: 40.0 ns)	22 MHz (SI: 45.5 ns)	120 MHz (SI: 8.3 ns)
Receiver trace stacking	64	25 (standard) 50 (polarimetric)	25
Effective PRF (post-stacking)	312.5 Hz	312.5 Hz (standard 2 waveforms)	125.1 Hz (5 waveforms) 208.5 Hz (3 waveforms)
ADC resolution	12-bit	14-bit	16-bit
Equivalent sustained data rate per ADCs (FPGA)	100 MB/s	176 MB/s (standard) 352 MB/s (polarimetric)	960 MB/s (system: 2.88 GB/s)
Average data storage rate for full PRI	1 MB/s	11 MB/s (maximum)	173 MB/s (all arrays)
Radar range resolution[b]	21.0 m (pulse) 8.4 m (chirp)	8.4 m	6.5 m

ering in the upper ∼1.5-2 km of the ice sheet, whereas the deeper-sounding chirp is best suited to assess englacial layering and bed characteristics in deep-ice conditions (Fig. 5.9c-e). The radar is capable of sounding ice to depths of up to 5 km

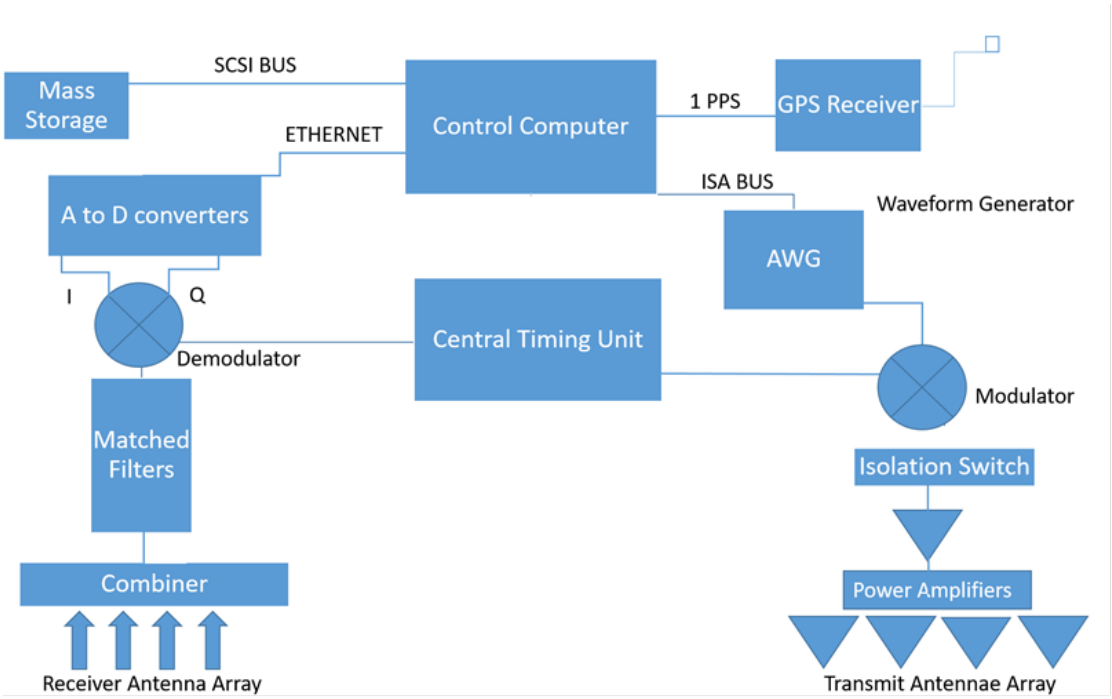

Figure 5.6: Digitised version of the diagram describing the set-up for the "BAS-built" radar system (Corr and Popple, 1994).

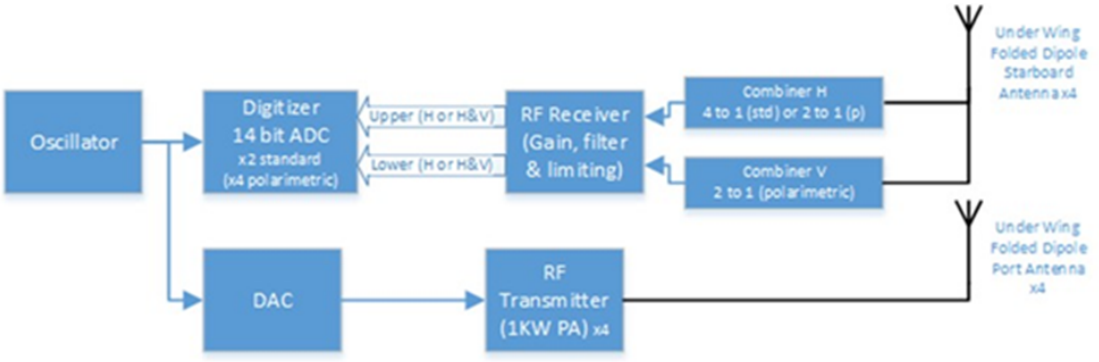

Figure 5.7: Diagram describing the set-up for the PASIN-1 radar system.

with a horizontal resolution of 10 cm (before processing) and a depth resolution in the vertical direction of 8.4 m (PASIN-1) and 6.5 m (PASIN-2).

The pulse repetition frequency of the PASIN (1/2) system is 15,635 Hz and hardware stacking is typically set to 25 in standard mode, which results in an effective pulse-coded waveform acquisition rate of 312.5 Hz for each transmit pulse (Table 5.2). Following stacking, the final sampling frequency of PASIN-1 is 22

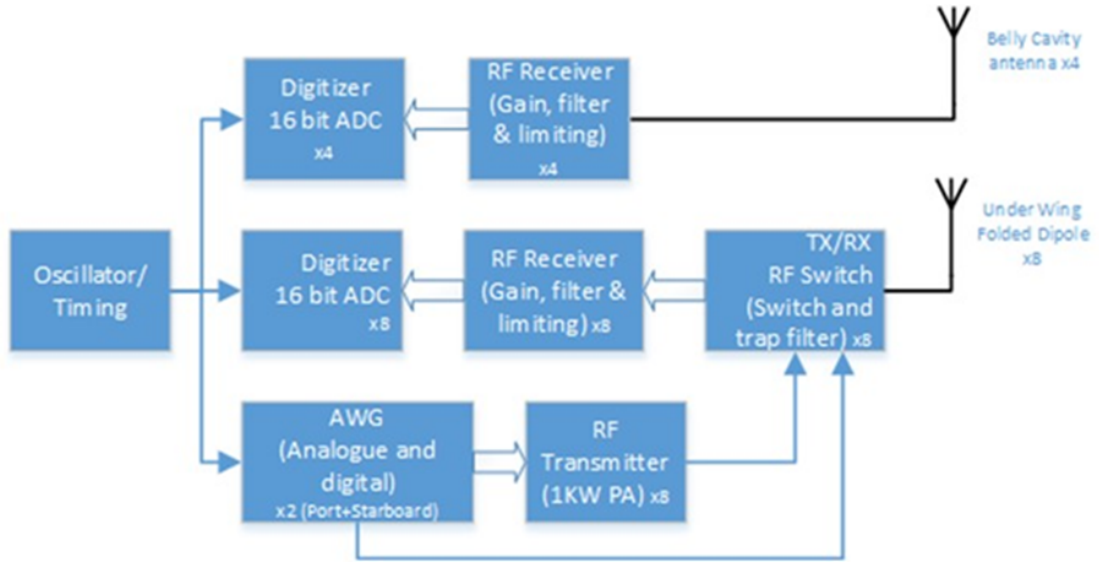

Figure 5.8: Diagram describing the set-up for the PASIN-2 radar system.

MHz and PASIN-2 is 120 MHz (Table 5.2).

TABLE 5.3: PASIN-2 Radar Transmit (Tx) and Receive (Rx) Description. *indicates Tukey-weighted.

Waveform type (frame uS*)	Port	Starboard
1. 0 to 64 uS	Tx 4 uS chirp*, Rx for remaining frame	Rx full frame
2. 64 to 128 uS	Rx full frame	Tx 4 uS chirp*, Rx for remaining frame
3. 128 to 192 uS	Tx 4 uS chirp* 180° out of phase with waveform 1, Rx for remaining frame	Rx full frame
4. 192 to 256 uS	Rx full frame	Tx 4 uS chirp* 180° out of phase with waveform 2, Rx for remaining frame
5. 256 to 320 uS	Tx 1 uS chirp* (15dB down), Rx for remaining frame	Rx full frame

5.4.1.4 GPS and lidar

Since 1978, navigation has transitioned from basic aircraft data, imagery, and dead reckoning to more modern means, including the use of the carrier-phase Global Positioning Systems (GPS).

Between 1994 and 2004, the BAS Twin Otter aircraft was equipped with a Trimble GPS system (1994–1995 surveys: Trimble 4000SSE; 1996–2003 surveys: Trimble 4000SSI). Since 2004, the aircraft is equipped with two, 10 Hz GPS receivers (Leica 500 and ASHTEC Z12 for 2004–2018 surveys; Javad Delta and Nova-

tel Span for post-2018 surveys) installed on board the aircraft. On the ground, two Leica 500 GPS base stations (replaced by Javad TRIUMPH-2 for post-2018 surveys) are positioned and equipped with choke-ring antennas, set up specifically to obtain an unobstructed view of the sky above. Aircraft turns are typically limited to 10 banking angles in order to avoid losing lock with GNSS (Global navigation satellite system) satellites orbiting close to the horizon. The estimated accuracy of the absolute position of the aircraft is 10 cm or less, with the relative accuracy approximately 1 order of magnitude better. Since 2010, the aircraft altitude and inertial information has been provided by an iMAR FSAS Inertial Measurement Unit (IMU), with the data logged on a Novatel Span receiver. Additional altitude information from the strap-down gravity system is also available for post processing of other datasets.

For all modern surveys (2002 onwards), the aircraft was also equipped with a Riegl Q240i-80 laser altimeter system (or lidar) in the floor camera hatch to accurately detect the ice surface. The lidar data used for correction of the radar data are typically extracted from the nadir point value with no correction for aircraft altitude. The system has a repetition frequency up to 2 kHz which results in an along-track measurement every 3 cm with an accuracy of up to 5 cm. The lidar is used up to altitudes of 700 m and is constrained by cloud-/fog-free conditions. From 2010 onwards, the lidar onboard the Twin Otter was capable of obtaining swath lidar data, although only the single-point data along the centre line were provided as part of this data release.

5.4.2 Data processing

5.4.2.1 Gravity

The raw aerogravity data are processed to obtain levelled free-air gravity anomalies. Although additional survey-specific processing might have been applied to the data, general processing steps for the LaCoste and Romberg system include the calculation of the observed gravity and a range of corrections and filtering functions as described in Jordan et al. (2007, 2010) and Valliant (1992). In particular, corrections for vertical acceleration, Eotvos horizontal motion (Harlan, 1968), latitude (Moritz, 1980), and free air (Hackney and Featherstone, 2003) were applied to obtain the final free-air anomalies before subsequent 9–12 km low-pass filtering. As the free-air values refer to the WGS84 ellipsoid, they are defined in geodesy as gravity disturbance (Hackney and Featherstone, 2003).

The strap-down gravity method adopted from 2015 onwards directly combined observations of acceleration in all three axes, with orientation and GPS observa-

tions combined in a Kalman filter to simultaneously solve for aircraft position and variations in the Earth's gravitational field (Becker et al., 2015). For subsequent strap-down-acquisition surveys, some amount of thermal drift levelling/correction is required. Spectral analysis suggests that the strap-down system can resolve wavelengths on the order of ∼5 km (Jordan et al., 2020). Error estimates for the gravity data can be found in the respective survey metadata (see Table 5.4), or in specific studies utilising the BAS aerogravity data (e.g. Ferraccioli et al., 2006; Forsberg et al., 2018; Jordan and Becker, 2018).

Additional processing may include the use of masks to remove aircraft turns, start and end of lines, and other regions of noisy data, or producing an upward continued free-air anomaly by the upward continuation of each line segment from the collected flight altitude to the highest altitude in the survey. The first level of free-air anomaly for all published BAS data is shown in Figure 5.2a, although it is worth noting that no correction such as downward continuation has been applied to compile the data shown in Figure 5.2a. It is considered that at the scale of the map, the vertical gradient of residual gravity anomalies at flight altitude is inferior to 2 mGal. Additionally, as the gravity surveys are acquired over the ice sheet, the distance to the bedrock is not only dependent on the flight altitude but also on the ice thickness.

5.4.2.2 Magnetics

The raw aeromagnetic data have been processed using the SCAR ADMAP2 data-release protocols (Golynsky et al., 2018). Data were collected at 10 Hz, allowing for modelling and removal of aircraft dynamic movements using a so-called compensation correction (Ferraccioli et al., 2007). This correction typically requires a dedicated calibration flight in the direction of the survey lines and tie-lines to have been flown. For some surveys with radial design, or where magnetic-data acquisition was opportunistic, logistical constraints meant no calibration flight could be conducted. In these cases, the generally large depth-to-source estimates due to the thick ice allowed for a 10–15 s filter to be applied to minimise noise generated by aircraft motion without compromising the geological signal. Given the redundancy of collecting 10 Hz (∼6 m spaced) observations over thick ice, most surveys were downsampled to 1 Hz (∼60 m) prior to further processing.

After magnetic compensation, the magnetic data were corrected for the International Geomagnetic Reference Field (IGRF), which is a standard mathematical description of the Earth's main magnetic field. Data impacted by operation of aircraft systems such as pumps and heaters were manually determined. Typically, such data were discarded, but survey design and lack of alternative data sources

mean that sometimes important geophysical signatures may be present. In some cases, the contaminated data were therefore corrected using an offset correction, accepting that the data segment may be more noisy.

Magnetic data were then corrected for diurnal variations in the magnetic field using observations at a fixed base station, typically filtered with a 30 min filter to remove short-wavelength noise potentially not seen on the aircraft. Further statistical levelling of the data based on internal intersections and crossovers with previous surveys was carried out at times to remove systematic errors associated with flight direction (i.e. heading corrections) and additional long-wavelength errors associated with incomplete removal of diurnal variations. In some cases, continuation to a fixed altitude above the ice-sheet bed and a final grid-based micro-levelling procedure were applied (Ferraccioli et al., 1998). The magnetic anomaly map shown in Figure 5.2b shows the spatial coverage and magnitude of magnetic data available. Errors in the data are typically presented as the standard deviation of the crossover errors and can be found in the respective survey metadata (see Table 5.4).

5.4.2.3 Radar

All data acquired with the earlier "BAS-built" radar system (1994–2004) were read using C code software to convert the LeCroy data to formats readable by Halliburton Landmark's seismic-processing software, SeisSpace ProMAX (hereafter referred to as ProMAX). Basic processing was applied to the data in the hardware analogue domain and later using ProMAX, including power normalisation and final SEG-Y export. Following the transition from the LeCroy oscilloscope to ADC cards on the "BAS-built" system (see Section 5.4.1.3), MATLAB replaced the IDL language for data processing.

As opposed to the "BAS-built" system which, by design, had some level of processing done on the raw data internally, the PASIN system was designed to retain much of the sampled data in the rawest form possible to allow for evolving processing techniques to be applied to the data in the future. For all PASIN data (2004 onwards), the first high-level step was to extract the raw data from the tape drives, convert the 3-byte values to conventional 4-byte integers, combine the waveforms associated with each pulse transmit type, and then export the data into MATLAB-formatted binary files. The second high-level step was to minimise side-lobe levels by applying a chirp-decompression technique using a Blackman window from a custom-built MATLAB toolbox, resulting in a processing gain of $\sim$10 decibels (dB).

The next step was to apply processing techniques both to enhance along-track resolution and improve the signal-to-noise ratio. For the 2004–2005 BBAS survey, incoherent stacking of 10 consecutive traces was applied and a moving-average window filter used; however, no SAR techniques were initially applied to these data. First tested on previously acquired PASIN radar data (see Hélière et al., 2007), 2-D SAR processing based on the Omega-K algorithm and subsequently improved versions using Doppler-beam sharpening were applied systematically to all the deep-sounding chirp data from 2005–2006 onwards to increase spatial resolution and remove backscattering hyperbolae in the along-track direction (Corr et al., 2007; Jeofry et al., 2018). The benefit of using along-track SAR processing is that it resolves the bed in much finer detail compared with non-SAR processed data (see Figure 5.9d-e). However, SAR-processing can also lead to distortions of the amplitude of the ice structure and bed reflection in inhomogeneous areas of the ice sheet (e.g. near the grounding line; see Hélière et al., 2007) and thus might not always be appropriate for assessing internal layering or absolute amplitudes such as required for bed-reflectivity analysis (e.g. Peters et al., 2007; Castelletti et al., 2019). Additional moving-average filters of varying lengths have also been applied to enhance englacial reflections and improve visualisation of the radar data.

Figure 5.9 shows the three processed radar products provided for the 2010–2011 IMAFI survey over West Antarctica. Figure 5.9c shows the shallow-sounding pulse and Figure 5.9d-e the deep-sounding chirp radar data using the focused SAR-processing technique from Hélière et al. (2007) (Fig. 5.9d) and a version of the chirp product processed with coherent summations using doppler processing (also known as unfocused SAR) (Fig. 5.9e). Internal layering is more clearly visible in the upper part of the ice column on the pulse data compared with the chirp data (see black-bordered insets in Fig. 5.9c and e). In contrast, deeper internal layering is much more visible on the focused SAR-chirp than on the unfocused SAR-chirp (Fig. 5.9d-e). Additionally, the peak amplitude of the bed is better resolved in the focused SAR-processed chirp than in the unfocused SAR-processed chirp (see white-bordered inset in Fig. 5.9d-e).

Further processing of the PASIN data has also been applied by others using simple image-processing techniques such as moving-average filters to enhance the internal layering of the ice and reduce incoherent noise (Ashmore et al., 2020a; Bodart et al., 2021a) or by applying more complex SAR-processing techniques over previously incoherently processed radar data (Castelletti et al., 2019; Chu et al., 2021). Additional techniques have also been employed in areas where side echoes from steep valley walls lead to ambiguous bed reflections, as previously employed over Flask Glacier (Antarctic Peninsula) using PASIN SAR-processed data and

a combination of velocity and digital elevation models to obtain more accurate ice-thickness estimates (Farinotti et al., 2013).

Following radar data processing, bed and ice-surface reflections were determined by picking the onset of the basal echo (i.e. where the echo amplitude is greater than the noise floor). We note that this is not a universal method applied by all radar data providers, who may pick the half-amplitude delay or the peak value, leading in turn to measurement biases across data providers and products (e.g. Peters et al., 2005; Chu et al., 2021).

The BAS approach to picking the bed was to use a semi-automatic first-break pick algorithm on the chirp data below a top-mute window in ProMAX (generally ∼100 samples above the approximate bed reflection) to locate the precise bed return, followed by manual checks and re-picking to exclude any unrealistic spikes. In areas where multiple closely spaced reflections were sounded at the bed, the shallowest reflection was assumed to be the bed as off-axis reflections would likely appear lower down in this section. However, in some cases, deeper reflections were chosen, with shallower weak reflections assumed to reflect entrained debris, accreted ice, or uncompensated refraction hyperbolae close to the bed. We note, however, that this method has evolved over the years, and that its success is inherently reliant on the radio-glaciological experience of the human picker to quality-check the results from the semi-automatic picker and manually re-pick the data if necessary. The uncertainty associated with the picking procedure can be partially approximated by calculating the root mean square error (RMSE) of the bed elevations at crossover points across the survey area. Although these errors are site-specific and can depend on factors such as varying bed topography and roughness, larger errors may reflect uncertainties in data processing or analysis (i.e. picking in this case). Areas of more extreme topography typically show the highest crossover errors, likely associated with off-axis reflections and entrained debris close to subglacial cliffs, which make deciding on the correct bed pick challenging. In isolated cases, such errors can exceed several hundred metres. In contrast, regions dominated by smooth and flat beds typically show lower crossover errors, on the order of several metres only. Survey-wide RMSEs are typically reported in each survey's metadata (see Table 5.4) and average ∼9–22 m depending on the survey (see Rippin et al., 2003a; Vaughan et al., 2006; Ross et al., 2012; Jeofry et al., 2018).

To estimate ice thickness and hence obtain the bed elevation, the location of the surface reflection in the radar data must be known accurately. However, since the PASIN system does not resolve the ice surface well due to errors in the phase

centre of the pulse through the firn layer, the surface reflection in the radargram was only rarely used on its own to calculate the ice surface. Usually, range-to-surface from coincident on board-acquired lidar, or alternatively, if lidar was not available (i.e. due to clouds or ground clearance higher than 750 m), using the aircraft's radar altimeter or surface elevation from an accurate Digital Elevation Model (DEM) (i.e. REMA 8 m DEM for latest surveys; Howat et al., 2019), was used to calculate a "theoretical" surface pick, as follows:

Firstly, the same semi-automatic picker used for picking the bed was used on a subset of the shallow-sounding pulse radargrams with a bottom-mute window set at ∼100 samples below the surface reflection. Secondly, once aircraft-to-surface range was obtained from lidar, a linear trend between the surface pick from the radargram and the surface range from the lidar was calculated, and a resulting slope and offset was used to calculate the theoretical location of the surface. Where possible, the range-to-ground value was derived from the lidar data or interpolated from the mean lidar elevation within ∼700 m. In those rare cases where the surface reflection was picked directly from the radargram, a regression, local to the data gap, was used to fit the radar range-to-terrain clearance. If lidar was not available to calculate range-to-ground, the height of the aircraft above the surface was obtained by the aircraft's radar altimeter which was then converted into a radar delay time. This conversion was done after a two-stage calibration process which involved recording the terrain clearance over a sea surface with the two instruments, and then correction for the penetration depth of the radar altimeter was obtained from the difference in the height above ellipsoid for a surveyed "flat" snow surface and the aircraft. Where possible, the reference surface was chosen to be in the centre of the targeted area.

Once bed and surface were calculated, ice thickness was obtained by calculating the difference between the bed and surface pick in range samples (relative to the BAS system). The picked travel time was then converted to depth in metres using a radar wave speed of 168 m μs^{-1} and a constant firn correction of 10 m. Bed and surface elevations were then integrated with a high-precision kinematic dual-frequency GPS position solution to provide the final point dataset of elevations relative to the WGS84 ellipsoid. To ensure the best accuracy of satellite-orbit definitions and atmospheric corrections, the interpolated survey locations and aircraft elevations were processed from 10 Hz coupled Precise Point Positioning (PPP) GNSS/INS solutions 1 month after data acquisition.

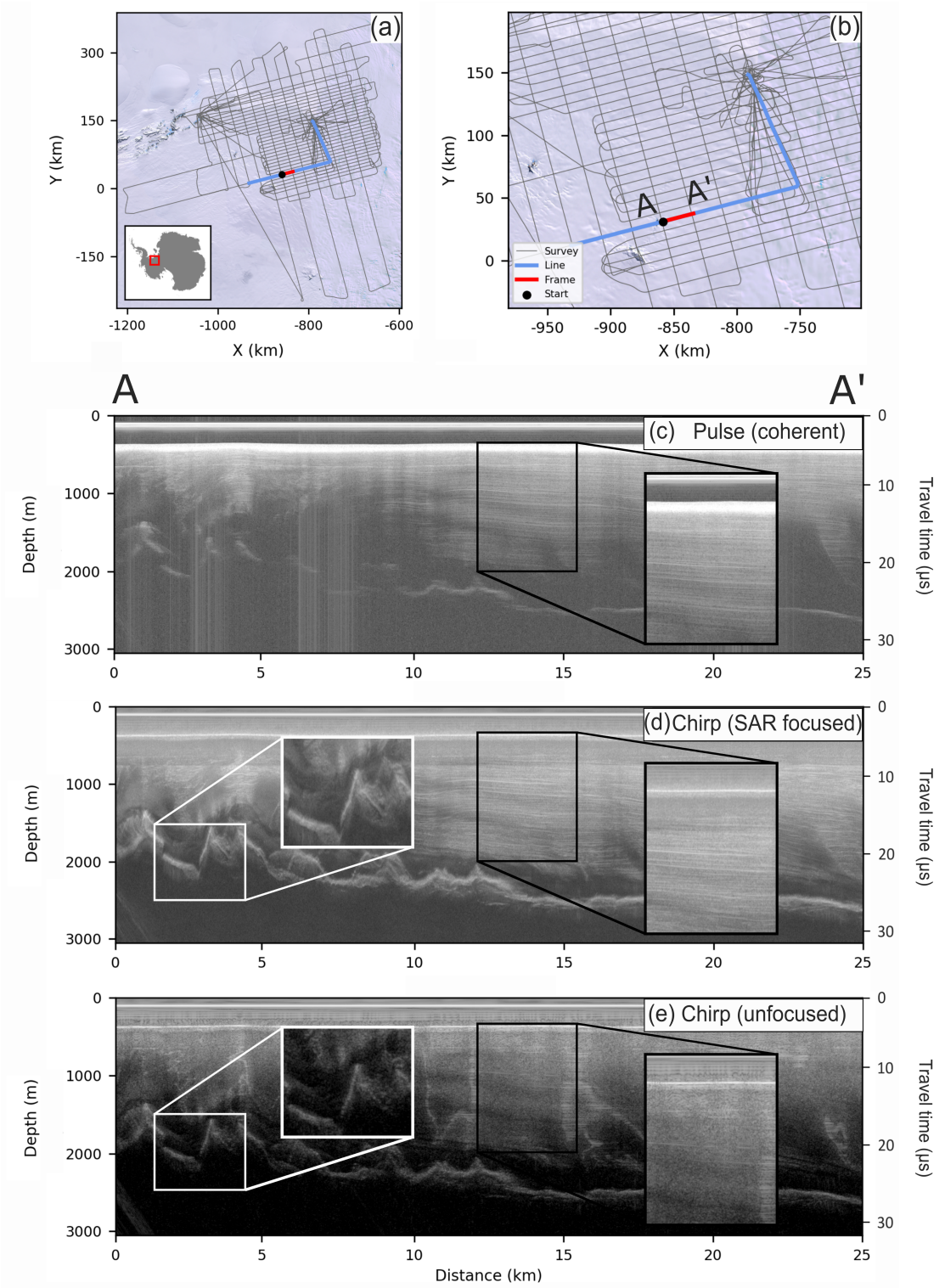

Figure 5.9: A 25 km segment of flight line 15d of the 2010–2011 IMAFI survey, showing the three radar products and processing attributes. (a) shows an overview map of the entire survey with an inset over Antarctica, and (b) shows a zoomed-in map over the specific flight line with the 25 km radar segment (defined as A–A) shown in red. The background satellite image in (a)–(b) is from the Landsat Image Mosaic of Antarctica (LIMA) dataset (Bindschadler et al., 2008). Images (c)–(e) show a 25 km segment of the data for the three products provided for the 2010–2011 IMAFI survey as follows: (c) the coherently processed, shallow-sounding pulse, (d) the focused 2-D SAR-processed, deep-sounding chirp, and (e) the coherently processed, deep-sounding chirp processed with doppler filtering. The black-bordered insets zoom to the internal layering in the upper portion of the ice column for (c)–(e) and the white-bordered insets show the difference in bed characteristics between (d) and (e).

5.5 FAIR data publishing

In total, we have published 64 datasets from 24 surveys as part of this data release, representing ∼566 GB of data and ∼1,800 files. This amounts to a total of 3.62 million gravity and 7.41 million magnetic data points, as well as 14.5 million ice-thickness and bed-elevation measurements. The complete list of published datasets is provided in Table 5.4, including the short digital object identifiers (DOIs), which redirect to the metadata sheets and download folders for each respective dataset archived on the PDC Discovery Metadata System (DMS) data catalogue (https://data.bas.ac.uk, last access: 05 April 2023).

We note that individual profiles acquired opportunistically following larger aerogeophysical surveys (i.e. flight lines over Flask Glacier; Farinotti et al., 2013) are not included in this data release unless specifically mentioned in the metadata for each survey (see Table 5.4). Such small-scale datasets will be added to the data portal in future releases (see Section 5.6.3).

Below, we discuss the release of the datasets centred around the four FAIR data principles (i.e. findable, accessible, interoperable and re-usable; Wilkinson et al., 2016), starting with the formats and attributes used to store and describe the data (Interoperability; Sect. 5.5.1), the metadata and Digital Object Identifiers assigned to each dataset (Findability; Sect. 5.5.2), the data-portal interface and functionalities (Accessibility; Sect. 5.5.3), and finally the creation of a user guide and open-access tutorials written in Python and MATLAB for reading the data programmatically (Re-usability; Sect. 5.5.4).

5.5.1 Interoperability: data formats and attributes

In order to make our data as interoperable as possible, the choice of an open format for all our datasets was a priority. We followed the best practices of the geophysics community and used common data formats and naming conventions to describe the variable names. These are detailed further here.

The gravity, magnetic, and bed-pick data are stored in open ASCII data formats, namely XYZ and CSV files, to ensure long-term access and unrestricted use of the data in the future (Fig. 5.4). Additionally, we followed the SCAR ADMAP2 data-release protocols (Golynsky et al., 2018) for the naming convention of the channels for the magnetic data. For the radar data, we chose to release the bed-pick data separately from the full radar data (see Figure 5.4), although the full radar product contains most of the information stored in the ASCII bed-pick

TABLE 5.4: Short digital object identifiers (DOIs) for the gravity, magnetic, bed-pick, and 2-D radar datasets of each survey flown by BAS and included in this data release. Abbreviations used are the same as in Table 5.1. The links in this table can also be accessed by adding the short DOI preceded by "https://doi.org/". For the AGAP radar data, the US-led survey lines can be found at https://doi.org/10.1594/IEDA/313685 (Bell, 2011). 2 For the PolarGAP survey, data can be downloaded from both the ESA and BAS data catalogues, but the DOI for the gravity and magnetic data (https://doi.org/10.5270/esa-8ffoo3e, Forsberg et al., 2017) belongs to ESA. If using the PDC data catalogue, the PolarGAP gravity and magnetic data can be downloaded from https://data.bas.ac.uk/full-record.php?id=GB/NERC/BAS/PDC/01583 (last access: 05 April 2023) and https://data.bas.ac.uk/full-record.php?id=GB/NERC/BAS/PDC/01584 (last access: 05 April 2023), respectively. "*" indicates that the data are not held at BAS, but instead are available on the CReSIS data portal (https://data.cresis.ku.edu/, last access: 05 April 2023).

Survey	Year	Region	Gravity	Magnetic	Bed-pick	Radar
EVANS	1994-95	WAIS	10/d549	-	10/d548	-
Black Coast	1996-97	APIS	-	10/d54x	-	-
CHARCOT	1996-97	APIS	-	10/d54z	-	-
JRI	1997-98	APIS	10/d55g	10/d55f	-	-
LARSEN	1997-98	APIS	-	10/d55k	-	-
DUFEK	1998-99	WAIS	10/d546	10/d544	10/d542	-
AFI Coats Land	2001-02	EAIS	-	10/dpnw	10/dpnx	-
MAMOG	2001-02	EAIS	10/dpqg	10/dpqh	10/dpqd	-
TORUS	2001-02	WAIS	10/dpqm	10/dpqj	10/dpqf	-
SPARC	2002-03	APIS	10/d552	10/d55x	-	-
BBAS	2004-05	WAIS	10/dpn6	10/dpn3	10/dpnz	10/gzqs
WISE-ISODYN	2005-06	EAIS	10/d554	10/d553	10/cncc	10/gzqq
GRADES-IMAGE	2006-07	WAIS	-	10/d55d	10/d55c	10/gzqj
AGAP	2007-09	EAIS	10/dpnf	10/dpnn	10/dpnr	10/gzqw[1]
ANDRILL HRAM	2008-09	WAIS	-	10/d54w	-	-
Adelaide Island	2010-11	APIS	-	10/dn8b	-	-
IMAFI	2010-11	WAIS	10/dn8g	10/dn8h	10/dn8f	10/gzqr
PIG Ice Shelf	2010-11	WAIS	-	10/d55m	10/d55n	-
ICEGRAV	2012-13	EAIS	10/dpqb	10/dpp9	10/cjzn	10/gzqt
FISS 2015	2015-16	WAIS	-	10/g36h	10/g35q	10/g35m
PolarGAP	2015-16	EAIS	10/g7kw[2]	10/g7kw[2]	10/g7qq	10/g7qp
FISS 2016	2016-17	WAIS	10/g36f	10/g36j	10/g35t	10/g35p
ITGC 2018	2018-19	WAIS	10/dn26	10/dn24	**	**
ITGC 2019	2019-20	WAIS	10/g68r	10/g68q	10/gp4z	10/g7qn

files. Publishing the bed-pick data separately from the radar data was a deliberate choice: it alleviates the need for users to download the full radar datasets to access light-weight tabular data, and improves the accessibility of the point data for large gridded products such as SCAR's Bedmap (Fretwell et al., 2013) and NASA's BedMachine (Morlighem et al., 2020) projects. The bed-pick data are

stored as ASCII-formatted files (namely XYZ and CSV), whereas the full radar data are stored as SEG-Y and NetCDF files, reasons for which are described below.

The SEG-Y format has been used extensively by radar scientists since the early 1980s to store radar data. This is primarily due to the lack of a radar-specific format, SEG-Y having been developed primarily to store seismic data. The advantage of using SEG-Y files is that data can be readily imported into seismic-interpretation software for data interpretation and analysis. The drawbacks of using SEG-Y, however, are numerous, making this option unsuitable for long-term data storage. These include: (1) limited space for metadata, (2) the choice of byte-information to store the radar data is subjective due to the nature of the SEG-Y format, (3) until recently, the byte stream structure which includes the geolocation of each radar trace (i.e. the X and Y positions) was restricted to integer format leading to large inaccuracies in the actual trace position, despite the use of high-resolution, sub-metre GPS data (see Section 5.4.1.4). Recognising, however, the geophysical community's need to view and analyse the radar data in conventional data formats, we have decided to continue producing SEG-Y files for each flight line and acquisition mode (e.g. pulse and chirp). The SEG-Y files were produced using the Revision 1.0 SEG-Y format and georeferenced using the navigational position of each trace from the GPS on board the aircraft in polar stereographic (EPSG: 3031) projection. Each SEG-Y file contains the following byte-information: trace number (byte: 1–4 and 5–8), PRI-Number (byte: 9–12), Cartesian X coordinate (byte: 73–76), Cartesian Y coordinate (byte: 77–80), number of samples for each SEG-Y trace (byte: 115–116), and the sampling interval (byte: 117–118).

As a result of the issues mentioned above, we also exported and published the radar data in NetCDF-formatted files. We chose the NetCDF format due to its portability and array-oriented structure, the ability to store large amounts of metadata and variables into one portable file, its machine-readable capability, and to harmonise our data products with other fields such as climate science (e.g. ECMWF ERA5 reanalysis products; NCAR climate data), glaciology (e.g. Le Brocq et al., 2010; Morlighem et al., 2017; Lei et al., 2022) and, increasingly, radar geophysics itself (e.g. Paden et al., 2014; Blankenship et al., 2017), which already all make use of this data format effectively. The NetCDF files we produced contain extensive metadata relating to the acquisition and processing of the radar data, as well as a set of Climate and Forecast (CF)-compliant variables that are tied to the radar data (https://cfconventions.org/, last access: 05 April 2023) (Table 5.5). As a minimum, each NetCDF file contains a radar data variable (one for the pulse and/or one for the chirp, if both exist) in 2-D format, and a set of

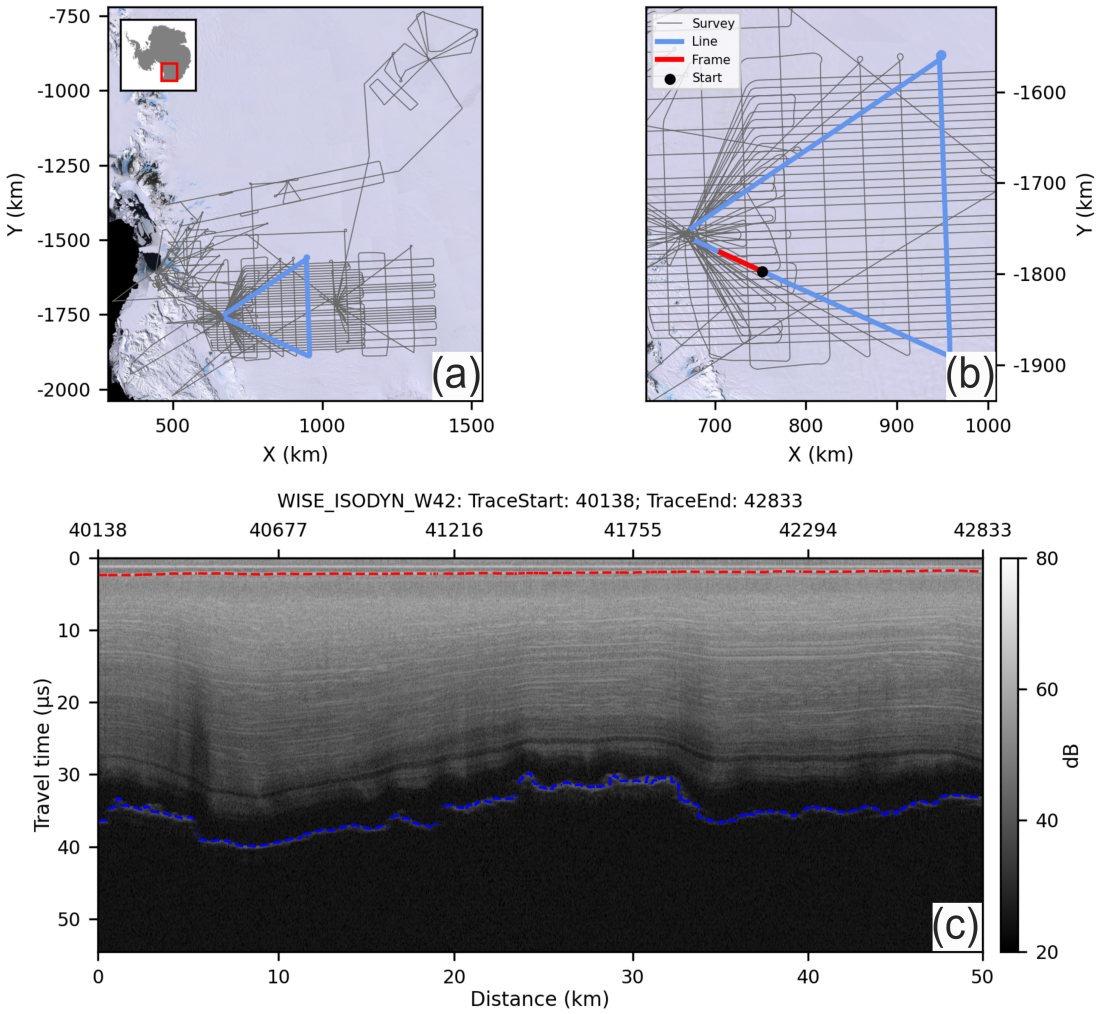

Figure 5.10: Example of a segmented quick-look image from the 2005–2006 WISE-ISODYN survey. (a) Overview map of the survey flight lines (grey lines) with an inset over Antarctica and the specific flight line highlighted in blue. (b) Zoomed in version of (a) showing the specific flight line with the footprint of the 50 km segment (red line) and start point for the radargram (black dot) shown in (c). The background satellite image in (a)–(b) is from the LIMA dataset (Bindschadler et al., 2008). (c) 50 km segmented radar image of the chirp data with distance in kilometres shown in the bottom x axis and the trace number shown in the top x axis. The y axis shows the travel time in microseconds. The format of the title in (c) is as follows: survey name and flight ID, first trace of segment, last trace of segment. The dashed red and blue lines on the radargram in (c) show the surface and bed pick, respectively.

1-D variables relating directly to the radar data, such as the trace number, PRI number, fast time, and the X and Y coordinates (Table 5.5). We also provided

additional radar-related variables which were extracted from the radar data following processing, such as the surface and bed picks, the surface and bed elevation, the ice thickness, longitude and latitude, time of the trace, and the elevation of the aircraft (Table 5.5). Additional 1-D variables include the source of the surface pick (from lidar or radar) if this exists, the range between the aircraft and the ice surface, and in case the pulse- and chirp-radar variables do not have the same length, we provide two sets of variables for the trace number and PRI number.

Lastly, to aid visualisation and improve efficiency in navigating the datasets, we created lightweight quick-look PDF files of the radar data for each flight line of each survey (see example for the WISE-ISODYN survey in Figure 5.10). The choice of ∼25 or ∼50 km length for the 2-D radargram was chosen based on clarity of the image and varies from survey to survey. The quick-look PDF files are stored alongside the SEG-Y and NetCDF files and are accessible using the links provided in Table 5.4.

5.5.2 Findability: metadata and digital object identifiers

ISO 19115/19139 Geographic information metadata are provided for each data type of each survey and is archived alongside the datasets into the PDC DMS catalogue (https://data.bas.ac.uk, last access: 05 April 2023; see Table 5.4). Each metadata record provides detailed information about the dataset, including an abstract, list of personnel involved in the acquisition or analysis of the dataset, and detailed lineage information about the acquisition and processing steps used to produce the dataset, amongst others. All our data are covered under the UK Open Government License (https://www.nationalarchives.gov.uk/doc/open-government-licence/, last access: 05 April 2023), enabling the re-use of the data freely and with flexibility, whilst at the same time ensuring acknowledgement of those involved in the collection and processing of the data. In addition, we use earth science-specific keywords and vocabularies from the Global Change Master Directory (GCMD, 2021) to describe our data in a consistent and comprehensive manner in accordance with ISO 19115 standards. Lastly, a DOI is minted for each dataset so that it can be discoverable and adequately cited. The end goal is to provide all the information necessary for effective, long-term data re-use.

TABLE 5.5: Attributes for each variable stored in the NetCDF files. For each attribute name, we provide the long name, the dimension (1- or 2-D, x or y axis), the short or CF-compliant standard name, and the unit of the measurement. The standard name is only provided if it exists as part of the CF convention (https://cfconventions.org/, last access: 05 April 2023), otherwise a short name is provided. The abbreviation "dBm" stands for decibel-milliwatts and "a.s.l." stands for above sea level. Note that the surface and bed-pick data are referenced to the sampling time of the BAS radar systems across the 64 μs pulse repetition interval window, and digitised according to the receiver sampling frequency (see Table 5.2).

NetCDF Attributes	Long Name	Dimension	Short / Standard Name	Unit
traces	Trace number for the radar data	1-D (x-axis)	traceNum	integer count (unitless)
fast_time	Two-way travel time	1-D (y-axis)	time	microseconds
x_coordinates	Cartesian x-coordinates for the radar data	1-D (x-axis)	projection_x_coordinate	metres (WGS84 EPSG: 3031)
y_coordinates	Cartesian y-coordinates for the radar data	1-D (x-axis)	projection_y_coordinate	metres (WGS84 EPSG: 3031)
chirp_data	Radar data for the processed chirp	2-D (x- and y-axis)	-	power (dBm)
pulse_data	Radar data for the processed pulse	2-D (x- and y-axis)	-	power (dBm)
longitude_layerData	Longitudinal position of the trace number	1-D (x-axis)	longitude	degree_east (WGS84 EPSG: 4326)
latitude_layerData	Latitudinal position of the trace number	1-D (x-axis)	latitude	degree_north (WGS84 EPSG: 4326)
UTC_time_layerData	Coordinated Universal Time (UTC) of trace number	1-D (x-axis)	resTime	seconds of the day
PriNumber_layerData	Incremental integer reference number related to initialisation of the radar system	1-D (x-axis)	PriNum	integer count (unitless)
terrainClearance_layerData	Terrain clearance distance from platform to air interface with ice, sea or ground	1-D (x-axis)	resHt	metres
aircraft_altitude_layerData	Aircraft altitude	1-D (x-axis)	Eht	metres a.s.l. (WGS84 ellipsoid)
surface_altitude_layerData	Ice surface elevation for the trace number	1-D (x-axis)	surface_altitude	metres a.s.l. (WGS84 ellipsoid)
surface_pick_layerData	Location down trace of surface pick (BAS system)	1-D (x-axis)	surfPickLoc	time sample (microseconds)
bed_altitude_layerData	Bedrock elevation for the trace number	1-D (x-axis)	bed_altitude	metres a.s.l. (WGS84 ellipsoid)
bed_pick_layerData	Location down trace of bed pick (BAS system)	1-D (x-axis)	bedPickLoc	time sample (microseconds)
land_ice_thickness_layerData	Ice thickness for the trace number	1-D (x-axis)	land_ice_thickness	metres

The data are shared via the web-based Repository for Archiving and MAnaging Diverse DAta (RAMADDA; https://geodesystems.com/, last access: 05 April 2023) which is an open-source content and data management platform. The download of the data is done through a standard HTTP-protocol where no login account is required. In the back-end, the data are stored following a simple folder structure on the PDC server that is mirrored onto RAMADDA. This simple structure allows us to maintain a balance between the services we can provide and our ability to move away from specific tools – RAMADDA in this case – and potentially adopt more performant systems in the future. The goal is to stay as independent of the platform we use as possible while providing the most effective service possible.

5.5.3 Accessibility: Polar Airborne Geophysics Data Portal

To increase the accessibility and discoverability of our data, we developed a new data portal, the Polar Airborne Geophysics Data Portal (accessible from (https://www.bas.ac.uk/project/nagdp/, last access: 05 April 2023). The portal interactively showcases the wide coverage of aerogeophysical datasets collected by BAS and enables users to easily discover and download the published datasets via a series of widgets and functionalities aimed at enhancing the user experience.

The portal is divided into five layer menus: "Aerogravity", "Aeromagnetics", "AeroRadar", "Boundaries Features", and "Basemaps". The first three menus contain shapefile layers for the gravity, magnetic, and radar datasets, respectively. The "Boundaries Features" menu contains a set of specific boundary layers, such as the Antarctic Coastline and Ice Drainage boundaries, amongst others, and the "Basemaps" menu contains background gridded maps of ice thickness, surface and bed elevations, magnetic anomaly, and geothermal heat flow, amongst others.

The track lines for each dataset correspond to individual polyline shapefiles (either segmented in 25 or 50 km, or by flight line) which contain key statistics such as the minimum, maximum, and median gravity and magnetic anomalies, and minimum, maximum, and median ice surface, bed elevation, and ice thickness. The shapefiles also contain direct links to the survey's metadata and to direct links to download the data via the RAMADDA interface.

A powerful functionality of the portal is the ability to view the aerogeophysical data rapidly via the creation of quick-look gravity, magnetic, and radar plots for each flight line (see Section 5.6.2; Figure 5.10c). For the magnetic and gravity

data, graphs showing the magnetic or free-air anomaly along straight lines were created in the westernmost–easternmost direction if the profile is mainly in the direction of the longitude, or northernmost–southernmost if the profile is predominantly in the direction of the latitude. For the radar data, the segmented images were produced in a similar format to Figure 5.10c and split into ∼25 and∼50 km segments depending on the survey.

5.5.4 Re-Usability: user guide and tutorials

To further increase the re-usability of our data, we provided a user guide for the data portal as well as interactive, open-source Jupyter Notebook tutorials written in Python and MATLAB for reading the gravity, magnetic, and radar datasets and conducting first-order analyses of the data. These are archived on the BAS GitHub repository and provided via an interactive web interface using Jupyter Book (https://antarctica.github.io/PDC_GeophysicsBook, last access: 05 April 2023). We believe these to be particularly beneficial for ensuring accessibility and re-usability of our data to the widest range of users possible, primarily as a result of the complexity around reading in aerogeophysical data formats.

5.6 Discussion

This final section exemplifies the potential re-usability of the newly released aerogeophysical data via the interrogation of the englacial architecture of the ice as sounded by the BAS Radio-Echo Sounding (RES) systems. We also explore the future use of the new data portal and discuss opportunities in terms of data release and further potential re-use of the BAS aerogeophysical data.

5.6.1 Internal Layering Continuity Index

Internal Reflecting Horizons (IRHs), as imaged by RES, is a powerful means of extracting information on past ice-dynamical processes (Rippin et al., 2003b; Siegert et al., 2003; Bingham et al., 2015). For example, the presence of well-preserved and continuous englacial layering may reflect stable ice conditions and suggest limited changes in past ice-flow conditions, ice-divide migration, or melting within or at the base of an ice sheet (Karlsson et al., 2012). In contrast, poor continuity in englacial layering, primarily characterised by buckled or absent layering, may be indicative of past ice-flow switching or increased englacial stress gradients (Siegert et al., 2003; Bingham et al., 2015). Thus, quantifying the continuity of englacial layering is essential in our understanding of past and current ice dynamical conditions, as well as in other application such as selecting ice-core drilling

sites (Karlsson et al., 2018; Beem et al., 2021; Fudge et al., 2022).

Several methods have been developed for mapping the continuity of englacial layering from RES data (e.g. Karlsson et al., 2012; Sime et al., 2014; Delf et al., 2020). One such technique, the Internal Layer Continuity Index (or ILCI; Karlsson et al., 2012) is the first to provide an automated tool for quantitatively assessing the continuity of englacial layering based on A-scope radar profiles. This method has the advantage of being much less laborious than manual methods (e.g. Rippin et al., 2003a; Siegert et al., 2003; Bingham et al. 2007) and removes the potential subjectivity in assessing layer continuity. Additionally, the large amount of radar data now available precludes the ability to identify layer continuity manually, making the ILCI a powerful tool in our ability to extract this valuable metric. First tested over selected 2004-2005 BBAS flightlines covering the Pine Island Glacier (Karlsson et al., 2012), the ILCI was subsequently employed over Institute and Möller Ice Streams (Bingham et al., 2015; Winter et al., 2015) and selected sectors of East Antarctica (Karlsson et al., 2018; Luo et al., 2020). Using the ILCI previously calculated for the 2010-11 IMAFI radar data, Ashmore et al. (2020a) further demonstrated that the ILCI was statistically higher where manually picked IRHs could be traced, thus showing for the first time that this method has the potential to be applied at a larger scale with reliable results. However, until now, this approach had not been tested at a regional scale over Antarctica and with the use of multiple radar datasets.

Here, our main objective is to provide a first-order assessment of the continuity of englacial layering across Antarctica in order to assess the feasibility of developing a pan-Antarctic age-depth model from existing radar data. Enabled by the comprehensive release of large swaths of fully standardised and open-access aerogeophysical data described in this chapter, we aim to demonstrate that much more information can be extracted from these data on a regional to continental-scale.

The ILCI represents the mean of the absolute value of the derivative for each radar trace (Karlsson et al., 2012), as follow:

$$\psi = \frac{1}{2\Delta r N} \sum_{i=n_1}^{n_N} \mid P_{i+1} - P_{i-1} \mid, \tag{5.1}$$

where n is the sample number of reflected relative power values within the selected section length, N, between the surface and the bed, P_i is the reflected relative power in decibels at point i, and Δr is the depth in metres. Although ψ is technically a product of the reflected relative power and depth, it is considered

dimensionless as the depth variable is considered a scaling factor that is set to 1 in Eq. 5.1. By design, the ILCI is sensitive to the number and strength of englacial layering situated between the surface and the bed, such that low values indicate discontinuity in, or absence of, englacial layering, and high values indicate clear englacial layering.

We have calculated the ILCI on the ten PASIN radar datasets that have been published as part of this data release (Figs. 5.11-5.12). This includes a total of ∼300,00 line-km of 2-D radar data from the BBAS-AGASEA (2004-2005), WISE-ISODYN (2005-2006), GRADES-IMAGE (2006-2007), AGAP (2007-2009), IMAFI (2010-2011), ICEGRAV (2012-2013), FISS (2015-2017), PolarGAP (2015-2016), and ITGC Thwaites (2019-2020) surveys (see Table 5.4). Since we were primarily interested in regional changes in layer continuity, the ILCI was smoothed using a horizontal window of 1,000 samples (representing ∼25-45 km distance depending on the dataset) to remove any small-scale anomalies in the data. Additionally, we only made use of the deep-sounding chirp PASIN product due to its capability of imaging deeper IRHs, particularly in areas with thick ice such as the South Pole plateau. The upper and lower 20% of the ice were also omitted in the processing due to the inability of the PASIN system to resolve continuous englacial layering in the upper portion of the ice column, and because englacial layering is typically absent near the ice-bed interface (Drews et al., 2009; Karlsson et al., 2012).

An important consideration in employing the ILCI over multiple datasets is that the results will vary based on data acquisition (i.e. radar frequency, system resolution) and processing applied (i.e. incoherent vs 2-D SAR), thus a pan-Antarctic comparison of internal layer continuity must be analysed in this context. This is especially the case here, where we have applied the ILCI to processed Z-scope radar data acquired over a period of >15 years with two different systems (PASIN-1 and PASIN-2) and using different processing regimes. Therefore, care must be taken when interpreting the results from different surveys together, as for example, a low level of layer continuity in the main trunk of Pine Island Glacier on the BBAS survey may not reflect the same level of discontinuity on the low-continuity areas of the PolarGAP survey. With this caution noted, the results presented here offer an opportunity to identify some regional patterns of potential value for future work, as we now discuss.

Figure 5.11 shows that there is a clear correspondence between discontinuous layering where ice flow is fast (>200 m a^{-1}) such as over Foundation Ice Stream (FISS) and the main trunk of Pine Island Glacier (BBAS) and Slessor Glacier (ICEGRAV) (Figs. 5.11 and 5.12a). Whilst layer discontinuity is mainly present

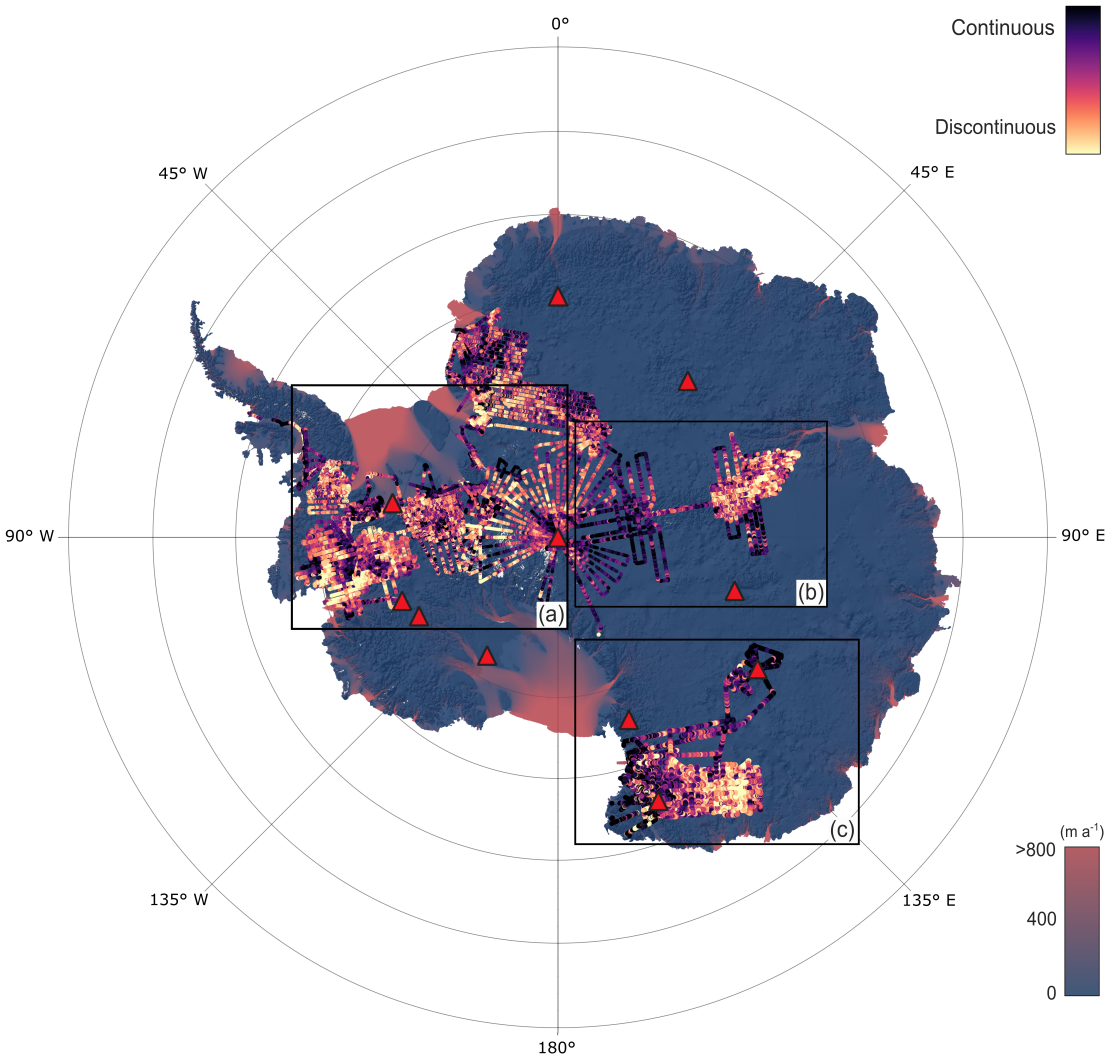

Figure 5.11: The ILCI for the ten PASIN datasets for which the fully processed 2-D radar data were released as part of this chapter (see Table 5.4). The background map shows ice-flow velocities from the In-SAR MEaSUREs dataset (Rignot et al., 2017) superimposed over a hill shade from the BedMachine bed-elevation v2 dataset (Morlighem, 2020). The red and blue colour bar shows ice-flow velocities in metres per annum, and the magma colour bar shows the continuity of englacial layering throughout the radar dataset (low continuity: yellow; high continuity: dark purple). The black-bordered rectangles (a–c) correspond to the close-up plots in Figure 5.12a-c. The red triangles correspond to existing deep ice cores located near the BAS radar surveys.

over the WAIS due to the high concentration of fast-flowing ice streams in this region, several sections covering the EAIS also show signs of layer discontinuity, particularly in the upstream portions of the fast-flowing Lambert Glacier (AGAP), as well as over David and Ninnis glaciers (WISE-ISODYN) (yellow arrows in Fig.

5.12b-c).

Unsurprisingly, areas of high continuity are mainly observed over the interior of the EAIS, particularly on flight lines extending deep into East Antarctica and South Pole (Figs. 5.11, 5.12a-b, and 5.13), as well as into the deeper parts of the Wilkes Subglacial Basin and Dome C (black arrow in Fig. 5.12c) where deep ice cores have been drilled (red triangles in Figures 5.11-5.12). Areas of high layer continuity over the WAIS include numerous ice rises (i.e. Bungenstock, Fletcher, Henry, and Korff) as imaged on the GRADES-IMAGE, IMAFI, and FISS surveys (black arrows in Fig. 5.12a), the deeper sections of the southern Pine Island Glacier basin on the BBAS data, as well as on PolarGAP survey lines upstream of the FISS grids covering Foundation Ice Stream and Recover and Slessor glaciers (Fig. 5.12a).

Also visible are the disruptive effects of local bed topography on the continuity of englacial layering, such as over the Ellsworth Subglacial Highlands (BBAS), the Transantarctic Mountains (IMAFI and PolarGAP), and the Gamburtsev Subglacial Mountains (AGAP) (see yellow arrows in Fig. 5.12a-b), with relatively flat bed topography in the deep interior of the EAIS allowing layering to remain relatively undisturbed (Fig. 5.11 and black arrows in Fig. 5.12b).

Altogether, the results presented in Figures 5.11 and 5.12 show the potential for those radar datasets to be exploited further in the future, particularly with regards to tracking or otherwise characterising the englacial architecture of the ice and as motivated by the SCAR AntArchitecture group. At present, only two BAS radar datasets (BBAS and IMAFI) have been comprehensively assessed for deep englacial layering (Karlsson et al., 2009; Ashmore et al., 2020a; Bodart et al., 2021a). Thus, the release here of large swaths of additional radar datasets, including over the more stable regions of the EAIS (namely the AGAP, ICEGRAV, PolarGAP, and WISE-ISODYN datasets), and the evidence of continuous englacial layering in this region will likely offer more promising opportunities for englacial work to be conducted on these datasets. In particular, the close proximity of deep ice cores, such as the WAIS Divide (Buizert et al., 2015; Sigl et al., 2016), EPICA Dome C (EPICA Community Members, 2004), and South Pole (Winski et al., 2019), to these newly released surveys (Figs. 5.11-5.12) provide ready opportunities for IRHs to be dated, significantly increasing their use for wider applications such as estimating past accumulation rates and constrain changes in past ice-flow dynamics (c.f. Siegert and Payne, 2004; Parrenin and Hindmarsh, 2007; Cavitte et al., 2018; Sutter et al., 2021).

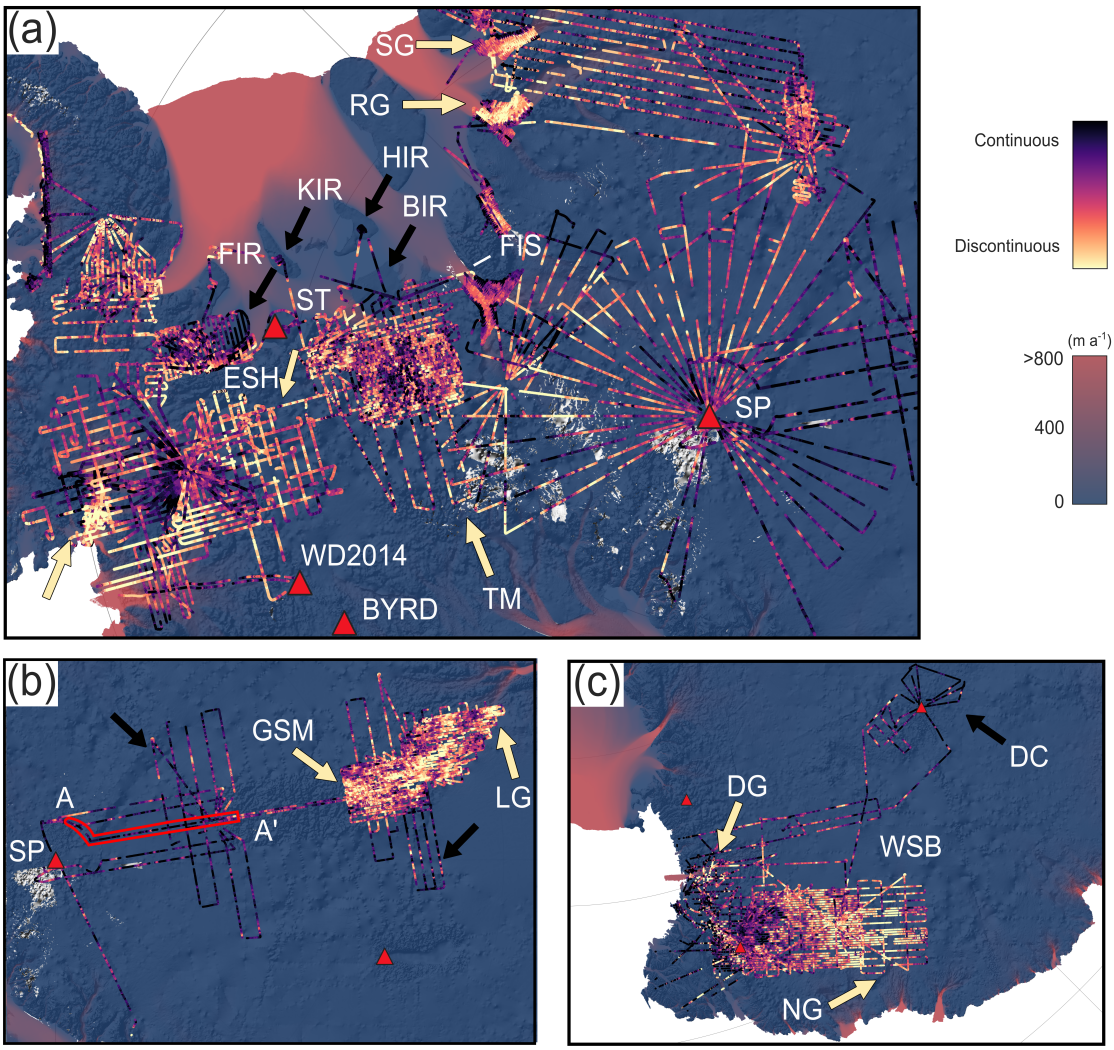

Figure 5.12: Zoomed-in sections of the ILCI shown in the black-bordered rectangles in Figure 5.11. Abbreviations correspond to locations mentioned in the text, as follows: BIR (Bungenstock Ice Rise); BYRD (Byrd ice core); DC (Dome C); DG (David Glacier); ESH (Ellsworth Subglacial Highlands); FIR (Filchner Ice Rise); FIS (Foundation Ice Stream); GSM (Gamburtsev Subglacial Mountains); HIR (Henry Ice Rise); KIR (Korff Ice Rise); LG (Lambert Glacier); NG (Ninnis Glacier); RG (Recovery Glacier); SG (Slessor Glacier); SP (South Pole); ST (Sky Train ice core); TM (Transantarctic Mountains); WD2014 (WAIS Divide ice core); WSB (Wilkes Subglacial Basin). (a) ILCI results over the WAIS (including Pine Island Glacier, Rutford Ice Stream, Institute–Möller Ice Stream, and FIS) and bottleneck with the EAIS (including SP, TM, and SG); (b) ILCI results for the AGAP survey over East Antarctica's Dome A and SP; (c) ILCI results for the WISE-ISODYN survey over East Antarctica's Wilkes Subglacial Basin and DC. Arrows refer to locations mentioned in the text, with black arrows highlighting examples of high-layer continuity and yellow arrows low-layer continuity. The red polygon in (b) shows the position of the 700-km segment A-A' shown in Figure 5.13. The basemap, red triangles, and colour scales are the same as in Figure 5.11.

This is in addition to already existing IRH stratigraphies across Antarctica which could provide dated constraints on the BAS RES data and compare the depth and/or age of IRHs between survey providers and radar systems, as previously conducted over East Antarctica (Winter et al., 2017). In particular, a previously traced IRH over East Antarctica, dated at 161 ka BP at the EPICA Dome C ice core (Winter et al., 2019), intersects an AGAP flightline over a distance of 700-km where englacial layering is particularly well-preserved on the newly released data (Fig. 5.13). There, the ILCI mean for this particular 700-km segment is higher (0.036) than the ILCI mean for the rest of the survey (0.026), and importantly, this profile intersects multiple flightlines from the PolarGAP survey where ILCI values are also high (Fig. 5.12a-b). Thus, this profile may provide an ideal starting point for linking stratigraphies from BAS RES surveys over East Antarctica, but also with dated stratigraphies from other survey providers across the ice sheet.

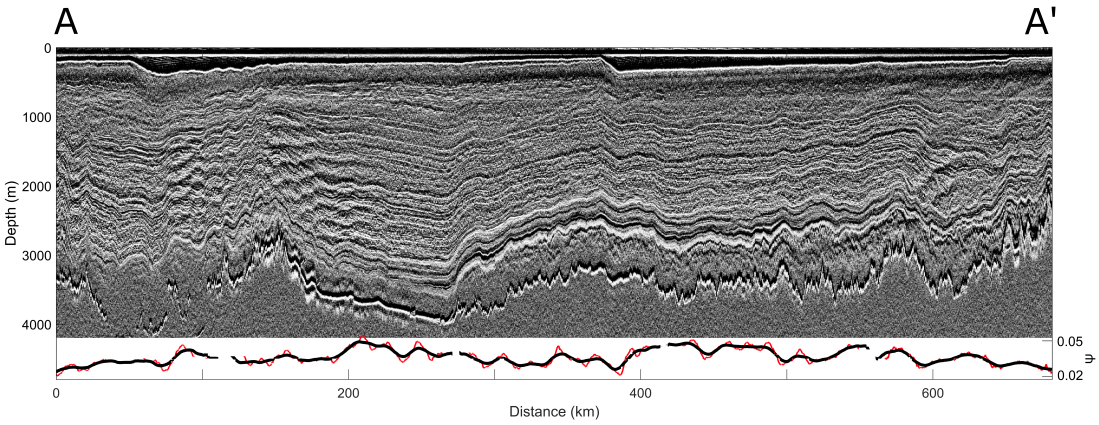

Figure 5.13: Segment A-A' from the AGAP survey (flightline: A10B) showing continuous layering at depth and high ILCI values. The ILCI is shown at the bottom of the radargram for the 20-80% portion of the ice thickness along the 700-km segment (red: unsmoothed; black: smoothed with moving-average filter) (see red polygon in Figure 5.12 for segment location).

Aside from offering promising opportunities for future englacial layering studies, we also expect this data release to be useful in a series of other ice-dynamical applications in the future. Examples applied to individual BAS datasets so far include comparing balance velocities with IRH geometries (Rippin et al., 2003b), analyses of water routing systems and bed reflectivity (Rippin et al., 2006a; Chu et al., 2021), as well as assessments of the bed roughness and local topography (Rippin et al., 2003a; 2011; 2014), amongst others. It is our aspiration that this data release will enable further such studies in the future.

5.6.2 Polar Airborne Geophysics Data Portal

One specificity of the platform is that it offers three types of geophysical datasets – gravity, magnetic, and radar – at the same time, geospatially. Although some surveys were acquired more than 25 years ago, they may never have been exploited or analysed fully in a form that reached peer-reviewed publications, nor combined with other geophysical data before, thereby increasing their re-usability. By publishing this resource, we anticipate that the portal and datasets will foster new research and discoveries related to our understanding of ice-sheet processes and crust and lithosphere heterogeneity beneath the Antarctic Ice Sheet.

Additionally, the portal enables users to combine the published line datasets with gridded products to compare the ability of the interpolated datasets to match the direct observations. For instance, as shown in Figure 5.14 for the 2012–2013 ICEGRAV survey, the portal allows users to readily investigate the free-air gravity anomaly with the bed topography from Bedmap2 or assess the consistency between the measured ICEGRAV magnetic anomalies and the gridded aeromagnetic product (Fig. 5.14). Alternatively, the quick-look radargrams can be compared with the ice-thickness and bed-elevation grid cells from Bedmap to assess sub-kilometre variations in along- and across-flow on the radar data which may have been smoothed out in the 1 km gridded product.

With its ∼207,000 line-km of gravity, ∼338,000 line-km of magnetic, and ∼352,000 line-km of radar data published, the Polar Airborne Geophysics Data Portal provides a robust platform for the dissemination of the BAS aerogeophysical data. Further opportunities offered by the data portal are the potential for the platform to be used to plan future field surveys or encourage future compilation efforts based on gaps in the data coverage or quality of the data.

5.6.3 Future work

Although most of data published here have already been incorporated into previous data compilations such as Bedmap2 or ADMAP2, the more recent datasets presented here will provide useful additions to future editions of such initiatives. Examples of this are the data acquired as part of the 2012–2013 ICEGRAV aeromagnetic campaign in Dronning Maud Land where the last compilation effort of magnetic anomalies had shown a large gap (Goodge and Finn, 2010; Fig. 5.14), or the new ice-thickness and bed-elevation data acquired over Thwaites Glacier (2018–2020), South Pole (2015–2016), and Filchner Ice Shelf (2015–2017), which are expected to be added to the new Bedmap3 compilation.

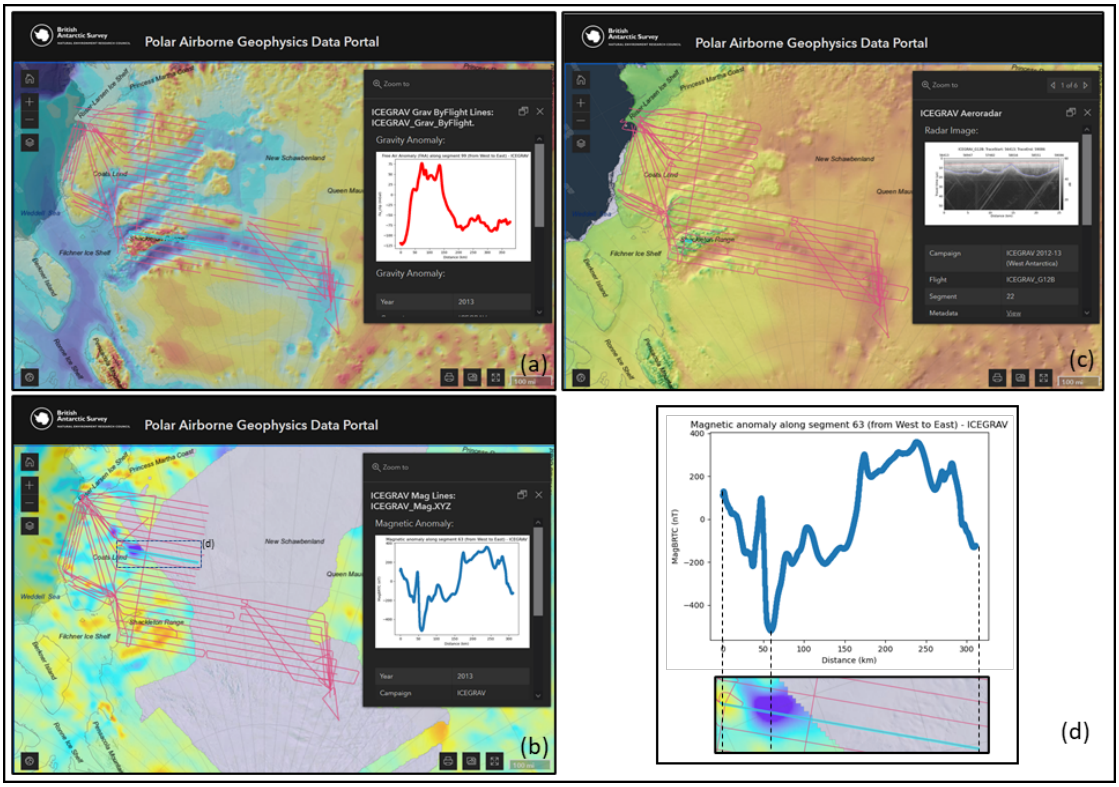

Figure 5.14: Screenshots of the Polar Airborne Geophysics Data Portal showing the three aerogeophysical products for the 2012–2013 ICEGRAV survey with different basemaps. (a) ICEGRAV aerogravity survey with the Bedmap2 bed-elevation basemap. (b) ICEGRAV aeromagnetic survey with the magnetic-anomaly basemap from Goodge and Finn (2010). (c) ICEGRAV aeroradar survey with the ice-thickness basemap from Bedmap2. (d) Magnetic anomaly along the profile highlighted in (c) with a comparison with the aeromagnetic anomaly map from Goodge and Finn (2010).

Even though most of the gravity, magnetic, and bed-pick data acquired since the mid-1990s are now fully published, radar data from older surveys, (1994–2004) for which the bed-pick data are published and already integrated into larger gridded products (e.g. Bedmap; Fretwell et al., 2013), are yet to be published in full as per the more modern surveys (2004–2020) released here (see Table 5.4). This is primarily due to poorer data management practices at times of acquisition and less well-documented processing procedures which restrict the re-usability of these older radar datasets. Much older analogue radar data acquired on films and video tapes prior to the deployment of digital radars (i.e. pre-1994) also offer additional opportunities, although the necessity for manual digitisation makes this task much more time consuming and challenging. It is worth noting, however,

that many of the regions broadly covered by these older surveys have recently been re-flown using more modern instruments as part of NASA's Operation IceBridge programme (MacGregor et al., 2021), although reprocessing and modernising older radar data can bring substantial benefits, as already demonstrated by Schroeder et al. (2019). Additional reprocessing of older radar data using modern 2-D SAR techniques would also be beneficial, as recently demonstrated on BAS data (see Castelletti et al., 2020; Chu et al., 2021).

As a result of the very flexible configuration of the PASIN-2 system, much more data can also be extracted from the raw radar files already acquired, including fully polarised data used to image ice crystal-fabric orientation for estimating ice-deformation processes (i.e. Young et al., 2021), or 3-D swath radar data used to reconstruct the sub-surface at finer resolution and without compromising on across-track resolution as for conventional 2-D data (Holschuh et al., 2020).

Combined, these will likely add further opportunities for future data releases, alongside our intention to publish newly acquired data regularly via the data portal and following the procedures detailed in this chapter.

5.7 Conclusion

We have presented the release of 64 aerogeophysical datasets from 24 surveys flown by BAS between 1994 and 2020 over West Antarctica, East Antarctica, and the Antarctic Peninsula. Altogether, the data release consists of ∼450,000 line-km (or ∼5.3 million km^2) of aerogeophysical data on gravity, magnetic, and radar measurements (including bed pick from 1994 onwards and the fully processed 2-D radar data from 2004 onwards) which have all been standardised according to the FAIR (findable, accessible, interoperable and re-usable) data principles. A new data portal, the Polar Airborne Geophysics Data Portal (https://www.bas.ac.uk/project/nagdp/, last access: 18 July 2022), and interactive, open-access tutorials written in Python and MATLAB have also been created to improve the interactivity and user accessibility of our datasets.

Aside from discussing the data acquisition and processing steps, we have demonstrated that much more information can be extracted from the newly released aerogeophysical data by assessing the continuity of englacial layering along ∼300,000 line-km of the RES data. Using an automated layer continuity extraction method on all ten fully published 2-D radar datasets, we have shown that large volumes of radar lines contain well-preserved englacial layering from which further glaciolog-

ical and geophysical information could be extracted. In particular, the presence of extensive continuous englacial layering on RES profiles crossing large sections of East Antarctica could significantly contribute to the recovery of an age-depth model of the ice sheet from dated IRHs, as motivated by the SCAR AntArchitecture Initiative. We note that the analysis shown in Section 5.6.1 is only possible because the data have been comprehensively standardised and made openly accessible. Whilst we acknowledge that this type of work may suffer from a lack of funding opportunities, the results presented here would suggest that re-modernising already-acquired data may be as important as acquiring new data. It also enables their use in emerging fields such as artificial intelligence, which rely on large amounts of standardised data.

Although all of the datasets released here have so far made a significant contribution to our understanding of past and current ice-dynamical and lithospheric influences, partly through their contributions to major international collaborative projects such as the SCAR Bedmap and ADMAP programmes, until now they have remained largely unpublished in their full form, thus restricting the further usage of the data beyond the life cycle of the science projects. It is our hope that these newly released data will offer further research opportunities and enable the wider scientific community to benefit from the abundance of newly published aerogeophysical data over Antarctica, particularly within the context of recently established international projects such as the SCAR AntArchitecture and RINGS Action groups, the latter of which focuses primarily on fillings gaps in radar observations at the boundaries of the Antarctic Ice Sheet.

Reflecting on our collaboration between data managers and scientists, we believe that this project sets a positive example for further release of aerogeophysical data, particularly for future international initiatives that are aiming to harmonise the availability and findability of aerogeophysical data collected across Antarctica. A full list of all available datasets can be found in Table 5.4 of this paper, or via the BAS Discovery Metadata System (https://data.bas.ac.uk, last access: 05 April 2023).

5.8 Data availability

All the data included in this chapter are freely available via the BAS Discovery Metadata System (https://data.bas.ac.uk, British Antarctic Survey, 2022), with direct links to the datasets found in Table 5.4 of this chapter. The user guide for the data portal and the Jupiter Notebook tutorials designed for reading the grav-

ity, magnetic, and radar data in Python and MATLAB are freely accessible on the Jupyter Book interface (https://antarctica.github.io/PDC_GeophysicsBook, Polar Data Centre, 2022) or via the BAS GitHub repository (https://github.com/antarctica/PDC_GeophysicsBook, last access: 05 April 2023). The code used to produce the Internal Layer Continuity Index over the whole BAS radar data (Figs. 5.11-5.12) is available on the GitHub page of Julien A. Bodart (https://github.com/julbod, last access: 05 April 2023) and on Zenodo (https://doi.org/10.5281/zenodo.6858932, Bodart, 2022).

6 Discussion

6.1 Thesis overview

The overall aim of this thesis was to develop and extend age-depth models of the Antarctic Ice Sheet (AIS) from Internal Reflecting Horizons (IRHs) to assess the past stability of the AIS. The three research objectives, described in Section 2.6, are summarised below:

- To build a spatially extensive age-depth model of the Pine Island Glacier (PIG) and upper Thwaites Glacier (THW) from airborne Radio-Echo Sounding (RES) data and high-resolution ice-core stratigraphy.
- To estimate mid-Holocene accumulation rates over the West Antarctic Ice Sheet (WAIS) using a pervasive IRH and a one-dimensional (1-D) ice-flow model.
- To provide a community resource of standardised aerogeophysical data and identify areas of continuous IRH profiles that will facilitate the development of an age-depth model of the AIS.

These three research objectives were addressed using large swaths of airborne RES data across the AIS, a database of IRHs spanning large portions of the WAIS, high-resolution ice-core stratigraphies, and climate datasets. By meeting these objectives, this thesis has led to significant progress in our understanding of the availability, spatial extent, and attributes of IRHs across the AIS, which will ultimately lead to the development of the first ice-sheet wide age-depth model, as motivated by the AntArchitecture initiative (Sect. 1.1.2). Section 6.2 reviews the key findings from this thesis, whilst Section 6.3 discusses the key limitations associated with this work and highlights opportunities for future work to be conducted in order to complete the development of an Antarctic-wide age-depth model.

6.2 Thesis outcome

In Chapter 3, I reported on the presence of four spatially extensive IRHs identified on airborne RES data over PIG and upper THW. Using intersections with other previously traced IRHs over PIG and Institute and Möller Ice Streams (IMIS), I showed that three of the four IRHs found across both catchments were identical. By connecting the IRHs to the WAIS Divide Ice Core (WD2014), and employing a 1-D age-depth model, I was able to date these IRHs at 2.31-2.92 ka, 4.72 ± 0.28, 6.94 ± 0.31, and 16.50 ± 0.79 ka Before the Present (BP), demonstrating their temporal span back through the Holocene and into the late Pleistocene. I found that below the deepest IRH (16.50 ka), there were no clear and continuous IRHs predating the Last Glacial Maximum (LGM), thus suggesting that an age-depth model of this sector of Antarctica is unlikely to span more than the last 20 ka on existing airborne RES data. By comparing the age and depth of strong acidity spikes in the WD2014, I was able to match the depth and age of the upper three IRHs with strong volcanic signals in the ice core, suggesting that their origin is from past volcanic activity that is unprecedented in the 68,000 year-old record. The main conclusion from Chapter 3 is that, together with the IRHs present over IMIS, a ubiquitous set of precisely dated volcanic markers spanning the Holocene is present across 20% of West Antarctica, which is a significant step forward in our ability to build an age-depth model of the WAIS.

In Chapter 4, I focused on the ubiquitous 4.72 ± 0.28 IRH from Chapter 3, extending its known geographical coverage to encompass THW, and used it to estimate past accumulation rates across 30% of the WAIS. Using a 1-D ice-flow model over the slow-flowing parts of these catchments and modern datasets of modelled (RACMO2) and observational (snow, firn, and ice cores) accumulation rates, I found that accumulation rates were 18% greater during the mid-Holocene compared with current rates over the Amundsen-Weddell-Ross Divide. Though no changes in the spatial pattern of accumulation rates were evident, I reported that the higher mid-Holocene accumulation rates inferred across large parts of the WAIS corresponded to the peak of a sustained increase in accumulation rates between $\sim$7 and 4 ka BP, evidenced in the WD2014 record and by targeted ground-based RES studies across West Antarctica. I also discussed the potential connection between the accumulation-rate change and grounding-line evolution over the WAIS during the mid-Holocene, which in the absence of downstream ice-dynamical processes counter-balancing the increase in accumulation upstream, would result in ice thickening and issuing grounding-line readvance, as previously suggested over the Ross and Weddell Sea side of the WAIS. The main conclusion from Chapter 4 is that the higher-than-present accumulation rates across most of the WAIS dur-

ing the mid-Holocene must be accounted for by regional and continental ice-sheet models in order to improve past ice-sheet reconstructions across Antarctica. These studies could use the reconstructed accumulation rates at the WD2014 site, which as I showed in this chapter, are representative of past conditions across the wider WAIS.

In Chapter 5, I presented the release of 25 years of aerogeophysical data acquired by the British Antarctic Survey (BAS) between 1994 and 2020 over Antarctica. I discussed how the data were acquired, processed, and standardised following the FAIR (Findable, Accessible, Interoperable, and Re-Usable) data principles, and presented the new Polar Airborne Geophysics Data Portal where all the data can be viewed and downloaded interactively. Of particular relevance to this thesis is the standardisation and release of ∼300,000 line-km of airborne RES data, which, aside from being used here in this thesis, are expected to also form part of future studies aiming to extract further IRH stratigraphies across the AIS. To assess the extent to which these RES products can be used to extract an ice-sheet wide age-depth model, I applied to the ten fully processed RES datasets a now well-established technique for identifying regions of well preserved IRHs, namely the Internal Layering Continuity Index (ILCI). This analysis demonstrated that large sections of continuous englacial layering are visible on the East Antarctic plateau and Wilkes Subglacial Basin where deep ice-core stratigraphies could enable the dating of future IRH stratigraphies. In particular, I identified a specific 700-km segment connecting both the South Pole and East Antarctic plateau that directly intersects an existing IRH stratigraphy dating back to the last ∼161 ka BP, which could be used to expand an age-depth model across two large regions covered by the BAS PolarGAP and AGAP surveys. The main conclusion from Chapter 5 is that the newly released RES data across both East and West Antarctica contain large sections of well-preserved and continuous englacial layering which, if dated, could bring us significantly closer to developing an Antarctic-wide age-depth model from dated IRHs.

6.3 Thesis limitations and future developments

6.3.1 Chapter 3

In Chapter 3, I showed that there was an offset of between 23 and 28 m between the sulphate peaks recorded at the WD2014 ice-core site and the depth of the three IRHs at the nearest RES crossover. Whilst this is a relatively small difference given that ice thickness in the area around WD2014 exceeds ∼3.5 km, it is worth considering where this offset originates from. In this chapter, I postulated

that the vertical offset between the IRHs and the sulphate peaks may be caused by roughness-induced changes in ice stratigraphy near WD2014, as reported by Laird et al. (2010), given that the two sets of measurements are not exactly co-located (∼1.2 km apart).

However, an alternative explanation may come from the surface correction applied to the BAS RES data. Typically, the gap between the elevation of the aircraft and the ice surface is removed in post-processing and the elevation of the ice surface on the radargram is set to zero, so that any depths measured below the surface are true depths in the ice thickness. For this study, the air-to-ice-surface gap in the RES data was cut using the surface-pick variable instead of the surface-altitude variable. However, the surface altitude associated with the BAS RES data is usually obtained from the lidar onboard the aircraft, which has a resolution of a few centimetres, whereas the surface pick is obtained by following the brightest reflection in the RES data which is influenced by the resolution at which it was acquired (equivalent to several metres). Thus the first reflection may in fact represent multiple layers within the firn and hence not represent the exact ice surface. This approach has likely resulted in several metres of uncertainty in the actual IRH depths, which may have contributed to the IRHs not aligning more precisely with the strong acidity peaks present in WD2014. To account for this offset in the chapter, I increased the IRH age uncertainties so that they overlapped with the ages of the acidity peaks at WD2014. However, it is likely that accounting more precisely for the surface correction in the post-processing of the RES data may have resulted in closer depths between the IRHs and the ice-core sulphate peaks, and thus lower age uncertainties.

Another limitation of Chapter 3 was that I was unable to identify the IRHs across available RES data linking West and East Antarctica (e.g. at the "bottleneck"; see Winter et al., 2018), thus limiting our understanding of their spatial extent over other regions of the AIS. Whilst this may be achieved in the future with greater access to already acquired RES data (e.g. MacGregor et al., 2021; Chapter 5), improved processing techniques (e.g. Chu et al., 2021), or the acquisition of new RES data, an alternative may be to query the available ice-core records across other parts of Antarctica for evidence of strong volcanic events which match the ages of the already acquired IRHs over the WAIS. I explore this possibility further here.

Firstly, and using an updated processing technique on the sulphate data shown in Figure 3.8 of Chapter 3, Cole-Dai et al. (2021) showed that out of 426 volcanic eruptions occurring during the Holocene and recorded in the WD2014 record, ten

were considered "Very Large" (VL) events where volcanic deposition is greater than 30 kg km^{-2}. As a matter of comparison, these VL events corresponded to higher sulphate concentration than that associated with the Tambora volcanic eruption of 1815 in Indonesia, one of the largest volcanic eruptions of the last 10,000 years (Stothers, 1984). Importantly, this volcanic signal is widely visible in ice-core records across the AIS and is commonly used as a benchmark to calibrate and compare all other signals of explosive volcanism in Antarctic ice cores (Cole-Dai et al., 2009).

TABLE 6.1: Largest volcanic events in the WAIS Divide ice core during the Holocene. f refers to the sulphate flux at the ice core (in kg km^{-2}) and f/f_{Tambora} refers to the ratio of relative magnitude between the volcanic flux of an event and the 1815 Tambora event in the same ice core (see Cole-Dai et al., 2021). Note that BP is relative to 1950 and that event 11 refers to the Tambora 1815 event. Table adapted from Cole-Dai et al. (2021).

Rank	*Year (BP)*	*Depth*	f	f/f_{Tambora}
1	10,957	1,897	182.1	2.09
2	7,177	1,475	160.9	1.84
3	7,572	1,526	153.7	1.76
4	4,860	1,099	110.8	1.27
5	10,115	1,812	108.2	1.24
6	10,080	1,809	105.7	1.21
7	491	143	94.9	1.09
8	2,376	584	92.3	1.06
9	10,356	1,836	91	1.04
10	7,793	1,554	88.3	1.01
11	135	59	87.3	1

Out of those ten VL eruptions, the second and third strongest events were dated at 7.18 and 7.57 ka BP respectively (Table 6.1), closely matching the age of the 6.94 ± 0.31 ka IRH which is often identified as the shallowest reflection from a couplet of closely spaced IRHs in the ice column (see Karlsson et al., 2014; Ashmore et al., 2020a; Chapter 3). The fourth largest event is a distinctive signal dated at 4.86 ka BP that closely matches the age of the 4.72 ± 0.28 ka IRH (Table 6.1), which this thesis has shown is found across at least 30% of West Antarctica (see Chapter 4). Finally, Cole-Dai et al. (2021) also found that the eighth largest event in the ice core was dated at 2.38 ka BP, which falls within the age-range of R1 calculated using a 1-D age-depth model over PIG (2.31-2.92 ka; see Chapter 3 and Table 6.1).

By comparing the VL volcanic events from WD2014 in Table 6.1 with the 1815 Tambora eruption, Cole-Dai et al. (2021) pointed to the potential for these signals

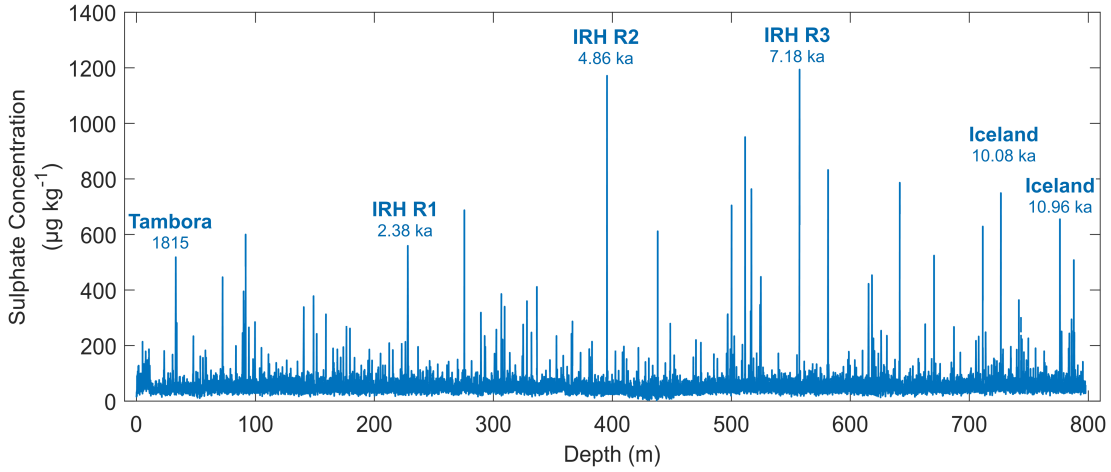

Figure 6.1: Sulphate concentrations (μg kg^{-1}) as a function of depth (m) at the South Pole ice core. Peaks of sulphate concentration matching the age and depth of R1-3 and dated at 2.38 ka, 4.86 ka, and 7.18 ka are shown, as well as the major 1815 Tambora eruption and the Icelandic Grímsvötn "Saksunarvatn Ash" eruption series from ~10 ka BP. The ages shown are in years before 1950, except for the 1815 Tambora eruption which is in years before the common era. Data is from Winski et al. (2021).

to be found across other sectors of the WAIS, and perhaps even across other parts of the wider AIS. Using the newly recovered South Pole ice core, East Antarctica, Winski et al. (2019) showed that similarly strong volcanic signals match those at WD2014 during the Holocene period (Fig. 6.1; Winski et al., 2019), suggesting that the IRHs identified over PIG and IMIS may be more widespread across the East Antarctic plateau. There, Winski et al. (2019) found that whilst the median annual sulphate maximum for the Holocene period is 60 μg kg^{-1}, several peaks matching the ages of the IRHs traced over PIG and IMIS exceed the sulphate concentrations of the strong 1850 Tambora eruption (518 μg kg^{-1}), reaching unmatched values in excess of 1,100 μg kg^{-1} for R2 and R3 (Fig. 6.1). Similarly at the Siple Dome ice core, West Antarctica, Kurbatov et al. (2006) showed that two signals dated at 2.28 ka and 4.77 ka were the second and fourth events with the highest sulphate concentration in the entire 12,000 year-old record. Comparatively at Dome C (East Antarctica), Castellano et al. (2005) showed that the EDC96 ice core also contained volcanic signals that matched closely the ages of the IRHs from Chapter 3. There, a band of large volcanic material was found between the ages of 6.21 and 7.49 ka BP (Castellano et al., 2005), which matches closely the age and characteristics of the 6.94 ± 0.31 ka IRH, the second-most spatially extensive IRH found over PIG and IMIS. Similarly, the fifth and nineteenth largest events in the record, dated at 2.33 ka BP and 4.79 ka BP respectively (Castellano et al., 2005), match the ages of the uppermost two IRHs, R1 and R2. Over Dronning Maud

Land, East Antarctica, Sigl et al. (2022) showed that large peaks matching the ages of the upper three IRHs were found within the EDML/B40 ice core (Severi et al., 2007), with a particularly strong peak that falls within the age range of the uppermost IRH (2.31-2.92 ka). These together suggest that the IRHs from Chapter 3 are also likely present over other sections of Antarctica, particularly over East Antarctica where the 2.31-2.92 ka and 6.94 ± 0.31 ka IRHs appear strongly in the ice-core records, whereas the 4.72 ± 0.28 is likely constrained to West Antarctica and the South Pole plateau. Promisingly, Holschuh et al. (2018) and Beem et al. (2021) both recently identified a prominent IRH matching closely the age of R2 and respectively traced on spatially targeted RES survey of Kamb Ice Stream (West Antarctica) and Titan Dome (East Antarctica). Together, the results from these studies suggest that even if we may never be able to directly track IRHs between West and East Antarctica on available RES data, an indirect approach of comparing age-depths and IRH characteristics between West and East Antarctica from available ice-core stratigraphies and RES data may be a suitable alternative.

One last limitation of this chapter was that I was unable to identify the sources of the volcanic eruptions which, as I showed in this chapter, are the likely cause of the IRHs due to the match in age and depth of the three strong sulphate peaks present in the WD2014 data. Whilst Cole-Dai et al. (2021) were unable to identify the exact sources of the VL eruptions from Table 6.1, they postulated that they must originate from explosive volcanic eruptions in the Southern Hemisphere or the low latitudes. This was largely based on analysis of glass shards in the first 600 m (<11 ka BP) of the Siple Dome ice core in West Antarctica by Kurbatov et al. (2006), which suggested that the dominant source of volcanic material detected in the core was likely local (i.e. Southern Ocean's Balleny Islands, Victoria Land's Pleiades, Marie Byrd Land's Mount Takahe and and Mount Berlin) or from volcanically active regions in the Southern Hemisphere (i.e. Mexico, Columbia, Chile, or New Zealand) (Kurbatov et al., 2006).

More recently, Sigl et al. (2022) used matching signals in sulphate and sulphur records from ice cores recovered from both Greenland and Antarctica to approximate the magnitudes and source latitudes of major volcanic events throughout the Holocene. Due to the limited amount of known eruptions during this time period, they were only able to provide average latitudes for the unknown eruptions, where 48°N, 37°S, and 5°N were assigned to eruptions likely originating in the Northern hemisphere, Southern hemisphere, and the tropics respectively. If matching signals from unknown volcanic eruptions were found in ice cores from both Greenland and Antarctica, the latitude was given as 5°N. This is largely based on previous evidence, which suggests that for a volcanic signal to be present in ice cores from

both poles, a volcanic eruption must be located in the tropics between latitudes of 20°N and 10°S and have a column height of at least 25 km, corresponding to a Volcanic Explosivity Index (VEI) ≥5 (Kohno and Fuji, 2001). However, previous evidence has also shown that a synchronous signal in both poles may not necessarily relate to the same tropical eruption, as individual eruptions of similar magnitudes in each respective hemisphere could occur at similar times (Yalcin et al., 2006; Hartman et al., 2019).

According to Sigl et al. (2022), out of 850 volcanic eruptions with injections greater than 1 teragram of sulphur (Tg S), 39% originated from the tropics, 50% from the Northern hemisphere extratropics, and 10% from the Southern hemisphere extratropics; however, tropical eruptions were responsible for 70% of the total sulphur injections in the stratosphere compared with 25% for Northern Hemisphere eruptions. Based on this analysis, Sigl et al. (2022) showed that most large peaks matching the ages of the IRHs I tracked across the WAIS likely originated from eruptions in the tropics, with a total peak sulphur injection value of 142, 211, and 516 Tg S for IRHs R1 to R3 respectively, obtained by summing all sulphur-injection values that fall within the age uncertainty of the IRHs at the ice core from Sigl et al. (2022). For comparison, it is estimated that the 1815 Tambora eruption emitted approximately 50-60 Tg S (Dai et al., 1991), which is relatively small in magnitude compared with the total concentration of sulphate associated with the upper two IRHs R1 and R2 that I traced across PIG and upper THW. Moreover, the total concentration of sulphate associated with the age of IRH R3 was much greater than that of the 1815 Tambora eruption (Cole-Dai et al., 2021; Sigl et al., 2022; Table 6.1), evincing a far-reaching volcanic eruption likely originating in the tropics whose impact across the WAIS was unrivalled through the Holocene. Whilst a precise source for these eruption is unlikely to be determined without improved geochemical data (Sigl et al., 2022), evidence suggests that even large eruptions tentatively assigned to the tropics have the ability to leave markers in Antarctica's ice stratigraphy which are significant enough to be detected in both ice cores (Sigl et al., 2022) and RES data (Chapter 3). To assess further whether the volcanic signals are local (i.e. Antarctic region) or regional (i.e. tropics), future studies could assess how far an IRH dated using sulphate peaks in ice cores can be traced away from the ice-core site on RES data, as similarly conducted by Corr and Vaughan (2008) over PIG. This could reveal the maximum spatial extent of a specific volcanic tracer and thus more precisely determine the source of a strong event based on its distance away from the strongest reflectivities in RES data.

Additionally, whilst Table 6.1 shows 5 events that match the characteristics, age, and depth of the upper-most three IRHs from Chapter 3 (Rank 2-3, 4, 8, and

10 in Table 6.1), and ignoring the two shallow events (Rank 7 and 11 in Table 6.1) which would not be visible on the BAS airborne RES data alone due to the inability for the RES system to image IRHs precisely in the first few hundred metres of the ice column (see Chapter 5), I note that four VL events may potentially be identified in BAS RES data in the future: Rank 1, 5, 6, and 9, with a depth range in the ice of 1,812-1,897 m and an age range of 10.12-11.00 ka BP (Table 6.1; Fig. 6.1). These four events appear to form part of a period of enhanced volcanic activity visible in most Antarctic and Greenland ice cores, and attributed to the Grímsvötn "Saksunarvatn Ash" eruption series from ∼10 ka in Iceland (Sigl et al., 2022; Fig. 6.1). Whilst Chapter 3 did not discuss evidence of continuous IRHs between R3 and R4, RES data across PIG shows the presence of bright and continuous IRHs in this part of the ice column that would be worth investigating further (see Figure 3.2 of Chapter 3). Because the resolution of the BAS RES system is best suited to resolve multi-annual IRHs, this series of closely spaced volcanic events from ∼10 ka BP may represent an ideal opportunity to extract a spatially extensive coverage of IRHs dated in the early stages of the Holocene across the PIG, THW and IMIS catchments.

6.3.2 Chapter 4

In Chapter 4, I showed that accumulation rates were 18% higher during the mid-Holocene than present rates across the Amundsen-Weddell-Ross Divide of the WAIS. Using a 1-D ice-flow model and the depth of a pervasive IRH found across most of PIG, THW, and IMIS, I showed that Holocene accumulation rates can be estimated without the need for more complex ice-flow models. This approach, however, was limited to regions where it can be reasonably assumed that the depth of an IRH is the primary product of accumulation rates at the surface, which meant that no calculations could be performed over fast-flowing regions of the WAIS, such as the tributaries and central trunks of PIG and THW.

Whilst the results presented in Chapter 4 are in good agreement with reconstructed accumulation rates at WD2014 (Fudge et al., 2016) and accumulation estimates derived from RES data and the use of multi-dimensional ice-flow models (Neumann et al., 2008; Koutnik et al., 2016), it would be beneficial to compare the accumulation estimates from Chapter 4 with a full 2-D or 3-D model that could account for the effects of convergent and divergent flow on the IRH stratigraphy, as previously employed over Antarctica (Karlsson et al., 2014; Leysinger-Vieli et al., 2011; Sutter et al., 2021). Indeed, the 1-D ice-flow model used here, although valid, does not take into account horizontal advection or the effect of basal melt rates, which can occur in faster-flow areas and at the divide, respectively. Unfortu-

nately, 2-D or 3-D models are much more complex to run and require substantially more computing resources than 1-D models, particularly over such a large area (i.e. 30% of the WAIS). Whilst the potential ice-dynamical effects on IRH depths were accounted for in the accumulation-rate uncertainty by using an alternative ice-flow model that considers the effect of vertical strain rates on the position of IRHs in the ice column, the results presented in this chapter could benefit from being compared with more sophisticated ice-flow models, particularly in the downstream parts of the PIG and THW catchments where differences between modern and Holocene accumulation rates were particularly high (see Section 4.4.1 for more details).

As also discussed in Chapter 4, other 1-D ice-flow models exist, including the Dansgaard-Johnsen (DJ) model (Dansgaard and Johnsen, 1969) and the shallow strain-rate model of MacGregor et al. (2016). It is therefore worth exploring whether other 1-D models may be more appropriate to estimate accumulation rates over the study area under consideration. For an ice sheet in steady state, the age-depth relationship is primarily controlled by accumulation of snow at the surface and thinning of ice due to horizontal gradients in ice flow (Fahnestock et al., 2001a). The 1-D models mentioned above are all designed to reproduce the age-depth relationship from ice cores by estimating vertical strain rates based on surface accumulation and ice thickness. The key difference between the Nye model used in Chapter 4, and the other two 1-D models mentioned above, is how this vertical strain rate is quantified, which is largely dependent on conditions at the ice-bed interface. In the Nye model, vertical strain rate is kept constant throughout the ice column to balance snow accumulation at the surface, thus implying that ice thinning is primarily controlled by sliding velocity gradients in a shallow layer at the ice-bed interface (Nye, 1957; Fahnestock et al., 2001a). A more complex alternative to this model is the DJ model, where ice deforms in the same way as for the Nye model (constant through depth) above a shearing section, h, below which vertical strain rates drop linearly to zero to accommodate a no-slip (frozen) bed (Dansgaard and Johnsen, 1969). If $h = 0$, the DJ model is equivalent to the Nye model where thinning is caused by gradients in basal sliding (i.e. assuming plug-flow conditions). However, the addition of the linear function $h > 0$ to account for thinning by internal deformation in the ice produces better results in areas where the ice is frozen to the bed (Dansgaard and Johnsen, 1969; Fahnestock et al., 2001a). One of the key limitations of the DJ model is that it depends on a good approximation of the basal-shear layer thickness parameter, h, which is largely unknown and varies over spatial and temporal scales (Siegert and Payne, 2004). Previous studies have used a series of values ranging from 10-70% of the ice thickness (where high values represent near-frozen conditions and a stable divide position), resulting in varying degrees of accumulation rates for the same age-depth

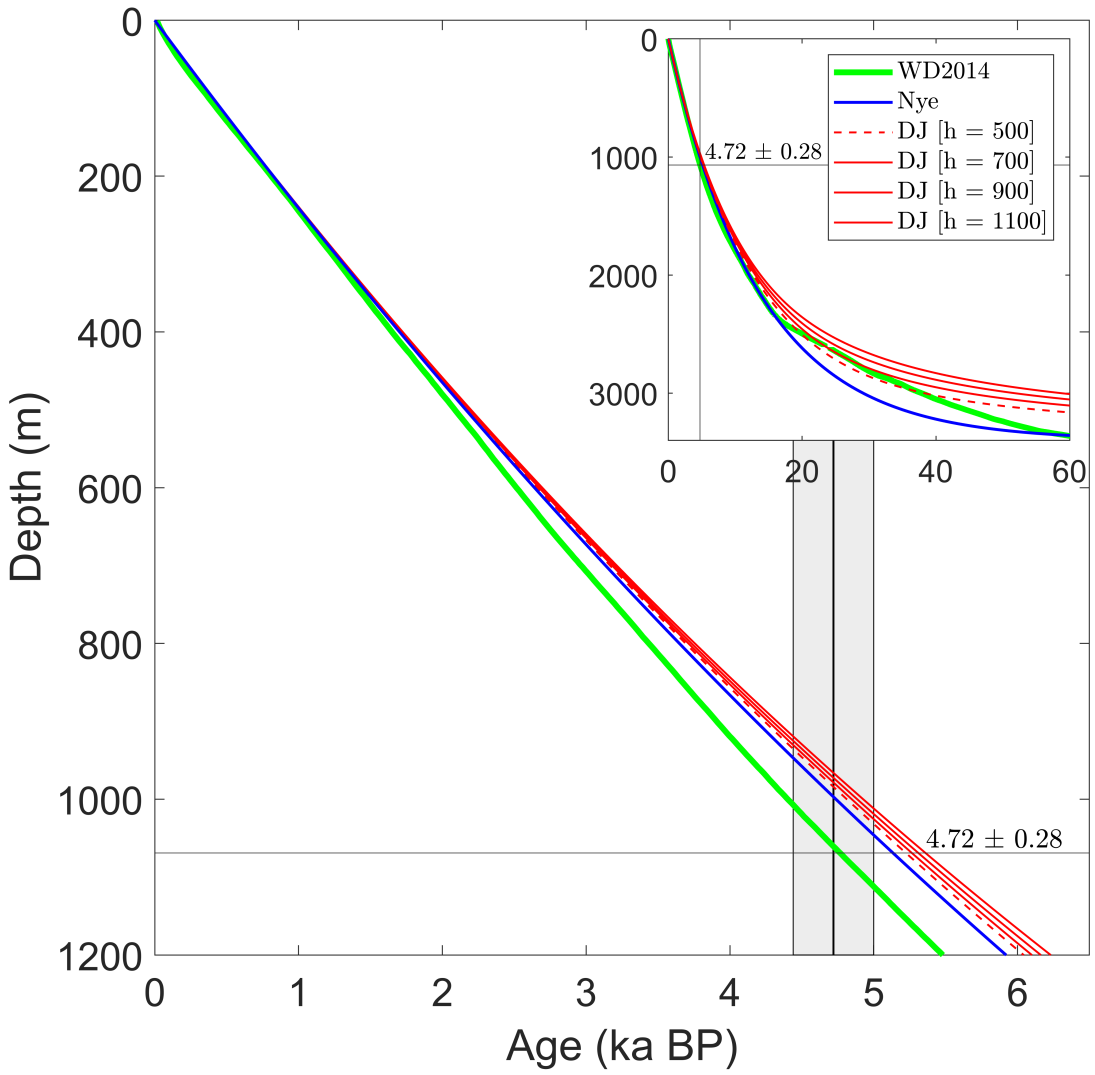

Figure 6.2: Comparison of age-depth relationships between two 1-D ice-flow models and the WAIS Divide ice core profile. The main figure shows the age-depth relationship for the 0-6 ka (x-axis) and 0-1,200 m (y-axis) portion of the ice column at WD2014. The horizontal line represents the depth of the 4.72 ka IRH at the ice core, and the vertical bold line represents the age of the 4.72 ka IRH from intersection with WD2014 (with the shaded area representing the upper and lower age uncertainties of the IRH). The top right inset shows the same data but for the full portion of the ice column (0-3,400 m) and age range (0-68 ka BP) at the ice core. The accumulation rate used to produce the age-depth relationship from the two 1-D models was set at 0.25 m a^{-1}, as reconstructed at the WD2014 Ice Core site for the 0-4.72 ka portion of the ice column (see Chapter 4). The three estimates for the DJ model (shown in red) are for different basal shear layer thickness scenarios, ranging from 500 (dashed line) to between 700 and 1,100 m (bold lines). The actual age-depth relationship observed at WD2014 is shown in green.

relationship (see Fahnestock et al., 2001a; Siegert and Payne, 2004; Neumann et al., 2008; Karlsson et al., 2014; Ashmore et al., 2020a; Chapter 3). Additionally, evidence from observational studies suggests that the Amundsen-Weddell Divide has unlikely been frozen to the bed, primarily due to the presence of water at the bottom of Byrd and WAIS Divide ice cores, the lack of a typical Raymond Arch below the Amundsen-Weddell Divide indicating a stable divide through time, and high geothermal heat flux in the area (Gow et al., 1968; Neumann et al., 2008; Buizert et al., 2015; Cuffey et al., 2016; Fudge et al., 2019; Chu et al., 2021). Thus, the addition of the parameter $h > 0$ (i.e. implying a frozen bed and negligible basal sliding) would likely not be appropriate here. A comparison of the age-depth relationship between the two models and the actual age-depth profile at WD2014 shows that the DJ model produces older ages with depth in the upper part of the ice column than the Nye model, though this is negligible ($\sim$0.1 ka at 4.72 ka BP) and falls within the age uncertainty of the IRH (Figure 6.2). Further down the ice column, both models appear unable to match the age-depth relationship from WD2014, with the DJ and Nye model producing much older and younger ages respectively than the WD2014 age-depth profile.

A key conclusion from Figure 6.2 is that there is relatively little difference between the two models in the upper part of the ice column where the 4.72 ka IRH is found, even when considering different scenarios for the basal shear layer thickness, although the Nye model appears to match better the age-depth profile of the ice core. This is not surprising, as both models are expected to perform well for estimating accumulation rates from IRHs that are found in the relatively shallow parts of the ice column ($\sim$35% at WD2014 for R2), albeit with consideration of the models' structural uncertainties (estimated at 14% over this sector of the WAIS for Nye-inferred accumulation rates; see Chapter 4). This noted, the added uncertainty associated with characterising the basal shear layer thickness in the DJ model means that the Nye model is likely more appropriate here, particularly when employed over larger spatial scales where the basal shear layer thickness will differ due to spatial variations in ice thicknesses and vertical strain rates.

Another 1-D model recently used to estimate accumulation rates from IRHs over the last 9 ka is the shallow strain-rate model adopted by MacGregor et al. (2016) over Greenland, which I used in Chapter 4 to infer uncertainties in accumulation rates. This model is similar to the Nye and DJ models in that it assumes uniform vertical strain rates, but only within the upper part of the ice column up to the age of the oldest IRH. One advantage of this model is that the vertical strain rate is not tied to the ice thickness, as per the DJ model, and is instead obtained by calculating the best-fit values using non-linear unconstrained minimi-

sation of a χ^2 statistic (MacGregor et al., 2016). Whilst this is a useful approach, the model requires at minimum two, and ideally several more, well-dated IRHs to constrain mean-accumulation and mean-vertical strain rates at one given point. For their Greenland application, MacGregor et al. (2016) used up to 24 well-dated IRHs in the central ice divides to calculate these parameters. For my study area, I was limited to only one IRH shallower than 4.72 ka over PIG/ISS to constrain accumulation and vertical strain rates; with the added complexity that it had not been dated at an ice core and was also much younger than R2, which, together, limited the suitability of this model for estimating accumulation rates over the WAIS using currently available IRHs.

6.3.3 Chapter 5

In Chapter 5, I showed that significant sections of continuous englacial layering are present over large swaths of the newly released BAS airborne RES data, particularly over East Antarctica. A follow-on comparison between the coverage of existing Antarctic IRH stratigraphies dated at ice cores and the newly released RES data presented in Chapter 5 shows that significant opportunities now exist for extending existing age-depth models acquired over spatially targeted sections of RES data to larger glacier catchments of both the WAIS and EAIS (Figure 6.3). In particular, the WISE-ISODYN, AGAP, and PolarGAP surveys over East Antarctica intersect both ice-core stratigraphies (going as far back as 740 ka; EPICA Community Members, 2004) and existing IRH stratigraphies (ranging from ∼5 to 705 ka) (Leysinger-Vieli et al., 2011; Winter et al., 2019; Beem et al., 2021; Cavitte et al., 2021), thus making them key surveys to prioritise for extracting an age-depth model of this region. The assessment of englacial layer continuity presented in Section 5.6.1 shows that these three surveys are promising for recovering continuous IRHs across large distances (Figs. 5.11-5.12), with a particular 700-km long profile that directly connects both the AGAP and PolarGAP surveys (Fig. 5.13) and dated stratigraphies extending to the Dome C Ice Core and the BAS WISE-ISODYN survey (Fig. 6.3).

This suggests that a link across ∼2.5 million km^2 of BAS RES data (representing ∼30% of East Antarctica) now exists for extracting a spatially extensive age-depth model of the region. In a first instance, future studies should attempt to identify IRHs in the BAS RES data that match the age-depth profile of existing IRH stratigraphies across the AIS, as these would bolster the coverage of existing age-depth profiles spanning several glacial cycles (up to the last 700 ka BP). In a second instance, it would be beneficial to expand this age-depth model to other key sectors of East Antarctica using intersections with other spatially extensive surveys, such as the ICECAP campaigns over the coastal sector of Wilkes Land

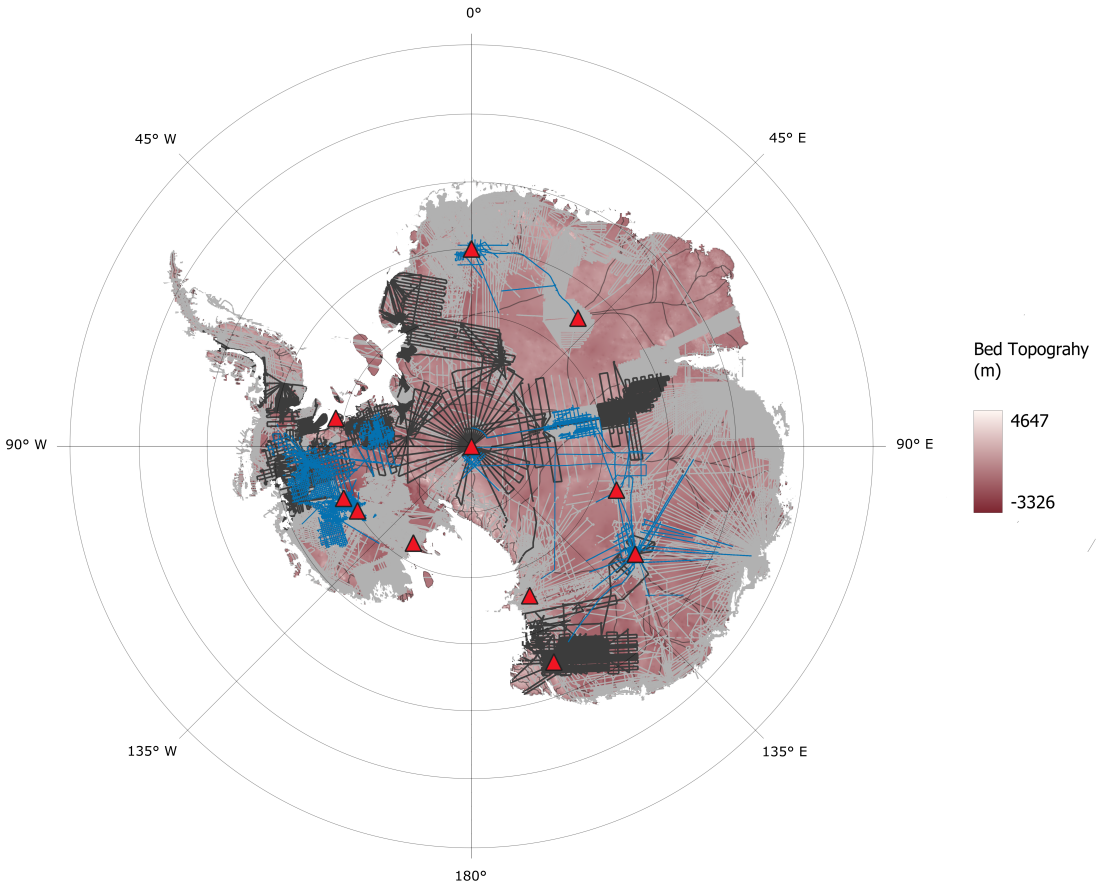

Figure 6.3: Coverage of dated IRH stratigraphies across Antarctica against existing RES data from Bedmap2-3 and the newly released data from Chapter 5. The line colours represent each dataset, as follows: the Bedmap2-3 data coverage (grey, Frémand et al., 2023), the recently released BAS airborne RES data (dark grey; Chapter 5), and the existing dated IRH stratigraphies from airborne RES surveys accessible in open-access format (light blue; Siegert and Payne, 2004; Leysinger-Vieli et al., 2011; Muldoon et al., 2018; Winter et al., 2019; Ashmore et al., 2020a; Beem et al., 2021; Cavitte et al., 2021; and Chapter 3). The red triangles show the locations of deep ice cores over the grounded part of the ice sheet. The background map shows bed topography from BedMachine (Morlighem, 2020) and the thin black lines in the background show the major ice divides from Mouginot et al. (2017). Note that RES coverage over ice shelves has been removed, as well as coverage of older RES data from Bedmap1.

(Frederik et al., 2016) and the Alfred Wegener Institute's surveys over Dronning Maud Land (Eagles et al., 2018), once these become fully available in open-access formats. Extending IRH stratigraphies to these sectors, as well as over additional catchments of West Antarctica such as over the newly released GRADES-IMAGE and FISS surveys (Chapter 5), would provide the AntArchitecture community with the first iteration of a pan-Antarctic age-depth model, which could be used

as boundary constraints for reconstructing past ice-sheet extents, as previously conducted by Sutter et al. (2021) with a subset of IRHs shown in Figure 6.3.

One limitation associated with Section 5.6.1 is that the ILCI values varied from survey to survey due to differences in processing applied to the data (e.g. incoherent versus 2-D Synthetic Aperture Radar (SAR) processing). As a result, caution is required when comparing ILCI values between different surveys, as high continuity values on the upstream portion of the fast-flowing WAIS may not represent the same level of continuity values measured on the stable plateau of East Antarctica. An alternative to this would be to re-apply the ILCI on RES data with a low-level of processing applied. Indeed, Karlsson et al. (2012) initially developed the ILCI for RES data for which a limited amount of processing had been applied (i.e. along-track stacking to reduce noise, but no background removal or migration), which enables this method to be transferred to other digital RES datasets irrespective of processing or data acquisition regimes. Unfortunately, only the RES data with a high-level of processing was released as part of Chapter 5. In addition to this issue, inconsistent surface or bed-pick information for some RES profiles directly impacted the retrieval of an ILCI value. To overcome this limitation, it would be beneficial to re-pick the surface and bed visible on previously acquired digital RES data with a community-agreed best automatic picker, particularly for older campaigns such as the BBAS survey where significant gaps in bed information exist (see Figure 5.3e).

Alternatively, re-processing older digital RES data with community-agreed SAR processing algorithms designed to facilitate the recovery of IRHs on RES data would be highly beneficial to AntArchitecture, as previously demonstrated by Castelletti et al. (2019).

Another limitation of Chapter 5 was that the data release did not include the pre-2004 2-D RES profiles. In particular, the analogue RES data acquired prior to 1994 by BAS (see Lythe et al., 2001 and Fretwell et al., 2013 for a listing of these further surveys), and recorded on acquisition directly to films and video tapes, exist in the BAS archives but are difficult to upgrade to modern standards due to the need to digitise manually each film. However, and despite the fact that these datasets were acquired over much smaller spatial scales and with lower spatial accuracy due to the lack of GPS technology at the time, they provide an important time capsule for fast-changing areas of the AIS (e.g. outlet glaciers of the Antarctic Peninsula and WAIS) where multidecadal-scale observations could improve our long-term understanding of the evolution of the grounding-line in these sectors, as previously exemplified by Schroeder et al. (2019) over the Thwaites Eastern Ice

Shelf. In addition to these analogue records, digital RES data acquired between 1994 and 2004 using the BAS-build RES system remain unavailable to the wider scientific community, primarily because the data and metadata that is used to reconnect the navigational information of each trace to the RES data is currently limited or lacking altogether. Whilst some of these surveys have been reflown recently with more modern RES systems, primarily as part of NASA Operation IceBridge campaigns, specific surveys such as the AFI Coats Land and Dufek surveys (Fig. 5.1) cover important areas that remain relatively unsurveyed. In the future, it would therefore be useful to digitise the pre-1994 analogue RES data and reconnect the navigational information on the 1994-2004 BAS-built RES data in order to provide a much longer record of ice-dynamical conditions over the AIS.

7 Conclusion

This thesis sought to develop and extend age-depth models across Antarctica from Internal Reflecting Horizons (IRHs) as imaged by Radio-Echo Sounding (RES) techniques to assess the past stability of the Antarctic Ice Sheet (AIS). Prior to this thesis, our knowledge of the coverage and availability of IRHs in both the West and East Antarctic Ice Sheets (WAIS and EAIS, respectively) was limited due, in part, to the lack of suitable datasets, which in turn impacted our ability to assess past ice-sheet changes. Together, the research presented in this thesis has resulted in significant progress in our ability to build an ice-sheet wide age-depth model of Antarctica. The key research findings resulting from Chapters 3, 4, and 5 are summarised as follows:

1. Using spatially extensive airborne RES data from multiple RES surveys and systems, I traced four isochronous IRHs over the Pine Island and upper Thwaites Glaciers and dated these using the high-resolution stratigraphy of the WAIS Divide ice core, with the youngest and oldest IRHs respectively ranging between 2.31-2.92 and 16.50±0.79 thousand years before the present. By comparing these with previously extracted IRHs over the Institute and Möller Ice Streams, I showed that this particular set of IRHs is found across 20% of the WAIS and corresponds to unprecedented peaks in sulphate concentrations in the 68,000 year-old ice-core record, suggesting that the origin of these IRHs is from past explosive volcanic eruptions. The limited presence of continuous and bright reflections below the depth of the deepest IRH on existing RES data suggests that extracting a spatially extensive age-depth model older than the late Pleistocene over the WAIS will be challenging using current RES data.

2. Using a ubiquitous IRH dated at 4.72 ± 0.28 ka BP and found across 30% of the WAIS (including over the Pine Island, Thwaites, and Institute and Möller ice-streams catchments) and a 1-D ice-flow model, I showed that accumulation rates during the mid-Holocene were 18% greater than current rates over the Amundsen-Weddell-Ross Divide; however, no spatial changes in accumulation patterns were found. Based on previous evidence, I showed that

these higher accumulation estimates occurred at a time when the grounding line of the Weddell and Ross sea sectors readvanced from its previously retreated position during the Holocene, suggesting that these sectors may be sensitive to changes in accumulation rates in the ice-sheet interior. Based on the similarity between the spatially extensive accumulation rates inferred across the Amundsen-Weddell-Ross Divide from the 1-D model, and those reconstructed at the WAIS Divide ice core, I concluded that future numerical ice-sheet models should base their climate boundary on the ice-core record in order to better simulate past ice-sheet configurations across the wider WAIS.

3. Whilst the results from Chapters 3 and 4 contributed significantly to our understanding of the spatial extent of IRHs across the WAIS, significantly less was known of the presence and extent of IRHs at a regional scale over the EAIS, which in turn impacted our ability to develop a spatially extensive age-depth model of the region. To address this challenge, I standardised and released 300,000 line-km of airborne RES data acquired by the British Antarctic Survey between 2004 and 2020 across large glacier catchments covering the EAIS and WAIS. Using the Internal Layer Continuity Index to automatically assess the continuity of englacial layering on the newly released RES data, I showed that large sections of continuous englacial layering are present across the RES data, particularly over the East Antarctic plateau and the Wilkes Subglacial basin where deep ice-core stratigraphies and existing age-depth profiles already exist. This chapter exemplified the ready opportunities that now exist for IRHs to be extracted in this region in order to build a spatially extensive age-depth model of the AIS, as motivated by the AntArchitecture Initiative.

Within the context of international research groups, such as the SCAR AntArchitecture Action Group and INSTANT Action Group, extracting an age-depth model of the ice sheet will be critical as it will provide important boundary conditions that can help constrain numerical ice-sheet model predictions of past and future ice-sheet wide changes. This is particularly relevant for our objective of providing a long-term context to the recent changes that Antarctica is currently facing as a result of climate change, and how the ice sheet is likely to respond to future anthropogenic forcing. In the future, further work should make use of the newly available RES data released as part of this thesis to extend existing IRH stratigraphies across the WAIS and EAIS in order to develop the first iteration of an ice-sheet wide age-depth model of Antarctica, as motivated by the AntArchitecture Initiative. The previous developments of similar data products over Greenland (MacGregor et al., 2015) and the WAIS (this thesis) have demonstrated that extracting regional age-depth models of ice sheets can significantly

increase our understanding of past ice-sheet processes, including estimating past accumulation rates, balance velocities, and the basal thermal state of the ice sheet. It is therefore expected that once produced by the AntArchitecture consortium, an age-depth model spanning the entire AIS will be a highly valuable resource for the Antarctic geophysical and glaciological communities.

References

Alley, R.B., Clark, P.U., Huybrechts, P. and Joughin, I., 2005. Ice-sheet and sea-level changes. *Science*, 310(5747), pp.456-460. DOI: 10.1126/science.1114613

Anderson, J.B., Shipp, S.S., Lowe, A.L., Wellner, J.S. and Mosola, A.B., 2002. The Antarctic Ice Sheet during the Last Glacial Maximum and its subsequent retreat history: a review. *Quaternary Science Reviews*, 21(1-3), pp.49-70. DOI: 10.1016/S0277-3791(01)00083-X

Arndt, J.E., Schenke, H.W., Jakobsson, M., Nitsche, F.O., Buys, G., Goleby, B., Rebesco, M., Bohoyo, F., Hong, J., Black, J. and Greku, R., 2013. The International Bathymetric Chart of the Southern Ocean (IBCSO) Version 1.0—A new bathymetric compilation covering circum-Antarctic waters. *Geophysical Research Letters*, 40(12), pp.3111-3117. DOI: 10.1002/grl.50413

Arndt, J.E., Hillenbrand, C.D., Grobe, H., Kuhn, G. and Wacker, L., 2017. Evidence for a dynamic grounding line in outer Filchner Trough, Antarctica, until the early Holocene. *Geology*, 45(11), pp.1035-1038. DOI: 10.1130/G39398.1

Arthern, R.J., Winebrenner, D.P. and Vaughan, D.G., 2006. Antarctic snow accumulation mapped using polarization of 4.3-cm wavelength microwave emission. *Journal of Geophysical Research: Atmospheres*, 111(D6), D06107. DOI: 10.1029/2004JD005667

Ashmore, D.W., Bingham, R.G., Hindmarsh, R.C., Corr, H.F. and Joughin, I.R., 2014. The relationship between sticky spots and radar reflectivity beneath an active West Antarctic ice stream. *Annals of Glaciology*, 55(67), pp.29-38. DOI: 10.3189/2014AoG67A052

Ashmore, D.W., Bingham, R.G., Ross, N., Siegert, M.J., Jordan, T.A. and Mair, D.W., 2020a. Englacial architecture and age-depth constraints across the West Antarctic Ice Sheet. *Geophysical Research Letters*, 47(6), e2019GL086663.

DOI: 10.1029/2019GL086663

Ashmore, D.W., Bingham, R.G., Ross, N., Siegert, M., Jordan, T.A. and Mair, D.W.F., 2020b. Radiostratigraphy of the Weddell Sea sector of West Antarctica, v2.0.0. *Zenodo* [data set]. DOI: 10.5281/zenodo.4945301

Bamber, J.L., Ferraccioli, F., Joughin, I., Shepherd, T., Rippin, D.M., Siegert, M.J. and Vaughan, D.G., 2006. East Antarctic ice stream tributary underlain by major sedimentary basin. *Geology*, 34(1), pp.33-36. DOI: 10.1130/G22160.1

Balco, G., Brown, N., Nichols, K., Venturelli, R.A., Adams, J., Braddock, S., Campbell, S., Goehring, B., Johnson, J.S., Rood, D.H., Wilcken, K., Hall, B. and Woodward, J. 2023. Reversible ice sheet thinning in the Amundsen Sea Embayment during the Late Holocene. *The Cryosphere*, 17, pp. 1787–1801. DOI: 10.5194/tc-17-1787-2023

Becker, D., Nielsen, J.E., Ayres-Sampaio, D., Forsberg, R., Becker, M. and Bastos, L., 2015. Drift reduction in strapdown airborne gravimetry using a simple thermal correction. *Journal of Geodesy*, 89(11), pp.1133-1144. DOI: 10.1007/s00190-015-0839-8

Beem, L.H., Cavitte, M.G.P., Blankenship, D.D., Carter, S.P., Young, D.A., Muldoon, G.R., Jackson, C.S. and Siegert, M.J., 2018. Ice-flow reorganization within the East Antarctic Ice Sheet deep interior. *Geological Society, London, Special Publications*, 461(1), pp.35-47. DOI: 10.1144/SP461.14

Beem, L.H., Young, D.A., Greenbaum, J.S., Blankenship, D.D., Cavitte, M.G., Guo, J. and Bo, S., 2021. Aerogeophysical characterization of Titan Dome, East Antarctica, and potential as an ice core target. *The Cryosphere*, 15(4), pp.1719-1730. DOI: 10.5194/tc-15-1719-2021

Bell, R.E., Blankenship, D.D., Finn, C.A., Morse, D.L., Scambos, T.A., Brozena, J.M. and Hodge, S.M., 1998. Influence of subglacial geology on the onset of a West Antarctic ice stream from aerogeophysical observations. *Nature*, 394(6688), pp.58-62. DOI: 10.1038/27883

Bell, R.E., Studinger, M., Fahnestock, M.A. and Shuman, C.A., 2006. Tectonically controlled subglacial lakes on the flanks of the Gamburtsev Subglacial Mountains, East Antarctica. *Geophysical Research Letters*, 33(2), L02504. DOI: 10.1029/2005GL025207

Bell, R.E., Ferraccioli, F., Creyts, T.T., Braaten, D., Corr, H., Das, I., Damaske, D., Frearson, N., Jordan, T., Rose, K. and Studinger, M., 2011. Widespread persistent thickening of the East Antarctic Ice Sheet by freezing from the base. *Science*, 331(6024), pp.1592-1595. DOI: 10.1126/science.1200109

Bentley, M.J., Fogwill, C.J., Le Brocq, A.M., Hubbard, A.L., Sugden, D.E., Dunai, T.J. and Freeman, S.P., 2010. Deglacial history of the West Antarctic Ice Sheet in the Weddell Sea embayment: Constraints on past ice volume change. *Geology*, 38(5), pp.411-414. DOI: 10.1130/G30754.1

Bindschadler, R., Vornberger, P., Fleming, A., Fox, A., Mullins, J., Binnie, D., Paulsen, S.J., Granneman, B. and Gorodetzky, D., 2008. The Landsat image mosaic of Antarctica. *Remote Sensing of the Environment*, 112(12), pp.4214-4226. DOI: 10.1016/j.rse.2008.07.006

Bindschadler, R.A.; Choi, H., Wichlacz, A, Bingham, R., Bohlander, J., Brunt, K., Corr, H., Drews, R., Fricker, H., Hall, M., Hindmarsh, R., Kohler, J., Padman, L., Rack, W., Rotschky, G., Urbini, S., Vornberger, P. and Young, N., 2011. Getting around Antarctica: New high-resolution mappings of the grounded and freely-floating boundaries of the Antarctic ice sheet created for the International Polar Year. *The Cryosphere*, 5(3), pp.569-588. DOI: 10.5194/tc-5-569-2011

Bingham, R.G. and Siegert, M.J., 2007. Radio-echo sounding over polar ice masses. *Journal of Environmental and Engineering Geophysics*, 12(1), pp.47-62. DOI: 10.2113/JEEG12.1.47

Bingham, R.G., Siegert, M.J., Young, D.A. and Blankenship, D.D., 2007. Organized flow from the South Pole to the Filchner-Ronne ice shelf: An assessment of balance velocities in interior East Antarctica using radio echo sounding data. *Journal of Geophysical Research: Earth Surface*, 112(F3), F03S26. DOI: 110.1029/2006JF000556

Bingham, R.G. and Siegert, M.J., 2009. Quantifying subglacial bed roughness in Antarctica: implications for ice-sheet dynamics and history. *Quaternary Science Reviews*, 28(3-4), pp.223-236. DOI: 10.1016/j.quascirev.2008.10.014

Bingham, R.G., King, E.C., Smith, A.M. and Pritchard, H.D., 2010. Glacial geomorphology: towards a convergence of glaciology and geomorphology. *Progress in Physical Geography*, 34(3), pp.327-355. DOI: 0.1177/0309133309360631

Bingham, R.G., Ferraccioli, F., King, E.C., Larter, R.D., Pritchard, H.D., Smith, A.M. and Vaughan, D.G., 2012. Inland thinning of West Antarctic Ice Sheet steered along subglacial rifts. *Nature*, 487(7408), pp.468-471. DOI: 10.1038/nature11292

Bingham, R.G., Rippin, D.M., Karlsson, N.B., Corr, H.F., Ferraccioli, F., Jordan, T.A., Le Brocq, A.M., Rose, K.C., Ross, N. and Siegert, M.J., 2015. Ice-flow structure and ice dynamic changes in the Weddell Sea sector of West Antarctica from radar-imaged internal layering. *Journal of Geophysical Research: Earth Surface*, 120(4), pp.655-670. DOI: 10.1002/2014JF003291

Bingham, R.G., Vaughan, D.G., King, E.C., Davies, D., Cornford, S.L., Smith, A.M., Arthern, R.J., Brisbourne, A.M., Rydt, J., Graham, A.G. and Spagnolo, M., 2017. Diverse landscapes beneath Pine Island Glacier influence ice flow. *Nature Communications*, 8(1), 1618. DOI: 10.1038/s41467-017-01597-y

Blankenship, D.D., Morse, D.L., Finn, C.A., Bell, R.E., Peters, M.E., Kempf, S.D., Hodge, S.M., Studinger, M., Behrendt, J.C. and Brozena, J.M., 2001. Geologic controls on the initiation of rapid basal motion for West Antarctic ice streams: A geophysical perspective including new airborne radar sounding and laser altimetry results. *The West Antarctic Ice Sheet: Behavior and Environment*, 77, pp.105-121. DOI: 10.1029/AR077p0105

Blankenship, D. D., S. D. Kempf, D. A. Young, T. G. Richter, D. M. Schroeder, J. S. Greenbaum, T. van Ommen, R. C. Warner, J. L. Roberts, N. W. Young, E. Lemeur, M. J. Siegert, and J. W. Holt., 2017. IceBridge HiCARS 1 L1B Time-Tagged Echo Strength Profiles, v.1.0.0. *NASA National Snow and Ice Data Center* [data set]. DOI: 10.5067/W2KXX0MYNJ9G

Bodart, J.A. and Bingham, R.J., 2019. The Impact of the Extreme 2015–2016 El Niño on the Mass Balance of the Antarctic Ice Sheet. *Geophysical Research Letters*, 46(23), pp.13862-13871. DOI: 10.1029/2019GL084466

Bodart, J.A., Bingham, R.G., Ashmore, D.W., Karlsson, N.B., Hein, A.S. and Vaughan, D.G., 2021a. Age-depth stratigraphy of Pine Island Glacier inferred from airborne radar and ice-core chronology *Journal of Geophysical Research: Earth Surface*, 126(4), e2020JF005927. DOI: 10.1029/2020JF005927

Bodart, J.A., Bingham, R.G., Ashmore, D.W., Karlsson, N.B., Hein, A.S., and Vaughan, D.G., 2021b. Dated radar stratigraphy of the Pine Island Glacier catchment (West Antarctica) derived from BBAS-PASIN (2004-05) and OIB-MCoRDS2 (2016/2018) surveys, v.1.0.0. *UK Polar Data Centre, Natural Environment Research Council* [data set]. DOI: 10.5285/F2DE31AF-9F83-44F8-9584-F0190A2CC3EB

Bodart, J.A., 2022. Calculate englacial layer continuity from BAS airborne radar data, v1.0.0. *Zenodo*[code]. DOI: 10.5281/zenodo.6858932

Bodart, J.A., Bingham, R.G., Young, D.A., MacGregor, J.A., Ashmore, D.W., Quartini, E., Vaughan, D.G., and Blankenship D.D., 2023a. Gridded depth and accumulation products from dated airborne radar stratigraphy over West Antarctica during the mid-Holocene, v.1.0.0. *Zenodo* [data set]. DOI: 10.5281/zenodo.7738654

Bodart, J.A., Bingham, R.G., Young, D.A., MacGregor, J.M., Ashmore, D.W., Quartini, E., Hein, A.S., Vaughan, D.G., and Blankenship D.D., 2023b. High mid-Holocene accumulation rates over West Antarctica inferred from a pervasive ice-penetrating radar reflector. *The Cryosphere*, 17(4), 1497-1512. DOI: 10.5194/tc-17-1497-2023

Bozzo, E. and Ferraccioli, F., 2007. The Italian-British Antarctic geophysical and geological survey in northern Victoria Land 2005-06-towards the International Polar Year 2007-08. *Terra Antartica Reports*, 13. DOI: https://nora.nerc.ac.uk/id/eprint/15403(last access: 05 April 2023)

Bracegirdle, T.J., Colleoni, F., Abram, N.J., Bertler, N.A., Dixon, D.A., England, M., Favier, V., Fogwill, C.J., Fyfe, J.C., Goodwin, I. and Goosse, H., 2019. Back to the future: Using long-term observational and paleo-proxy reconstructions to improve model projections of Antarctic climate. *Geosciences*, 9(6), 255. DOI: 10.3390/geosciences9060255

Braddock, S., Hall, B.L., Johnson, J.S., Balco, G., Spoth, M., Whitehouse, P.L., Campbell, S., Goehring, B.M., Rood, D.H. and Woodward, J., 2022. Relative sea-level data preclude major late Holocene ice-mass change in Pine Island Bay. *Nature Geoscience*, 15(7), pp.568-572. DOI: 10.1038/s41561-022-00961-y

Bradley, S.L., Hindmarsh, R.C., Whitehouse, P.L., Bentley, M.J. and King, M.A., 2015. Low post-glacial rebound rates in the Weddell Sea due to Late

Holocene ice-sheet readvance. *Earth and Planetary Science Letters*, 413, pp.79-89. DOI: 10.1016/j.epsl.2014.12.039

British Antarctic Survey (BAS), 2022. Discovery Metadata System. https://data.bas.ac.uk (last access: 05 April 2023)

Buizert, C., Cuffey, K.M., Severinghaus, J.P., Baggenstos, D., Fudge, T.J., Steig, E.J., Markle, B.R., Winstrup, M., Rhodes, R.H., Brook, E.J. and Sowers, T.A., 2015. The WAIS Divide deep ice core WD2014 chronology–Part 1: Methane synchronization (68–31 kaBP) and the gas age–ice age difference. *Climate of the Past*, 11(2), pp.153-173. DOI: 10.5194/cp-11-153-2015

Buizert, C., Fudge, T.J., Roberts, W.H., Steig, E.J., Sherriff-Tadano, S., Ritz, C., Lefebvre, E., Edwards, J., Kawamura, K., Oyabu, I. and Motoyama, H., 2021. Antarctic surface temperature and elevation during the Last Glacial Maximum. *Science*, 372(6546), pp.1097-1101. DOI: 10.1126/science.abd2897

Burgener, L., Rupper, S., Koenig, L., Forster, R., Christensen, W.F., Williams, J., Koutnik, M., Miege, C., Steig, E.J., Tingey, D. and Keeler, D., 2013. An observed negative trend in West Antarctic accumulation rates from 1975 to 2010: Evidence from new observed and simulated records. *Journal of Geophysical Research: Atmosphere*, 118(10), pp.4205-4216. DOI: 10.1002/jgrd.50362

Carter, S.P., Blankenship, D.D., Peters, M.E., Young, D.A., Holt, J.W. and Morse, D.L., 2007. Radar-based subglacial lake classification in Antarctica. *Geochemistry, Geophysics, Geosystems*, 8(3), Q03016. DOI: 10.1029/2006GC001408

Carter, S.P., Blankenship, D.D., Young, D.A. and Holt, J.W., 2009. Using radar-sounding data to identify the distribution and sources of subglacial water: application to Dome C, East Antarctica. *Journal of Glaciology*, 55(194), pp.1025-1040. DOI: 10.3189/002214309790794931

Castellano, E., Becagli, S., Hansson, M., Hutterli, M., Petit, J.R., Rampino, M.R., Severi, M., Steffensen, J.P., Traversi, R. and Udisti, R., 2005. Holocene volcanic history as recorded in the sulfate stratigraphy of the European Project for Ice Coring in Antarctica Dome C (EDC96) ice core. *Journal of Geophysical Research: Atmospheres*, 110(D6), D06114. DOI: 10.1029/2004JD005259

Castelletti, D., Schroeder, D.M., Mantelli, E. and Hilger, A., 2019. Layer optimized SAR processing and slope estimation in radar sounder data. *Journal of*

Glaciology, 65(254), pp.983-988. DOI: 10.1017/jog.2019.72

Catania, G.A., Conway, H.B., Gades, A.M., Raymond, C.F. and Engelhardt, H., 2003. Bed reflectivity beneath inactive ice streams in West Antarctica. *Annals of Glaciology*, 36, pp.287-291. DOI: 10.3189/172756403781816310

Catania, G.A., Conway, H., Raymond, C.F. and Scambos, T.A., 2006. Evidence for floatation or near floatation in the mouth of Kamb Ice Stream, West Antarctica, prior to stagnation. *Journal of Geophysical Research: Earth Surface*, 111(F1), F01005. DOI: 10.1029/2006GL026430

Catania, G., Hulbe, C. and Conway, H., 2010. Grounding-line basal melt rates determined using radar-derived internal stratigraphy. *Journal of Glaciology*, 56(197), pp.545-554. DOI: 10.3189/002214310792447842

Cavitte, M.G., Blankenship, D.D., Young, D.A., Schroeder, D.M., Parrenin, F., Lemeur, E.,Macgregor, J.A. and Siegert, M.J., 2016. Deep radiostratigraphy of the East Antarctic plateau: connecting the Dome C and Vostok ice core sites. *Journal of Glaciology*, 62(232), pp.323-334. DOI: 10.1017/jog.2016.11

Cavitte, M.G., Parrenin, F., Ritz, C., Young, D.A., Liefferinge, B., Blankenship, D.D., Frezzotti, M. and Roberts, J., 2018. Accumulation patterns around Dome C, East Antarctica, in the last 73 kyr. *The Cryosphere*, 12(4), pp.1401-1414. DOI: 10.5194/tc-12-1401-2018

Cavitte, M.G., Dalaiden, Q., Goosse, H., Lenaerts, J. and Thomas, E.R., 2020. Reconciling the surface temperature–surface mass balance relationship in models and ice cores in Antarctica over the last two centuries. *The Cryosphere*, 14(11), pp.4083–4102. DOI: 10.5194/tc-14-4083-2020

Cavitte, M.G., Young, D.A., Mulvaney, R., Ritz, C., Greenbaum, J.S., Ng, G., Kempf, S.D., Quartini, E., Muldoon, G.R., Paden, J. and Frezzotti, M., 2021. A detailed radiostratigraphic data set for the central East Antarctic Plateau spanning from the Holocene to the mid-Pleistocene. *Earth System Science Data*, 13(10), pp.4759-4777. DOI: 10.5194/essd-13-4759-2021

Cavitte, M.G., Goosse, H., Wauthy, S., Kausch, T., Tison, J.L., Van Liefferinge, B., Pattyn, F., Lenaerts, J.T. and Claeys, P., 2022. From ice core to ground-penetrating radar: representativeness of SMB at three ice rises along the Princess Ragnhild Coast, East Antarctica. textitJournal of Glaciology, 68(272),

pp.1-13. DOI: 10.1017/jog.2022.39

Chavaillaz, Y., Codron, F. and Kageyama, M., 2013. Southern westerlies in LGM and future (RCP4. 5) climates. *Climate of the Past*, 9(2), pp.517-524. DOI: 10.5194/cp-9-517-2013

Christianson, K., Bushuk, M., Dutrieux, P., Parizek, B.R., Joughin, I.R., Alley, R.B., Shean, D.E., Abrahamsen, E.P., Anandakrishnan, S., Heywood, K.J. and Kim, T.W., 2016. Sensitivity of Pine Island Glacier to observed ocean forcing. *Geophysical Research Letters*, 43(20), pp.10817-10825. DOI: 10.1002/2016GL070500

Chu, W., Hilger, A.M., Culberg, R., Schroeder, D.M., Jordan, T.M., Seroussi, H., Young, D.A., Blankenship, D.D. and Vaughan, D.G., 2021. Multi-system synthesis of radar sounding observations of the Amundsen Sea sector from the 2004-2005 field season. *Journal of Geophysical Research: Earth Surface*, 126(10), e2021JF006296. DOI: 10.1029/2021JF006296

Clough, J.W., 1977. Radio-echo sounding: reflections from internal layers in ice sheets. *Journal of Glaciology*, 18(78), pp.3-14. DOI: 10.3189/S002214300002147X

Cole-Dai, J., Ferris, D., Lanciki, A., Savarino, J., Baroni, M. and Thiemens, M.H., 2009. Cold decade (AD 1810–1819) caused by Tambora (1815) and another (1809) stratospheric volcanic eruption. *Geophysical Research Letters*, 36(22), L22703. DOI: 10.1029/2009GL040882

Cole-Dai, J., 2014. Major Ion Chemistry Data of WAIS Divide Ice Core Brittle Ice. *U.S. Antarctic Program Data Center* [data set]. DOI: 10.7265/N5RF5S0D

Cole-Dai, J., Ferris, D.G., Kennedy, J.A., Sigl, M., McConnell, J.R., Fudge, T.J., Geng, L., Maselli, O.J., Taylor, K.C. and Souney, J.M., 2021. Comprehensive record of volcanic eruptions in the Holocene (11,000 years) from the WAIS Divide, Antarctica ice core. *Journal of Geophysical Research: Atmospheres*, 126(7), e2020JD032855. DOI: 10.1029/2020JD032855

Constantino, R.R., Tinto, K.J., Bell, R.E., Porter, D.F. and Jordan, T.A., 2020. Seafloor depth of George VI Sound, Antarctic Peninsula, from inversion of aerogravity data. *Geophysical Research Letters*, 47(21), e2020GL088654. DOI: 10.1029/2020GL088654

Conway, H., Hall, B.L., Denton, G.H., Gades, A.M. and Waddington, E.D., 1999. Past and future grounding-line retreat of the West Antarctic Ice Sheet. *Science*, 286(5438), pp.280-283. DOI: 10.1126/science.286.5438.280

Conway, H., Catania, G., Raymond, C.F., Gades, A.M., Scambos, T.A. and Engelhardt, H., 2002. Switch of flow direction in an Antarctic ice stream. *Nature*, 419(6906), pp.465-467. DOI: 10.1038/nature01081

Conway, H. and Rasmussen, L. A., 2009. Recent thinning and migration of the Western Divide, central West Antarctica. *Geophysical Research Letters*, 36(12), L12502. DOI: 10.1029/2009GL038072

Corr, H. and Popple, M., 1994. Airborne radio echo sounding on the Evans flowline, Ronne Ice Shelf. *Filchner-Ronne Ice Shelf Programme Report*, 8, pp.9-11. DOI: http://nora.nerc.ac.uk/id/eprint/515954 (last access: 05 April 2023)

Corr, H.F., Ferraccioli, F., Frearson, N., Jordan, T., Robinson, C., Armadillo, E., Caneva, G., Bozzo, E. and Tabacco, I., 2007. Airborne radio-echo sounding of the Wilkes Subglacial Basin, the Transantarctic Mountains and the Dome C region. *Terra Antartica Reports*, 13, pp.55-63. DOI: https://nora.nerc.ac.uk/id/eprint/13578/ (last access: 05 April 2023)

Corr, H.F. and Vaughan, D.G., 2008. A recent volcanic eruption beneath the West Antarctic ice sheet. *Nature Geoscience*, 1(2), pp.122-125. DOI: 10.1038/ngeo106

CReSIS, 2018. *CReSIS Radar Depth Sounder Data*, Lawrence, Kansas, USA. Digital Media. DOI: http://data.cresis.ku.edu/ (last access: 05 April 2023)

Creyts, T.T., Ferraccioli, F., Bell, R.E., Wolovick, M., Corr, H., Rose, K.C., Frearson, N., Damaske, D., Jordan, T., Braaten, D. and Finn, C., 2014. Freezing of ridges and water networks preserves the Gamburtsev Subglacial Mountains for millions of years. *Geophysical Research Letters*, 41(22), pp.8114-8122. DOI: 10.1002/2014GL061491

Cui, X., Jeofry, H., Greenbaum, J.S., Guo, J., Li, L., Lindzey, L.E., Habbal, F.A., Wei, W., Young, D.A., Ross, N. and Morlighem, M., 2020. Bed topography of princess Elizabeth land in east Antarctica. *Earth System Science Data*, 12(4), pp.2765-2774. DOI: 10.5194/essd-12-2765-2020

Cuffey, K.M., Clow, G.D., Steig, E.J., Buizert, C., Fudge, T.J., Koutnik, M., Waddington, E.D., Alley, R.B. and Severinghaus, J.P., 2016. Deglacial temperature history of West Antarctica. *Proceedings of the National Academy of Sciences*, 113(50), pp.14249-14254. DOI: 10.1073/pnas.1609132113

Dai, J., Mosley-Thompson, E. and Thompson, L.G., 1991. Ice core evidence for an explosive tropical volcanic eruption 6 years preceding Tambora. *Journal of Geophysical Research: Atmospheres*, 96(D9), pp.17361-17366. DOI: 10.1029/91JD01634

Dalaiden, Q., Goosse, H., Klein, F., Lenaerts, J., Holloway, M., Sime, L. and Thomas, E.R., 2020. How useful is snow accumulation in reconstructing surface air temperature in Antarctica? A study combining ice core records and climate models. *The Cryosphere*, 14(4), pp.1187–1207. DOI: 10.5194/tc-14-1187-2020

Dansgaard, W. and Johnsen, S.J., 1969. A flow model and a time scale for the ice core from Camp Century, Greenland. *Journal of Glaciology*, 8(53), pp.215-223. DOI: 10.3189/S0022143000031208

Das, I., Padman, L., Bell, R.E., Fricker, H.A., Tinto, K.J., Hulbe, C.L., Siddoway, C.S., Dhakal, T., Frearson, N.P., Mosbeux, C. and Cordero, S.I., 2020. Multidecadal basal melt rates and structure of the Ross Ice Shelf, Antarctica, using airborne ice penetrating radar. *Journal of Geophysical Research: Earth Surface*, 125(3), e2019JF005241. DOI: 10.1029/2019JF005241

Dattler, M.E., Lenaerts, J.T. and Medley, B., 2019. Significant spatial variability in radar-derived west Antarctic accumulation linked to surface winds and topography. *Geophysical Reseach Letters*, 46(22), pp.13126-13134. DOI: 10.1029/2019GL085363

Davies, D., Bingham, R.G., King, E.C., Smith, A.M., Brisbourne, A.M., Spagnolo, M., Graham, A.G., Hogg, A.E. and Vaughan, D.G., 2018. How dynamic are ice-stream beds?. *The Cryosphere*, 12(5), pp.1615-1628. DOI: 10.5194/tc-12-1615-2018

DeConto, R.M. and Pollard, D., 2016. Contribution of Antarctica to past and future sea-level rise. *Nature*, 531(7596), pp.591-597. DOI: 10.1038/nature17145

DeConto, R.M., Pollard, D., Alley, R.B., Velicogna, I., Gasson, E., Gomez, N., Sadai, S., Condron, A., Gilford, D.M., Ashe, E.L. and Kopp, R.E., 2021. The Paris

Climate Agreement and future sea-level rise from Antarctica. *Nature*, 593(7857), pp.83-89. DOI: 10.1038/s41586-021-03427-0

Delf, R., Schroeder, D.M., Curtis, A., Giannopoulos, A. and Bingham, R.G., 2020. A comparison of automated approaches to extracting englacial-layer geometry from radar data across ice sheets. *Annals of Glaciology*, 61(81), pp.234-241. DOI: 10.1017/aog.2020.42

Denton, G.H. and Hughes, T.J., 2002. Reconstructing the Antarctic ice sheet at the Last Glacial Maximum. *Quaternary Science Reviews*, 21(1-3), pp.193-202. DOI: 10.1016/S0277-3791(01)00090-7

Depoorter, M.A., Bamber, J.L., Griggs, J.A., Lenaerts, J.T.M., Ligtenberg, S.R.M., Van den Broeke, M.R. and Moholdt, G., 2013. Calving fluxes and basal melt rates of Antarctic ice shelves. *Nature*, 502(7469), pp.89-92. DOI: 10.1038/nature12567. DOI: 10.1038/nature12567

Diez, A., Matsuoka, K., Ferraccioli, F., Jordan, T.A., Corr, H.F., Kohler, J., Olesen, A.V. and Forsberg, R., 2018. Basal settings control fast ice flow in the Recovery/Slessor/Bailey Region, East Antarctica. *Geophysical Research Letters*, 45(6), pp.2706-2715. DOI: 10.1002/2017GL076601

Diez, A., Matsuoka, K., Jordan, T.A., Kohler, J., Ferraccioli, F., Corr, H.F., Olesen, A.V., Forsberg, R. and Casal, T.G., 2019. Patchy lakes and topographic origin for fast flow in the Recovery Glacier system, East Antarctica. *Journal of Geophysical Research: Earth Surface*, 124(2), pp.287-304. DOI: 10.1029/2018JF004799

Dow, C.F., Ross, N., Jeofry, H., Siu, K. and Siegert, M.J., 2022. Antarctic basal environment shaped by high-pressure flow through a subglacial river system. *Nature Geoscience*, 15(11), pp.892-898. DOI: 10.1038/s41561-022-01059-1

Dowdeswell, J.A. and Evans, S., 2004. Investigations of the form and flow of ice sheets and glaciers using radio-echo sounding. *Reports on Progress in Physics*, 67(10), pp.1821-1861. DOI: 10.1088/0034-4885/67/10/R03

Drewry, D.J., Jordan, S.R. and Jankowski, E., 1982. Measured properties of the Antarctic ice sheet: surface configuration, ice thickness, volume and bedrock characteristics. *Annals of Glaciology*, 3, pp.83-91. DOI: 10.3189/S0260305500002573

Drewry, D. J., 1983. *Antarctica: glaciological and geophysical folio*. University of Cambridge, Scott Polar Research Institute Cambridge, United Kingdom

Drews, R., Eisen, O., Weikusat, I., Kipfstuhl, S., Lambrecht, A., Steinhage, D., Wilhelms, F. and Miller, H., 2009. Layer disturbances and the radio-echo free zone in ice sheets. *The Cryosphere*, 3(2), pp.195-203. DOI: 10.5194/tc-3-195-2009

Drews, R., Matsuoka, K., Martín, C., Callens, D., Bergeot, N. and Pattyn, F., 2015. Evolution of Derwael ice rise in Dronning Maud Land, Antarctica, over the last millennia. *Journal of Geophysical Research: Earth Surface*, 120(3), pp.564-579. DOI: 10.1002/2014JF003246

Drews, R., Pattyn, F., Hewitt, I.J., Ng, F.S.L., Berger, S., Matsuoka, K., Helm, V., Bergeot, N., Favier, L. and Neckel, N., 2017. Actively evolving subglacial conduits and eskers initiate ice shelf channels at an Antarctic grounding line. *Nature communications*, 8(1), 15228. DOI: 10.1038/ncomms15228

Dutrieux, P., De Rydt, J., Jenkins, A., Holland, P.R., Ha, H.K., Lee, S.H., Steig, E.J., Ding, Q., Abrahamsen, E.P. and Schröder, M., 2014. Strong sensitivity of Pine Island ice-shelf melting to climatic variability. *Science*, 343(6167), pp.174-178. DOI: 10.1126/science.1244341

Edwards, T.L., Brandon, M.A., Durand, G., Edwards, N.R., Golledge, N.R., Holden, P.B., Nias, I.J., Payne, A.J., Ritz, C. and Wernecke, A., 2019. Revisiting Antarctic ice loss due to marine ice-cliff instability. *Nature*, 566(7742), pp.58-64. DOI: 10.1038/s41586-019-0901-4

Eagles, G., Karlsson, N.B., Ruppel, A., Steinhage, D., Jokat, W. and Läufer, A., 2018. Erosion at extended continental margins: Insights from new aerogeophysical data in eastern Dronning Maud Land. Gondwana Research, 63, pp.105-116. DOI: 10.1016/j.gr.2018.05.011

Elderfield, H., Ferretti, P., Greaves, M., Crowhurst, S., McCave, I.N., Hodell, D. and Piotrowski, A.M., 2012. Evolution of ocean temperature and ice volume through the mid-Pleistocene climate transition. Science, 337(6095), pp.704-709. DOI: 10.1126/science.1221294

Evans, S., Drewry, D.J. and Robin, G.D.Q., 1972. Radio-echo sounding in Antarctica, 1971–72. *Polar Record*, 16(101), pp.207-212. DOI: 10.1017/S003224740006280X

Fahnestock, M., Abdalati, W., Joughin, I., Brozena, J., and Gogineni, P., 2001a. High geothermal heat flow, basal melt, and the origin of rapid ice flow in central Greenland. *Science*, 294(5550), pp.2238–2342. DOI: 1126/science.1065370

Fahnestock, M., Abdalati, W., Luo, S. and Gogineni, S., 2001b. Internal layer tracing and age-depth-accumulation relationships for the northern Greenland ice sheet. *Journal of Geophysical Research: Atmospheres*, 106(D24), pp.33789-33797. DOI: 10.1029/2001JD900200

Farinotti, D., Corr, H. and Gudmundsson, G.H., 2013. The ice thickness distribution of Flask Glacier, Antarctic Peninsula, determined by combining radio-echo soundings, surface velocity data and flow modelling. *Annals of Glaciology*, 54(63), pp.18-24. DOI: 10.3189/2013AoG63A603

Favier, V., Agosta, C., Parouty, S., Durand, G., Delaygue, G., Gallée, H., Drouet, A.-S., Trouvilliez, A., and Krinner, G., 2013. An updated and quality controlled surface mass balance dataset for Antarctica. *The Cryosphere*, 7(2), pp.583-597. DOI: 10.5194/tc-7-583-2013

Favier, L., Durand, G., Cornford, S.L., Gudmundsson, G.H., Gagliardini, O., Gillet-Chaulet, F., Zwinger, T., Payne, A.J. and Le Brocq, A.M., 2014. Retreat of Pine Island Glacier controlled by marine ice-sheet instability. *Nature Climate Change*, 4(2), pp.117-121. DOI: 10.1038/NCLIMATE2094

Ferraccioli, F., Gambetta, M. and Bozzo, E., 1998. Microlevelling procedures applied to regional aeromagnetic data: an example from the Transantarctic Mountains (Antarctica). *Geophysical Prospect*, 46(2), pp.177-196. DOI: 10.1046/j.1365-2478.1998.00080.x

Ferraccioli, F., Jones, P.C., Curtis, M.L. and Leat, P.T., 2005a. Subglacial imprints of early Gondwana break-up as identified from high resolution aerogeophysical data over western Dronning Maud Land, East Antarctica. *Terra Nova*, 17(6), pp.573-579. DOI: 10.1111/j.1365-3121.2005.00651.x

Ferraccioli, F., Jones, P. C., Curtis, M. L., Leat, P. T., and Riley, T. R., 2005b. Tectonic and magmatic patterns in the Jutulstraumen rift (?) region, East Antarctica, as imaged by high-resolution aeromagnetic data. *Earth, Planets and Space*, 57(8), pp.767-780. DOI: 10.1186/BF03351856

Ferraccioli, F., Jones, P.C., Vaughan, A.P.M. and Leat, P.T., 2006. New aerogeophysical view of the Antarctic Peninsula: More pieces, less puzzle. *Geophysical Research Letters*, 33(5), L05310. DOI: 10.1029/2005GL024636

Ferraccioli, F., Jordan, T., Armadillo, E., Bozzo, E., Corr, H., Caneva, G., Robinson, C., Frearson, N. and Tabacco, I., 2007. Collaborative aerogeophysical campaign targets the Wilkes Subglacial Basin, the Transantarctic Mountains and the Dome C region. *Terra Antarctica Report*, 13, pp.1-36. DOI: https://nora.nerc.ac.uk/id/eprint/13741 (last access: 05 April 2023)

Ferraccioli, F., Armadillo, E., Jordan, T., Bozzo, E. and Corr, H., 2009. Aeromagnetic exploration over the East Antarctic Ice Sheet: a new view of the Wilkes Subglacial Basin. *Tectonophysics*, 478(1-2), pp.62-77. DOI: 10.1016/j.tecto.2009.03.013

Ferraccioli, F., Finn, C.A., Jordan, T.A., Bell, R.E., Anderson, L.M. and Damaske, D., 2011. East Antarctic rifting triggers uplift of the Gamburtsev Mountains. *Nature*, 479(7373), pp.388-392. DOI: 10.1038/nature10566

Ferris, J.K., Vaughan, A.P. and King, E.C., 2002. A window on West Antarctic crustal boundaries: the junction between the Antarctic Peninsula, the Filchner Block, and Weddell Sea oceanic lithosphere. *Tectonophysics*, 347(1-3), pp.13-23. DOI: 10.1016/S0040-1951(01)00235-9

Ferris, J.K., Storey, B.C., Vaughan, A.P., Kyle, P.R. and Jones, P.C., 2003. The Dufek and Forrestal intrusions, Antarctica: A centre for Ferrar large igneous province dike emplacement?. *Geophysical Research Letters*, 30(6), 1348. DOI: 10.1029/2002GL016719

Forsberg, R., Olesen, A. V., Ferraccioli, F., Jordan, T., Corr, H., and Matsuoka, K., 2017. PolarGap 2015/16 Filling the GOCE polar gap in Antarctica and ASIRAS flight around South Pole. *European Space Agency* [data set]. DOI: 10.5270/esa-8ffoo3e

Forsberg, R., Olesen, A.V., Ferraccioli, F., Jordan, T.A., Matsuoka, K., Zakrajsek, A., Ghidella, M. and Greenbaum, J.S., 2018. Exploring the Recovery Lakes region and interior Dronning Maud Land, East Antarctica, with airborne gravity, magnetic and radar measurements. *Geological Society of London Special Publications*, 461(1), pp.23-34. DOI: 10.1144/SP461.17

Frederick, B.C., Young, D.A., Blankenship, D.D., Richter, T.G., Kempf, S.D., Ferraccioli, F. and Siegert, M.J., 2016. Distribution of subglacial sediments across the Wilkes Subglacial Basin, East Antarctica. *Journal of Geophysical Research: Earth Surface*, 121(4), pp.790-813. DOI: 10.1002/2015JF003760

Frémand, A.C., Bodart, J.A., Jordan, T.A., Ferraccioli, F., Robinson, C., Corr, H.F., Peat, H.J., Bingham, R.G. and Vaughan, D.G., 2022. British Antarctic Survey's Aerogeophysical Data: Releasing 25 Years of Airborne Gravity, Magnetic, and Radar Datasets over Antarctica. *Earth System Science Data*, 14(7), pp.3379–3410. DOI: 10.5194/essd-14-3379-2022

Frémand, A.C., Fretwell, P., Bodart, J.A., Pritchard, H.D., Aitken, A., Bamber, J.L., Bell, R., Bianchi, C., Bingham, R.G., Blankenship, D.D., Casassa, G., et al., 2023. Antarctic Bedmap data: FAIR sharing of 60 years of ice bed, surface and thickness data. *Earth System Science Data Discussions*. DOI: 10.5194/essd-2022-355 [in press]

Fretwell, P., Pritchard, H.D., Vaughan, D.G., Bamber, J.L., Barrand, N.E., Bell, R., Bianchi, C., Bingham, R.G., Blankenship, D.D., Casassa, G. and Catania, G., 2013. Bedmap2: improved ice bed, surface and thickness datasets for Antarctica. *The Cryosphere*, 7(1), pp.375-393. DOI: 10.5194/tc-7-375-2013

Fudge, T.J., Markle, B.R., Cuffey, K.M., Buizert, C., Taylor, K.C., Steig, E.J., Waddington, E.D., Conway, H. and Koutnik, M., 2016. Variable relationship between accumulation and temperature in West Antarctica for the past 31,000 years. *Geophysical Research Letters*, 43(8), pp.3795-3803. DOI: 10.1002/2016GL068356

Fudge, T. J., Buizert, C., Conway, H., and Waddington, E. D., 2017. Accumulation Rates from the WAIS Divide Ice Core, v.1.0.0. *U.S. Antarctic Program Data Center* [data set]. DOI: 10.15784/601004

Fudge, T.J., Biyani, S.C., Clemens-Sewall, D. and Hawley, R.L., 2019. Constraining geothermal flux at coastal domes of the Ross Ice Sheet, Antarctica. *Geophysical Research Letters*, 46(22), pp.13090-13098. DOI: 10.1029/2019GL08433

Fudge, T.J., Hills, B.H., Horlings, A.N., Holschuh, N., Christian, J.E., Davidge, L., Hoffman, A., O'Connor, G.K., Christianson, K. and Steig, E.J., 2022. A site for deep ice coring at West Hercules Dome: results from ground-based geophysics and modeling. Journal of Glaciology, pp.1-13. DOI: 10.1017/jog.2022.80

Fujita, S., Matsuoka, T., Ishida, T., Matsuoka, K., and Mae, S., 2000. *A summary of the complex dielectric permittivity of ice in the megahertz range and its applications for radar sounding of polar ice sheets.* In T. Hondoh (Ed.), Physics of ice core records (pp. 185–212). Sapporo: Hokkaido University Press

Eisen, O., Wilhelms, F., Nixdorf, U. and Miller, H., 2003. Identifying isochrones in GPR profiles from DEP-based forward modeling. *Annals of Glaciology*, 37, pp.344-350. DOI: 10.3189/172756403781816068

Eisen, O., Rack, W., Nixdorf, U. and Wilhelms, F., 2005. Characteristics of accumulation around the EPICA deep-drilling site in Dronning Maud Land, Antarctica. *Annals of Glaciology*, 41, pp.41-46. DOI: 10.3189/172756405781813276

Eisen, O., Wilhelms, F., Steinhage, D. and Schwander, J., 2006. Improved method to determine radio-echo sounding reflector depths from ice-core profiles of permittivity and conductivity. *Journal of Glaciology*, 52(177), pp.299-310. DOI: 10.3189/172756506781828674

Eisen, O., Frezzotti, M., Genthon, C., Isaksson, E., Magand, O., van den Broeke, M.R., Dixon, D.A., Ekaykin, A., Holmlund, P., Kameda, T. and Karlöf, L., 2008. Ground-based measurements of spatial and temporal variability of snow accumulation in East Antarctica. *Reviews of Geophysics*, 46(2), RG2001. DOI: 10.1029/2006RG000218

Eisen, O., Winter, A., Steinhage, D., Kleiner, T. and Humbert, A., 2020. Basal roughness of the East Antarctic Ice Sheet in relation to flow speed and basal thermal state. *Annals of Glaciology*, 61(81), pp.162-175. DOI: 10.1017/aog.2020.47

EPICA Community Members, 2004. Eight glacial cycles from an Antarctic ice core. *Nature*, 429(6992), pp.623-628. DOI: 10.1038/nature02599

Gades, A.M., Raymond, C.F., Conway, H. and Jagobel, R.W., 2000. Bed properties of Siple Dome and adjacent ice streams, West Antarctica, inferred from radio-echo sounding measurements.*Journal of Glaciology*, 46(152), pp.88-94. DOI: 172756500781833467

Gardner, A.S., Moholdt, G., Scambos, T., Fahnestock, M., Ligtenberg, S., van den Broeke, M. and Nilsson, J., 2018. Increased West Antarctic and unchanged East Antarctic ice discharge over the last 7 years. *The Cryosphere*, 12(2), pp.521-547. DOI: 10.5194/tc-12-521-2018

Global Change Master Directory (GCMD), 2021. *GCMD Keywords, v.12.2.* Greenbelt, MD: Earth Science Data and Information System, Earth Science Projects Division, Goddard Space Flight Center (GSFC) National Aeronautics and Space Administration (NASA). DOI: https://forum.earthdata.nasa.gov/app.php/tag/GCMD+Keywords (last access: 05 April 2023)

Golledge, N.R., Fogwill, C.J., Mackintosh, A.N. and Buckley, K.M., 2012. Dynamics of the last glacial maximum Antarctic ice-sheet and its response to ocean forcing. *Proceedings of the National Academy of Sciences*, 109(40), pp.16052-16056. DOI: 10.1073/pnas.1205385109

Golledge, N.R., Levy, R.H., McKay, R.M., Fogwill, C.J., White, D.A., Graham, A.G., Smith, J.A., Hillenbrand, C.D., Licht, K.J., Denton, G.H. and Ackert Jr, R.P., 2013. Glaciology and geological signature of the Last Glacial Maximum Antarctic ice sheet. textitQuaternary Science Reviews, 78, pp.225-247. DOI: 10.1016/j.quascirev.2013.08.011

Golledge, N.R., Menviel, L., Carter, L., Fogwill, C.J., England, M.H., Cortese, G. and Levy, R.H., 2014. Antarctic contribution to meltwater pulse 1A from reduced Southern Ocean overturning. *Nature Communications*, 5(1), 5107. DOI: 10.1038/ncomms6107

Golledge, N.R., Clark, P.U., He, F., Dutton, A., Turney, C.S.M., Fogwill, C.J., Naish, T.R., Levy, R.H., McKay, R.M., Lowry, D.P. and Bertler, N.A., 2021. Retreat of the Antarctic Ice Sheet during the Last Interglaciation and implications for future change. *Geophysical Research Letters*, 48(17), e2021GL094513. DOI: 10.1029/2021GL094513

Golynsky, A.V., Ferraccioli, F., Hong, J.K., Golynsky, D.A., von Frese, R.R.B., Young, D.A., Blankenship, D.D., Holt, J.W., Ivanov, S.V., Kiselev, A.V. and Masolov, V.N., 2018. New magnetic anomaly map of the Antarctic. *Geophysical Research Letters*, 45(13), pp.6437-6449. DOI: 10.1029/2018GL078153

Goodge, J.W. and Finn, C.A., 2010. Glimpses of East Antarctica: Aeromagnetic and satellite magnetic view from the central Transantarctic Mountains of East Antarctica. *Journal of Geophysical Research: Solid Earth*, 115(B9), B09103. DOI: 10.1029/2009JB006890

Gow, A.J., Ueda, H.T., Garfield, D.E., 1968. Antarctic ice sheet: preliminary results of first core hole to bedrock. *Science*, 161(3845), pp.1011-1013. DOI: 10.1126/science.161.3845.1011

Gow, A. J. (1970). *Preliminary results of studies of ice cores from the 2164m-deep drill hole, Byrd Station, Antarctica.* Antarctic Glaciological Exploration (ISAGE), Redbooks, 86, pp.78–90. UK: IAHS

Greenbaum, J.S., Blankenship, D.D., Young, D.A., Richter, T.G., Roberts, J.L., Aitken, A.R.A., Legresy, B., Schroeder, D.M., Warner, R.C., Van Ommen, T.D. and Siegert, M.J., 2015. Ocean access to a cavity beneath Totten Glacier in East Antarctica. *Nature Geoscience*, 8(4), pp.294-298. DOI: 10.1038/ngeo2388

Greene, C. A., Gwyther, D. E., and Blankenship, D. D., 2017. Antarctic Mapping Tools for Matlab. *Computers and Geosciences.* 104, pp.151-157. DOI: 10.1016/j.cageo.2016.08.003

Hackney, R.I. and Featherstone, W.E., 2003. Geodetic versus geophysical perspectives of the 'gravity anomaly'. *Geophysical Journal International*, 154(1), pp.35-43. DOI: 10.1046/j.1365-246X.2003.01941.x

Hammer, C.U., 1977. Past volcanism revealed by Greenland ice sheet impurities. *Nature*, 270, pp.482-486. DOI: 10.1038/270482a0

Hammer, C.U., 1980. Acidity of polar ice cores in relation to absolute dating, past volcanism, and radio–echoes. *Journal of Glaciology*, 25(93), pp.359-372. DOI: 10.3189/S0022143000015227

Hammer, C.U., Clausen, H.B. and Langway, C.C., 1997. 50,000 years of recorded global volcanism. *Climatic Change*, 35(1), pp.1-15. DOI: 10.1023/A:1005344225434

Haran, T., M. Klinger, J. Bohlander, M. Fahnestock, T. Painter, and T. Scambos, 2018. MEaSUREs MODIS Mosaic of Antarctica 2013-2014 (MOA2014) Image Map, v.1.0.0. *NASA National Snow and Ice Data Center* [data set]. DOI: 10.5067/RNF17BP824UM

Harlan, R.B., 1968. Eotvos corrections for airborne gravimetry. *Journal of Geophysical Research*, 73(14), pp.4675-4679. DOI: 10.1029/JB073i014p04675

Harrison, C.H., 1973. Radio echo sounding of horizontal layers in ice. *Journal of glaciology*, 12(66), pp.383-397. DOI: 10.3189/S0022143000031804

Hartman, L.H., Kurbatov, A.V., Winski, D.A., Cruz-Uribe, A.M., Davies, S.M., Dunbar, N.W., Iverson, N.A., Aydin, M., Fegyveresi, J.M., Ferris, D.G. and Fudge, T.J., 2019. Volcanic glass properties from 1459 CE volcanic event in South Pole ice core dismiss Kuwae caldera as a potential source. *Scientific reports*, 9(1), pp.1-7. DOI: 10.1038/s41598-019-50939-x

Hein, A.S., Woodward, J., Marrero, S.M., Dunning, S.A., Steig, E.J., Freeman, S.P., Stuart, F.M., Winter, K., Westoby, M.J. and Sugden, D.E., 2016a. Evidence for the stability of the West Antarctic Ice Sheet divide for 1.4 million years. *Nature communications*, 7(1), 10325. DOI: 10.1038/ncomms10325

Hein, A.S., Marrero, S.M., Woodward, J., Dunning, S.A., Winter, K., Westoby, M.J., Freeman, S.P., Shanks, R.P. and Sugden, D.E., 2016b. Mid-Holocene pulse of thinning in the Weddell Sea sector of the West Antarctic ice sheet. *Nature Communications*, 7(1), 12511. DOI: 10.1038/ncomms12511

Hélière, F., Lin, C.C., Corr, H. and Vaughan, D., 2007. Radio echo sounding of Pine Island Glacier, West Antarctica: Aperture synthesis processing and analysis of feasibility from space. *IEEE Transactions on Geoscience and Remote Sensing*, 45(8), pp.2573-2582. DOI: 10.1109/TGRS.2007.897433

Hillenbrand, C.D., Kuhn, G., Smith, J.A., Gohl, K., Graham, A.G., Larter, R.D., Klages, J.P., Downey, R., Moreton, S.G., Forwick, M. and Vaughan, D.G., 2013. Grounding-line retreat of the west Antarctic ice sheet from inner Pine island Bay. *Geology*, 41(1), pp.35-38. DOI: 10.1130/G33469.1

Hillenbrand, C.D., Bentley, M.J., Stolldorf, T.D., Hein, A.S., Kuhn, G., Graham, A.G., Fogwill, C.J., Kristoffersen, Y., Smith, J.A., Anderson, J.B. and Larter, R.D., 2014. Reconstruction of changes in the Weddell Sea sector of the Antarctic Ice Sheet since the Last Glacial Maximum. *Quaternary Science Reviews*, 100, pp.111-136. DOI: 10.1016/j.quascirev.2013.07.020

Hillenbrand, C.D., Smith, J.A., Hodell, D.A., Greaves, M., Poole, C.R., Kender, S., Williams, M., Andersen, T.J., Jernas, P.E., Elderfield, H. and Klages, J.P., 2017. West Antarctic Ice Sheet retreat driven by Holocene warm water incursions. *Nature*, 547(7661), 43-48. DOI: 10.1038/nature22995

Hindmarsh, R.C., Gwendolyn, J.M. and Parrenin, F., 2009. A large-scale numerical model for computing isochrone geometry. *Annals of Glaciology*, 50(51), pp.130-140. DOI: 10.3189/172756409789097450

Hindmarsh, R.C., King, E.C., Mulvaney, R., Corr, H.F., Hiess, G. and Gillet-Chaulet, F., 2011. Flow at ice-divide triple junctions: 2. Three-dimensional views of isochrone architecture from ice-penetrating radar surveys. *Journal of Geophysical Research: Earth Surface*, 116(F2), F02024. DOI: 10.1029/2009JF001622

Hodgson, D.A., Jordan, T.A., Rydt, J.D., Fretwell, P.T., Seddon, S.A., Becker, D., Hogan, K.A., Smith, A.M. and Vaughan, D.G., 2019. Past and future dynamics of the Brunt Ice Shelf from seabed bathymetry and ice shelf geometry. *The Cryosphere*, 13(2), pp.545-556. DOI: 10.5194/tc-13-545-2019

Hofstede, C., Beyer, S., Corr, H., Eisen, O., Hattermann, T., Helm, V., Neckel, N., Smith, E.C., Steinhage, D., Zeising, O. and Humbert, A., 2021. Evidence for a grounding line fan at the onset of a basal channel under the ice shelf of Support Force Glacier, Antarctica, revealed by reflection seismics. *The Cryosphere*, 15(3), pp.1517-1535. DOI: 10.5194/tc-15-1517-2021

Hogan, K.A., Larter, R.D., Graham, A.G., Arthern, R., Kirkham, J.D., Totten Minzoni, R., Jordan, T.A., Clark, R., Fitzgerald, V., Wåhlin, A.K. and Anderson, J.B., 2020. Revealing the former bed of Thwaites Glacier using sea-floor bathymetry: implications for warm-water routing and bed controls on ice flow and buttressing. *The Cryosphere*, 14(9), pp.2883-2908. DOI: 10.5194/tc-14-2883-2020

Holland, P.R., Corr, H.F., Vaughan, D.G., Jenkins, A. and Skvarca, P., 2009. Marine ice in Larsen ice shelf. *Geophysical Research Letters*, 36(11), L11604. DOI: 10.1029/2009GL038162

Holland, P.R., Jenkins, A. and Holland, D.M., 2010. Ice and ocean processes in the Bellingshausen Sea, Antarctica. *Journal of Geophysical Research: Oceans*, 115(C5), C05020. DOI: 10.1029/2008JC005219

Holland, P.R., Corr, H.F., Pritchard, H.D., Vaughan, D.G., Arthern, R.J., Jenkins, A. and Tedesco, M., 2011. The air content of Larsen ice shelf. *Geophysical Research Letters*, 38(10), L10503. DOI: 10.1029/2011GL047245

Holland, P.R., Bracegirdle, T.J., Dutrieux, P., Jenkins, A. and Steig, E.J., 2019.

West Antarctic ice loss influenced by internal climate variability and anthropogenic forcing.*Nature Geoscience*, 12(9), pp.718-724. DOI: 10.1038/s41561-019-0420-9

Holloway, M.D., Sime, L.C., Singarayer, J.S., Tindall, J.C., Bunch, P. and Valdes, P.J., 2016. Antarctic last interglacial isotope peak in response to sea ice retreat not ice-sheet collapse. *Nature communications*, 7(1), pp.12293. DOI: 10.1038/ncomms12293

Holschuh, N., Christianson, K. and Anandakrishnan, S., 2014. Power loss in dipping internal reflectors, imaged using ice-penetrating radar. *Annals of Glaciology*, 55(67), pp.49-56. DOI: 10.3189/2014AoG67A005

Holschuh, N., Parizek, B.R., Alley, R.B. and Anandakrishnan, S., 2017. Decoding ice sheet behavior using englacial layer slopes. *Geophysical Research Letters*, 44(11), pp.5561-5570. DOI: 10.1002/2017GL073417

Holschuh, N., Christianson, K., Conway, H., Jacobel, R.W. and Welch, B.C., 2018. Persistent tracers of historic ice flow in glacial stratigraphy near Kamb Ice Stream, West Antarctica. *The Cryosphere*, 12(9), pp.2821-2829. DOI: 10.5194/tc-12-2821-2018

Holschuh, N., Christianson, K., Paden, J., Alley, R.B. and Anandakrishnan, S., 2020. Linking postglacial landscapes to glacier dynamics using swath radar at Thwaites Glacier, Antarctica. *Geology*, 48(3), pp.268-272. DOI: 10.1130/G46772.1

Holt, J.W., Blankenship, D.D., Morse, D.L., Young, D.A., Peters, M.E., Kempf, S.D., Richter, T.G., Vaughan, D.G. and Corr, H.F., 2006. New boundary conditions for the West Antarctic Ice Sheet: Subglacial topography of the Thwaites and Smith glacier catchments. *Geophysical Research Letters*, 33(9), L09501. DOI: 10.1029/2005GL025561

Howat, I.M., Porter, C., Smith, B.E., Noh, M.J. and Morin, P., 2019. The reference elevation model of Antarctica. *The Cryosphere*, 13(2), pp.665-674. DOI: 10.5194/tc-13-665-2019

IPCC AR6, 2021: Climate Change 2021: *The Physical Science Basis. Contribution of Working Group I to the Sixth Assessment Report of the Intergovernmental Panel on Climate Change* [Masson-Delmotte, V., P. Zhai, A. Pirani, S.L. Connors, C. Péan, S. Berger, N. Caud, Y. Chen, L. Goldfarb, M.I. Gomis, M.

Huang, K. Leitzell, E. Lonnoy, J.B.R. Matthews, T.K. Maycock, T. Waterfield, O. Yelekçi, R. Yu, and B. Zhou (eds.)]. Cambridge University Press. In Press. DOI: 10.1017/9781009157896

Jacobel, R.W., Gades, A.M., Gottschling, D.L., Hodge, S.M., and Wright, L.M., 1993. Interpretation of radar-detected internal layer folding in West Antarctic ice streams. *Journal of Glaciology*, 39(133), pp. 528-537. DOI: 110.3189/S0022143000016427

Jacobel, R.W., Scambos, T.A., Raymond, C.F. and Gades, A.M., 1996. Changes in the configuration of ice stream flow from the West Antarctic Ice Sheet. *Journal of Geophysical Research: Solid Earth*, 101(B3), pp.5499-5504. DOI: 10.1029/95JB03735

Jacobel, R.W., Scambos, T.A., Nereson, N.A. and Raymond, C.F., 2000. Changes in the margin of Ice Stream C, Antarctica. *Journal of Glaciology*, 46(152), pp.102-110. DOI: 10.3189/172756500781833485

Jacobel, R.W. and Welch, B.C., 2005. A time marker at 17.5 ka BP detected throughout West Antarctica. *Annals of Glaciology*, 41, pp.47-51. DOI: 10.3189/172756405781813348

Jakobsson, M., Anderson, J.B., Nitsche, F.O., Dowdeswell, J.A., Gyllencreutz, R., Kirchner, N., Mohammad, R., O'Regan, M., Alley, R.B., Anandakrishnan, S. and Eriksson, B., 2011. Geological record of ice shelf break-up and grounding line retreat, Pine Island Bay, West Antarctica. *Geology*, 39(7), pp.691-694. DOI: 10.1130/G32153.1

Jeofry, H., Ross, N., Corr, H.F., Li, J., Morlighem, M., Gogineni, P. and Siegert, M.J., 2018. A new bed elevation model for the Weddell Sea sector of the West Antarctic Ice Sheet. *Earth System Science Data*, 10(2), pp.711-725. DOI: 10.5194/essd-10-711-2018

Johnson, A., Cheeseman, S. and Ferris, J., 1999. Improved compilation of Antarctic Peninsula magnetic data by new interactive grid suturing and blending methods. *Annals of Geophysics - Italy*, 42(2), pp.249-259. DOI: 10.4401/ag-3717

Johnson, J.S., Bentley, M.J. and Gohl, K., 2008. First exposure ages from the Amundsen Sea embayment, West Antarctica: The late Quaternary context for recent thinning of Pine Island, Smith, and Pope Glaciers. *Geology*, 36(3), pp.223-

226. DOI: 10.1130/G24207A.1

Johnson, J.S., Bentley, M.J., Smith, J.A., Finkel, R.C., Rood, D.H., Gohl, K., Balco, G., Larter, R.D. and Schaefer, J.M., 2014. Rapid thinning of Pine Island Glacier in the early Holocene. *Science*, 343(6174), pp.999-1001. DOI: 10.1126/science.1247385

Johnson, J.S., Smith, J.A., Schaefer, J.M., Young, N.E., Goehring, B.M., Hillenbrand, C.D., Lamp, J.L., Finkel, R.C. and Gohl, K., 2017. The last glaciation of Bear Peninsula, central Amundsen Sea Embayment of Antarctica: Constraints on timing and duration revealed by in situ cosmogenic 14C and 10Be dating. *Quaternary Science Reviews*, 178, pp.77-88. DOI: 10.1016/j.quascirev.2017.11.003

Johnson, J.S., Roberts, S.J., Rood, D.H., Pollard, D., Schaefer, J.M., Whitehouse, P.L., Ireland, L.C., Lamp, J.L., Goehring, B.M., Rand, C. and Smith, J.A., 2020. Deglaciation of Pope Glacier implies widespread early Holocene ice sheet thinning in the Amundsen Sea sector of Antarctica. *Earth and Planetary Science Letters*, 548, 116501. DOI: 10.1016/j.epsl.2020.116501

Johnson, J.S., Pollard, D., Whitehouse, P.L., Roberts, S.J., Rood, D.H. and Schaefer, J.M., 2021. Comparing glacial-geological evidence and model simulations of ice sheet change since the last glacial period in the Amundsen Sea sector of Antarctica. *Journal of Geophysical Research: Earth Surface*, 126(6), e2020JF005827. DOI: 10.1029/2020JF005827

Johnson, J.S., Venturelli, R.A., Balco, G., Allen, C.S., Braddock, S., Campbell, S., Goehring, B.M., Hall, B.L., Neff, P.D., Nichols, K.A. and Rood, D.H., 2022. Existing and potential evidence for Holocene grounding line retreat and readvance in Antarctica. *The Cryosphere*, 16(5), pp.1543-1562. DOI: 10.5194/tc-16-1543-2022

Jones, P.C., Johnson, A.C., von Frese, R.R. and Corr, H., 2002. Detecting rift basins in the Evans Ice Stream region of West Antarctica using airborne gravity data. *Tectonophysics*, 347(1-3), pp.25-41. DOI: 10.1016/S0040-1951(01)00236-0

Jones, R.S., Johnson, J.S., Lin, Y., Mackintosh, A.N., Sefton, J.P., Smith, J.A., Thomas, E.R. and Whitehouse, P.L., 2022 Stability of the Antarctic Ice Sheet during the pre-industrial Holocene. *Nature Reviews Earth and Environment*, 3(8), pp.500-515. DOI: 10.1038/s43017-022-00309-5

Jordan, T., Ferraccioli, F., Corr, H., Robinson, C., Caneva, G., Armadillo, E., Bozzo, E. and Frearson, N., 2007. Linking the Wilkes Subglacial Basin the Transantarctic Mountains and the Ross Sea with a new airborne gravity survey. *Terra Antarctica Reports*, 13, pp.37-54. DOI: https://nora.nerc.ac.uk/id/eprint/15749 (last access: 05 April 2023)

Jordan, T.A., Ferraccioli, F., Jones, P.C., Smellie, J.L., Ghidella, M. and Corr, H., 2009. Airborne gravity reveals interior of Antarctic volcano. *Physics of the Earth and Planetary Interiors*, 175(3-4), pp.127-136. DOI: 10.1016/j.pepi.2009.03.004

Jordan, T.A., Ferraccioli, F., Corr, H., Graham, A., Armadillo, E. and Bozzo, E., 2010. Hypothesis for mega-outburst flooding from a palaeo-subglacial lake beneath the East Antarctic Ice Sheet. *Terra Nova*, 22(4), pp.283-289. DOI: 10.1111/j.1365-3121.2010.00944.x

Jordan, T. A., Ferraccioli, F., Vaughan, D. G., Holt, J. W., Corr, H., Blankenship, D. D., and Diehl, T. M., 2010b. Aerogravity evidence for major crustal thinning under the Pine Island Glacier region (West Antarctica). *Bulletin*, 122(5-6), pp.714-726. DOI: 10.1130/B26417.1

Jordan, T.A., Ferraccioli, F., Armadillo, E. and Bozzo, E., 2013. Crustal architecture of the Wilkes Subglacial Basin in East Antarctica, as revealed from airborne gravity data. *Tectonophysics*, 585, pp.196-206. DOI: 10.1016/j.tecto.2012.06.041

Jordan, T.A., Neale, R.F., Leat, P.T., Vaughan, A.P.M., Flowerdew, M.J., Riley, T.R., Whitehouse, M.J. and Ferraccioli, F., 2014. Structure and evolution of Cenozoic arc magmatism on the Antarctic Peninsula: a high resolution aeromagnetic perspective. *Geophysical Journal International*, 198(3), pp.1758-1774. DOI: 10.1093/gji/ggu233

Jordan, T.A., Martín, C., Ferraccioli, F., Matsuoka, K., Corr, H., Forsberg, R., Olesen, A. and Siegert, M., 2018. Anomalously high geothermal flux near the South Pole. *Scientific Reports*, 8(1), pp.1-8. DOI: 10.1038/s41598-018-35182-0

Jordan, T.A. and Becker, D., 2018. Investigating the distribution of magmatism at the onset of Gondwana breakup with novel strapdown gravity and aeromagnetic data. *Physics of the Earth and Planetary Interiors*, 282, pp.77-88. DOI: 10.1016/j.pepi.2018.07.007

Jordan, T.A., Porter, D., Tinto, K., Millan, R., Muto, A., Hogan, K., Larter, R.D., Graham, A.G. and Paden, J.D., 2020. New gravity-derived bathymetry for the Thwaites, Crosson, and Dotson ice shelves revealing two ice shelf populations. *The Cryosphere*, 14(9), pp.2869-2882. DOI: 10.5194/tc-14-2869-2020

Joughin, I., Smith, B.E. and Medley, B., 2014. Marine ice sheet collapse potentially under way for the Thwaites Glacier Basin, West Antarctica. Science, 344(6185), pp.735-738. DOI: 10.1126/science.1249055

Karlsson, N.B., Rippin, D.M., Vaughan, D.G. and Corr, H.F., 2009. The internal layering of Pine Island Glacier, West Antarctica, from airborne radar-sounding data. *Annals of Glaciology*, 50(51), pp.141-146. DOI: 10.3189/S0260305500250660

Karlsson, N.B., Rippin, D.M., Bingham, R.G. and Vaughan, D.G., 2012. A 'continuity-index'for assessing ice-sheet dynamics from radar-sounded internal layers. *Earth and Planetary Science Letters*, 335, pp.88-94. DOI: 10.1016/j.epsl.2012.04.034

Karlsson, N.B., Bingham, R.G., Rippin, D.M., Hindmarsh, R.C., Corr, H.F. and Vaughan, D.G., 2014. Constraining past accumulation in the central Pine Island Glacier basin, West Antarctica, using radio-echo sounding. *Journal of Glaciology*, 60(221), pp.553-562. DOI: 10.3189/2014JoG13j180

Karlsson, N.B., Binder, T., Eagles, G., Helm, V., Pattyn, F., Liefferinge, B.V. and Eisen, O., 2018. Glaciological characteristics in the Dome Fuji region and new assessment for "Oldest Ice". *The Cryosphere*, 12(7), pp.2413-2424. DOI: 10.5194/tc-12-2413-2018

Kausch, T., Lhermitte, S., Lenaerts, J., Wever, N., Inoue, M., Pattyn, F., Sun, S., Wauthy, S., Tison, J.L. and Van De Berg, W.J., 2020. Impact of coastal East Antarctic ice rises on surface mass balance: insights from observations and modeling. *The Cryosphere*, 14(10), pp.3367-3380. DOI: 10.5194/tc-14-3367-2020

King, E.C., 2009. Flow dynamics of the Rutford Ice Stream ice-drainage basin, West Antarctica, from radar stratigraphy. *Annals of Glaciology*, 50(51), pp.42-48. DOI: 10.3189/172756409789097586

King, E.C., 2011. Ice stream or not? Radio-echo sounding of Carlson Inlet, West Antarctica. *The Cryosphere*, 5(4), pp.907-916. DOI: 10.5194/tc-5-907-2011

King, E.C., 2020. The precision of radar-derived subglacial bed topography: a case study from Pine Island Glacier, Antarctica. *Annals of Glaciology*, 61(81), pp.154–161. DOI: 10.1017/aog.2020.33

King, M.A., Watson, C.S. and White, D., 2022. GPS rates of vertical bedrock motion suggest Late Holocene Ice-Sheet readvance in a critical sector of East Antarctica. *Geophysical Research Letters*, 49(4), e2021GL097232. DOI: 10.1029/2021GL097232

Kingslake, J., Martín, C., Arthern, R.J., Corr, H.F. and King, E.C., 2016. Ice-flow reorganization in West Antarctica 2.5 kyr ago dated using radar-derived englacial flow velocities. *Geophysical Research Letters*, 43(17), pp.9103-9112. DOI: 10.1002/2016GL070278

Kingslake, J., Scherer, R.P., Albrecht, T., Coenen, J., Powell, R.D., Reese, R., Stansell, N.D., Tulaczyk, S., Wearing, M.G. and Whitehouse, P.L., 2018. Extensive retreat and re-advance of the West Antarctic Ice Sheet during the Holocene. *Nature*, 558(7710), pp.430-434. DOI: 10.1038/s41586-018-0208-x

Kohno, M. and Fujii, Y., 2002. Past 220 year bipolar volcanic signals: remarks on common features of their source volcanic eruptions. *Annals of Glaciology*, 35, pp.217-223. DOI: 10.3189/172756402781816807

Konrad, H., Gilbert, L., Cornford, S.L., Payne, A., Hogg, A., Muir, A. and Shepherd, A., 2017. Uneven onset and pace of ice-dynamical imbalance in the Amundsen Sea Embayment, West Antarctica. *Geophysical Research Letters*, 44(2), pp.910-918. DOI: 10.1002/2016GL070733

Koutnik, M.R., Fudge, T.J., Conway, H., Waddington, E.D., Neumann, T.A., Cuffey, K.M., Buizert, C. and Taylor, K.C., 2016. Holocene accumulation and ice flow near the West Antarctic Ice Sheet Divide ice core site. *Journal of Geophysical Research: Earth Surface*, 121(5), pp.907-924. DOI: 10.1002/2015JF003668

Kurbatov, A.V., Zielinski, G.A., Dunbar, N.W., Mayewski, P.A., Meyerson, E.A., Sneed, S.B. and Taylor, K.C., 2006. A 12,000 year record of explosive volcanism in the Siple Dome Ice Core, West Antarctica. *Journal of Geophysical Research: Atmospheres*, 111(D12), D12307. DOI: 10.1029/2005JD006072

Laird, C.M., Blake, W.A., Matsuoka, K., Conway, H., Allen, C.T., Leuschen, C.J. and Gogineni, S., 2010. Deep ice stratigraphy and basal conditions in central

West Antarctica revealed by coherent radar. *IEEE Geoscience and Remote Sensing Letters*, 7(2), pp.246-250. DOI: 10.1109/LGRS.2009.2032304

Le Brocq, A.M., Payne, A.J. and Vieli, A., 2010. An improved Antarctic dataset for high resolution numerical ice sheet models (ALBMAP v1). *Earth System Science Data*, 2(2), pp.247-260. DOI: 10.5194/essd-2-247-2010

Le Brocq, A.M., Bentley, M.J., Hubbard, A., Fogwill, C.J., Sugden, D.E. and Whitehouse, P.L., 2011. Reconstructing the Last Glacial Maximum ice sheet in the Weddell Sea embayment, Antarctica, using numerical modelling constrained by field evidence. *Quaternary Science Reviews*, 30(19-20), pp.2422-2432. DOI: 10.1016/j.quascirev.2011.05.009

Le Brocq, A.M., Ross, N., Griggs, J.A., Bingham, R.G., Corr, H.F., Ferraccioli, F., Jenkins, A., Jordan, T.A., Payne, A.J., Rippin, D.M. and Siegert, M.J., 2013. Evidence from ice shelves for channelized meltwater flow beneath the Antarctic Ice Sheet. *Nature Geoscience*, 6(11), pp.945-948. DOI: 10.1038/ngeo1977

Lei, Y., Gardner, A.S. and Agram, P., 2022. Processing methodology for the ITS LIVE Sentinel-1 ice velocity product. *Earth System Science Data*, 14(11), pp.5111–5137. DOI: 10.5194/essd-14-5111-2022

Lenaerts, J.T., Van den Broeke, M.R., Van de Berg, W.J., Van Meijgaard, E. and Kuipers Munneke, P., 2012. A new, high-resolution surface mass balance map of Antarctica (1979–2010) based on regional atmospheric climate modeling. *Geophysical Research Letters*, 39(4), L04501. DOI: 10.1029/2011GL050713

Leysinger Vieli, G.J.M., Siegert, M.J. and Payne, A.J., 2004. Reconstructing ice-sheet accumulation rates at ridge B, East Antarctica. *Annals of Glaciology*, 39, pp.326-330. DOI: 10.3189/172756404781814519

Leysinger Vieli, G.J.M., Hindmarsh, R.C. and Siegert, M.J., 2007. Three-dimensional flow influences on radar layer stratigraphy. *Annals of Glaciology*, 46, pp.22-28. DOI: 10.3189/172756407782871729

Leysinger Vieli, G.J.M., Hindmarsh, R.C., Siegert, M.J. and Bo, S., 2011. Time-dependence of the spatial pattern of accumulation rate in East Antarctica deduced from isochronic radar layers using a 3-D numerical ice flow model. *Journal of Geophysical Research: Earth Surface*, 116(F2), F02018. DOI:

10.1029/2010JF001785

Leysinger Vieli, G.M., Martín, C., Hindmarsh, R.C.A. and Lüthi, M.P., 2018. Basal freeze-on generates complex ice-sheet stratigraphy. *Nature Communications*, 9(1), 4669. DOI: 10.1038/s41467-018-07083-3

Li, X., Rignot, E., Morlighem, M., Mouginot, J. and Scheuchl, B., 2015. Grounding line retreat of Totten Glacier, east Antarctica, 1996 to 2013. *Geophysical Research Letters*, 42(19), pp.8049-8056. DOI: 10.1002/2015GL065701

Lindow, J., Castex, M., Wittmann, H., Johnson, J.S., Lisker, F., Gohl, K. and Spiegel, C., 2014. Glacial retreat in the Amundsen Sea sector, West Antarctica–first cosmogenic evidence from central Pine Island Bay and the Kohler Range. *Quaternary Science Reviews*, 98, pp.166-173. DOI: 10.1016/j.quascirev.2014.05.010

Lliboutry, L. A. (1979). A critical review of analytical approximate solutions for steady state velocities and temperatures in cold ice sheets. *Gletscherkd Glazialgeol*, 15, pp.135–148

Lowe, A.L. and Anderson, J.B., 2002. Reconstruction of the West Antarctic ice sheet in Pine Island Bay during the Last Glacial Maximum and its subsequent retreat history. *Quaternary Science Reviews*, 21(16-17), pp.1879-1897. DOI: 10.1016/S0277-3791(02)00006-9

Luo, K., Liu, S., Guo, J., Wang, T., Li, L., Cui, X., Sun, B. and Tang, X., 2020. Radar-Derived Internal Structure and Basal Roughness Characterization along a Traverse from Zhongshan Station to Dome A, East Antarctica. *Remote Sensing*, 12(7), 1079. DOI: 10.3390/rs12071079

Luo, K., Tang, X., Liu, S., Guo, J., Greenbaum, J.S., Li, L. and Sun, B., 2022. Deep Radiostratigraphy Constraints Support the Presence of Persistent Wind Scouring Behavior for More Than 100 Ka in the East Antarctic Ice Sheet. *IEEE Transactions on Geoscience and Remote Sensing*, 60, pp.1-13. DOI: 10.1109/TGRS.2022.3209543

Luyendyk, B.P., Wilson, D.S. and Siddoway, C.S., 2003. Eastern margin of the Ross Sea Rift in western Marie Byrd Land, Antarctica: Crustal structure and tectonic development. *Geochemistry, Geophysics, Geosystems*, 4(10), 1090. DOI: 10.1029/2002GC000462

Lythe, M.B., Vaughan, D.G., and the BEDMAP Consortium, 2001. BEDMAP: A new ice thickness and subglacial topographic model of Antarctica. *Journal of Geophysical Research: Solid Earth*, 106(B6), pp.11335-11351. DOI: 10.1029/2000JB900449

MacGregor, J.A., Matsuoka, K., Koutnik, M.R., Waddington, E.D., Studinger, M. and Winebrenner, D.P., 2009. Millennially averaged accumulation rates for the Vostok Subglacial Lake region inferred from deep internal layers. *Annals of Glaciology*, 50(51), pp.25-34. DOI: 10.3189/172756409789097441

MacGregor, J.A., Catania, G.A., Conway, H., Schroeder, D.M., Joughin, I., Young, D.A., Kempf, S.D. and Blankenship, D.D., 2013. Weak bed control of the eastern shear margin of Thwaites Glacier, West Antarctica. *Journal of Glaciology*, 59(217), pp.900-912. DOI: 10.3189/2013JoG13J050

MacGregor, J.A., Fahnestock, M.A., Catania, G.A., Paden, J.D., Gogineni, S.P., Young, S.K., Rybarski, S.C., Mabrey, A.N., Wagman, B.M. and Morlighem, M., 2015. Radiostratigraphy and age structure of the Greenland Ice Sheet. *Journal of Geophysical Research: Earth Surface*, 120(2), pp.212-241. DOI: 10.1002/2014JF003215

MacGregor, J.A., Colgan, W.T., Fahnestock, M.A., Morlighem, M., Catania, G.A., Paden, J.D. and Gogineni, S.P., 2016. Holocene deceleration of the Greenland ice sheet. *Science*, 351(6273), pp.590-593. DOI: 10.1126/science.aab1702

MacGregor, J.A., Boisvert, L.N., Medley, B., Petty, A.A., Harbeck, J.P., Bell, R.E., Blair, J.B., Blanchard-Wrigglesworth, E., Buckley, E.M., Christoffersen, M.S. and Cochran, J.R., 2021. The scientific legacy of NASA's Operation Icebridge. *Reviews of Geophysics*, 59(2), e2020RG000712. DOI: 10.1029/2020RG000712

Mackintosh, A.N., Verleyen, E., O'Brien, P.E., White, D.A., Jones, R.S., McKay, R., Dunbar, R., Gore, D.B., Fink, D., Post, A.L. and Miura, H., 2014. Retreat history of the East Antarctic Ice Sheet since the last glacial maximum. *Quaternary Science Reviews*, 100, pp.10-30. DOI: 10.1016/j.quascirev.2013.07.024

Martín, C., Hindmarsh, R.C. and Navarro, F.J., 2006. Dating ice flow change near the flow divide at Roosevelt Island, Antarctica, by using a thermomechanical model to predict radar stratigraphy. *Journal of Geophysical Research: Earth Surface*, 111(F1), F01011. DOI: 10.1029/2005JF000326

Matsuoka, K., Power, D., Fujita, S. and Raymond, C.F., 2012. Rapid development of anisotropic ice-crystal-alignment fabrics inferred from englacial radar polarimetry, central West Antarctica. *Journal of Geophysical Research: Earth Surface*, 117(F3), F03029. DOI: 10.1029/2012JF002440

Mayewski, P. A. and Dixon, D.A, 2013. US International TransAntarctic Scientific Expedition (US ITASE) Glaciochemical Data, v. 2.0.0. *NASA National Snow and Ice Data Center* [data set]. DOI: 10.7265/N51V5BXR

McConnell, J.R., Burke, A., Dunbar, N.W., Köhler, P., Thomas, J.L., Arienzo, M.M., Chellman, N.J., Maselli, O.J., Sigl, M., Adkins, J.F. and Baggenstos, D., 2017. Synchronous volcanic eruptions and abrupt climate change 17.7 ka plausibly linked by stratospheric ozone depletion. *Proceedings of the National Academy of Sciences*, 114(38), pp.10035-10040. DOI: 10.1073/pnas.1705595114

Medley, B., Joughin, I., Das, S.B., Steig, E.J., Conway, H., Gogineni, S., Criscitiello, A.S., McConnell, J.R., Smith, B.E., van den Broeke, M.R. and Lenaerts, J.T., 2013. Airborne-radar and ice-core observations of annual snow accumulation over Thwaites Glacier, West Antarctica confirm the spatiotemporal variability of global and regional atmospheric models. *Geophysical Research Letters*, 40(14), pp.3649-3654. DOI: 10.1002/grl.50706

Medley, B., Joughin, I.R., Smith, B.E., Das, S.B., Steig, E.J., Conway, H., Gogineni, S., Lewis, C.S., Criscitiello, A.S., McConnell, J.R. and van den Broeke, M.R., 2014. Constraining the recent mass balance of Pine Island and Thwaites glaciers, West Antarctica, with airborne observations of snow accumulation. *The Cryosphere*, 8(4), pp.1375–1392. DOI: 10.5194/tc-8-1375-2014

Medley, B., McConnell, J.R., Neumann, T.A., Reijmer, C.H., Chellman, N., Sigl, M. and Kipfstuhl, S., 2018. Temperature and snowfall in western Queen Maud Land increasing faster than climate model projections. *Geophysical Research Letters*, 45(3), pp.1472-1480. DOI: 10.1002/2017GL075992

Miles, B.W., Jordan, J.R., Stokes, C.R., Jamieson, S.S., Gudmundsson, G.H. and Jenkins, A., 2021. Recent acceleration of Denman Glacier (1972–2017), East Antarctica, driven by grounding line retreat and changes in ice tongue configuration. *The Cryosphere*, 15(2), pp.663-676. DOI: 10.5194/tc-15-663-2021

Millan, R., Rignot, E., Bernier, V., Morlighem, M. and Dutrieux, P., 2017.

Bathymetry of the Amundsen Sea Embayment sector of West Antarctica from Operation IceBridge gravity and other data. *Geophysical Research Letters*, 44(3), pp.1360-1368. DOI: 10.1002/2016GL072071

Millar, D.H.M., 1981. Radio-echo layering in polar ice sheets and past volcanic activity. *Nature*, 292(5822), pp.441-443. DOI: 10.1038/292441a0

Millar, D.H.M., 1982. Acidity levels in ice sheets from radio echo-sounding. *Annals of Glaciology*, 3, pp.199-203. DOI: 10.3189/S0260305500002779

Moore, J.C., 1988. Dielectric variability of a 130 m Antarctic ice core: implications for radar sounding. *Annals of Glaciology*, 11, pp.95-99. DOI: 10.3189/S026030550000639X

Moritz, H., 1980. Geodetic reference system 1980. *Bulletin Géodésique*, 54(3), pp.395-405. DOI: 10.1007/s001900050278

Morlighem, M., Williams, C.N., Rignot, E., An, L., Arndt, J.E., Bamber, J.L., Catania, G., Chauché, N., Dowdeswell, J.A., Dorschel, B. and Fenty, I., 2017. BedMachine v3: Complete bed topography and ocean bathymetry mapping of Greenland from multibeam echo sounding combined with mass conservation. *Geophysical Research Letters*, 44(21), pp.11051–11061. DOI: 10.1002/2017GL074954

Morlighem, M., 2020. MEaSUREs BedMachine Antarctica, v2.0.0. *NASA National Snow and Ice Data Center* [data set]. DOI: 10.5067/E1QL9HFQ7A8M

Morlighem, M., Rignot, E., Binder, T., Blankenship, D., Drews, R., Eagles, G., Eisen, O., Ferraccioli, F., Forsberg, R., Fretwell, P. and Goel, V., 2020. Deep glacial troughs and stabilizing ridges unveiled beneath the margins of the Antarctic ice sheet. *Nature Geoscience*, 13(2), pp.132-137. DOI: 10.1038/s41561-019-0510-8

Mouginot, J., Rignot, E. and Scheuchl, B., 2014. Sustained increase in ice discharge from the Amundsen Sea Embayment, West Antarctica, from 1973 to 2013. *Geophysical Research Letters*, 41(5), pp.1576-1584. DOI: 10.1002/2013GL059069

Mouginot, J., Scheuchl, B., and Rignot., E., 2017. MEaSUREs Antarctic Boundaries for IPY 2007-2009 from Satellite Radar, v.2.0.0. *NASA National Snow and Ice Data Center* [data set]. DOI: 10.5067/AXE4121732AD

Muldoon, G.R., 2018. West Antarctic Ice Sheet retreat during the Last In-

terglacial. *The University of Texas at Austin ScholarWorks Repository.* DOI: http://hdl.handle.net/2152/65631 (last access: 05 April 2023)

Muldoon, G.R., Jackson, C.S., Young, D.A. and Blankenship, D.D., 2018. Bayesian estimation of englacial radar chronology in Central West Antarctica. *Dynamics and Statistics of the Climate System*, 3(1), dzy004. DOI: 10.1093/climatesystem/dzy004

Muldoon, G., Blankenship, D. D., Jackson, C., and Young, D. A., 2023. AGASEA 4.7 ka Englacial Isochron over the Thwaites Glacier Catchment. *U.S. Antarctic Program Data Center*[data set]. DOI: 10.15784/601673

Napoleoni, F., Jamieson, S.S., Ross, N., Bentley, M.J., Rivera, A., Smith, A.M., Siegert, M.J., Paxman, G.J., Gacitúa, G., Uribe, J.A. and Zamora, R., 2020. Subglacial lakes and hydrology across the Ellsworth Subglacial Highlands, West Antarctica. *The Cryosphere*, 14(12), pp.4507-4524. DOI: 10.5194/tc-14-4507-2020

Neuhaus, S.U., Tulaczyk, S.M., Stansell, N.D., Coenen, J.J., Scherer, R.P., Mikucki, J.A. and Powell, R.D., 2021. Did Holocene climate changes drive West Antarctic grounding line retreat and readvance? *The Cryosphere*, 15(10), pp.4655-4673. DOI: 10.5194/tc-15-4655-2021

Nereson, N.A., Raymond, C.F., Waddington, E.D. and Jacobel, R.W., 1998. Migration of the Siple Dome ice divide, West Antarctica. *Journal of Glaciology*, 44(148), pp.643-652. DOI: 10.3189/S0022143000002148

Nereson, N.A., Raymond, C.F., Jacobel, R.W. and Waddington, E.D., 2000. The accumulation pattern across Siple Dome, West Antarctica, inferred from radar-detected internal layers. *Journal of Glaciology*, 46(152), pp.75-87. DOI: 10.3189/172756500781833449

Neumann, T.A., Conway, H., Price, S.F., Waddington, E.D., Catania, G.A. and Morse, D.L., 2008. Holocene accumulation and ice sheet dynamics in central West Antarctica. *Journal of Geophysical Research: Earth Surface*, 113(F2), F02018. DOI: 10.1029/2007JF000764

Ng, F. and Conway, H., 2004. Fast-flow signature in the stagnated Kamb Ice Stream, West Antarctica. *Geology*, 32(6), pp.481-484. DOI: 10.1130/G20317.1

Nichols, K.A., Goehring, B.M., Balco, G., Johnson, J.S., Hein, A.S. and Todd, C., 2019. New last glacial maximum ice thickness constraints for the Weddell Sea Embayment, Antarctica. *The Cryosphere*, 13(11), pp.2935-2951. DOI: 10.5194/tc-13-2935-2019

Nielsen, L.T., Karlsson, N.B. and Hvidberg, C.S., 2015. Large-scale reconstruction of accumulation rates in northern Greenland from radar data. *Annals of Glaciology*, 56(70), pp.70-78. DOI: 10.3189/2015AoG70A062

Nielsen, L.T., Aalgeirsdóttir, G., Gkinis, V., Nuterman, R. and Hvidberg, C.S., 2018. The effect of a Holocene climatic optimum on the evolution of the Greenland ice sheet during the last 10 kyr. *Journal of Glaciology*, 64(245), pp.477-488. DOI: 10.1017/jog.2018.40

Nitsche, F.O., Porter, D., Williams, G., Cougnon, E.A., Fraser, A.D., Correia, R. and Guerrero, R., 2017. Bathymetric control of warm ocean water access along the East Antarctic Margin. *Geophysical Research Letters*, 44(17), pp.8936-8944. DOI: 10.1002/2017GL074433

Nixdorf, U., Steinhage, D., Meyer, U., Hempel, L., Jenett, M., Wachs, P. and Miller, H., 1999. The newly developed airborne radio-echo sounding system of the AWI as a glaciological tool. *Annals of Glaciology*, 29, pp.231-238. DOI: 10.3189/172756499781821346

Nye, J.F., 1957. The distribution of stress and velocity in glaciers and ice-sheets. *Proceedings of the Royal Society of London.* Series A. Mathematical and Physical Sciences, 239(1216), pp.113-133. DOI: 10.1098/rspa.1957.0026

Otosaka, I.N., Shepherd, A., Ivins, E.R., Schlegel, N.J., Amory, C., van den Broeke, M., Horwath, M., Joughin, I., King, M., Krinner, G. and Nowicki, S., 2022. Mass Balance of the Greenland and Antarctic Ice Sheets from 1992 to 2020. *Earth System Science Data*, 15(4), pp. 1597-1616. DOI: 10.5194/essd-15-1597-2023

Paden, J., Li, J., Leuschen, C., Rodriguez-Morales, F., and Hale, R., 2014. IceBridge MCoRDS L1B Geolocated Radar Echo Strength Profiles, v.2.0.0. *NASA National Snow and Ice Data Center* [data set]. DOI: 10.5067/90S1XZRBAX5N [Accessed: 01/12/2021]

Palerme, C., Genthon, C., Claud, C., Kay, J.E., Wood, N.B. and L'Ecuyer, T., 2017. Evaluation of current and projected Antarctic precipitation in CMIP5

models. *Climate dynamics*, 48(1-2), pp.225-239. DOI: 10.1007/s00382-016-3071-1

Parrenin, F., Hindmarsh, R.C.A. and Rémy, F., 2006. Analytical solutions for the effect of topography, accumulation rate and lateral flow divergence on isochrone layer geometry. *Journal of Glaciology*, 52(177), pp.191-202. DOI: 10.3189/172756506781828728

Parrenin, F., Barnola, J.M., Beer, J., Blunier, T., Castellano, E., Chappellaz, J., Dreyfus, G., Fischer, H., Fujita, S., Jouzel, J. and Kawamura, K., 2007. The EDC3 chronology for the EPICA Dome C ice core. *Climate of the Past*, 3(3), pp.485-497. DOI: 10.5194/cp-3-485-2007

Parrenin, F., Hindmarsh, R., 2007. Influence of a non-uniform velocity field on isochrone geometry along a steady flowline of an ice sheet. *Journal of Glaciology*, 53(183), pp.612-622. DOI: 10.3189/002214307784409298

Parrenin, F., Cavitte, M.G., Blankenship, D.D., Chappellaz, J., Fischer, H., Gagliardini, O., Masson-Delmotte, V., Passalacqua, O., Ritz, C., Roberts, J. and Siegert, M.J., 2017. Is there 1.5-million-year-old ice near Dome C, Antarctica?. *The Cryosphere*, 11(6), pp.2427-2437. DOI: 10.5194/tc-11-2427-2017

Pattyn, F., 2010. Antarctic subglacial conditions inferred from a hybrid ice sheet/ice stream model. *Earth and Planetary Science Letters*, 295(3-4), pp.451-461. DOI: 10.1016/j.epsl.2010.04.025

Pattyn, F. and Morlighem, M., 2020. The uncertain future of the Antarctic Ice Sheet. *Science*, 367(6484), pp.1331-1335. DOI: 10.1126/science.aaz5487

Paxman, G.J., Jamieson, S.S., Ferraccioli, F., Jordan, T.A., Bentley, M.J., Ross, N., Forsberg, R., Matsuoka, K., Steinhage, D., Eagles, G. and Casal, T.G., 2019. Subglacial Geology and Geomorphology of the Pensacola-Pole Basin, East Antarctica. *Geochemistry, Geophysics and Geosystems*, 20(6), pp.2786-2807. DOI: 10.1029/2018GC008126

Pelle, T., Morlighem, M. and McCormack, F.S., 2020. Aurora Basin, the weak underbelly of East Antarctica. *Geophysical Research Letters*, 47(9), e2019GL086821. DOI: 10.1029/2019GL086821

Peters, M.E., Blankenship, D.D. and Morse, D.L., 2005. Analysis techniques for coherent airborne radar sounding: Application to West Antarctic ice streams.

Journal of Geophysical Research: Solid Earth, 110(B6), B06303. DOI: 10.1029/2004JB003222

Peters, M.E., Blankenship, D.D., Carter, S.P., Kempf, S.D., Young, D.A. and Holt, J.W., 2007. Along-track focusing of airborne radar sounding data from West Antarctica for improving basal reflection analysis and layer detection. *IEEE Transactions on Geoscience and Remote Sensing*, 45(9), pp.2725-2736. DOI: 10.1109/TGRS.2007.897416

Petit, J.R., Jouzel, J., Raynaud, D., Barkov, N.I., Barnola, J.M., Basile, I., Bender, M., Chappellaz, J., Davis, M., Delaygue, G. and Delmotte, M., 1999. Climate and atmospheric history of the past 420,000 years from the Vostok ice core, Antarctica. *Nature*, 399(6735), pp.429-436. DOI: 10.1038/20859

Plewes, L.A. and Hubbard, B., 2001. A review of the use of radio-echo sounding in glaciology. *Progress in Physical Geography*, 25(2), pp.203-236. DOI: 10.1177/030913330102500203

Polar Data Centre, 2022. BAS Aerogeophysics Book. https://antarctica.github.io/PDC_GeophysicsBook (last access: 05 April 2023)

Pollard, D. and DeConto, R.M., 2009. Modelling West Antarctic ice sheet growth and collapse through the past five million years. *Nature*, 458(7236), pp.329-332. DOI: 10.1038/nature07809

Pollard, D., DeConto, R.M. and Alley, R.B., 2015. Potential Antarctic Ice Sheet retreat driven by hydrofracturing and ice cliff failure. *Earth and Planetary Science Letters*, 412, pp.112-121. DOI: 10.1016/j.epsl.2014.12.035

RAISED Consortium: A community-based geological reconstruction of Antarctic Ice Sheet deglaciation since the Last Glacial Maximum, 2014. *Quaternary Science Reviews*, 100, pp.1-9. DOI: 10.1016/j.quascirev.2014.06.025

Retzlaff, R. and Bentley, C.R., 1993. Timing of stagnation of Ice Stream C, West Antarctica, from short-pulse radar studies of buried surface crevasses. *Journal of Glaciology*, 39(133), pp.553-561. DOI: 10.3189/S0022143000016440

Rignot, E., Jacobs, S., Mouginot, J. and Scheuchl, B., 2013. Ice-shelf melting around Antarctica. *Science*, 341(6143), pp.266-270. DOI: 10.1126/science.1235798

Rignot, E., Mouginot, J., Morlighem, M., Seroussi, H. and Scheuchl, B., 2014. Widespread, rapid grounding line retreat of Pine Island, Thwaites, Smith, and Kohler glaciers, West Antarctica, from 1992 to 2011. *Geophysical Research Letters*, 41(10), pp.3502-3509. DOI: 10.1002/2014GL060140

Rignot, E., Mouginot, J., and Scheuchl, B., 2017. MEaSUREs InSAR-Based Antarctica Ice Velocity Map, v 2.0.0. *NASA National Snow and Ice Data Center* [data set]. DOI: 10.5067/D7GK8F5J8M8R

Rignot, E., Mouginot, J., Scheuchl, B., van den Broeke, M., van Wessem, M.J. and Morlighem, M., 2019. Four decades of Antarctic Ice Sheet mass balance from 1979–2017. *Proceedings of the National Academy of Sciences*, 116(4), pp.1095-1103. DOI: 10.1073/pnas.1812883116

Rippin, D.M., Bamber, J.L., Siegert, M.J., Vaughan, D.G. and Corr, H.F.J., 2003a. Basal topography and ice flow in the Bailey/Slessor region of East Antarctica. *Journal of Geophysical Research: Earth Surface*, 108(F1), 6008. DOI: 10.1029/2003JF000039

Rippin, D.M., Siegert, M.J. and Bamber, J.L., 2003b. The englacial stratigraphy of Wilkes Land, East Antarctica, as revealed by internal radio-echo sounding layering, and its relationship with balance velocities. *Annals of Glaciology*, 36, pp.189-196. DOI: 10.3189/172756403781816356

Rippin, D.M., Bamber, J.L., Siegert, M.J., Vaughan, D.G. and Corr, H.F., 2004. The role of ice thickness and bed properties on the dynamics of the enhanced-flow tributaries of Bailey Ice Stream and Slessor Glacier, East Antarctica. *Annals of Glaciology*, 39, pp.366-372. DOI: 10.3189/172756404781814375

Rippin, D.M., Bamber, J.L., Siegert, M.J., Vaughan, D.G. and Corr, H.F.J., 2006a. Basal conditions beneath enhanced-flow tributaries of Slessor Glacier, East Antarctica. *Journal of Glaciology*, 52(179), pp.481-490. DOI: 10.3189/172756506781828467

Rippin, D.M., Siegert, M.J., Bamber, J.L., Vaughan, D.G. and Corr, H.F., 2006b. Switch-off of a major enhanced ice flow unit in East Antarctica. *Geophysical research letters*, 33(15). DOI: 10.1029/2006GL026648

Rippin, D.M., Vaughan, D.G. and Corr, H.F., 2011. The basal roughness of

Pine Island Glacier, West Antarctica. *Journal of Glaciology*, 57(201), pp.67-76. DOI: 10.3189/002214311795306574

Rippin, D.M., Bingham, R.G., Jordan, T.A., Wright, A.P., Ross, N., Corr, H.F., Ferraccioli, F., Le Brocq, A.M., Rose, K.C. and Siegert, M.J., 2014. Basal roughness of the Institute and Möller Ice Streams, West Antarctica: Process determination and landscape interpretation. *Geomorphology*, 214, pp.139-147. DOI: 10.1016/j.geomorph.2014.01.021

Ritz, C., Rommelaere, V. and Dumas, C., 2001. Modeling the evolution of Antarctic ice sheet over the last 420,000 years: Implications for altitude changes in the Vostok region.*Journal of Geophysical Research: Atmospheres*, 106(D23), pp.31943-31964. DOI: 10.1029/2001JD900232

Ritz, C., Edwards, T.L., Durand, G., Payne, A.J., Peyaud, V. and Hindmarsh, R.C., 2015. Potential sea-level rise from Antarctic ice-sheet instability constrained by observations. *Nature*, 528(7580), pp.115-118. DOI: 10.1038/nature16147

Robel, A.A., Seroussi, H. and Roe, G.H., 2019. Marine ice sheet instability amplifies and skews uncertainty in projections of future sea-level rise. Proceedings of the National Academy of Sciences, 116(30), pp.14887-14892. DOI: 10.1073/pnas.1904822116

Robin, G.D.Q., Swithinbank, C.W.M. and Smith, B.M.E., 1970. Radio echo exploration of the Antarctic ice sheet. *International Association of Scientific Hydrology Publication*, 86, pp.97-115

Robin, G.D.Q., Drewry, D.J. and Meldrum, D.T., 1977. International studies of ice sheet and bedrock. *Philosophical Transactions of the Royal Society of London*, 279(963), pp.185-196. DOI: 10.1098/rstb.1977.0081

Rose, K.C., Ferraccioli, F., Jamieson, S.S., Bell, R.E., Corr, H., Creyts, T.T., Braaten, D., Jordan, T.A., Fretwell, P.T. and Damaske, D., 2013. Early east Antarctic Ice Sheet growth recorded in the landscape of the Gamburtsev Subglacial Mountains. *Earth Planet Science Letters*, 375, pp.1-12. DOI: 10.1016/j.epsl.2013.03.053

Rose, K.C., Ross, N., Bingham, R.G., Corr, H.F., Ferraccioli, F., Jordan, T.A., Le Brocq, A.M., Rippin, D.M. and Siegert, M.J., 2014. A temperate former West Antarctic ice sheet suggested by an extensive zone of subglacial meltwater chan-

nels. *Geology*, 42(11), pp.971-974. DOI: 10.1130/G35980.1

Ross, N., Siegert, M.J., Woodward, J., Smith, A.M., Corr, H.F., Bentley, M.J., Hindmarsh, R.C., King, E.C. and Rivera, A., 2011. Holocene stability of the Amundsen-Weddell ice divide, West Antarctica. *Geology*, 39(10), pp.935-938. DOI: 10.1130/G31920

Ross, N., Bingham, R.G., Corr, H.F., Ferraccioli, F., Jordan, T.A., Le Brocq, A., Rippin, D.M., Young, D., Blankenship, D.D. and Siegert, M.J., 2012. Steep reverse bed slope at the grounding line of the Weddell Sea sector in West Antarctica. *Nature Geoscience*, 5(6), pp.393-396. DOI: 10.1038/ngeo1468

Ross, N., Jordan, T.A., Bingham, R.G., Corr, H.F., Ferraccioli, F., Le Brocq, A., Rippin, D.M., Wright, A.P. and Siegert, M.J., 2014. The Ellsworth subglacial highlands: inception and retreat of the West Antarctic Ice Sheet. *Bulletin*, 126(1-2), pp.3-15. DOI: 10.1130/B30794.1

Ross, N. and Siegert, M., 2020. Basal melting over Subglacial Lake Ellsworth and its catchment: insights from englacial layering. *Annals of Glaciology*, 61(81), pp.198-205. DOI: 10.1017/aog.2020.50

Ross, N., Corr, H. and Siegert, M., 2020. Large-scale englacial folding and deep-ice stratigraphy within the West Antarctic Ice Sheet. *The Cryosphere*, 14(6), pp.2103–2114. DOI: 10.5194/tc-14-2103-2020

Rotschky, G., Eisen, O., Wilhelms, F., Nixdorf, U. and Oerter, H., 2004. Spatial distribution of surface mass balance on Amundsenisen plateau, Antarctica, derived from ice-penetrating radar studies. *Annals of Glaciology*, 39, pp.265-270. DOI: 10.3189/172756404781814618

Scambos, T.A., Haran, T.M., Fahnestock, M.A., Painter, T.H. and Bohlander, J., 2007. MODIS-based Mosaic of Antarctica (MOA) data sets: Continent-wide surface morphology and snow grain size. *Remote Sensing of the Environment*, 111(2-3), pp.242-257. DOI: 10.1016/j.rse.2006.12.020

Scambos, T.A., Bell, R.E., Alley, R.B., Anandakrishnan, S., Bromwich, D.H., Brunt, K., Christianson, K., Creyts, T., Das, S.B., DeConto, R. and Dutrieux, P., 2017. How much, how fast?: A science review and outlook for research on the instability of Antarctica's Thwaites Glacier in the 21st century. *RGlobal and Planetary Change*, 153, pp.16-34. DOI: 10.1016/j.gloplacha.2017.04.008

Schroeder, D.M., Blankenship, D.D. and Young, D.A., 2013. Evidence for a water system transition beneath Thwaites Glacier, West Antarctica. *Proceedings of the National Academy of Sciences*, 110(30), pp.12225-12228. DOI: 10.1073/pnas.1302828110

Schroeder, D.M., Blankenship, D.D., Young, D.A. and Quartini, E., 2014. Evidence for elevated and spatially variable geothermal flux beneath the West Antarctic Ice Sheet. *Proceedings of the National Academy of Sciences*, 111(25), pp.9070-9072. DOI: 10.1073/pnas.1405184111

Schroeder, D.M., Dowdeswell, J.A., Siegert, M.J., Bingham, R.G., Chu, W., MacKie, E.J., Siegfried, M.R., Vega, K.I., Emmons, J.R. and Winstein, K., 2019. Multidecadal observations of the Antarctic ice sheet from restored analog radar records.*Proceedings of the National Academy of Sciences*, 116(38), pp.18867-18873. DOI: 10.1073/pnas.1821646116

Schroeder, D.M., Bingham, R.G., Blankenship, D.D., Christianson, K., Eisen, O., Flowers, G.E., Karlsson, N.B., Koutnik, M.R., Paden, J.D. and Siegert, M.J., 2020. Five decades of radioglaciology. *Annals of Glaciology*, 61(81), pp.1-13. DOI: 10.1017/aog.2020.11

Schwander, J., Jouzel, J., Hammer, C.U., Petit, J.R., Udisti, R. and Wolff, E., 2001. A tentative chronology for the EPICA Dome Concordia ice core. *Geophysical Research Letters*, 28(22), pp.4243-4246. DOI: 10.1029/2000GL011981

Schoof, C., 2007. Ice sheet grounding line dynamics: Steady states, stability, and hysteresis. *Journal of Geophysical Research: Earth Surface*, 112(F3), F03S28. DOI: 10.1029/2006JF000664

Seroussi, H., Nowicki, S., Simon, E., Abe-Ouchi, A., Albrecht, T., Brondex, J., Cornford, S., Dumas, C., Gillet-Chaulet, F., Goelzer, H. and Golledge, N.R., 2019. initMIP-Antarctica: an ice sheet model initialization experiment of ISMIP6. *The Cryosphere*, 13(5), pp.1441-1471. DOI: 10.5194/tc-13-1441-2019

Severi, M., Becagli, S., Castellano, E., Morganti, A., Traversi, R., Udisti, R., Ruth, U., Fischer, H., Huybrechts, P., Wolff, E. and Parrenin, F., 2007. Synchronisation of the EDML and EDC ice cores for the last 52 kyr by volcanic signature matching. *Climate of the Past*, 3(3), pp.367-374. DOI: 10.5194/cp-3-367-2007

Shepherd, T., Bamber, J.L. and Ferraccioli, F., 2006. Subglacial geology in Coats Land, East Antarctica, revealed by airborne magnetics and radar sounding. *Earth and Planetary Science Letters*, 244(1-2), pp.323-335. DOI: 10.1016/j.epsl.2006.01.068

Shepherd, A., Ivins, E. R., Geruo, A., Barletta, V. R., Bentley, M. J., Bettadpur, S., Briggs, K. H., Bromwich, D. H., Forsberg, R., Galin, N., Horwath, M., Jacobs, S., Joughin, I., King, M. A., Lenaerts, J. T. M., Li, J. L., Ligtenberg, S. R. M., Luckman, A., Luthcke, S. B., McMillan, M., Meister, R., Milne, G., Mouginot, J., Muir, A., Nicolas, J. P., Paden, J., Payne, A. J., Pritchard, H., Rignot, E., Rott, H., Sorensen, L. S., Scambos, T. A., Scheuchl, B., Schrama, E. J. O., Smith, B., Sundal, A. V., van Angelen, J. H., van de Berg, W. J., van den Broeke, M. R., Vaughan, D. G., Velicogna, I., Wahr, J., Whitehouse, P. L., Wingham, D. J., Yi, D. H., Young, D., and Zwally, H. J., 2012. A reconciled estimate of ice-sheet mass balance. *Science*, 338(6111), pp.1183-1189. DOI: 10.1126/science.1228102

Shepherd, A., Ivins, E. R., Rignot, E., Smith, B., Van Den Broeke, M., Velicogna, I., and the IMBIE team (2018). Mass balance of the Antarctic Ice Sheet from 1992 to 2017. *Nature*, 556, pp. 219–222. DOI: 10.1038/s41586-018-0179-y

Siegert, M.J., Hodgkins, R. and Dowdeswell, J.A., 1998. A chronology for the Dome C deep ice-core site through radio-echo layer Correlation with the Vostok Ice Core, Antarctica. *Geophysical Research Letters*, 25(7), pp.1019-1022. DOI: 10.1029/98GL00718

Siegert, M.J., 1999. On the origin, nature and uses of Antarctic ice-sheet radio-echo layering. *Progress in physical geography*, 23(2), pp.159-179. DOI: 10.1177/030913339902300201

Siegert, M.J., 2000. Antarctic subglacial lakes. *Earth-Science Reviews*, 50(1-2), pp.29-50. DOI: 10.1016/S0012-8252(99)00068-9

Siegert, M.J., 2003. Glacial–interglacial variations in central East Antarctic ice accumulation rates. *Quaternary Science Reviews*, 22(5-7), pp.741-750. DOI: 10.1016/S0277-3791(02)00191-9

Siegert, M.J., Payne, A.J. and Joughin, I., 2003. Spatial stability of Ice Stream D and its tributaries, West Antarctica, revealed by radio-echo sounding and interferometry. *Annals of Glaciology*, 37, pp.377-382. DOI:

10.3189/172756403781816022

Siegert, M.J. and Payne, A.J., 2004. Past rates of accumulation in central West Antarctica. *Geophysical Research Letters*, 31(12), L12403. DOI: 10.1029/2004GL020290

Siegert, M.J., Welch, B., Morse, D., Vieli, A., Blankenship, D.D., Joughin, I., King, E.C., Gwendolyn, J.M., Payne, A.J. and Jacobel, R., 2004a. Ice flow direction change in interior West Antarctica. *Science*, 305(5692), pp.1948-1951. DOI: 10.1126/science.1101072

Siegert, M.J., Taylor, J., Payne, A.J. and Hubbard, B., 2004b. Macro-scale bed roughness of the Siple Coast ice streams in West Antarctica. *Earth Surface Processes and Landforms: The Journal of the British Geomorphological Research Group*, 29(13), pp.1591-1596. DOI: 10.1002/esp.1100

Siegert, M.J., Pokar, M., Dowdeswell, J.A. and Benham, T., 2005. Radio-echo layering in West Antarctica: a spreadsheet dataset. *Earth Surface Processes and Landforms: The Journal of the British Geomorphological Research Group*, 30(12), pp.1583-1591. DOI: 10.1002/esp.1238

Siegert, M., Ross, N., Corr, H., Kingslake, J. and Hindmarsh, R., 2013. Late Holocene ice-flow reconfiguration in the Weddell Sea sector of West Antarctica. *Quaternary Science Reviews*, 78, pp.98-107. DOI: 10.1016/j.quascirev.2013.08.003

Siegert, M.J., Ross, N., Corr, H., Smith, B., Jordan, T., Bingham, R.G., Ferraccioli, F., Rippin, D.M. and Le Brocq, A., 2014. Boundary conditions of an active West Antarctic subglacial lake: implications for storage of water beneath the ice sheet. *The Cryosphere*, 8(1), pp.15-24. DOI: 10.5194/tc-8-15-2014

Siegert, M.J., Ross, N., Li, J., Schroeder, D.M., Rippin, D., Ashmore, D., Bingham, R. and Gogineni, P., 2016. Subglacial controls on the flow of Institute Ice Stream, West Antarctica. *Annals of Glaciology*, 57(73), pp.19-24. DOI: 10.1017/aog.2016.17

Siegert, M.J., Jeofry, H., Corr, H.F.J., Ross, N., Jordan, T.A., Ferraccioli, F., Bingham, R.G., Le Brocq, A.M., Rippin, D.M., and Robinson, C., 2017. Synthetic-aperture radar (SAR) processed airborne radio-echo sounding data from the Institute and Moller ice streams, West Antarctica, 2010-11. *UK Polar Data Centre, Natural Environment Research Council* [data set]. DOI: 10.1029/AR077p0075

Siegert, M.J., Kingslake, J., Ross, N., Whitehouse, P.L., Woodward, J., Jamieson, S.S., Bentley, M.J., Winter, K., Wearing, M., Hein, A.S. and Jeofry, H., 2019. Major ice sheet change in the Weddell Sea sector of West Antarctica over the last 5,000 years. *Reviews of Geophysics*, 57(4), pp.1197-1223. DOI: 10.1029/2019RG000651

Siegert, M., Alley, R.B., Rignot, E., Englander, J. and Corell, R., 2020. Twenty-first century sea-level rise could exceed IPCC projections for strong-warming futures. *One Earth*, 3(6), pp.691-703. DOI: 10.1016/j.oneear.2020.11.002

Siegert, M., Hein, A.S., White, D.A., Gore, D.B., De Santis, L. and Hillenbrand, C.D., 2022. Chapter 11: Antarctic ice sheet changes since the Last Glacial Maximum. *In Antarctic Climate Evolution (second edition)*, Amsterdam, Elsevier, pp.623–687. DOI: 10.1016/B978-0-12-819109-5.00002-5

Sigl, M., Fudge, T.J., Winstrup, M., Cole-Dai, J., Ferris, D., McConnell, J.R., Taylor, K.C., Welten, K.C., Woodruff, T.E., Adolphi, F. and Bisiaux, M., 2016. The WAIS Divide deep ice core WD2014 chronology–Part 2: Annual-layer counting (0–31 ka BP). *Climate of the Past*, 12(3), pp.769-786. DOI: 10.5194/cp-12-769-2016

Sigl, M., Toohey, M, McConnell, J.R., Cole-Dai, J., and Severi, M., 2022. Volcanic stratospheric sulfur injections and aerosol optical depth during the Holocene (past 11 500 years) from a bipolar ice-core array. *Earth System Science Data*, 14(7), pp.3167–3196. DOI: 10.5194/essd-14-3167-2022

Sime, L. C., Karlsson, N. B., Paden, J. D., and Prasad Gogineni, S., 2014. Isochronous information in a Greenland ice sheet radio echo sounding data set. *Geophysical Research Letters*, 41(5), pp.1593–1599. DOI: 10.1002/2013GL057928

Smith, J.A., Andersen, T.J., Shortt, M., Gaffney, A.M., Truffer, M., Stanton, T.P., Bindschadler, R., Dutrieux, P., Jenkins, A., Hillenbrand, C.D. and Ehrmann, W., 2017. Sub-ice-shelf sediments record history of twentieth-century retreat of Pine Island Glacier. *Nature*, 541(7635), pp.77-80. DOI: 10.1038/nature20136

Smith, B., Fricker, H.A., Gardner, A.S., Medley, B., Nilsson, J., Paolo, F.S., Holschuh, N., Adusumilli, S., Brunt, K., Csatho, B. and Harbeck, K., 2020. Pervasive ice sheet mass loss reflects competing ocean and atmosphere processes. *Science*, 368(6496), pp.1239-1242. DOI: 10.1126/science.aaz5845

Spector, P., Stone, J. and Goehring, B., 2019. Thickness of the divide and flank of the West Antarctic Ice Sheet through the last deglaciation. *The Cryosphere*, 13(11), pp.3061-3075. DOI: 10.5194/tc-13-3061-2019

Spikes, V.B., Hamilton, G.S., Arcone, S.A., Kaspari, S. and Mayewski, P.A., 2004. Variability in accumulation rates from GPR profiling on the West Antarctic plateau. *Annals of Glaciology*, 39, pp.238-244. DOI: 10.3189/172756404781814393

Sproson, A.D., Yokoyama, Y., Miyairi, Y., Aze, T. and Totten, R.L., 2022. Holocene melting of the West Antarctic Ice Sheet driven by tropical Pacific warming. *Nature Communications*, 13(2434). DOI: 10.1038/s41467-022-30076-2

Steig, E.J., Fastook, J.L., Zweck, C., Goodwin, I.D., Licht, K.J., White, J.W. and Ackert Jr, R.P., 2001. West Antarctic ice sheet elevation changes. *The West Antarctic Ice Sheet: Behavior and Environment*, 77, pp.75-90. DOI: 10.1029/AR077p0075

Steinhage, D., Kipfstuhl, S., Nixdorf, U. and Miller, H., 2013. Internal structure of the ice sheet between Kohnen station and Dome Fuji, Antarctica, revealed by airborne radio-echo sounding. *Annals of Glaciology*, 54(64), pp.163-167. DOI: 10.3189/2013AoG64A113

Stokes, C.R., Abram, N.J., Bentley, M.J., Edwards, T.L., England, M.H., Foppert, A., Jamieson, S.S., Jones, R.S., King, M.A., Lenaerts, J.T. and Medley, B., 2022. Response of the East Antarctic Ice Sheet to past and future climate change. *Nature*, 608(7922), pp.275-286. DOI: 10.1038/s41586-022-04946-0

Stone, J.O., Balco, G.A., Sugden, D.E., Caffee, M.W., Sass III, L.C., Cowdery, S.G. and Siddoway, C., 2003. Holocene deglaciation of Marie Byrd land, west Antarctica. *Science*, 299(5603), pp.99-102. DOI: 10.1126/science.1077998

Stothers, R.B., 1984. The great Tambora eruption in 1815 and its aftermath. *Science*, 224(4654), pp.1191-1198. DOI: 10.1126/science.224.4654.1191

Studinger, M., Bell, R.E., Blankenship, D.D., Finn, C.A., Arko, R.A., Morse, D.L. and Joughin, I., 2001. Subglacial sediments: A regional geological template for ice flow in West Antarctica. *Geophysical Research Letters*, 28(18), pp.3493-3496. DOI: 10.1029/2000GL011788

Studinger, M., Bell, R.E., Buck, W.R., Karner, G.D. and Blankenship, D.D.,

2004. Sub-ice geology inland of the Transantarctic Mountains in light of new aerogeophysical data. *Earth and Planetary Science Letters*, 220(3-4), pp.391-408. DOI: 10.1016/S0012-821X(04)00066-4

Suganuma, Y., Miura, H., Zondervan, A. and Okuno, J.I., 2014. East Antarctic deglaciation and the link to global cooling during the Quaternary: Evidence from glacial geomorphology and 10Be surface exposure dating of the Sør Rondane Mountains, Dronning Maud Land. *Quaternary Science Reviews*, 97, pp.102-120. DOI: 10.1016/j.quascirev.2014.05.007

Sutter, J., Gierz, P., Grosfeld, K., Thoma, M. and Lohmann, G., 2016. Ocean temperature thresholds for last interglacial West Antarctic Ice Sheet collapse. *Geophysical Research Letters*, 43(6), pp.2675-2682. DOI: 10.1002/2016GL067818

Sutter, J., Fischer, H., Grosfeld, K., Karlsson, N.B., Kleiner, T., Van Liefferinge, B. and Eisen, O., 2019. Modelling the Antarctic Ice Sheet across the mid-Pleistocene transition–implications for Oldest Ice. *The Cryosphere*, 13(7), pp.2023-2041. DOI: 10.5194/tc-13-2023-2019

Sutter, J., Fischer, H. and Eisen, O., 2021. Investigating the internal structure of the Antarctic ice sheet: the utility of isochrones for spatiotemporal ice-sheet model calibration. *The Cryosphere*, 15(8), pp.3839-3860. DOI: 10.5194/tc-15-3839-2021

Taylor, J., Siegert, M.J., Payne, A.J. and Hubbard, B., 2004. Regional-scale bed roughness beneath ice masses: measurement and analysis. *Computers and Geosciences*, 30(8), pp.899-908. DOI: 10.1016/j.cageo.2004.06.007

Tinto, K.J. and Bell, R.E., 2011. Progressive unpinning of Thwaites Glacier from newly identified offshore ridge: Constraints from aerogravity. *Geophysical Research Letters*, 38(20), L20503. DOI: 10.1029/2011GL049026

Tinto, K.J., Padman, L., Siddoway, C.S., Springer, S.R., Fricker, H.A., Das, I., Tontini, F.C., Porter, D.F., Frearson, N.P., Howard, S.L. and Siegfried, M.R., 2019. Ross Ice Shelf response to climate driven by the tectonic imprint on seafloor bathymetry. *Nature Geoscience*, 12(6), pp.441-449. DOI: 10.1038/s41561-019-0370-2

Valliant, H.D., 1992. *LaCoste and Romberg Air/Sea Meters: An Overview*. CRC Handbook of Geophysical Exploration at Sea. London, CRC Press. DOI:

10.1201/9780367812751

van Den Broeke, M.R. and Van Lipzig, N.P., 2004. Changes in Antarctic temperature, wind and precipitation in response to the Antarctic Oscillation. *Annals of Glaciology*, 39, pp.119-126. DOI: 10.3189/172756404781814654

van Wessem, J.M., Jan Van De Berg, W., Noë l, B.P., Van Meijgaard, E., Amory, C., Birnbaum, G., Jakobs, C.L., Krüger, K., Lenaerts, J., Lhermitte, S. and Ligtenberg, S.R., 2018. Modelling the climate and surface mass balance of polar ice sheets using RACMO2: Part 2: Antarctica (1979-2016). *The Cryosphere*, 12(4), pp.1479-1498. DOI: 10.5194/tc-12-1479-2018

Vaughan, D.G., Corr, H.F., Ferraccioli, F., Frearson, N., O'Hare, A., Mach, D., Holt, J.W., Blankenship, D.D., Morse, D.L. and Young, D.A., 2006. New boundary conditions for the West Antarctic ice sheet: Subglacial topography beneath Pine Island Glacier. *Geophysical Research Letters*, 33(9), L09501. DOI: 10.1029/2005GL025588

Vaughan, D.G., Corr, H.F., Smith, A.M., Pritchard, H.D. and Shepherd, A., 2008. Flow-switching and water piracy between Rutford ice stream and Carlson inlet, West Antarctica. *Journal of Glaciology*, 54(184), pp.41-48. DOI: 10.3189/002214308784409125

Vaughan, D.G., Corr, H.F., Bindschadler, R.A., Dutrieux, P., Gudmundsson, G.H., Jenkins, A., Newman, T., Vornberger, P. and Wingham, D.J., 2012. Subglacial melt channels and fracture in the floating part of Pine Island Glacier, Antarctica. *Journal of Geophysical Research: Earth Surface*, 117(F3), F03012. DOI: 10.1029/2012JF002360

Venturelli, R.A., Siegfried, M.R., Roush, K.A., Li, W., Burnett, J., Zook, R., Fricker, H.A., Priscu, J.C., Leventer, A. and Rosenheim, B.E., 2020. Mid-Holocene grounding line retreat and readvance at Whillans Ice Stream, West Antarctica. *Geophysical Research Letters*, 47(15), e2020GL088476. DOI: 10.1029/2020GL088476

Verfaillie, D., Fily, M., Le Meur, E., Magand, O., Jourdain, B., Arnaud, L. and Favier, V., 2012. Snow accumulation variability derived from radar and firn core data along a 600 km transect in Adelie Land, East Antarctic plateau. *The Cryosphere*, 6(6), pp.1345-1358. DOI: 10.5194/tc-6-1345-2012

Waddington, E.D., Conway, H., Steig, E.J., Alley, R.B., Brook, E.J., Taylor, K.C. and White, J.W.C., 2005. Decoding the dipstick: thickness of Siple Dome, West Antarctica, at the last glacial maximum. *Geology*, 33(4), pp.281-284. DOI: 10.1130/G21165.1

Waddington, E.D., Neumann, T.A., Koutnik, M.R., Marshall, H.P. and Morse, D.L., 2007. Inference of accumulation-rate patterns from deep layers in glaciers and ice sheets. *Journal of Glaciology*, 53(183), pp.694-712. DOI: 10.3189/002214307784409351

WAIS Divide Project Members, 2013. Onset of deglacial warming in West Antarctica driven by local orbital forcing. *Nature*, 500(7463), pp.440-444. DOI: 10.1038/nature12376

Wang, Y., Ding, M., Van Wessem, J.M., Schlosser, E., Altnau, S., van den Broeke, M.R., Lenaerts, J.T., Thomas, E.R., Isaksson, E., Wang, J. and Sun, W., 2016. A comparison of Antarctic Ice Sheet surface mass balance from atmospheric climate models and in situ observations. *Journal of Climate*, 29(14), pp.5317-5337. DOI: 10.1175/JCLI-D-15-0642.1

Wearing, M.G. and Kingslake, J., 2019. Holocene Formation of Henry Ice Rise, West Antarctica, Inferred from Ice-Penetrating Radar. *Journal of Geophysical Research: Earth Surface*, 124(8), pp.2224-2240. DOI: 10.1029/2018JF004988

Weertman, J., 1974. Stability of the junction of an ice sheet and an ice shelf. *Journal of Glaciology*, 13(67), pp.3-11. DOI: 10.3189/S0022143000023327

Werner, M., Jouzel, J., Masson-Delmotte, V. and Lohmann, G., 2018. Reconciling glacial Antarctic water stable isotopes with ice sheet topography and the isotopic paleothermometer. Nature communications, 9(1), pp.3537. DOI: 10.1038/s41467-018-05430-y

Whillans, I.M., 1976. Radio-echo layers and the recent stability of the West Antarctic ice sheet. *Nature*, 264(5582), pp.152-155. DOI: 10.1038/264152a0

Wilkinson, M.D., Dumontier, M., Aalbersberg, I.J., Appleton, G., Axton, M., Baak, A., Blomberg, N., Boiten, J.W., da Silva Santos, L.B., Bourne, P.E. and Bouwman, J., 2016. The FAIR Guiding Principles for scientific data management and stewardship. *Scientific Data*, 3(1), pp.1-9. DOI: 10.1038/sdata.2016.18

Winski, D.A., Fudge, T.J., Ferris, D.G., Osterberg, E.C., Fegyveresi, J.M., Cole-Dai, J., Thundercloud, Z., Cox, T.S., Kreutz, K.J., Ortman, N. and Buizert, C., 2019. The SP19 chronology for the South Pole Ice Core–Part 1: volcanic matching and annual layer counting. *Climate of the Past*, 15(5), pp.1793-1808. DOI: 10.5194/cp-15-1793-2019

Winski, D.A., Osterberg, E.C., Kreutz, K.J., Ferris, D.G., Cole-Dai, J., Thundercloud, Z., Huang, J., Alexander, B., Jaeglé, L., Kennedy, J.A. and Larrick, C., 2021. Seasonally resolved Holocene sea ice variability inferred from South Pole ice core chemistry. *Geophysical Research Letters*, 48(8), e2020GL091602. DOI: 10.1029/2020GL091602

Winter, A., Steinhage, D., Arnold, E.J., Blankenship, D.D., Cavitte, M.G., Corr, H.F., Paden, J.D., Urbini, S., Young, D.A. and Eisen, O., 2017. Comparison of measurements from different radio-echo sounding systems and synchronization with the ice core at Dome C, Antarctica. *The Cryosphere*, 11(1), pp.653-668. DOI: 10.5194/tc-11-653-2017

Winter, A., Steinhage, D., Creyts, T.T., Kleiner, T. and Eisen, O., 2019. Age stratigraphy in the East Antarctic Ice Sheet inferred from radio-echo sounding horizons. *Earth System Science Data*, 11(3), pp.1069-1081. DOI: 10.5194/essd-11-1069-2019

Winter, K., Woodward, J., Ross, N., Dunning, S.A., Bingham, R.G., Corr, H.F. and Siegert, M.J., 2015. Airborne radar evidence for tributary flow switching in Institute Ice Stream, West Antarctica: Implications for ice sheet configuration and dynamics. *Journal of Geophysical Research: Earth Surface*, 120(9), pp.1611-1625. DOI: 10.1002/2015JF003518

Winter, K., Ross, N., Ferraccioli, F., Jordan, T.A., Corr, H.F., Forsberg, R., Matsuoka, K., Olesen, A.V. and Casal, T.G., 2018. Topographic steering of enhanced ice flow at the bottleneck between East and West Antarctica. *Geophysical Research Letters*, 45(10), pp.4899-4907. DOI: 10.1029/2018GL077504

Woodward, J. and King, E.C., 2009. Radar surveys of the Rutford Ice Stream onset zone, West Antarctica: indications of flow (in) stability?. *Annals of Glaciology*, 50(51), pp.57-62. DOI: 10.3189/17275640978909

Wright, A.P., Young, D.A., Roberts, J.L., Schroeder, D.M., Bamber, J.L., Dowdeswell, J.A., Young, N.W., Le Brocq, A.M., Warner, R.C., Payne, A.J.

and Blankenship, D.D., 2012. Evidence of a hydrological connection between the ice divide and ice sheet margin in the Aurora Subglacial Basin, East Antarctica. *Journal of Geophysical Research: Earth Surface*, 117(F1), F01033. DOI: 10.1029/2011JF002066

Wright, A.P., Young, D.A., Bamber, J.L., Dowdeswell, J.A., Payne, A.J., Blankenship, D.D. and Siegert, M.J., 2014. Subglacial hydrological connectivity within the Byrd Glacier catchment, East Antarctica. *Journal of Glaciology*, 60(220), pp.345-352. DOI: 10.3189/2014JoG13J014

Yalcin, K., Wake, C.P., Kreutz, K.J., Germani, M.S. and Whitlow, S.I., 2006. Ice core evidence for a second volcanic eruption around 1809 in the Northern Hemisphere. *Geophysical Research Letters*, 33(14), L14706. DOI: 10.1029/2006GL026013

Young, D.A., Wright, A.P., Roberts, J.L., Warner, R.C., Young, N.W., Greenbaum, J.S., Schroeder, D.M., Holt, J.W., Sugden, D.E., Blankenship, D.D. and van Ommen, T.D., 2011. A dynamic early East Antarctic Ice Sheet suggested by ice-covered fjord landscapes. *Nature*, 474(7349), pp.72-75. DOI: 10.1038/nature10114

Young, D.A., Schroeder, D.M., Blankenship, D.D., Kempf, S.D. and Quartini, E., 2016. The distribution of basal water between Antarctic subglacial lakes from radar sounding. *Philosophical Transactions of the Royal Society A: Mathematical, Physical and Engineering Sciences*, 374(2059), 20140297. DOI: 10.1098/rsta.2014.0297

Young, D.A., Roberts, J.L., Blankenship, D.D., Van Ommen, T., Ritz, C., Cavitte, M.G. and Frezzotti, M., 2021. ICECAP radargrams in support of the international old ice search at Dome C - 2016, v.1.0.0. *Australian Antarctic Data Centre* [data set]. DOI: 10.26179/5wkf-7361

Young, T.J., Schroeder, D.M., Jordan, T.M., Christoffersen, P., Tulaczyk, S.M., Culberg, R. and Bienert, N.L., 2021. Inferring ice fabric from birefringence loss in airborne radargrams: Application to the eastern shear margin of Thwaites Glacier, West Antarctica. *Journal of Geophysical Research: Earth Surface*, 126(5), e2020JF006023. DOI: 10.1029/2020JF006023

Zwally, H. J, Giovinetto, M. B., Beckley, M. A., and Saba, J. L., 2012. *Antarctic and Greenland drainage systems*, GSFC Cryospheric Sciences Laboratory. Acces-

sible from: http://imbie.org/imbie-3/drainage-basins/ (last access: 05 April 2023)

Appendix

Appendix A: Age-Depth Stratigraphy of Pine Island Glacier Inferred From Airborne Radar and Ice-Core Chronology

Check for updates

AGU ADVANCING EARTH AND SPACE SCIENCE

JGR Earth Surface

RESEARCH ARTICLE
10.1029/2020JF005927

Age-Depth Stratigraphy of Pine Island Glacier Inferred From Airborne Radar and Ice-Core Chronology

J. A. Bodart[1,4], R. G. Bingham[1], D. W. Ashmore[2], N. B. Karlsson[3], A. S. Hein[1], and D. G. Vaughan[4]

[1]School of GeoSciences, University of Edinburgh, Edinburgh, UK, [2]School of Environmental Sciences, University of Liverpool, Liverpool, UK, [3]Geological Survey of Denmark and Greenland, Copenhagen, Denmark, [4]British Antarctic Survey, Cambridge, UK

Key Points:

- Using airborne radar, we trace four isochronous internal reflecting horizons over Pine Island Glacier, West Antarctica
- Isochrone ages calculated using the WAIS Divide ice core and a 1-D model are 2.31–2.92, 4.72 ± 0.28, 6.94 ± 0.31, and 16.50 ± 0.79 ka
- We show that these isochrones are widespread across Pine Island Glacier and extend into neighboring Weddell and Amundsen Sea regions

Supporting Information:

Supporting Information may be found in the online version of this article.

Correspondence to:

J. A. Bodart,
julien.bodart@ed.ac.uk

Citation:

Bodart, J. A., Bingham, R. G., Ashmore, D. W., Karlsson, N. B., Hein, A. S., & Vaughan, D. G. (2021). Age-depth stratigraphy of Pine Island Glacier inferred from airborne radar and ice-core chronology. *Journal of Geophysical Research: Earth Surface*, *126*, e2020JF005927. https://doi.org/10.1029/2020JF005927

Received 30 SEP 2020
Accepted 17 MAR 2021

© 2021. The Authors.
This is an open access article under the terms of the Creative Commons Attribution License, which permits use, distribution and reproduction in any medium, provided the original work is properly cited.

Abstract Understanding the contribution of the West Antarctic Ice Sheet (WAIS) to past and future sea level has been a major scientific priority over the last three decades. In recent years, observed thinning and ice-flow acceleration of the marine-based Pine Island Glacier has highlighted that understanding dynamic changes is critical to predicting the long-term stability of the WAIS. However, relatively little is known about the evolution of the catchment during the Holocene. Internal reflecting horizons (IRHs) provide a cumulative record of accumulation, basal melt, and ice dynamics that, if dated, can be used to constrain ice-flow models. Here, we use airborne radars to trace four spatially extensive IRHs deposited in the late Quaternary across the Pine Island Glacier catchment. We use the WAIS Divide ice-core chronology to assign ages to three IRHs: 4.72 ± 0.28, 6.94 ± 0.31, and 16.50 ± 0.79 ka. We use a 1-D model, constrained by observational and modeled accumulation rates, to produce an independent validation of our ice-core-derived ages and provide an age estimate for our shallowest IRH (2.31–2.92 ka). We find that our upper three IRHs correspond to three large peaks in sulfate concentrations in the WAIS Divide ice-core record and hypothesize that the origin of these spatially extensive IRHs is from past volcanic activity. The clear correspondence between our IRHs and the ones previously identified over the Weddell Sea Sector, altogether representing ~20% of the WAIS, indicates that a unique set of stratigraphic markers spanning the Holocene exists over a large part of West Antarctica.

1. Introduction

The West Antarctic Ice Sheet (WAIS) has been losing mass at an accelerating rate since satellite records began, averaging 94 ± 27 Gt yr^{-1} of mass loss since 1992 (Shepherd et al., 2018). Approximately 40% of this loss was through Pine Island Glacier (PIG), which alone has contributed ~3 mm of the total ~7 mm sea-level-rise contribution of the WAIS between 1979 and 2017 (Rignot et al., 2019). The increasing mass-loss trend of PIG has been primarily driven by interannual and decadal-scale atmospheric and oceanic forcing, triggering grounding-line retreat and consequent inland dynamical adjustments (Bodart & Bingham, 2019; Christianson et al., 2016; Dutrieux et al., 2014; Favier et al., 2014; Holland et al., 2019; Konrad et al., 2017; Rignot et al., 2019; Smith et al., 2017). However, placing the observed changes over the last four decades within the context of long-term dynamic changes and sea-level rise contribution is challenging (Medley et al., 2018; Palerme et al., 2017), as the short observational satellite record captures only slight perturbations in the forcing and response which are not sufficient to predict a future in which changes are likely to be rapid and large. This lack of long-term observations currently limits our understanding of the likely future evolution of this sensitive sector of the WAIS. Reaching further back into the past will help us capture a wider set of ice-sheet configurations, and so create a more robust basis for future predictions of the Antarctic Ice Sheet evolution (Bracegirdle et al., 2019; DeConto & Pollard, 2016; Ritz et al., 2001).

Past research has focused primarily on using in situ observations and ice-sheet models to reconstruct the evolution of the WAIS since the Last Glacial Maximum (LGM, ~20 ka BP), indicating that WAIS contained significantly more ice than at present, with the potential to have raised sea level by more than 9 m at the LGM (Denton & Hughes, 2002). Several studies have reported evidence of short-lived episodes of rapid grounding-line retreat in the Amundsen Sea Embayment (ASE) between the LGM and the start of the Holocene (~11.5 ka BP) (Hillenbrand et al., 2013; Jakobsson et al., 2011; Lowe & Anderson, 2002). However, much less is known about the interior ice-sheet history of this region during the Holocene. Cosmogenic

nuclide studies on isolated nunataks across the ASE suggest significant ice thinning occurred during the early- to mid-Holocene in the central ASE (Johnson et al., 2017, 2020; Lindow et al., 2014), with thinning complete by the mid-Holocene in the eastern ASE near PIG (Johnson et al., 2008, 2014). More recent evidence, based on sediment cores, ice-penetrating radar, and ice-sheet modeling, showed possible retreat and re-advance of the WAIS grounding line over millennial timescales during the Holocene (Kingslake et al., 2018), although evidence of such behavior is not available in the ASE region.

Internal reflecting horizons (IRHs), as observed by ice-penetrating radars, provide a powerful and complementary resource to point-based geochronological measurements. Excluding basal ice and erosional surfaces, the majority of specular, continuous IRHs are isochronous (Whillans, 1976); many can be traced for several hundreds of kilometers and provide a record of accumulation rates and patterns, convolved with key information on past ice-dynamical processes (Bingham & Siegert, 2007; Eisen et al., 2005, 2008; Siegert et al., 1998). IRHs can thus serve as a valuable resource for constraining past changes in surface mass balance (SMB) and ice-flow velocities (e.g., Rotschky et al., 2004), and, where they can be dated, can be incorporated into ice-flow models, as previously shown for Greenland (Fahnestock, et al., 2001; MacGregor et al., 2016) and Antarctica (Cavitte et al., 2018; Koutnik et al., 2016; Leysinger Vieli et al., 2011; Waddington et al., 2007).

Despite the large spatial coverage of radar data across Antarctica, information on dated IRHs is limited over much of the WAIS. This is partly due to the restricted availability of deep ice cores, the multitude of radar-system families operating at varying frequencies and using different post-processing methods to generate the radar data, and the challenge in tracing deep continuous IRHs, particularly through areas of high strain rate (i.e., at the onset of fast-flowing tributaries). Nonetheless, previous studies over the WAIS have used IRHs for the direct purpose of linking major deep ice cores (Koutnik et al., 2016; Neumann et al., 2008), while others have used a wider, catchment-scale approach to constrain information on past accumulation rates and ice-flow reconfiguration. Such studies have ranged across the central WAIS (Jacobel & Welch, 2005; Muldoon, 2018; Siegert & Payne, 2004) or focused on specific sub-regions, for example, Siple Dome (Jacobel et al., 1996), Kamb Ice Stream (Catania et al., 2006; Holschuh et al., 2018) and Thwaites Glacier (Muldoon et al., 2018).

Over PIG, Karlsson et al. (2014) identified two IRHs spanning much of the slow-flowing parts of the catchment, which they roughly dated to 5.3–6.2 and 8.6–13.4 ka. More recently, Ashmore et al. (2020) recovered three IRHs ranging across Institute and Möller Ice Streams and crossing the Institute/PIG divide which they broadly dated to 1.9–3.2, 3.5–6.0, and 4.6–8.1 ka. They demonstrated a correspondence between their IRH package and the IRHs previously identified by Karlsson et al. (2014) and Siegert et al. (2005), suggesting that a spatially extensive network of IRHs may span much of the WAIS.

Here, we build on previous studies to present a spatially extensive, dated-radiostratigraphy of PIG. We use ice-penetrating radar data collected from two airborne platforms to trace four IRHs throughout PIG. We use a published ice-core chronology as well as a steady-state vertical-strain model to date these IRHs, and show that they span much of the Late Pleistocene and Holocene. We first discuss the specifications of the radar systems and their respective uncertainties, and then describe the methods used to assign ages to each of our four IRHs. We present the dated age-depth stratigraphy of the catchment and make inferences for the rest of WAIS by comparing our recent findings to other age-depth studies. Finally, we investigate the link between sulfate activity in the WAIS Divide ice-core record and the depth of our upper three IRHs, and discuss the potential to recover records of older (i.e., pre-LGM) ice in the region using currently available radar data sets.

2. Data Sets and Methods

2.1. Data

The principal data used in this study were acquired during two large-scale airborne radar surveys of West Antarctica.

The first of these was acquired over the 2004–05 austral season, when PIG's 175,000 km^2 catchment was surveyed extensively using the British Antarctic Survey's Polarimetric Airborne Survey INstrument (PASIN)

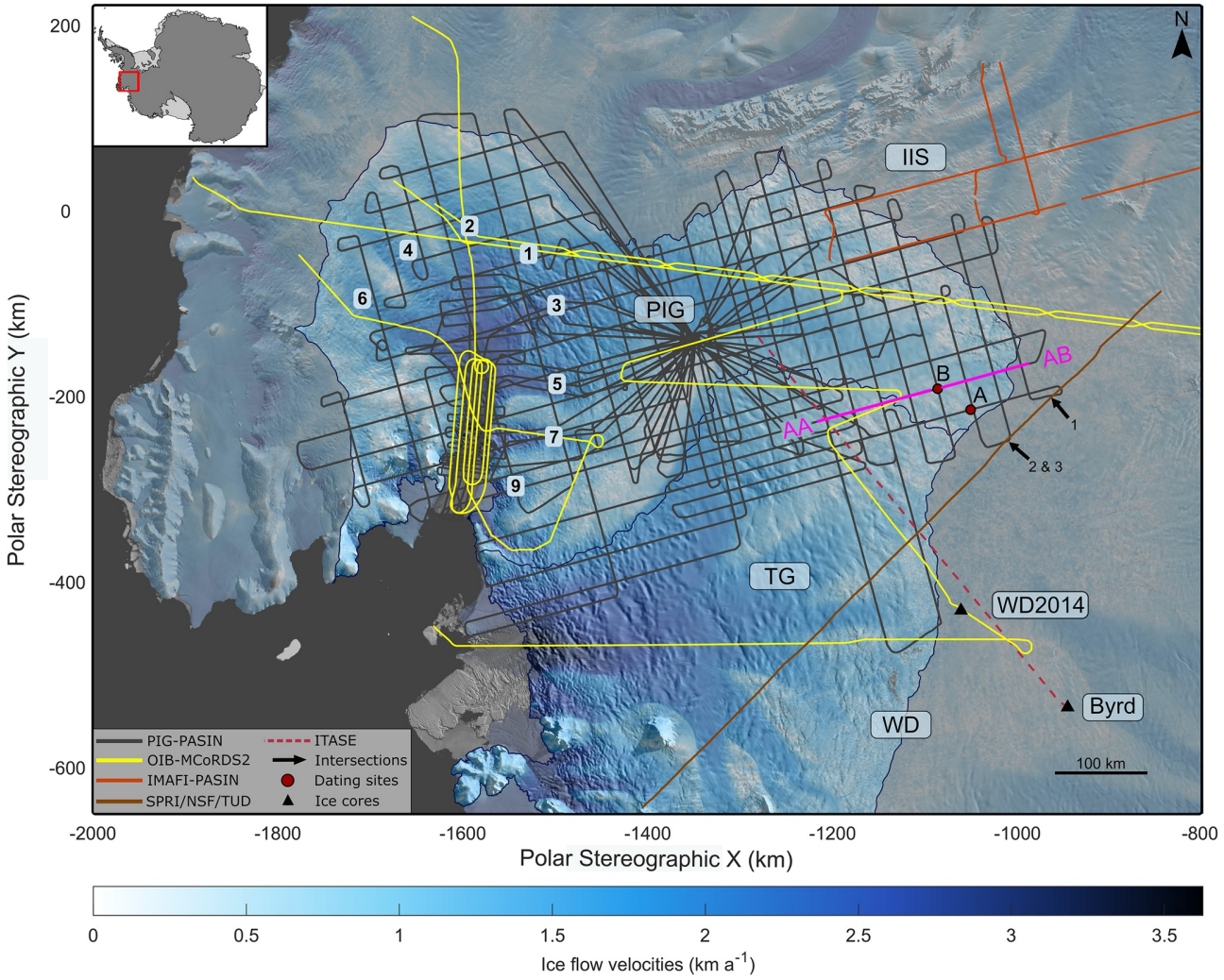

Figure 1. Map of study area with the data sets and key locations mentioned in this study. The inset in top left corner shows the region of interest (red box). Airborne survey lines included in this study: PIG-PASIN (gray), OIB-MCoRDS2 (yellow), IMAFI-PASIN transects flown over Institute Ice Stream (IIS) and intersecting the PIG catchment (orange), SPRI/NSF/TUD line (brown), overlaid on top of ice flow velocities from Rignot et al. (2017) and MODIS Mosaic of Antarctica (Scambos et al., 2007). Also included is the long, ITASE GPR-transect (dashed red) through which the 17.5 ± 0.5 ka layer from Jacobel and Welch (2005) was traced. The numbers shown over PIG's trunk represent the eight fast-flowing tributaries (1–7, 9) mentioned in this study. The WAIS Divide (WD2014) and Byrd ice cores are represented by the two black triangles, and the black arrows represent the three intersections between the SPRI/NSF/TUD-traced IRHs and this study. The two red circles show the two sites (Sites A and B) where the 1-D age-depth model was used. The AA–AB segment (magenta) shows a subset of the control line where IRHs were first identified over PIG-PASIN (see Figure 2). The Western Divide is shown as WD on the map. The ICESat IMBIE basins of Pine Island Glacier (PIG) and Thwaites Glacier (TG) (Zwally et al., 2012) are annotated on the map and delimited by the blue outline lines.

system (Vaughan et al., 2006). This survey, hereafter termed "PIG-PASIN", acquired ~35,000 line-km of airborne radar data across the region (Figure 1). Data were collected with two interleaved radar modes. The first was a deep-sounding, 150 MHz center-frequency, 4-μs, 10-MHz chirp mode, which has been used previously to identify and trace the bed (Vaughan et al., 2006) and some IRHs (Karlsson et al., 2009, 2014). The second was a 150 MHz, 0.1-μs pulse mode designed to image shallow IRHs but from which we are also able to recover IRHs deeper (~2 km, see Figure 2a) in the ice column. Over much of the surveyed region, flight lines form 30 km spaced grids that contain multiple crossovers, ensuring consistency when tracing IRHs across neighboring lines (Figure 1). Following techniques outlined in Ashmore et al. (2020), here, we used both modes of PASIN interchangeably during our IRH-tracing procedures (see Section 2.2). For the purposes of linking our stratigraphy further across the WAIS, we also refer to further PASIN-acquired data from a survey of Institute and Möller Ice Streams undertaken in 2010–11 (hereafter "IMAFI-PASIN"),

Table 1
Characteristics and Resolution of the Two Airborne Radar Systems Used in This Study

System	Platform	Center frequency	Bandwidth/ pulse width	Vertical sampling frequency	Vertical resolution	Horizontal sampling distance
PASIN	Twin Otter	150 MHz	10 MHz/100 ns	22 MHz	12.89/8.42 m	45 m
MCoRDS2	DC8	190 MHz	50 MHz	150 MHz	2.58 m	14 m

Note: for the PASIN system, we provide values for both the chirp- and pulse-acquisition mode in the bandwidth/ pulse width column, as well as in the vertical resolution column. The vertical resolution of the chirped systems was calculated as per CReSIS (2016) using a scaling factor "*k*" which accounts for resolution degradation due to receiver characteristics and processing (see Equation S1).

which provided tie-lines connecting PIG with its neighboring basins (Figure 1; see Ashmore et al., 2020, and references therein, for further details).

The second survey was conducted in 2016 and 2018 by NASA's Operation IceBridge (OIB) mission, and yielded ~3,000 line-km of airborne radar data over PIG, Institute and Möller Ice Streams, and Thwaites Glacier (Figure 1). The system deployed by the Center for Remote Sensing of Ice Sheets (CReSIS) was the Multichannel Coherent Radar Depth Sounder 2 (MCoRDS2) with a 190 MHz center frequency and 50 MHz bandwidth. We used the CReSIS L1B standard products, produced with pulse compression, focused-SAR processing, and along-track motion compensation. More information on the radar system and processing is given by CReSIS (2016). Critically for this study, one of the OIB flight tracks over PIG also flew over the WAIS Divide Ice Core (79.48°S, 112.11°W; hereafter referred to as WD2014) (Figure 1), making it possible to assign relatively unambiguous dates to the traced IRHs.

More details on each of the radar systems are provided in Table 1. For the purposes of increasing IRH traceability on the PIG-PASIN data, we quadratically detrended each radar trace, normalized each pixel in a moving vertical window, and then applied a 10-trace horizontal average to reduce incoherent noise (after Ashmore et al., 2020). For both the PIG-PASIN and the OIB-MCoRDS2 data, we removed the air-to-ice two-way travel time and shifted the surface elevation to time zero, before exporting the data to standard 2-D SEG-Y format for data interpretation.

2.2. IRH-Tracing Workflow

We conducted all IRH-tracing in the Schlumberger Petrel® 3-D seismic software using a semi-automated tracing algorithm that uses an adjustable window to track the local maxima of received reflected power between traces.

We initiated our workflow on the PIG-PASIN data set as it is the most spatially extensive survey of the PIG catchment. From a "control line" crossing the ice divides between PIG, Thwaites Glacier, and Institute Ice Stream (Figure 1), in which clearly visible englacial stratigraphy is ubiquitous in both chirp- and pulse-mode data, we identified four prominent IRHs that we term R1–4 (Figure 2). The upper three IRHs (R1–3) were chosen on the basis of high spatial continuity, high signal-to-noise ratio (SNR), and as being analogous to "IRH packages" traced over part of PIG by Karlsson et al. (2014) and through IMAFI-PASIN radar profiles by Ashmore et al. (2020). All four IRHs occur in the middle part of the ice column where IRHs likely result from contrasts in acidity from past volcanic eruptions (Gow & Williamson, 1971; Millar, 1981, 1982), rather than the result of density variations occurring primarily at the near-surface (Clough, 1977; Gow, 1970; Moore, 1988) or orientation of anisotropic material due to ice foliation in the basal zone (Fujita et al., 1999; Harrison, 1973); and thus can be assumed to be isochronous (Siegert et al., 1998; Whillans, 1976).

Expanding out from the control line, we progressively traced and mapped IRHs across the catchment using IRH intersections at each crossover as calibration points. This ensured reliability in our reflection tracing as the software is capable of detecting intersecting IRHs at the crossover with orthogonal radar lines. Since our tracing strategy was based on reflector echo strength and continuity, the reflection tracing was terminated when it was no longer possible to distinguish visually between adjacent reflections, either as a result of similar brightness levels or a loss in continuity. This was particularly common in areas of steep bed topography

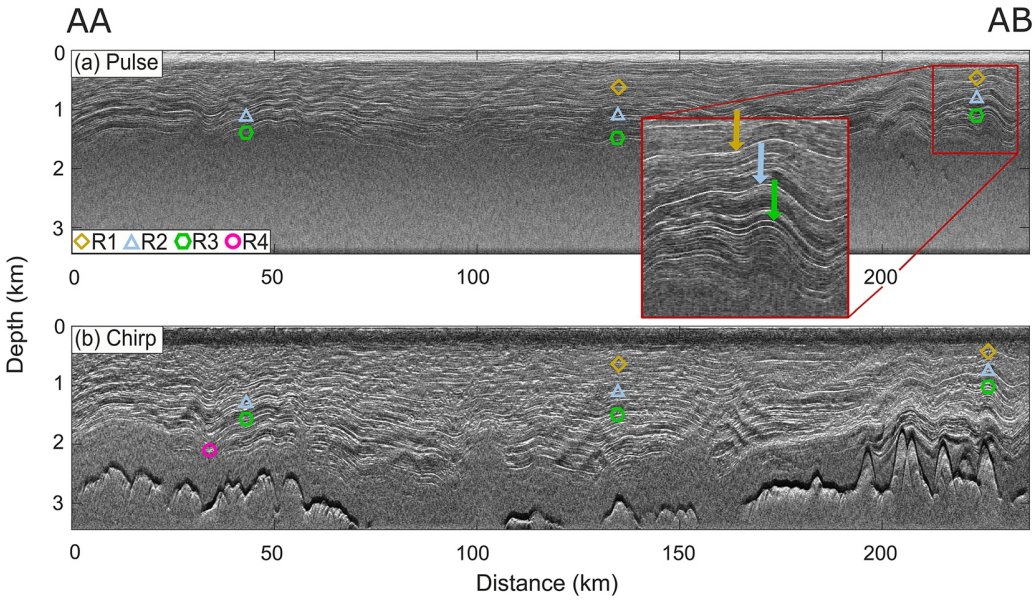

Figure 2. Subset of the control line with the unmodulated pulse (a) and chirp (b) modes from the PIG-PASIN survey along transect AA– AB (see Figure 1). Traced IRHs are marked as per the legend on panel (a). The zoomed inset on the pulse radargram shows the characteristics of R1–3 in more detail, with the color of the arrows corresponding to the legend in (a).

causing IRHs to dip significantly, or where enhanced ice-flow speeds disrupted IRH continuity, notably into the main flow features of PIG's northern catchment. In some places, IRHs faded without such clear topography/flow-induced reasons, likely due to the attenuation of the radar signal with depth or the type of processing used (Holschuh et al., 2014). In some locations more distant from the upper PIG catchment (i.e., westward of tributary 6; Figure 1), extensive englacial layering was visible in radar profiles but, due to a dearth of connecting lines and crossovers, we could not, with confidence, identify R1–4.

When tracing between crossovers, we relied upon the distinctiveness of our IRHs. At the vertical resolution of PASIN, R1 and R2 manifest as single-amplitude peaks, with R2 representing a particularly bright reflector widely visible across our radar data (Figure 2, Figure S1). R3 consists of the shallowest of a series of closely spaced bright horizons, often manifested as a couplet (zoomed inset in Figure 2, Figure S1), and previously identified by Karlsson et al. (2014; their "Layer 2") and Ashmore et al. (2020; their "H3"). The lowermost IRH, R4, forms the upper part of a band of bright reflectors visible at the intersection with the 17.5 ± 0.5 ka layer widely imaged on radar data from the International Trans-Antarctic Scientific Expedition (ITASE) connecting the PIG catchment with the Byrd Ice Core chronology (Hammer et al., 1997; Jacobel & Welch, 2005) (Figures 1, 2, and S1).

Once R1–4 were traced through the PIG-PASIN survey, we looked for the same IRHs on the OIB-MCoRDS2 data using available crossovers between each survey (Figures 1 and 3). We found R2–3 to be equally distinguishable in OIB-MCoRDS2 profiles, with R2 representing a particularly bright reflector similar to that on PIG-PASIN, whilst R3 also formed the shallower part of an easily distinguishable couplet. We did not recover R1 independently on the OIB-MCoRDS2 profile crossing the WAIS Divide Ice Core and used intersections with PIG-PASIN to trace it across to the Institute Ice Stream catchment. Similarly, we used several intersections with the 17.5 ± 0.5 ka layer from Jacobel and Welch (2005) in and around the WD2014 site to recover R4 in the OIB-MCoRDS2 data (Figures 1 and 3).

It is worth noting that the OIB-MCoRDS2 data were acquired 12–14 years later than the PIG-PASIN survey, and so the same IRHs will, in principle, lie slightly lower in the ice column. However, considering a present-day mean accumulation rate of ~0.30–0.35 m a^{-1} (meters of ice equivalent per year) at the intersection between the two surveys, the maximum change in IRH depth is < 5 m. This is well within the bounds of the total depth uncertainty calculated for each radar system (see Section 2.3) and does not affect the pattern

of englacial layering or the identification of our IRHs across the different surveys. Crossover analysis at key intersections on the airborne radar data showed that the mean depth difference for R1–4 falls within the uncertainty range of all surveys (Figure S2, Tables S1 and S2) (see Section 2.3). At 10 intersections on PIG-PASIN, the mean depth difference for R1–4 is < 6 m. Similarly, the mean depth difference for R2–3 at 11 intersections between PIG-PASIN and OIB-MCoRDS2 is 14 and 29 m, respectively, and < 18 m at 5 intersections between R4 on OIB-MCoRDS2 and the 17.5 ± 0.5 ka from Jacobel and Welch (2005) (Figure S2, Table S2).

With our objective being to produce an age-depth radiostratigraphy across PIG, we converted all IRHs traced above in the time domain (t_{IRH}) to depth (d_{IRH}) using

$$d_{IRH} = \frac{v_{ice}\, t_{IRH}}{2} + Z_f, \tag{1}$$

where $v_{ice} = 168.5\,\text{m}\,\mu\text{s}^{-1}$ is the speed of electromagnetic waves through ice (cf. Fujita et al., 2000) and $Z_f = 10$ m is a spatially invariant firn correction, appropriate for West Antarctica (Ashmore et al., 2020). All our depth measurements are given in meters below the surface. We then calculated IRH depth as a function of ice thickness using the ice-thickness measurement from each respective radar mission, and complemented these with ice-thickness measurements from BedMachine (Morlighem et al., 2020) in places where the radar did not sound the bed.

2.3. Catchment-Wide Depth Uncertainties

To assess the accuracy of our IRH depths at the catchment scale, we consider the uncertainties associated with the imaging of IRHs with ice-penetrating-radar. These uncertainties primarily depend on three factors: variations in the speed of electromagnetic (EM) waves through the ice, the firn-density correction, and the radar system's range precision (Cavitte et al., 2016) (Text S1).

The maximum uncertainty arising from selecting an EM value ranging between 168 and 169.5 m μs^{-1} is 16 m on the maximum depth of the deepest reflection on PIG-PASIN and 14 m on OIB-MCoRDS2. The uncertainty associated with the firn correction is ±3 m, owing to minor variations in firn densification across the catchment (Ashmore et al., 2020) (Text S1). The precision of IRH depth estimates also depends on the range accuracy, $\sigma(r^*)$, of the radar system, which refers to how accurately changes can be located in 3-D space (Cavitte et al., 2016; King, 2020). This is a combination of the SNR of each IRH and the range resolution, Δr, of the radar system, which is mainly a function of sampling frequency, bandwidth, source wavelets, and the type of post-processing applied. The range resolution for each system, from coarser to finer is: PASIN chirp (12.89 m), PASIN pulse (8.42 m), and MCoRDS2 (2.58 m) (Table 1, Text S1).

We undertook an empirical error analysis to calculate the maximum uncertainty associated with the deepest IRH by calculating the root-mean-square error of the depth uncertainties from EM wave through the ice, the firn correction, and the radar range accuracy. We obtained a combined maximum uncertainty of ±17 m and attached this uncertainty to all IRHs traced on the PIG-PASIN data (Text S1). Similarly, we estimated a combined maximum uncertainty of ±14 m on the OIB-MCoRDS2 data (Text S1). Given that this uncertainty represents the maximum uncertainty on the deepest IRH over our entire data set, we also calculate IRH-specific uncertainties at the ice-core site (see Section 2.4.1).

2.4. Age-Depth Attribution

To estimate the absolute age of our IRHs, we employ two primary dating methods: we use (a) the WAIS Divide ice-core chronology to provide a direct age to our three deepest IRHs, namely R2–4; and (b) the Dansgaard-Johnsen 1-D model to independently compare the ages calculated at the ice core and to provide an approximate age range to our shallowest IRH, R1. Once dated, we also compared the ages and depths of R1–3 with dated IRHs traced across PIG (Karlsson et al., 2014; Siegert & Payne, 2004) and Institute and Möller Ice Streams (Ashmore et al., 2020); as well as the age and depth of R4 with the 17.5 ± 0.5 ka layer dated using the Byrd ice-core chronology (Hammer et al., 1997) and traced across the WAIS (Jacobel &

Welch, 2005). Finally, we also compare the depth and age of our upper three IRHs with sulfate concentrations from the WD2014 ice-core record (Cole-Dai, 2014; McConnell et al., 2017).

2.4.1. Connection to the WAIS Divide Ice-Core Chronology

We used the 2016 OIB-MCoRDS2 data linking central PIG to the WD2014 site to date IRHs across PIG relative to the ice-core chronology, where annual-layer counting goes back to the last ~31 ka BP (Buizert et al., 2015; Sigl et al., 2016). We take the recorded depth at the ice core which most-closely matches our IRH depth at WD2014, and calculate the upper and lower age bounds using the radar depth and ice-core

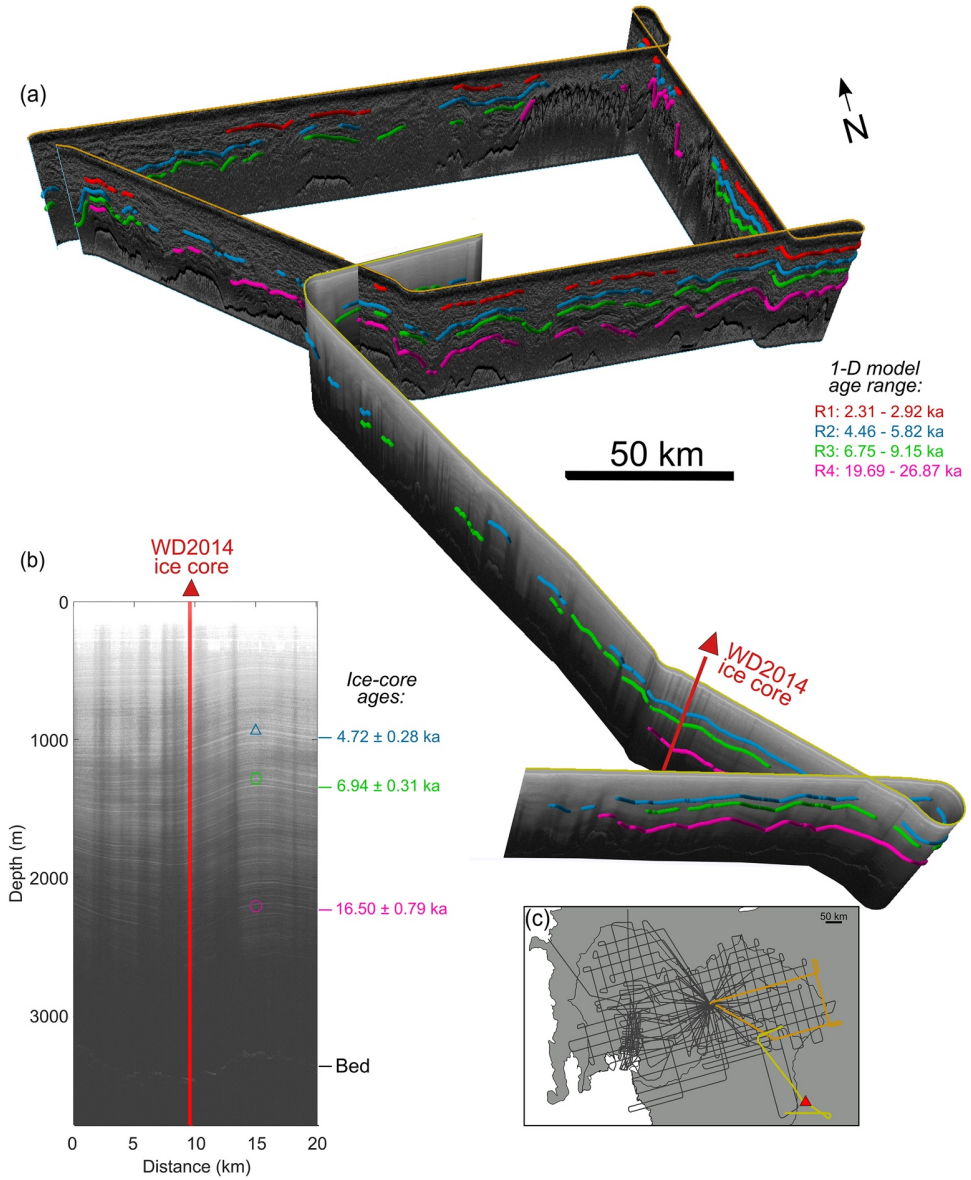

Figure 3. (a) Intersecting radar profiles from PIG-PASIN and OIB-MCoRDS2 with IRHs R1 (red), R2 (blue), R3 (green), and R4 (pink) traced along radargrams. The age range shown on the PIG-PASIN profile in the top right corner is from the 1-D model for R1–4 (see Section 3.2). (b) Englacial layering on the OIB-MCoRDS2 radar profile where it intersects the WD2014 ice core (red line), with ages and total age uncertainties for R2–4 inferred from the ice-core chronology (see Section 3.2) shown on the right-hand side. (c) Inset showing the PIG-PASIN (orange line) and OIB-MCoRDS2 (yellow line) profiles in (a) and the full PIG-PASIN radar flight lines shown in gray in the background, as well as the position of the WD2014 ice core (red triangle).

uncertainties. Following MacGregor et al. (2015), the age uncertainty (Δa_{comb}) associated with each IRH is the root-mean-square combination of the age uncertainty associated with the unweighted mean IRH depth at the ice core ($\Delta a_{\Delta depth}$) and the age uncertainty associated with the ice core at the IRH depth (Δa_{core}), following

$$\Delta a_{comb} = \sqrt{\Delta a_{\Delta depth}{}^2 + \Delta a_{core}{}^2}, \quad (2)$$

where (Δa_{core}) is a function of the age of the individual IRH at the ice core site (Sigl et al., 2016) and the published uncertainty associated with the ice core age (1% and 3% for ages ranging between 0–15 ka and 15–31 ka BP, respectively; Sigl et al., 2016), while ($\Delta a_{\Delta depth}$) is a function of the depth uncertainty of each IRH at the ice-core site. Since the uncertainty in the EM wave through the ice increases with depth, using the maximum uncertainty calculated on the deepest IRH to calculate $\Delta depth$ at a catchment scale (see Section 2.3) would result in less accurate age uncertainties at the ice core. We have therefore calculated a depth uncertainty for each individual IRH at the ice core, and undertook the same empirical error analysis to calculate $\Delta depth$ at WD2014. This resulted in IRH-specific radar depth uncertainties which we used to calculate the age uncertainty for each IRH at WD2014, as per Equation 2.

Whilst Δa_{comb} represents the combined maximum uncertainty from the radar and the ice-core chronology, we found that our IRHs are systematically lower in the ice column compared with strong peaks in acidity concentrations at WD2014 matching closely the age and depth of our IRHs and which we can assume to be the likely cause of our IRHs (see Section 4.2). To account for this offset in ages between the IRHs and the strong sulfate peaks observed at WD2014, we calculated a total age uncertainty (Δa_{total}, Table 3) which represents the maximum age difference between our IRHs and the sulfate peaks at the ice core. This was obtained by adding a systematic factor of 0.22 ka to Δa_{comb}, which represents the total age difference between the maximum IRH age calculated using Δa_{comb} and the age of the strong sulfate peaks (see Section 4.2). We provide the total uncertainty values in Table 3 and Section 3.2.

2.4.2. Age-Depth Modeling

To provide an independent validation of our ice-core derived IRH ages, we also applied the Dansgaard and Johnsen (1969) 1-D vertical ice-strain rate model to derive approximate dating of the IRHs traced over the central PIG catchment. This model has been used previously to date IRHs across West Antarctica (Ashmore et al., 2020; Corr & Vaughan, 2008; Karlsson et al., 2012, 2014), assess divide migration (Waddington et al., 2005), and calculate past accumulation rates at or near ice divides (Jacobel & Welch, 2005; Siegert & Payne, 2004). We chose the Dansgaard-Johnsen model here for its simplicity and as it allows us to test the effect of ice deformation on the ages of our IRHs. However, we note that other alternatives exist such as the Nye (1957) and Lliboutry (1979) models, or the more developed quasi-Nye model (MacGregor et al., 2015).

Under the assumption that the ice sheet is, and has been, in steady state, close to an ice divide, the Dansgaard-Johnsen model gives

$$t = \frac{2H - h}{2a} \ln\left(\frac{2H - h}{2z - h}\right), h \le z \le H, \quad (3)$$

where t (ka; thousand years) is the age of an IRH, H (m) is the ice thickness (assumed constant in time), h (m) is the thickness of the basal shear layer, a (in m a^{-1} ice-equivalent) is the average accumulation rate since deposition of the IRH, and z (m) is the elevation of the IRH above the bed (Dansgaard & Johnsen, 1969).

For this model, several assumptions are made: (a) negligible horizontal velocity component; (b) time-averaged accumulation rates and no temporal change in accumulation patterns; and (c) constant ice deformation from the surface to some depth, h, below which vertical strain rate is assumed to decrease linearly toward the bed. Considering the above, we initiated the model on the PIG-PASIN data at two sites (A and B in Figure 1) located ~50 km from the ice divide where horizontal ice flow is minimal (<3 m a^{-1}), the ice

is thick (>3 km) and the bed relatively flat. Site A (80.15°S, 101.56°W) was selected due to its relative proximity within PIG to WD2014 (~215 km). At this site, R1–3 were traced, as well as R4. This provided us with initial constraints for age-depth estimates for the upper IRHs (namely R1–3), and allowed us to evaluate the model results based on the approximate known age of R4. To ensure representativeness, however, we also selected a second site, Site B (79.87°S, 100.03°W), where R1–3 were traced but not R4.

We based our estimates for a in the equation on advection-corrected accumulation rates from the WD2014 ice core (Fudge et al., 2016) for each IRH R1–4, and with current accumulation estimates to correct for any elevation-dependent change in accumulation between the WD2014 site and our PIG Sites A and B. Tentatively treating our R1–3 as broadly equivalent to three of Siegert and Payne's (2004) dated IRHs based on depth associations at three crossovers (see Text S2, Table S3), we derived mean advection-corrected accumulation rates at WD2014 for each reference age: 0.247 ± 0.062 m a^{-1} (3 ka BP, with BP defined as years before 1950 CE), 0.248 ± 0.062 m a^{-1} (5 ka BP), and 0.243 ± 0.061 m a^{-1} (7 ka BP), as well as a rate of 0.226 ± 0.051 m a^{-1} (17.5 ka BP) based on the intersection with Jacobel and Welch (2005). The errors correspond to uncertainties in the firn-densification model used by Fudge et al. (2016). These provide us with estimates of what would be required to reproduce each layer if accumulation had remained constant between the time of the deposition of the layer and the present at WD2014. Under the assumption that spatial accumulation patterns have not changed during the Holocene over the WAIS (Koutnik et al., 2016; Neumann et al., 2008; Siegert & Payne, 2004), and considering that accumulation rates at the Ice Core are generally smaller than at Sites A and B (Table S4), we use modern accumulation rates from modeled and observational data to calculate the regional difference between accumulation at WD2014 and our Sites A and B. The four sources of accumulation data used here are: (a) SMB estimates for the period 1979–2015 using the Modèle Atmosphérique Régional (MAR, Version 3.6.4; Agosta et al., 2019); (b) SMB estimates for the period 1979–2018 from the Regional Atmospheric Climate Model 2 (RACMO2; van Wessem et al., 2018); (c) accumulation rates interpolated from ground measurements and AMSR-E polarisation (Arthern et al., 2006; hereafter referred to as ART06); and (d) a combination of catchment-wide, snow and accumulation radar measurements obtained in 2009–11 from ultra-wideband airborne platforms and intersecting a series of shallow ice cores (Medley et al., 2014), combined with a set of GPR tracks acquired in 2002–04 over the Western Divide (Neumann et al., 2008) (hereafter referred to as MED14) (Text S2). From these data sets, we calculate a percentage of change between WD2014 and Sites A and B and apply this to the mean advection-corrected rates calculated at WAIS Divide for R1–4 (Table S4). Together, these provided us with a range of realistic values of a for each IRH at Sites A and B to use as input into the 1-D model.

The thickness of the basal shear layer, h, is largely unknown as it is dependent on accurate knowledge of the bed topography and temperature of the ice (Neumann et al., 2008). Previous studies have used a value of $h = 400$ m for Greenland and West Antarctica (Fahnestock et al., 2001; Jacobel & Welch, 2005; Karlsson et al., 2012; Siegert & Payne, 2004), whilst Karlsson et al. (2014) and Ashmore et al. (2020) explored the effects of fuller ranges of $100 \text{ m} \leq h \geq 1200$ m. We refined this range to $0.2H \leq h \geq 0.3H$ (Neumann et al., 2008), rounding to the nearest 100, hence investigating the effect of h ranging from 700 to 1,100 m at both sites (Text S2). We note, however, that large uncertainties in basal deformation at WD2014 (Cuffey et al., 2016; Fudge et al., 2019) could result in h values being smaller than 20% of the ice thickness and thus lead to an overestimation of our ages (see Text S2).

3. Results

3.1. Englacial Stratigraphy

We successfully traced four IRHs R1–4 across a large proportion of the PIG catchment, including in areas where annual velocities reach up to ~350 m a^{-1} (Figure 4). The most extensive IRH traced in our study is R2, closely followed by R3 (Figure 4), with mean depths across the catchment of 1,175 and 1,463 m, respectively (Table 2). The shallowest IRH, R1, was located on average at ~30% of the ice depth, whilst the deepest, R4, was on average found at ~68% depth (Table 2).

The traceability of R1–3 does not vary greatly and is primarily constrained by topography (Figures 4a–4c). By contrast, R4 was only detected across the upper Thwaites/PIG catchments (Figure 4d), even though

Table 2
Summary Statistics for Each IRH Traced Throughout the PIG-PASIN and OIB-MCoRDS2 Surveys

	IRH depth statistics							
	Depth below the surface (m)				Depth as fraction of ice thickness			
	Mean	1σ	Range	IQ range	Mean	1σ	Range	IQ range
R1	722	191	204–1,302	623–873	0.30	0.10	0.12–0.63	0.22–0.36
R2	1,175	240	304–2,014	1,069–1,347	0.46	0.09	0.21–0.82	0.40–0.52
R3	1,463	298	650–2,486	1,324–1,650	0.54	0.08	0.29–0.82	0.48–0.60
R4	1,929	257	697–2,640	1,799–2,080	0.68	0.05	0.42–0.92	0.66–0.71

Note. We provide these for both depths below the surface and depth as a fraction of ice thickness. "1σ" refers to one standard deviation, "Range" refers to the minimum and maximum values, and "IQ range" refers to the interquartile range (25th and 75th percentile). A maximum uncertainty of ±17 m is assumed here.

it has previously been detected much further north into the PIG basin in the ITASE survey (Jacobel & Welch, 2005), likely due to the different frequency range used by the two radar systems. We come back to this point in Section 4.1. We were also able to trace R1–3 in the upper parts of the Institute and Möller ice-stream catchment, and R2–4 in the upper parts of the Thwaites catchment toward the WD2014 site (Figure 4). The traced IRHs are generally deeper southward of the onset of PIG tributaries 7 and 9 and at the center of the PIG catchment, and relatively shallow at its southern margin and at the divides with Thwaites Glacier and Institute Ice Stream (Figures 4e–4h). We were unable to identify the IRHs in several locations, mainly north of the main trunk of PIG near the Hudson Mountains range and west of tributary 6 (Figure 4a). We were also unable to detect continuous IRHs in any PIG-PASIN profiles traversing the main trunk and tributaries of Thwaites Glacier, nor those that cover the main trunk and fast-flowing tributaries of PIG (Figure 4).

3.2. Age-Depth Estimates

Having clearly identified R2–4 near the WD2014 site, we attempt to date these using the WD2014 chronology. The OIB-MCoRDS2 radar profile passes within ~1.2 km of the ice-core site, and the stable ice conditions in the area mean that flow-induced disturbance on layer geometry is relatively limited (Laird et al., 2010). Following MacGregor et al. (2015), we calculate the unweighted mean reflection depth within a distance of ±250 m along transect from the trace that is closest to the ice-core site to obtain $\Delta a_{\Delta depth}$, resulting in mean depths at the ice core of 1,060 ± 7 (R2), 1,430 ± 9 (R3), and 2,371 ± 14 m (R4) (Table 3). Considering the radar-depth and ice-core uncertainties (Equation 2), and to account for the age offset between our IRHs and the strong sulfate peaks at the ice core (see Sections 2.4.1 and 4.2), we determined the age and associated age uncertainty for each IRH at WD2014 as: 4.72 ± 0.28 (R2), 6.94 ± 0.31 (R3), and 16.50 ± 0.79 ka (R4) (Table 3).

Table 3
IRH Mean Depths (m), Ages (ka; in Years Before 2020 AD), and Uncertainties (Δ) at the WD2014 Site for R2–4

	Depth (m)	Δdepth (±m)	*a* (ka)	$\Delta a_{\Delta depth}$ (±ka)	Δa_{core} (±ka)	Δa_{comb} (±ka)	Δa_{total} (±ka)
R2	1,060	7	4.72	0.04	0.05	0.06	0.28
R3	1,430	9	6.94	0.06	0.07	0.09	0.31
R4	2,371	14	16.50	0.28	0.50	0.57	0.79

Note. Column "a (ka)" refers to the IRH age obtained from the radar-depth and the depth at the WD2014 ice core. Column "Δa_{comb}" refers to the combined age uncertainty from the radar and the ice-core chronology, whilst "Δa_{total}" refers to the maximum age uncertainty of our IRHs calculated from the age difference between our IRHs and the strong sulfate peaks at WD2014 (see Sections 2.4.1 and 4.2).
Abbreviation: IRH, internal reflecting horizon.

To compare the ages independently from the WD2014 chronology and provide an approximate age-range estimate for our shallowest isochrone R1, we use the 1-D model at Sites A and B. The age estimates returned from the 1-D model at both sites are as follows: R1 (2.31–2.92), R2 (4.46–5.82), R3 (6.75–9.15), and R4 (19.69–26.87 ka) (Table 4).

The ages calculated for R2–3 at WD2014 (Table 3) are within the upper and lower bounds of the modeled age-range estimates from the 1-D model (Table 4), with the MED14 and RACMO2 accumulation products best able to reproduce the ages at WD2014 to within < 10%. However, the returned age estimate for R4 at Site A, 19.69–26.87 ka, is 20%–60% greater than the age of R4 at WD2014 (16.50 ± 0.79 ka) and that of Jacobel and Welch (2005) (17.5 ± 0.5 ka). We come back to these points in Sections 4.1 and 4.3.

Table 4
Modeled IRH Age-Range Estimates (ka) Returned From the 1-D Steady-State Model for Varying Accumulation Data Sets (see Section 2.4.2) and Basal Shear Layer Thickness (h, in m) Scenarios at Sites A and B for IRHs R1–4 (see Section 2.4.2)

		Site A			Site B		
		$h = 700$	$h = 900$	$h = 1{,}100$	$h = 700$	$h = 900$	$h = 1{,}100$
R1	MAR	2.84	2.85	2.86	2.89	2.90	2.92
	ART06	2.68	2.69	2.70	2.78	2.80	2.81
	RACMO2	2.36	2.37	2.38	2.32	2.33	2.34
	MED14	2.31	2.32	2.33	2.36	2.37	2.38
R2	MAR	5.72	5.77	5.82	5.55	5.61	5.67
	ART06	5.40	5.44	5.49	5.35	5.40	5.46
	RACMO2	4.75	4.79	4.84	4.46	4.50	4.55
	MED14	4.65	4.69	4.73	4.57	4.62	4.67
R3	MAR	8.88	9.01	9.15	8.41	8.54	8.69
	ART06	8.38	8.50	8.63	8.10	8.23	8.37
	RACMO2	7.38	7.48	7.60	6.75	6.86	6.98
	MED14	7.22	7.32	7.43	6.92	7.03	7.15
R4	MAR	24.22	25.40	26.87	–	–	–
	ART06	22.85	24.00	25.40	–	–	–
	RACMO2	20.13	21.10	22.32	–	–	–
	MED14	19.69	20.64	21.84	–	–	–

Note: At Site B, R4 was not retrieved. The accumulation rates (m a^{-1}) used to obtain each IRH age estimate can be found in Table S4. We calculate an empirical error estimate of between ±2% and 4% for each modeled age estimate based on the uncertainties in radar depth (±17 m) and ice thickness (±23 m, Vaughan et al., 2006).
Abbreviation: IRH, internal reflecting horizon

4. Discussion

4.1. IRH Comparison Across the WAIS

Karlsson et al. (2014) traced two distinctive IRHs through the middle ice depths across parts of the central PIG catchment using the same PIG-PASIN data set as that used here, but only focusing on flight lines flown at constant elevation and only exploiting the data in its chirp mode. This earlier study highlighted the existence of a distinctive IRH package between an upper bound, "Layer 1", approximately dated to 5.3–6.2 ka, and a lower bound "Layer 2", approximately dated to 8.6–13.4 ka. Here, by additionally exploiting the full spatial extent of the PIG-PASIN data set, the simultaneously acquired pulse-mode PASIN data, and complementing these with recent OIB-MCoRDS2 data, we have expanded the reach of that earlier radiostratigraphy across the fuller PIG catchment, and across the ice divides into neighboring regions, notably Thwaites Glacier and Institute Ice Stream. Direct comparison between both sets of results suggests that Karlsson et al.'s (2014) Layers 1 and 2 are equivalent to the IRHs traced in this study as R2 and R3, with a median difference ranging between 6 and 12 m, which is within the depth uncertainty of the IRHs (Figure S3).

Throughout the neighboring Institute and Möller ice-stream catchments, Ashmore et al. (2020) also recently traced three prominent IRHs (H1–3), broadly dated at 1.9–3.2 (H1), 3.5–6.0 (H2), and 4.6–8.1 ka (H3), using the same 1-D model described here. They posited that their deeper two IRHs (namely H2–3) were also similar to Karlsson et al.'s (2014) Layers 1 and 2 (and hence are likely equivalent to our R2 and R3), but the association was untested with any direct crossovers. Here, we were able to trace our upper three IRHs R1–3 along an OIB-MCoRDS2 profile extending across the upper Institute Ice Stream catchment (Figures 4a–4c), intersecting eight IMAFI-PASIN profiles in which H1–3 were traced. Across these intersections, the mean difference between OIB-MCoRDS2 R1-3 and IMAFI-PASIN H1-3 is 15 m, which is within the uncertainty bounds of the respective radar systems (±14 m for OIB-MCoRDS2; ±15 m for IMAFI-PASIN, Ashmore

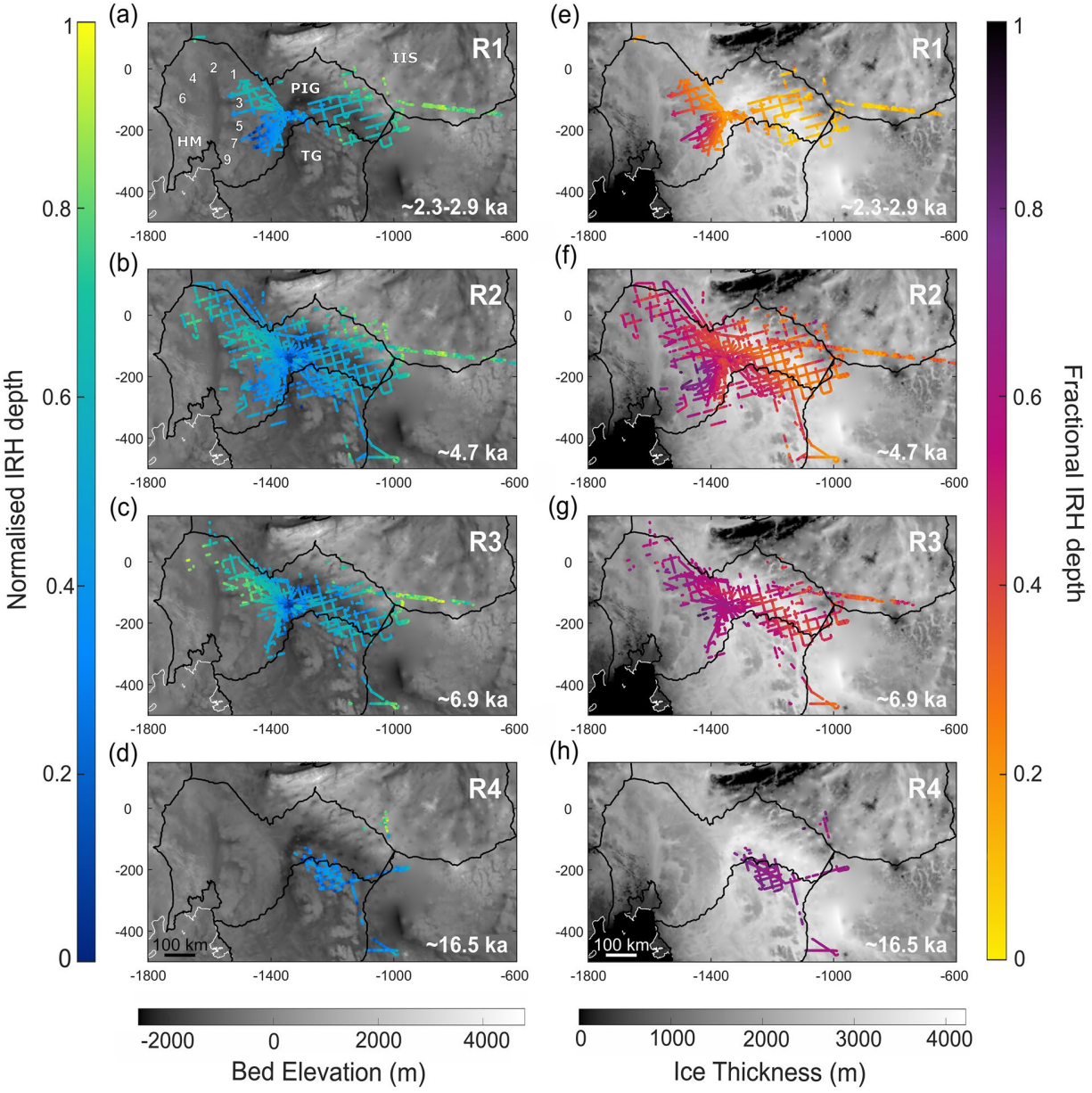

Figure 4. Normalized (a–d) and fractional (e–h) depth for the four IRHs traced over the PIG-PASIN and OIB-MCoRDS2 data from shallowest to deepest. Also shown are the IRH ages (ka) (see Section 3.2) for R1 (age-range estimate from 1-D model) and R2–4 (ages from WD2014 ice-core intersection). For (a–d), lower (blue) values correspond to relatively deep IRH depths, higher (yellow) values correspond to shallow IRH depths. Background is bed elevation in meters (referenced to the WGS84 ellipsoid) from BedMachine (Morlighem et al., 2020). For (e–h), lower (yellow) values correspond to the shallowest IRHs, higher (purple) values correspond to the deepest IRHs. Background is ice thickness in meters from BedMachine (Morlighem et al., 2020). The white line is the Antarctic coast line. The numbers and annotations in (a) are the eight fast-flowing tributaries (1–7 and 9) of Pine Island Glacier, the location of the Hudson Mountain Range (HM), and the ICESat IMBIE basins containing Pine Island Glacier (PIG), Thwaites Glacier (TG) and Institute Ice Stream (ISS) (Zwally et al., 2012).

et al. 2020), and hence provides additional evidence that we observe the same IRHs across both catchments. Two sets of parallel profiles, laterally offset by ~1.5 km, and acquired across the PIG/Institute Ice Stream divide in the PIG-PASIN and IMAFI-PASIN data sets (Figure 1), provide a further opportunity to confirm these equivalences with data from the same radar system. Only in three short sections of these transects could we compare our IRHs with those from the IMAFI-PASIN study (inset Figure S3a); in these locations,

we could not identify R1 and R3. Nevertheless, at two intersections (black arrows in inset on Figure S3a), the respective depths for PIG-PASIN R2 and IMAFI-PASIN H2 were 794 and 797 m at Intersection 1 and 776 and 778 m at Intersection 2, respectively, which is remarkably close considering ice thickness in this area exceeds 2 km. This, alongside the crossovers on the OIB-MCoRDS2 data, gives us high confidence that our R2, Ashmore et al.'s (2020) H2, and therefore Karlsson et al.'s (2014) Layer 1, all represent the same internal marker in the ice. This study, by using additional data that allowed direct dating at the WD2014 site, is therefore able to ascribe more accurate and precise ages to the IRH package ranging across PIG and Institute and Möller Ice Streams of 4.72 ± 0.28 ka (Layer 1/H2/R2) and 6.94 ± 0.31 ka (Layer 2/H3/R3), respectively, based on the WD2014 ice-core chronology.

We also note that all three studies identify R2 as their most spatially extensive IRH, indicating the presence of a particularly ubiquitous isochrone, similar in age to a 4.72 ± 0.24 ka isochrone detected and also extensively mapped elsewhere across central West Antarctica (Muldoon et al., 2018). Whilst we were not able to provide a more refined age to our shallowest IRH, R1, from direct intersection of the WD2014 Ice Core, the 1-D model returned an age-range estimate (2.31–2.92 ka) that is in broad agreement with that of Ashmore et al. (2020) (1.9–3.2 ka; their H1) and Siegert and Payne (2004) (3.10 ± 0.16 ka; their L07). Together, these studies demonstrate considerable promise for unifying an age-depth stratigraphy across the WAIS back to at least ~7 ka, while tying our IRHs to the WD2014 Ice Core has yielded more accurate, and younger, ages, for the isochrones detected across PIG and, by extension, Institute and Möller Ice Streams.

The age assigned to R4 at WD2014 (16.50 ± 0.79 ka) is slightly younger than the 17.5 ± 0.5 ka layer tied by Jacobel and Welch (2005) to the Byrd Ice Core (Hammer et al., 1997), although there is an overlap of 0.29 ka when fully accounting for the age uncertainties. We offer two potential explanations for this disparity. First, the low-frequency ground-radar system used as part of the ITASE survey has a much longer wavelength than the high-frequency airborne systems used here, meaning that the 17.5 ± 0.5 ka layer appears as a single-amplitude peak measuring tens of meters in thickness (cf. Jacobel & Welch, 2005), whereas the shorter-wavelength on the airborne radars allows for the delineation of individual peaks, thus resolving the strong singular reflector from Jacobel and Welch (2005) as a series of closely spaced reflectors. As a result, when attempting to connect the ITASE profile with the airborne radar data, it is likely that the closest bright reflector identified on the airborne radar forms the upper part of the wider reflector imaged by Jacobel and Welch (2005), thus leading to younger ages at the intersection with the WD2014 Ice Core. Second, the uncertainties in the radar data at the intersection between OIB-MCoRDS2 (±14 m) and Jacobel and Welch's (2005) profile (±10 m) increase the chance to misinterpret the correct position of the 17.5 ka layer over the airborne data, although we show in Table S2 that the mean depth difference between R4 and Jacobel and Welch's (2005) layer is < 18 m, which is within the uncertainty range of both studies. Whilst these points are relevant when comparing the ages of R4 at WD2014 with the age of Jacobel and Welch's (2005) layer, it is worth mentioning that the exact age and depth of the strong reflector at WD2014 are known from electrical conductivity and chemistry measurements. At the ice core, this layer is characterized by nine distinctive peaks ranging in depths between 2,420 and 2,427 m and dated at 17.75 ± 0.19 ka (McConnell et al., 2017; Sigl et al., 2016), a full 35 m below the depth of R4 at WD2014. Even taking into account the maximum depth of our IRH along the ±250 m transect (2,378 ± 14 m; see Section 3.1), R4 is still found 28 m above the depth of the 17.75 ± 0.19 ka at WD2014. Considering all the above, it is likely that R4 is not the same layer as the strong volcanic layer dated at 17.75 ± 0.19 ka at WD2014 (McConnell et al., 2017), but rather forms the upper part of the wide reflector imaged by Jacobel and Welch (2005) in the ground-radar data.

4.2. Linkage with the WAIS Divide Ice-Core Record

Whilst determining the cause of R4 remains ambiguous due to the limitations mentioned above, the existence of R2 and R3 offers an opportunity to link them directly to the ice-core sulfate record at WD2014. High sulfate content from volcanic sulfuric acid is known to correspond to high acidity levels in englacial layers in ice cores (Castellano et al., 2005; Gow & Williamson, 1971; Hammer et al., 1997; Millar, 1982) and, because the radar is sensitive to acidity contrasts (Fujita et al., 1999; Millar, 1981), we can attempt to link the sulfate record at the ice core with our IRH stratigraphy. Figure S4 shows the presence of three large peaks in sulfate concentration at the WD2014 ice core, which are particularly close in age and depth to IRHs R2–3 traced on the OIB-MCoRDS2 profile near WD2014. In particular, a layer dated at 4.94 ka (depth: 1,099 m)

contains sulfate concentrations that are unmatched (405 μg/kg) for much of the core up until a depth of ~2,400 m (equal to the last ~18,000 years BP) (Figure S4). Even taking into account the entire profile, this layer contains the fourth largest amount of sulfate concentrations in the last ~68,000 years BP. We also notice the presence of two closely spaced peaks in the sulfate record which are dated at 7.25 ka (depth: 1,475 m; sulfate concentration: 306 μg/kg) and 7.64 ka (depth: 1,526 m; sulfate concentration: 271 μg/kg), corresponding to the 9th and 10th highest sulfate concentrations on record (Figure S4b). Not only do these ages match closely the age of R3 at the ice core, they also match the characteristics of R3, which is often found as a couplet across most of Pine Island, upper Thwaites, and Institute and Möller ice-stream catchments on the airborne radar data (Figures 2 and S1). Additionally, the second largest peak on record before ~18,000 years BP is found at a depth of 584 m and dated at 2.45 ka (sulfate concentration: 309 μg/kg), which falls within the modeled age-range estimate for R1 (2.31–2.92 ka) at Sites A and B (Table 4, Figure S4a).

Whilst this offers us the opportunity to directly link our IRHs to the WAIS Divide record, we note that the depths of R2–3 at WD2014 are slightly shallower (R2: 1,060 ± 7 m; R3: 1,430 ± 9 m) than the sulfate peaks in Figure S4, resulting in slightly younger ages at the ice core. We cannot exclude the possibility that we traced a layer that is slightly above R2 and R3 at the Ice Core, although this is unlikely as we base our tracing on depth intersections (Figure S2) and IRH characteristics (Figure S1). Even taking into account the maximum depth of R2–3 along our ±250 m transect to account for the fact the OIB-MCoRDS2 line did not fly directly over the WD2014 site but instead ~1.2 km away (see Section 2.4.1), R2 (1,069 ± 7 m) and R3 (1,438 ± 9 m) would still be found 23 and 28 m higher than the sulfate peaks at the ice core, respectively. Whilst this is a relatively small disparity considering ice thickness in the area exceeds ~3.5 km and that we are effectively comparing airborne-radar data (meter-scale accuracy) with ice-core data (mm-scale accuracy), the reason for our IRHs not aligning more closely with the sulfate peaks remains unclear. One potential explanation could relate to the distance between our transect and the location of the WD2014 ice-core site. Although Laird et al. (2010) suggested that flow-induced disturbance on layer geometry is limited in the area around the WD2014 site, changes in bed roughness were found to affect englacial stratigraphy near WD2014. This could lead to small undulation in IRH elevations between our transect and WD2014 and thus cause in several meters of discrepancy. To acknowledge this, and considering that the sulfate peaks are most likely the cause of our IRHs as we show above, we have increased the age uncertainty of our IRHs to account for the offset between our IRH ages and the age of the sulfate peaks (see Section 2.4.1, Table 3). This results in more conservative uncertainties for our deeper three IRHs dated at the ice core: 4.72 ± 0.28 (R2), 6.94 ± 0.31 (R3), and 16.50 ± 0.79 ka (R4).

By linking three of our four IRHs to the sulfate record at WAIS Divide, we can hypothesize that the origin of our spatially extensive IRHs is from past explosive volcanic activity during the Holocene. Previous studies in Antarctica have demonstrated the correspondence between bright reflectors in radar data and past volcanic activity (e.g., Corr & Vaughan, 2008; Jacobel & Welch, 2005). Karlsson et al. (2014) previously attempted to link their deeper layer (Layer 2/R3) to acidity peaks at Byrd Ice Core; however, the absence of a direct link between the PIG catchment and a complete ice-core chronology was lacking at the time. The evidence presented here suggests that our IRHs may also originate from past explosive volcanism; but, the precise source of these eruptions, whether regional or global, remains unknown.

4.3. Accumulation Rate and IRH-Age Comparison

The correspondence in isochrone-age estimates for IRHs R2–3 derived from intersecting the WD2014 site (Table 3) and using the 1-D model (Table 4) at the PIG/Thwaites divide (~250 km away) (our Sites A and B; Figure 1) suggests that accumulation patterns have remained broadly similar across the Amundsen-Ross divide for at least the last ~7 ka. Whilst this is based on a relatively limited amount of data points, it complements previous studies (Fudge et al., 2016; Koutnik et al., 2016; Neumann et al., 2008), including Siegert and Payne (2004) who, using the same SPRI/NSF/TUD radar transect as that in Figure 1, concluded that accumulation patterns have remained stable over the last 6.4 ka. We suggest future research make use of the accurately dated IRHs provided here to model Holocene accumulation rates and patterns, as well as regional ice-sheet balance velocities, as previously conducted over Greenland (e.g., MacGregor et al., 2016)

and on individual sections of the WAIS (Koutnik et al., 2016; Neuman et al., 2008). This will provide additional information on the terrestrial ice-sheet history of the ASE during the Holocene, and in turn help us to constrain better the future of the WAIS.

Previous studies have successfully combined ice-core records with modeled modern-day accumulation rates to reconstruct Holocene accumulation (Cavitte et al., 2018; Fudge et al., 2016; Nielsen et al., 2018), although non-climatic noise in the observations and model biases have resulted in small discrepancies between ice-core and model reconstructions (Cavitte et al., 2020; Dalaiden et al., 2020). When assessing the ability of the 1-D model to reproduce the ages for R2-3 derived at the WD2014 Ice Core, we find that the best match (to within < 10%) is achieved using the modern accumulation rates provided by the MED14 and RACMO2 products. This is not surprising as both have higher spatial resolution than MAR and ART06, but it also likely reflects the fact that MED14 is an observational product and that RACMO2 has been shown to agree well with geophysical estimates of accumulation rates (Lenaerts et al., 2012; Medley et al., 2014; van Wessem et al., 2018; Wang et al., 2016). In contrast, when using present-day accumulation estimates from ART06 and MAR to calculate past accumulation rates, model-derived ages are up to 1.1 ka (~23%) greater for R2 and 2.2 ka (~32%) greater for R3 compared with ice-core derived ages (Tables 3 and 4). This discrepancy is primarily dominated by different modern accumulation gradients estimated between WD2014 and the PIG/Thwaites divide (i.e., Sites A and B), with the MED14 and RACMO2 products suggesting a slightly more homogenous gradient than ART06 and MAR (Table S4). Lower in the ice, the poor correspondence between the age of R4 derived by links to the WD2014 (16.50 ± 0.79 ka) relative to the age returned by the 1-D model (19.69–26.87 ka) is worthy of investigation. Even taking into account the maximum age uncertainty at the ice core, the minimum and maximum age returned by the 1-D model is 2.6 (15%) and 9.8 ka (57%) greater than at the ice core (Tables 3 and 4), a difference that cannot solely be attributed to the different modern-day accumulation gradients mentioned above. The most likely explanation is that the assumptions required for the 1-D model (see Section 2.4.2) break down for older IRHs, where local accumulation rate is no longer a primary factor in determining the depth of an IRH. This could be due to complex flow dynamics such as longitudinal strain or lateral shearing at the boundary between slow and fast-flowing ice, resulting in high internal stress impacting IRH stratigraphy in the deeper part of the ice column (Waddington et al., 2007). Moreover, R4 (16.50 ± 0.79 ka) was deposited pre-Holocene as the WAIS was transitioning from a glacial to an interglacial period during which ice thickness has likely not remained constant (Golledge et al., 2014; Johnson et al., 2017), implying possible changes in ice-flow configurations for which the steady-state model is not able to account.

4.4. Characteristics of Englacial Stratigraphy

Previous research over East Antarctica has shown that common bright reflectors can be interchangeably traced over long distances using radar systems operating at different center frequencies (Cavitte et al., 2016; Winter et al., 2017). Our findings provide further evidence of this over West Antarctica, having successfully identified common IRHs across different airborne radar systems. However, although IRHs younger than 7 ka can be traced widely across the WAIS using existing data sets, tracing deeper, pre-Holocene IRHs has not been widely possible across PIG (this study) nor the Weddell Sea Sector (Ashmore et al., 2020). Relative to the interior of East Antarctica, where much lower snow accumulation and ice-flow velocities have facilitated the tracing of isochrones pre-dating the LGM (~20 ka BP) and even the past glacial-interglacial periods (up to ~366 ka BP) (Cavitte et al., 2016; Parrenin et al., 2017; Steinhage et al., 2013; Winter et al., 2019), the extremely variable deep-ice conditions in the WAIS will challenge the recovery of pre-Holocene radiostratigraphy. Compounding the challenge, Ross et al. (2020) have demonstrated that large packages of ice older than ~16 ka in the Weddell Sea sector of the WAIS are rheologically different to the ice above, containing large proportions of deformed and folded ice. These packages typically show poor continuity of englacial stratigraphy across Institute and Möller Ice Streams (Bingham et al., 2015) and, indeed, where we could see IRHs deeper than R4 in PASIN and MCoRDS2 for this study, very few were continuous for long distances. Over other parts of the WAIS, an IRH dating back to 24.9 ± 0.3 ka has been traced in limited radar profiles connecting the Byrd and WAIS divide ice cores, where it was found at 68% and 80% of ice depth at Byrd and WD2014, respectively (Muldoon et al., 2018); however, they were also unable to recover deeper continuous IRHs more widely.

Overall, with the existing data sets available across the WAIS, the prospects for tracing and dating Holocene radiostratigraphy widely across the ice sheet with existing data are excellent, but diminish rapidly for older ice, going back to the LGM and beyond. Yet, much deeper, and thus older IRHs, are visible throughout the ice column with ground-based radars (e.g., Bingham et al., 2017; King, 2011; Laird et al., 2010) and hence the interrogation of older ice in the WAIS may be best suited to strategic ground campaigns that can be linked into the airborne-derived radiostratigraphy. In the PIG catchment, older ice is suggested by our results to lie below the PIG/Thwaites divide, where on average ~900 m of ice (30% of the mean ice thickness) underlies R4 (~17 ka) (Figure S5).

5. Conclusion

We have identified four spatially extensive IRHs in airborne radar surveys that are present across much of the Pine Island Glacier catchment in West Antarctica. Extending into neighboring Thwaites Glacier and Institute Ice Stream, these IRHs can be considered isochrones that span the late Pleistocene and Holocene, with ages of 2.31–2.92, 4.72 ± 0.28, 6.94 ± 0.31, and 16.50 ± 0.79 ka derived from intersecting the WAIS Divide Ice Core and the use of a 1-D ice-flow model. Our most spatially extensive IRH, R2, is remarkably similar in age and depth to another extensive IRH previously identified by other studies over Pine Island Glacier, Institute and Möller Ice Streams, and the Marie Byrd Land region. More broadly, we have also shown that our IRH package is similar to previously traced IRHs over the Weddell Sea sector of the WAIS, which, together with the Pine Island Glacier catchment represents ~20% of West Antarctica. Finally, we have shown that our upper three IRHs correspond to large peaks in sulfate concentrations at the WAIS Divide Ice Core, suggesting that our IRHs are of volcanic origin.

When assessing the presence of older ice across the catchment, we observe that the relative proportion of ice older than R4 in the ice column is limited and does not contain many continuous reflections. Indeed, we find that the deepest (and thus oldest) continuous IRH identified in this study, R4, is found at an average depth of 68% in the ice column despite its age (~17 ka), only representing 25% of the estimated age of the oldest ice recovered at the WAIS Divide Ice Core (~68 ka). This indicates that the majority of ice older than the LGM is found within the bottom ~30% of the ice thickness across PIG/Upper Thwaites. Whilst this is to be expected as the age-depth profile of an ice sheet does not increase linearly, the absence of continuous reflections dating back to the LGM and older currently limits our ability to reconstruct longer-term changes using existing airborne data sets.

As isochronous features, the dated IRHs generated here offer a new set of large-scale boundary conditions that could be a valuable resource, if incorporated into ice-flow models seeking to improve our understanding of past ice-sheet evolution. We anticipate that these well-dated IRHs will provide constraints for models simulating past accumulation rates and patterns, which in turn will shed more light onto the terrestrial ice sheet history of this very sensitive catchment of the WAIS.

Acknowledgments
This study was motivated by the AntArchitecture Action Group of the Scientific Committee for Antarctic Research (SCAR). J. A. Bodart was supported by the NERC Doctoral Training Partnership grant (NE/L002558/1), hosted in the Edinburgh E^3 DTP program. The authors would like to thank the reviewers, Marie Cavitte and T. J. Fudge, for their constructive suggestions, which greatly improved this manuscript. The authors thank the BAS scientists and logistics personnel for acquiring the PASIN data over Pine Island Glacier, which will be made fully available upon publication from the Polar Airborne Geophysics Data Portal of the UK Polar Data Center (https://secure.antarctica.ac.uk/data/aerogeo/). The authors also thank CReSIS for acquiring and providing the processed MCoRDS2 data, which can be downloaded from the OIB data portal (https://data.cresis.ku.edu/). The authors thank Brooke Medley and Howard Conway for providing the airborne and ground snow accumulation products.

Data Availability Statement

The RACMO2 and MAR SMB outputs were downloaded from (https://www.projects.science.uu.nl/iceclimate/publications/data/2018) and (https://zenodo.org/record/2547638) respectively. Parts of the figures included in this study were produced with outputs from the Antarctic Mapping Toolbox in MATLAB® (Greene et al., 2017). The full picking information for each IRH can be downloaded from the UK Polar Data Center (https://doi.org/10.5285/f2de31af-9f83-44f8-9584-f0190a2cc3eb; Bodart et al., 2021).

References

Agosta, C., Amory, C., Kittel, C., Orsi, A., Favier, V., Gallée, H., et al. (2019). Estimation of the Antarctic surface mass balance using the regional climate model MAR (1979–2015) and identification of dominant processes. *The Cryosphere*, *13*(1), 281–296. https://doi.org/10.5194/tc-2018-76

Arthern, R. J., Winebrenner, D. P., & Vaughan, D. G. (2006). Antarctic snow accumulation mapped using polarization of 4.3-cm wavelength microwave emission. *The Journal of Geophysical Research*, *111*(D6). https://doi.org/10.1029/2004JD005667

Ashmore, D. W., Bingham, R. G., Ross, N., Siegert, M. J., Jordan, T. A., & Mair, D. W. F. (2020). Englacial architecture and age-depth constraints across the West Antarctic Ice Sheet. *Geophysical Research Letters*, *47*. https://doi.org/10.1029/2019GL086663

Bingham, R. G., Rippin, D. M., Karlsson, N. B., Corr, H. F. J., Ferraccioli, F., Jordan, T. A., et al. (2015). Ice-flow structure and ice dynamic changes in the Weddell Sea sector of West Antarctica from radar-imaged internal layering. *Journal of Geophysical Research: Earth Surface*, *120*(4), 655–670. https://doi.org/10.1002/2014JF003291

Bingham, R. G., & Siegert, M. J. (2007). Radio-echo sounding over polar ice masses. *Journal of Environmental and Engineering Geophysics*, *12*(1), 47–62. https://doi.org/10.2113/JEEG12.1.47

Bingham, R. G., Vaughan, D. G., King, E. C., Davies, D., Cornford, S. L., Smith, A. M., et al. (2017). Diverse landscapes beneath Pine Island Glacier influence ice flow. *Nature Communications*, *8*(1), 1618. https://doi.org/10.1038/s41467-017-01597-y

Bodart, J. A., Bingham, R. G., Ashmore, D. W., Karlsson, N. B., Hein, A. S., & Vaughan, D. G. (2021). Dated radar stratigraphy of the Pine Island Glacier catchment (West Antarctica) derived from BBAS-PASIN (2004-05) and OIB-MCoRDS2 (2016/2018) surveys. UK Polar Data Centre, Natural Environment Research Council, UK Research & Innovation. https://doi.org/10.5285/f2de31af-9f83-44f8-9584-f0190a2cc3eb

Bodart, J. A., & Bingham, R. J. (2019). The impact of the extreme 2015-2016 El Niño on the mass balance of the Antarctic Ice Sheet. *Geophysical Research Letters*, *46*(23), 13862–13871. https://doi.org/10.1029/2019GL084466

Bracegirdle, T. J., Colleoni, F., Abram, N. J., Bertler, N. A. N., Dixon, D. A., England, M., et al. (2019). Back to the future: Using long-term observational and paleo-proxy reconstructions to improve model projections of Antarctic climate. *Geosciences*, *9*(6), 255. https://doi.org/10.3390/geosciences9060255

Buizert, C., Cuffey, K. M., Severinghaus, J. P., Baggenstos, D., Fudge, T. J., Steig, E. J., et al. (2015). The WAIS Divide deep ice core WD2014 chronology – Part 1: Methane synchronization (68-31 ka BP) and the gas age-ice age difference. *Climate of the Past*, *11*(2), 153. https://doi.org/10.5194/cp-11-153-2015

Castellano, E., Becagli, S., Hansson, M., Hutterli, M., Petit, J. R., Rampino, M. R., et al. (2005). Holocene volcanic history as recorded in the sulphate stratigraphy of the European Project for Ice Coring in Antarctica Dome C (EDC96) ice core. *Journal of Geophysical Research*, *110*(D6). https://doi.org/10.1029/2004JD005259

Catania, G. A., Scambos, T. A., Conway, H., & Raymond, C. F. (2006). Sequential stagnation of Kamb Ice Stream, West Antarctica. *Geophysical Research Letters*, *33*(F1). https://doi.org/10.1029/2006GL026430

Cavitte, M. G. P., Blankenship, D. D., Young, D. A., Schroeder, D. M., Parrenin, F., Lemeur, E., et al. (2016). Deep radiostratigraphy of the East Antarctic plateau: Connecting the Dome C and Vostok ice core sites. *Journal of Glaciology*, *62*(232), 323–334. https://doi.org/10.1017/jog.2016.11

Cavitte, M. G. P., Dalaiden, Q., Goosse, H., Lenaerts, J. T. M., & Thomas, E. R. (2020). Reconciling the surface temperature-surface mass balance relationship in models and ice cores in Antarctica over the last 2 centuries. *The Cryosphere*, *14*, 4083–4102. https://doi.org/10.5194/tc-14-4083-2020

Cavitte, M. G. P., Parrenin, F., Ritz, C., Young, D. A., Van Liefferinge, B., Blankenship, D. D., et al. (2018). Accumulation patterns around Dome C, East Antarctica, in the last 73 kyr. *The Cryosphere*, *12*, 1401–1414. https://doi.org/10.5194/tc-12-1401-2018

Christianson, K., Bushuk, M., Dutrieux, P., Parizek, B. R., Joughin, I. R., Alley, R. B., et al. (2016). Sensitivity of Pine Island Glacier to observed ocean forcing. *Geophysical Research Letters*, *43*(20), 10817–10825. https://doi.org/10.1002/2016GL070500

Clough, J. W. (1977). Radio-echo sounding: Reflections from internal layers in ice sheets. *Journal of Glaciology*, *18*(78), 3–14. https://doi.org/10.3189/S002214300002147X

Cole - Dai, J. (2014). "Major ion chemistry data of WAIS Divide ice core brittle ice". U.S. Antarctic Program (USAP) Data Center. https://doi.org/10.7265/N5RF5S0D

Corr, H. F. J., & Vaughan, D. G. (2008). A recent volcanic eruption beneath the West Antarctic Ice Sheet. *Nature Geoscience*, *1*(2), 122–125. https://doi.org/10.1038/ngeo106

CReSIS (2016). CReSIS radar depth sounder data. Digital Media. Retrieved from http://data.cresis.ku.edu/

Cuffey, K. M., Clow, G. D., Steig, E. J., Buizert, C., Fudge, T. J., Koutnik, M., et al. (2016). Deglacial temperature history of West Antarctica. *Proceedings of the National Academy of Sciences of the United States of America*, *113*(50), 14249–14254. https://doi.org/10.1073/pnas.1609132113

Dalaiden, Q., Goosse, H., Klein, F., Lenaerts, J. T. M., Holloway, M., Sime, L., & Thomas, E. R. (2020). How useful is snow accumulation in reconstructing surface air temperature in Antarctica? A study combining ice core records and climate models. *The Cryosphere*, *14*(4), 1187. https://doi.org/10.5194/tc-14-1187-2020

Dansgaard, W., & Johnsen, S. J. (1969). A flow model and a time scale for the ice core from Camp Century, Greenland. *Journal of Glaciology*, *8*(53), 215–223. https://doi.org/10.3189/S002214300003120810.1017/s0022143000031208

DeConto, R. M., & Pollard, D. (2016). Contribution of Antarctica to past and future sea-level rise. *Nature*, *531*(7596), 591–597. https://doi.org/10.1038/nature17145

Denton, G. H., & Hughes, T. J. (2002). Reconstructing the Antarctic ice sheet at the Last Glacial Maximum. *Quaternary Science Reviews*, *21*(1–3), 193–202. https://doi.org/10.1016/S0277-3791(01)00090-7

Dutrieux, P., De Rydt, J., Jenkins, A., Holland, P. R., Ha, H. K., Lee, S. H., et al. (2014). Strong sensitivity of Pine Island ice-shelf melting to climatic variability. *Science*, *343*(6167), 174–178. https://doi.org/10.1126/science.1244341

Eisen, O., Frezzotti, M., Genthon, C., Isaksson, E., Magand, O., van den Broeke, M. R., et al. (2008). Ground-based measurements of spatial and temporal variability of snow accumulation in East Antarctica. *Reviews of Geophysics*, *46*(2). https://doi.org/10.1029/2006RG000218

Eisen, O., Rack, W., Nixdorf, U., & Wilhelms, F. (2005). Characteristics of accumulation around the EPICA deep-drilling site in Dronning Maud Land, Antarctica. *Annals of Glaciology*, *41*, 41–46. https://doi.org/10.3189/172756405781813276

Fahnestock, M., Abdalati, W., Joughin, I., Brozena, J., & Gogineni, P. (2001). High geothermal heat flow, basal melt, and the origin of rapid ice flow in central Greenland. *Science*, *294*(5550), 2338–2342. https://doi.org/10.1126/science.1065370

Fahnestock, M., Abdalati, W., Luo, S., & Gogineni, S. (2001). Internal layer tracing and age-depth-accumulation relationships for the northern Greenland ice sheet. *Journal of Geophysical Research*, *106*(D24), 33789–33797. https://doi.org/10.1029/2001JD900200

Favier, L., Durand, G., Cornford, S. L., Gudmundsson, G. H., Gagliardini, O., Gillet-Chaulet, F., et al. (2014). Retreat of Pine Island Glacier controlled by marine ice-sheet instability. *Nature Climate Change*, *4*(2), 117. https://doi.org/10.1038/nclimate2094

Fudge, T. J., Biyani, S. C., Clemens-Sewall, D., & Hawley, R. L. (2019). Constraining geothermal flux at coastal domes of the Ross Ice Sheet, Antarctica. *Geophysical Research Letters*, *46*(22), 13090–13098. https://doi.org/10.1029/2019GL084332

Fudge, T. J., Markle, B. R., Cuffey, K. M., Buizert, C., Taylor, K. C., Steig, E. J., et al. (2016). Variable relationship between accumulation and temperature in West Antarctica for the past 31,000 years. *Geophysical Research Letters*, *43*(8), 3795–3803. https://doi.org/10.1002/2016GL068356

Fujita, S., Maeno, H., Uratsuka, S., Furukawa, T., Mae, S., Fujii, Y., & Watanabe, O. (1999). Nature of radio echo layering in the Antarctic Ice Sheet detected by a two-frequency experiment. *Journal of Geophysical Research*, *104*(B6), 13013–13024. https://doi.org/10.1029/1999JB900034

Fujita, S., Matsuoka, T., Ishida, T., Matsuoka, K., & Mae, S. (2000). A summary of the complex dielectric permittivity of ice in the megahertz range and its applications for radar sounding of polar ice sheets. In T. Hondoh (Ed.), Ed., *Physics of ice core records* (pp. 185–212). Hokkaido University Press.

Golledge, N. R., Menviel, L., Carter, L., Fogwill, C. J., England, M. H., Cortese, G., & Levy, R. H. (2014). Antarctic contribution to meltwater pulse 1A from reduced Southern Ocean overturning. *Nature Communications*, *5*, 5107. https://doi.org/10.1038/ncomms6107

Gow, A. J. (1970). Preliminary results of studies of ice cores from the 2164m-deep drill hole, Byrd Station, Antarctica. Paper presented at the international symposium on Antarctic Glaciological Exploration, IAHS Publication (Vol. 86 (pp. 78–90). IAHS.

Gow, A. J., & Williamson, T. (1971). Volcanic ash in the Antarctic ice sheet and its possible climatic implications. *Earth and Planetary Science Letters*, *13*(1), 210–218. https://doi.org/10.1016/0012-821X(71)90126-9

Greene, C. A., Gwyther, D. E., & Blankenship, D. D. (2017). Antarctic mapping tools for Matlab. *Computers & Geosciences*, *104*, 151–157. https://doi.org/10.1016/j.cageo.2016.08.003

Hammer, C. U., Clausen, H. B., & Langway, C. C., Jr. (1997). 50,000 years of recorded global volcanism. *Climatic Change*, *35*(1), 1–15. https://doi.org/10.1023/A:1005344225434

Harrison, C. H. (1973). Radio echo sounding of horizontal layers in ice. *Journal of Glaciology*, *12*(66), 383–397. https://doi.org/10.3189/S0022143000031804

Hillenbrand, C.-D., Kuhn, G., Smith, J. A., Gohl, K., Graham, A. G. C., Larter, R. D., et al. (2013). Grounding-line retreat of the west Antarctic ice sheet from inner Pine island Bay. *Geology*, *41*(1), 35–38. https://doi.org/10.1130/G33469.1

Holland, P. R., Bracegirdle, T. J., Dutrieux, P., Jenkins, A., & Steig, E. J. (2019). West Antarctic ice loss influenced by internal climate variability and anthropogenic forcing. *Nature Geoscience*, *12*(9), 718–724. https://doi.org/10.1038/s41561-019-0420-9

Holschuh, N., Christianson, K., & Anandakrishnan, S. (2014). Power loss in dipping internal reflectors, imaged using ice-penetrating radar. *Annals of Glaciology*, *55*(67), 49–56. https://doi.org/10.3189/2014AoG67A005

Holschuh, N., Christianson, K., Conway, H., Jacobel, R. W., & Welch, B. C. (2018). Persistent tracers of historic ice flow in glacial stratigraphy near Kamb Ice Stream, West Antarctica. *The Cryosphere*, *12*(9), 2821–2829. https://doi.org/10.5194/tc-12-2821-2018

Jacobel, R. W., Scambos, T. A., Raymond, C. F., & Gades, A. M. (1996). Changes in the configuration of ice stream flow from the West Antarctic Ice Sheet. *Journal of Geophysical Research*, *101*(B3), 5499–5504. https://doi.org/10.1029/95JB03735

Jacobel, R. W., & Welch, B. C. (2005). A time marker at 17.5 kyr BP detected throughout West Antarctica. *Annals of Glaciology*, *41*, 47–51. https://doi.org/10.3189/172756405781813348

Jakobsson, M., Anderson, J. B., Nitsche, F. O., Dowdeswell, J. A., Gyllencreutz, R., Kirchner, N., et al. (2011). Geological record of ice shelf break-up and grounding line retreat, Pine Island Bay, West Antarctica. *Geology*, *39*(7), 691–694. https://doi.org/10.1130/G32153.1

Johnson, J. S., Bentley, M. J., & Gohl, K. (2008). First exposure ages from the Amundsen Sea embayment, West Antarctica: The late Quaternary context for recent thinning of Pine Island, Smith, and Pope Glaciers. *Geology*, *36*(3), 223–226. https://doi.org/10.1130/G24207A.1

Johnson, J. S., Bentley, M. J., Smith, J. A., Finkel, R. C., Rood, D. H., Gohl, K., et al. (2014). Rapid thinning of Pine Island Glacier in the early Holocene. *Science*, *343*(6174), 999–1001. https://doi.org/10.1126/science.1247385

Johnson, J. S., Roberts, S. J., Rood, D. H., Pollard, D., Schaefer, J. M., Whitehouse, P. L., et al. (2020). Deglaciation of Pope Glacier implies widespread early Holocene ice sheet thinning in the Amundsen Sea sector of Antarctica. *Earth and Planetary Science Letters*, *548*, 116501. https://doi.org/10.1016/j.epsl.2020.116501

Johnson, J. S., Smith, J. A., Schaefer, J. M., Young, N. E., Goehring, B. M., Hillenbrand, C.-D., et al. (2017). The last glaciation of Bear Peninsula, central Amundsen Sea Embayment of Antarctica: Constraints on timing and duration revealed by in situ cosmogenic 14C and 10Be dating. *Quaternary Science Reviews*, *178*, 77–88. https://doi.org/10.1016/j.quascirev.2017.11.003

Karlsson, N. B., Bingham, R. G., Rippin, D. M., Hindmarsh, R. C. A., Corr, H. F. J., & Vaughan, D. G. (2014). Constraining past accumulation in the central Pine Island Glacier basin, West Antarctica, using radio-echo sounding. *Journal of Glaciology*, *60*(221), 553–562. https://doi.org/10.3189/2014JoG13j180

Karlsson, N. B., Rippin, D. M., Bingham, R. G., & Vaughan, D. G. (2012). A 'continuity-index' for assessing ice-sheet dynamics from radar-sounded internal layers. *Earth and Planetary Science Letters*, *335–336*, 88–94. https://doi.org/10.1016/j.epsl.2012.04.034

Karlsson, N. B., Rippin, D. M., Vaughan, D. G., & Corr, H. F. J. (2009). The internal layering of Pine Island Glacier, West Antarctica, from airborne radar-sounding data. *Annals of Glaciology*, *50*(51), 141–146. https://doi.org/10.3189/S0260305500250660

King, E. C. (2011). Ice stream or not? Radio-echo sounding of Carlson Inlet, West Antarctica. *The Cryosphere*, *5*(4), 907–916. https://doi.org/10.5194/tc-5-907-2011

King, E. C. (2020). The precision of radar-derived subglacial bed topography: A case study from Pine Island Glacier, Antarctica. *Annals of Glaciology*, *61*, 154–161. https://doi.org/10.1017/aog.2020.33

Kingslake, J., Scherer, R. P., Albrecht, T., Coenen, J., Powell, R. D., Reese, R., et al. (2018). Extensive retreat and re-advance of the West Antarctic Ice Sheet during the Holocene. *Nature*, *558*(7710), 430. https://doi.org/10.1038/s41586-018-0208-x

Konrad, H., Gilbert, L., Cornford, S. L., Payne, A., Hogg, A., Muir, A., & Shepherd, A. (2017). Uneven onset and pace of ice-dynamical imbalance in the Amundsen Sea Embayment, West Antarctica. *Geophysical Research Letters*, *44*(2), 910–918. https://doi.org/10.1002/2016GL070733

Koutnik, M. R., Fudge, T. J., Conway, H., Waddington, E. D., Neumann, T. A., Cuffey, K. M., et al. (2016). Holocene accumulation and ice flow near the West Antarctic Ice Sheet Divide ice core site. *Journal of Geophysical Research: Earth Surface*, *121*(5), 907–924. https://doi.org/10.1002/2015JF003668

Laird, C. M., Blake, W. A., Matsuoka, K., Conway, H., Allen, C. T., Leuschen, C. J., & Gogineni, S. (2010). Deep ice stratigraphy and basal conditions in central West Antarctica revealed by coherent radar. *IEEE Geoscience and Remote Sensing Letters*, *7*(2), 246–250. https://doi.org/10.1109/LGRS.2009.2032304

Lenaerts, J. T. M., Van den Broeke, M. R., Van de Berg, W. J., Van Meijgaard, E., & Kuipers Munneke, P. (2012). A new, high-resolution surface mass balance map of Antarctica (1979-2010) based on regional atmospheric climate modeling. *Geophysical Research Letters*, *39*(4). https://doi.org/10.1029/2011GL050713

Leysinger Vieli, G. J.-M. C., Hindmarsh, R. C. A., Siegert, M. J., & Bo, S. (2011). Time-dependence of the spatial pattern of accumulation rate in East Antarctica deduced from isochronic radar layers using a 3-D numerical ice flow model. *Journal of Geophysical Research*, *116*(F2). https://doi.org/10.1029/2010JF001785

Lindow, J., Castex, M., Wittmann, H., Johnson, J. S., Lisker, F., Gohl, K., & Spiegel, C. (2014). Glacial retreat in the Amundsen Sea sector, West Antarctica – First cosmogenic evidence from central Pine Island Bay and the Kohler Range. *Quaternary Science Reviews*, *98*, 166–173. https://doi.org/10.1016/j.quascirev.2014.05.010

Lliboutry, L. A. (1979). A critical review of analytical approximate solutions for steady state velocities and temperatures in cold ice sheets. *Zeitschr Gletscherkde Glazialgeology*, *15*, 135–148.

Lowe, A. L., & Anderson, J. B. (2002). Reconstruction of the West Antarctic ice sheet in Pine Island Bay during the Last Glacial Maximum and its subsequent retreat history. *Quaternary Science Reviews*, *21*(16–17), 1879–1897. https://doi.org/10.1016/S0277-3791(02)00006-9

MacGregor, J. A., Colgan, W. T., Fahnestock, M. A., Morlighem, M., Catania, G. A., Paden, J. D., & Gogineni, S. P. (2016). Holocene deceleration of the Greenland ice sheet. *Science*, *351*(6273), 590–593. https://doi.org/10.1126/science.aab1702

MacGregor, J. A., Fahnestock, M. A., Catania, G. A., Paden, J. D., Prasad Gogineni, S., Young, S. K., et al. (2015). Radiostratigraphy and age structure of the Greenland Ice Sheet. *Journal of Geophysical Research: Earth Surface*, *120*(2), 212–241. https://doi.org/10.1002/2014JF003215

McConnell, J. R., Burke, A., Dunbar, N. W., Köhler, P., Thomas, J. L., Arienzo, M. M., et al. (2017). Synchronous volcanic eruptions and abrupt climate change ~17.7 ka plausibly linked by stratospheric ozone depletion. *Proceedings of the National Academy of Sciences of the United States of America*, *114*(38), 10035–10040. https://doi.org/10.1073/pnas.1705595114

Medley, B., Joughin, I., Smith, B. E., Das, S. B., Steig, E. J., Conway, H., et al. (2014). Constraining the recent mass balance of Pine Island and Thwaites glaciers, West Antarctica, with airborne observations of snow accumulation. *The Cryosphere*, *8*, 1375–1392. https://doi.org/10.5194/tc-8-1375-2014

Medley, B., McConnell, J. R., Neumann, T. A., Reijmer, C. H., Chellman, N., Sigl, M., & Kipfstuhl, S. (2018). Temperature and snowfall in western Queen Maud Land increasing faster than climate model projections. *Geophysical Research Letters*, *45*(3), 1472–1480. https://doi.org/10.1002/2017GL075992

Millar, D. H. M. (1981). Radio-echo layering in polar ice sheets and past volcanic activity. *Nature*, *292*(5822), 441–443. https://doi.org/10.1038/292441a0

Millar, D. H. M. (1982). Acidity levels in ice sheets from radio echo-sounding. *Annals of Glaciology*, *3*, 199–203. https://doi.org/10.3189/S0260305500002779 10.1017/s0260305500002779

Moore, J. C. (1988). Dielectric variability of a 130 m Antarctic ice core: Implications for radar sounding. *Annals of Glaciology*, *11*, 95–99. https://doi.org/10.3189/S026030550000639X

Morlighem, M., Rignot, E., Binder, T., Blankenship, D., Drews, R., Eagles, G., et al. (2020). Deep glacial troughs and stabilizing ridges unveiled beneath the margins of the Antarctic ice sheet. *Nature Geoscience*, *13*(2), 132–137. https://doi.org/10.1038/s41561-019-0510-8

Muldoon, G. R. (2018). West Antarctic ice sheet retreat during the last interglacial (Doctoral dissertation). The University of Texas at Austin ScholarWorks Repository. https://doi.org/10.15781/T23B5WS0D

Muldoon, G. R., Jackson, C. S., Young, D. A., & Blankenship, D. D. (2018). Bayesian estimation of englacial radar chronology in Central West Antarctica. *Dynamics and Statistics of the Climate System*, *3*(1), dzy004. https://doi.org/10.1093/climatesystem/dzy004

Neumann, T. A., Conway, H., Price, S. F., Waddington, E. D., Catania, G. A., & Morse, D. L. (2008). Holocene accumulation and ice sheet dynamics in central West Antarctica. *Journal of Geophysical Research*, *113*(F2). https://doi.org/10.1029/2007JF000764

Nielsen, L. T., Aðalgeirsdóttir, G., Gkinis, V., Nuterman, R., & Hvidberg, C. S. (2018). The effect of a Holocene climatic optimum on the evolution of the Greenland ice sheet during the last 10 kyr. *Journal of Glaciology*, *64*(245), 477–488. https://doi.org/10.1017/jog.2018.40

Nye, J. F. (1957). The distribution of stress and velocity in glaciers and ice-sheets. *Proceedings of the Royal Society of London - Series A: Mathematical and Physical Sciences*, *239*(1216), 113–133. https://doi.org/10.1098/rspa.1957.0026

Palerme, C., Genthon, C., Claud, C., Kay, J. E., Wood, N. B., & L'Ecuyer, T. (2017). Evaluation of current and projected Antarctic precipitation in CMIP5 models. *Climate Dynamics*, *48*(1–2), 225–239. https://doi.org/10.1007/s00382-016-3071-1

Parrenin, F., Cavitte, M. G. P., Blankenship, D. D., Chappellaz, J., Fischer, H., Gagliardini, O., et al. (2017). Is there 1.5-million-year-old ice near Dome C, Antarctica? *The Cryosphere*, *11*(6), 2427–2437. https://doi.org/10.5194/tc-11-2427-2017

Rignot, E., Mouginot, J., & Scheuchl, B. (2017). MEaSUREs InSAR-based Antarctica ice velocity map, version 2. NASA National Snow and Ice Data Center Distributed Active Archive Center. https://doi.org/10.5067/D7GK8F5J8M8R

Rignot, E., Mouginot, J., Scheuchl, B., van den Broeke, M., van Wessem, M. J., & Morlighem, M. (2019). Four decades of Antarctic Ice Sheet mass balance from 1979-2017. *Proceedings of the National Academy of Sciences of the United States of America*, *116*(4), 1095–1103. https://doi.org/10.1073/pnas.1812883116

Ritz, C., Rommelaere, V., & Dumas, C. (2001). Modeling the evolution of Antarctic ice sheet over the last 420,000 years: Implications for altitude changes in the Vostok region. *Journal of Geophysical Research*, *106*(D23), 31943–31964. https://doi.org/10.1029/2001JD900232

Ross, N., Corr, H., & Siegert, M. (2020). Large-scale englacial folding and deep-ice stratigraphy within the West Antarctic Ice Sheet. *The Cryosphere*, *14*, 2103–2114. https://doi.org/10.5194/tc-14-2103-2020

Rotschky, G., Eisen, O., Wilhelms, F., Nixdorf, U., & Oerter, H. (2004). Spatial distribution of surface mass balance on Amundsenisen plateau, Antarctica, derived from ice-penetrating radar studies. *Annals of Glaciology*, *39*, 265–270. https://doi.org/10.3189/172756404781814618

Scambos, T. A., Haran, T. M., Fahnestock, M. A., Painter, T. H., & Bohlander, J. (2007). MODIS-based Mosaic of Antarctica (MOA) data sets: Continent-wide surface morphology and snow grain size. *Remote Sensing of Environment*, *111*(2–3), 242–257. https://doi.org/10.1016/j.rse.2006.12.020

Shepherd, A., Ivins, E. R., Rignot, E., Smith, B., Van Den Broeke, M., Velicogna, I., et al. (2018). Mass balance of the Antarctic Ice Sheet from 1992 to 2017. *Nature*, *556*, 219–222. https://doi.org/10.1038/s41586-018-0179-y

Siegert, M. J., Hodgkins, R., & Dowdeswell, J. A. (1998). A chronology for the Dome C deep ice-core site through radio-echo layer Correlation with the Vostok Ice Core, Antarctica. *Geophysical Research Letters*, *25*(7), 1019–1022. https://doi.org/10.1029/98GL00718

Siegert, M. J., & Payne, A. J. (2004). Past rates of accumulation in central West Antarctica. *Geophysical Research Letters*, *31*(12). https://doi.org/10.1029/2004GL020290

Siegert, M. J., Pokar, M., Dowdeswell, J. A., & Benham, T. (2005). Radio-echo layering in West Antarctica: A spreadsheet dataset. *Earth Surface Processes and Landforms*, *30*(12), 1583–1591. https://doi.org/10.1002/esp.1238

Sigl, M., Fudge, T. J., Winstrup, M., Cole-Dai, J., Ferris, D., McConnell, J. R., et al. (2016). The WAIS Divide deep ice core WD2014 chronology – Part 2: Annual-layer counting (0-31 ka BP). *Climate of the Past*, *12*(3), 769–786. https://doi.org/10.5194/cp-12-769-2016

Smith, J. A., Andersen, T. J., Shortt, M., Gaffney, A. M., Truffer, M., Stanton, T. P., et al. (2017). Sub-ice-shelf sediments record history of twentieth-century retreat of Pine Island Glacier. *Nature*, *541*(7635), 77–80. https://doi.org/10.1038/nature20136

Steinhage, D., Kipfstuhl, S., Nixdorf, U., & Miller, H. (2013). Internal structure of the ice sheet between Kohnen station and Dome Fuji, Antarctica, revealed by airborne radio-echo sounding. *Annals of Glaciology*, *54*(64), 163–167. https://doi.org/10.3189/2013AoG64A113

van Wessem, J. M., van de Berg, W. J., Noël, B. P. Y., Van Meijgaard, E., Amory, C., Birnbaum, G., et al. (2018). Modeling the climate and surface mass balance of polar ice sheets using RACMO2 – Part 2: Antarctica (1979-2016). *The Cryosphere*, *12*(4), pp.1479–1498. https://doi.org/10.5194/tc-12-1479-2018

Vaughan, D. G., Corr, H. F. J., Ferraccioli, F., Frearson, N., O'Hare, A., Mach, D., et al. (2006). New boundary conditions for the West Antarctic ice sheet: Subglacial topography beneath Pine Island Glacier. *Geophysical Research Letters*, *33*(9). https://doi.org/10.1029/2005GL025588

Waddington, E. D., Conway, H., Steig, E. J., Alley, R. B., Brook, E. J., Taylor, K. C., & White, J. W. C. (2005). Decoding the dipstick: Thickness of Siple Dome, West Antarctica, at the last glacial maximum. *Geology*, *33*(4), 281–284. https://doi.org/10.1130/G21165.1

Waddington, E. D., Neumann, T. A., Koutnik, M. R., Marshall, H.-P., & Morse, D. L. (2007). Inference of accumulation-rate patterns from deep layers in glaciers and ice sheets. *Journal of Glaciology*, *53*(183), 694–712. https://doi.org/10.3189/002214307784409351

Wang, Y., Ding, M., Van Wessem, J. M., Schlosser, E., Altnau, S., van den Broeke, M. R., et al. (2016). A comparison of Antarctic Ice Sheet surface mass balance from atmospheric climate models and in situ observations. *Journal of Climate*, *29*(14), 5317–5337. https://doi.org/10.1175/JCLI-D-15-0642.1

Whillans, I. M. (1976). Radio-echo layers and the recent stability of the West Antarctic ice sheet. *Nature*, *264*(5582), 152–155. https://doi.org/10.1038/264152a0

Winter, A., Steinhage, D., Arnold, E. J., Blankenship, D. D., Cavitte, M. G. P., Corr, H. F. J., et al. (2017). Comparison of measurements from different radio-echo sounding systems and synchronization with the ice core at Dome C, Antarctica. *The Cryosphere*, *11*(1), 653–668. https://doi.org/10.5194/tc-11-653-2017

Winter, A., Steinhage, D., Creyts, T. T., Kleiner, T., & Eisen, O. (2019). Age stratigraphy in the East Antarctic Ice Sheet inferred from radio-echo sounding horizons. *Earth System Science Data*, *11*(3), 1069–1081. https://doi.org/10.5194/essd-11-1069-2019

Zwally, H. J., Giovinetto, M. B., Beckley, M. A., & Saba, J. L. (2012). Antarctic and Greenland drainage systems. Retrieved from GSFC Cryospheric Sciences Laboratory. https://icesat4.gsfc.nasa.gov/cryo_data/ant_grn_drainage_systems.php

References From the Supporting Information

Conway, H., & Rasmussen, L. A. (2009). Recent thinning and migration of the Western Divide, central West Antarctica. *Geophysical Research Letters*, *36*, L12502. https://doi.org/10.1029/2009GL038072

Dowdeswell, J. A., & Evans, S. (2004). Investigations of the form and flow of ice sheets and glaciers using radio-echo sounding. *Reports on Progress in Physics*, *67*(10), 1821. https://doi.org/10.1088/0034-4885/67/10/R03

Hein, A. S., Woodward, J., Marrero, S. M., Dunning, S. A., Steig, E. J., Freeman, S. P. H. T., et al. (2016). Evidence for the stability of the West Antarctic Ice Sheet divide for 1.4 million years. *Nature Communications*, *7*(1), 1–8. https://doi.org/10.1038/ncomms10325

Ross, N., Bingham, R. G., Corr, H. F. J., Ferraccioli, F., Jordan, T. A., Le Brocq, A., et al. (2012). Steep reverse bed slope at the grounding line of the Weddell Sea sector in West Antarctica. *Nature Geoscience*, *5*, 393–396. https://doi.org/10.1038/ngeo1468

Ross, N., Siegert, M. J., Woodward, J., Smith, A. M., Corr, H. F. J., Bentley, M. J., et al. (2011). Holocene stability of the Amundsen-Weddell ice divide, West Antarctica. *Geology*, *39*(10), 935–938. https://doi.org/10.1130/G3192010.1130/g31920.1

Schroeder, D. M., Dowdeswell, J. A., Siegert, M. J., Bingham, R. G., Chu, W., MacKie, E. J., et al. (2019). Multidecadal observations of the Antarctic ice sheet from restored analog radar records. *Proceedings of the National Academy of Sciences of the United States of America*, *116*(38), 18867–18873. https://doi.org/10.1073/pnas.1821646116

Schwander, J., Jouzel, J., Hammer, C. U., Petit, J.-R., Udisti, R., & Wolff, E. (2001). A tentative chronology for the EPICA Dome Concordia ice core. *Geophysical Research Letters*, *28*(22), 4243–4246. https://doi.org/10.1029/2000GL011981

Siegert, M. J., Ross, N., Corr, H., Kingslake, J., & Hindmarsh, R. (2013). Late Holocene ice-flow reconfiguration in the Weddell Sea sector of West Antarctica. *Quaternary Science Reviews*, *78*, 98–107. https://doi.org/10.1016/j.quascirev.2013.08.003

Appendix B: High mid-Holocene accumulation rates over West Antarctica inferred from a pervasive ice-penetrating radar reflector

The Cryosphere, 17, 1497–1512, 2023
https://doi.org/10.5194/tc-17-1497-2023
© Author(s) 2023. This work is distributed under
the Creative Commons Attribution 4.0 License.

The Cryosphere Open Access EGU

High mid-Holocene accumulation rates over West Antarctica inferred from a pervasive ice-penetrating radar reflector

Julien A. Bodart[1], Robert G. Bingham[1], Duncan A. Young[2], Joseph A. MacGregor[3], David W. Ashmore[4,5], Enrica Quartini[2,6], Andrew S. Hein[1], David G. Vaughan[7,†], and Donald D. Blankenship[2]

[1]School of GeoSciences, University of Edinburgh, Edinburgh, UK
[2]Institute for Geophysics, University of Texas at Austin, Austin, Texas, USA
[3]Cryospheric Sciences Laboratory, NASA Goddard Space Flight Center, Greenbelt, Maryland, USA
[4]School of Environmental Sciences, University of Liverpool, Liverpool, UK
[5]Met Office, Exeter, UK
[6]Department of Astronomy, Cornell University, Ithaca, New York, USA
[7]British Antarctic Survey, Cambridge, UK
[†]deceased

Correspondence: Julien A. Bodart (julien.bodart@ed.ac.uk)

Received: 14 October 2022 – Discussion started: 1 November 2022
Revised: 15 March 2023 – Accepted: 19 March 2023 – Published: 6 April 2023

Abstract. Understanding the past and future evolution of the Antarctic Ice Sheet is challenged by the availability and quality of observed paleo-boundary conditions. Numerical ice-sheet models often rely on these paleo-boundary conditions to guide and evaluate their models' predictions of sea-level rise, with varying levels of confidence due to the sparsity of existing data across the ice sheet. A key data source for large-scale reconstruction of past ice-sheet processes are internal reflecting horizons (IRHs) detected by radio-echo sounding (RES). When IRHs are isochronal and dated at ice cores, they can be used to determine paleo-accumulation rates and patterns on large spatial scales. Using a spatially extensive IRH over the Pine Island Glacier (PIG), Thwaites Glacier (THW), and the Institute and Möller ice streams (IMIS, covering a total of 610 000 km^2 or 30 % of the West Antarctic Ice Sheet (WAIS)), and a local layer approximation model, we infer mid-Holocene accumulation rates over the slow-flowing parts of these catchments for the past ∼ 4700 years. By comparing our results with modern climate reanalysis models (1979–2019) and observational syntheses (1651–2010), we estimate that accumulation rates over the Amundsen–Weddell–Ross Divide were on average 18 % higher during the mid-Holocene than modern rates. However, no significant spatial changes in the accumulation pattern were observed. The higher mid-Holocene accumulation-rate estimates match previous paleo-accumulation estimates from ice-core records and targeted RES surveys over the ice divide, and they also coincide with periods of grounding-line readvance during the Holocene over the Weddell and Ross sea sectors. We find that our spatially extensive, mid-Holocene-to-present accumulation estimates are consistent with a sustained late-Holocene period of higher accumulation rates occurring over millennia reconstructed from the WAIS Divide ice core (WD14), thus indicating that this ice core is spatially representative of the wider West Antarctic region. We conclude that future regional and continental ice-sheet modelling studies should base their climatic forcings on time-varying accumulation rates from the WAIS Divide ice core through the Holocene to generate more realistic predictions of the West Antarctic Ice Sheet's past contribution to sea-level rise.

Highlights.

- We estimate mean accumulation rates for the past ∼ 4700 years across the Pine Island Glacier, Thwaites Glacier, and the Institute and Möller ice-stream catchments in West Antarctica using a ubiquitous, ice-core dated internal radar reflection.
- Accumulation rates were 18 % higher during the mid-Holocene compared to modern rates over the Amundsen–Weddell–Ross Divide.

Published by Copernicus Publications on behalf of the European Geosciences Union.

– Spin-up of regional and continental ice-sheet models should include time-varying changes in Holocene accumulation rates from the WAIS Divide ice core to generate more realistic grounding-line evolution and past sea-level rise contribution across this region.

1 Introduction

Improving our knowledge of past climatic changes over the Antarctic Ice Sheet is required if we are to understand its present evolution and model its future under increasingly rapid climatic changes (IPCC, 2021). Most studies of past ice-sheet behaviour over Antarctica have focused on modelling changes in ice volume and grounding-line retreat following the Last Glacial Maximum (LGM, $\sim$ 20 ka BP) (Denton and Hughes, 2002; Golledge et al., 2012, 2013; Hillenbrand et al., 2013, 2014; Le Brocq et al., 2011; Kingslake et al., 2018); however, less attention has been paid to ice-sheet evolution during the Holocene ($\sim$ 11.7 ka BP to present). Recent evidence suggests that parts of the grounding line of West Antarctica may have retreated several hundred kilometres inland from its current position at $\sim$ 10 ka and subsequently readvanced to reach its modern position sometime during the Holocene, due to isostatic rebound and climate-induced changes, particularly over the Weddell Sea and western Ross Sea sectors (Siegert et al., 2013; Bradley et al., 2015; Kingslake et al., 2018; Wearing and Kingslake, 2019; Venturelli et al., 2020; Neuhaus et al., 2021; Johnson et al., 2022). However, the atmospheric and ice-dynamical conditions farther inland, which could also have induced grounding-line migration, remain poorly constrained. An early investigation by Whillans (1976) using radar data near the Byrd ice core indicated stability during the Late Pleistocene and Holocene epochs. Records of temperature and precipitation from the WAIS Divide ice core (hereafter abbreviated as WD14; Fig. 1) in the central West Antarctic Ice Sheet (WAIS) suggest higher accumulation rates during the Holocene than at present (Fudge et al., 2016), a trend that is also observed across small parts of the Amundsen–Weddell–Ross Divide (Fig. 1) where isolated radio-echo sounding (RES) surveys have shown 15 %–30 % higher accumulation rates during the mid-Holocene compared to modern values (Siegert and Payne, 2004; Neumann et al., 2008; Koutnik et al., 2016).

Many numerical ice-sheet models that aim to predict Antarctica's long-term (past and future) contribution to sea-level rise use past ice-sheet reconstructions from after the LGM to guide and evaluate their models (Chavaillaz et al., 2013; DeConto and Pollard, 2016; Bracegirdle et al., 2019). However, even well-used ice-sheet reconstructions assume that the ice sheet retreated continuously throughout the Holocene (e.g. RAISED Consortium, 2014), a finding that has been challenged recently for the WAIS (e.g. Kingslake et al., 2018). Further, significant discrepancies between model simulations and the paleoproxy record currently impede our ability to confidently predict how the ice sheet will respond to future changes in the climate (e.g. Johnson et al., 2021). While improvements in model parameterizations are needed to close this gap (Bracegirdle et al., 2019; Sutter et al., 2021), considerable improvement in the availability and quality of paleoproxy records, particularly during the Holocene, is also needed to provide better constraints for ice-sheet models and ultimately better resolve past ice-sheet changes (Kingslake et al., 2018; Jones et al., 2022). Paleoproxy data have traditionally come from point-based measurements, such as ice cores (e.g. Petit et al., 1999; Parrenin et al., 2007; WAIS Divide Project Members, 2013; Buizert et al., 2021), sediment cores (e.g. Hillenbrand et al., 2013; Arndt et al., 2017; Hillenbrand et al., 2017; Kingslake et al, 2018; Venturelli et al., 2020; Neuhaus et al., 2021; Sproson et al., 2022), or surface-exposure dating (e.g. Stone et al., 2003; Suganuma et al., 2014; Johnson et al., 2014; Hein et al., 2016; Nichols et al., 2019; Johnson et al., 2020; Braddock et al., 2022). A complementary and spatially extensive alternative data source for inferring past climate across an ice sheet is provided by internal reflecting horizons (IRHs) detected by RES. They primarily result from englacial acidity contrasts and are often detected for hundreds of kilometres on RES data (Harrison, 1973; Bingham and Siegert, 2007). When employed in combination with ice-core stratigraphies, IRHs can be used to extend age–depth relationships away from an ice core by following peaks in electromagnetic return power in the radar data (e.g. Beem et al., 2021; Bodart et al., 2021a; Cavitte et al., 2016; Jacobel and Welch, 2005; MacGregor et al., 2015; Whillans, 1976; Winter et al., 2019).

In contrast to East Antarctica and Greenland, the IRH extension of WAIS ice cores has been challenging so far due to fewer deep ice cores there and, until recently, the lack of well-dated IRH datasets. However, efforts have intensified in recent years to improve our understanding of ice stratigraphy over this sector. In particular, four recent studies using airborne RES data (Karlsson et al., 2014; Muldoon et al., 2018; Ashmore et al., 2020a; Bodart et al., 2021a) all identified a distinct and bright IRH dated using the Byrd and WD14 ice-core chronologies to 4.72 ± 0.28 ka BP (Muldoon et al., 2018; Bodart et al., 2021a). A comparison of volcanic sulfate deposition within the WD14 and Siple Dome ice cores revealed a large peak in sulfate concentration that matches the age and depth of this ubiquitous IRH (Kurbatov et al., 2006; Bodart et al., 2021a; Cole-Dai et al., 2021; Sigl et al., 2022), which we hereafter term the "4.72 ka IRH". This IRH has now been observed by multiple RES systems and extends throughout much of the slower-flowing ice of the Amundsen and Weddell sea embayments ($< 400\,\mathrm{m\,a^{-1}}$), including across the divides demarcating regions draining into the Amundsen, Weddell, and Ross seas.

Despite their potential wide-ranging applications, the incorporation of IRHs into ice-sheet models has been limited so far compared to other types of paleoproxy data, primarily

because the inference of accumulation-rate or ice-flow history from IRHs is an ill-posed inverse problem (Waddington et al., 2007). Previous applications using IRHs to inform regional and continental models include the following: (a) constraining decadal-scale surface mass balance (SMB) estimates from atmospheric models using annually resolved IRHs found in the shallow firn (Medley et al., 2013, 2014; Van Wessem et al., 2018; Dattler et al., 2019; Kausch et al., 2020; Cavitte et al., 2022); (b) inferring past accumulation rates going back further in time (i.e. hundreds to thousands of years) with the aim of comparing past accumulation estimates with modern times (e.g. Leysinger Vieli et al., 2004; Siegert and Payne, 2004; Neumann et al., 2008; MacGregor et al., 2009, 2016; Leysinger Vieli et al., 2011; Cavitte et al., 2018); or (c) integrating both their characteristics (e.g. elevation in the ice) and the information inferred from them (e.g. accumulation or basal-melt rates) to evaluate the output from regional and continental ice-sheet models (Leysinger Vieli et al., 2011, 2018; Holschuh et al., 2017; Sutter et al., 2021). Promisingly, Sutter et al. (2021) recently showed that spatially extensive Antarctic IRHs can provide unique benchmarks for constraining ice-sheet model parameterizations (i.e. climate forcing and simulated ice flow), which are then used to simulate paleo-ice-sheet evolution. Together, these studies indicate multiple avenues for ice-sheet models to assimilate IRHs to further improve estimates of past, current, and future ice-sheet changes.

Here, we estimate mid-Holocene accumulation rates across the WAIS from first-order calculations using a one-dimensional (1-D) model, constrained by the spatially extensive 4.72 ka IRH. We first describe the data, the model used and their limitations and uncertainties (Sect. 2). We then present our accumulation-rate estimates and compare them to observed and modelled modern accumulation rates to reveal a longer-term perspective on changes between the mid-Holocene and the present (Sect. 3). Finally, we place our results in the context of previous studies that consider WAIS evolution during the Holocene (Sect. 4).

2 Data and methods

2.1 Along-track IRH data

We used data from extensive ($\sim$ 91 000 km) RES surveys acquired across West Antarctica between 2004 and 2018. The main contributing surveys are the University of Texas Institute for Geophysics (UTIG) 2004–2005 AGASEA (Airborne Geophysical Survey of the Amundsen Embayment), flown over the Thwaites Glacier (THW) and Marie Byrd Land which deployed the 60 MHz High Capability Airborne Radar Sounder (HiCARS) radar system (Holt et al., 2006; Peters et al., 2007); the British Antarctic Survey (BAS) 2004–2005 BBAS survey over the Pine Island Glacier (PIG); and the 2010–2011 Institute–Möller Antarctic Funding Initiative (IMAFI) survey over the Institute and Möller ice streams (IMIS) which deployed the 150 MHz Polarimetric Airborne Survey INstrument (PASIN) radar system (Vaughan et al., 2006; Corr et al., 2007; Ross et al., 2012; Frémand et al., 2022) (Fig. 1; Table 1). Additional profiles from NASA's Operation Ice Bridge (OIB; MacGregor et al., 2021) 2016 and 2018 surveys, flown with the 195 MHz Multichannel Coherent Radar Depth Sounder 2 (MCoRDS-2) radar system (CReSIS, 2018), were also used to extract IRH information near the WD14 and upper IMIS catchments (Bodart et al., 2021a; Fig. 1 and Table 1). We refer the reader to the above references for comprehensive details on each system's capabilities.

These RES surveys were used to track and date six IRHs spanning the Late Pleistocene and Holocene (25.7–2.3 ka BP) that collectively cover much of the WAIS, including IMIS (Ashmore et al., 2020a), PIG (Karlsson et al., 2014; Bodart et al., 2021a), and THW (Muldoon et al., 2018). Here, we only consider the 4.72 ka IRH mapped in all four studies and shown in Fig. 1, as it is by far both the most spatially extensive and the only commonly traced IRH across all studies. We first merged all data points from the 4.72 ka IRH across the three catchments, resulting in a cumulative distance of $\sim$ 40 000 line-km of IRH profiles (44 % of the RES surveys' total coverage; Table 1). Although the along-track RES data were acquired with a trace spacing of between 10 and 35 m, depending on the dataset used, we resampled these points to 500 m in the along-track direction. We then added a spatially invariant firn correction of 10 m onto the Muldoon et al. (2018) dataset to match the same firn correction applied by the other studies to correct the IRH depth. Finally, we calculated the median value of all ice thicknesses and IRH depths falling within each 500 m interval.

2.2 Inferring accumulation rates

To infer accumulation rates from the 4.72 ka IRH, we used the Nye model, a 1-D ice-flow model widely used for estimating accumulation rates and age–depth relationships over relatively slow-flowing parts of an ice sheet (Nye, 1957; Fahnestock et al., 2001a). This model invokes the local-layer approximation (LLA), i.e. it assumes that the time-averaged accumulation rate that the IRH has experienced since its upstream inception at the surface can be adequately represented by its depth where it is observed presently. Other 1-D models exist, including the Dansgaard–Johnsen (Dansgaard and Johnsen, 1969) and the shallow-strain rate model (MacGregor et al., 2016), but were less suitable for estimating accumulation rates here due to uncertainty in the basal shear layer thickness across our survey area and because we are limited to only one IRH to constrain the ice-flow model, respectively. The Nye model assumes that ice thickness is constant and therefore that the ice sheet has been in a steady state since the deposition of the IRH, an acceptable assumption for the

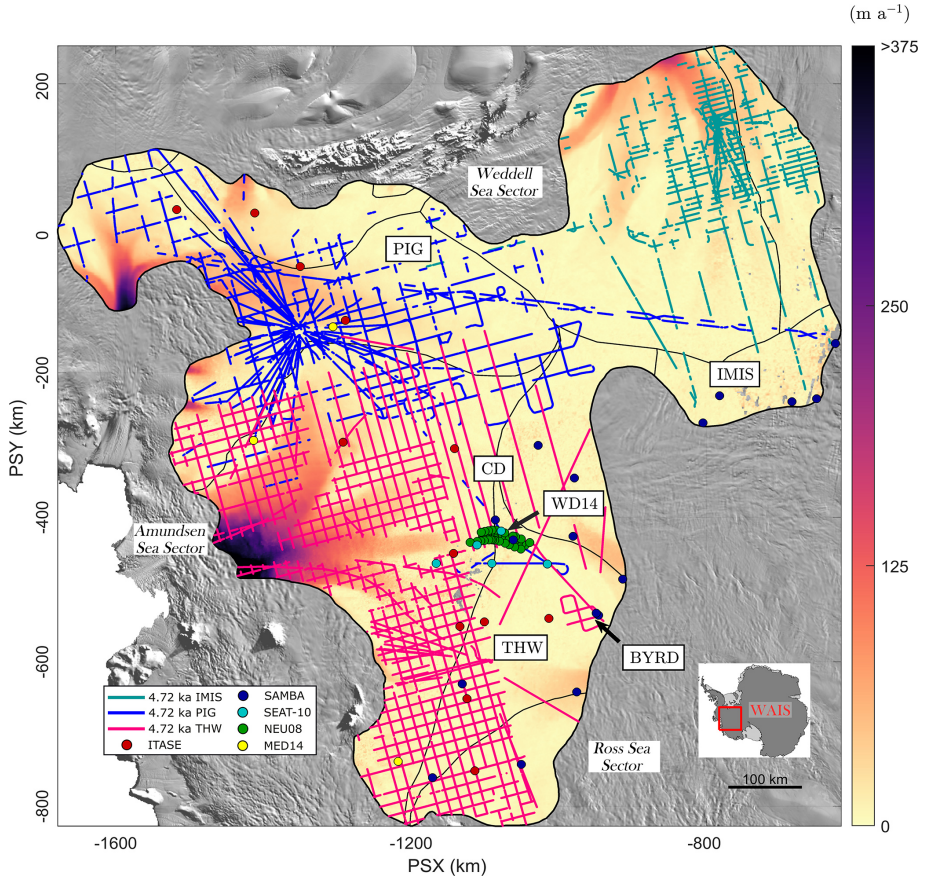

Figure 1. Map of the datasets and key locations in this study. The three datasets that contain the 4.72 ka IRH are colour-coded as IMIS (green), PIG (blue), and THW (pink). IRH data where $D > 1$ are excluded (see Sect. 2.2.1; Fig. S1). Points represent the snow, firn, and ice cores used in this study to compare modern accumulation rates with those inferred from the 4.72 ka IRH (Sect. 2.4). The background colour map shows modern surface speeds from Rignot et al. (2017). Locations mentioned in this paper are abbreviated on the map as follows: BYRD (Byrd Ice Core), IMIS (Institute and Möller ice streams), PIG (Pine Island Glacier), THW (Thwaites Glacier), WAIS (West Antarctic Ice Sheet), CD (Central Amundsen–Weddell–Ross Divide), WD14 (WAIS Divide ice core). Major ice divides are from Mouginot et al. (2017). The background image is the 2014 MODIS mosaic of Antarctica (Haran et al., 2018). For all analyses and figures in this study, the SCAR Antarctic Polar Stereographic projection is used (PSX/PSY; EPSG: 3031).

Table 1. Characteristics of each IRH dataset used in this study that contain the 4.72 ka IRH. "Reflector 1" in Muldoon et al. (2018) is abbreviated here as "R1".

Survey name	Survey provider	RES system	Dataset reference	Cumulative IRH distance (10^3 km)
IMAFI	BAS	PASIN 150 MHz	H2 in Ashmore et al. (2020a)	6
BBAS/OIB	BAS/NASA	PASIN 150 MHz/MCoRDS-2 195-MHz	R2 in Bodart et al. (2021a)	15
AGASEA	UTIG	HiCARS 60 MHz	R1 in Muldoon et al. (2018)	19

period under investigation here. The Nye model states:

$$\dot{b}_a = \ln\left(\frac{z_a}{H}\frac{H}{a}\right), \quad (1)$$

where $\dot{b}_a$ is the mean accumulation rate during the Holocene epoch between an IRH of age a and the present, z_a represents the depth of the IRH dated at the ice core, and H is the ice thickness. The model assumes that the vertical strain rate, $\dot{\varepsilon}^a_{zz}$, is also constant and vertically uniform, so that it exactly balances the overburden of local ice accumulation:

$$\dot{\varepsilon}^a_{zz} = \frac{\dot{b}_a}{H}. \quad (2)$$

We iterated Eq. (1) over the resampled 500 m spaced dataset using the depth of the 4.72 ka IRH for z_a and used the median

radar-derived ice-thickness measurement, resampled over the 500 m grid to obtain H, when this information was available. In areas where the radar did not sound the bed, we used the BedMachine Antarctica v2 gridded product to obtain a value for H (Morlighem, 2020; Morlighem et al., 2020). Note that accumulation-rate values presented in this study are all reported in metres per annum ($\mathrm{m\,a^{-1}}$) of ice equivalent using a density value in ice of $917\,\mathrm{kg\,m^{-3}}$.

2.2.1 Assessing the suitability of the 1-D model

To quantify the suitability of the LLA which is used here to estimate accumulation rates, we calculated the effects of horizontal gradients in modern ice thickness and accumulation rates along particle paths in their ability to affect IRH depths across our grid, as per Waddington et al. (2007). Where these gradients are large, estimates of accumulation rates from IRHs likely require a more complete treatment of ice flow and its effect upon IRH depths, which multi-dimensional models and more physically complete models can better resolve (e.g. Waddington et al., 2007; Leysinger Vieli et al., 2011; Karlsson et al., 2014; Nielsen et al., 2015; Koutnik et al., 2016). However, such models are significantly more computationally expensive over such a larger area and depend on well-constrained boundary conditions from along-flow radar profiles which are not often available at an ice-sheet level (MacGregor et al., 2009).

We quantified the effect of horizontal gradients on an IRH of age a by first estimating the total horizontal particle path length L_{path} that each "particle" of the 4.72 ka IRH has travelled since a, and then the characteristic lengths of variability in ice thickness (L_H) and apparent accumulation rate ($L_{\dot{b}}$) (Supplement). These three components were then combined to generate a non-dimensional parameter D (Fig. S1d), which we used as a confidence metric for our inferred accumulation rates. Both Waddington et al. (2007) and MacGregor et al. (2009) suggested a value of $D \ll 1$ over Antarctica, whereas MacGregor et al. (2016) used a maximum value of $D = 1$ to estimate where the LLA is acceptable over Greenland. Since D cannot be translated simply into an uncertainty in an LLA-inferred accumulation rate, it is not yet clear what exact value is appropriate. Smaller values of D indicate that local horizontal gradients in ice thickness and accumulation rates have a smaller effect on IRH depth of age a, and thus that the LLA may be valid (Waddington et al., 2007; MacGregor et al., 2009, 2016). Where $D \geq 1$, the depth of an IRH is less likely to be the result of accumulation rates at the surface or vertical strain rates further down, and thus a more sophisticated model is likely required (Sect. 2.2.2) (Waddington et al., 2007). However, MacGregor et al. (2009) found that even along a flow band across Lake Vostok where the mean value of D is 0.50 for a 41 ka IRH, the difference in accumulation rate inferred from the LLA and from a more sophisticated flow-band model could be relatively small (4 %–16 %). This similarly suggests that accumulation rate can be inferred acceptably using the LLA where D is higher.

For our study area, D values are mostly well below unity (median: 0.19; 25th quartile: 0.09; 75th quartile: 0.34), which suggests relatively little effect from ice-dynamical processes upon IRH depths across most of our grid. We used the upper quartile of the D distribution across our model domain (i.e. $D \leq 0.34$) to show areas where we can have confidence that accumulation rate remains the dominant factor influencing the vertical position of our IRHs in the ice column (i.e. where the $D \ll 1$ criterion is likely met; Fig. S1d). While accumulation rates inferred from IRHs situated in the upper quartile (Fig. S1d) may still be valid, we suggest additional caution in interpreting our results there due to the potential impact of larger flow gradients on IRH depths.

2.2.2 Model limitations and uncertainty

One of the main limitations of the Nye model is that it assumes that gradients in sliding velocity are mostly concentrated in a thin layer at the ice–bed interface and that the ice column deforms by pure shear only (Nye, 1957; Fahnestock et al., 2001a). For this reason, the Nye model is generally only appropriate for IRHs found in the upper part of the ice column, as is the case here. Additionally, the use of the model is restricted to areas where ice flow is relatively slow and horizontal strain rates are also relatively low.

Here, we focus on a shallower IRH situated in the upper part of the ice column (median: 40 %; 25th quartile: 30 %; 75th quartile: 50 %; Fig. 2b and c), for which we can reasonably assume that the ice sheet has remained close to a steady state and where IRHs are likely shallow enough not to have experienced appreciable flow disturbances that would affect the Nye model assumptions. Additionally, due to the inherent nature of tracking IRHs through RES data, our coverage is limited to areas where ice-flow speeds are relatively low and IRHs are undisturbed. In some portions of our study area, the IRH is found deeper in the ice column or in faster-flowing sections of the ice sheet (e.g. in the downstream sectors of our grid, Figs. 1 and 2b, c), both of which challenge the assumptions that the 1-D model is based upon and thus where uncertainties in accumulation estimates are likely to be higher.

Estimating uncertainty in accumulation rates from the Nye model is non-trivial. Previous studies have used the misfit between the accumulation rate calculated using multiple proximal IRHs in the ice column (e.g. Fahnestock et al., 2001a, b; Leysinger Vieli et al., 2004; MacGregor et al., 2016). Unfortunately, this method is not suitable here due to the dearth of spatially extensive IRHs younger than 4.72 ka over our model domain.

Instead, uncertainty in the Nye-inferred accumulation rates were calculated using (a) the lowest and highest possible accumulation rates from Eq. (1) using the age uncertainty (± 0.28 ka) of the 4.72 ka IRH and (b) the lowest and highest

possible accumulation rates inferred from an additional 1-D model (Eq. S5) which accounts for the effect of strain rates on accumulation rates (i.e. the shallow-strain rate model from MacGregor et al., 2016; Supplement, Figs. S2–S4).

This calculation provides lower and upper bounds for the IRH-inferred accumulation rates (Fig. S4a and b), which were then averaged to generate a relative uncertainty (Fig. S4c). From this assessment, we estimate a median relative uncertainty in the Nye-inferred accumulation rates for the 4.72 ka IRH of 14 % across our grid. This uncertainty is higher in the downstream edges of our grids, particularly over the PIG, THW, and IMIS catchments, and generally low over the Amundsen–Weddell–Ross Divide (Fig. S4), reflecting the effect of spatially variable strain rates on the inferred accumulation rates. When combined with the assessment of the suitability of the LLA and exclusion of IRHs where the $D > 1$ (Sect. 2.2.1–2.2.2), we conclude that it supports our application of a 1-D modelling approach here.

2.3 Gridding and filtering

Once IRH depths and accumulation rates for the 4.72 ka IRH were obtained at regular 500 m points along RES flight paths, we filtered the results using a moving-average Gaussian filter of length 30 samples (equivalent to $\sim$ 15 km) to reduce along-track noise in the IRH depth. We then gridded the filtered result using a Delaunay-triangulation-based natural neighbour interpolation method onto a 1 km polar stereographic grid. We further smoothed the gridded data using an 18 km square cell mean filter to limit the localized interpolation artefacts in areas of poor survey coverage. Figure S5 shows the maximum distance away from the nearest 500 m along-track point used to produce Figs. 2 and 3, and thus where errors in the interpolated grids are expected to be larger. The median value of this maximum distance is 5 km and its maximum value is 75 km, which is comparable to previous studies that infer SMB from IRHs in the shallow firn (e.g. Medley et al., 2014). We evaluated other possible interpolation methods (e.g. kriging and using different semi-variogram models), but they resulted in similar or poorer quality and were thus discounted.

2.4 Comparison with modern observations

To compare our inferred accumulation estimates for the past 4.72 ka with modern values (defined here as 1651–2019), we derived information on modern accumulation rates from two sources, one modelled (gridded) and one from a series of observational (point-based) datasets.

We used modelled gridded accumulation rates from the Regional Atmospheric Climate Model 2.3p2 (hereafter RACMO2) 1979–2019 SMB product forced at its margin with the ERA-Interim product (native resolution: 27 km) as an estimate for modern accumulation rates (Van Wessem et al., 2018). Although SMB is not technically equivalent to the accumulation rate, runoff and sublimation are negligible in our survey area (Medley et al., 2013), so we assume that SMB is equal to accumulation rate in this region. We converted modelled values from kilograms per square metre per annum ($\mathrm{kg\,m^{-2}\,a^{-1}}$) to metres per annum ($\mathrm{m\,a^{-1}}$) of ice equivalent using an ice density value of $917\,\mathrm{kg\,m^{-3}}$, calculated the 40-year mean, and then bi-linearly interpolated the gridded RACMO2 product to the same 1 km grid resolution as our 4.72 ka-to-present accumulation grid (Sect. 2.3) to ensure consistency when comparing both datasets.

Observational point-based measurements were obtained from a series of snow, firn and ice cores from the ITASE (Mayewski and Dixon, 2013), MED14 (Medley et al., 2014), SAMBA (Favier et al., 2013), and SEAT-10 (Burgener et al., 2013) datasets, as well as from a network of centennially-averaged modern accumulation rates derived from shallow IRHs traced on ground-based RES data over the central divide and dated using a shallow ITASE Ice Core (Neumann et al., 2008) (Fig. 1). This resulted in 79 point-based accumulation measurements from cores covering the period 1651–2010 CE (Common Era) and spread across our model domain (see Fig. 1). Further detail on these datasets can be found in the above references.

To compare the Holocene gridded product with the point-based measurements, we first calculated the average value of the accumulation rate at the point measurement for the entire period. We converted these values to ice-equivalent accumulation rates and then extracted two paired values, i.e. the value for the point measurement for modern accumulation rates and the value for the nearest grid cell in the gridded 4.72 ka-to-present accumulation estimates to this measurement.

3 Results

The final grids for depth and accumulation rates for the 4.72 ka IRH are shown in Figs. 2 and 3. In total, these grids are made of $\sim$ 89 000, 500 m spaced points, which cover an area of $\sim 610\,000\,\mathrm{km^2}$, or $\sim$ 30 % of the total surface area of the WAIS. The grids span most of the PIG and THW catchments, as well as the Ronne (upper Rutford, Institute, and Möller) and upper western Ross (Bindschadler, Kamb, MacAyeal, and Whillans) catchments (IPY Antarctic boundaries G-H, J-Jpp, and Ep-F; Mouginot et al. (2017); Figs. 1 and 2). Overall, the 4.72 ka IRH is shallower within the IMIS and upper PIG and THW catchments, as well as on the Ross side of the central divide where ice thickness is particularly deep (Fig. 2b). Conversely, the 4.72 ka IRH is deeper in the ice near a 400 m high bedrock plateau that separates the northern and southern basins of PIG (Vaughan et al., 2006) and at two locations in the upstream parts of the main trunk of THW where ice flows over highs in subglacial topography (Fig. 2b).

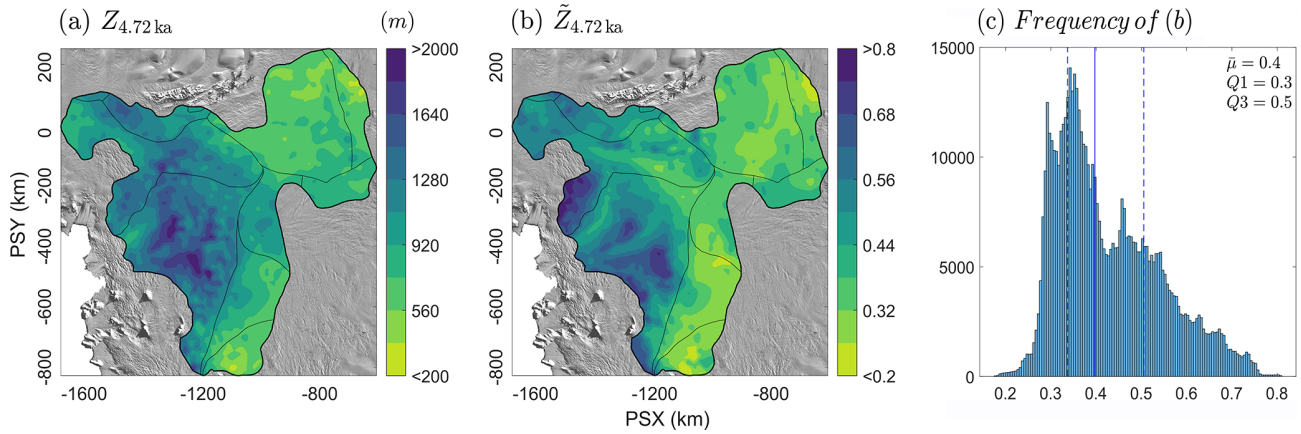

Figure 2. Gridded depths for the 4.72 ka IRH across the model domain covering the PIG, THW, and Institute and Möller ice-stream catchments. **(a)** Gridded depth of the 4.72 ka IRH. **(b)** Normalized depth of the 4.72 ka IRH relative to ice thickness. **(c)** Histogram showing the distribution of values in **(b)** with the median ($\tilde{\mu}$) and interquartile range (i.e. 25th (Q1) and 75th (Q3) quartiles) shown as solid and dashed blue lines, respectively. The background image is the 2014 MODIS mosaic of Antarctica (Haran et al., 2018).

3.1 Catchment-scale accumulation estimates

Figure 3 shows a comparison of the ice-equivalent accumulation rates we inferred for the 4.72 ka IRH (Fig. 3a) and modern SMB estimates from RACMO2 (Fig. 3b). We observe that the IRH accumulation rate pattern for the last 4.72 ka is similar to the modern pattern of accumulation rates for the Amundsen Sea sector of the WAIS, which is dominated by higher coastal accumulation rates that progressively decrease inland to reach their lowest rates over the Ross side of the divide (Fig. 3a and b). Differences in accumulation rates between the 4.72 ka-to-present estimates and modern values are mainly observed directly upstream of the main trunks of PIG and THW, where modern rates are much higher (up to 0.2 m a^{-1} ice equivalent) than for the 4.72 ka-to-present estimates (Fig. 3c). In comparison, higher accumulation rates for the last 4.72 ka relative to modern rates are observed for the entire stretch of the Amundsen–Weddell–Ross Divide (Fig. 3c; Table 2). Over the IMIS catchment, little change is observed between the two periods. Over the entire model domain, we observe a median percentage change value of 6 % higher accumulation since 4.72 ka compared with modern rates (Fig. 4); however, when considering only the values that fall within 100 km of either side of the Amundsen–Weddell–Ross Divide (i.e. in the accumulation zone of the Amundsen, Weddell, and Ross sea sectors and where mean surface speeds average ~ 7 m a^{-1}), we obtain a median percentage change value of 18 % higher accumulation compared with modern accumulation rates (Fig. 4).

Comparison between our 4.72 ka-to-present accumulation-rate estimates and 79 core-derived point-based accumulation measurements for modern times (1651–2010 CE) are shown in Figs. 3, 4, and S6. This evaluation shows that the 4.72 ka-to-present accumulation-rate estimates for the nearest grid cell to each point measurement are, on average, 22 % higher for cores situated across the entire grid ($p < 0.0015$, $n = 79$) and 23 % higher for cores found within 100 km of the divide compared with modern accumulation rates ($p < 0.0001$, $n = 59$; Figs. 4 and S6). In comparison, a similar analysis between grid cells from the 4.72 ka-to-present accumulation-rate estimates and RACMO2 at these 79 core locations shows mid-Holocene accumulation rate estimates are, on average, 32 % ($p < 0.00002$, $n = 79$) higher for cores situated across the entire grid and 36 % higher for cores found within 100 km of the divide ($p < 0.00001$, $n = 59$; Fig. S6). This result confirms that the relative change for gridded accumulation rates between the 4.72 ka-to-present and modern modelled accumulation rates is consistent with modern rates from point-based measurements.

Table 2. Summary statistics for the modern (modelled and observational) and 4.72 ka-to-present ice-equivalent accumulation rates at the catchment-scale and over the Amundsen–Weddell–Ross Divide (abbreviated CD for Central Divide here). Values for the Amundsen–Weddell–Ross Divide are for all points that fall within 100 km of either side of the divide (see dashed line in Fig. 4). $\tilde{\mu}$ refers to the median and IQR represents the interquartile range calculated by computing the difference between the 75th and 25th percentiles. Note that the values provided in the text represent the median relative change from the cell-by-cell change between each grid (Fig. 4), rather than the relative change of the median values provided here.

	Catchment-wide		CD only	
Accumulation rate (m a^{-1})	$\tilde{\mu}$	IQR	$\tilde{\mu}$	IQR
Modern (model)	0.23	0.23	0.22	0.10
Modern (cores)	0.24	0.12	0.24	0.09
4.72 ka-to-present	0.27	0.18	0.27	0.11

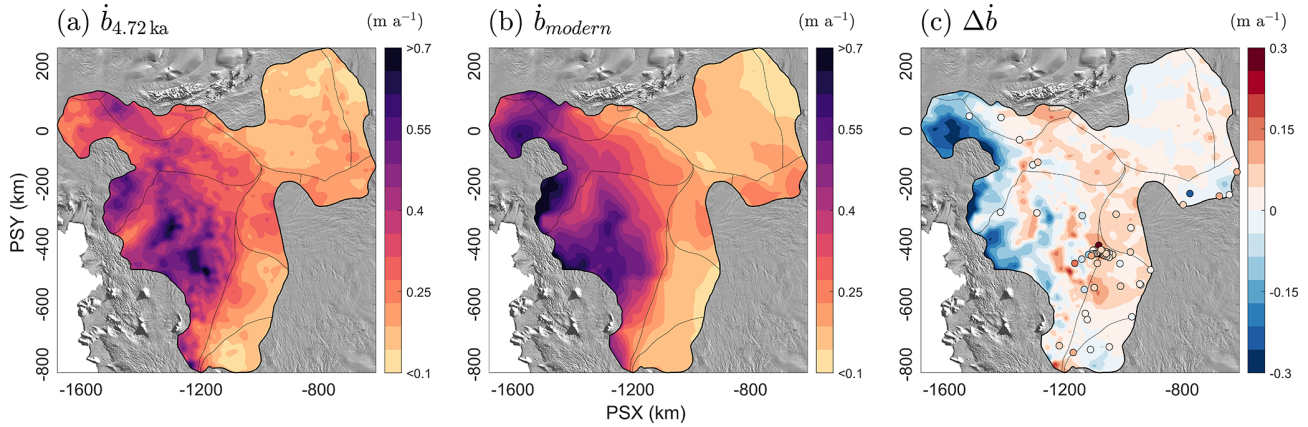

Figure 3. Gridded estimates of ice-equivalent accumulation rates for the last 4.72 ka and modern times. **(a)** Gridded accumulation rates inferred from the 4.72 ka IRH. **(b)** Modern (1979–2019) modelled SMB rates from RACMO2. **(c)** Difference between 4.72 ka-to-present and modern accumulation rates (red = 4.72 ka-to-present accumulation higher than modern times, blue = 4.72 ka-to-present accumulation lower than modern times). The dots represent the difference between the value for the nearest grid cell in **(a)** and time-averaged accumulation rates at each of the 79 core locations (see Sect. 2.4; Fig. S6). The background image is the 2014 MODIS mosaic of Antarctica (Haran et al., 2018).

3.2 Elevation-dependent accumulation estimates

While Figs. 3 and 4 help to assess potential differences in patterns and rates across spatial scales, considering accumulation-rate differences in terms of elevation can inform how topography influences accumulation and whether this has changed over time. We binned the ice-equivalent accumulation values by 50 m elevation bands across the three main catchments covering our grid (Amundsen, Weddell, and Ross) for both the 4.72 ka-to-present estimates and modern model rates and calculated the mean accumulation rate and the total accumulation rate for each bin over the entire elevation gradient (Fig. 5). We again find that the accumulation-rate estimates for the period since 4.72 ka are lower at low elevations ($\sim$ 700–1400 m) over the Amundsen sector compared with RACMO2, but they begin to exceed RACMO2 near the 1400 m elevation band where the 4.72 ka-to-present accumulation rate is higher than modern times across the divide (Fig. 5a and b). We also note that whilst an elevation-dependent gradient in accumulation rates, dominated by high accumulation at the coast and decreasing inland, exists over this sector for the mid-Holocene, it is much less marked than for present rates. This is not surprising, as this sector is where we observe the largest relative uncertainties in inferred accumulation rates across our grid (Fig. S4), indicating that the 1-D model is less able to produce realistic accumulation rates in the downstream end of our grid where ice flow is faster and strain rates are likely higher. In comparison to the Amundsen sector, accumulation rates since 4.72 ka are generally higher at all elevations for the Weddell and Ross sectors compared with the present, although this difference is less than over the Amundsen sector (Fig. 5c–f).

4 Discussion

4.1 Comparison with other Holocene accumulation estimates

Previous studies of past accumulation rates over the WAIS have shown that accumulation varied temporally during the Holocene. Using a single airborne RES profile over the Amundsen Sea sector, Siegert and Payne (2004) showed that accumulation rates were approximately the same at 3.1 ka compared with modern rates, but $\sim 0.3\,m\,a^{-1}$ greater ($\sim$ 15 %) than current rates between 3.1–6.4 ka, before which accumulation was $\sim$ 50 % of modern rates between 6.4 and 16.0 ka. Similarly, Neumann et al. (2008) found that accumulation rates at the Amundsen–Weddell–Ross Divide were $\sim$ 30 % higher between 3–5 ka than modern values based on a dense network of IRHs traced on ground-based RES data, while Karlsson et al. (2014) found that accumulation patterns had likely changed twice during the early to mid-Holocene over PIG from the lack of a model fit between the depths and ages of two prominent IRHs. Using the updated WD14 record, Fudge et al. (2016) showed that accumulation rates were higher there in the mid to late-Holocene (19 % between 4.72 ka BP and the present), a trend that was also observed by Koutnik et al. (2016), who found a 20 % increase in accumulation rates between 2–4 ka compared with modern rates from a ground-based RES profile across the ice divide.

These studies together point to a period of increasing accumulation observed at the WD14 from $\sim$ 7 ka onwards (Fudge et al., 2016; their Fig. 2), with its peak matching the age of the 4.72 ka IRH used here. Thus, our accumulation-rate estimates likely form part of a wider pattern of a sustained increase in accumulation across the Amundsen–Weddell–Ross Divide over several millennia. In showing that mean accumu-

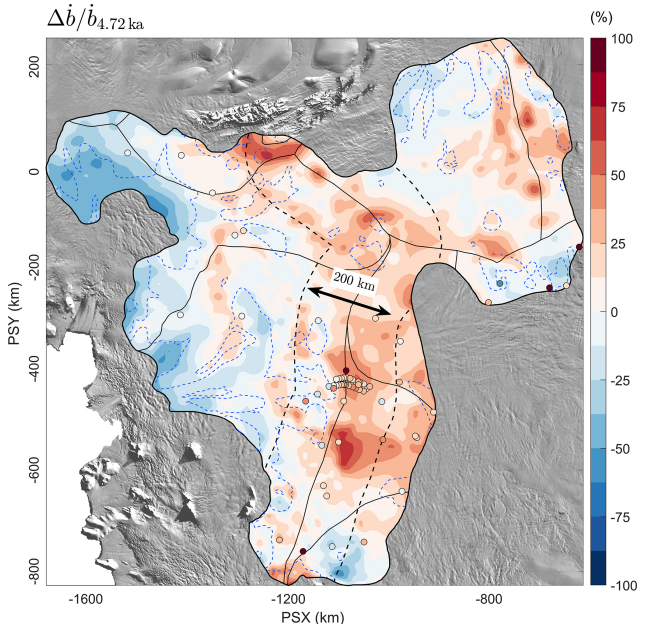

Figure 4. Relative change in accumulation rates between the 4.72 ka-to-present estimates and modern rates. The points on the map represent the relative change in ice-equivalent accumulation rate between the nearest grid cell in the 4.72 ka-to-present grid and the 79 modern observations from cores (Figs. 1 and S6; Sect. 2.4). The dashed black outline line represents the 100 km boundary on either side of the Amundsen–Weddell–Ross Divide used to provide the summary statistics in Sect. 3.1 and Table 2. The dashed blue line shows the contours of the upper limit of the interquartile range for the D parameter ($D \leq 0.34$), whereby all values situated inside of this boundary may satisfy the $D \ll 1$ criteria and those outside may require re-evaluating with the use of multi-dimensional models (Sect. 2.2.1–2.2.2). The background image is the 2014 MODIS mosaic of Antarctica (Haran et al., 2018).

lation rates since 4.72 ka were 18 % greater than modern rates modelled from RACMO2 across the Amundsen–Weddell–Ross Divide, our results provide much wider regional support for the hypothesis that accumulation rates during the mid-Holocene exceeded modern rates across central West Antarctica. A possible explanation for the higher accumulation rates during the mid-Holocene compared with modern values is that they represent a continued climatic transition from the LGM (Steig et al., 2001). Alternatively, it has been suggested that seasonal or interannual variability, such as a weaker circumpolar vortex (van Den Broeke and van Lipzig, 2004; Neumann et al., 2008), or teleconnections to tropical Pacific Ocean warming (Sproson et al., 2022), may also lead to such difference. We did not find evidence for significant changes in accumulation patterns between the mid-Holocene and modern times, suggesting that the current spatial pattern of high accumulation on the Amundsen side of the divide transitioning to low accumulation on the Ross side of the divide was stable throughout the mid-Holocene, as previously suggested by others (Siegert and Payne, 2004; Neumann et al., 2008; Koutnik et al., 2016).

We also find that accumulation estimates for the 4.72 ka-to-present are smaller than modern rates in the lowest elevation bands (< 1400 m), particularly over the Amundsen sector (Fig. 5a–d). This pattern was also found by Medley et al. (2014), who compared modern observational and modelled data over this sector and hypothesized that this discrepancy at low elevations resulted primarily from a lack of sufficient accumulation measurements in the lower sections of their survey area. In our case, these low-elevation values are close to the boundary where we consider the LLA acceptable for the 4.72 ka IRH, albeit where D values are higher than for the rest of the catchment (Fig. S1d), so it is more likely that accumulation rates calculated there are affected by ice-flow gradients and their influence upon IRH depths leading to lower accumulation rates there. Despite this caveat, Fig. 5b and d show that values at low elevations contribute relatively little to the total accumulation (by mass) over our survey area.

We suggest that future ice-sheet modelling studies investigate the difference in accumulation rates inferred from our 1-D model using multi-dimensional flow-band models to assess effects of divergent and convergent flow on IRH depth and ultimately accumulation rates, as previously considered elsewhere in Antarctica (MacGregor et al., 2009). This could be conducted along a flowline transitioning from the slow-flowing regions directly downstream of the Amundsen–Weddell–Ross Divide to the coastal margins of our grid, particularly over THW where we observe the largest uncertainties in accumulation rates. In addition, we suggest that future modelling studies use the accumulation-rate variability from the WD14 as a climate forcing in their ice-sheet models. Koutnik et al. (2016) previously showed that the WD14 record is unique in that it provides a reliable record of accumulation-rate variability during the Holocene, which other East Antarctic ice-core records, often used to reconstruct the evolution of the WAIS, do not possess. We found that these higher accumulation rates are spatially extensive across nearly one third of the WAIS, further suggesting that the WD14 is indeed representative of the wider WAIS and can be used in regional or continental ice-sheet models as a reliable climate forcing for the region. Future regional and continental ice-sheet models should make use of this record to adjust their climatic boundary conditions to provide improved estimates of ice-elevation change and grounding-line evolution over Antarctica.

4.2 Impact for ice-sheet elevation change during the Holocene

Model results from Steig et al. (2001) suggest that the maximum elevation of the WAIS was most likely reached during the early to mid-Holocene (around $\sim$ 7 ka) following higher accumulation rates at the late glacial–interglacial tran-

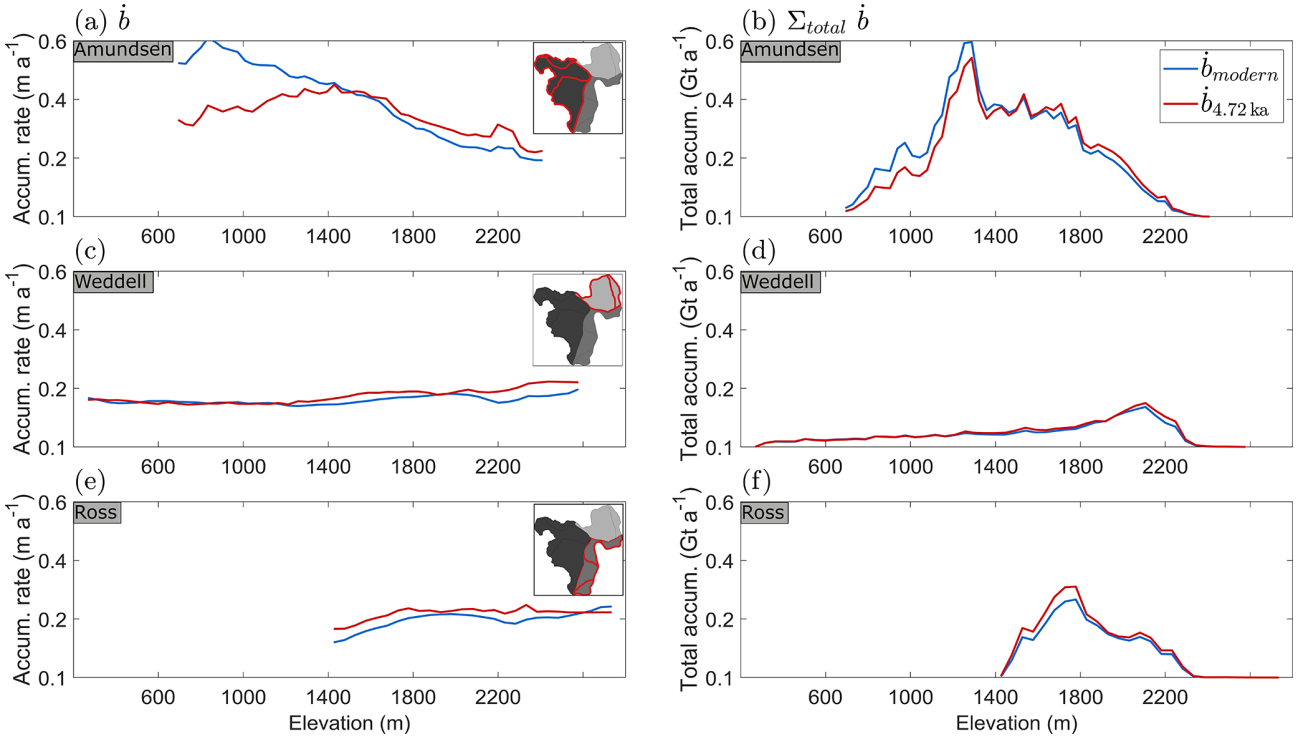

Figure 5. Comparison of ice-equivalent accumulation rates between the 4.72 ka-to-present estimates and modern rates (RACMO2) binned by 50 m elevation bands across the three main catchments considered here (Amundsen, Weddell, and Ross). **(a, c, e)** Mean accumulation rate averaged per 50 m elevation band across the specific catchment area in metres per annum (m a^{-1}). **(b, d, f)** Total accumulation rate per 50 m elevation band across the specific catchment area in gigatonnes per annum (Gt a^{-1}).

sition, after which the WAIS slowly declined to present conditions as the sea-level-rise-induced kinematic wave reached the ice-sheet interior and outpaced the increase in accumulation rates. However, higher accumulation rates in the mid-Holocene relative to the present, which our results suggest occurred spatially across the WAIS, would likely delay the timing of this thinning by several thousand years (Steig et al., 2001).

Using a flow-band model, Koutnik et al. (2016) suggested that an increase of up to 40 % in accumulation rates for the period 9–2 ka would likely have led to an increase in ice thickness of tens of metres during the mid-Holocene. Although this finding was warranted by physical assumptions around the response time of the ice-sheet interior to adjust to an increase in accumulation in the model, it points to the potential for the divide to have thickened by several metres over a relatively short period of time from increased accumulation rates alone. Because the WAIS is also sensitive to ice-dynamical changes at the ice-sheet margins (e.g. grounding-line retreat or calving), an increase in accumulation rates in the upper part of the ice sheet may not necessarily result in enough thickening to counteract potential dynamical losses farther downstream (Jones et al., 2022). Conway and Rasmussen (2009) reported that the Amundsen–Ross Divide is currently thinning and migrating towards the Ross Sea at a speed of 10 m a^{-1}, but they were unable to determine whether this was in response to long-term (last two millennia) accumulation-rate changes there or short-term (last few centuries) ice-dynamical forcing from the coastal margins of the Amundsen and Ross sectors. More recently, Balco et al. (2022) showed that Thwaites and Pope glaciers experienced 35 m of thickening in the mid-to-late Holocene, when accumulation rates were higher than present. While this thickening relative to present was attributed to glacio-isostatic rebound, it is also possible that higher accumulation rates in the upstream sections of the WAIS contributed to this thickening, if sustained over millennia.

The lack of an ice-dynamical component in the model used here precludes us from evaluating any ice-surface-elevation change associated with changing accumulation rates. However, 18 % higher accumulation rates during the mid-Holocene relative to the present across 30 % of the WAIS could be consistent with an elevation increase of several tens of metres in ice thickness, according to Koutnik et al. (2016). Even if tens of metres of ice-surface-elevation change occurred, it is still unlikely to significantly affect the steady-state assumption of the 1-D model used here (constant ice thickness over time), because such changes are small (a few percent of the ice thickness) and that ice thickness exceeds 3500 m in places over our survey area.

4.3 Impact for grounding-line evolution during the Holocene over the WAIS

Finally, we consider the possibility for Holocene ice thickening at the divide from increased accumulation rates to affect downstream grounding-line evolution. Recent evidence from ice-sheet modelling and field measurements suggest that grounding-line retreat during the Holocene was not monotonic, particularly at the Ross and Weddell sea sides of the WAIS (Bradley et al., 2015; Kingslake et al., 2018; Neuhaus et al., 2021). Rather, Kingslake et al. (2018) showed that the grounding-line position in the Ross and Weddell sea sectors initially retreated from the LGM inland until $\sim$ 10.2–9.7 ka, and then readvanced to its modern position sometime during the Holocene. Although they attributed this change in grounding-line position to the solid Earth viscoelastic response due to ice-sheet mass change and the subsequent re-grounding around pinning points, it has also been suggested that an increase in accumulation rates upstream of the grounding line could lead to a readvance via ice thickening there and a subsequent increase in ice flow (Steig et al., 2001; Koutnik et al., 2016; Jones et al., 2022). Across parts of the Weddell Sea Embayment, several studies have produced evidence for stability of the LGM ice thickness there until the early to mid-Holocene (Ross et al., 2011; Hein et al., 2016; Ashmore et al., 2020a), contrary to most of the WAIS, after which abrupt thinning of $\sim$ 400 m contributed $\sim$ 1.4–2 m of sea-level rise (Hein et al., 2016). A possible explanation for this delayed thinning in the Weddell Sea Embayment is that increased snowfall in the upper WAIS might have counteracted ice-dynamical processes at the coast until the mid-to-late Holocene (Hein et al., 2016; Spector et al., 2019). Similarly, over part of the Ross Sea sector, Neuhaus et al. (2021) showed that the grounding line over the Whillans, Kamb, and Bindschadler ice streams retreated to its minimum Holocene position in the mid to late-Holocene, and then readvanced between 2–1 ka, coinciding with periods of warmer and colder climates, respectively. They concluded that the reported grounding-line migration was likely dominated by modest climate-induced changes upstream rather than ice dynamics further downstream, as suggested for the Weddell Sea sector (Hein et al., 2016).

Our results, which provide strong and widespread evidence for higher accumulation along the Amundsen–Weddell–Ross Divide during the mid-Holocene compared with the present, support these hypotheses further, as higher accumulation rates at the divide would likely result in upstream thickening (Sect. 4.2). In the absence of ice-dynamical processes counter-balancing this increase in accumulation rates, the grounding-line should advance in these regions. However, we note that the pattern of grounding-line retreat and readvance has not been observed over the Amundsen Sea sector (Kingslake et al., 2018; Johnson et al., 2020, 2021; Braddock et al., 2022) despite the accumulation-rate increase we also observed along the Amundsen–Weddell–Ross Divide and the recent results from Balco et al. (2022). This complication may indicate that the Amundsen sector is more strongly influenced by coastal changes in ice dynamics, for which even moderate changes in accumulation rate cannot compensate.

5 Conclusion

Using a ubiquitous internal reflecting horizon found across most of the Pine Island, Thwaites, and Institute and Möller ice-stream catchments, we have estimated mid-Holocene accumulation rates in the relatively slow-flowing parts of West Antarctica, representing 30 % of total surface area of the WAIS.

By comparing our Holocene accumulation-rate estimates with a modern climate reanalysis model and observational syntheses, we estimated that accumulation rates across the Amundsen–Weddell–Ross Divide since 4.72 ka were, on average, 18 % higher than modern values. Our results suggest that spatial patterns of accumulation across the WAIS have remained stable during this period, i.e. higher accumulation rates on the Amundsen side of the divide transitioning to lower accumulation rates on the Ross side of the divide. The higher accumulation rates reported here for the mid-Holocene compared to the present agree well with earlier, spatially focused studies of accumulation rates, all of which indicate higher accumulation rates (+15 %–30 %) over the past $\sim$ 5 ka. This change in magnitude occurred at a time of asynchronous grounding-line migration over the WAIS, including readvances of the grounding line in the Weddell and Ross sectors and evidence for delayed deglaciation in the Weddell Sea side of the WAIS.

The higher mid-Holocene accumulation estimates inferred here over large sectors of the WAIS occurred at a time of sustained, millennial-scale increase in accumulation rates found at the WAIS Divide ice core. This pattern indicates that the ice core is suitably representative of the climatic conditions of the wider region over time. We suggest that future regional or continental ice-sheet modelling studies base their paleoclimate forcing on modern spatial SMB products that are modulated over time using the WAIS Divide ice core record. This will enable those models to obtain a more realistic climatic forcing representative of the past conditions of the wider WAIS, and ultimately, constrain ice-sheet volume change and grounding-line evolution during the Holocene.

Code availability. All the codes used to produce the results presented in this paper are available on the GitHub page of Julien A. Bodart (https://github.com/julbod, last access: 15 March 2023) and on Zenodo (https://doi.org/10.5281/zenodo.7738654, Bodart et al., 2023).

Data availability. The IRH information for each of the three surveys used in this paper are archived in open-access repositories (https://doi.org/10.5281/zenodo.4945301, Ashmore et al., 2020b; https://doi.org/10.5285/F2DE31AF-9F83-44F8-9584-F0190A2CC3EB, Bodart et al., 2021b; https://doi.org/10.15784/601673, Muldoon et al., 2023) with references and links provided in the reference list. The BAS airborne radar data which were used to extract the IRHs used in this paper are fully available at the UK Polar Data Centre via the Polar Airborne Geophysics Data Portal (see Frémand et al., 2022). The RACMO2 product is available on request from j.m.vanwessem@uu.nl or m.r.vandenbroeke@uu.nl. Links to access the observational point-based datasets used here are available from the respective references mentioned in the text (Sect. 2.4). The gridded depth and accumulation outputs, as well as the codes used in this study, are archived on Zenodo (https://doi.org/10.5281/zenodo.7738654; Bodart et al., 2023).

Supplement. The supplement related to this article is available online at: https://doi.org/10.5194/tc-17-1497-2023-supplement.

Author contributions. JAB designed the study with supervision from RGB, DAY, and DDB. JAB performed the data processing, gridding, and 1-D modelling, with contributions from JAM for the modelling approach. JAB interpreted the results with input from RGB, DAY, DDB, and JAM. JAB wrote the paper, with edits from RGB, DAY, JAM, DWA, EQ, ASH, DGV, and DDB.

Competing interests. At least one of the (co-)authors is a member of the editorial board of *The Cryosphere*. The peer-review process was guided by an independent editor, and the authors also have no other competing interests to declare.

Disclaimer. Publisher's note: Copernicus Publications remains neutral with regard to jurisdictional claims in published maps and institutional affiliations.

Acknowledgements. The authors would like to dedicate this work to our dear friend and colleague, David G. Vaughan, who recently passed away. This study was motivated by the AntArchitecture SCAR Action Group. UTIG acknowledges the high school students who did the original AGASEA layer interpretation. We would like to thank the editor, Olaf Eisen, as well as Michelle Koutnik and an anonymous reviewer for thorough and constructive reviews, which improved this paper.

Financial support. Julien A. Bodart was supported by the NERC Doctoral Training Partnership grant (grant no. NE/L002558/1), hosted in the Edinburgh E^3 DTP programme. Julien A. Bodart was also supported by the Scottish Alliance for Geoscience, Environment and Society (SAGES) with funding of a Postdoctoral and Early Career Researcher Exchanges scheme to UTIG. Support for UTIG data analysis was received from NSF (grant nos. CDI-0941678, PLR-1443690, and PLR-10437661) as well as the G. Unger Vetlesen Foundation and the UTIG Gale White and Ewing/-Worzel fellowships. This is the UTIG contribution no. 3955 and ITGC contribution no. 102.

Review statement. This paper was edited by Olaf Eisen and reviewed by Michelle Koutnik and one anonymous referee.

References

Arndt, J. E., Hillenbrand, C. D., Grobe, H., Kuhn, G., and Wacker, L.: Evidence for a dynamic grounding line in outer Filchner Trough, Antarctica, until the early Holocene, Geology, 45, 1035–1038, https://doi.org/10.1130/G39398.1, 2017.

Ashmore, D. W., Bingham, R. G., Ross, N., Siegert, M. J., Jordan, T. A., and Mair, D. W.: Englacial architecture and age-depth constraints across the West Antarctic Ice Sheet, Geophys. Res. Lett., 47, e2019GL086663, https://doi.org/10.1029/2019GL086663, 2020a.

Ashmore, D. W., Bingham, R. G., Ross, N., Siegert, M., Jordan, T. A., and Mair, D. W. F.: Radiostratigraphy of the Weddell Sea sector of West Antarctica, v2.0.0, Zenodo [data set], https://doi.org/10.5281/zenodo.4945301, 2020b.

Balco, G., Brown, N., Nichols, K., Venturelli, R. A., Adams, J., Braddock, S., Campbell, S., Goehring, B., Johnson, J. S., Rood, D. H., Wilcken, K., Hall, B., and Woodward, J.: Reversible ice sheet thinning in the Amundsen Sea Embayment during the Late Holocene, The Cryosphere Discuss. [preprint], https://doi.org/10.5194/tc-2022-172, in review, 2022.

Beem, L. H., Young, D. A., Greenbaum, J. S., Blankenship, D. D., Cavitte, M. G. P., Guo, J., and Bo, S.: Aerogeophysical characterization of Titan Dome, East Antarctica, and potential as an ice core target, The Cryosphere, 15, 1719–1730, https://doi.org/10.5194/tc-15-1719-2021, 2021.

Bingham, R. G. and Siegert, M. J.: Radio-echo sounding over polar ice masses, J. Environ. Eng. Geoph., 12, 47–62, https://doi.org/10.2113/JEEG12.1.47, 2007.

Bodart, J. A., Bingham, R. G., Ashmore, D. W., Karlsson, N. B., Hein, A. S., and Vaughan, D. G.: Age-depth stratigraphy of Pine Island Glacier inferred from airborne radar and ice core chronology, J. Geophys. Res.-Earth, 126, e2020JF005927, https://doi.org/10.1029/2020JF005927, 2021a.

Bodart, J. A., Bingham, R. G., Ashmore, D. W., Karlsson, N. B., Hein, A. S., and Vaughan, D. G.: Dated radar stratigraphy of the Pine Island Glacier catchment (West Antarctica) derived from BBAS-PASIN (2004–05) and OIB-MCoRDS2 (2016/2018) surveys, v.1.0.0, UK Polar Data Centre, Natural Environment Research Council, UK Research and Innovation [data set], https://doi.org/10.5285/F2DE31AF-9F83-44F8-9584-F0190A2CC3EB, 2021b.

Bodart, J. A., Bingham, R. G., Young, D. A., MacGregor, J. A., Ashmore, D. W., Quartini, E., Vaughan, D. G., and Blankenship, D. D.: Gridded depth and accumulation products from dated airborne radar stratigraphy over West Antarctica during the mid-Holocene, v.1.0.0, Zenodo [data set], https://doi.org/10.5281/zenodo.7738654, 2023.

Bracegirdle, T. J., Colleoni, F., Abram, N. J., Bertler, N. A., Dixon, D. A., England, M., Favier, V., Fogwill, C. J., Fyfe, J. C., Goodwin, I., and Goosse, H.: Back to the future: Using long-term observational and palaeo-proxy reconstructions to improve model projections of Antarctic climate, Geosci. J., 9, 255, https://doi.org/10.3390/geosciences9060255, 2019.

Braddock, S., Hall, B. L., Johnson, J. S., Balco, G., Spoth, M., Whitehouse, P. L., Campbell, S., Goehring, B. M., Rood, D. H., and Woodward, J.: Relative sea-level data preclude major late Holocene ice-mass change in Pine Island Bay, Nat. Geosci., 15, 568–572, https://doi.org/10.1038/s41561-022-00961-y, 2022.

Bradley, S. L., Hindmarsh, R. C., Whitehouse, P. L., Bentley, M. J., and King, M. A.: Low post-glacial rebound rates in the Weddell Sea due to Late Holocene ice-sheet readvance, Earth Planet. Sc. Lett., 413, 79–89, https://doi.org/10.1016/j.epsl.2014.12.039, 2015.

Buizert, C., Fudge, T. J., Roberts, W. H., Steig, E. J., Sherriff-Tadano, S., Ritz, C., Lefebvre, E., Edwards, J., Kawamura, K., Oyabu, I., and Motoyama, H.: Antarctic surface temperature and elevation during the Last Glacial Maximum, Science, 372, 1097–1101, https://doi.org/10.1126/science.abd2897, 2021.

Burgener, L., Rupper, S., Koenig, L., Forster, R., Christensen, W. F., Williams, J., Koutnik, M., Miege, C., Steig, E. J., Tingey, D., and Keeler, D.: An observed negative trend in West Antarctic accumulation rates from 1975 to 2010: Evidence from new observed and simulated records, J. Geophys. Res.-Atmos., 118, 4205–4216, https://doi.org/10.1002/jgrd.50362, 2013.

Cavitte, M. G., Blankenship, D. D., Young, D. A., Schroeder, D. M., Parrenin, F., Lemeur, E., Macgregor, J. A., and Siegert, M. J.: Deep radiostratigraphy of the East Antarctic plateau: connecting the Dome C and Vostok ice core sites, J. Glaciol., 62, 323–334, https://doi.org/10.1017/jog.2016.11, 2016.

Cavitte, M. G. P., Parrenin, F., Ritz, C., Young, D. A., Van Liefferinge, B., Blankenship, D. D., Frezzotti, M., and Roberts, J. L.: Accumulation patterns around Dome C, East Antarctica, in the last 73 kyr, The Cryosphere, 12, 1401–1414, https://doi.org/10.5194/tc-12-1401-2018, 2018.

Cavitte, M. G., Goosse, H., Wauthy, S., Kausch, T., Tison, J. L., Van Liefferinge, B., Pattyn, F., Lenaerts, J. T., and Claeys, P.: From ice core to ground-penetrating radar: representativeness of SMB at three ice rises along the Princess Ragnhild Coast, East Antarctica, J. Glaciol., 68, 1221–1233, https://doi.org/10.1017/jog.2022.39, 2022.

Chavaillaz, Y., Codron, F., and Kageyama, M.: Southern westerlies in LGM and future (RCP4.5) climates, Clim. Past, 9, 517–524, https://doi.org/10.5194/cp-9-517-2013, 2013.

Cole-Dai, J., Ferris, D. G., Kennedy, J. A., Sigl, M., McConnell, J. R., Fudge, T. J., Geng, L., Maselli, O. J., Taylor, K. C., and Souney, J. M.: Comprehensive record of volcanic eruptions in the Holocene (11,000 years) from the WAIS Divide, Antarctica ice core, J. Geophys. Res.-Atmos., 126, e2020JD032855, https://doi.org/10.1029/2020JD032855, 2021.

Conway, H. and Rasmussen, L. A.: Recent thinning and migration of the Western Divide, central West Antarctica, Geophys. Res. Let., 36, https://doi.org/10.1029/2009GL038072, 2009.

Corr, H. F., Ferraccioli, F., Frearson, N., Jordan, T., Robinson, C., Armadillo, E., Caneva, G., Bozzo, E., and Tabacco, I.: Airborne radio-echo sounding of the Wilkes Subglacial Basin, the Transantarctic Mountains and the Dome C region, Terra Ant. Rep., 13, 55–63, 2007.

CReSIS: CReSIS Radar Depth Sounder Data, Lawrence, Kansas, USA, Digital Media, http://data.cresis.ku.edu/ (last access: 15 October 2022), 2018.

Dansgaard, W. and Johnsen, S. J.: A flow model and a time scale for the ice core from Camp Century, Greenland, J. Glaciol., 8, 215–223, https://doi.org/10.3189/S0022143000031208, 1969.

Dattler, M. E., Lenaerts, J. T., and Medley, B.: Significant spatial variability in radar-derived west Antarctic accumulation linked to surface winds and topography, Geophys. Res. Lett., 46, 13126–13134, https://doi.org/10.1029/2019GL085363, 2019.

DeConto, R. M. and Pollard, D.: Contribution of Antarctica to past and future sea-level rise, Nature, 531, 591–597, https://doi.org/10.1038/nature17145, 2016.

Denton, G. H. and Hughes, T. J.: Reconstructing the Antarctic ice sheet at the Last Glacial Maximum, Quaternary Sci. Rev., 21, 193–202, https://doi.org/10.1016/S0277-3791(01)00090-7, 2002.

Fahnestock, M., Abdalati, W., Joughin, I., Brozena, J., and Gogineni, P.: High geoSthermal heat flow, basal melt, and the origin of rapid ice flow in central Greenland, Science, 294, 2338–2342, https://doi.org/10.1126/science.1065370, 2001a.

Fahnestock, M., Abdalati, W., Luo, S., and Gogineni, S.: Internal layer tracing and age-depth-accumulation relationships for the northern Greenland ice sheet, J. Geophys. Res.-Atmos, 106, 33789–33797, https://doi.org/10.1029/2001JD900200, 2001b.

Favier, V., Agosta, C., Parouty, S., Durand, G., Delaygue, G., Gallée, H., Drouet, A.-S., Trouvilliez, A., and Krinner, G.: An updated and quality controlled surface mass balance dataset for Antarctica, The Cryosphere, 7, 583–597, https://doi.org/10.5194/tc-7-583-2013, 2013.

Frémand, A. C., Bodart, J. A., Jordan, T. A., Ferraccioli, F., Robinson, C., Corr, H. F. J., Peat, H. J., Bingham, R. G., and Vaughan, D. G.: British Antarctic Survey's aerogeophysical data: releasing 25 years of airborne gravity, magnetic, and radar datasets over Antarctica, Earth Syst. Sci. Data, 14, 3379–3410, https://doi.org/10.5194/essd-14-3379-2022, 2022.

Fudge, T. J., Markle, B. R., Cuffey, K. M., Buizert, C., Taylor, K. C., Steig, E. J., Waddington, E. D., Conway, H., and Koutnik, M.: Variable relationship between accumulation and temperature in West Antarctica for the past 31,000 years, Geophys. Res. Lett., 43, 3795–3803, https://doi.org/10.1002/2016GL068356, 2016.

Golledge, N. R., Fogwill, C. J., Mackintosh, A. N., and Buckley, K. M.: Dynamics of the last glacial maximum Antarctic ice-sheet and its response to ocean forcing, P. Natl. Acad. Sci. USA, 109, 16052–16056, https://doi.org/10.1073/pnas.1205385109, 2012.

Golledge, N. R., Levy, R. H., McKay, R. M., Fogwill, C. J., White, D. A., Graham, A. G., Smith, J. A., Hillenbrand, C. D., Licht, K. J., Denton, G. H., and Ackert Jr., R. P.: Glaciology and geological signature of the Last Glacial Maximum Antarctic ice sheet, Quaternary Sci. Rev., 78, 225–247, https://doi.org/10.1016/j.quascirev.2013.08.011, 2013.

Haran, T., Klinger, M., Bohlander, J., Fahnestock, M., Painter, T., and Scambos, T.: MEaSUREs MODIS Mosaic of Antarctica 2013–2014 (MOA2014) Image Map, v.1.0.0., NASA National Snow and Ice Data Center Distributed Active Archive Center [data set], https://doi.org/10.5067/RNF17BP824UM, 2018.

Harrison, C. H.: Radio Echo Sounding of Horizontal Layers in Ice, J. Glaciol., 12, 383–397, https://doi.org/10.3189/S0022143000031804, 1973.

Hein, A. S., Marrero, S. M., Woodward, J., Dunning, S. A., Winter, K., Westoby, M. J., Freeman, S. P., Shanks, R. P., and Sugden, D. E.: Mid-Holocene pulse of thinning in the Weddell Sea sector of the West Antarctic ice sheet, Nat. Commun., 7, 1–8, https://doi.org/10.1038/ncomms12511, 2016.

Hillenbrand, C. D., Kuhn, G., Smith, J. A., Gohl, K., Graham, A. G., Larter, R. D., Klages, J. P., Downey, R., Moreton, S. G., Forwick, M., and Vaughan, D. G.: Grounding-line retreat of the west Antarctic ice sheet from inner Pine island Bay, Geology, 41, 35–38, https://doi.org/10.1130/G33469.1, 2013.

Hillenbrand, C. D., Bentley, M. J., Stolldorf, T. D., Hein, A. S., Kuhn, G., Graham, A. G., Fogwill, C. J., Kristoffersen, Y., Smith, J. A., Anderson, J. B., and Larter, R. D.: Reconstruction of changes in the Weddell Sea sector of the Antarctic Ice Sheet since the Last Glacial Maximum, Quaternary Sci. Rev., 100, 111–136, https://doi.org/10.1016/j.quascirev.2013.07.020, 2014.

Hillenbrand, C. D., Smith, J. A., Hodell, D. A., Greaves, M., Poole, C. R., Kender, S., Williams, M., Andersen, T. J., Jernas, P. E., Elderfield, H., and Klages, J. P.: West Antarctic Ice Sheet retreat driven by Holocene warm water incursions, Nature, 547, 43–48, https://doi.org/10.1038/nature22995, 2017.

Holschuh, N., Parizek, B. R., Alley, R. B., and Anandakrishnan, S.: Decoding ice sheet behavior using englacial layer slopes, Geophys. Res. Lett., 44, 5561–5570, https://doi.org/10.1002/2017GL073417, 2017.

Holt, J. W., Blankenship, D. D., Morse, D. L., Young, D. A., Peters, M. E., Kempf, S. D., Richter, T. G., Vaughan, D. G., and Corr, H. F.: New boundary conditions for the West Antarctic Ice Sheet: Subglacial topography of the Thwaites and Smith glacier catchments, Geophys. Res. Lett., 33, L09502, https://doi.org/10.1029/2005GL025561, 2006.

IPCC: Climate Change 2021: The Physical Science Basis. Contribution of Working Group I to the Sixth Assessment Report of the Intergovernmental Panel on Climate Change, edited by: Masson-Delmotte, V., Zhai, P., Pirani, A., Connors, S. L., Péan, C., Berger, S., Caud, N., Chen, Y., Goldfarb, L., Gomis, M. I., Huang, M., Leitzell, K., Lonnoy, E., Matthews, J. B. R., Maycock, T. K., Waterfield, T., Yelekçi, O., Yu, R., and Zhou, B., Cambridge University Press, Cambridge, United Kingdom and New York, NY, USA, 147–286, https://doi.org/10.1017/9781009157896.003, in press, 2021.

Jacobel, R. W. and Welch, B. C.: A time marker at 17.5 kyr BP detected throughout West Antarctica, Ann. Glaciol., 41, 47–51, https://doi.org/10.3189/172756405781813348, 2005.

Johnson, J. S., Bentley, M. J., Smith, J. A., Finkel, R. C., Rood, D. H., Gohl, K., Balco, G., Larter, R. D., and Schaefer, J. M.: Rapid thinning of Pine Island Glacier in the early Holocene, Science, 343, 999–1001, https://doi.org/10.1126/science.1247385, 2014.

Johnson, J. S., Roberts, S. J., Rood, D. H., Pollard, D., Schaefer, J. M., Whitehouse, P. L., Ireland, L. C., Lamp, J. L., Goehring, B. M., Rand, C., and Smith, J. A.: Deglaciation of Pope Glacier implies widespread early Holocene ice sheet thinning in the Amundsen Sea sector of Antarctica, Earth Planet Sc. Lett., 548, 116501, https://doi.org/10.1016/j.epsl.2020.116501, 2020.

Johnson, J. S., Pollard, D., Whitehouse, P. L., Roberts, S. J., Rood, D. H., and Schaefer, J. M.: Comparing glacial-geological evidence and model simulations of ice sheet change since the last glacial period in the Amundsen Sea sector of Antarctica, J. Geophys. Res.-Earth, 126, e2020JF005827, https://doi.org/10.1029/2020JF005827, 2021.

Johnson, J. S., Venturelli, R. A., Balco, G., Allen, C. S., Braddock, S., Campbell, S., Goehring, B. M., Hall, B. L., Neff, P. D., Nichols, K. A., Rood, D. H., Thomas, E. R., and Woodward, J.: Review article: Existing and potential evidence for Holocene grounding line retreat and readvance in Antarctica, The Cryosphere, 16, 1543–1562, https://doi.org/10.5194/tc-16-1543-2022, 2022.

Jones, R. S., Johnson, J. S., Lin, Y., Mackintosh, A. N., Sefton, J. P., Smith, J. A., Thomas, E. R., and Whitehouse, P. L.: Stability of the Antarctic Ice Sheet during the pre-industrial Holocene, Nat. Rev. Earth Environ., 3, 500–515, https://doi.org/10.1038/s43017-022-00309-5, 2022.

Karlsson, N. B., Bingham, R. G., Rippin, D. M., Hindmarsh, R. C., Corr, H. F., and Vaughan, D. G.: Constraining past accumulation in the central Pine Island Glacier basin, West Antarctica, using radio-echo sounding, J. Glaciol., 60, 553–562, https://doi.org/10.3189/2014JoG13j180, 2014.

Kausch, T., Lhermitte, S., Lenaerts, J. T. M., Wever, N., Inoue, M., Pattyn, F., Sun, S., Wauthy, S., Tison, J.-L., and van de Berg, W. J.: Impact of coastal East Antarctic ice rises on surface mass balance: insights from observations and modeling, The Cryosphere, 14, 3367–3380, https://doi.org/10.5194/tc-14-3367-2020, 2020.

Kingslake, J., Scherer, R. P., Albrecht, T., Coenen, J., Powell, R. D., Reese, R., Stansell, N. D., Tulaczyk, S., Wearing, M. G., and Whitehouse, P. L.: Extensive retreat and re-advance of the West Antarctic Ice Sheet during the Holocene, Nature, 558, 430–434, https://doi.org/10.1038/s41586-018-0208-x, 2018.

Koutnik, M. R., Fudge, T. J., Conway, H., Waddington, E. D., Neumann, T. A., Cuffey, K. M., Buizert, C., and Taylor, K. C.: Holocene accumulation and ice flow near the West Antarctic Ice Sheet Divide ice core site, J. Geophys. Res.-Earth, 121, 907–924, https://doi.org/10.1002/2015JF003668, 2016.

Kurbatov, A. V., Zielinski, G. A., Dunbar, N. W., Mayewski, P. A., Meyerson, E. A., Sneed, S. B., and Taylor, K. C.: A 12,000 year record of explosive volcanism in the Siple Dome Ice Core, West Antarctica, J. Geophys. Res.-Atmos., 111, D12307, https://doi.org/10.1029/2005JD006072, 2006.

Le Brocq, A. M., Bentley, M. J., Hubbard, A., Fogwill, C. J., Sugden, D. E., and Whitehouse, P. L.: Reconstructing the Last Glacial Maximum ice sheet in the Weddell Sea embayment, Antarctica, using numerical modelling constrained by field evidence, Quaternary Sci. Rev., 30, 2422–2432, https://doi.org/10.1016/j.quascirev.2011.05.009, 2011.

Leysinger Vieli, G. J. M., Siegert, M. J., and Payne, A. J.: Reconstructing ice-sheet accumulation rates at ridge B, East Antarctica, Ann. Glaciol., 39, 326–330, https://doi.org/10.3189/172756404781814519, 2004.

Leysinger Vieli, G. J. M., Hindmarsh, R. C., Siegert, M. J., and Bo, S.: Time-dependence of the spatial pattern of accumulation rate in East Antarctica deduced from isochronic radar layers using a 3-D numerical ice flow model, J. Geophys. Res.-Earth, 116, F02018, https://doi.org/10.1029/2010JF001785, 2011.

Leysinger Vieli, G. M., Martin, C., Hindmarsh, R. C. A., and Lüthi, M. P., Basal freeze-on generates complex ice-sheet stratig-

raphy, Nat. Commun., 9, 4669, https://doi.org/10.1038/s41467-018-07083-3, 2018.

MacGregor, J. A., Matsuoka, K., Koutnik, M. R., Waddington, E. D., Studinger, M., and Winebrenner, D. P.: Millennially averaged accumulation rates for the Vostok Subglacial Lake region inferred from deep internal layers, Ann. Glaciol., 50, 25–34, https://doi.org/10.3189/172756409789097441, 2009.

MacGregor, J. A., Fahnestock, M. A., Catania, G. A., Paden, J. D., Prasad Gogineni, S., Young, S. K., Rybarski, S. C., Mabrey, A. N., Wagman, B. M., and Morlighem, M.: Radiostratigraphy and age structure of the Greenland Ice Sheet, J. Geophys. Res.-Earth Surf., 120, 212–241, https://doi.org/10.1002/2014JF003215, 2015.

MacGregor, J. A., Colgan, W. T., Fahnestock, M. A., Morlighem, M., Catania, G. A., Paden, J. D., and Gogineni, S. P.: Holocene deceleration of the Greenland ice sheet, Science, 351, 590–593, https://doi.org/10.1126/science.aab1702, 2016.

MacGregor, J. A., Boisvert, L. N., Medley, B., Petty, A. A., Harbeck, J. P., Bell, R. E., Blair, J. B., Blanchard-Wrigglesworth, E., Buckley, E.,M., Christoffersen, M. S., and Cochran, J. R.: The scientific legacy of NASA's Operation Icebridge, Rev. Geophys., 59, e2020RG000712, https://doi.org/10.1029/2020RG000712, 2021.

Mayewski, P. A. and Dixon, D. A.: US International TransAntarctic Scientific Expedition (US ITASE) Glaciochemical Data, v. 2.0.0., NASA National Snow and Ice Data Center [data set], https://doi.org/10.7265/N51V5BXR, 2013.

Medley, B., Joughin, I., Das, S. B., Steig, E. J., Conway, H., Gogineni, S., Criscitiello, A. S., McConnell, J. R., Smith, B. E., van den Broeke, M. R., and Lenaerts, J. T.: Airborne-radar and ice-core observations of annual snow accumulation over Thwaites Glacier, West Antarctica confirm the spatiotemporal variability of global and regional atmospheric models, Geophys. Res. Lett., 40, 3649–3654, https://doi.org/10.1002/grl.50706, 2013.

Medley, B., Joughin, I., Smith, B. E., Das, S. B., Steig, E. J., Conway, H., Gogineni, S., Lewis, C., Criscitiello, A. S., McConnell, J. R., van den Broeke, M. R., Lenaerts, J. T. M., Bromwich, D. H., Nicolas, J. P., and Leuschen, C.: Constraining the recent mass balance of Pine Island and Thwaites glaciers, West Antarctica, with airborne observations of snow accumulation, The Cryosphere, 8, 1375–1392, https://doi.org/10.5194/tc-8-1375-2014, 2014.

Morlighem, M.: MEaSUREs BedMachine Antarctica, v.2.0.0., NASA National Snow and Ice Data Center Distributed Active Archive Center [data set], https://doi.org/10.5067/E1QL9HFQ7A8M, 2020.

Morlighem, M., Rignot, E., Binder, T., Blankenship, D., Drews, R., Eagles, G., Eisen, O., Ferraccioli, F., Forsberg, R., Fretwell, P., and Goel, V.: Deep glacial troughs and stabilizing ridges unveiled beneath the margins of the Antarctic ice sheet, Nat. Geo., 13, 132–137, https://doi.org/10.1038/s41561-019-0510-8, 2020.

Mouginot, J., Scheuchl, B., and Rignot., E.: MEaSUREs Antarctic Boundaries for IPY 2007–2009 from Satellite Radar, v.2.0.0., NASA National Snow and Ice Data Center Distributed Active Archive Center [data set], https://doi.org/10.5067/AXE4121732AD, 2017.

Muldoon, G. R., Jackson, C. S., Young, D. A., and Blankenship, D. D.: Bayesian estimation of englacial radar chronology in Central West Antarctica, Dynamics and Statistics of the Climate System, 3, dzy004, https://doi.org/10.1093/climatesystem/dzy004, 2018.

Muldoon, G., Blankenship, D. D., Jackson, C., and Young, D. A.: AGASEA 4.7 ka Englacial Isochron over the Thwaites Glacier Catchment, U.S. Antarctic Program (USAP) Data Center [data set], https://doi.org/10.15784/601673, 2023.

Neuhaus, S. U., Tulaczyk, S. M., Stansell, N. D., Coenen, J. J., Scherer, R. P., Mikucki, J. A., and Powell, R. D.: Did Holocene climate changes drive West Antarctic grounding line retreat and readvance?, The Cryosphere, 15, 4655–4673, https://doi.org/10.5194/tc-15-4655-2021, 2021.

Neumann, T. A., Conway, H., Price, S. F., Waddington, E. D., Catania, G. A., and Morse, D. L.: Holocene accumulation and ice sheet dynamics in central West Antarctica, J. Geophys. Res.-Earth, 113, F02018, https://doi.org/10.1029/2007JF000764, 2008.

Nichols, K. A., Goehring, B. M., Balco, G., Johnson, J. S., Hein, A. S., and Todd, C.: New Last Glacial Maximum ice thickness constraints for the Weddell Sea Embayment, Antarctica, The Cryosphere, 13, 2935–2951, https://doi.org/10.5194/tc-13-2935-2019, 2019.

Nielsen, L. T., Karlsson, N. B., and Hvidberg, C. S.: Large-scale reconstruction of accumulation rates in northern Greenland from radar data, Ann. Glaciol., 56, 70–78 https://doi.org/10.3189/2015AoG70A062, 2015.

Nye, J. F.: The distribution of stress and velocity in glaciers and ice-sheets, P. Roy. Soc. Lond. A. Mat., 239, 113–133, https://doi.org/10.1098/rspa.1957.0026, 1957.

Parrenin, F., Barnola, J.-M., Beer, J., Blunier, T., Castellano, E., Chappellaz, J., Dreyfus, G., Fischer, H., Fujita, S., Jouzel, J., Kawamura, K., Lemieux-Dudon, B., Loulergue, L., Masson-Delmotte, V., Narcisi, B., Petit, J.-R., Raisbeck, G., Raynaud, D., Ruth, U., Schwander, J., Severi, M., Spahni, R., Steffensen, J. P., Svensson, A., Udisti, R., Waelbroeck, C., and Wolff, E.: The EDC3 chronology for the EPICA Dome C ice core, Clim. Past, 3, 485–497, https://doi.org/10.5194/cp-3-485-2007, 2007.

Peters, M. E., Blankenship, D. D., Carter, S. P., Kempf, S. D., Young, D. A., and Holt, J. W.: Along-track focusing of airborne radar sounding data from West Antarctica for improving basal reflection analysis and layer detection, IEEE T. Geosci. Remote, 45, 2725–2736, https://doi.org/10.1109/TGRS.2007.897416, 2007.

Petit, J. R., Jouzel, J., Raynaud, D., Barkov, N. I., Barnola, J. M., Basile, I., Bender, M., Chappellaz, J., Davis, M., Delaygue, G., and Delmotte, M.: Climate and atmospheric history of the past 420,000 years from the Vostok ice core, Antarctica, Nature, 399, 429–436, https://doi.org/10.1038/20859, 1999.

RAISED Consortium: A community-based geological reconstruction of Antarctic Ice Sheet deglaciation since the Last Glacial Maximum, Quaternary Sci. Rev., 100, 1–9, https://doi.org/10.1016/j.quascirev.2014.06.025, 2014.

Rignot, E., Mouginot, J., and Scheuchl, B.: MEaSUREs InSAR-based Antarctica ice velocity map, v.2.0.0., NASA National Snow and Ice Data Center Distributed Active Archive Center [data set], https://doi.org/10.5067/D7GK8F5J8M8R, 2017.

Ross, N., Siegert, M. J., Woodward, J., Smith, A. M., Corr, H. F., Bentley, M. J., Hindmarsh, R. C., King, E. C., and Rivera, A.: Holocene stability of the Amundsen-

Weddell ice divide, West Antarctica, Geology, 39, 935–938, https://doi.org/10.1130/G31920.1, 2011.

Ross, N., Bingham, R. G., Corr, H. F., Ferraccioli, F., Jordan, T. A., Le Brocq, A., Rippin, D. M., Young, D., Blankenship, D. D., and Siegert, M. J.: Steep reverse bed slope at the grounding line of the Weddell Sea sector in West Antarctica, Nat. Geosci., 5, 393–396, https://doi.org/10.1038/ngeo1468, 2012.

Siegert, M. J. and Payne, A. J.: Past rates of accumulation in central West Antarctica, Geophys. Res. Lett., 31, L12403, https://doi.org/10.1029/2004GL020290, 2004.

Siegert, M., Ross, N., Corr, H., Kingslake, J., and Hindmarsh, R.: Late Holocene ice-flow reconfiguration in the Weddell Sea sector of West Antarctica, Quaternary Sci. Rev., 78, 98–107, https://doi.org/10.1016/j.quascirev.2013.08.003, 2013.

Sigl, M., Toohey, M., McConnell, J. R., Cole-Dai, J., and Severi, M.: Volcanic stratospheric sulfur injections and aerosol optical depth during the Holocene (past 11 500 years) from a bipolar ice-core array, Earth Syst. Sci. Data, 14, 3167–3196, https://doi.org/10.5194/essd-14-3167-2022, 2022.

Spector, P., Stone, J., and Goehring, B.: Thickness of the divide and flank of the West Antarctic Ice Sheet through the last deglaciation, The Cryosphere, 13, 3061–3075, https://doi.org/10.5194/tc-13-3061-2019, 2019.

Sproson, A. D., Yokoyama, Y., Miyairi, Y., Aze, T., and Totten, R. L.: Holocene melting of the West Antarctic Ice Sheet driven by tropical Pacific warming, Nat. Commun., 13, 1–9, https://doi.org/10.1038/s41467-022-30076-2, 2022.

Steig, E. J., Fastook, J. L., Zweck, C., Goodwin, I. D., Licht, K. J., White, J. W., and Ackert Jr., R. P.: West Antarctic ice sheet elevation changes, The West Antarctic Ice Sheet: Behavior and Environment, 77, 75–90, https://doi.org/10.1029/AR077p0075, 2001.

Stone, J. O., Balco, G. A., Sugden, D. E., Caffee, M. W., Sass III, L. C., Cowdery, S. G., and Siddoway, C.: Holocene deglaciation of Marie Byrd land, west Antarctica, Science, 299, 99–102, https://doi.org/10.1126/science.1077998, 2003.

Suganuma, Y., Miura, H., Zondervan, A., and Okuno, J. I.: East Antarctic deglaciation and the link to global cooling during the Quaternary: Evidence from glacial geomorphology and 10Be surface exposure dating of the Sør Rondane Mountains, Dronning Maud Land, Quaternary Sci. Rev., 97, 102–120, https://doi.org/10.1016/j.quascirev.2014.05.007, 2014.

Sutter, J., Fischer, H., and Eisen, O.: Investigating the internal structure of the Antarctic ice sheet: the utility of isochrones for spatiotemporal ice-sheet model calibration, The Cryosphere, 15, 3839–3860, https://doi.org/10.5194/tc-15-3839-2021, 2021.

Van Den Broeke, M. R. and Van Lipzig, N. P.: Changes in Antarctic temperature, wind and precipitation in response to the Antarctic Oscillation, Ann. Glaciol., 39, 119–126, https://doi.org/10.3189/172756404781814654, 2004.

van Wessem, J. M., van de Berg, W. J., Noël, B. P. Y., van Meijgaard, E., Amory, C., Birnbaum, G., Jakobs, C. L., Krüger, K., Lenaerts, J. T. M., Lhermitte, S., Ligtenberg, S. R. M., Medley, B., Reijmer, C. H., van Tricht, K., Trusel, L. D., van Ulft, L. H., Wouters, B., Wuite, J., and van den Broeke, M. R.: Modelling the climate and surface mass balance of polar ice sheets using RACMO2 – Part 2: Antarctica (1979–2016), The Cryosphere, 12, 1479–1498, https://doi.org/10.5194/tc-12-1479-2018, 2018.

Vaughan, D. G., Corr, H. F., Ferraccioli, F., Frearson, N., O'Hare, A., Mach, D., Holt, J. W., Blankenship, D. D., Morse, D. L., and Young, D. A.: New boundary conditions for the West Antarctic ice sheet: Subglacial topography beneath Pine Island Glacier, Geophys. Res. Lett., 33, L09501, https://doi.org/10.1029/2005GL025588, 2006.

Venturelli, R. A., Siegfried, M. R., Roush, K. A., Li, W., Burnett, J., Zook, R., Fricker, H. A., Priscu, J. C., Leventer, A., and Rosenheim, B. E.: Mid-Holocene grounding line retreat and readvance at Whillans Ice Stream, West Antarctica, Geophys. Res. Lett., 47, e2020GL088476, https://doi.org/10.1029/2020GL088476, 2020.

Waddington, E. D., Neumann, T. A., Koutnik, M. R., Marshall, H.-P., and Morse, D. L.: Inference of accumulation-rate patterns from deep layers in glaciers and ice sheets, J. Glaciol., 53, 694–712, https://doi.org/10.3189/002214307784409351, 2007.

WAIS Divide Project Members: Onset of deglacial warming in West Antarctica driven by local orbital forcing, Nature, 500, 440–444, https://doi.org/10.1038/nature12376, 2013.

Wearing, M. G. and Kingslake, J.: Holocene Formation of Henry Ice Rise, West Antarctica, Inferred from Ice-Penetrating Radar, J. Geophys. Res.-Earth, 124, 2224–2240, https://doi.org/10.1029/2018JF004988, 2019.

Whillans, I. M.: Radio-echo layers and the recent stability of the West Antarctic ice sheet, Nature, 264, 152, https://doi.org/10.1038/264152a0, 1976.

Winter, A., Steinhage, D., Creyts, T. T., Kleiner, T., and Eisen, O.: Age stratigraphy in the East Antarctic Ice Sheet inferred from radio-echo sounding horizons, Earth Syst. Sci. Data, 11, 1069–1081, https://doi.org/10.5194/essd-11-1069-2019, 2019.

Appendix C: British Antarctic Survey's Aerogeophysical Data: Releasing 25 Years of Airborne Gravity, Magnetic, and Radar Datasets over Antarctica

Earth Syst. Sci. Data, 14, 3379–3410, 2022
https://doi.org/10.5194/essd-14-3379-2022
© Author(s) 2022. This work is distributed under
the Creative Commons Attribution 4.0 License.

Open Access Earth System Science Data

British Antarctic Survey's aerogeophysical data: releasing 25 years of airborne gravity, magnetic, and radar datasets over Antarctica

Alice C. Frémand[1,★], Julien A. Bodart[1,2,★], Tom A. Jordan[1], Fausto Ferraccioli[1,3], Carl Robinson[1], Hugh F. J. Corr[1], Helen J. Peat[1], Robert G. Bingham[2], and David G. Vaughan[1]

[1]British Antarctic Survey, Cambridge, UK
[2]School of GeoSciences, University of Edinburgh, Edinburgh, UK
[3]Istituto Nazionale di Oceanografia e di Geofisica Sperimentale, Trieste, Italy
[★]These authors contributed equally to this work.

Correspondence: Alice C. Frémand (almand@bas.ac.uk) and Julien A. Bodart (julien.bodart@ed.ac.uk)

Received: 5 February 2022 – Discussion started: 18 February 2022
Revised: 14 June 2022 – Accepted: 5 July 2022 – Published: 25 July 2022

Abstract. Over the past 50 years, the British Antarctic Survey (BAS) has been one of the major acquirers of aerogeophysical data over Antarctica, providing scientists with gravity, magnetic, and radar datasets that have been central to many studies of the past, present, and future evolution of the Antarctic Ice Sheet. Until recently, many of these datasets were not openly available, restricting further usage of the data for different glaciological and geophysical applications. Starting in 2020, scientists and data managers at BAS have worked on standardizing and releasing large swaths of aerogeophysical data acquired during the period 1994–2020, including a total of 64 datasets from 24 different surveys, amounting to ∼ 450 000 line-km (or 5.3 million km^2) of data across West Antarctica, East Antarctica, and the Antarctic Peninsula. Amongst these are the extensive surveys over the fast-changing Pine Island (BBAS 2004–2005) and Thwaites (ITGC 2018–2019 & 2019–2020) glacier catchments, and the first ever surveys of the Wilkes Subglacial Basin (WISE-ISODYN 2005–2006) and Gamburtsev Subglacial Mountains (AGAP 2007–2009). Considerable effort has been made to standardize these datasets to comply with the FAIR (findable, accessible, interoperable and re-usable) data principles, as well as to create the Polar Airborne Geophysics Data Portal (https://www.bas.ac.uk/project/nagdp/, last access: 18 July 2022), which serves as a user-friendly interface to interact with and download the newly published data. This paper reviews how these datasets were acquired and processed, presents the methods used to standardize them, and introduces the new data portal and interactive tutorials that were created to improve the accessibility of the data. Lastly, we exemplify future potential uses of the aerogeophysical datasets by extracting information on the continuity of englacial layering from the fully published airborne radar data. We believe these newly released data will be a valuable asset to future glaciological and geophysical studies over Antarctica and will significantly extend the life cycle of the data. All datasets included in this data release are now fully accessible at https://data.bas.ac.uk (British Antarctic Survey, 2022).

Published by Copernicus Publications.

Highlights. We present the release of 64 aerogeophysical datasets (including gravity, magnetic, bed-pick, and radar data) obtained from 24 surveys flown by the British Antarctic Survey over West Antarctica, East Antarctica, and the Antarctic Peninsula between 1994 and 2020.

The published datasets have been standardized according to the FAIR (findable, accessible, interoperable and re-usable) data principles and integrated into a user-friendly data interface, the Polar Airborne Geophysics Data Portal, to further enhance the interactivity of the datasets.

We discuss how the data were acquired and processed and show the potential re-usability of the newly released aerogeophysical data by investigating the englacial architecture of the ice from airborne radars using an automatic layer-continuity method.

1 Introduction

As one of the fastest changing environments on Earth, Antarctica has been at the epicentre of scientific research since the early 1960s. Understanding the past, present, and future of the Antarctic Ice Sheet is of special interest, particularly in the context of rapid climatic changes already affecting large parts of the Antarctic Peninsula and threatening the stability of the West Antarctic Ice Sheet (WAIS; IPCC, 2021). One way to quantify how the ice sheet will respond to these changes is to conduct studies of englacial and basal properties of the ice using geophysical techniques such as gravity, magnetic, and radar. By studying the bedrock topography beneath an ice sheet, we can better estimate where a retreating ice stream is more likely to stabilize or destabilize further (Holt et al., 2006; Vaughan et al., 2006; Tinto and Bell, 2011; Ross et al., 2012; Morlighem et al., 2020) and how landforms or subglacial water-routing systems can affect the flow regime of ice streams (Bell et al., 2011; Wright et al., 2012; Schroeder et al., 2013; Ashmore and Bingham, 2014; Siegert et al., 2014; Young et al., 2016; Napoleoni et al., 2020). By studying the subglacial geology, we can better understand magmatic, tectonic, and sedimentary influences on ice flow over timescales of hundreds, thousands or even millions of years (Bell et al., 1998; Blankenship et al., 2001; Studinger et al., 2001; Bamber et al., 2006; Bell et al., 2006; Jordan et al., 2010; Bingham et al., 2012), and quantify the influence of geothermal heat flux on ice dynamics (Schroeder et al., 2014; Jordan et al., 2018). Finally, the use of gravity techniques enables us to better understand the bathymetry beneath fast-changing ice shelves and ice-stream fronts and quantify areas of high sensitivity (Greenbaum et al., 2015; Millan et al., 2017; Tinto et al., 2019; Jordan et al., 2020).

Since the mid-1960s, the British Antarctic Survey (BAS) has been involved in acquiring aerogeophysical data with a particular focus on radar-data acquisition using a 35 and 60 MHz radio-echo sounder developed at the Scott Polar Research Institute (Robin et al., 1970), and, in collaboration with the Technical University of Denmark, using slightly improved versions of the same analogue radar system until the early 1990s (Robin et al., 1977). The subsequent development of an in-house digital radar system at BAS in 1993–1994 (Corr and Popple, 1994), and accompanying gravity and magnetic instruments, allowed for the first surveys over West Antarctica's Evans Ice Stream to be conducted in 1994–1995, marking the start of modern digital aerogeophysical surveying of the Antarctic by BAS. Further improvements in survey techniques and instruments have allowed BAS to develop its aerogeophysical capabilities further and become one of the leaders in aerogeophysics over the Antarctic.

Since the mid-1990s, aerogeophysical datasets acquired by BAS have played a vital role in understanding past and current ice-dynamical and lithospheric processes over the Antarctic Ice Sheet. In total, BAS flew 24 survey campaigns between 1994 and 2020, representing a total of $\sim 450\,000$ line-km of aerogeophysical data over the Antarctic Peninsula as well as over the WAIS and the East Antarctic Ice Sheet (EAIS) (Fig. 1, Table 1). The total cumulative survey coverage since 1994 is 5.3 million km^2, equivalent to $> 30\,\%$ of the total area of the Antarctic Ice Sheet (14.2 million km^2). Many of these surveys were acquired as part of large international collaborative projects such as the International Polar Year Antarctica's Gamburtsev Province Project (AGAP), the European Space Agency (ESA) PolarGAP project, and the US–UK International Thwaites Glacier Collaboration (ITGC), amongst others. Importantly, much of the data acquired since then have been central to the output of large international science groups, such as the Scientific Committee on Antarctic Research (SCAR) BEDMAP (I/II/III), ADMAP (I/II), AntArchitecture, and IBCSO projects (Lythe et al., 2001; Arndt et al., 2013; Fretwell et al., 2013; Golynsky et al., 2018).

Despite the importance of these surveys for understanding the Antarctic cryosphere and tectonics, until now the underlying data have been relatively inaccessible to wider scientific communities due to the scale of the data-management task required. This lack of accessibility has hampered the ability of the wider research community to extract further valuable information from these datasets. In 2020, a collaborative project between the UK Polar Data Centre (PDC, https://www.bas.ac.uk/data/uk-pdc/, last access: 18 July 2022) and the BAS Airborne Geophysics science team was set up to improve the FAIR-ness (Wilkinson et al., 2016) of these data. The main objectives of this collaboration were to comply with national and international policies on data sharing and accessibility, foster new collaborations, and allow the further re-use of these data beyond the lifespan of the science projects.

This paper presents the result of this successful collaboration between data managers and scientists to standardize and release most of BAS' aerogeophysical data acquired to date using modern instruments from 1994 onwards. Data acquired prior to this, while particularly useful to long-term monitoring of ice sheet conditions, are much more challenging and time-consuming to update to modern standards (see

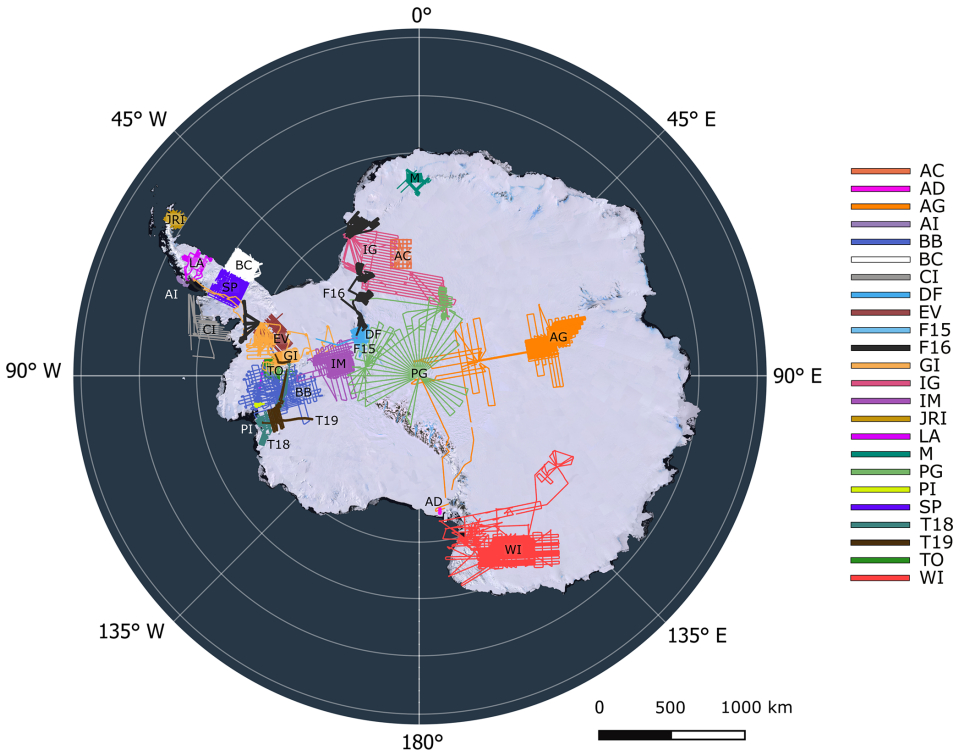

Figure 1. Map showing all the published datasets included in this data release. The colours are the same as those used on the data portal interface. Abbreviations are as follows: AC: AFI Coats Land (2001–2002); AD: Andrill HRAM (2008–2009); AG: AGAP (2007–2009); AI: Adelaide Island (2010–2011); BB: BBAS (2004–2005); BC: Black Coast (1996–1997); CI: Charcot Island (1996–1997); DF: DUFEK (1998–1999); EV: EVANS (1994–1995); F15: FISS 2015 (2015–2016); F16: FISS–EC–Halley 2016 (2015–2016); GI: GRADES-IMAGE (2006–2007); IG: ICEGRAV (2012–2013); IM: IMAFI (2010–2011); JRI: James Ross Island (1997–1998); LA: Larsen Ice Shelf (1997–1998); M: MAMOG (2001–2002); PG: PolarGAP (2015–2016); PI: Pine Island Glacier Ice Shelf (2010–2011); SP: SPARC (2002–2003); T18: ITGC (2018–2019); T19: ITGC (2019–2020); TO: TORUS (2001–2002); WI: WISE-ISODYN (2005–2006). The legend on the right-hand side of the figure shows the colour corresponding to each survey. The background image is from the Landsat Image Mosaic of Antarctica (LIMA; Bindschadler et al., 2008).

Schroeder et al., 2019; Sect. 5.3), and are thus not included in the data release discussed here. Section 2 of this paper reviews the main scientific findings from each survey flown between 1994 and 2020. Section 3 describes the various instruments and techniques used to acquire and process the data. Section 4 outlines the format and data publishing strategy for our datasets following the FAIR data principles, as well as the creation of a new data portal and interactive, open-access tutorials. Finally, Sect. 5 provides a case study for the reusability of the newly released aerogeophysical data, as well as suggestions on future uses of the data portal and aspirations for future data releases.

2 Background

The following section reviews the main scientific findings related to the acquisition of aerogeophysical data from BAS for the period 1994–2020 and is divided into two sub-sections: (i) findings from surveys conducted pre-2004 using older aerogeophysical instruments and for which the fully processed 2-D radar data are not published as part of this data release (see Table 1, Sect. 5.3), and (ii) surveys conducted post-2004 using the PASIN-1 (2004–2015) and PASIN-2 (2015–2020) radar systems and more modern data-acquisition methods. Figures 2–3 present the wide-ranging datasets of gravity and magnetic anomalies, bed elevation and ice thickness, and 2-D radar profiles ensuing from the surveys discussed in Sect. 2.1. and 2.2.

2.1 Aerogeophysical surveys for the period 1994–2004

The first surveys conducted by BAS since the mid-1990s involved extensive gravity and magnetic surveying of the western and eastern Antarctic Peninsula and Weddell Sea Embayment. Surveys over Evans Ice Stream (1994–1995), Black Coast (1996–1997), Charcot Island (1996–1997), and James Ross Island (1997–1998) (Fig. 1, Table 1) provided new insights into the history of crustal boundaries between the eastern Antarctic Peninsula and the Filchner Block (Ferris et al., 2002), evidence of crustal thinning below Evans

Ice Stream (Jones et al., 2002), and new understanding of the magmatic and tectonic processes around the Mount Haddington stratovolcano on James Ross Island (Jordan et al., 2009). A further study covering the Larsen Ice Shelf (Antarctic Peninsula) was conducted conjointly by BAS and the Instituto Antártico Argentino in 1997–1998. The radar data acquired during this survey were used in ocean (Holland et al., 2009) and firn-density (Holland et al., 2011) models to improve our understanding of ice–ocean interactions and ice-surface elevation changes on the ice shelf. In 1998–1999, extensive aeromagnetic surveying of the Dufek Massif (West Antarctica/East Antarctica) revealed the presence of a Jurassic dike swarm that likely acted as a magma transport and feeder system to the Ferrar Large Igneous Province (Ferris et al., 2003). In 2001–2002, an additional survey was flown as part of the initiative, Targeting ice-stream Onset Regions and Under-ice Systems (TORUS), to assess the factors controlling the dynamics of the Rutford Ice Stream using gravity, magnetic, and radar instruments over a high-resolution grid spacing of $\sim$10 km (Vaughan et al., 2008). Lastly, for the WAIS, the 2002–2003 Superterranes in the Pacific Margin Arc (SPARC) campaign over northern Palmer Land (Antarctic Peninsula) used gravity and magnetic instruments to reveal subglacial imprints of crustal growth linked with the Gondwana margin (Ferraccioli et al., 2006).

Over East Antarctica, two surveys conducted in 2001–2002 acquired detailed gravity, magnetic, and radar measurements over Slessor Glacier (as part of the Antarctic Funding Initiative (AFI) Coats Land survey) and Jutulstraumen Ice Stream (as part of the Magmatism as a Monitor of Gondwana breakup survey; MAMOG). The AFI Coats Land survey, a UK initiative between BAS and the University of Bristol, provided the first accurate measurements of ice thickness and bed elevation in the area (Rippin et al., 2003a) (Fig. 2), and led to the discovery of a $\sim$3 km thick sedimentary basin associated with a weak till layer at the bed which enhances basal motion and affects the flow regime of this part of the EAIS (Rippin et al., 2003a; Bamber et al., 2006; Shepherd et al., 2006). The MAMOG survey revealed the presence of a subglacial Jurassic continental rift in the area of western Dronning Maud Land, providing early evidence for the initial Gondwana breakup (Ferraccioli et al., 2005a, b).

2.2 Aerogeophysical Surveys for the Period 2004–2020

Building on the surveys prior to 2004, which were relatively small in areal extent, BAS began surveying larger areas from the mid-2000s onwards (Table 1), primarily due to enhanced international collaborations and improvements in data acquisition and instruments, which led to data being acquired both at higher resolution and over larger spatial scales. The acquisition strategy was to collect data from multiple geophysical sensors mounted on BAS' Twin Otter aircraft across every survey, giving a holistic view of vast and previously unsurveyed regions (Figs. 4–5). The core sensor suite included gravity and magnetic instruments used to understand the geological nature of the subglacial basins and mountains along with their tectonic structure, together with the radar system used to map ice thickness and bed elevation. The development of a new radar system, the Polarimetric Airborne System INstrument (PASIN) (PASIN-1, 2004–2015) (see Sect. 3.1.3), and an improved version of the same system (PASIN-2, 2015–2016 onwards), allowed for the efficient collection of high-quality digital radar data for BAS-led campaigns in the Antarctic.

We divide the findings from these surveys into two subsections (Sect. 2.2.1 for surveys between 2004 and 2015 and Sect. 2.2.2 for surveys between 2015 and 2020) to reflect the acquisition of data prior to and following the upgrade of the PASIN system (see Sect. 3.1.3).

2.2.1 2004–2015

The first mission to utilize the PASIN-1 radar system was the 2004–2005 BBAS survey of Pine Island Glacier, which aimed to characterize the subglacial conditions of this sensitive glacier of West Antarctica (Vaughan et al., 2006). This survey provided two key findings: (a) the discovery of a deep subglacial trough, 500 m at its deepest point and 250 km long, through which Pine Island Glacier flows; and (b) the existence of well-constrained valley walls, which would likely provide a buffer against a potential catastrophic collapse of the WAIS via Pine Island Glacier (Vaughan et al., 2006). Further studies utilizing this dataset focused primarily on bed characteristics and the subglacial hydrology of the catchment (Rippin et al., 2011; Napoleoni et al., 2020; Chu et al., 2021), as well as tracking englacial layers and quantifying past accumulation rates (Corr and Vaughan, 2008; Karlsson et al., 2009, 2014; Bodart et al., 2021). The survey was also conducted simultaneously with another covering the Thwaites Glacier catchment led by the University of Texas Institute for Geophysics and the National Science Foundation of the United States (Holt et al., 2006), enabling a comparison of the surveying capabilities where the surveys overlapped (e.g. Chu et al., 2021).

Following on from the BBAS data, the suite of geophysical instruments on board the BAS Twin Otter aircraft were used to survey the Wilkes Subglacial Basin, Dome C, and the Transantarctic Mountains as part of the 2005–2006 WISE-ISODYN survey between BAS and the Italian Programma Nazionale di Ricerche in Antartide (Bozzo and Ferraccioli, 2007; Corr et al., 2007; Ferraccioli et al., 2007; Jordan et al., 2007). This project revealed, for the first time, the crustal architecture of the Wilkes Subglacial Basin (Ferraccioli et al., 2009; Jordan et al., 2013) and the distribution of a well-preserved subglacial sedimentary basin underlying the Wilkes catchment (Frederick et al., 2016). The following year, the 2006–2007 survey, Glacial Retreat in Antarctica and Deglaciation of the Earth System – Inverse Modelling of Antarctica and Global Eustasy (GRADES-IMAGE), com-

Table 1. Information on the period, region, sub-region, type of data acquired, total line coverage (km), total coverage area (km^2), and key reference for each survey included in this data release. For "Data", the abbreviations are as follows: gravity (G), magnetic (M), radar (R). For "Regions", abbreviations are as follows: APIS (Antarctic Peninsula Ice Sheet), EAIS (East Antarctic Ice Sheet), WAIS (West Antarctic Ice Sheet). "DML" stands for Dronning Maud Land and "PIG" for Pine Island Glacier. The total area in km^2 is calculated as a cumulative total area of the spatial footprint of the survey's minimum and maximum extents. * For AGAP, the data release only consists of the BAS-acquired data, which represents approximately half of the total (∼ 120 000 km) survey coverage from the whole AGAP expedition (see Sect. 2.2.1).

Survey	Year	Region	Sub-region	Data	Total line coverage (km)	Total coverage area (km^2)	Reference
EVANS	1994–1995	WAIS/APIS	Evans Ice Stream	G, M, R	11 500	1.06×10^5	Jones et al. (2002)
Black Coast	1996–1997	APIS	Black Coast/ Weddell Sea	M	10 000	8.96×10^4	Ferris et al. (2002)
CHARCOT	1996–1997	APIS	Charcot Island	M	7500	1.67×10^5	Johnson et al. (1999)
James Ross Island	1997–1998	APIS	James Ross Island	G, M, R	10 000	3.32×10^4	Jordan et al. (2009)
LARSEN	1997–1998	APIS	Larsen Ice Shelf	M, R	5800	5.96×10^4	Holland et al. (2009)
DUFEK	1998–1999	WAIS/EAIS	Dufek Massif	G, M, R	8300	4.66×10^4	Ferris et al. (2003)
AFI Coats Land	2001–2002	EAIS	Slessor Glacier	G, M, R	5000	6.53×10^4	Rippin et al. (2003a)
MAMOG	2001–2002	EAIS	Jutulstraumen Ice Stream/DML	G, M, R	15 500	5.79×10^4	Ferraccioli et al. (2005a)
TORUS	2001–2002	WAIS	Rutford Ice Stream	G, M, R	8600	1.12×10^5	Vaughan et al. (2008)
SPARC	2002–2003	APIS	Northern Palmer Land	G, M	20 000	1.07×10^5	Ferraccioli et al. (2006)
BBAS	2004–2005	WAIS	Pine Island Glacier	G, M, R	35 000	4.09×10^5	Vaughan et al. (2006)
WISE-ISODYN	2005–2006	EAIS	Wilkes Land	G, M, R	61 000	7.91×10^5	Jordan et al. (2013)
GRADES-IMAGE	2006–2007	WAIS/APIS	Evans & Rutford ice streams	M, R	27 500	3.06×10^5	Ashmore et al. (2014)
AGAP	2007–2009	EAIS	Gamburtsev/Dome A	G, M, R	73 000*	6.22×10^5	Ferraccioli et al. (2011)
ANDRILL HRAM	2008–2009	WAIS	Ross Ice Shelf & Coulman High	M, R	1200	1.48×10^3	–
Adelaide Island	2010–2011	APIS	Adelaide Island	M, R	5500	3.76×10^3	Jordan et al. (2014)
IMAFI	2010–2011	WAIS	Institute and Möller ice streams	G, M, R	25 000	1.96×10^5	Ross et al. (2012)
PIG Ice Shelf	2010–2011	WAIS	Pine Island Shelf	M, R	1500	1.80×10^3	Vaughan et al. (2012)
ICEGRAV	2012–2013	EAIS	Recovery and Slessor glaciers, Bailey Ice Stream	G, M, R	29 000	4.75×10^5	Diez et al. (2018)
FISS 2015	2015–2016	WAIS	Foundation Ice Stream/Bungenstock Ice Rise	M, R	7000	1.43×10^4	–
PolarGAP	2015–2016	EAIS	South Pole	G, M, R	38 000	8.71×10^5	Jordan et al. (2018)
FISS 2016	2016–2017	WAIS	Filchner Ice Shelf/English Coast/Recovery & Support Force glaciers/Halley station	G, M, R	26 000	5.99×10^5	Hofstede et al. (2021)
ITGC 2018	2018–2020	WAIS	Thwaites Glacier	G, M, R	9872	6.43×10^4	Jordan et al. (2020)
ITGC 2019	2019–2020	WAIS	Thwaites Glacier/WAIS divide/Rutford Ice Stream	G, M, R	4432	4.85×10^4	–

prising surveys over the transitional area between the Antarctic Peninsula and the WAIS, provided detailed information on subglacial properties of Evans Ice Stream (Ashmore et al., 2014). Ice-thickness measurements along the grounding line were also used as key calibration for the Landsat-derived "ASAID" grounding-line product (Bindschadler et al., 2011), and englacial layers through Bungenstock Ice Rise were used to assess ice-divide stability and the wider ice-flow history and stability of the WAIS's Weddell Sea sector during the Holocene (Siegert et al., 2013).

Over two austral field seasons from 2007 to 2009, AGAP, coordinated as part of the fourth International Polar Year between the UK, USA, Germany, Japan, Australia and China, comprised a comprehensive survey of the interior of the EAIS, yielding important aerogeophysical data used to interrogate the origin and geophysical characteristics of the Gamburtsev Subglacial Mountains. Significant scientific discoveries generated by the AGAP survey included observations of widespread freeze-on at the bottom of the ice which leads to thickening of the EAIS from the base (Bell et al., 2011), a thick crustal root formed during the Proterozoic eon (1 Gyr ago) surrounded by a more recent $\sim$2500 km-long rift system (Ferraccioli et al., 2011), and the existence of ancient pre-glacial fluvial networks at the present ice bed which confirmed the presence of the Gamburtsev Subglacial Mountains prior to the start of glaciation at the Eocene–Oligocene climate boundary (ca. 34 Ma) (Rose et al., 2013; Creyts et al., 2014).

Between 2008 and 2011, three surveys utilized the magnetic and radar instruments on board the BAS Twin Otter to conduct high-spatial-resolution surveying of Coulman High on Ross Ice Shelf as part of the Antarctic Drilling – High Resolution Aeromagnetic (ANDRILL HRAM) project, Adelaide Island (Antarctic Peninsula), and Pine Island Glacier Ice Shelf (West Antarctica). The 2010–2011 Adelaide Island survey provided high-resolution aeromagnetic data to underpin a better understanding of the complex magmatic structure of the Antarctic Peninsula Cenozoic arc/forearc boundary (Jordan et al., 2014). The Pine Island Glacier Ice Shelf survey of the same year revealed a network of sinuous subglacial channels, 500 to 3000 m wide and up to 200 m high, in the ice-shelf base, which, combined with surface and basal crevasses formed as a result of the basal melting, could lead to structural weakening of the shelf in the future (Vaughan et al., 2012).

The early 2010s saw the deployment of the PASIN system used as part of two large collaborative projects, namely the 2010–2011 Institute–Möller Antarctic Funding Initiative (IMAFI) survey over the Institute and Möller ice streams of West Antarctica, and the 2012–2013 ICEGRAV survey over the Recovery and Slessor region of East Antarctica.

The 2010–2011 IMAFI project was a UK initiative between BAS and the universities of Edinburgh, York, Aberdeen and Exeter. The key aims were to investigate the potential stability of this sector of West Antarctica and test the ability of the subglacial sedimentary structure to control the flow of two large ice streams draining the WAIS into the Weddell Sea Embayment (Ross et al., 2012). Radar data revealed the presence of a reverse-bed slope with a 400 m decline over a 40 km distance away from the grounding line and that this region was relatively close to flotation, indicating the potential instability of this sector in light of future grounding-line migration upstream of its current position (Ross et al., 2012). Additional analysis using gravity and magnetic data revealed the extent of the Weddell Sea Rift System, adding further evidence for the early stages of the Gondwana breakup and Jurassic extension in the region (Jordan et al., 2013). Further analysis of the radar data acquired during the IMAFI survey led to a new digital elevation model of the subglacial topography around the ice streams of the Weddell Sea Embayment at 1 km resolution, revealing deep subglacial troughs between the ice-sheet interior and the grounding line, and well-preserved landforms associated with alpine glaciation (Ross et al., 2014; Jeofry et al., 2018), as well as evidence for a temperate former WAIS via the discovery of extensive subglacial meltwater channels (Rose et al., 2014). The data have also been used to assess the roughness of the subglacial bed (Rippin et al., 2014), investigate englacial properties across the catchment as an indicator of past ice-flow dynamics (Bingham et al., 2015; Winter et al., 2015; Ashmore et al., 2020; Ross et al., 2020), and show the presence of sub-ice shelf channels generated by water flowing from beneath the present ice sheet (Le Brocq et al., 2013).

The 2012–2013 ICEGRAV survey, an international collaboration between BAS and the Technical University of Denmark, National Science Foundation, Norwegian Polar Institute, and the Instituto Antártico Argentino, carried out aerogeophysical surveys over the poorly explored Recovery Glacier catchment and Recovery subglacial lakes (Forsberg et al., 2018), revealing a deep 800 km trough underlying Recovery Glacier, with evidence for subglacial water controlling the fast flow in the upstream portion of the ice stream (Diez et al., 2018).

2.2.2 2015–2020

The 2015–2016 PolarGAP survey was a major international collaboration, funded by ESA and led by BAS, the Technical University of Denmark, the Norwegian Polar Institute, and the National Science Foundation, to fill a gap in global gravity surveying that the ESA's Gravity field and steady-state Ocean Circulation Explorer (GOCE) satellite network was unable to cover. Alongside the large swath of gravity surveying, opportunistic magnetic and radar data were also acquired over the South Pole and parts of Support Force, Foundation, and Recovery ice streams using a further upgraded radar system, PASIN-2 (see Sect. 3.1.3). Additional funding from the Norwegian Polar Institute also allowed for a number of dedicated flights over the Recovery subglacial lakes. The acquired data have led to major scientific findings, including

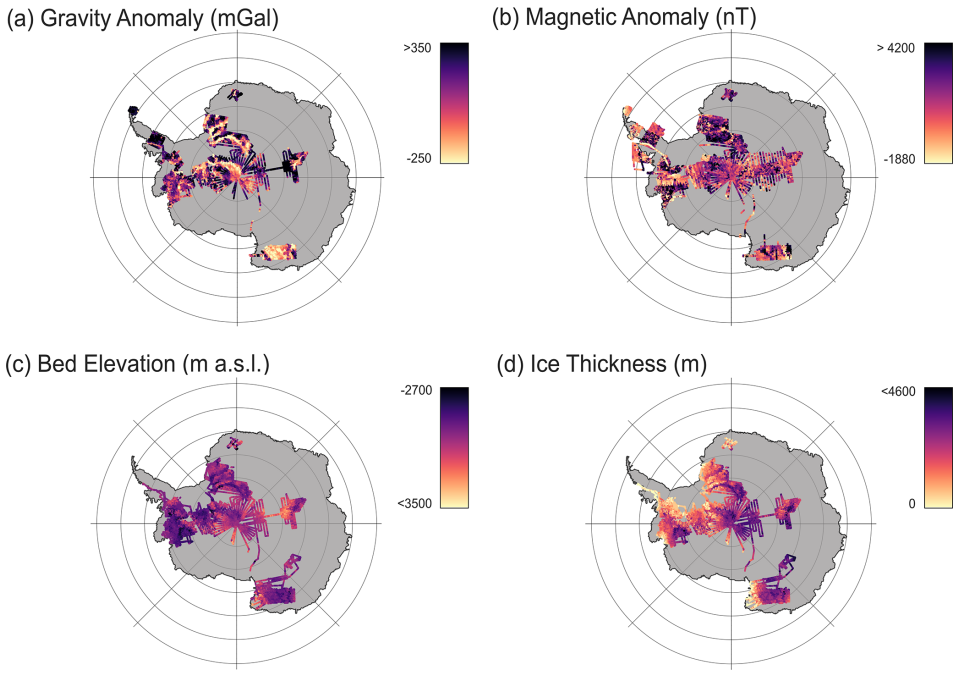

Figure 2. Maps of gravity, magnetic, and radar (bed elevation and ice thickness) point measurements for all surveys published as part of this data release. **(a)** Gravity anomaly points (in milligal, or mGal), **(b)** magnetic anomaly points (in nanotesla, or nT), **(c)** bed-elevation points from radar data (in metres above sea level, or m a.s.l.), **(d)** ice-thickness points from radar data (metres). In total, this data release consists of 3.62 million gravity, 7.41 million magnetics, and 14.5 million ice-thickness and bed-elevation data points. Note that no correction such as downward continuation has been applied to compile the gravity data shown in **(a)**.

(a) the presence of anomalously high geothermal heat flux near the South Pole (Jordan et al., 2018), (b) the delineation of two subglacial lakes (Recovery Lakes A and B) totalling $\sim 4320\,km^2$ in size and composed of saturated till, with evidence of bed lubrication and enhanced flow downstream of their location as a result of water drainage (Diez et al., 2019), and **(c)** the evidence of a large (500–700 km-wide) marginal embayment formed during late Neoproterozoic rifting along the craton margin and which cuts into the East Antarctic basement around the South Pole region (Jordan et al., 2022). Additional evidence showed that the Pensacola-Pole Basin is characterized by a topographic depression of ~ 0.5 km below sea level and contains a thick sedimentary layer of 2–3 km in the southern part of the catchment (Paxman et al., 2019). The radar data from the PolarGAP survey have also revealed large troughs at the bottleneck between East and West Antarctica, suggesting that the drawdown of the EAIS via the WAIS is unlikely (Winter et al., 2018).

In the austral summers of 2015–2016 and 2016–2017, two surveys were flown as part of the Filchner Ice Shelf system (FISS) project led by BAS with support from the Alfred Wegener Institute in Germany and several other UK institutions (UK National Oceanography Centre, Met Office Hadley Centre, universities of Exeter, Oxford, and University College London), with the aim to investigate the potential contribution of the Filchner Ice Shelf and feeding ice streams to sea-level rise. The 2015–2016 survey acquired ~ 7000 line-km of aerogeophysical data, primarily over Foundation Ice Stream and to a smaller extent over Bungenstock Ice Rise. In 2016–2017, $\sim 26\,000$ line-km of aerogeophysical data were acquired over Academy, Recovery, Slessor, and Support Force glaciers, and parts of the Filchner and Brunt ice shelves. Data were also collected over outlet glaciers of the English Coast (western Palmer Land, Antarctic Peninsula). Early findings from the 2016–2017 aerogeophysical survey revealed subglacial drainage channels beneath Support Force Glacier (Hofstede et al., 2021), provided evidence for a large $\sim 80 \times 30 \times 6$ km mafic intrusion, likely resulting from mantle melting during the Gondwana breakup (Jordan and Becker, 2018), and helped to delineate the subglacial bathymetry beneath Brunt Ice Shelf (Hodgson et al., 2019).

During the 2018–2019 and 2019–2020 seasons, BAS was involved in aerogeophysical surveying of Thwaites Glacier as part of the UK–US ITGC initiative. The 2018–2019 survey acquired ~ 9900 km of aerogeophysical data over the lower Thwaites Glacier and Thwaites Glacier Ice Shelf. The 2019–2020 survey acquired ~ 4500 line-km over the lower Thwaites Glacier, the WAIS Divide ice-core site, and Rutford Ice Stream. These surveys contributed to a new bathymetric map of Thwaites, Crosson, and Dotson ice shelves from gravity measurements, revealing a deep (> 800 m) ma-

rine channel extending beneath the ice shelf adjacent to the front of Thwaites Glacier (Jordan et al., 2020). These datasets have also contributed to a new bathymetry model of George VI Sound (Constantino et al., 2020) and were integrated with swath bathymetric data outboard from Thwaites Glacier (Hogan et al., 2020).

3 Data acquisition and processing

The typical acquisition and processing workflow for the aerogeophysical data is shown in Fig. 4. Usually, the aircraft is set up systematically to acquire gravity, magnetic, and radar data together, except in situations where surveying objectives are not compatible with the acquisition of all three datasets at once (i.e. flying at constant terrain clearance for the radar data affects the quality of the gravity data which is better flown at constant altitude, and vice versa); although novel gravity-acquisition methods are increasingly making this issue redundant (see Sect. 3.1.1). As shown in Table 1, the conventional gravity–magnetic–radar set-up was used in 15 out of 24 surveys, with the remaining 7 surveys using either a magnetic–radar- or gravity–magnetic-only set-up, and only 2 using a magnetic-only set-up. The data acquisition steps for each type of data are described in Sect. 3.1, and the processing of the data is described in Sect. 3.2.

3.1 Data acquisition and instrumentation

All BAS aerogeophysical data acquisition is conducted using Twin Otter aircraft due to their remote capabilities, long fuel range (up to 1000 km), and operability. The aircraft's twin turbo-prop engines enable it to conduct rapid take-off and landing as well as operate in small and remote airfields commonly covered in snow and icy terrains using mounted skis. All data acquisition since the early 1990s has been conducted using the BAS DeHavilland Twin Otter aircraft "*VP-FBL*" (Fig. 5). The aircraft typically flies at a nominal speed of $\sim 60\,\mathrm{m\,s^{-1}}$, which results in an along-track distance between each stacked radar trace of 0.2 m (prior to processing). The following sections describe the acquisition of the data for the gravity (Sect. 3.1.1), magnetic (Sect. 3.1.2), radar (Sect. 3.1.3), and GPS and lidar (Sect. 3.1.4) instruments on board the aircraft.

3.1.1 Gravity

Until 2012, BAS aerogravity measurements were acquired with a LaCoste and Romberg air–sea gravimeter modified by Zero-Length Spring (ZLS) Corporation. The gravimeter was mounted in a gyro-stabilized, shock-mounted platform at the centre of the aircraft to minimize the effect of vibrations and rotational motions.

Starting with the 2015–2016 PolarGAP survey, aerogravity data were acquired using a novel strap-down method which, unlike traditional surveys using a stabilized gravity platform, allowed for the collection of gravity data during draped or turbulent flights (Jordan and Becker, 2018). For this survey, both the LaCoste and Romberg and strap-down systems were operated, together with results from the two systems merged, to provide an optimum data product with the long-term low and predictable drift of the LaCoste and Romberg system and the dynamic stability of the strap-down system. Subsequent surveys used a strap-down sensor alone, removing the need to prioritize the quality of the gravity data over the radar data and allowing for flights at a constant terrain clearance for optimal radar-data collection. The optimum resolution of the system is approximately 100 s along-track (Jordan and Becker, 2018).

The first strap-down sensor deployed by BAS was the iMAR RQH-1003 system provided by the Technical University (TU) of Darmstadt, and consisting of three Honeywell QA2000 accelerometers (mounted in mutually perpendicular directions) and three Honeywell GG1230 ring laser gyroscopes. The subsequent 2018–2019 and 2019–3020 ITGC surveys over Thwaites Glacier used the iMAR iCORUS strap-down airborne gravimeter systems from Lamont-Doherty Earth Observatory and BAS respectively, which have approximately equivalent internal components to the TU Darmstadt system.

3.1.2 Magnetics

The Twin Otter is configured for fixed wing magnetometer operation. The aircraft modifications include inboard-positioned wingtip fuel pumps, pod-boom hard points and a demagnetized airframe to maximize magnetic-data collection. Scintrex CS3 Cesium sensors are used due to their high sensitivity, high cycling rates, excellent gradient tolerance, fast response, and low susceptibility to the electromagnetic interference. The resolution of the magnetometers has greatly increased over time, with the current systems having a measurement accuracy of 0.2 pT compared to the older systems used between 1973 and 1990 (500 pT; Geometrics G-803 Potassium) and between 1991 and 2003 (10 pT; Sintrex H8 Cesium).

3.1.3 Radar

Prior to 2004, BAS deployed a custom-built, 8-array element radar system, referred to here as "BAS-built" (Corr and Popple, 1994). This was a coherent radar system operating at a centre frequency of 150 MHz and using a transmit power of 1200 W (Rippin et al., 2003a). The radar system was equipped with eight folded dipole transmitting and receiving antennas fixed under the wings (four transmitting on the port wing, four receiving on the starboard wing). Similar to the current systems, the "BAS-built" system transmitted both a conventional narrow-sounding pulse mode of 0.25 µs and a deep-sounding 4 µs, 10 MHz chirp (Table 2). As developments in digital acquisition became commercially avail-

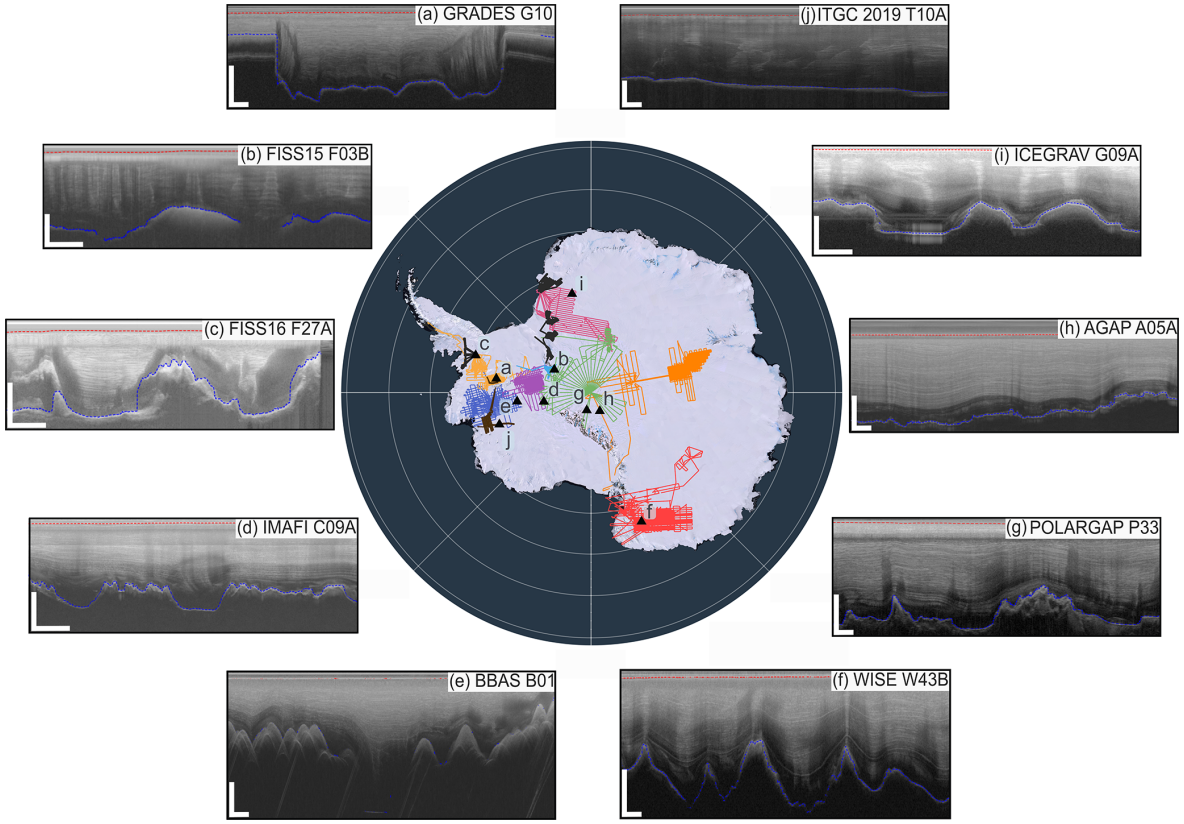

Figure 3. Sample radargrams from the 10 2-D radar datasets released with this paper. The colours for each survey on the map are the same as in Fig. 1 and the data portal. The location of each radargram **(a–j)** is marked on the map by black triangles. The dashed red and blue lines on the radargrams are the surface and bed picks, respectively. A description of each radargram is provided as follows: **(a)** flight line G10 (GRADES-IMAGE) showing well-defined subglacial valleys through which Evans Ice Stream flows (ice flow is approximately out of page), with stable layering present before and in the middle of the topographic low; **(b)** flight line F03B (FISS 2015) showing undulating bed topography and disrupted layering at the onset of Foundation Ice Stream; **(c)** flight line F27A (FISS 2016) showing variations in subglacial topography at the divide between the Antarctic Peninsula and West Antarctica, with potential evidence of basal freeze-on at the start of the segment; **(d)** flight line C09A (IMAFI) showing evidence of preserved layering despite changes in local topography at the bottleneck between East and West Antarctica; **(e)** flight line B01 (BBAS) over Ellsworth Subglacial Mountains showing a ~ 1.5 km trough in the ice-sheet bed and one of the deepest points in the PIG basin with ~ 3 km of ice underlying the surface; **(f)** flight line W43B (WISE-ISODYN) showing internal layers draping over the highs and lows in the local Wilkes Subglacial Basin topography, with two particularly bright reflections in the middle and bottom of the ice column; **(g)** flight line P33 (PolarGAP) showing clear and stable englacial layering throughout the ice column at the onset of the topographic highs of the Transantarctic Mountain Range; **(h)** flight line A05A (AGAP) showing stable internal layering characteristic of the interior of the EAIS; **(i)** flight line G09A (ICEGRAV) showing evidence of a bright reflection likely associated with a previously unidentified subglacial lake in the region; and **(j)** flight line T10A (ITGC 2019) showing a section of inland-sloping bed from a profile in the main trunk of Thwaites Glacier, > 200 km from the current grounding line position (ice flow is right to left). The horizontal and vertical white bars at the bottom of each radargram represent ~ 3 km in the horizontal direction (i.e. distance) and ~ 1 km in the vertical direction (i.e. depth), respectively.

able, several technical upgrades were applied to the radar system. These ranged from using a LeCroy scope to acquire logarithmic detected waveforms to accommodate complex coherent acquisition, as well as the replacement of the LeCroy oscilloscope by a low sample-frequency 12 bit dual ADC (analogue-to-digital converted) card in the later years of operation (see Fig. S1 in the Supplement). During this time, the dynamic range of the system was extended by the interleaved transmission of different waveforms, which were conventional short wave-train pulses at the centre frequency.

After operating for 10 successive field seasons, the "BAS-built" radar system was retired and was replaced by a more modern radar system, PASIN (Corr et al., 2007). In contrast to the "BAS-built" system, PASIN was designed to sound ice much deeper (up to 5 km compared to 3.3 km for the earlier system) thanks to improved digital electronics and added power in the transmitting antennas (see Table 2). Additionally, modern methods of digitization, enabled by the use of ADC cards rather than a digitizing scope, allowed phase and not just power to be recorded in greater resolution on PASIN,

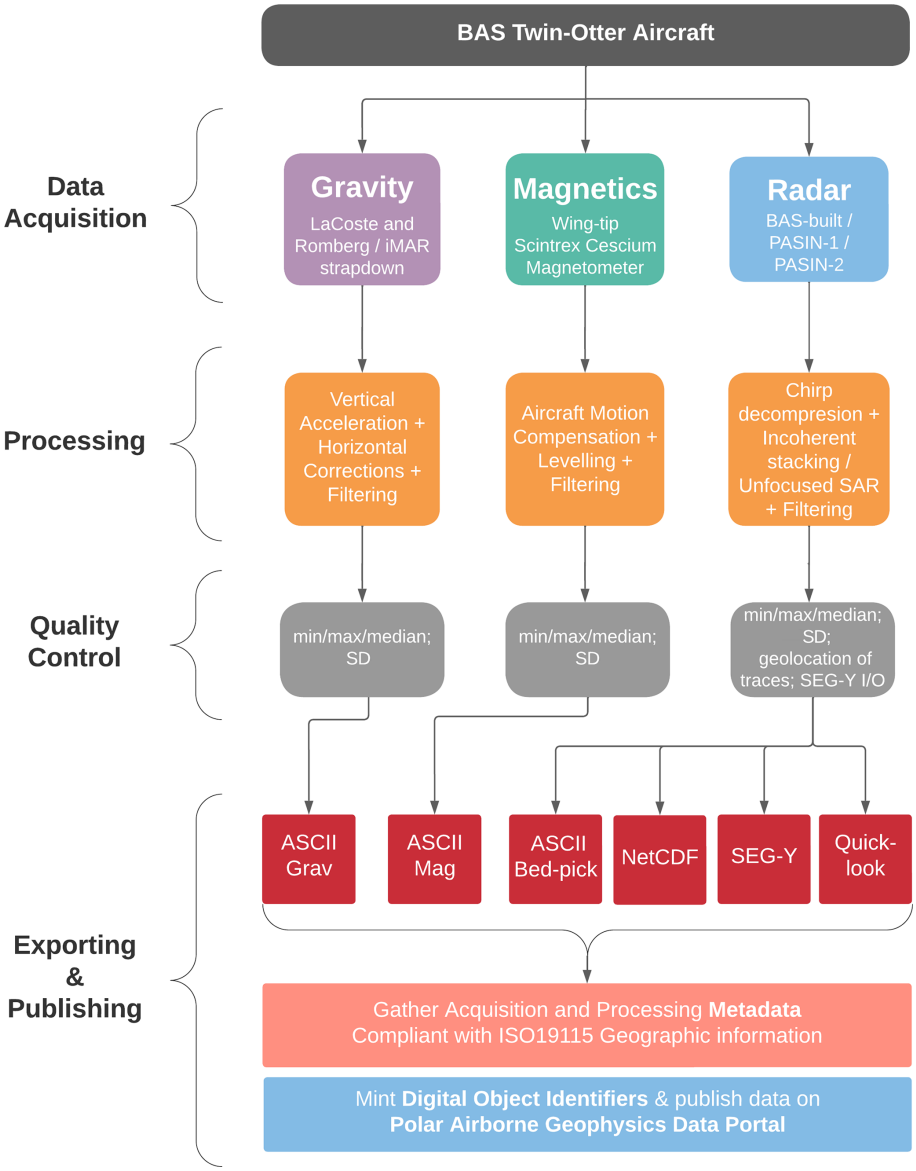

Figure 4. Workflow describing the data acquisition, processing, and publishing for the BAS aerogeophysical data included in this data release. Standard deviation is abbreviated as "SD", whilst "I/O" refers to the import of the SEG-Y files into seismic-interpretation software for quality check and the output of the files.

which eventually allowed for the use of more advanced processing techniques such as synthetic aperture radar (SAR) to be applied to the data (see Sect. 3.2.3).

The older PASIN-1 (2004–2015) and the newer PASIN-2 (2015–present) systems are bistatic radars operating at a 150 MHz centre frequency and configured as follows: (a) PASIN-1: 10 MHz bandwidth system with eight folded dipole transmitting and receiving antennas fixed under the wings (four transmitting on port wing, four receiving on starboard wing) operating in horizontal (H) orientation when in standard mode, and more rarely with the port (transmit) and starboard (receive) antennas positioned in both H and vertical (V) orientation when in polarimetric mode (see similar set-up of PASIN-2 in Fig. 5a) (Corr et al., 2007); and (b) PASIN-2: 13 MHz bandwidth system with eight folded dipole transmitting and receiving antennas fixed under the wings and inside the aircraft with radio frequency (RF) switches and an additional four receiving antennas in the belly enclosure (see Fig. 5b–c; Table 2). The main difference between the PASIN-1 and PASIN-2 systems is the ability for across-track swath processing to be applied to the PASIN-2 data by allowing both transmitting and receiving on the folded dipole antennas via the use of RF switches.

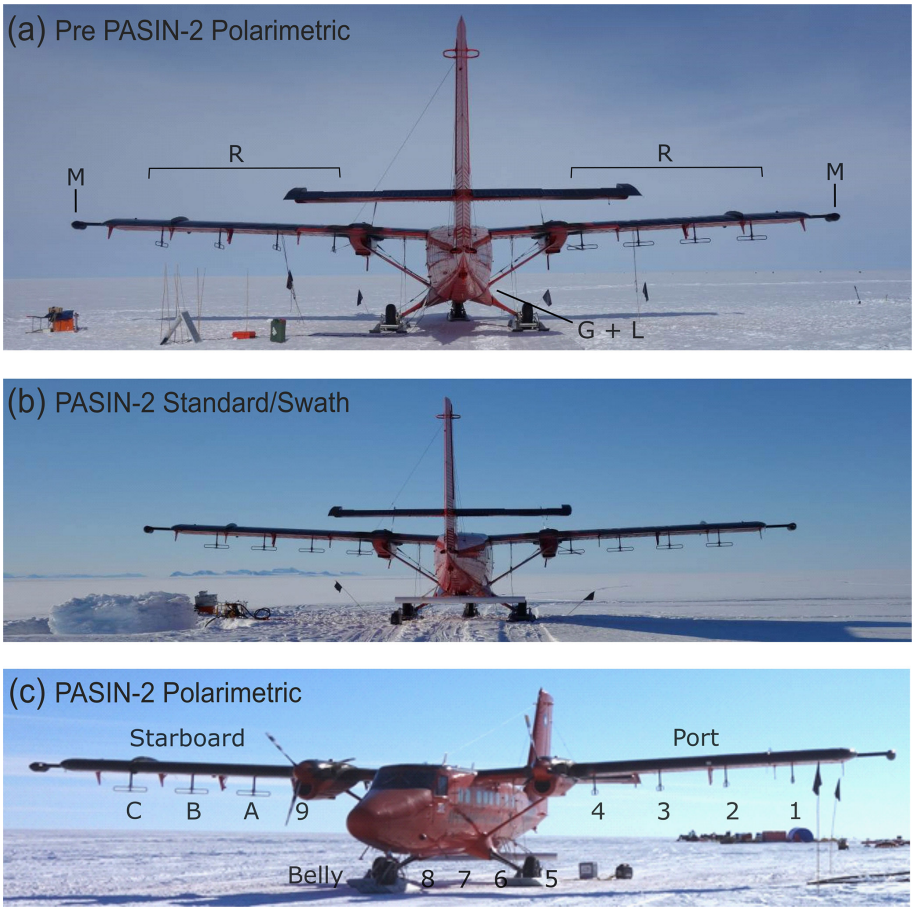

Figure 5. Photographs of the aerogeophysical set-up on the BAS Twin Otter aircraft "*VP-FBL*" for PASIN-2. **(a)** The pre-PASIN-2 (used in 2015–2016 PolarGAP only) configured to mimic the set-up of PASIN-1 data collection in polarimetric mode. The eight folded dipole transmitting and receiving antennas are fixed under the wings (two transmitting and two receiving antennas on each wing) with the port configured as vertical (V) and starboard as horizontal (H). The annotations show the location of the radar (R), magnetic (M), and gravity and lidar (G + L) instruments on board the aircraft. **(b)** The PASIN-2 set-up in standard/swath mode. The eight folded dipole transmitting and receiving antennas are fixed under the wings and inside the aircraft and are operated using a radio frequency (RF) switch, and an additional four receiving antennas are situated in the belly enclosure. When in standard swath mode, all antennas are configured in H orientation with the starboard and belly antennas also in H orientation. The PASIN-1 set-up in standard mode (not shown here) had a similar configuration as shown in **(b)** bar the belly antenna (i.e. only four transmitting on port and four receiving on starboard in H orientation). **(c)** The PASIN-2 set-up in polarimetric mode. The eight folded dipole transmitting and receiving antennas are fixed under the wings and inside the aircraft and are operated using an RF switch, and an additional four receiving antennas are situated in the belly enclosure. When in polarimetric mode, the port antennas are configured in V orientation and the starboard and belly antennas in H orientation. The PASIN-1 set-up in polarimetric mode (not shown here as rarely flown) had the two pairs of outboard antennas rotated to V configuration and the inboard to H configuration. Photo credit: Carl Robinson.

In further contrast with PASIN-1, the PASIN-2 radar has a very flexible configuration, with the standard configuration being as 12-channel swath radar (with 8 transmitting and 12 receiving). However, other configurations are also possible, including a polarimetric mode to give H and V data where the port antennas are rotated 180° (see Table S1 in the Supplement). A final configuration is a mixed antenna gain path for areas where ice is heavily disrupted and where the starboard signal can be attenuated by several decibels. Since 2016, the PASIN-2 system has undergone minor modifications to reduce noise and improve system operations, including (a) low-pass filters in the RF switches, (b) the use of a 10 GHz waveform generator, and (c) new 1 kW solid-state power amplifiers which have lowered transmitter system noise and increased transmitter and receiver isolation.

Data for both versions of the PASIN system are received using sub-Nyquist digitization and stacking and stored on removable solid-state disks or tapes, and then copied to duplicate spinning disks for data archiving. On average, a 4.5 h flight will generate ∼ 150–200 GB of data for PASIN-1 and up to 3 TB of data for PASIN-2. The systems systematically acquire a shallow-sounding 0.1 µs pulse (PASIN-1)/1 µs

short-attenuated chirp (PASIN-2), and a deep-sounding 4 µs, 10 MHz (PASIN-1)/13 MHz (PASIN-2) linear chirp (Table 2). The shallow-sounding pulse/short-attenuated chirp product is best used to assess internal layering in the upper ∼ 1.5–2 km of the ice sheet, whereas the deeper-sounding chirp is best suited to assess englacial layering and bed characteristics in deep-ice conditions (Fig. 6c–e). The radar is capable of sounding ice to depths of up to 5 km with a horizontal resolution of 10 cm (before processing) and a depth resolution in the vertical direction of 8.4 m (PASIN-1) and 6.5 m (PASIN-2).

The pulse repetition frequency of the PASIN (1/2) system is 15 635 Hz and hardware stacking is typically set to 25 in standard mode, which results in an effective pulse-coded waveform acquisition rate of 312.5 Hz for each transmit pulse (Table 2). Following stacking, the final sampling frequency of PASIN-1 is 22 MHz and PASIN-2 is 120 MHz (Table 2).

3.1.4 GPS and lidar

Since 1978, navigation has transitioned from basic aircraft data, imagery, and dead reckoning to more modern means, including the use of the carrier-phase Global Positioning Systems (GPS).

Between 1994 and 2004, the BAS Twin Otter aircraft was equipped with a Trimble GPS system (1994–1995 surveys: Trimble 4000SSE; 1996–2003 surveys: Trimble 4000SSI). Since 2004, the aircraft is equipped with two, 10 Hz GPS receivers (Leica 500 and ASHTEC Z12 for 2004–2018 surveys; Javad Delta and Novatel Span for post-2018 surveys) installed on board the aircraft. On the ground, two Leica 500 GPS base stations (replaced by Javad TRIUMPH-2 for post-2018 surveys) are positioned and equipped with choke-ring antennas, set up specifically to obtain an unobstructed view of the sky above. Aircraft turns are typically limited to 10° banking angles in order to avoid losing lock with GNSS satellites orbiting close to the horizon. The estimated accuracy of the absolute position of the aircraft is 10 cm or less, with the relative accuracy approximately 1 order of magnitude better. Since 2010, the aircraft altitude and inertial information has been provided by an iMAR FSAS inertial measurement unit (IMU), with the data logged on a Novatel Span receiver. Additional altitude information from the strap-down gravity system is also available for post processing of other datasets.

For all modern surveys, the aircraft was also equipped with a Riegl Q240i-80 laser altimeter system (or lidar) in the floor camera hatch to accurately detect the ice surface. The lidar data used for correction of the radar data are typically extracted from the nadir point value with no correction for aircraft altitude. The system has a repetition frequency up to 2 kHz which results in an along-track measurement every 3 cm with an accuracy of up to 5 cm. The lidar is used up to altitudes of 700 m and is constrained by cloud-/fog-free conditions. From 2010 onwards, the lidar onboard the Twin Otter was capable of obtaining swath lidar data, although only the single-point data along the centre line were provided as part of this data release.

3.2 Data processing

3.2.1 Gravity

The raw aerogravity data are processed to obtain levelled free-air gravity anomalies. Although additional survey-specific processing might have been applied to the data, general processing steps for the LaCoste and Romberg system include the calculation of the observed gravity and a range of corrections and filtering functions as described in Jordan et al. (2007, 2010) and Valliant (1992). In particular, corrections for vertical acceleration, Eotvos horizontal motion (Harlan, 1968), latitude (Moritz, 1980), and free air (Hackney and Featherstone, 2003) were applied to obtain the final free-air anomalies before subsequent 9–12 km low-pass filtering. As the free-air values refer to the WGS84 ellipsoid, they are defined in geodesy as gravity disturbance (Hackney and Featherstone, 2003).

The strap-down gravity method adopted from 2015 onwards directly combined observations of acceleration in all three axes, with orientation and GPS observations combined in a Kalman filter to simultaneously solve for aircraft position and variations in the Earth's gravitational field (Becker et al., 2015). For subsequent strap-down-acquisition surveys, some amount of thermal drift levelling/correction is required. Spectral analysis suggests that the strap-down system can resolve wavelengths on the order of ∼ 5 km (Jordan et al., 2020). Error estimates for the gravity data can be found in the respective survey metadata (see Table 3), or in specific studies utilizing the BAS aerogravity data (e.g. Ferraccioli et al., 2006; Forsberg et al., 2018; Jordan and Becker, 2018).

Additional processing may include the use of masks to remove aircraft turns, start and end of lines, and other regions of noisy data, or producing an upward continued free-air anomaly by the upward continuation of each line segment from the collected flight altitude to the highest altitude in the survey. The first level of free-air anomaly for all published BAS data is shown in Fig. 2a, although it is worth noting that no correction such as downward continuation has been applied to compile the data shown in Fig. 2a. It is considered that at the scale of the map, the vertical gradient of residual gravity anomalies at flight altitude is inferior to 2 mGal. Additionally, as the gravity surveys are acquired over the ice sheet, the distance to the bedrock is not only dependent on the flight altitude but also on the ice thickness.

Table 2. Radar parameters for the three radar systems deployed by BAS between 1994 and the present day. Note that PASIN-1/2 have a number of programmable settings for flight-specific objectives (e.g. one to eight waveforms programmable for PASIN-2), and the numbers provided here are for the most commonly used settings. For PASIN-2, a standard set-up consists of five waveforms as follows: 4 µs H (0°), 4 µs V (0°), 4 µs H (90°), 4 µs V (90°), 1 µs H (Table S1). Abbreviations in the table are as follows. ADC: analogue-to-digital converter; FPGA: field-programmable gate array; SF: sample frequency; SI: sample interval; PRF: pulse-repetition frequency; PRI: pulse-repetition interval. [a] BAS-built and PASIN-1 systems used RF combiners on the receiver to produce a single RF input-to-sample, with PASIN-1 splitting these into a high- and low-gain channel for standard mode (two ADC channels) and combining these for pairs of H and V in polarimetric mode (four ADC channels). [b] Radar Range Resolution is calculated using a radio-wave velocity in ice of 168 m µs^{-1} and does not include the effect of the processing on the vertical resolution of the system, which is expected to be ∼ 50 % greater than the values provided in the table, thus these numbers should be interpreted as the theoretical system performance. Diagrams showing the configurations of the three radar systems are provided in the Supplement (Figs. S1–S3).

Radar parameters	BAS-built (1994–2004)	PASIN-1 (2004–2015)	PASIN-2 (2015–present)
Antennas configuration	8× folded dipole (4 Tx/4 Rx)[a]	8× folded dipole (4 Tx/4 Rx)[a]	8× folded dipole + 4× belly (8 Tx/Rx + 4 Rx only)
Centre frequency	150 MHz	150 MHz	150 MHz
Transmitted pulse width	0.25 µs (pulse) 4 µs linear (chirp)	0.1 µs (pulse) 4 µs linear (chirp)	1 µs (Tukey envelope chirp) 4 µs linear (Tukey envelope chirp)
Chirp bandwidth	4 MHz (pulse) 10 MHz (chirp)	10 MHz	13 MHz
Antenna gain	11 dBi	11 dBi	11 dBi
PRF/PRI	20 000 Hz (PRI: 50 µs)	15 635 Hz (PRI: 64 µs)	15 635 Hz (PRI: 64 µs)
Peak transmit power	300 W/antenna (1.2 kW total)	1 kW/antenna (4 kW total)	1 kW/antenna (8 kW total)
Receiver SF	25 MHz (scope max single shot)	88 MHz	120 MHz
Receiver FPGA decimation	–	4	–
Receiver effective SF	25 MHz (SI: 40.0 ns)	22 MHz (SI: 45.5 ns)	120 MHz (SI: 8.3 ns)
Receiver trace stacking	64	25 (standard) 50 (polarimetric)	25
Effective PRF (post-stacking)	312.5 Hz	312.5 Hz (standard 2 waveforms)	125.1 Hz (5 waveforms) 208.5 Hz (3 waveforms)
ADC resolution	12 bit	14 bit	16 bit
Equivalent sustained data rate per ADCs (FPGA)	100 MB s^{-1}	176 MB s^{-1} (standard) 352 MB s^{-1} (polarimetric)	960 MB s^{-1} (system: 2.88 GB s^{-1})
Average data storage rate for full PRI	∼ 1 MB s^{-1}	11 MB s^{-1} (maximum)	173 MB s^{-1} (all arrays)
Radar range resolution[b]	21.0 m (pulse) 8.4 m (chirp)	8.4 m	6.5 m

3.2.2 Magnetics

The raw aeromagnetic data have been processed using the SCAR ADMAP2 data-release protocols (Golynsky et al., 2018). Data were collected at 10 Hz, allowing for modelling and removal of aircraft dynamic movements using a so-called compensation correction (Ferraccioli et al., 2007). This correction typically requires a dedicated calibration flight in the direction of the survey lines and tie-lines to have been flown. For some surveys with radial design, or where magnetic-data acquisition was opportunistic, logistical constraints meant no calibration flight could be conducted. In these cases, the generally large depth-to-source estimates due to the thick ice allowed for a 10–15 s filter to be applied to minimize noise generated by aircraft motion without compromising the geological signal. Given the redundancy of collecting 10 Hz ($\sim$ 6 m spaced) observations over thick ice, most surveys were downsampled to 1 Hz ($\sim$ 60 m) prior to further processing.

After magnetic compensation, the magnetic data were corrected for the International Geomagnetic Reference Field (IGRF), which is a standard mathematical description of the Earth's main magnetic field. Data impacted by operation of aircraft systems such as pumps and heaters were manually determined. Typically, such data were discarded, but survey design and lack of alternative data sources mean that sometimes important geophysical signatures may be present. In some cases, the contaminated data were therefore corrected using an offset correction, accepting that the data segment may be more noisy.

Magnetic data were then corrected for diurnal variations in the magnetic field using observations at a fixed base station, typically filtered with a 30 min filter to remove short-wavelength noise potentially not seen on the aircraft. Further statistical levelling of the data based on internal intersections and crossovers with previous surveys was carried out at times to remove systematic errors associated with flight direction (i.e. heading corrections) and additional long-wavelength errors associated with incomplete removal of diurnal variations. In some cases, continuation to a fixed altitude above the ice-sheet bed and a final grid-based micro-levelling procedure were applied (Ferraccioli et al., 1998). The magnetic anomaly map shown in Fig. 2b shows the spatial coverage and magnitude of magnetic data available. Errors in the data are typically presented as the standard deviation of the crossover errors and can be found in the respective survey metadata (see Table 3).

3.2.3 Radar

All data acquired with the earlier "BAS-built" radar system (1994–2004) were read using C code software to convert the LeCroy data to formats readable by Halliburton Landmark's seismic-processing software, SeisSpace ProMAX (hereafter referred to as ProMAX). Basic processing was applied to the data in the hardware analogue domain and later using ProMAX, including power normalization and final SEG-Y export. Following the transition from the LeCroy oscilloscope to ADC cards on the "BAS-built" system (see Sect. 3.1.3), MATLAB replaced the IDL language for data processing.

As opposed to the "BAS-built" system which, by design, had some level of processing done on the raw data internally, the PASIN system was designed to retain much of the sampled data in the rawest form possible to allow for evolving processing techniques to be applied to the data in the future. For all PASIN data (2004 onwards), the first high-level step was to extract the raw data from the tape drives, convert the 3-byte values to conventional 4-byte integers, combine the waveforms associated with each pulse transmit type, and then export the data into MATLAB-formatted binary files. The second high-level step was to minimize side-lobe levels by applying a chirp-decompression technique using a Blackman window from a custom-built MATLAB toolbox, resulting in a processing gain of $\sim$ 10 decibels (dB).

The next step was to apply processing techniques both to enhance along-track resolution and improve the signal-to-noise ratio. For the 2004–2005 BBAS survey, incoherent stacking of 10 consecutive traces was applied and a moving-average window filter used; however, no SAR techniques were initially applied to these data. First tested on previously acquired PASIN radar data (see Hélière et al., 2007), 2-D SAR processing based on the Omega-K algorithm and subsequently improved versions using Doppler-beam sharpening were applied systematically to all the deep-sounding chirp data from 2005–2006 onwards to increase spatial resolution and remove backscattering hyperbolae in the along-track direction (Corr et al., 2007; Jeofry et al., 2018). The benefit of using unfocused along-track SAR processing is that it resolves the bed in much finer detail compared with non-SAR focused data (see Fig. 6d–e). However, SAR-processing can also lead to distortions of the amplitude of the ice structure and bed reflection in inhomogeneous areas of the ice sheet (e.g. near the grounding line; see Hélière et al., 2007) and thus might not always be appropriate for assessing internal layering or absolute amplitudes such as required for bed-reflectivity analysis (e.g. Peters et al., 2007; Castelletti et al., 2019). Additional moving-average filters of varying lengths have also been applied to enhance englacial reflections and improve visualization of the radar data.

Figure 6 shows the three processed radar products provided for the 2010–2011 IMAFI survey over West Antarctica. Figure 6c shows the shallow-sounding pulse and Fig. 6d–e the deep-sounding chirp radar data using the unfocused SAR-processing technique from Hélière et al. (2007) (Fig. 6d) and a version of the chirp product processed with coherent summations but with no SAR-processing applied (Fig. 6e). Internal layering is more clearly visible in the upper part of the ice column on the pulse data compared with the chirp data (see black-bordered insets in Fig. 6c and e). In contrast, deeper internal layering is much more visible on the

SAR-chirp than on the non-SAR chirp (Fig. 6d–e). Additionally, the peak amplitude of the bed is better resolved in the SAR-processed chirp than in the non SAR-processed chirp (see white-bordered inset in Fig. 6d–e).

Further processing of the PASIN data has also been applied by others using simple image-processing techniques such as moving-average filters to enhance the internal layering of the ice and reduce incoherent noise (Ashmore et al., 2020; Bodart et al., 2021) or by applying more complex SAR-processing techniques over previously incoherently processed radar data (Castelletti et al., 2019; Chu et al., 2021). Additional techniques have also been employed in areas where side echoes from steep valley walls lead to ambiguous bed reflections, as previously employed over Flask Glacier (Antarctic Peninsula) using PASIN SAR-processed data and a combination of velocity and digital elevation models to obtain more accurate ice-thickness estimates (Farinotti et al., 2013).

Following radar data processing, bed and ice-surface reflections were determined by picking the onset of the basal echo (i.e. where the echo amplitude is greater than the noise floor). We note that this is not a universal method applied by all radar data providers, who may pick the half-amplitude delay or the peak value, leading in turn to measurement biases across data providers and products (e.g. Peters et al., 2005; Chu et al., 2021).

The BAS approach to picking the bed was to use a semi-automatic first-break pick algorithm on the chirp data below a top-mute window in ProMAX (generally ~ 100 samples above the approximate bed reflection) to locate the precise bed return, followed by manual checks and re-picking to exclude any unrealistic spikes. In areas where multiple closely spaced reflections were sounded at the bed, the shallowest reflection was assumed to be the bed as off-axis reflections would likely appear lower down in this section. However, in some cases, deeper reflections were chosen, with shallower weak reflections assumed to reflect entrained debris, accreted ice, or uncompensated refraction hyperbolae close to the bed. We note, however, that this method has evolved over the years, and that its success is inherently reliant on the radio-glaciological experience of the human picker to quality-check the results from the semi-automatic picker and manually re-pick the data if necessary. The uncertainty associated with the picking procedure can be partially approximated by calculating the root mean square error (RMSE) of the bed elevations at crossover points across the survey area. Although these errors are site-specific and can depend on factors such as varying bed topography and roughness, larger errors may reflect uncertainties in data processing or analysis (i.e. picking in this case). Areas of more extreme topography typically show the highest crossover errors, likely associated with off-axis reflections and entrained debris close to subglacial cliffs, which make deciding on the correct bed pick challenging. In isolated cases, such errors can exceed several hundred metres. In contrast, regions dominated by smooth and flat beds typically show lower crossover errors, on the order of several metres only. Survey-wide RMSEs are typically reported in each survey's metadata (see Table 3) and average ~ 9–22 m depending on the survey (see Rippin et al., 2003a; Vaughan et al., 2006; Ross et al., 2012; Jeofry et al., 2018).

To estimate ice thickness and hence obtain the bed elevation, the location of the surface reflection in the radar data must be known accurately. However, since the PASIN system does not resolve the ice surface well due to errors in the phase centre of the pulse through the firn layer, the surface reflection in the radargram was only rarely used on its own to calculate the ice surface. Usually, range-to-surface from coincident on board-acquired lidar, or alternatively, if lidar was not available (i.e. due to clouds or ground clearance higher than 750 m), using the aircraft's radar altimeter or surface elevation from an accurate digital elevation model (DEM) (i.e. REMA 8 m DEM for latest surveys; Howat et al., 2019), was used to calculate a "theoretical" surface pick, as follows:

Firstly, the same semi-automatic picker used for picking the bed was used on a subset of the shallow-sounding pulse radargrams with a bottom-mute window set at ~ 100 samples below the surface reflection. Secondly, once aircraft-to-surface range was obtained from lidar, a linear trend between the surface pick from the radargram and the surface range from the lidar was calculated, and a resulting slope and offset was used to calculate the theoretical location of the surface. Where possible, the range-to-ground value was derived from the lidar data or interpolated from the mean lidar elevation within ~ 700 m. In those rare cases where the surface reflection was picked directly from the radargram, a regression, local to the data gap, was used to fit the radar range-to-terrain clearance. If lidar was not available to calculate range-to-ground, the height of the aircraft above the surface was obtained by the aircraft's radar altimeter which was then converted into a radar delay time. This conversion was done after a two-stage calibration process which involved recording the terrain clearance over a sea surface with the two instruments, and then correction for the penetration depth of the radar altimeter was obtained from the difference in the height above ellipsoid for a surveyed "flat" snow surface and the aircraft. Where possible, the reference surface was chosen to be in the centre of the targeted area.

Once bed and surface were calculated, ice thickness was obtained by calculating the difference between the bed and surface pick in range samples (relative to the BAS system). The picked travel time was then converted to depth in metres using a radar wave speed of $168\ \mathrm{m\,\mu s^{-1}}$ and a constant firn correction of 10 m. Bed and surface elevations were then integrated with a high-precision kinematic dual-frequency GPS position solution to provide the final point dataset of elevations relative to the WGS84 ellipsoid. To ensure the best accuracy of satellite-orbit definitions and atmospheric corrections, the interpolated survey locations and aircraft elevations were processed from 10 Hz coupled Precise Point Position-

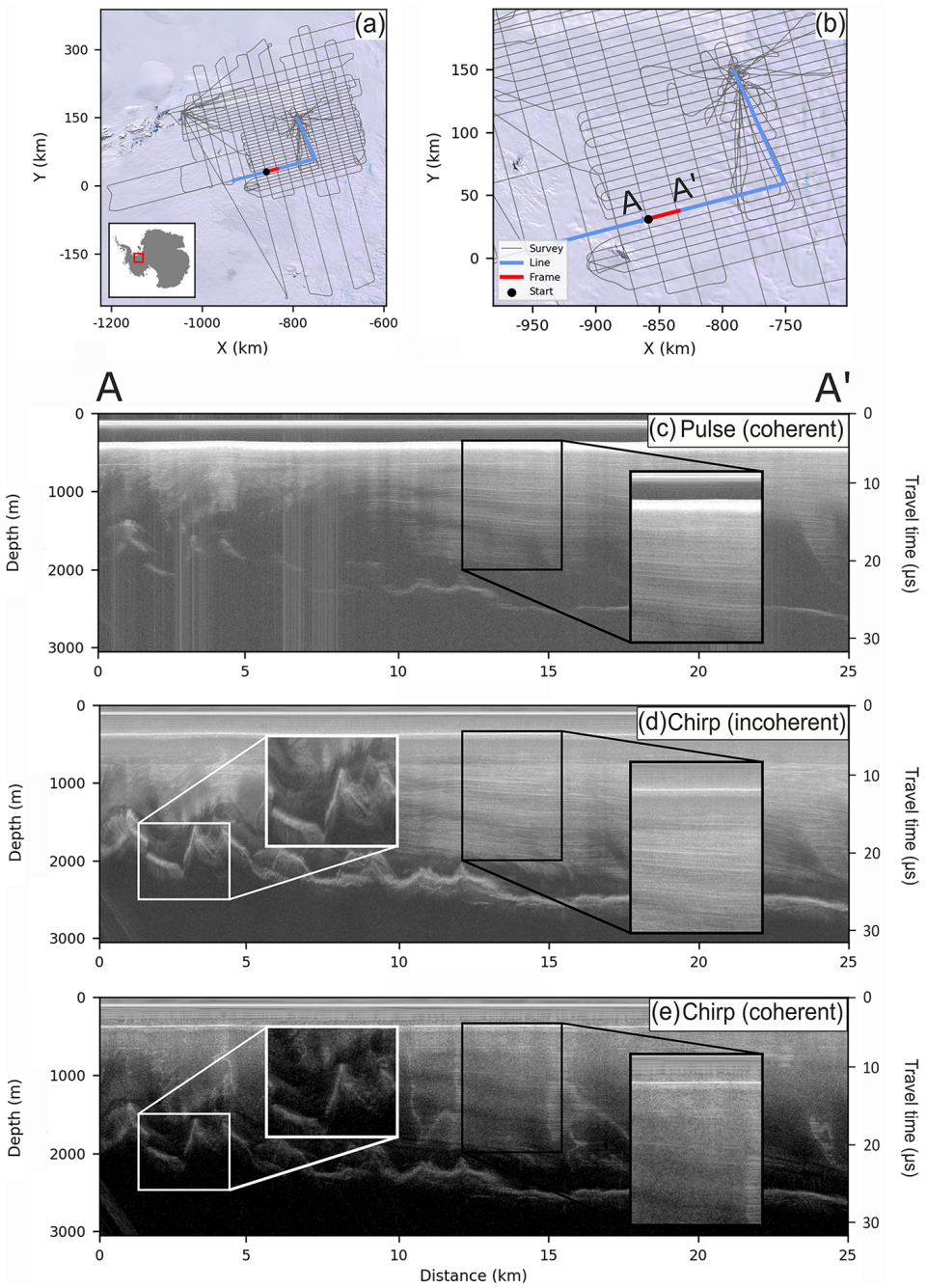

Figure 6. A 25 km segment of flight line 15d of the 2010–2011 IMAFI survey, showing the three radar products and processing attributes: **(a)** shows an overview map of the entire survey with an inset over Antarctica, and **(b)** shows a zoomed-in map over the specific flight line with the 25 km radar segment (defined as A–A′) shown in red. The background satellite image in **(a)**–**(b)** is from the Landsat Image Mosaic of Antarctica (LIMA) (Bindschadler et al., 2008). Images **(c)**–**(e)** show a 25 km segment of the data for the three products provided for the 2010–2011 IMAFI survey as follows: **(c)** the coherently processed, shallow-sounding pulse, **(d)** the unfocused 2-D SAR-processed, deep-sounding chirp, and **(e)** the coherently processed, deep-sounding chirp. The black-bordered insets zoom to the internal layering in the upper portion of the ice column for **(c)**–**(e)** and the white-bordered insets show the difference in bed characteristics between **(d)** and **(e)**.

ing (PPP) GNSS/INS solutions 1 month after data acquisition.

4 FAIR data publishing

In total, we have published 64 datasets from 24 surveys as part of this data release, representing ∼ 566 GB of data and ∼ 1800 files. This amounts to a total of 3.62 million gravity and 7.41 million magnetic data points, as well as 14.5 million ice-thickness and bed-elevation measurements. The complete list of published datasets is provided in Table 3, including the short digital object identifiers (DOIs), which redirect to the metadata sheets and download folders for each respective dataset archived on the PDC Discovery Metadata System (DMS) data catalogue (https://data.bas.ac.uk/, last access: 18 July 2022).

We note that individual profiles acquired opportunistically following larger aerogeophysical surveys (i.e. flight lines over Flask Glacier; Farinotti et al., 2013) are not included in this data release unless specifically mentioned in the metadata for each survey (see Table 3). Such small-scale datasets will be added to the data portal in future releases (see Sect. 4.3).

Below, we discuss the release of the datasets centred around the four FAIR data principles (i.e. findable, accessible, interoperable and re-usable; Wilkinson et al., 2016), starting with the formats and attributes used to store and describe the data (Interoperability; Sect. 4.1), the metadata and DOIs assigned to each dataset (Findability; Sect. 4.2), the data-portal interface and functionalities (Accessibility; Sect. 4.3), and finally the creation of a user guide and open-access tutorials written in Python and MATLAB for reading the data programmatically (Re-usability; Sect. 4.4).

4.1 Interoperability: data formats and attributes

In order to make our data as interoperable as possible, the choice of an open format for all our datasets was a priority. We followed the best practices of the geophysics community and used common data formats and naming conventions to describe the variable names. These are detailed further here.

The gravity, magnetic, and bed-pick data are stored in open ASCII data formats, namely XYZ and CSV files, to ensure long-term access and unrestricted use of the data in the future (Fig. 4). Additionally, we followed the SCAR ADMAP2 data-release protocols (Golynsky et al., 2018) for the naming convention of the channels for the magnetic data. For the radar data, we chose to release the bed-pick data separately from the full radar data (see Fig. 4), although the full radar product contains most of the information stored in the ASCII bed-pick files. Publishing the bed-pick data separately from the radar data was a deliberate choice: it alleviates the need for users to download the full radar datasets to access light-weight tabular data, and improves the accessibility of the point data for large gridded products such as SCAR's BEDMAP (Fretwell et al., 2013) and NASA's BedMachine (Morlighem et al., 2020) projects. The bed-pick data are stored as ASCII-formatted files (namely XYZ and CSV), whereas the full radar data are stored as SEG-Y and NetCDF files, reasons for which are described below.

The SEG-Y format has been used extensively by radar scientists since the early 1980s to store radar data. This is primarily due to the lack of a radar-specific format, SEG-Y having been developed primarily to store seismic data. The advantage of using SEG-Y files is that data can be readily imported into seismic-interpretation software for data interpretation and analysis. The drawbacks of using SEG-Y, however, are numerous, making this option unsuitable for long-term data storage. These include: (1) limited space for metadata, (2) the choice of byte-information to store the radar data is subjective due to the nature of the SEG-Y format, (3) until recently, the byte stream structure which includes the geolocation of each radar trace (i.e. the X and Y positions) was restricted to integer format leading to large inaccuracies in the actual trace position, despite the use of high-resolution, sub-metre GPS data (see Sect. 3.1.4). Recognizing, however, the geophysical community's need to view and analyse the radar data in conventional data formats, we have decided to continue producing SEG-Y files for each flight line and acquisition mode (e.g. pulse and chirp). The SEG-Y files were produced using the Revision 1.0 SEG-Y format and georeferenced using the navigational position of each trace from the GPS on board the aircraft in polar stereographic (EPSG: 3031) projection. Each SEG-Y file contains the following byte-information: trace number (byte: 1–4 and 5–8), PRI-Number (byte: 9–12), Cartesian X coordinate (byte: 73–76), Cartesian Y coordinate (byte: 77–80), number of samples for each SEG-Y trace (byte: 115–116), and the sampling interval (byte: 117–118).

As a result of the issues mentioned above, we also exported and published the radar data in NetCDF-formatted files. We chose the NetCDF format due to its portability and array-oriented structure, the ability to store large amounts of metadata and variables into one portable file, its machine-readable capability, and to harmonize our data products with other fields such as climate science (e.g. ECMWF ERA5 reanalysis products; NCAR climate data), glaciology (e.g. Le Brocq et al., 2010; Morlighem et al., 2017; Lei et al., 2021) and, increasingly, radar geophysics itself (e.g. Paden et al., 2014; Blankenship et al., 2017), which already all make use of this data format effectively. The NetCDF files we produced contain extensive metadata relating to the acquisition and processing of the radar data, as well as a set of Climate and Forecast (CF)-compliant variables that are tied to the radar data (https://cfconventions.org/, last access: 18 July 2022) (Table 4). As a minimum, each NetCDF file contains a radar data variable (one for the pulse and/or one for the chirp, if both exist) in 2-D format, and a set of 1-D variables relating directly to the radar data, such as the trace number, PRI number, fast time, and the X and Y coordinates (Table 4). We

Table 3. Short digital object identifiers (DOIs) for the gravity, magnetic, bed-pick, and 2-D radar datasets of each survey flown by BAS and included in this data release. Abbreviations used are the same as in Table 1. [1] For the AGAP radar data, the US-led survey lines can be found at https://doi.org/10.1594/IEDA/313685 (Bell, 2011). [2] For the PolarGAP survey, data can be downloaded from both the ESA and BAS data catalogues, but the DOI for the gravity and magnetic data (https://doi.org/10.5270/esa-8ffoo3e, Forsberg et al., 2017) belongs to ESA. If using the PDC data catalogue, the PolarGAP gravity and magnetic data can be downloaded from https://data.bas.ac.uk/full-record.php?id=GB/NERC/BAS/PDC/01583 (last access: 18 July 2022) and https://data.bas.ac.uk/full-record.php?id=GB/NERC/BAS/PDC/01584 (last access: 18 July 2022), respectively. "*" indicates that the data are not held at BAS, but instead are available on the CReSIS data portal (https://data.cresis.ku.edu/, last access: 18 July 2022).

Survey	Year	Region	Gravity	Magnetic	Bed-pick	Radar
EVANS	1994–1995	WAIS	https://doi.org/10/d549	–	https://doi.org/10/d548	–
Black Coast	1996–1997	APIS	–	https://doi.org/10/d54x	–	–
CHARCOT	1996–1997	APIS	–	https://doi.org/10/d54z	–	–
JRI	1997–1998	APIS	https://doi.org/10/d55g	https://doi.org/10/d55f	–	–
LARSEN	1997–1998	APIS	–	https://doi.org/10/d55k	–	–
DUFEK	1998–1999	WAIS	https://doi.org/10/d546	https://doi.org/10/d544	https://doi.org/10/d542	–
AFI Coats Land	2001–2002	EAIS	–	https://doi.org/10/dpnw	https://doi.org/10/dpnx	–
MAMOG	2001–2002	EAIS	https://doi.org/10/dpqg	https://doi.org/10/dpqh	https://doi.org/10/dpqd	-
TORUS	2001–2002	WAIS	https://doi.org/10/dpqm	https://doi.org/10/dpqj	https://doi.org/10/dpqf	–
SPARC	2002–2003	APIS	https://doi.org/10/d552	https://doi.org/10/d55x	–	–
BBAS	2004–2005	WAIS	https://doi.org/10/dpn6	https://doi.org/10/dpn3	https://doi.org/10/dpnz	https://doi.org/10/gzqs
WISE-ISODYN	2005–2006	EAIS	https://doi.org/10/d554	https://doi.org/10/d553	https://doi.org/10/cncc	https://doi.org/10/gzqq
GRADES-IMAGE	2006–2007	WAIS	–	https://doi.org/10/d55d	https://doi.org/10/d55c	https://doi.org/10/gzqj
AGAP	2007–2009	EAIS	https://doi.org/10/dpnf	https://doi.org/10/dpnn	https://doi.org/10/dpnr	https://doi.org/10/gzqw[1]
ANDRILL HRAM	2008–2009	WAIS	–	https://doi.org/10/d54w	–	–
Adelaide Island	2010–2011	APIS	–	https://doi.org/10/dn8b	–	–
IMAFI	2010–2011	WAIS	https://doi.org/10/dn8g	https://doi.org/10/dn8h	https://doi.org/10/dn8f	https://doi.org/10/gzqr
PIG Ice Shelf	2010–2011	WAIS	–	https://doi.org/10/d55m	https://doi.org/10/d55n	–
ICEGRAV	2011–2013	EAIS	https://doi.org/10/dpqb	https://doi.org/10/dpp9	https://doi.org/10/cjzn	https://doi.org/10/gzqt
FISS 2015	2015–2016	WAIS	–	https://doi.org/10/g36h	https://doi.org/10/g35q	https://doi.org/10/g35m
PolarGAP	2015–2016	EAIS	https://doi.org/10/g7kw[2]	https://doi.org/10/g7kw[2]	https://doi.org/10/g7qq	https://doi.org/10/g7qp
FISS 2016	2016–2017	WAIS	https://doi.org/10/g36f	https://doi.org/10/g36j	https://doi.org/10/g35t	https://doi.org/10/g35p
ITGC 2018	2018–2019	WAIS	https://doi.org/10/dn26	https://doi.org/10/dn24	*	*
ITGC 2019	2019–2020	WAIS	https://doi.org/10/g68r	https://doi.org/10/g68q	https://doi.org/10/gp4z	https://doi.org/10/g7qn

also provided additional radar-related variables which were extracted from the radar data following processing, such as the surface and bed picks, the surface and bed elevation, the ice thickness, longitude and latitude, time of the trace, and the elevation of the aircraft (Table 4). Additional 1-D variables include the source of the surface pick (from lidar or radar) if this exists, the range between the aircraft and the ice surface, and in case the pulse- and chirp-radar variables do not have the same length, we provide two sets of variables for the trace number and PRI number.

Lastly, to aid visualization and improve efficiency in navigating the datasets, we created lightweight quick-look PDF files of the radar data for each flight line of each survey (see example for the WISE-ISODYN survey in Fig. 7). The choice of ~ 25 or ~ 50 km length for the 2-D radargram was chosen based on clarity of the image and varies from survey to survey. The quick-look PDF files are stored alongside the SEG-Y and NetCDF files and are accessible using the links provided in Table 3.

4.2 Findability: metadata and digital object identifiers (DOIs)

ISO 19115/19139 Geographic information metadata are provided for each data type of each survey and is archived alongside the datasets into the PDC DMS catalogue (https://data.bas.ac.uk/, last access: 18 July 2022; see Table 3). Each metadata record provides detailed information about the dataset, including an abstract, list of personnel involved in the acquisition or analysis of the dataset, and detailed lineage information about the acquisition and processing steps used to produce the dataset, amongst others. All our data are covered under the UK Open Government License (http://www.nationalarchives.gov.uk/doc/open-government-licence/, last access: 18 July 2022), enabling the re-use of the data freely and with flexibility, whilst at the same time ensuring acknowledgement of those involved in the collection and processing of the data. In addition, we use earth science-specific keywords and vocabularies from the Global Change Master Directory (GCMD, 2021) to describe our data in a consistent and comprehensive manner in accordance with ISO 19115 standards. Lastly, a DOI is minted for each dataset so that it can be discoverable and adequately cited. The end goal is to

Table 4. Attributes for each variable stored in the NetCDF files. For each attribute name, we provide the long name, the dimension (1- or 2-D, *x* or *y* axis), the short or CF-compliant standard name, and the unit of the measurement. The standard name is only provided if it exists as part of the CF convention (https://cfconventions.org/, last access: 18 July 2022), otherwise a short name is provided. The abbreviation "dBm" stands for decibel-milliwatts and "a.s.l." stands for above sea level. Note that the surface and bed-pick data are referenced to the sampling time of the BAS radar systems across the 64 µs pulse repetition interval window, and digitized according to the receiver sampling frequency (see Table 2).

NetCDF attributes	Long name	Dimension	Short/standard name	Unit
traces	Trace number for the radar data	1-D (*x* axis)	traceNum	Integer count (unitless)
fast_time	Two-way travel time	1-D (*y* axis)	time	Microseconds
x_coordinates	Cartesian x coordinates for the radar data	1-D (*x* axis)	projection_x_coordinate	Metres (WGS84 EPSG: 3031)
y_coordinates	Cartesian y coordinates for the radar data	1-D (*x* axis)	projection_y_coordinate	Metres (WGS84 EPSG: 3031)
chirp_data	Radar data for the processed chirp	2-D (*x* and *y* axis)	–	Power (dBm)
pulse_data	Radar data for the processed pulse	2-D (*x* and *y* axis)	–	Power (dBm)
longitude_layerData	Longitudinal position of the trace number	1-D (*x* axis)	longitude	Degree_east (WGS84 EPSG: 4326)
latitude_layerData	Latitudinal position of the trace number	1-D (*x* axis)	latitude	Degree_north (WGS84 EPSG: 4326)
UTC_time_layerData	Coordinated Universal Time (UTC) of trace number	1-D (*x* axis)	resTime	Seconds of the day
PriNumber_layerData	Incremental integer reference number related to initialization of the radar system	1-D (*x* axis)	PriNum	Integer count (unitless)
terrainClearance_layerData	Terrain clearance distance from platform to air interface with ice, sea or ground	1-D (*x* axis)	resHt	Metres
aircraft_altitude_layerData	Aircraft altitude	1-D (*x* axis)	Eht	Metres a.s.l. (WGS84 ellipsoid)
surface_altitude_layerData	Ice surface elevation for the trace number	1-D (*x* axis)	surface_altitude	Metres a.s.l. (WGS84 ellipsoid)
surface_pick_layerData	Location down trace of surface pick (BAS system)	1-D (*x* axis)	surfPickLoc	Time sample (microseconds)
bed_altitude_layerData	Bedrock elevation for the trace number	1-D (*x* axis)	bed_altitude	Metres a.s.l. (WGS84 ellipsoid)
bed_pick_layerData	Location down trace of bed pick (BAS system)	1-D (*x* axis)	bedPickLoc	Time sample (microseconds)
land_ice_thickness_layerData	Ice thickness for the trace number	1-D (*x* axis)	land_ice_thickness	Metres

provide all the information necessary for effective, long-term data re-use.

The data are shared via the web-based Repository for Archiving and MAnaging Diverse DAta (RAMADDA; https://geodesystems.com/, last access: 18 July 2022) which is an open-source content and data management platform. The download of the data is done through a standard HTTP-protocol where no login account is required. In the back-end, the data are stored following a simple folder structure on the PDC server that is mirrored onto RAMADDA. This simple structure allows us to maintain a balance between the services we can provide and our ability to move away from

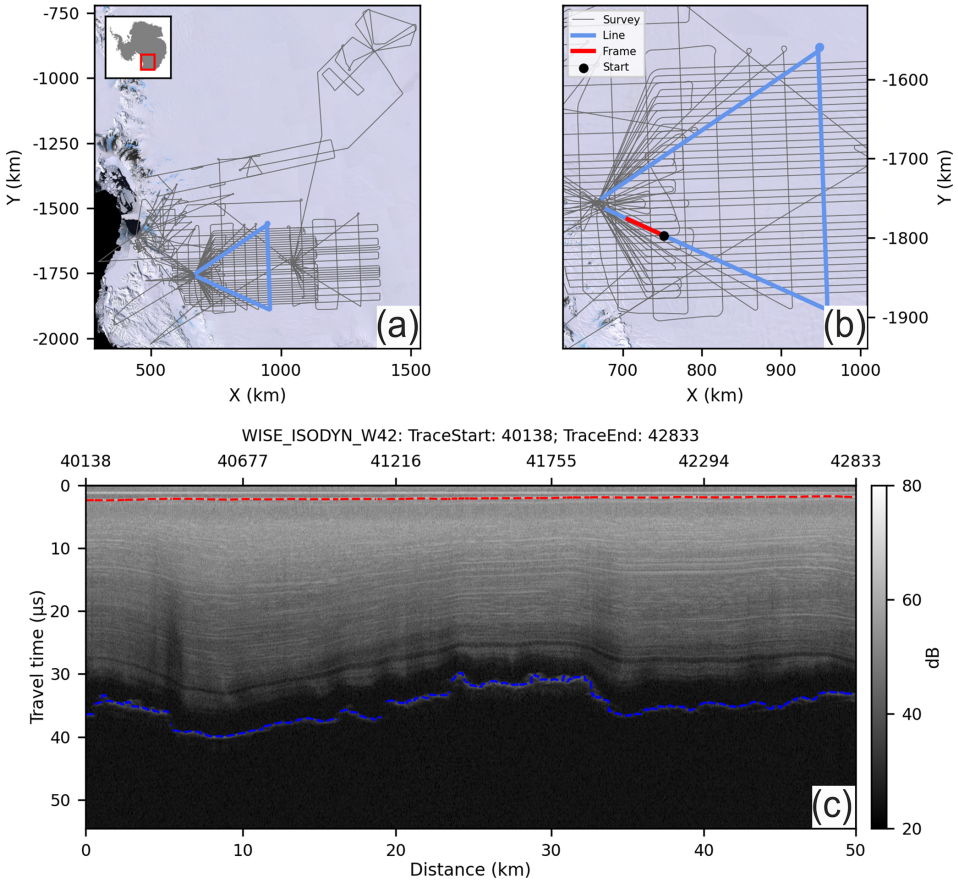

Figure 7. Example of a segmented quick-look image from the 2005–2006 WISE-ISODYN survey. **(a)** Overview map of the survey flight lines (grey lines) with an inset over Antarctica and the specific flight line highlighted in blue. **(b)** Zoomed in version of **(a)** showing the specific flight line with the footprint of the 50 km segment (red line) and start point for the radargram (black dot) shown in **(c)**. The background satellite image in **(a)**–**(b)** is from the Landsat Image Mosaic of Antarctica (LIMA) (Bindschadler et al., 2008). **(c)** 50 km segmented radar image of the chirp data with distance in kilometres shown in the bottom x axis and the trace number shown in the top x axis. The y axis shows the travel time in microseconds. The format of the title in **(c)** is as follows: survey name and flight ID, first trace of segment, last trace of segment. The dashed red and blue lines on the radargram in **(c)** show the surface and bed pick, respectively.

specific tools – RAMADDA in this case – and potentially adopt more performant systems in the future. The goal is to stay as independent of the platform we use as possible while providing the most effective service possible.

4.3 Accessibility: Polar Airborne Geophysics Data Portal

To increase the accessibility and discoverability of our data, we developed a new data portal, the Polar Airborne Geophysics Data Portal (accessible from https://www.bas.ac.uk/project/nagdp/, last access: 18 July 2022). The portal interactively showcases the wide coverage of aerogeophysical datasets collected by BAS and enables users to easily discover and download the published datasets via a series of widgets and functionalities aimed at enhancing the user experience.

The portal is divided into five layer menus: "Aerogravity", "Aeromagnetics", "AeroRadar", "Boundaries & Features", and "Basemaps". The first three menus contain shapefile layers for the gravity, magnetic, and radar datasets, respectively. The "Boundaries & Features" menu contains a set of specific boundary layers, such as the Antarctic Coastline and Ice Drainage boundaries, amongst others, and the "Basemaps" menu contains background gridded maps of ice thickness, surface and bed elevations, magnetic anomaly, and geothermal heat flow, amongst others.

The track lines for each dataset correspond to individual polyline shapefiles (either segmented in 25 or 50 km, or by flight line) which contain key statistics such as the minimum, maximum, and median gravity and magnetic anomalies, and minimum, maximum, and median ice surface, bed elevation, and ice thickness. The shapefiles also contain direct links to the survey's metadata and to direct links to download the data via the RAMADDA interface.

A powerful functionality of the portal is the ability to view the aerogeophysical data rapidly via the creation of

quick-look gravity, magnetic, and radar plots for each flight line (see Sect. 5.2; Fig. 7c). For the magnetic and gravity data, graphs showing the magnetic or free-air anomaly along straight lines were created in the westernmost–easternmost direction if the profile is mainly in the direction of the longitude, or northernmost–southernmost if the profile is predominantly in the direction of the latitude. For the radar data, the segmented images were produced in a similar format to Fig. 7c and split into ∼ 25 and ∼ 50 km segments depending on the survey.

4.4 Re-Usability: user guide and tutorials

To further increase the re-usability of our data, we provided a user guide for the data portal as well as interactive, open-source Jupyter Notebook tutorials written in Python and MATLAB for reading the gravity, magnetic, and radar datasets and conducting first-order analyses of the data. These are archived on the BAS GitHub repository and provided via an interactive web interface using Jupyter Book (https://antarctica.github.io/PDC_GeophysicsBook, last access: 18 July 2022). We believe these to be particularly beneficial for ensuring accessibility and re-usability of our data to the widest range of users possible, primarily as a result of the complexity around reading in aerogeophysical data formats.

5 Discussion

This final section exemplifies the potential re-usability of the newly released aerogeophysical data via the interrogation of the englacial architecture of the ice as sounded by BAS ice-penetrating radars. We also explore the future use of the new data portal and discuss opportunities in terms of data release and further potential re-use of the BAS aerogeophysical data.

5.1 Internal layering continuity index

Englacial layering, as imaged by ice-penetrating radars, is a powerful means of extracting information on past ice-dynamical processes (Rippin et al., 2003b; Siegert et al., 2003; Bingham et al., 2015), amongst others. For example, the presence of well-preserved and continuous englacial layering may reflect stable ice conditions and suggest limited changes in past ice-flow conditions, ice-divide migration, or melting within or at the base of an ice sheet (Karlsson et al., 2012). In contrast, poor continuity in englacial layering, primarily characterized by buckled or absent layering, may be indicative of past ice-flow switching or increased englacial stress gradients (Siegert et al., 2003; Bingham et al., 2015).

The Internal Layer Continuity Index (ILCI; Karlsson et al., 2012) provides an automated tool for quantitatively assessing the continuity of englacial layering based on A-scope radar profiles. This method has the advantage of being much less laborious than manual methods (e.g. Rippin et al., 2003a; Siegert et al., 2003; Bingham et al., 2007) and removes the potential subjectivity in assessing layer continuity. By design, the ILCI is sensitive to the number and strength of internal reflections, such that low values indicate discontinuity and high values indicate high continuity.

Whilst the ILCI has previously been calculated over individual surveys (Karlsson et al., 2012; Bingham et al., 2015; Winter et al., 2015; Karlsson et al., 2018; Luo et al., 2020), until now, this approach had not been tested at a regional scale over Antarctica and with the use of multiple radar datasets. Enabled by the comprehensive release of large swaths of fully standardized and open-access aerogeophysical data described in this paper, we aim to demonstrate that much more information can be extracted from these data on a regional to continental scale, which would not have otherwise been possible before.

Here, we have calculated the ILCI on the 10 PASIN radar datasets acquired between 2004 and 2020 that have been published as part of this data release (see Table 3; Figs. 8–9) and that amount to ∼ 300 000 line-km of data. Since we were primarily interested in regional changes in layer continuity, the ILCI was smoothed using a horizontal window of 1000 samples (representing ∼ 25–45 km distance depending on the dataset) to remove any small-scale anomalies in the data and only making use of the deep-sounding chirp product due to its capability of imaging deeper internal layers. The upper and lower 20 % of the ice were also omitted in the calculations due to the inability of the PASIN system to resolve continuous layers in the upper portion of the ice column, and because internal layering is typically absent near the ice-bed interface (Drews et al., 2009; Karlsson et al., 2012).

An important consideration in employing the ILCI over multiple datasets is that the results will vary based on data acquisition (i.e. radar frequency, system resolution) and processing applied (i.e. incoherent vs. 2-D SAR), and thus a pan-Antarctic comparison of internal layer continuity must be analysed in this context. This is especially the case here, where we have applied the ILCI to data acquired over a period of > 15 years with two slightly different systems (PASIN-1 and PASIN-2) and using different processing regimes. Therefore, care must be taken when interpreting the results from different surveys together, as for example, a low level of layer continuity in the main trunk of Pine Island Glacier on the BBAS survey may not reflect the same level of discontinuity on the low-continuity areas of the PolarGAP survey. With this caution noted, the results presented here offer an opportunity to identify some regional patterns of potential value for future work, which we now discuss.

Figure 8 shows that there is a good correspondence between discontinuous layering where ice flow is fast ($> 200\,\mathrm{m\,a^{-1}}$) such as over Foundation Ice Stream (FISS) and the main trunk of Pine Island Glacier (BBAS) and Slessor Glacier (ICEGRAV) (Figs. 8 and 9a). Whilst layer discontinuity is mainly present over the WAIS due to the high concentration of fast-flowing ice streams in this region, several sections covering the EAIS also show signs of layer

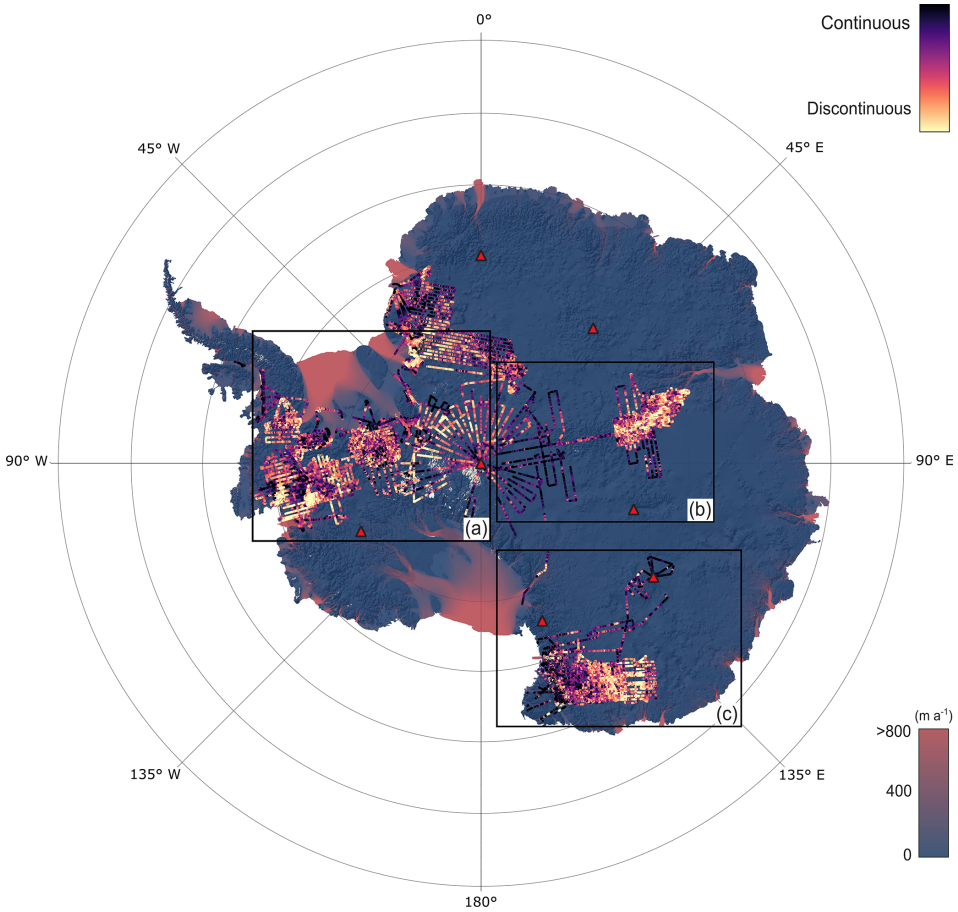

Figure 8. Internal Layer Continuity Index for the 10 PASIN datasets for which the fully processed 2-D radar data were released as part of this paper (see Table 3). The background map shows ice-flow velocities from the In-SAR MEaSUREs dataset (Rignot et al., 2017) superimposed over a hill shade from the BedMachine bed-elevation v2 dataset (Morlighem, 2020). The red and blue colour bar shows ice-flow velocities in metres per annum, and the magma colour bar shows the continuity of internal layers throughout the radar dataset (low continuity: yellow; high continuity: dark purple). The black-bordered rectangles **(a–c)** correspond to the close-up plots in Fig. 9a–c. The red triangles correspond to existing deep ice cores located near the BAS radar surveys.

discontinuity, particularly in the upstream portions of the fast-flowing Lambert Glacier (AGAP) and David and Ninnis glaciers (WISE-ISODYN) (yellow arrows in Fig. 9b–c).

Unsurprisingly, areas of high continuity are mainly observed over the interior of the EAIS, particularly on flight lines extending deep into East Antarctica and the South Pole (Figs. 8 and 9a–b) as well as into the deeper parts of Wilkes Subglacial Basin and Dome C (black arrow in Fig. 9c) where deep ice cores have been drilled (red triangles in Figs. 8–9). Areas of high-layer continuity over the WAIS include numerous ice rises (i.e. Bungenstock, Fletcher, Henry, and Korff) as imaged on the GRADES-IMAGE, IMAFI, and FISS surveys (black arrows in Fig. 9a), the deeper sections of the southern Pine Island Glacier basin on the BBAS data, as well as on PolarGAP survey lines upstream of the FISS grids covering Foundation Ice Stream and Recovery and Slessor glaciers (Fig. 9a).

Also visible are the disruptive effects of local bed topography on the continuity of internal layering, such as over the Ellsworth Subglacial Highlands (BBAS), the Transantarctic Mountains (IMAFI and PolarGAP), and the Gamburtsev Subglacial Mountains (AGAP) (see yellow arrows in Fig. 9a–b), whereas relatively flat bed topography in the deep interior of the EAIS allows layering to remain relatively undisturbed there (Fig. 8 and black arrows in Fig. 9b).

Altogether, the results presented in Figs. 8 and 9 show considerable promise for those radar datasets to be exploited further in the future, particularly with regards to tracking or otherwise characterizing the englacial architecture of the ice, as motivated by the SCAR AntArchitecture group. At present, only two BAS radar datasets (BBAS and IMAFI) have been comprehensively assessed for deep englacial layers (Karlsson et al., 2009; Ashmore et al., 2020; Ross et al., 2020; Bodart et al., 2021). Importantly, the close proximity of deep ice cores, such as the WAIS Divide (Buizert et al., 2015; Sigl et

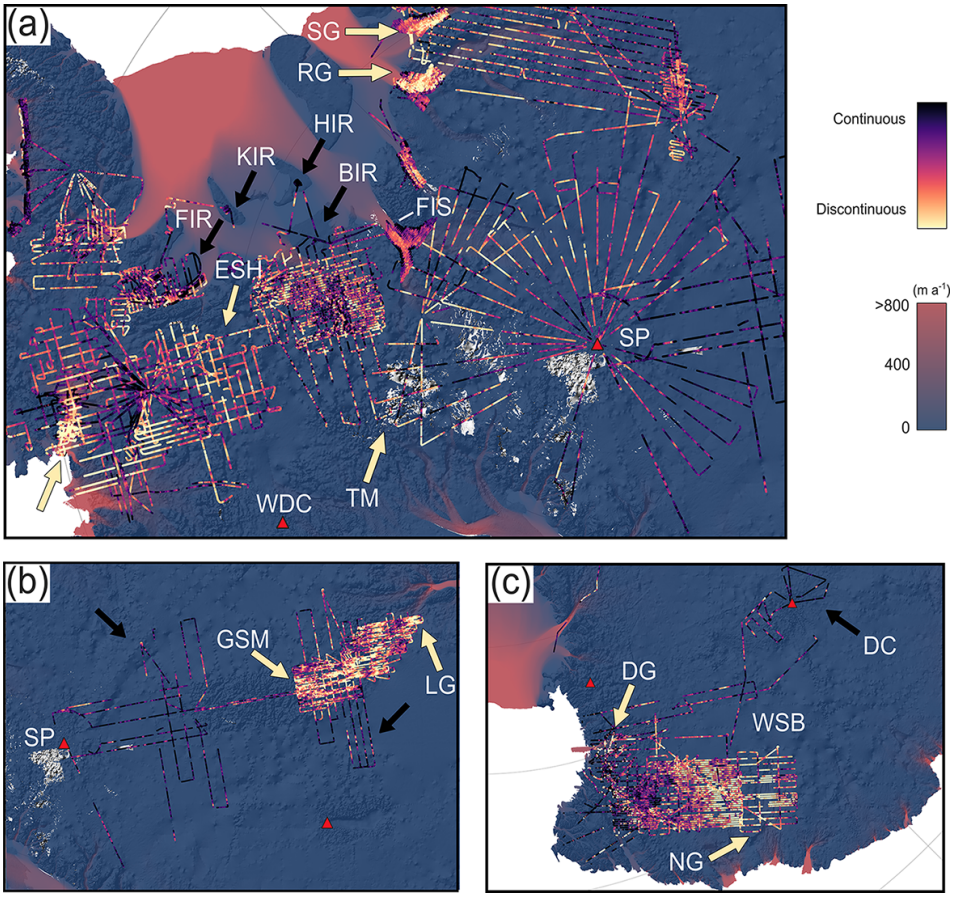

Figure 9. Zoomed-in sections of the Internal Layer Continuity Index (ICLI) shown in the black-bordered rectangles in Fig. 8. The basemap datasets and colour scales are the same as in Fig. 8. **(a)** ILCI results over the WAIS (including Pine Island Glacier, Rutford Ice Stream, Institute–Möller Ice Stream, and Foundation Ice Stream) and bottleneck with the EAIS (including the South Pole, Pensacola Mountains and Slessor Glacier), **(b)** ILCI results for the AGAP survey over East Antarctica's Dome A and South Pole, **(c)** ILCI results for the WISE-ISODYN survey over East Antarctica's Wilkes Subglacial Basin and Dome C. Arrows refer to locations mentioned in the text, with black arrows highlighting examples of high-layer continuity and yellow arrows low-layer continuity. As per Fig. 8, the red triangles correspond to existing deep ice cores located near the BAS radar surveys. Abbreviations correspond to locations mentioned in the text, as follows: BIR (Bungenstock Ice Rise); DC (Dome C); DG (David Glacier); ESH (Ellsworth Subglacial Highlands); FIR (Filchner Ice Rise); FIS (Foundation Ice Stream); GSM (Gamburtsev Subglacial Mountains); HIR (Henry Ice Rise); KIR (Korff Ice Rise); LG (Lambert Glacier); NG (Ninnis Glacier); RG (Recovery Glacier); SG (Slessor Glacier); SP (South Pole); TM (Transantarctic Mountains); WDC (WAIS Divide Core); WSB (Wilkes Subglacial Basin).

al., 2016), EPICA Dome C (EPICA Community Members, 2004), and the South Pole (Winski et al., 2019), to these newly released surveys (Fig. 8, 9) provides ready opportunities for these layers to be dated, significantly increasing their wider use for glaciological and geophysical applications (e.g. Siegert and Payne, 2004; Parrenin and Hindmarsh, 2007; Cavitte et al., 2018; Sutter et al., 2021).

5.2 Polar Airborne Geophysics Data Portal

One specificity of the platform is that it offers three types of geophysical datasets – gravity, magnetic, and radar – at the same time, geospatially. Although some surveys were acquired more than 25 years ago, they may never have been exploited or analysed fully in a form that reached peer-reviewed publications, nor combined with other geophysical data before, thereby increasing their re-usability. By publishing this resource, we anticipate that the portal and datasets will foster new research and discoveries related to our understanding of ice-sheet processes and crust and lithosphere heterogeneity beneath the Antarctic Ice Sheet.

Additionally, the portal enables users to combine the published line datasets with gridded products to compare the ability of the interpolated datasets to match the direct observations. For instance, as shown in Fig. 10 for the 2012–2013 ICEGRAV survey, the portal allows users to readily investigate the free-air gravity anomaly with the bed topography from BEDMAP2 or assess the consistency between

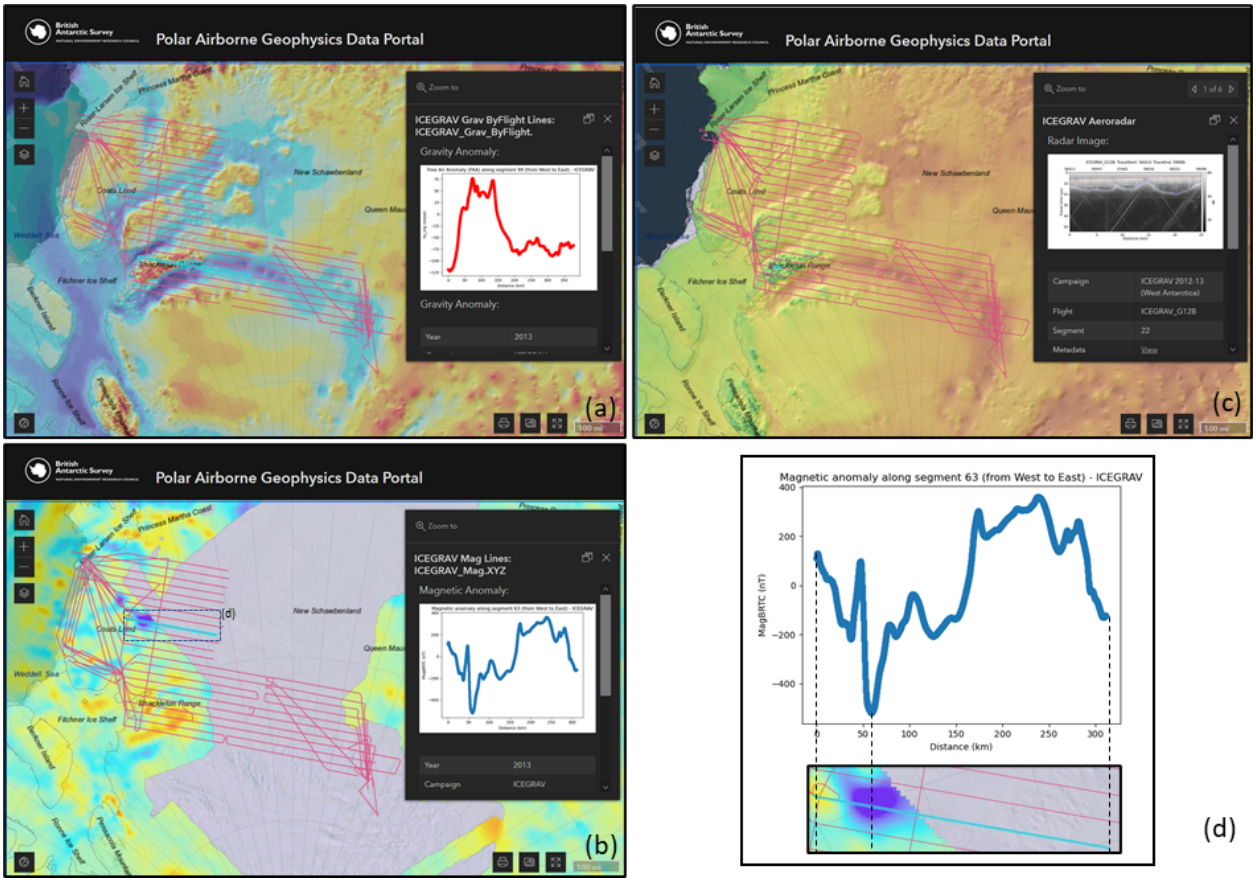

Figure 10. Screenshots of the Polar Airborne Geophysics Data Portal showing the three aerogeophysical products for the 2012–2013 ICEGRAV survey with different basemaps. **(a)** ICEGRAV aerogravity survey with the BEDMAP2 bed-elevation basemap. **(b)** ICEGRAV aeromagnetic survey with the magnetic-anomaly basemap from Goodge and Finn (2010). **(c)** ICEGRAV aeroradar survey with the ice-thickness basemap from BEDMAP2. **(d)** Magnetic anomaly along the profile highlighted in **(c)** with a comparison with the aeromagnetic anomaly map from Goodge and Finn (2010).

the measured ICEGRAV magnetic anomalies and the gridded aeromagnetic product (Fig. 10). Alternatively, the quick-look radargrams can be compared with the ice-thickness and bed-elevation grid cells from BEDMAP to assess sub-kilometre variations in along- and across-flow on the radar data which may have been smoothed out in the 1 km gridded product.

With its ∼ 207 000 line-km of gravity, ∼ 338 000 line-km of magnetic, and ∼ 352 000 line-km of radar data published, the Polar Airborne Geophysics Data Portal provides a robust platform for the dissemination of the BAS aerogeophysical data. Further opportunities offered by the data portal are the potential for the platform to be used to plan future field surveys or encourage future compilation efforts based on gaps in the data coverage or quality of the data.

5.3 Future Work

Although most of data published here have already been incorporated into previous data compilations such as BEDMAP2 or ADMAP2, the more recent datasets presented here will provide useful additions to future editions of such initiatives. Examples of this are the data acquired as part of the 2012–2013 ICEGRAV aeromagnetic campaign in Dronning Maud Land where the last compilation effort of magnetic anomalies had shown a large gap (Goodge and Finn, 2010; Fig. 10), or the new ice-thickness and bed-elevation data acquired over Thwaites Glacier (2018–2020), South Pole (2015–2016), and Filchner Ice Shelf (2015–2017), which are expected to be added to the new BEDMAP3 compilation.

Even though most of the gravity, magnetic, and bed-pick data acquired since the mid-1990s are now fully published, radar data from older surveys, (1994–2004) for which the bed-pick data are published and already integrated into larger gridded products (e.g. BEDMAP; Fretwell et al., 2013), are yet to be published in full as per the more modern surveys (2004–2020) released here (see Table 3). This is primarily due to poorer data management practices at times of acquisition and less well-documented processing procedures which restrict the re-usability of these older radar datasets.

Much older analogue radar data acquired on films and video tapes prior to the deployment of digital radars (i.e. pre-1994) also offer additional opportunities, although the necessity for manual digitization makes this task much more time consuming and challenging. It is worth noting, however, that many of the regions broadly covered by these older surveys have recently been re-flown using more modern instruments as part of NASA's Operation IceBridge programme (MacGregor et al., 2021), although reprocessing and modernizing older radar data can bring substantial benefits, as already demonstrated by Schroeder et al. (2019). Additional reprocessing of older radar data using modern 2-D SAR techniques would also be beneficial, as recently demonstrated on BAS data (see Castelletti et al., 2020; Chu et al., 2021).

As a result of the very flexible configuration of the PASIN-2 system, much more data can also be extracted from the raw radar files already acquired, including fully polarized data used to image ice crystal-fabric orientation for estimating ice-deformation processes (i.e. Young et al., 2021), or 3-D swath radar data used to reconstruct the sub-surface at finer resolution and without compromising on across-track resolution as for conventional 2-D data (Holschuh et al., 2020).

Combined, these will likely add further opportunities for future data releases, alongside our intention to publish newly acquired data regularly via the data portal and following the procedures detailed in this paper.

6 Data availability

All the data included in this paper are freely available via the BAS Discovery Metadata System (https://data.bas.ac.uk, British Antarctic Survey, 2022), with direct links to the datasets found in Table 3 of this paper. The user guide for the data portal and the Jupiter Notebook tutorials designed for reading the gravity, magnetic, and radar data in Python and MATLAB are freely accessible on the Jupyter Book interface (https://antarctica.github.io/PDC_GeophysicsBook, Polar Data Centre, 2022) or via the BAS GitHub repository (https://github.com/antarctica/PDC_GeophysicsBook, last access: 18 July 2022). The code used to produce the Internal Layer Continuity Index over the whole BAS radar data (Figs. 8–9) is available on the GitHub page of Julien A. Bodart (https://github.com/julbod, last access: 18 July 2022) and on Zenodo (https://doi.org/10.5281/zenodo.6858932, Bodart, 2022).

7 Conclusions

We have presented the release of 64 aerogeophysical datasets from 24 surveys flown by BAS between 1994 and 2020 over West Antarctica, East Antarctica, and the Antarctic Peninsula. Altogether, the data release consists of $\sim$ 450 000 line-km (or $\sim$ 5.3 million km^2) of aerogeophysical data on gravity, magnetic, and radar measurements (including bed pick from 1994 onwards and the fully processed 2-D radar data from 2004 onwards) which have all been standardized according to the FAIR (findable, accessible, interoperable and re-usable) data principles. A new data portal, the Polar Airborne Geophysics Data Portal (https://www.bas.ac.uk/project/nagdp/, last access: 18 July 2022), and interactive, open-access tutorials written in Python and MATLAB have also been created to improve the interactivity and user accessibility of our datasets.

Aside from discussing the data acquisition and processing steps, we have demonstrated that much more information can be extracted from the newly released aerogeophysical data by assessing the continuity of englacial layering along $\sim$ 300 000 line-km of the ice-penetrating radar data. Using an automated layer continuity extraction method on all 10 fully published 2-D radar datasets, we have shown that large volumes of radar lines contain well-preserved englacial layering from which further glaciological and geophysical information could be extracted. We note that the analysis shown in Sect. 5.1 is only possible because the data have been comprehensively standardized and made openly accessible. Whilst we acknowledge that this type of work may suffer from a lack of funding opportunities, the results presented here would suggest that re-modernizing already-acquired data may be as important as acquiring new data. It also enables their use in emerging fields such as artificial intelligence, which rely on large amounts of standardized data.

Although all of the datasets released here have so far made a significant contribution to our understanding of past and current ice-dynamical and lithospheric influences, partly through their contributions to major international collaborative projects such as the SCAR BEDMAP and ADMAP programmes, until now they have remained largely unpublished in their full form, thus restricting the further usage of the data beyond the life cycle of the science projects. It is our hope that these newly released data will offer further research opportunities and enable the wider scientific community to benefit from the abundance of newly published aerogeophysical data over Antarctica, particularly within the context of recently established international projects such as the SCAR AntArchitecture and RINGS Action groups, the latter of which focuses primarily on fillings gaps in radar observations at the boundaries of the Antarctic Ice Sheet.

Reflecting on our collaboration between data managers and scientists, we believe that this project sets a positive example for further release of aerogeophysical data, particularly for future international initiatives that are aiming to harmonize the availability and findability of aerogeophysical data collected across Antarctica. A full list of all available datasets can be found in Table 3 of this paper, or via the BAS Discovery Metadata System (https://data.bas.ac.uk, last access: 18 July 2022).

Supplement. The supplement related to this article is available online at: https://doi.org/10.5194/essd-14-3379-2022-supplement.

Author contributions. ACF and JAB co-led this data release. ACF initiated the collaboration between the Polar Data Centre and the BAS Airborne Geophysics science team, with input from HJP. ACF quality-checked and published the gravity, magnetic, and bed-pick datasets, with input from TAJ, FF, and JAB. JAB reprocessed, quality-checked, and published the fully processed radar datasets and accompanying files, with input from ACF, TAJ, and CR. The three BAS radar systems and accompanying radar processing software libraries were designed by HFJC. The aerogeophysical data were primarily acquired and processed by HFJC, CR, FF, and TAJ. JAB created the data portal, with input from ACF, TAJ, and FF. ACF and JAB populated the data portal with the gravity, magnetic, and radar track lines. ACF created the Jupyter Notebook tutorials, with input from JAB for the radar tutorials and user guide. JAB wrote the code and analysed the results for the layer continuity index. JAB wrote the initial manuscript and created the figures, with input from ACF. All the authors commented and contributed to the final edits of the manuscript prior to publication.

Competing interests. The contact author has declared that none of the authors has any competing interests.

Disclaimer. Publisher's note: Copernicus Publications remains neutral with regard to jurisdictional claims in published maps and institutional affiliations.

Acknowledgements. We would like to thank the many BAS personnel involved over the last three decades in developing and maintaining the aerogeophysical instruments and in acquiring and processing the data presented in this paper. In particular, we would like to credit and thank Hugh Corr and Nick Frearson for designing the PASIN radar systems. We are also especially grateful to the many pilots that flew the BAS Twin Otter aicraft "*VP-FBL*" throughout the years, including Lee Proudfoot, Greg Harris, Pete Buckley, Doug Pearson, Mark Beasley, Doug Cochrane, Andy Vidamour, Oli Smith, and particularly David Leatherdale and Ian Potten, who flew most of the survey kilometres. We would also like to highlight the scientific contribution of the late Richard Hindmarsh, particularly with regards to the GRADES-IMAGE survey. Many campaigns that BAS conducted were in partnership with national and international collaborators and institutes, which we would also like to thank more widely. We are also grateful for the help from the BAS PDC and Mapping and GIS (MAGIC) teams for their valuable input throughout this project. Lastly, the authors thank Neil Ross and an anonymous reviewer for their constructive suggestions, which improved this paper.

Financial support. This research has been supported by the NERC National Capability Environmental Data Service. Julien A. Bodart was also supported by the NERC Doctoral Training Partnership (grant reference number: NE/L002558/1) hosted in the Edinburgh E3 DTP program.

Review statement. This paper was edited by Kirsten Elger and reviewed by Neil Ross and one anonymous referee.

References

Arndt, J. E., Schenke, H. W., Jakobsson, M., Nitsche, F. O., Buys, G., Goleby, B., Rebesco, M., Bohoyo, F., Hong, J., Black, J., and Greku, R.: The International Bathymetric Chart of the Southern Ocean (IBCSO) Version 1.0 – A new bathymetric compilation covering circum-Antarctic waters, Geophys. Res. Lett., 40, 3111–3117, https://doi.org/10.1002/grl.50413, 2013.

Ashmore, D. W. and Bingham, R. G.: Antarctic subglacial hydrology: current knowledge and future challenges, Antarct. Sci., 26, 758–773, https://doi.org/10.1017/S0954102014000546, 2014.

Ashmore, D. W., Bingham, R. G., Hindmarsh, R. C., Corr, H. F., and Joughin, I. R.: The relationship between sticky spots and radar reflectivity beneath an active West Antarctic ice stream, Ann. Glaciol., 55, 29–38, https://doi.org/10.3189/2014AoG67A052, 2014.

Ashmore, D. W., Bingham, R. G., Ross, N., Siegert, M. J., Jordan, T. A., and Mair, D. W.: Englacial architecture and age-depth constraints across the West Antarctic Ice Sheet, Geophys. Res. Lett., 47, e2019GL086663, https://doi.org/10.1029/2019GL086663, 2020.

Bamber, J. L., Ferraccioli, F., Joughin, I., Shepherd, T., Rippin, D. M., Siegert, M. J., and Vaughan, D. G.: East Antarctic ice stream tributary underlain by major sedimentary basin, Geology, 34, 33–36, https://doi.org/10.1130/G22160.1, 2006.

Becker, D., Nielsen, J. E., Ayres-Sampaio, D., Forsberg, R., Becker, M., and Bastos, L.: Drift reduction in strapdown airborne gravimetry using a simple thermal correction, J. Geodesy, 89, 1133–1144, https://doi.org/10.1007/s00190-015-0839-8, 2015.

Bell, R.: Processed Ice Penetrating Radar Altimeter Data from the Gamburtsev Mountainsin Antarctica acquired during the GAMBIT Twin Otter expedition AGAP_GAMBIT (2008), Interdisciplinary Earth Data Alliance (IEDA) [data set], https://doi.org/10.1594/IEDA/313685, 2011.

Bell, R. E., Blankenship, D. D., Finn, C. A., Morse, D. L., Scambos, T. A., Brozena, J. M., and Hodge, S. M.: Influence of subglacial geology on the onset of a West Antarctic ice stream from aerogeophysical observations, Nature, 394, 58–62, https://doi.org/10.1038/27883, 1998.

Bell, R. E., Studinger, M., Fahnestock, M. A., and Shuman, C. A.: Tectonically controlled subglacial lakes on the flanks of the Gamburtsev Subglacial Mountains, East Antarctica, Geophys. Res. Lett., 33, L02504, https://doi.org/10.1029/2005GL025207, 2006.

Bell, R. E., Ferraccioli, F., Creyts, T. T., Braaten, D., Corr, H., Das, I., Damaske, D., Frearson, N., Jordan, T., Rose, K., and Studinger, M.: Widespread persistent thickening of the East Antarctic Ice Sheet by freezing from the base, Science, 331, 1592–1595, https://doi.org/10.1126/science.1200109, 2011.

Bindschadler, R., Vornberger, P., Fleming, A., Fox, A., Mullins, J., Binnie, D., Paulsen, S. J., Granneman, B., and Gorodetzky, D.: The Landsat image mosaic of Antarctica, Remote Sens. Envi-

ron., 112, 4214–4226, https://doi.org/10.1016/j.rse.2008.07.006, 2008.

Bindschadler, R., Choi, H., Wichlacz, A., Bingham, R., Bohlander, J., Brunt, K., Corr, H., Drews, R., Fricker, H., Hall, M., Hindmarsh, R., Kohler, J., Padman, L., Rack, W., Rotschky, G., Urbini, S., Vornberger, P., and Young, N.: Getting around Antarctica: new high-resolution mappings of the grounded and freely-floating boundaries of the Antarctic ice sheet created for the International Polar Year, The Cryosphere, 5, 569–588, https://doi.org/10.5194/tc-5-569-2011, 2011.

Bingham, R. G., Siegert, M. J., Young, D. A., and Blankenship, D. D.: Organized flow from the South Pole to the Filchner-Ronne ice shelf: An assessment of balance velocities in interior East Antarctica using radio echo sounding data, J. Geophys. Res.-Earth, 112, F03S26, https://doi.org/10.1029/2006JF000556, 2007.

Bingham, R. G., Ferraccioli, F., King, E. C., Larter, R. D., Pritchard, H. D., Smith, A. M., and Vaughan, D. G.: Inland thinning of West Antarctic Ice Sheet steered along subglacial rifts, Nature, 487, 468–471, https://doi.org/10.1038/nature11292, 2012.

Bingham, R. G., Rippin, D. M., Karlsson, N. B., Corr, H. F., Ferraccioli, F., Jordan, T. A., Le Brocq, A. M., Rose, K. C., Ross, N., and Siegert, M. J.: Ice-flow structure and ice dynamic changes in the Weddell Sea sector of West Antarctica from radar-imaged internal layering, J. Geophys. Res.-Earth, 120, 655–670, https://doi.org/10.1002/2014JF003291, 2015.

Blankenship, D. D., Morse, D. L., Finn, C. A., Bell, R. E., Peters, M. E., Kempf, S. D., Hodge, S. M., Studinger, M., Behrendt, J. C., and Brozena, J. M.: Geologic controls on the initiation of rapid basal motion for West Antarctic ice streams: A geophysical perspective including new airborne radar sounding and laser altimetry results, in: The West Antarctic Ice Sheet: Behavior and Environment, edited by: Alley, R. B. and Bindschadle, R. A., Antarctic Research Series, 77, 105–121, https://doi.org/10.1029/AR077p0105, 2001.

Blankenship, D. D., Kempf, S. D., Young, D. A., Richter, T. G., Schroeder, D. M., Greenbaum, J. S., van Ommen, T., Warner, R. C., Roberts, J. L., Young, N. W., Lemeur, E., Siegert, M. J., and Holt, J. W.: IceBridge HiCARS 1 L1B Time-Tagged Echo Strength Profiles, Version 1. Boulder, Colorado USA, NASA National Snow and Ice Data Center Distributed Active Archive Center [data set], https://doi.org/10.5067/W2KXX0MYNJ9G, 2017.

Bodart, J. A.: Calculate englacial layer continuity from BAS airborne radar data, v1.0.0, Zenodo [code], https://doi.org/10.5281/zenodo.6858932, 2022.

Bodart, J. A., Bingham, R. G., Ashmore, D. W., Karlsson, N. B., Hein, A. S., and Vaughan, D. G.: Age-depth stratigraphy of Pine Island Glacier inferred from airborne radar and ice-core chronology, J. Geophys. Res.-Earth, 126, e2020JF005927, https://doi.org/10.1029/2020JF005927, 2021.

Bozzo, E. and Ferraccioli, F.: The Italian-British Antarctic geophysical and geological survey in northern Victoria Land 2005–2006-towards the International Polar Year 2007-08, https://nora.nerc.ac.uk/id/eprint/15403 (last access: 18 July 2022), 2007.

British Antarctic Survey (BAS): Discovery Metadata System, https://data.bas.ac.uk, last access: 18 July 2022.

Buizert, C., Cuffey, K. M., Severinghaus, J. P., Baggenstos, D., Fudge, T. J., Steig, E. J., Markle, B. R., Winstrup, M., Rhodes, R. H., Brook, E. J., Sowers, T. A., Clow, G. D., Cheng, H., Edwards, R. L., Sigl, M., McConnell, J. R., and Taylor, K. C.: The WAIS Divide deep ice core WD2014 chronology – Part 1: Methane synchronization (68–31 ka BP) and the gas age–ice age difference, Clim. Past, 11, 153–173, https://doi.org/10.5194/cp-11-153-2015, 2015.

Castelletti, D., Schroeder, D. M., Mantelli, E., and Hilger, A.: Layer optimized SAR processing and slope estimation in radar sounder data, J. Glaciol., 65, 983–988, https://doi.org/10.1017/jog.2019.72, 2019.

Cavitte, M. G. P., Parrenin, F., Ritz, C., Young, D. A., Van Liefferinge, B., Blankenship, D. D., Frezzotti, M., and Roberts, J. L.: Accumulation patterns around Dome C, East Antarctica, in the last 73 kyr, The Cryosphere, 12, 1401–1414, https://doi.org/10.5194/tc-12-1401-2018, 2018.

Chu, W., Hilger, A. M., Culberg, R., Schroeder, D. M., Jordan, T. M., Seroussi, H., Young, D. A., Blankenship, D. D., and Vaughan, D. G.: Multi-system synthesis of radar sounding observations of the Amundsen Sea sector from the 2004–2005 field season, J. Geophys. Res.-Earth, 126, e2021JF006296, https://doi.org/10.1029/2021JF006296, 2021.

Constantino, R. R., Tinto, K. J., Bell, R. E., Porter, D. F., and Jordan, T. A.: Seafloor depth of George VI Sound, Antarctic Peninsula, from inversion of aerogravity data. Geophys. Res. Lett., 47, e2020GL088654, https://doi.org/10.1029/2020GL088654, 2020.

Corr, H. and Popple, M.: Airborne radio echo sounding on the Evans flowline, Ronne Ice Shelf, Filchner-Ronne Ice Shelf Programme Report, 8, 9–11, http://nora.nerc.ac.uk/id/eprint/515954 (last access: 18 July 2022), 1994.

Corr, H. F. and Vaughan, D. G.: A recent volcanic eruption beneath the West Antarctic ice sheet, Nat. Geosci., 1, 122–125, https://doi.org/10.1038/ngeo106, 2008.

Corr, H. F., Ferraccioli, F., Frearson, N., Jordan, T., Robinson, C., Armadillo, E., Caneva, G., Bozzo, E., and Tabacco, I.: Airborne radio-echo sounding of the Wilkes Subglacial Basin, the Transantarctic Mountains and the Dome C region, Terra Ant. Rep., 13, 55–63, https://nora.nerc.ac.uk/id/eprint/13578 (last access: 18 July 2022), 2007.

Creyts, T. T., Ferraccioli, F., Bell, R. E., Wolovick, M., Corr, H., Rose, K. C., Frearson, N., Damaske, D., Jordan, T., Braaten, D., and Finn, C.: Freezing of ridges and water networks preserves the Gamburtsev Subglacial Mountains for millions of years. Geophys. Res. Lett., 41, 8114–8122, https://doi.org/10.1002/2014GL061491, 2014.

Diez, A., Matsuoka, K., Ferraccioli, F., Jordan, T. A., Corr, H. F., Kohler, J., Olesen, A. V., and Forsberg, R.: Basal settings control fast ice flow in the Recovery/Slessor/Bailey Region, East Antarctica, Geophys. Res. Lett., 45, 2706–2715, https://doi.org/10.1002/2017GL076601, 2018.

Diez, A., Matsuoka, K., Jordan, T. A., Kohler, J., Ferraccioli, F., Corr, H. F., Olesen, A. V., Forsberg, R., and Casal, T. G.: Patchy lakes and topographic origin for fast flow in the Recovery Glacier system, East Antarctica, J. Geophys. Res.-Earth, 124, 287–304, https://doi.org/10.1029/2018JF004799, 2019.

Drews, R., Eisen, O., Weikusat, I., Kipfstuhl, S., Lambrecht, A., Steinhage, D., Wilhelms, F., and Miller, H.: Layer disturbances and the radio-echo free zone in ice sheets, The Cryosphere, 3, 195–203, https://doi.org/10.5194/tc-3-195-2009, 2009.

EPICA Community Members: Eight glacial cycles from an Antarctic ice core, Nature, 429, 623–628, https://doi.org/10.1038/nature02599, 2004.

Farinotti, D., Corr, H. and Gudmundsson, G. H.: The ice thickness distribution of Flask Glacier, Antarctic Peninsula, determined by combining radio-echo soundings, surface velocity data and flow modelling, Ann. Glaciol., 54, 18–24, https://doi.org/10.3189/2013AoG63A603, 2013.

Ferraccioli, F., Gambetta, M., and Bozzo, E.: Microlevelling procedures applied to regional aeromagnetic data: an example from the Transantarctic Mountains (Antarctica), Geophys. Prospect, 46, 177–196, https://doi.org/10.1046/j.1365-2478.1998.00080.x, 1998.

Ferraccioli, F., Jones, P. C., Curtis, M. L., and Leat, P. T.: Subglacial imprints of early Gondwana break-up as identified from high resolution aerogeophysical data over western Dronning Maud Land, East Antarctica, Terra Nova, 17, 573–579, https://doi.org/10.1111/j.1365-3121.2005.00651.x, 2005a.

Ferraccioli, F., Jones, P. C., Curtis, M. L., Leat, P. T., and Riley, T. R.: Tectonic and magmatic patterns in the Jutulstraumen rift region, East Antarctica, as imaged by high-resolution aeromagnetic data, Earth Planet. Space, 57, 767–780, https://doi.org/10.1186/BF03351856, 2005b.

Ferraccioli, F., Jones, P. C., Vaughan, A. P. M., and Leat, P. T.: New aerogeophysical view of the Antarctic Peninsula: More pieces, less puzzle, Geophys. Res. Lett., 33, L05310, https://doi.org/10.1029/2005GL024636, 2006.

Ferraccioli, F., Jordan, T., Armadillo, E., Bozzo, E., Corr, H., Caneva, G., Robinson, C., Frearson, N., and Tabacco, I.: Collaborative aerogeophysical campaign targets the Wilkes Subglacial Basin, the Transantarctic Mountains and the Dome C region, Terra Ant. Rep., 13, 1–36, https://nora.nerc.ac.uk/id/eprint/13741 (last access: 18 July 2022), 2007.

Ferraccioli, F., Armadillo, E., Jordan, T., Bozzo, E., and Corr, H.: Aeromagnetic exploration over the East Antarctic Ice Sheet: a new view of the Wilkes Subglacial Basin, Tectonophysics, 478, 62–77, https://doi.org/10.1016/j.tecto.2009.03.013, 2009.

Ferraccioli, F., Finn, C. A., Jordan, T. A., Bell, R. E., Anderson, L. M., and Damaske, D.: East Antarctic rifting triggers uplift of the Gamburtsev Mountains, Nature, 479, 388–392, https://doi.org/10.1038/nature10566, 2011.

Ferris, J. K., Vaughan, A. P., and King, E. C.: A window on West Antarctic crustal boundaries: the junction between the Antarctic Peninsula, the Filchner Block, and Weddell Sea oceanic lithosphere. Tectonophysics, 347, 13–23, https://doi.org/10.1016/S0040-1951(01)00235-9, 2002.

Ferris, J. K., Storey, B. C., Vaughan, A. P., Kyle, P. R., and Jones, P. C.: The Dufek and Forrestal intrusions, Antarctica: A centre for Ferrar large igneous province dike emplacement?, Geophys. Res. Lett., 30, 1348, https://doi.org/10.1029/2002GL016719, 2003.

Forsberg, R., Olesen, A. V., Ferraccioli, F., Jordan, T., Corr, H., and Matsuoka, K.: PolarGap 2015/16 Filling the GOCE polar gap in Antarctica and ASIRAS flight around South Pole, European Space Agency (ESA) [data set], https://doi.org/10.5270/esa-8ffoo3e, 2017.

Forsberg, R., Olesen, A. V., Ferraccioli, F., Jordan, T. A., Matsuoka, K., Zakrajsek, A., Ghidella, M., and Greenbaum, J. S.: Exploring the Recovery Lakes region and interior Dronning Maud Land, East Antarctica, with airborne gravity, magnetic and radar measurements, Geol. Soc. Lond. Spec. Publ., 461, 23–34, https://doi.org/10.1144/SP461.17, 2018.

Frederick, B. C., Young, D. A., Blankenship, D. D., Richter, T. G., Kempf, S. D., Ferraccioli, F., and Siegert, M. J.: Distribution of subglacial sediments across the Wilkes Subglacial Basin, East Antarctica, J. Geophys. Res.-Earth, 121, 790–813, https://doi.org/10.1002/2015JF003760, 2016.

Fretwell, P., Pritchard, H. D., Vaughan, D. G., Bamber, J. L., Barrand, N. E., Bell, R., Bianchi, C., Bingham, R. G., Blankenship, D. D., Casassa, G., Catania, G., Callens, D., Conway, H., Cook, A. J., Corr, H. F. J., Damaske, D., Damm, V., Ferraccioli, F., Forsberg, R., Fujita, S., Gim, Y., Gogineni, P., Griggs, J. A., Hindmarsh, R. C. A., Holmlund, P., Holt, J. W., Jacobel, R. W., Jenkins, A., Jokat, W., Jordan, T., King, E. C., Kohler, J., Krabill, W., Riger-Kusk, M., Langley, K. A., Leitchenkov, G., Leuschen, C., Luyendyk, B. P., Matsuoka, K., Mouginot, J., Nitsche, F. O., Nogi, Y., Nost, O. A., Popov, S. V., Rignot, E., Rippin, D. M., Rivera, A., Roberts, J., Ross, N., Siegert, M. J., Smith, A. M., Steinhage, D., Studinger, M., Sun, B., Tinto, B. K., Welch, B. C., Wilson, D., Young, D. A., Xiangbin, C., and Zirizzotti, A.: Bedmap2: improved ice bed, surface and thickness datasets for Antarctica, The Cryosphere, 7, 375–393, https://doi.org/10.5194/tc-7-375-2013, 2013.

Global Change Master Directory (GCMD): GCMD Keywords, Version 12.2. Greenbelt, MD: Earth Science Data and Information System, Earth Science Projects Division, Goddard Space Flight Center (GSFC) National Aeronautics and Space Administration (NASA), https://forum.earthdata.nasa.gov/aphp/tag/GCMD+Keywords, last access: 1 December 2021.

Golynsky, A. V., Ferraccioli, F., Hong, J. K., Golynsky, D. A., von Frese, R. R. B., Young, D. A., Blankenship, D. D., Holt, J. W., Ivanov, S. V., Kiselev, A. V., and Masolov, V. N.: New magnetic anomaly map of the Antarctic, Geophys. Res. Lett., 45, 6437–6449, https://doi.org/10.1029/2018GL078153, 2018.

Goodge, J. W. and Finn, C. A.: Glimpses of East Antarctica: Aeromagnetic and satellite magnetic view from the central Transantarctic Mountains of East Antarctica, J. Geophys. Res.-Sol. Ea., 115, B09103, https://doi.org/10.1029/2009JB006890, 2010.

Greenbaum, J. S., Blankenship, D. D., Young, D. A., Richter, T. G., Roberts, J. L., Aitken, A. R. A., Legresy, B., Schroeder, D. M., Warner, R. C., Van Ommen, T. D., and Siegert, M. J.: Ocean access to a cavity beneath Totten Glacier in East Antarctica, Nat. Geosci., 8, 294–298, https://doi.org/10.1038/ngeo2388, 2015.

Hackney, R. I. and Featherstone, W. E.: Geodetic versus geophysical perspectives of the "gravity anomaly", Geophys. J. Int., 154, 35–43, https://doi.org/10.1046/j.1365-246X.2003.01941.x, 2003.

Harlan, R. B.: Eotvos corrections for airborne gravimetry, J. Geophys. Res., 73, 4675–4679, https://doi.org/10.1029/JB073i014p04675, 1968.

Hélière, F., Lin, C. C., Corr, H., and Vaughan, D.: Radio echo sounding of Pine Island Glacier, West Antarctica: Aperture synthesis processing and analysis of feasibility from space, IEEE T. Geosci. Remote, 45, 2573–2582, https://doi.org/10.1109/TGRS.2007.897433, 2007.

Hodgson, D. A., Jordan, T. A., De Rydt, J., Fretwell, P. T., Seddon, S. A., Becker, D., Hogan, K. A., Smith, A. M., and Vaughan, D. G.: Past and future dynamics of the Brunt Ice Shelf from seabed

bathymetry and ice shelf geometry, The Cryosphere, 13, 545–556, https://doi.org/10.5194/tc-13-545-2019, 2019.

Hofstede, C., Beyer, S., Corr, H., Eisen, O., Hattermann, T., Helm, V., Neckel, N., Smith, E. C., Steinhage, D., Zeising, O., and Humbert, A.: Evidence for a grounding line fan at the onset of a basal channel under the ice shelf of Support Force Glacier, Antarctica, revealed by reflection seismics, The Cryosphere, 15, 1517–1535, https://doi.org/10.5194/tc-15-1517-2021, 2021.

Hogan, K. A., Larter, R. D., Graham, A. G. C., Arthern, R., Kirkham, J. D., Totten Minzoni, R., Jordan, T. A., Clark, R., Fitzgerald, V., Wåhlin, A. K., Anderson, J. B., Hillenbrand, C.-D., Nitsche, F. O., Simkins, L., Smith, J. A., Gohl, K., Arndt, J. E., Hong, J., and Wellner, J.: Revealing the former bed of Thwaites Glacier using sea-floor bathymetry: implications for warm-water routing and bed controls on ice flow and buttressing, The Cryosphere, 14, 2883–2908, https://doi.org/10.5194/tc-14-2883-2020, 2020.

Holland, P. R., Corr, H. F., Vaughan, D. G., Jenkins, A., and Skvarca, P.: Marine ice in Larsen ice shelf, Geophys. Res. Lett., 36, L11604, https://doi.org/10.1029/2009GL038162, 2009.

Holland, P. R., Corr, H. F., Pritchard, H. D., Vaughan, D. G., Arthern, R. J., Jenkins, A., and Tedesco, M.: The air content of Larsen ice shelf, Geophys. Res. Lett., 38, L10503, https://doi.org/10.1029/2011GL047245, 2011.

Holschuh, N., Christianson, K., Paden, J., Alley, R. B., and Anandakrishnan, S.: Linking postglacial landscapes to glacier dynamics using swath radar at Thwaites Glacier, Antarctica, Geology, 48, 268–272, https://doi.org/10.1130/G46772.1, 2020.

Holt, J. W., Blankenship, D. D., Morse, D. L., Young, D. A., Peters, M. E., Kempf, S. D., Richter, T. G., Vaughan, D. G., and Corr, H. F.: New boundary conditions for the West Antarctic Ice Sheet: Subglacial topography of the Thwaites and Smith glacier catchments, Geophys. Res. Lett., 33, L09502, https://doi.org/10.1029/2005GL025561, 2006.

Howat, I. M., Porter, C., Smith, B. E., Noh, M.-J., and Morin, P.: The Reference Elevation Model of Antarctica, The Cryosphere, 13, 665–674, https://doi.org/10.5194/tc-13-665-2019, 2019.

IPCC: Climate Change 2021: The Physical Science Basis. Contribution of Working Group I to the Sixth Assessment Report of the Intergovernmental Panel on Climate Change, edited by: Masson-Delmotte, V., Zhai, P., Pirani, A., Connors, S. L., Péan, C., Berger, S., Caud, N., Chen, Y., Goldfarb, L., Gomis, M. I., Huang, M., Leitzell, K., Lonnoy, E., Matthews, J. B. R., Maycock, T. K., Waterfield, T., Yelekçi, O., Yu, R., and Zhou B., Cambridge University Press, Cambridge, United Kingdom and New York, NY, USA, 147–286, https://doi.org/10.1017/9781009157896.003, in press, 2021.

Jeofry, H., Ross, N., Corr, H. F. J., Li, J., Morlighem, M., Gogineni, P., and Siegert, M. J.: A new bed elevation model for the Weddell Sea sector of the West Antarctic Ice Sheet, Earth Syst. Sci. Data, 10, 711–725, https://doi.org/10.5194/essd-10-711-2018, 2018.

Johnson, A., Cheeseman, S., and Ferris, J.: Improved compilation of Antarctic Peninsula magnetic data by new interactive grid suturing and blending methods, Ann. Geophys., 42, 249–259, https://doi.org/10.4401/ag-3717, 1999.

Jones, P. C., Johnson, A. C., von Frese, R. R., and Corr, H.: Detecting rift basins in the Evans Ice Stream region of West Antarctica using airborne gravity data, Tectonophysics, 347, 25–41, https://doi.org/10.1016/S0040-1951(01)00236-0, 2002.

Jordan, T., Ferraccioli, F., Corr, H., Robinson, C., Caneva, G., Armadillo, E., Bozzo, E., and Frearson, N.: Linking the Wilkes Subglacial Basin the Transantarctic Mountains and the Ross Sea with a new airborne gravity survey, Terra Ant. Rep., 13, 37–54, https://nora.nerc.ac.uk/id/eprint/15749 (last access: 18 July 2022), 2007.

Jordan, T. A. and Becker, D.: Investigating the distribution of magmatism at the onset of Gondwana breakup with novel strapdown gravity and aeromagnetic data, Phys. Earth Planet In., 282, 77–88, https://doi.org/10.1016/j.pepi.2018.07.007, 2018.

Jordan, T. A., Ferraccioli, F., Jones, P. C., Smellie, J. L., Ghidella, M., and Corr, H.: Airborne gravity reveals interior of Antarctic volcano, Phys. Earth Planet In., 175, 127–136, https://doi.org/10.1016/j.pepi.2009.03.004, 2009.

Jordan, T. A., Ferraccioli, F., Vaughan, D. G., Holt, J. W., Corr, H., Blankenship, D. D., and Diehl, T. M.: Aerogravity evidence for major crustal thinning under the Pine Island Glacier region (West Antarctica), Bulletin, 122, 714–726, https://doi.org/10.1130/B26417.1, 2010.

Jordan, T. A., Ferraccioli, F., Armadillo, E., and Bozzo, E.: Crustal architecture of the Wilkes Subglacial Basin in East Antarctica, as revealed from airborne gravity data, Tectonophysics, 585, 196–206, https://doi.org/10.1016/j.tecto.2012.06.041, 2013.

Jordan, T. A., Neale, R. F., Leat, P. T., Vaughan, A. P. M., Flowerdew, M. J., Riley, T. R., Whitehouse, M. J., and Ferraccioli, F.: Structure and evolution of Cenozoic arc magmatism on the Antarctic Peninsula: a high resolution aeromagnetic perspective, Geophys. J. Int., 198, 1758–1774, https://doi.org/10.1093/gji/ggu233, 2014.

Jordan, T. A., Martin, C., Ferraccioli, F., Matsuoka, K., Corr, H., Forsberg, R., Olesen, A., and Siegert, M.: Anomalously high geothermal flux near the South Pole, Sci. Rep.-UK, 8, 1–8, https://doi.org/10.1038/s41598-018-35182-0, 2018.

Jordan, T. A., Porter, D., Tinto, K., Millan, R., Muto, A., Hogan, K., Larter, R. D., Graham, A. G. C., and Paden, J. D.: New gravity-derived bathymetry for the Thwaites, Crosson, and Dotson ice shelves revealing two ice shelf populations, The Cryosphere, 14, 2869–2882, https://doi.org/10.5194/tc-14-2869-2020, 2020.

Jordan, T. A., Ferraccioli, F., and Forsberg, R.: An embayment in the East Antarctic basement constrains the shape of the Rodinian continental margin, Communications Earth & Environment, 3, 1–8, https://doi.org/10.1038/s43247-022-00375-z, 2022.

Karlsson, N. B., Rippin, D. M., Vaughan, D. G., and Corr, H. F.: The internal layering of Pine Island Glacier, West Antarctica, from airborne radar-sounding data, Ann. Glaciol., 50, 141–146, https://doi.org/10.3189/S0260305500250660, 2009.

Karlsson, N. B., Rippin, D. M., Bingham, R. G., and Vaughan, D. G.: A "continuity-index" for assessing ice-sheet dynamics from radar-sounded internal layers, Earth Planet Sc. Lett., 335, 88–94, https://doi.org/10.1016/j.epsl.2012.04.034, 2012.

Karlsson, N. B., Bingham, R. G., Rippin, D. M., Hindmarsh, R. C., Corr, H. F., and Vaughan, D. G.: Constraining past accumulation in the central Pine Island Glacier basin, West Antarctica, using radio-echo sounding, J. Glaciol., 60, 553–562, https://doi.org/10.3189/2014JoG13j180, 2014.

Karlsson, N. B., Binder, T., Eagles, G., Helm, V., Pattyn, F., Van Liefferinge, B., and Eisen, O.: Glaciological characteristics in the Dome Fuji region and new assessment for "Oldest Ice", The

Cryosphere, 12, 2413–2424, https://doi.org/10.5194/tc-12-2413-2018, 2018.

Le Brocq, A. M., Payne, A. J., and Vieli, A.: An improved Antarctic dataset for high resolution numerical ice sheet models (ALBMAP v1), Earth Syst. Sci. Data, 2, 247–260, https://doi.org/10.5194/essd-2-247-2010, 2010.

Le Brocq, A. M., Ross, N., Griggs, J. A., Bingham, R. G., Corr, H. F., Ferraccioli, F., Jenkins, A., Jordan, T. A., Payne, A. J., Rippin, D. M., and Siegert, M. J.: Evidence from ice shelves for channelized meltwater flow beneath the Antarctic Ice Sheet, Nat. Geosci., 6, 945–948, https://doi.org/10.1038/ngeo1977, 2013.

Lei, Y., Gardner, A. S., and Agram, P.: Processing methodology for the ITS_LIVE Sentinel-1 ice velocity product, Earth Syst. Sci. Data Discuss. [preprint], https://doi.org/10.5194/essd-2021-393, in review, 2021.

Luo, K., Liu, S., Guo, J., Wang, T., Li, L., Cui, X., Sun, B., and Tang, X.: Radar-Derived Internal Structure and Basal Roughness Characterization along a Traverse from Zhongshan Station to Dome A, East Antarctica, Remote Sens., 12, 1079, https://doi.org/10.3390/rs12071079, 2020.

Lythe, M. B., Vaughan, D. G., and the BEDMAP Consortium: BEDMAP: A new ice thickness and subglacial topographic model of Antarctica, J. Geophys. Res.-Sol. Ea., 106, 11335–11351, https://doi.org/10.1029/2000JB900449, 2001.

MacGregor, J. A., Boisvert, L. N., Medley, B., Petty, A. A., Harbeck, J. P., Bell, R. E., Blair, J. B., Blanchard-Wrigglesworth, E., Buckley, E.,M., Christoffersen, M. S., and Cochran, J. R.: The scientific legacy of NASA's Operation Icebridge, Rev. Geophys., 59, e2020RG000712, https://doi.org/10.1029/2020RG000712, 2021.

Millan, R., Rignot, E., Bernier, V., Morlighem, M., and Dutrieux, P.: Bathymetry of the Amundsen Sea Embayment sector of West Antarctica from Operation IceBridge gravity and other data, Geophys. Res. Lett., 44, 1360–1368, https://doi.org/10.1002/2016GL072071, 2017.

Moritz, H.: Geodetic reference system 1980, B. Geod., 54, 395–405, https://doi.org/10.1007/s001900050278, 1980.

Morlighem, M.: MEaSUREs BedMachine Antarctica, Version 2. Boulder, Colorado USA, NASA National Snow and Ice Data Center Distributed Active Archive Center [data set], https://doi.org/10.5067/E1QL9HFQ7A8M, 2020.

Morlighem, M., Williams, C., Rignot, E., An, L., Arndt, J. E., Bamber, J., Catania, G., Chauché, N., Dowdeswell, J. A., Dorschel, B., Fenty, I., Hogan, K., Howat, I., Hubbard, A., Jakobsson, M., Jordan, T. M., Kjeldsen, K. K., Millan, R., Mayer, L., Mouginot, J., Noël, B., O'Cofaigh, C., Palmer, S. J., Rysgaard, S., Seroussi, H., Siegert, M. J., Slabon, P., Straneo, F., van den Broeke, M. R., Weinrebe, W., Wood, M., and Zinglersen, K.: BedMachine v3: Complete bed topography and ocean bathymetry mapping of Greenland from multi-beam echo sounding combined with mass conservation, Geophys. Res. Lett., 44, 11051–11061, https://doi.org/10.1002/2017GL074954, 2017.

Morlighem, M., Rignot, E., Binder, T., Blankenship, D., Drews, R., Eagles, G., Eisen, O., Ferraccioli, F., Forsberg, R., Fretwell, P., and Goel, V.: Deep glacial troughs and stabilizing ridges unveiled beneath the margins of the Antarctic ice sheet, Nat. Geosci., 13, 132–137, https://doi.org/10.1038/s41561-019-0510-8, 2020.

Napoleoni, F., Jamieson, S. S. R., Ross, N., Bentley, M. J., Rivera, A., Smith, A. M., Siegert, M. J., Paxman, G. J. G., Gacitúa, G., Uribe, J. A., Zamora, R., Brisbourne, A. M., and Vaughan, D. G.: Subglacial lakes and hydrology across the Ellsworth Subglacial Highlands, West Antarctica, The Cryosphere, 14, 4507–4524, https://doi.org/10.5194/tc-14-4507-2020, 2020.

Paden, J., Li, J., Leuschen, C., Rodriguez-Morales, F., and Hale, R.: IceBridge MCoRDS L1B Geolocated Radar Echo Strength Profiles, Version 2. Boulder, Colorado USA, NASA National Snow and Ice Data Center Distributed Active Archive Center [data set], https://doi.org/10.5067/90S1XZRBAX5N, 2014.

Parrenin, F. and Hindmarsh, R.: Influence of a non-uniform velocity field on isochrone geometry along a steady flowline of an ice sheet, J. Glaciol., 53, 612–622, https://doi.org/10.3189/002214307784409298, 2007.

Paxman, G. J., Jamieson, S. S., Ferraccioli, F., Jordan, T. A., Bentley, M. J., Ross, N., Forsberg, R., Matsuoka, K., Steinhage, D., Eagles, G., and Casal, T. G.: Subglacial Geology and Geomorphology of the Pensacola-Pole Basin, East Antarctica, Geochem. Geophy. Geosy., 20, 2786–2807, https://doi.org/10.1029/2018GC008126, 2019.

Peters, M. E., Blankenship, D. D., and Morse, D. L.: Analysis techniques for coherent airborne radar sounding: Application to West Antarctic ice streams, J. Geophys. Res.-Sol. Ea., 110, B06303, https://doi.org/10.1029/2004JB003222, 2005.

Peters, M. E., Blankenship, D. D., Carter, S. P., Kempf, S. D., Young, D. A., and Holt, J. W.: Along-track focusing of airborne radar sounding data from West Antarctica for improving basal reflection analysis and layer detection, IEEE T. Geosci. Remote, 45, 2725–2736, https://doi.org/10.1109/TGRS.2007.897416, 2007.

Polar Data Centre: BAS Aerogeophysics Book, https://antarctica.github.io/PDC_GeophysicsBook, last access: 18 July 2022

Rignot, E., Mouginot, J., and Scheuchl, B.: MEaSUREs InSAR-based Antarctica ice velocity map, version 2, NASA National Snow and Ice Data Center Distributed Active Archive Center [data set], https://doi.org/10.5067/D7GK8F5J8M8R, 2017.

Rippin, D. M., Bamber, J. L., Siegert, M. J., Vaughan, D. G., and Corr, H. F. J.: Basal topography and ice flow in the Bailey/Slessor region of East Antarctica, J. Geophys. Res.-Earth, 108, 6008, https://doi.org/10.1029/2003JF000039, 2003a.

Rippin, D. M., Siegert, M. J., and Bamber, J. L.: The englacial stratigraphy of Wilkes Land, East Antarctica, as revealed by internal radio-echo sounding layering, and its relationship with balance velocities, Ann. Glaciol., 36, 189–196, https://doi.org/10.3189/172756403781816356, 2003b.

Rippin, D. M., Vaughan, D. G., and Corr, H. F.: The basal roughness of Pine Island Glacier, West Antarctica, J. Glaciol., 57, 67–76, https://doi.org/10.3189/002214311795306574, 2011.

Rippin, D. M., Bingham, R. G., Jordan, T. A., Wright, A. P., Ross, N., Corr, H. F., Ferraccioli, F., Le Brocq, A. M., Rose, K. C., and Siegert, M. J.: Basal roughness of the Institute and Möller Ice Streams, West Antarctica: Process determination and landscape interpretation, Geomorphology, 214, 139–147, https://doi.org/10.1016/j.geomorph.2014.01.021, 2014.

Robin, G. D. Q., Swithinbank, C. W. M., and Smith, B. M. E.: Radio echo exploration of the Antarctic ice sheet, International Association of Scientific Hydrology Publication, 86, 97–115, 1970.

Robin, G. D. Q., Drewry, D. J., and Meldrum, D. T.: International studies of ice sheet and bedrock, Philos. T. Roy. Soc. B., 279, 185–196, https://doi.org/10.1098/rstb.1977.0081, 1977.

Rose, K. C., Ferraccioli, F., Jamieson, S. S., Bell, R. E., Corr, H., Creyts, T. T., Braaten, D., Jordan, T. A., Fretwell, P. T., and Damaske, D.: Early east Antarctic Ice Sheet growth recorded in the landscape of the Gamburtsev Subglacial Mountains, Earth Planet Sc. Lett., 375, 1–12, https://doi.org/10.1016/j.epsl.2013.03.053, 2013.

Rose, K. C., Ross, N., Bingham, R. G., Corr, H. F., Ferraccioli, F., Jordan, T. A., Le Brocq, A. M., Rippin, D. M., and Siegert, M. J.: A temperate former West Antarctic ice sheet suggested by an extensive zone of subglacial meltwater channels, Geology, 42, 971–974, https://doi.org/10.1130/G35980.1, 2014.

Ross, N., Bingham, R. G., Corr, H. F., Ferraccioli, F., Jordan, T. A., Le Brocq, A., Rippin, D. M., Young, D., Blankenship, D. D., and Siegert, M. J.: Steep reverse bed slope at the grounding line of the Weddell Sea sector in West Antarctica, Nat. Geosci., 5, 393–396, https://doi.org/10.1038/ngeo1468, 2012.

Ross, N., Jordan, T. A., Bingham, R. G., Corr, H. F., Ferraccioli, F., Le Brocq, A., Rippin, D. M., Wright, A. P., and Siegert, M. J.: The Ellsworth subglacial highlands: inception and retreat of the West Antarctic Ice Sheet, Bulletin, 126, 3–15, https://doi.org/10.1130/B30794.1, 2014.

Ross, N., Corr, H., and Siegert, M.: Large-scale englacial folding and deep-ice stratigraphy within the West Antarctic Ice Sheet, The Cryosphere, 14, 2103–2114, https://doi.org/10.5194/tc-14-2103-2020, 2020.

Schroeder, D. M., Blankenship, D. D., and Young, D. A.: Evidence for a water system transition beneath Thwaites Glacier, West Antarctica, P. Natl. A. Sci., 110, 12225–12228, https://doi.org/10.1073/pnas.1302828110, 2013.

Schroeder, D. M., Blankenship, D. D., Young, D. A., and Quartini, E.: Evidence for elevated and spatially variable geothermal flux beneath the West Antarctic Ice Sheet, P. Natl. Acad. Sci. USA, 111, 9070–9072, https://doi.org/10.1073/pnas.1405184111, 2014.

Schroeder, D. M., Dowdeswell, J. A., Siegert, M. J., Bingham, R. G., Chu, W., MacKie, E. J., Siegfried, M. R., Vega, K. I., Emmons, J. R., and Winstein, K.: Multidecadal observations of the Antarctic ice sheet from restored analog radar records, P. Natl. Acad. Sci. USA, 116, 18867–18873, https://doi.org/10.1073/pnas.1821646116, 2019.

Shepherd, T., Bamber, J. L., and Ferraccioli, F.: Subglacial geology in Coats Land, East Antarctica, revealed by airborne magnetics and radar sounding, Earth Planet Sc. Lett., 244, 323–335, https://doi.org/10.1016/j.epsl.2006.01.068, 2006.

Siegert, M. J., Payne, A. J., and Joughin, I.: Spatial stability of Ice Stream D and its tributaries, West Antarctica, revealed by radio-echo sounding and interferometry, Ann. Glaciol., 37, 377–382, https://doi.org/10.3189/172756403781816022, 2003.

Siegert, M., Ross, N., Corr, H., Kingslake, J., and Hindmarsh, R.: Late Holocene ice-flow reconfiguration in the Weddell Sea sector of West Antarctica, Quaternary Sci. Rev., 78, 98–107, https://doi.org/10.1016/j.quascirev.2013.08.003, 2013.

Siegert, M. J. and Payne, A. J.: Past rates of accumulation in central West Antarctica, Geophys. Res. Lett., 31, L12403, https://doi.org/10.1029/2004GL020290, 2004.

Siegert, M. J., Ross, N., Corr, H., Smith, B., Jordan, T., Bingham, R. G., Ferraccioli, F., Rippin, D. M., and Le Brocq, A.: Boundary conditions of an active West Antarctic subglacial lake: implications for storage of water beneath the ice sheet, The Cryosphere, 8, 15–24, https://doi.org/10.5194/tc-8-15-2014, 2014.

Sigl, M., Fudge, T. J., Winstrup, M., Cole-Dai, J., Ferris, D., McConnell, J. R., Taylor, K. C., Welten, K. C., Woodruff, T. E., Adolphi, F., Bisiaux, M., Brook, E. J., Buizert, C., Caffee, M. W., Dunbar, N. W., Edwards, R., Geng, L., Iverson, N., Koffman, B., Layman, L., Maselli, O. J., McGwire, K., Muscheler, R., Nishiizumi, K., Pasteris, D. R., Rhodes, R. H., and Sowers, T. A.: The WAIS Divide deep ice core WD2014 chronology – Part 2: Annual-layer counting (0–31 ka BP), Clim. Past, 12, 769–786, https://doi.org/10.5194/cp-12-769-2016, 2016.

Studinger, M., Bell, R. E., Blankenship, D. D., Finn, C. A., Arko, R. A., Morse, D. L., and Joughin, I.: Subglacial sediments: A regional geological template for ice flow in West Antarctica, Geophys. Res. Lett., 28, 3493–3496, https://doi.org/10.1029/2000GL011788, 2001.

Sutter, J., Fischer, H., and Eisen, O.: Investigating the internal structure of the Antarctic ice sheet: the utility of isochrones for spatiotemporal ice-sheet model calibration, The Cryosphere, 15, 3839–3860, https://doi.org/10.5194/tc-15-3839-2021, 2021.

Tinto, K. J. and Bell, R. E.: Progressive unpinning of Thwaites Glacier from newly identified offshore ridge: Constraints from aerogravity, Geophys. Res. Lett., 38, L20503, https://doi.org/10.1029/2011GL049026, 2011.

Tinto, K. J., Padman, L., Siddoway, C. S., Springer, S. R., Fricker, H. A., Das, I., Tontini, F. C., Porter, D. F., Frearson, N. P., Howard, S. L., and Siegfried, M. R.: Ross Ice Shelf response to climate driven by the tectonic imprint on seafloor bathymetry, Nat. Geosci., 12, 441–449, https://doi.org/10.1038/s41561-019-0370-2, 2019.

Valliant, H. D.: LaCoste & Romberg Air/Sea Meters: An Overview, CRC Handbook of Geophysical Exploration at Sea, London, CRC Press, https://doi.org/10.1201/9780367812751, 1992.

Vaughan, D. G., Corr, H. F., Ferraccioli, F., Frearson, N., O'Hare, A., Mach, D., Holt, J. W., Blankenship, D. D., Morse, D. L., and Young, D. A.: New boundary conditions for the West Antarctic ice sheet: Subglacial topography beneath Pine Island Glacier, Geophys. Res. Lett., 33, L09501, https://doi.org/10.1029/2005GL025588, 2006.

Vaughan, D. G., Corr, H. F., Smith, A. M., Pritchard, H. D., and Shepherd, A.: Flow-switching and water piracy between Rutford ice stream and Carlson inlet, West Antarctica, J. Glaciol., 54, 41–48, https://doi.org/10.3189/002214308784409125, 2008.

Vaughan, D. G., Corr, H. F., Bindschadler, R. A., Dutrieux, P., Gudmundsson, G. H., Jenkins, A., Newman, T., Vornberger, P., and Wingham, D. J.: Subglacial melt channels and fracture in the floating part of Pine Island Glacier, Antarctica. J. Geophys. Res.-Earth, 117, F03012, https://doi.org/10.1029/2012JF002360, 2012.

Wilkinson, M. D., Dumontier, M., Aalbersberg, I. J., Appleton, G., Axton, M., Baak, A., Blomberg, N., Boiten, J. W., da Silva Santos, L. B., Bourne, P. E., and Bouwman, J.: The FAIR Guiding Principles for scientific data management and stewardship, Sci. Data, 3, 1–9, https://doi.org/10.1038/sdata.2016.18, 2016.

Winski, D. A., Fudge, T. J., Ferris, D. G., Osterberg, E. C., Fegyveresi, J. M., Cole-Dai, J., Thundercloud, Z., Cox, T. S., Kreutz, K. J., Ortman, N., Buizert, C., Epifanio, J., Brook, E. J., Beaudette, R., Severinghaus, J., Sowers, T., Steig, E. J., Kahle, E. C., Jones, T. R., Morris, V., Aydin, M., Nicewonger, M. R.,

Casey, K. A., Alley, R. B., Waddington, E. D., Iverson, N. A., Dunbar, N. W., Bay, R. C., Souney, J. M., Sigl, M., and McConnell, J. R.: The SP19 chronology for the South Pole Ice Core – Part 1: volcanic matching and annual layer counting, Clim. Past, 15, 1793–1808, https://doi.org/10.5194/cp-15-1793-2019, 2019.

Winter, K., Woodward, J., Ross, N., Dunning, S. A., Bingham, R. G., Corr, H. F., and Siegert, M. J.: Airborne radar evidence for tributary flow switching in Institute Ice Stream, West Antarctica: Implications for ice sheet configuration and dynamics, J. Geophys. Res.-Earth, 120, 1611–1625, https://doi.org/10.1002/2015JF003518, 2015.

Winter, K., Ross, N., Ferraccioli, F., Jordan, T. A., Corr, H. F., Forsberg, R., Matsuoka, K., Olesen, A. V., and Casal, T. G.: Topographic steering of enhanced ice flow at the bottleneck between East and West Antarctica, Geophys. Res. Lett., 45, 4899–4907, https://doi.org/10.1029/2018GL077504, 2018.

Wright, A. P., Young, D. A., Roberts, J. L., Schroeder, D. M., Bamber, J. L., Dowdeswell, J. A., Young, N. W., Le Brocq, A. M., Warner, R. C., Payne, A. J. and Blankenship, D. D.: Evidence of a hydrological connection between the ice divide and ice sheet margin in the Aurora Subglacial Basin, East Antarctica, J. Geophys. Res.-Earth, 117, F01033, https://doi.org/10.1029/2011JF002066, 2012.

Young, D. A., Schroeder, D. M., Blankenship, D. D., Kempf, S. D., and Quartini, E.: The distribution of basal water between Antarctic subglacial lakes from radar sounding, Philos. T. R. Soc. A., 374, 20140297, https://doi.org/10.1098/rsta.2014.0297, 2016.

Young, T. J., Schroeder, D. M., Jordan, T. M., Christoffersen, P., Tulaczyk, S. M., Culberg, R., and Bienert, N. L.: Inferring ice fabric from birefringence loss in airborne radargrams: Application to the eastern shear margin of Thwaites Glacier, West Antarctica, J. Geophys. Res.-Earth, 126, 2020JF006023, https://doi.org/10.1029/2020JF006023, 2021.

This dissertation was typeset in LaTeX by the author, Julien Bodart.

LaTeX is a document preparation system developed by Leslie Lamport as a special version of Donald Knuth's TeX Programs